OVERPRESSURE AND COMPACTION IN THE LOWER KUTAI BASIN, INDONESIA

AGUS MOCHAMAD RAMDHAN

OVERPRESSURE AND COMPACTION IN THE LOWER KUTAI BASIN, INDONESIA

By

Agus Mochamad Ramdhan

This thesis was submitted as partial fulfilment of the requirements
for the degree of Doctor of Philosophy
at the Department of Earth Sciences, Durham University,
United Kingdom

Durham

2010

ABSTRACT

Agus M. Ramdhan

The Lower Kutai Basin is a Tertiary sedimentary basin located on the eastern coast of Kalimantan, Indonesia, underlying the area around the Mahakam Delta. Concerning overpressuring, previous workers agreed that the principal mechanism of overpressure generation is disequilibrium compaction, with sand–mudrock pressure discrepancies being present above the transition zone into hard overpressure as a result of lateral reservoir drainage.

The pressure data, wireline logs and other data such as temperature and vitrinite reflectance data have been re-examined to analyse the overpressuring in this area. Unloading mechanisms have been considered as alternatives to disequilibrium compaction. The reasons for doing so are the high temperatures in this basin, which promote unloading mechanisms, together with some evidence ignored by previous researchers, from wireline log and vitrinite reflectance data, that also suggest unloading mechanisms play an important role.

Clear evidence of unloading has been found in the form of trend reversals in sonic and resistivity logs, without coincident reversals in density logs, and of substantial chemical compaction with mudrock densities exceeding 2.6 g/cm^3 at the top of overpressure. In the Peciko Field, a field located in the shelfal area of the basin, mudrock density continues to increase with depth in the overpressured section. All these circumstances are in conflict with the disequilibrium compaction hypothesis; instead, the mudrocks are inferred to be overcompacted.

The top of the transition zone into hard overpressure coincides with the onset of gas generation indicating that the gas generation is the principal cause of unloading. Chemical compaction processes must also be ongoing in the overpressured zone, including illitization of mixed layer illite-smectite, illitization of kaolinite, and quartz dissolution and reprecipitation.

The result of this research is novel and possibly controversial: there is no other Neogene basin where the role of disequilibrium compaction in overpressure generation has been discounted.

OVERPRESSURE AND COMPACTION IN THE LOWER KUTAI BASIN, INDONESIA

By

Agus Mochamad Ramdhan

This thesis was submitted as partial fulfilment of the requirements
for the degree of Doctor of Philosophy
at the Department of Earth Sciences, Durham University,
United Kingdom

Durham

2010

TABLE OF CONTENTS

	Page
ABSTRACT	i
TITLE	ii
TABLE OF CONTENTS	iii
LIST OF FIGURES	ix
LIST OF TABLES	xxii
DECLARATION	xxiii
STATEMENT OF COPYRIGHT	xxiv
ACKNOWLEDGEMENTS	xxv
CHAPTER 1 INTRODUCTION	1
1.1 Research problems	1
1.2 Objectives	8
1.3 Data	9
1.4 Synopsis	9
CHAPTER 2 GEOLOGY AND PETROLEUM SYSTEM	11
2.1 Geology	11
2.1.1 Regional tectonics and basin development	11
2.1.2 Basin structure	15
2.1.3 Stratigraphy and sedimentation	17
2.2 Petroleum system	20
2.2.1 Palaeogene petroleum system	22
2.2.2 Neogene fluvio-deltaic petroleum system	23
2.2.3 Deep water turbidite petroleum system	27
CHAPTER 3 THEORETICAL BACKGROUND	29
3.1 Basic terminology	29
Normal hydrostatic pressure	29

Vertical stress 31
Minimum horizontal stress 32
Effective stress 34
Overpressure 34
3.2 Overpressure generating mechanisms 35
3.2.1 Loading mechanisms 36
Disequilibrium compaction 36
Tectonic compression 36
3.2.2 Unloading mechanisms 37
Clay diagenetic processes 38
Hydrocarbon generation 39
Aquathermal pressuring 39
Erosion/exhumation 41
3.2.3 Other minor processes 41
Hydrocarbon buoyancy 41
Hydraulic head 42
Osmosis 43
3.3 Transient overpressure phenomenon 43
3.4 Worldwide examples of overpressuring 46
3.5 Overpressure characteristics 48
3.5.1 Disequilibrium compaction characteristics 48
3.5.2 Unloading characteristics 50
3.6 Overpressure estimation methods 52
3.6.1 Overview of mudrock compaction 53
3.6.2 Mudrock compaction from wireline data 56
3.6.2.1 Direct use of wireline logs 56
Sonic log 56
Resistivity log 58
Density log 59
3.6.2.2 Sonic porosity versus effective stress 59
3.6.2.3 Cross-plots of wireline parameters 60

3.6.3 Overpressure estimation methods 61
Eaton's ratio method 63
Effective stress method 64
Bowers' method 65
3.7 Overpressure implications: lateral reservoir drainage and hydrodynamic trapping 66
CHAPTER 4 RESEARCH METHODOLOGY 74
4.1 Pressure data 74
4.2 Wireline log suites 78
4.3 Other data 82
4.4 Interpretation 83
CHAPTER 5 OVERPRESSURE AND COMPACTION IN THE PECIKO FIELD 85
5.1 The Peciko Field 86
5.2 Pressure data 92
5.3 Wireline log suites 96
5.4 Data analysis 98
5.4.1 Overpressure generating mechanisms 98
Observation 98
Interpretation 102
5.4.2 Compaction 105
5.4.3 Overpressure estimation 108
5.4.4 Lateral reservoir drainage 112
5.5 Summary 114
CHAPTER 6 OVERPRESSURE AND COMPACTION IN THE LOWER KUTAI BASIN 115
6.1 Data analysis 115
6.1.1 Deep water area 115
6.1.2 External Axis 116
6.1.2.1 Pressure data 116
6.1.2.2 Wireline log suites 121

6.1.3 Median Axis 125
6.1.3.1 Pressure data 129
Bekapai 129
Tunu 131
6.1.3.2 Wireline log suites 135
Bekapai 135
Tunu 138
6.1.4 Internal Axis 139
6.1.4.1 Pressure data 139
Handil 139
Tambora 143
Nilam 145
6.1.4.2 Wireline log suites 146
Handil 146
Tambora 148
Nilam 149
6.1.5 Onshore area 149
6.1.5.1 Pressure data 152
Mutiara 152
Semberah 153
6.1.5.2 Wireline log suites 155
Mutiara 155
Semberah 156
6.2 Interpretation 158
6.2.1 Overpressure distribution and its characteristics 158
6.2.2 Overpressure generating mechanisms and compaction 161
6.2.3 Hydrodynamic implications 168
6.3 Overpressure estimation 169
6.4 Summary 172
CHAPTER 7 DISCUSSION 173
7.1 Overpressuring and compaction in the Lower Kutai Basin 173

7.2 Overpressure detection and estimation 176
Pre-drill prediction 176
Prediction while drilling 177
7.3 Role of overpressure in the petroleum system 178
7.4 Global comparison 179
7.4.1 Overpressuring 179
7.4.2 Compaction 181
CHAPTER 8 CONCLUSIONS AND SUGGESTIONS FOR FUTURE RESEARCH 186
8.1 Main findings 186
8.1.1 The cause of overpressure 186
8.1.2 The state of mudrock compaction 187
8.1.3 Overpressure detection and estimation 188
8.1.4 Relationship between overpressure and the petroleum system 188
8.1.5 Comparison of overpressure and compaction with other basins 188
8.2 Future research 189

APPENDICES 192
APPENDIX 1 PECIKO FIELD 192
Appendix 1a Pressure–depth plots for intermediate stratigraphic units, as shown in Figure 5.2 192
Appendix 1b Pressure–depth plots, wireline log responses, and cross-plots for mudrocks in 16 wells 198
Appendix 1c Overpressure map in selected stratigraphic units, as shown in Figure 5.2 231
APPENDIX 2 EXTERNAL AXIS 236
Appendix 2a Pressure–depth plots for each stratigraphic unit, as shown in Figure 5.2 236
Appendix 2b Pressure–depth plots, wireline log responses, and 241

cross-plots for mudrocks in overpressured wells

APPENDIX 3 MEDIAN AXIS 251

Appendix 3a Pressure–depth plots for intermediate stratigraphic units, Tunu Field, as shown in Figure 5.2 251

Appendix 3b Pressure–depth plots, wireline log responses, and cross-plots for mudrocks in overpressured wells, Bekapai Field 258

Appendix 3c Pressure–depth plots, wireline log responses, and cross-plots for mudrocks in overpressured wells, Tunu Field 265

APPENDIX 4 ONSHORE AREA 272

Appendix 4a Pressure–depth plots, wireline log responses, and cross-plots for mudrocks in overpressured wells, Mutiara Field 272

Appendix 4b Pressure–depth plots, wireline log responses, and cross-plots for mudrocks in overpressured wells, Semberah Field 282

REFERENCES 289

LIST OF FIGURES

		Page
Figure 1.1	Known hydrocarbon accumulations and major shallow faults in the Lower Kutai Basin, Kalimantan, Indonesia. The main north-south anticlines are indicated by the outlines of the hydrocarbon accumulations.	2
Figure 1.2	Results of the previous evaluation of overpressure in the SS-1 well, Sisi Field, Lower Kutai Basin by Bois et al. (1994). Pore pressures were measured in the sands, and estimated from the sonic log in the mudrocks. Overpressure was thought to be caused by disequilibrium compaction, and substantial sand-mudrock pressure discrepancies were thought to be present. On the left is a simplified lithologic column of this well, showing intensively interbedded sand-mudrock sequences.	3
Figure 1.3	Evidence ignored by Bates (1996) showing a coincidence between the top of overpressure and the onset of hydrocarbon maturation in the NLM-109X well, Nilam Field.	5
Figure 1.4	Porosity-effective stress relationship introduced by Burrus (1998) for mudrocks in the Sisi Field (arrows on the green lines indicate increasing depth).	6
Figure 1.5	Hydrodynamic trapping observed in the Peciko Field explained by lateral drainage of water that had flowed into the sands from overpressured, undercompacted mudrocks (modified from Lambert et al., 2003).	7

Figure 2.1	Present day tectonic elements in the area around the Lower Kutai Basin (modified from Van de Weerd and Armin, 1992).	12
Figure 2.2	Tectonic plates in the region of South East Asia at 45 Ma (Eocene). The Kutai Basin was being initiated at this time, as a consequence of regional extension (simplified from Hall, 2009).	13
Figure 2.3	Tectono-stratigraphic column of the Lower Kutai Basin showing basin initiation, basin development, tectonic processes and the resulting stratigraphic section (simplified from Chambers et al., 2004).	14
Figure 2.4	Regional cross-section showing stratigraphic and structural elements of the Lower Kutai Basin (simplified from Hall et al., 2009) (not to scale).	15
Figure 2.5	Schematics of structural development of the Lower Kutai Basin with the hypothesis of thick-skinned basement involvement inversion (simplified from Chambers et al., 2004).	16
Figure 2.6	Schematics of structural development of the Lower Kutai Basin with the hypothesis of the thin-skinned tectonics (McClay et al., 2000).	18
Figure 2.7	Detail structural-stratigraphic section of Neogene section, Lower Kutai Basin (after Total E&P Indonesie, 2003a).	19
Figure 2.8	Detailed sequence stratigraphic section of Neogene strata, Lower Kutai Basin (simplified from Duval et al., 1998).	20
Figure 2.9	Distribution of sands and mudrocks on the Median Axis in the form of net to gross maps for sediments of age 7–6.6 Ma (left) and 10–9.5 Ma (right) (simplified from Total E&P Indonesie, 2000a).	21
Figure 2.10	Burial history of Neogene section, shelfal area, Lower Kutai Basin (data source: Lambert et al., 2003).	21

Figure 2.11 Schematic of the Neogene petroleum system (simplified from Duval et al., 1998). 24

Figure 2.12 Schematic showing complexity of reservoir geometry (stacked sandstone bodies), pore fluid distribution, and reservoir quality (permeability) in the Neogene petroleum system (compiled from Lambert et al., 2003, Samson et al., 2005, and Total E&P Indonesie, 2010a). 25

Figure 2.13 Displaced gas accumulations (red) on the western flank of the structure in the Tunu Field, indicating hydrodynamic trapping (simplified from Lambert et al., 2003). 26

Figure 3.1 Typical pressure/stress–depth profile commonly encountered in a sedimentary basin. 30

Figure 3.2 A schematic of an XLOT test (modified from White et al., 2002). 33

Figure 3.3 Underpressuring due to reservoir isolation from recharge area (modified from Swarbrick and Osborne, 1998). 35

Figure 3.4 Schematic of overpressure generation due to load transfer from load-bearing grains (red) into pore fluid (e.g. due to transformation of load-bearing kerogen into oil and gas) (after Swarbrick and Osborne, 1998). 37

Figure 3.5 Effect of aquathermal pressuring on overpressure development (modified from Osborne and Swarbrick, 1997). 40

Figure 3.6 **Figure 3.6** Overpressure due to gas buoyancy where the pore water in the water-saturated reservoir is at normal hydrostatic pressure. The maximum overpressure is located in the crest of the structure, while the overpressure due to buoyancy is zero at the gas-water contact. 42

Figure 3.7 Overpressure due to hydraulic head. The maximum head, *H*, due to this mechanism is equal to the elevation of the reservoir at outcrop, and the corresponding overpressure is $\rho_w gH$. 43

Figure 3.8 Illustration showing overpressure caused by osmotic flow through clay membrane (modified from Swarbrick and Osborne, 1998). 44

Figure 3.9 Illustration showing overpressure dissipation through a more permeable sequence. 44

Figure 3.10 **Figure 3.10** Illustration showing 'centroid' effect which causes the pore pressure in the sand to be lower and higher than the regional pore pressure in the mudrock at the base and top of the sand body, respectively. 45

Figure 3.11 Lateral reservoir drainage causing overpressure bleed-off in the Palaeocene fan sandstones of the Central Graben, North Sea (simplified from Dennis et al., 2000). 46

Figure 3.12 Worldwide occurrences of overpressure (shaded areas) (after Mouchet and Mitchell, 1989). 47

Figure 3.13 Cartoon to show the pressure-depth profile and wireline log responses anticipated where overpressure is due to disequilibrium compaction. 49

Figure 3.14 Cartoon to show the pressure-depth profile and wireline log responses anticipated where overpressure is due to unloading. 51

Figure 3.15 Properties of storage and connecting pores (after Bowers and Katsube, 2002). 52

Figure 3.16 Bjorlykke's compaction model dividing compaction into two regimes: mechanical compaction and chemical compaction. The transition between the two regimes is marked by temperatures of around 70–100°C (Bjorlykke, 1998). 55

Figure 3.17 Comparison between published porosity trends with laboratory experiments in mechanically compacting synthetic mudrocks of different clay composition (modified from Mondol et al., 2007). 55

Figure 3.18 Comparison of normal compaction trends (NCTs) between direct exponential decay (2P-NCT) and exponential decay + matrix transit time (3P-NCT). 57

Figure 3.19 Upper panel: sonic velocity–density cross-plot as used by Bowers (2001). Lower panel: Density–sonic transit time cross-plot as used by Dutta (2002). 62

Figure 3.20 Schematic of Eaton's method and the effective stress method. In Eaton's method, pore pressure is estimated by comparing the wireline log reading (sonic in this illustration) with the expected wireline log value for normally compacted mudrocks at the same depth. 63

Figure 3.21 Divergent migration of oil and gas due to hydrodynamic condition (simplified from Hubbert, 1953). 67

Figure 3.22 Cartoon illustrating the difference between hydrodynamically tilted hydrocarbon water contacts (left panel) and a hydrostatic flat hydrocarbon water contact (right panel). 67

Figure 3.23 Cartoon illustrating one pressure gradient in a single gas accumulation accompanied by different water pressure gradients in different wells, indicating hydrodynamic trapping. 68

Figure 3.24 Cartoon showing shoulder effects on the pressure–depth profile as a consequence of lateral reservoir drainage. The green dashed line showing sub-lithostatic parallel pressure profile indicates that overpressure is caused by disequilibrium compaction. The higher overpressure in the mudrock compared to the laterally drained reservoir triggers the fluid flow from the mudrocks toward the reservoir, causing the development of the 'shoulder effect'. 69

Figure 3.25 Possible shoulder effects at the Shiunji gas field, Japan (simplified from Magara, 1969). The red line indicates the normal compaction trend. 70

Figure 3.26 Possible shoulder effects in the Taglu Well, Beaufort Basin, Canada (simplified from Magara, 1978). 70

Figure 3.27 Possible shoulder effects in the Pan America A-5 Well, Manchester Field, Louisiana Gulf Coast (simplified from Schmidt, 1973). 72

Figure 3.28 Reservoir-mudrock pressure discrepancy in Azerbaijan (simplified from Gurevich and Chilingar, 1995). 72

Figure 3.29 Possible shoulder effect from an offshore India well (simplified from O'Connor and Swarbrick, 2008). 73

Figure 4.1 Research workflow. 75

Figure 4.2 Typical pressure data available for analysis in this research. 76

Figure 4.3 Flowchart for pressure QC. 77

Figure 4.4 Example of spreadsheet calculation of vertical stress in a well. In this well, the density data start to available at the depth of 480.024 m. Above this depth, the value of 1.9 g/cm^3 for the density is used to calculate the total vertical stress from surface down to 480.024 m. 79

Figure 4.5 Cartoon illustrating the underlying reason why there are differences between the physical characteristics of sandstone and mudrock (modified from Katahara, 2008). 80

Figure 4.6	Mudrock discrimination based on the gamma ray log (after Katahara, 2008).	81
Figure 4.7	Cartoon illustrating where simple three-component mudrocks can lie on a cross-plot of density porosity versus neutron density (modified from Katahara, 2008).	81
Figure 4.8	Mudrock discrimination based on the difference between neutron porosity and density porosity (after Katahara, 2008).	82
Figure 5.1	Structural map of one stratigraphic horizon within the Tunu Main Zone at the Peciko Field. The depth contour interval is 200 ft. The thick line demarcates the lateral extent of hydrocarbon accumulations in all reservoirs.	87
Figure 5.2	Stratigraphic column of the shelfal area Lower Kutai Basin, including the Peciko Field (simplified from Total E&P Indonesie, 2000b).	88
Figure 5.3	Schematic section showing stacked mouth bars in a stratigraphic interval between two local flooding surfaces (after Samson et al., 2005).	88
Figure 5.4	Thermal gradient in the Peciko Field.	89
Figure 5.5	Vitrinite reflectance data from well PEC-1.	89
Figure 5.6	Schematic section through the Peciko Field showing gas accumulations (red) with tilted GWCs in the Tunu Main Zone. SU1 – SU5 are stratigraphic units of the Tunu Main Zone. A simplified lithological column for SU3 is shown on the right: yellow denotes sand-rich interval and green mudrock intervals.	90

Figure 5.7	Upper: lateral overpressure distribution in the uppermost reservoir of SU3 in the Peciko Field before production started. Overpressure contours are at intervals of 50 psi. Lower: pore fluid distribution in the same stratigraphic unit showing that the gas accumulation is located on the north flank of the structure. Red line: limit of the gas accumulation in this stratigraphic unit. Diameter of the well symbols is proportional to reservoir thickness.	91
Figure 5.8	Pressure–depth plot for all Class A pressure data.	92
Figure 5.9	Pressure–depth plot in stratigraphic layer SU3 in the Peciko Field.	93
Figure 5.10	Pressure–depth plot for stratigraphic layer SU3a showing hydrodynamically tilted gas-water contacts: one gas line accompanied by several water lines.	94
Figure 5.11	Typical overpressure profile in the Peciko Field.	95
Figure 5.12	Overpressure cross-section in the Peciko Field showing that both top of overpressure and the top of the transition zone deepen to the north.	95
Figure 5.13	Sand-mudrock discrimination in the Peciko Field.	96
Figure 5.14	Examples of vertical stress in wells NWP-9 and NWP-16.	97
Figure 5.15	Pressure data from well PEC-1 showing that top of the transition zone coincides with the onset of gas generation.	98
Figure 5.16	Pressure–depth plot, wireline log suites in the mudrock section, and simplified lithological column for the Tunu Main Zone in well NWP-9, Peciko Field.	100
Figure 5.17	Cross-plots of density against sonic transit time and resistivity in mudrocks in well NWP-9, Peciko Field.	101
Figure 5.18	Pressure–depth plot, wireline log suites in the mudrock section, and simplified lithological column for the Tunu Main Zone in well NWP-16, Peciko Field.	103

Figure 5.19 Cross-plots of density against sonic transit time and resistivity in mudrocks in well NWP-16, Peciko Field. 104

Figure 5.20 Composite density plot for mudrocks, defined by Φ_N - Φ_D > 0.18, in all the NWP wells, Peciko Field: left figure for hydrostatically pressured interval only; and right figure for all the density log data. The red and blue lines are running averages of the data, using a window length of 100 ft, for the hydrostatically pressured and overpressured section, respectively. 106

Figure 5.21 Empirical fitting exponential-decay curve for porosity as a function of depth for the depth interval of 6000 – 15,000 ft derived from 16 density logs in the Peciko Field. 107

Figure 5.22 Various empirical NCTs for sonic transit time versus depth fitted empirically to mudrock data from the Peciko Field. 108

Figure 5.23 Estimated pore pressure profiles in the mudrocks in well NWP-9 using 3P-NCT + Eaton's Method with exponents 3 and 7. 109

Figure 5.24 Estimated pore pressure profile in the mudrocks in well NWP-16 using 3P-NCT + Eaton's Method with exponent 3. 110

Figure 5.25 Estimated pore pressure profile in the mudrocks in well NWP-9 using 2P-NCT + Eaton's Method with exponent 3. 111

Figure 5.26 Typical sonic log through a sand-mudrock sequence in the Peciko Field, showing the absence of shoulder effect (taken from NWP-16). 113

Figure 5.27 A south-north cross-section showing that the top of the transition zone into hard overpressure follows the 140°C isotherm. 113

Figure 5.28 Top of overpressure in relation to sand-mudrock facies distribution. 114

Figure 6.1 Structural map of the Sisi–Nubi Field at the top of the Beta marker (Total E&P Indonesie, 1995). 117

Figure 6.2 Pressure–depth plot for all Class A pressure data, Sisi–Nubi Field. 118

Figure 6.3 Pressure–depth plot for the Shallow Reservoir Zone, Sisi–Nubi Field, showing a constant shift in the water pressure from the normal hydrostatic line. 119

Figure 6.4 Pressure–depth plot for the Sisi Main Zone, Sisi–Nubi Field. 119

Figure 6.5 Pressure–depth plot for the Sisi Main Zone, Sisi–Nubi Field. 121

Figure 6.6 Pressure–depth plot and wireline log values in the mudrocks for well SS-1, Sisi–Nubi Field. 122

Figure 6.7 Cross-plots of density against sonic transit time and resistivity in mudrocks in well SS-1, Sisi–Nubi Field. 123

Figure 6.8 Vitrinite reflectance data from well SS-1, Sisi–Nubi Field showing that the top of the overpressure transition zone coincides with the onset of gas generation. 124

Figure 6.9 Pressure–depth plot and wireline log values in the mudrocks for well SS-4, Sisi Field. 126

Figure 6.10 Cross-plots of density against sonic transit time and resistivity in mudrocks in well SS-4, Sisi Field. 127

Figure 6.11 Vertical section through the Bekapai Field showing main faults and some stratigraphic horizons. Unfortunately, only the two deeper horizons are marked on Figure 5.2 (Total E&P Indonesie, 2010c). 128

Figure 6.12 Pressure–depth plot for all Class A and B pressure data, Bekapai Field. 129

Figure 6.13 Pressure–depth plot for wells B-J-1, B-11, and W-B-1, Bekapai Field, showing that the top of overpressure is shallower at the crest. 130

Figure 6.14 Pressure–depth plot for all Class A and B pressure data, Tunu Field. 131

Figure 6.15 Pressure–depth plot in SU1, Tunu Main Zone, Tunu Field. 132

Figure 6.16 Pressure–depth plot in SU-4, Tunu Main Zone, Tunu Field. 132
Figure 6.17 Overpressure profile in well TN-G6, Tunu Field. 133
Figure 6.18 Map of depth to top of overpressure in the Tunu Field. 134
Figure 6.19 West-east cross-section showing variation in depth of top of overpressure relative to stratigraphic horizons in the Tunu Field. 135
Figure 6.20 Pressure–depth plot and wireline log values in the mudrocks in well B-11, Bekapai Field. 136
Figure 6.21 Cross-plots of density against sonic transit time and resistivity in mudrocks in well B-11, Bekapai Field. 137
Figure 6.22 Pressure–depth plot and wireline log values in the mudrocks in well TN-G6, Tunu Field. 138
Figure 6.23 Structure of the Handil Field (after Bellorini et al., 1989) for horizon R27 in the Middle Miocene (Figure 5.2). 140
Figure 6.24 Structural map of the Nilam and Tambora fields at the top of F Zone (see Figure 5.2 for stratigraphic column) (Total E&P Indonesie, 2003c). 141
Figure 6.25 Pressure–depth plot for all Class A and B pressure data, Handil Field. 142
Figure 6.26 Pressure–depth plot for well H-9-B-1, Handil Field. 142
Figure 6.27 Pressure–depth plot showing top of overpressure for wells located in the Handil Field (see Figure 6.23 for well locations). 143
Figure 6.28 Pressure–depth plot for all Class A and B pressure data, Tambora Field. 144
Figure 6.29 Pressure–depth plot for well TM-84, Tambora Field. 144
Figure 6.30 Pressure–depth plot for all Class A and B pressure data, Nilam Field. 145
Figure 6.31 Pressure–depth plot for well NLM-109X, Nilam Field. 146
Figure 6.32 Pressure–depth plot and wireline log values in the mudrocks in well B-11, Bekapai Field. 147

Figure 6.33 Cross-plot of density against sonic transit time in mudrocks in well H-9-B1, Handil Field. 148

Figure 6.34 Pressure–depth plot and density log values in the mudrocks in well TM-84, Tambora Field. 149

Figure 6.35 Structure of the Mutiara Field: (a) map for one stratigraphic horizon; and (b) south-north cross-section (modified from Safarudin and Manulang, 1989). 150

Figure 6.36 Structural map for one stratigraphic horizon in the Semberah Field (modified from Ramdhan, 2002). 151

Figure 6.37 Pressure–depth plot for all Class A pressure data, Mutiara Field. 152

Figure 6.38 Pressure–depth plot for well MUT-21, Mutiara Field. 153

Figure 6.39 Pressure–depth plot for all Class A pressure data, Semberah Field. 154

Figure 6.40 Pressure–depth plot for well SEM-39, Semberah Field. 154

Figure 6.41 Pressure–depth plot and wireline log values in the mudrocks in well MUT-21, Mutiara Field. 155

Figure 6.42 Pressure–depth plot and wireline log values in the mudrocks in well SEM-39, Semberah Field. 157

Figure 6.43 Cross-plots of density against sonic transit time and resistivity in mudrocks in well SEM-39, Semberah Field. 158

Figure 6.44 Schematic west-east geological cross-section of the Lower Kutai Basin (after Total E&P Indonesie, 2003a) and top of overpressure. Top of overpressure comes from several wells in the Mutiara, Handil, Tunu, Sisi-Nubi, and the deep water area located close to the line of section. 159

Figure 6.45 Characteristic overpressure profiles in each area of the Lower Kutai Basin. 160

Figure 6.46 Geothermal gradient of the Lower Kutai Basin. 162

Figure 6.47 Salinity variations across the Internal, Median, and External axes (Total E&P Indonesie, 2003b). 163

Figure 6.48 Enrichment of deuterium (D) and oxygen-18 (^{18}O) isotopes compared to the 'normal' lines for formation water (Total E&P Indonesie, 2003b). 164

Figure 6.49 Mixing formation water with the third source (compaction water) as the cause of isotope enrichment. Bottom panel: example of calculation of compaction water contribution to the observed formation water composition (after Total E&P Indonesie, 2003b). 166

Figure 6.50 Composite pressure–depth plot and vitrinite reflectance data for wells in the Tunu Field and well PEC-1, Peciko Field. All the vitrinite reflectance data from the Tunu Field come from depth intervals in the respective wells where the pore pressure is known to be hydrostatic. 167

Figure 6.51 Pressure–depth plot and vitrinite reflectance data for wells H-9-B1, Handil Field and NLM-109X, Nilam Field. 167

Figure 6.52 Possible hydrodynamically tilted hydrocarbon accumulation in the very deep zone, Bekapai Field. 169

Figure 6.53 Plot of velocity versus vertical effective stress showing the normal compaction trend (the'virgin' curve) and unloading paths. 170

Figure 6.54 Application of Bowers' unloading relation and standard Eaton's method in predicting overpressure in mudrocks in well B-11, Bekapai Field. 171

Figure 7.1 Average rates of sedimentation in various basins around the world (data source: Swarbrick et al., 2002). 180

Figure 7.2 Comparison of the porosity–depth compaction trend at Peciko with other published compaction trends. 181

Figure 7.3 Porosity–temperature compaction trends for mudrocks in the Peciko Field compared to the Sclater–Christie curve and Baldwin-Butler 1. 185

LIST OF TABLES

Page

Table 1 Data used in this research. 9

DECLARATION

1. *The materials contained in this thesis have not previously been submitted for a degree in this or any other institution,*
2. *This thesis is not based on joint research.*

STATEMENT OF COPYRIGHT

ACKNOWLEDGEMENTS

First and foremost, thanks goes to my principal supervisor, Prof. Neil Goulty. His excellent supervision in teaching the philosophy of research and challenging the ideas, together with his willingness and friendly attitude, has helped me throughout my PhD studies. Neil and his family have also made me feel not far away from home. I could ask no more during my stay at Durham.

Special thanks go to Total E&P Indonesie. It would simply have been impossible for me to undertake this research without the scholarship and data provided by Total.

Sincere thanks also belongs to my co-supervisors, Prof. Richard Swarbrick and Prof. Richard Davies. Richard S. forwarded my PhD research proposal to Total, which made it possible for me to study at Durham, and always provided me with food for thought, which helped me to sharpen the research. Richard D. arranged for me to enter the PhD programme at Durham, and helped me to settle in after I had arrived.

Guillaume Smagghe has constantly challenged our ideas, organised the research materials, arranged my presentations to Total in Balikpapan and Pau, and helped to obtain agreement to publish results and helping to deal with some non-technical issues. It has been a great pleasure to work with him: mille mercis!

Noor Syarifuddin, Patrick Zaugg, Jean-Michel Gaulier, and Aussie Gautama initiated my PhD project over six months with a pilot research project in Balikpapan. They mentored me in defining and understanding the technical background necessary for the research, and it was because of them that I was able to get the scholarship from Total. I offer them my sincerest gratitude. Alan Mitchell has also helped me a lot during my annual visits to Indonesia, not least with constructive criticism of the research ideas. Many other people at Total have helped me during my pilot project and annual visits, including Cepi, Andre, Riswandi, Ruli, Rasdianto. Terima kasih!

I owe my biggest thanks to my ‘guru’ at the Institute of Technology Bandung (ITB), Dr. Lambok Hutasoit. Pak Lambok has motivated and helped me at all times. It was Pak Lambok’s encouragement to keep learning, learning, and learning that brought me into this level of study. Mauliate, Pak!

My special thanks also go to all my fellow PhD students at the Department of Earth Sciences, Durham University. Alex Cicchino is the man who has always challenged my ideas and he is a friend indeed. Grazie, my mate! My fellow Indonesian students and their families at Durham also deserve my special thanks: Rifki, Erwin, Abdi, Arham, Yuda, Sekar, Edo, Jay, Eddy, and Farid.

My parents in Indonesia, Ibu Heni Rohaeni, Ibu Lilis Nurhayati, ‘Almarhum’ Bapak Eman Sulaeman, and Bapak Oo Kristiana, have given me every support since my birth. A million words are not enough to express my gratitude to them.

Finally, I would like to dedicate all my research work to my wife, Ami, and our twin sons, Danish and Darish. I could not have succeeded without their love, patience, and help. Ami has supported me throughout, and has been the most wonderful companion on this long and winding road. Durham is a very peaceful city but I have never missed the rock ‘n’ roll because of the lads. Howay the lads!

CHAPTER 1
INTRODUCTION

1.1 Research problems

The Lower Kutai Basin is a Tertiary Basin which underlies the region surrounding the Mahakam Delta, on the east coast of Kalimantan, Indonesia. It is the second largest hydrocarbon province in Indonesia after the Central Sumatra Basin, and the largest for gas production (Burrus et al., 1992; Pertamina BPPKA, 1997). As of 2003, the proven and probable hydrocarbon reserves in the basin are 4 bbl of oil and 47 tcf of gas (Lambert et al., 2003). These numbers exclude the recently discovered new reserves in the deep water area.

Geographically, the basin can be divided into three areas: onshore, shelfal (shallow water), and deep water areas (Figure 1.1). The onshore area and the shelfal area surrounding the Mahakam Delta are mature areas for hydrocarbon exploration and production. The shelfal area includes fields located along three major anticlines lying parallel to the coast, known as Internal, Median and External axes. Recent exploration in the deep water area has resulted in some new discoveries (Guritno et al., 2003), including the oil fields to the north-east. None of the fields in the deep water area are yet in production.

There are three important previous publications concerning overpressures in the research area, by Bois et al. (1994), Bates (1996), and Burrus (1998). One important conclusion from those studies, agreed by all the authors, is that the cause of overpressuring in the Lower Kutai Basin is disequilibrium compaction or undercompaction. Furthermore, Bois et al. (1994) claimed to have identified differences between the sand and mudrock pore pressures in the shallower part of the hydrocarbon-bearing sequences, known as sand-mudrock pressure discrepancies (Figure 1.2). For all depth plots in this thesis, the depth is given as

TVDSS and for all plots where all fluid type has been identified, the fluid type was determined by Total E&P Indonesie from fluid analysis or wireline log interpretation.

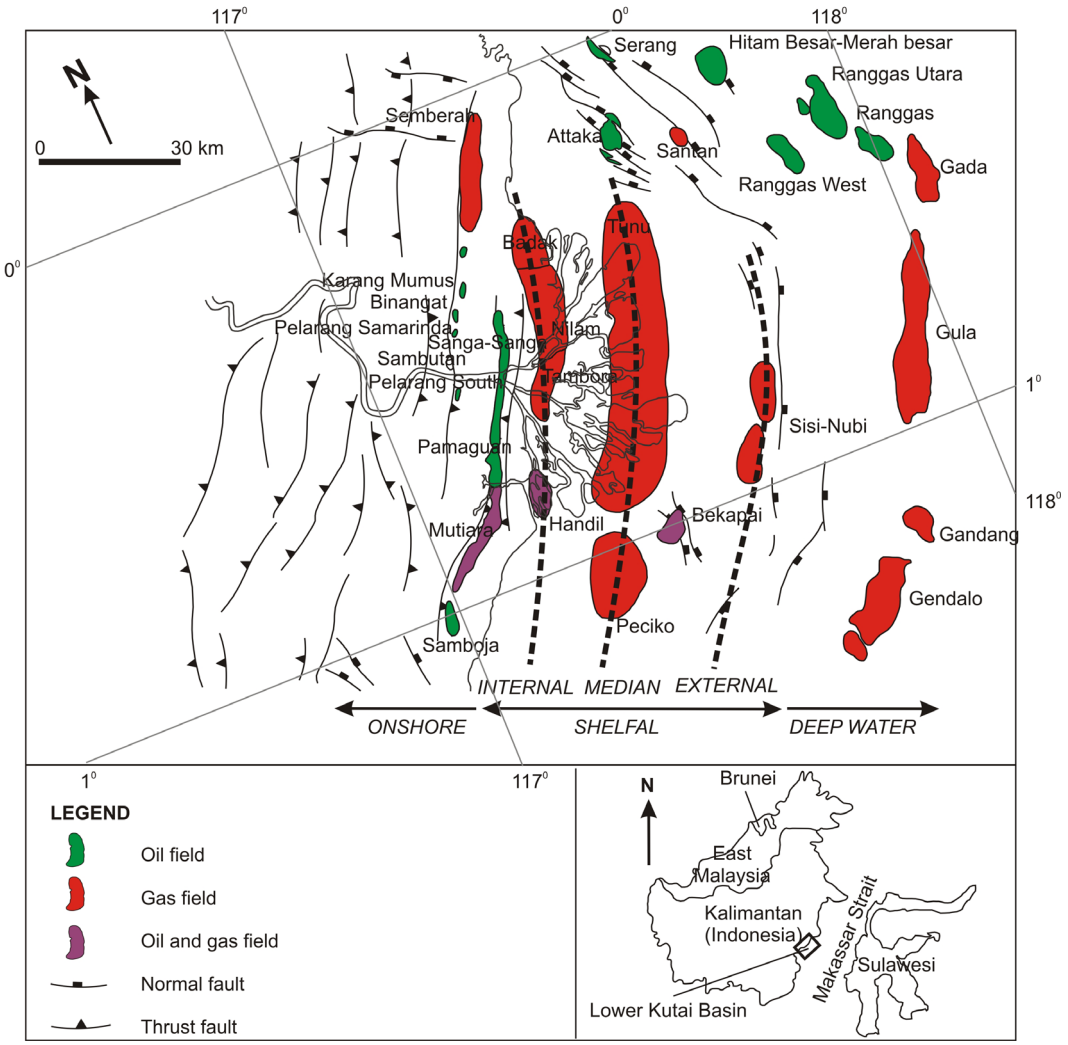

Figure 1.1 Known hydrocarbon accumulations and major shallow faults in the Lower Kutai Basin, Kalimantan, Indonesia. The main north-south anticlines are indicated by the outlines of the hydrocarbon accumulations.

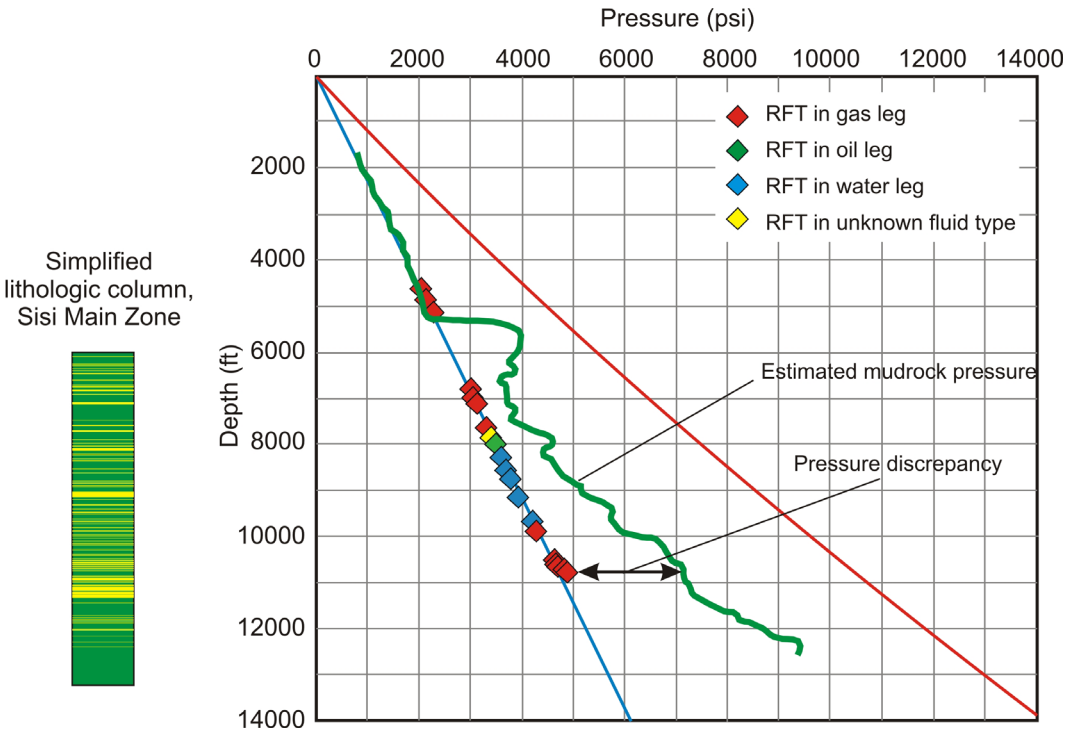

Figure 1.2 Results of the previous evaluation of overpressure in the SS-1 well, Sisi Field, Lower Kutai Basin by Bois et al. (1994). Pore pressures were measured in the sands, and estimated from the sonic log in the mudrocks. Overpressure was thought to be caused by disequilibrium compaction, and substantial sand-mudrock pressure discrepancies were thought to be present. On the left is a simplified lithologic column of this well, showing intensively interbedded sand-mudrock sequences.

Interestingly, several facts relevant to the overpressuring mechanisms in the area were ignored by the previous researchers. Bates (1996) ignored the fact that in one of his wells, i.e. Nilam NLM-109X (Figure 1.3), top of overpressure coincides with top of hydrocarbon maturation. Burrus (1998) ignored the fact that in the Sisi Field he found a relationship between porosity and effective stress (Figure 1.4) in which porosity is not a single-valued function of effective stress. Such a relationship is contrary to the disequilibrium compaction hypothesis. Instead, he introduced what he described as 'Biot's coefficient', subsequently criticised by Goulty (1998) as simply being a fudge factor, to align the porosity and 'Biot effective stress' values into a single relationship so that the data appeared to fit the disequilibrium compaction model.

The research reported here has reviewed available data relevant to overpressuring in the Lower Kutai Basin in an attempt to test the hypothesis that disequilibrium compaction is the main overpressure generating mechanism in this area. The shelfal area, with a sea water temperature of 30°C and a geothermal gradient within the sedimentary column of almost 10°C/1000 ft may be categorised as a 'warm' basin. This warm condition is very favourable for the temperature-driven overpressuring mechanisms of clay diagenesis and hydrocarbon maturation. These fluid-expansion overpressuring mechanisms, broadly categorised as unloading mechanisms, are considered here as viable alternative mechanisms for generating overpressure in the Lower Kutai Basin, and the suggestion that these mechanisms are the principal mechanisms of overpressure generation is put forward as a hypothesis.

The claim of Bois et al. (1994) that there are sand-mudrock pressure discrepancies (Figure 1.2) is also examined here. The reason for doubting the reality of such huge pressure discrepancies (up to ~2000 psi) is the nature of the deltaic succession in the research area, i.e. thin sand-mudrock intercalations.

Hydrodynamic trapping of gas was recognised in the Peciko Field by Grosjean et al. (1994, 2009) and Lambert et al. (2003), and was explained by the concept of mudrock dewatering into the sands (Figure 1.5) due to sand-mudrock pressure discrepancies. In this conceptual model, the lateral flow through the

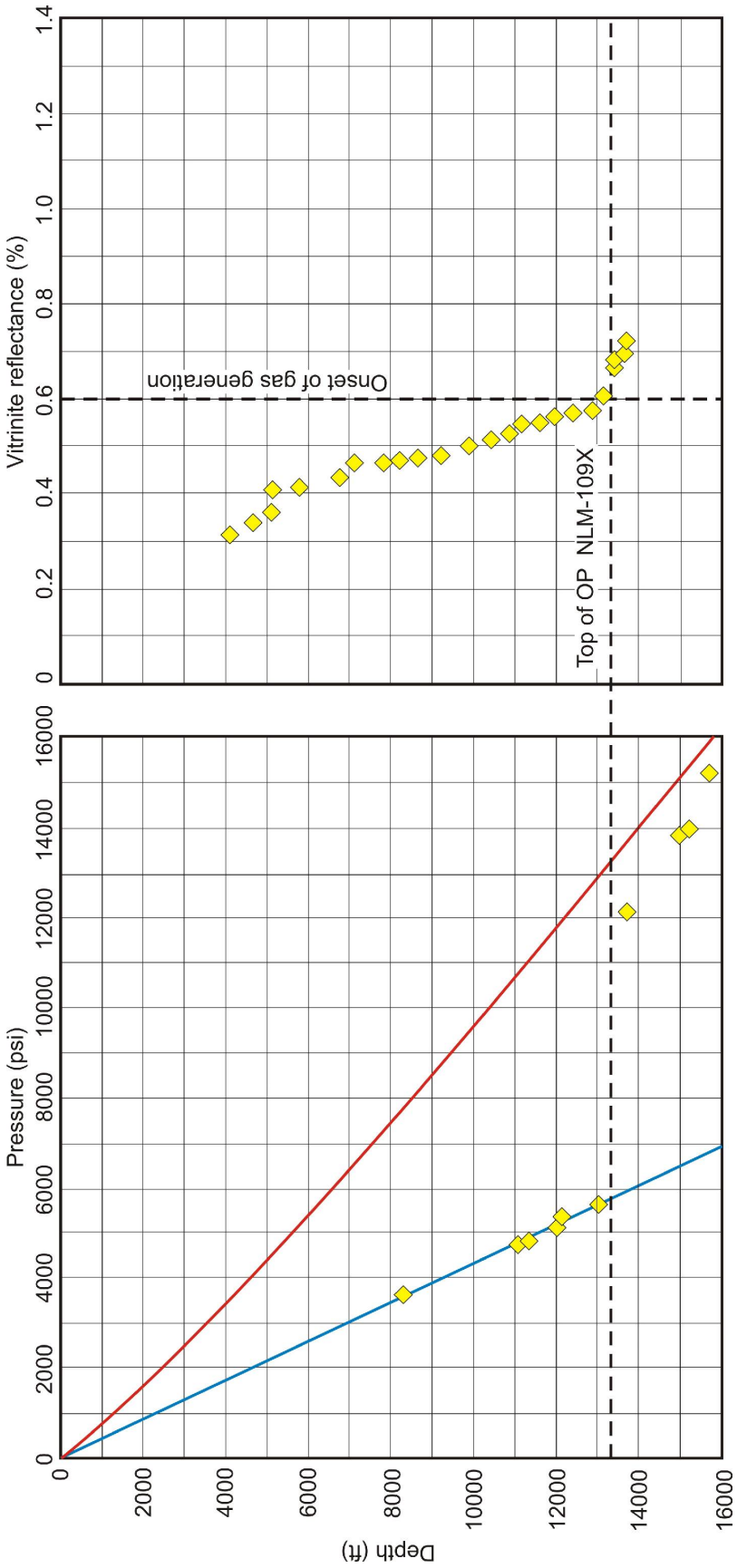

Figure 1.3 Evidence ignored by Bates (1996) showing a coincidence between the top of overpressure and the onset of hydrocarbon maturation in the NLM-109X well, Nilam Field.

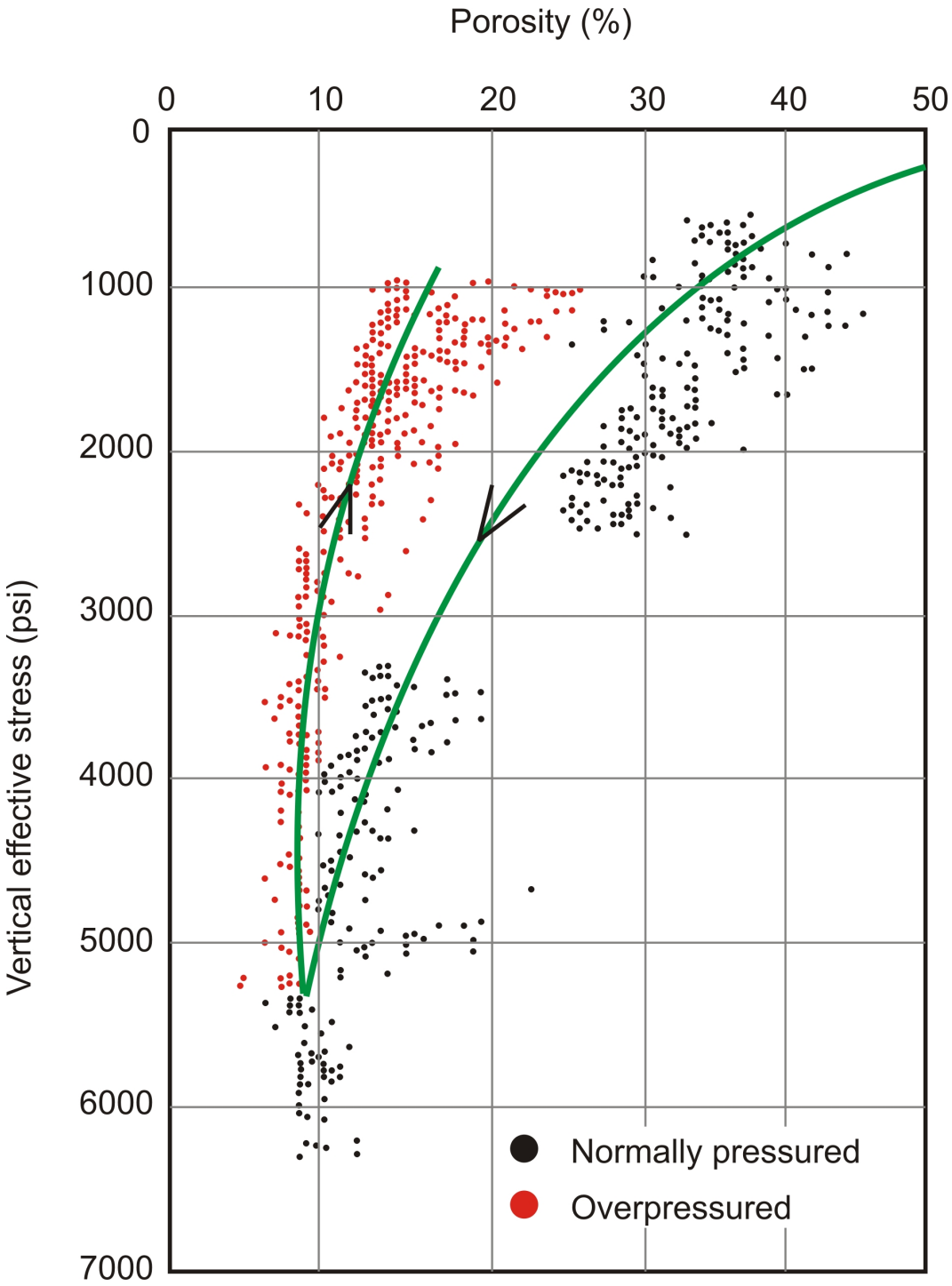

Figure 1.4 Porosity-effective stress relationship introduced by Burrus (1998) for mudrocks in the Sisi Field (arrows on the green lines indicate increasing depth).

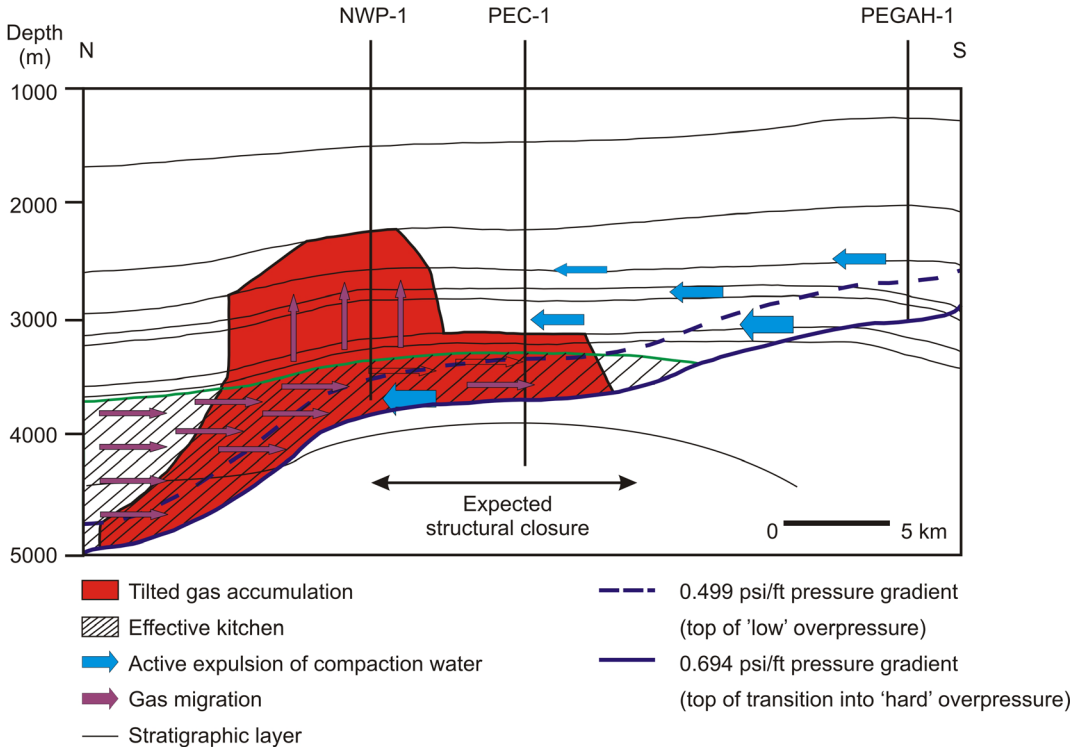

Figure 1.5 Hydrodynamic trapping observed in the Peciko Field explained by lateral drainage of water that had flowed into the sands from overpressured, undercompacted mudrocks (modified from Lambert et al., 2003).

sands at the present time, is maintained by the movement of water from the highly overpressured mudrocks into the weakly overpressured sands. Since the hypothesized pressure discrepancies are implausible, it is also necessary to consider alternative sources for the fluid that is being laterally drained through the reservoirs.

1.2 Objectives

The objectives of this research are:-

1. Determine the cause of overpressure in the Lower Kutai Basin.
2. Determine the state of mudrock compaction in the basin.
3. Consider how the overpressure in the basin can be detected and estimated.
4. Consider how the role of overpressure relates to the petroleum system in the basin.
5. Compare the overpressure generating mechanism and the state of compaction in the Lower Kutai Basin with other basins world-wide.

In fulfilling the above objectives, the overall aim is to get a new insight on overpressuring in a relatively young and warm sedimentary succession. To date, the two mainstream schools of thought on overpressuring come from two distinct areas: 1) the relatively cool basins in the Gulf of Mexico, and 2) the warm but older basins of the North Sea area.

In terms of petroleum system analysis, the understanding of overpressuring may help in the determination of migration and trapping mechanisms. The Peciko Field was discovered by applying the hydrodynamic concept and discovering gas down flank from the crest of the structure, in the direction of fluid flow and decreasing overpressure (Grosjean et al., 1994). Other examples of fields where hydrocarbons are hydrodynamically trapped are given by Dennis et al. (2000).

For a practical point of view, the understanding of the overpressure distribution is of paramount importance for well planning, both from safety and cost considerations, and also to ensure that the target depths can be reached. As

far as possible, the depths of casing points and the appropriate mud weights to be used in drilling need to be accurately estimated in advance of drilling (Mouchet and Mitchell, 1989).

1.3 Data

The summary of data used in this project is given as Table 1.1.

Table 1.1 Data used in this research

No	Type of data	Onshore	Shelfal	Deep water
1	Reservoir pressure measurements	590 points	7855 points	Not available
2	Wireline log suites	8 wells	32 wells	Not available
3	Temperature data	262 points		Not available
4	Hydrocarbon maturation data	74 points		Not available

1.4 Synopsis

In this first chapter, the research problem and objectives have been stated, and previous ideas about overpressure generating mechanisms in the Lower Kutai Basin have been briefly reviewed. The geology and petroleum system in the basin are described in Chapter 2. The theoretical background and methodologies used in this research are discussed in Chapter 3 and Chapter 4, respectively.

Chapter 5 mainly comprises an analysis of overpressure and compaction in the Peciko Field. To put this analysis in context, the chapter starts with a review of the results from previous research. The Peciko Field was chosen as the field to test the methodologies that will be used throughout the basin. This choice was made because this field has the largest number of pre-production pressure

measurements (‘virgin’ pressures), unaffected by production and consequent pore pressure drawdown. This field also has many complete suites of high quality wireline logs, because the use of oil-based drilling mud minimised the caving of the borehole wall which resulted in poor wireline log quality in other fields in the basin where water-based muds were used. This excellent dataset is ideal for studying overpressure generating mechanisms and compaction. The work reported in this chapter has been accepted for publication in Petroleum Geoscience (Ramdhan and Goulty, 2010a).

Chapter 6 consists of analyses of overpressure and compaction in the whole Lower Kutai Basin, using the same methodologies as those used for the Peciko Field. Objectives 1 – 4 are addressed in this chapter, and the work reported in it has been submitted for publication to AAPG Bulletin (Ramdhan and Goulty, 2010b).

Chapter 7 compares overpressure and compaction in the Lower Kutai Basin with other areas in the world in order to put the new insights gained in this relatively young and warm basin into a wider context. Conclusions from this research are given in Chapter 8 along with suggestions for further work.

CHAPTER 2
GEOLOGY AND PETROLEUM SYSTEM

2.1 Geology

2.1.1 Regional tectonics and basin development

Tectonically, the Lower Kutai Basin lies within the greater South East Asia tectonic system. The present day tectonic elements of South East Asia are shown in Figure 2.1. Indonesia is located on the Eurasia Plate close to a junction between three major plates: the Indian-Australian Plate to the south, the Pacific Plate to the east, and the Eurasia Plate to the north. Development of the Kutai Basin has been very much affected by the interactions between those plates (Van de Weerd and Armin, 1992; McClay et al., 2000; Hall, 2002, 2009). Among the interactions are the opening of the South China Sea to the north, at the margin of the Eurasia Plate (Figure 2.1), the westward motion of Pacific Plate, and the northward motion of the Indian-Australian Plate. An example of the plate movements during the Middle Eocene, when the basin was initiated, is shown in Figure 2.2.

Moss and Chambers (1999) and Chambers et al. (2004) comprehensively investigated the development of the Kutai Basin (Figure 2.3). There are four major development phases of the basin:

1. Middle – Late Eocene: basin initiation marked by the development of half grabens as a consequence of tectonic extension experienced by the South East Asia region, including the Kalimantan area (e.g. Hall, 2009). This process was accompanied by syn-rift sedimentation.
2. Latest Eocene – Late Oligocene: sag period, marked by deep marine mudrock sedimentation in the basin centre and carbonate platform development at the basin edge near the basement high.

3. Latest Oligocene – Early Miocene: early development of deltaic sediments in the Lower Kutai Basin. There are two phases of tectonics related to this development: inversion/uplift and volcanism in the hinterland, followed by a second extensional phase in the basin centre.
4. Middle Miocene – Present: the main inversion stage with development of the Samarinda Anticlinorium, the major anticlinal structure in the Kutai Basin (Figure 1.1), and progradation of the delta toward the present-day Mahakam Delta.

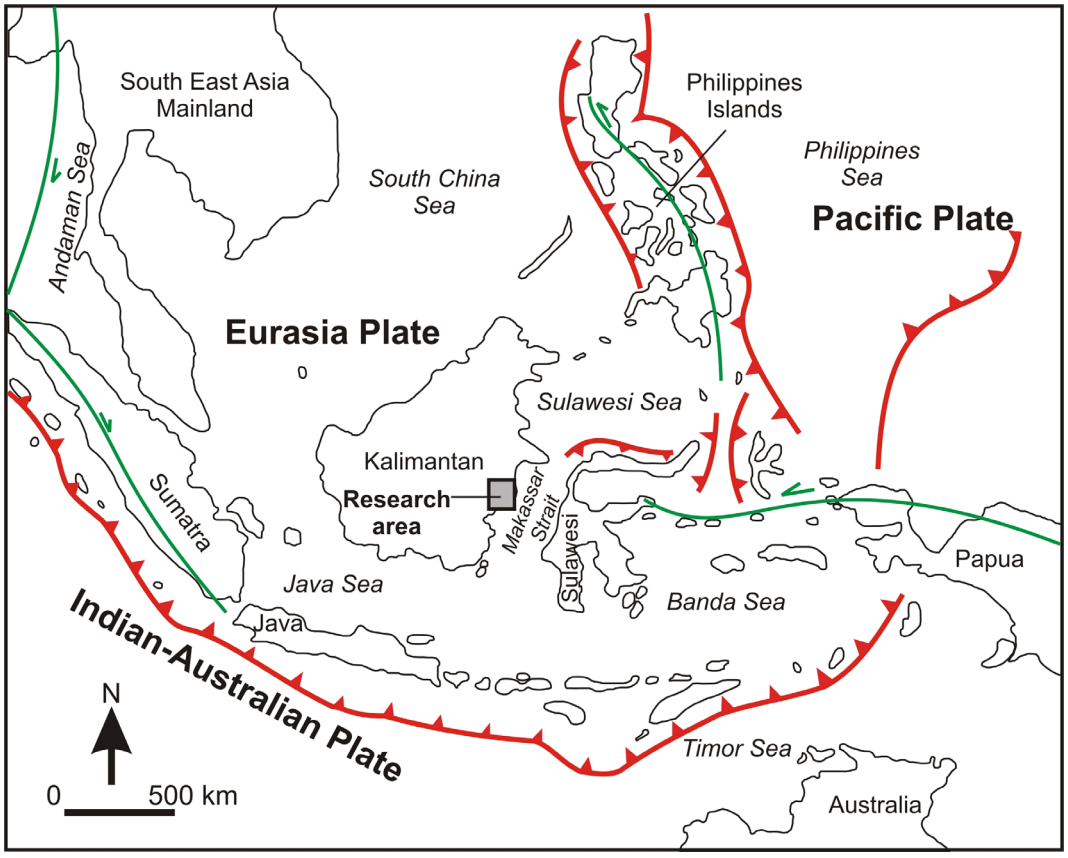

Figure 2.1 Present day tectonic elements in the area around the Lower Kutai Basin (modified from Van de Weerd and Armin, 1992).

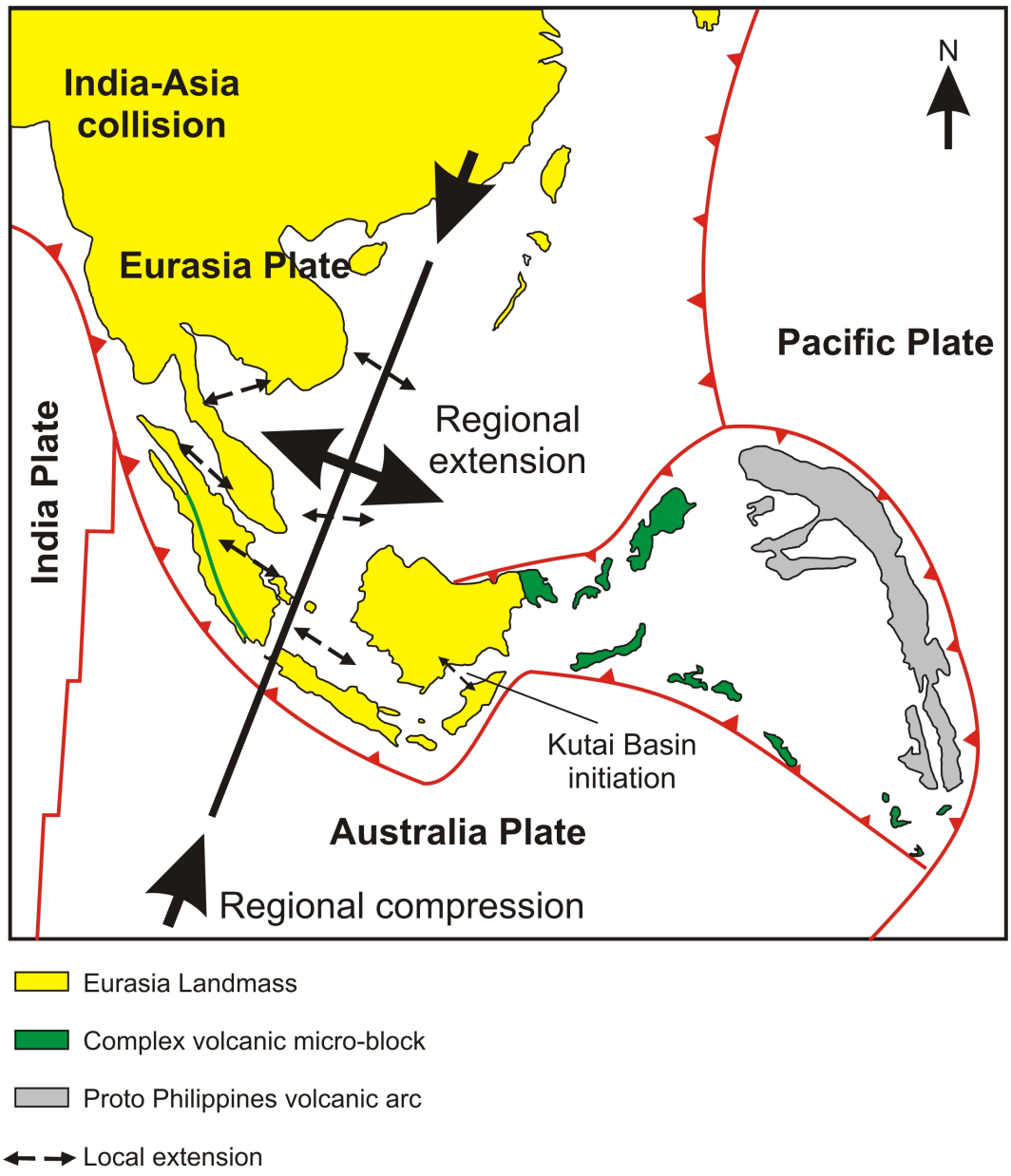

Figure 2.2. Tectonic plates in the region of South East Asia at 45 Ma (Eocene). The Kutai Basin was being initiated at this time, as a consequence of regional extension (simplified from Hall, 2009).

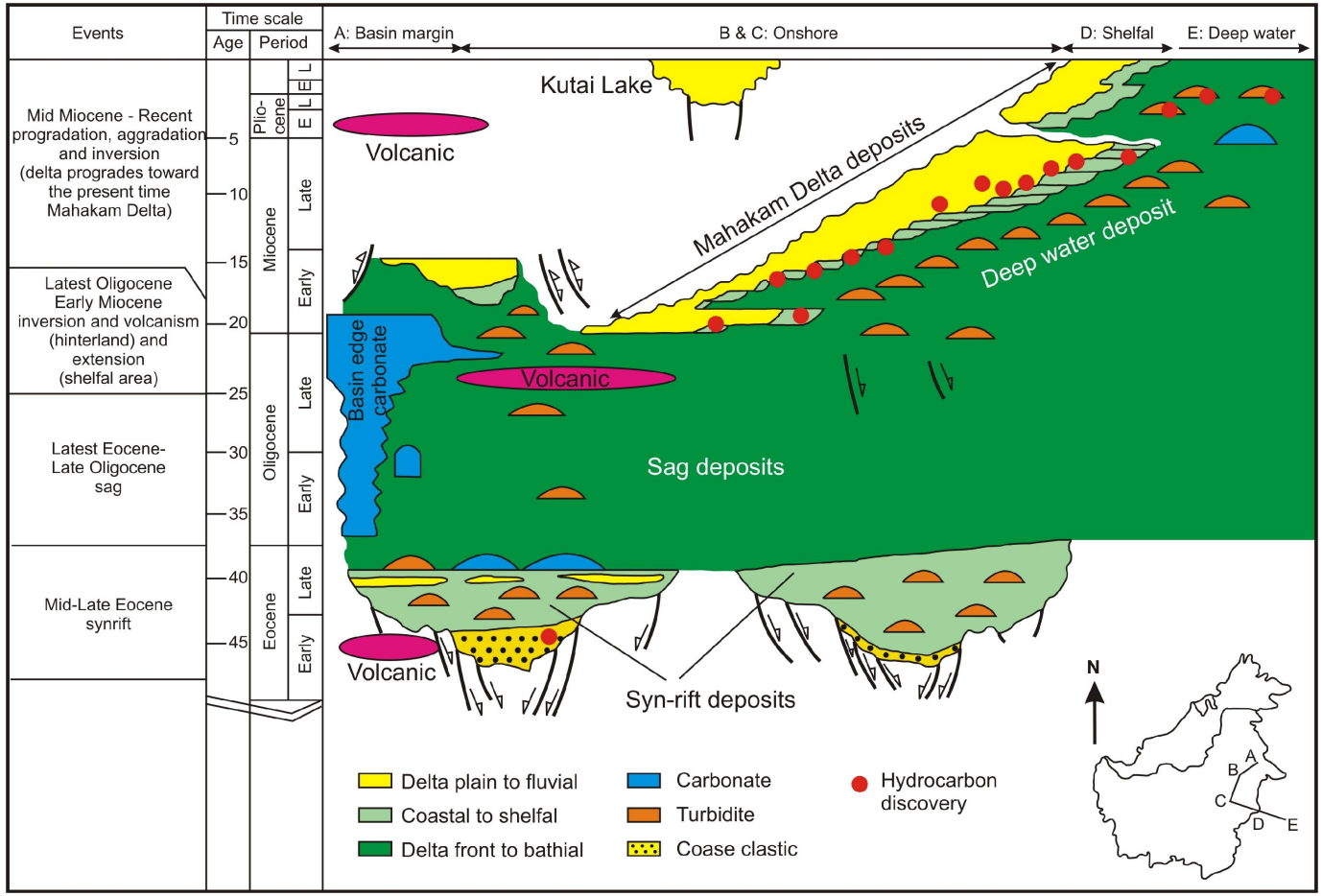

Figure 2.3 Tectono-stratigraphic column of the Lower Kutai Basin showing basin initiation, basin development, tectonic processes and the resulting stratigraphic section (simplified from Chambers et al., 2004).

A regional cross-section reflecting the basin development, tectonic events, and structural elements in the Kutai Basin has been compiled by Hall et al. (2009) and is shown as Figure 2.4.

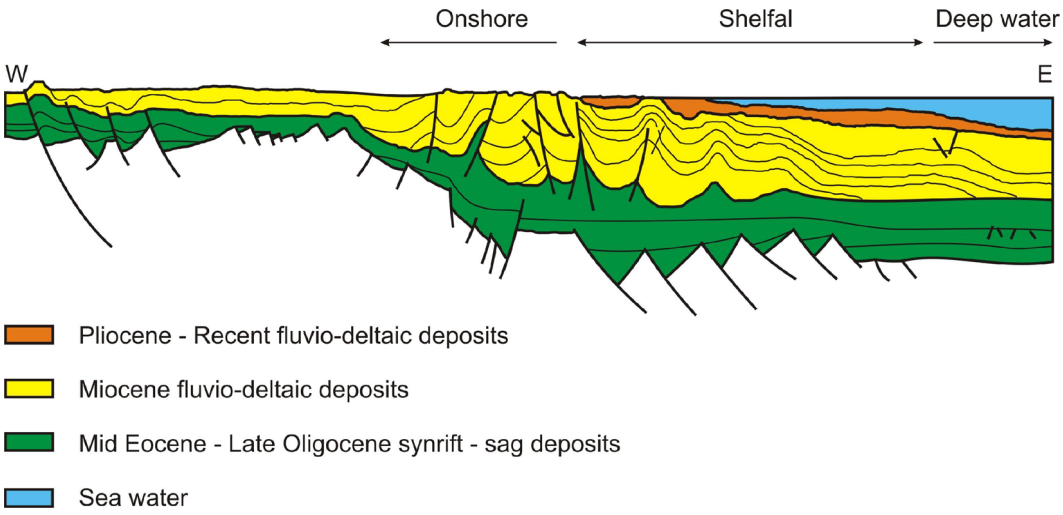

Figure 2.4 Regional cross-section showing stratigraphic and structural elements of the Lower Kutai Basin (simplified from Hall et al., 2009) (not to scale).

2.1.2 Basin structure

The major structural feature in the Lower Kutai Basin is the Samarinda Anticlinorium, consisting of a series of anticlines and synclines with axes oriented approximately north-south (Figures 1.1 and 2.4). This anticlinorium is highly folded and faulted on the onshore area, whereas dips are gentle in the shelfal and deep water areas.

The development of the structures in the Lower Kutai Basin is a subject of debate up to the present day. Ott (1978) proposed a regional gravity gliding hypothesis, caused by uplift in the basin margin, to explain the Samarinda Anticlinorium. In this hypothesis, the uplift caused sediments to collapse in the uplifted area, and by the force of gravity, they moved towards the east, forming the Samarinda Anticlinorium. He recognized the importance of top surface of the bathial Oligocene overpressured mudrocks as an ideal detachment surface for the gravity gliding.

Recently, two models have been proposed for the structural development of the Lower Kutai Basin. In the first model, reactivation of basement faults and inversion caused the development of structures in the shallower section, including the Samarinda Anticlinorium (Chambers and Daley, 1995, 1997; Moss et al., 1997; Cloke et al., 1997; Moss and Chambers, 1999; Chambers et al., 2004). This is the thick-skinned tectonics model, and it is shown schematically in Figure 2.5. It is interesting that the top of the overpressured prodelta mudrocks is proposed by Chambers et al. (2004) to be the detachment surface of the subhorizontal detachment fault at the base of the Miocene deltaic sediments. This model implies that the top of overpressure lies at the top of the prodelta sediments. This research investigates whether the top of overpressure really lies at the top of the prodelta sediments. The relationship between overpressure and structural development of the basin is not addressed, although that would be an interesting subject for further work. For example, if the top of overpressure is not located in the prodelta mudrocks, will the model of the structural development of the basin be changed?

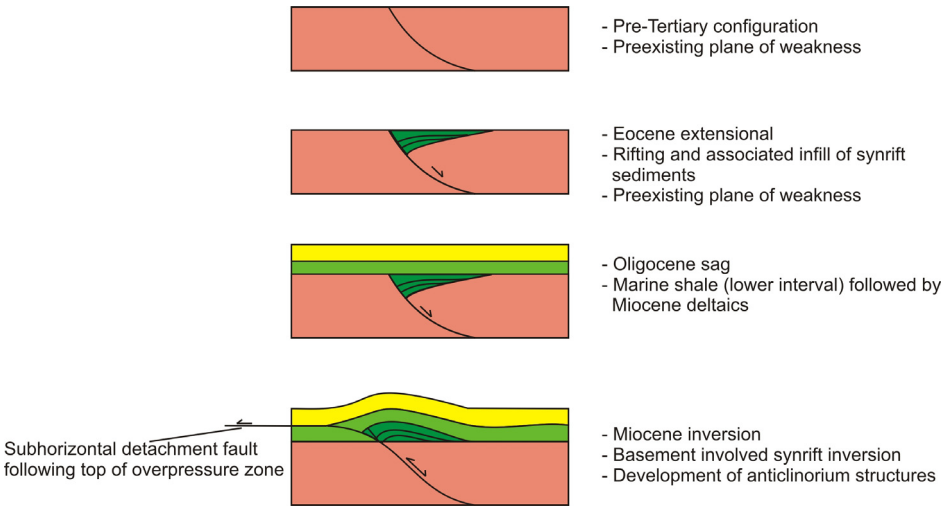

Figure 2.5 Schematics of structural development of the Lower Kutai Basin with the hypothesis of thick-skinned basement involvement inversion (simplified from Chambers et al., 2004).

The second model is the thin-skinned tectonics model. According to this model, the Samarinda Anticlinorium formed as the result of reactivation of the early delta-top extensional growth fault (Ferguson and McClay, 1997; McClay et al., 2000) (Figure 2.6). The structure then developed as the rapidly accumulating and prograding deltaic sediments detached on the overpressured prodelta mudrocks. As in the thick-skinned tectonics model, the thin-skinned model also stresses the importance of the top of the prodelta mudrocks as the detachment surface for the structural development.

2.1.3 Stratigraphy and sedimentation

A generalised stratigraphic column for the Lower Kutai Basin is shown in Figure 2.3. The sedimentation regimes can be divided into two: overall transgression during the Palaeogene (rift-filled sedimentation and sag), and overall regression during the Neogene (delta progradation and aggradation) (Allen and Chambers, 1998).

The main process throughout the Palaeogene was rift-filled sedimentation. In the northeastern area, the Palaeogene sediments vary from alluvial fans and deltaic sediments to deep marine sediments, but are dominantly fluvio-deltaic sediments. In the eastern area, surrounding the present-day Mahakam Delta, the sediments are dominantly deep marine sediments.

A schematic structural-stratigraphic section of the Neogene strata in the Lower Kutai Basin is shown in Figure 2.7. The lithologies of the Neogene section comprise intercalations of sand, mudrock and coal of fluvial–deltaic sediments in the onshore and shelfal areas, and dominantly marine mudrocks with confined turbiditic sand-mudrock sequences on the deep water area.

Duval et al. (1998) performed a detailed sequence stratigraphic study of the shelfal area (Figure 2.8). The evolution of the deltaic system, from delta plain to delta front, can be recognized clearly in that section. It can also be seen in

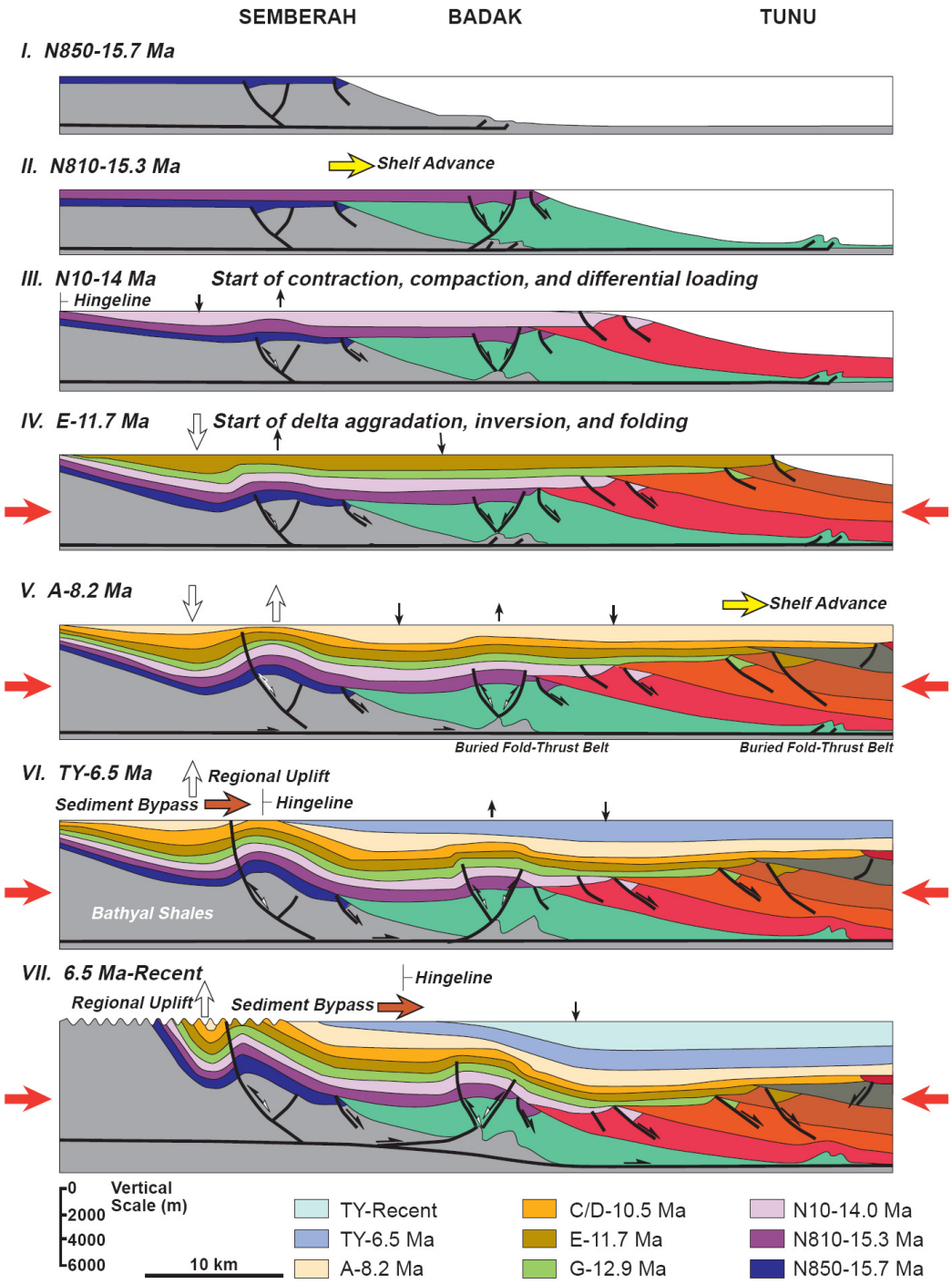

Figure 2.6 Schematics of structural development of the Lower Kutai Basin with the hypothesis of the thin-skinned tectonics (McClay et al., 2000).

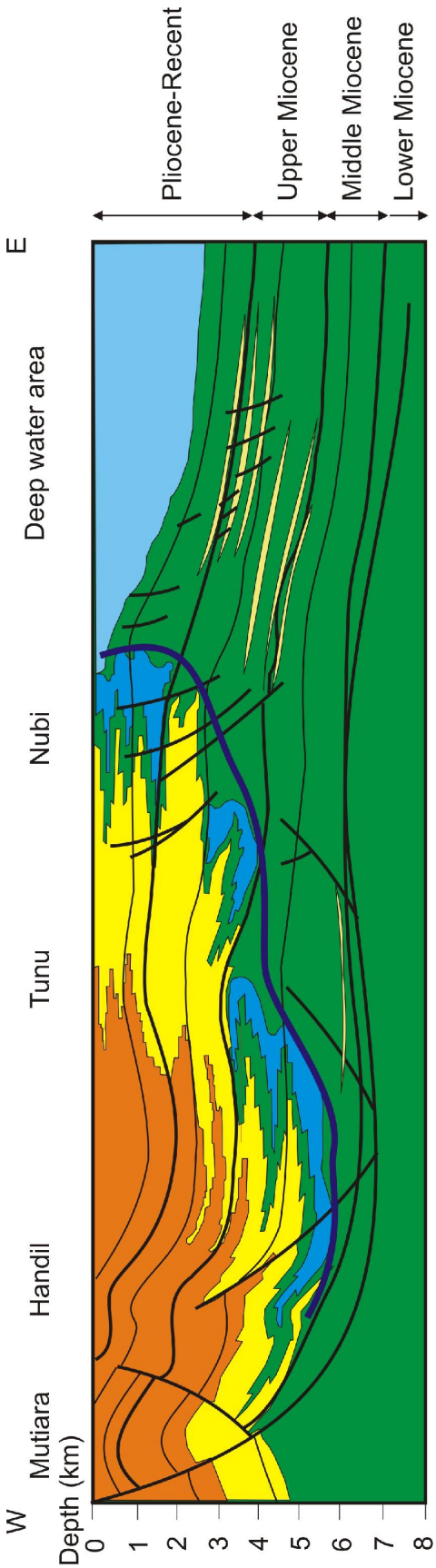

Figure 2.7 Detail structural-stratigraphic section of Neogene section, Lower Kutai Basin (after Total E&P Indonesie, 2003a).

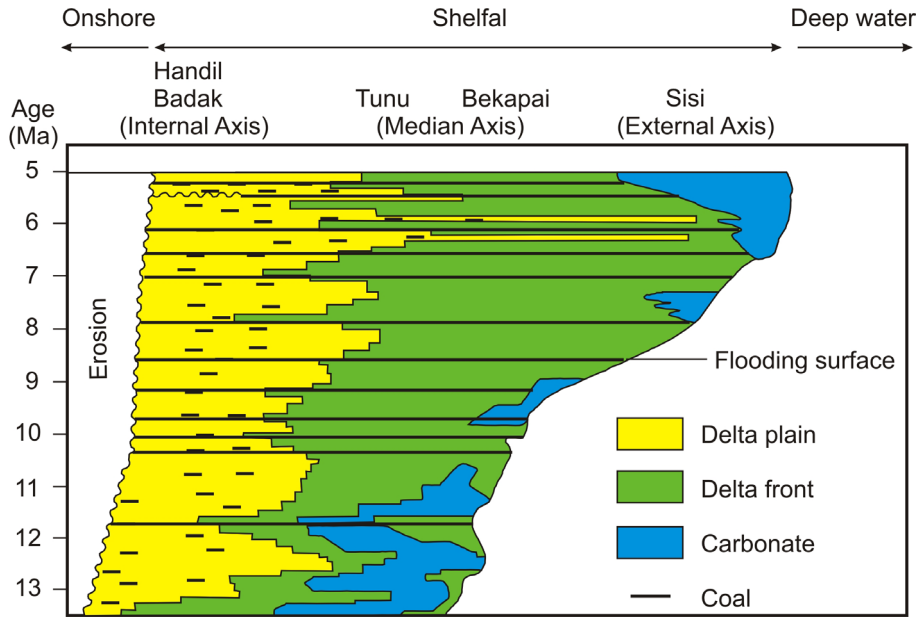

Figure 2.8 Detailed sequence stratigraphic section of Neogene strata, Lower Kutai Basin (simplified from Duval et al., 1998).

Figure 2.8 that, in several parts of the onshore area, the Upper Miocene–Pliocene sediments have been eroded, resulting in only Middle Miocene and older sediments remaining. The movement of the carbonate shelf during the Miocene is a clear indicator of a prograding deltaic sequence during the Neogene. This sequence has resulted a distinct sand–mudrock distribution which becomes increasingly shaly with depth and towards the east, as illustrated by Figure 2.9.

The burial history of the Neogene section is shown in Figure 2.10. During the last 8 Ma, the sedimentation rate was fairly constant at around 300 m/Ma, while during 10–8 Ma, it was around 700 m/Ma. The burial history information for the Palaeogene section is not available for analysis in this project.

2.2 Petroleum system

Based on the history of basin development and the stratigraphy described above, the petroleum system in the Kutai Basin can be divided into three: a Palaeogene petroleum system, a Neogene fluvio-deltaic petroleum system, and a Neogene

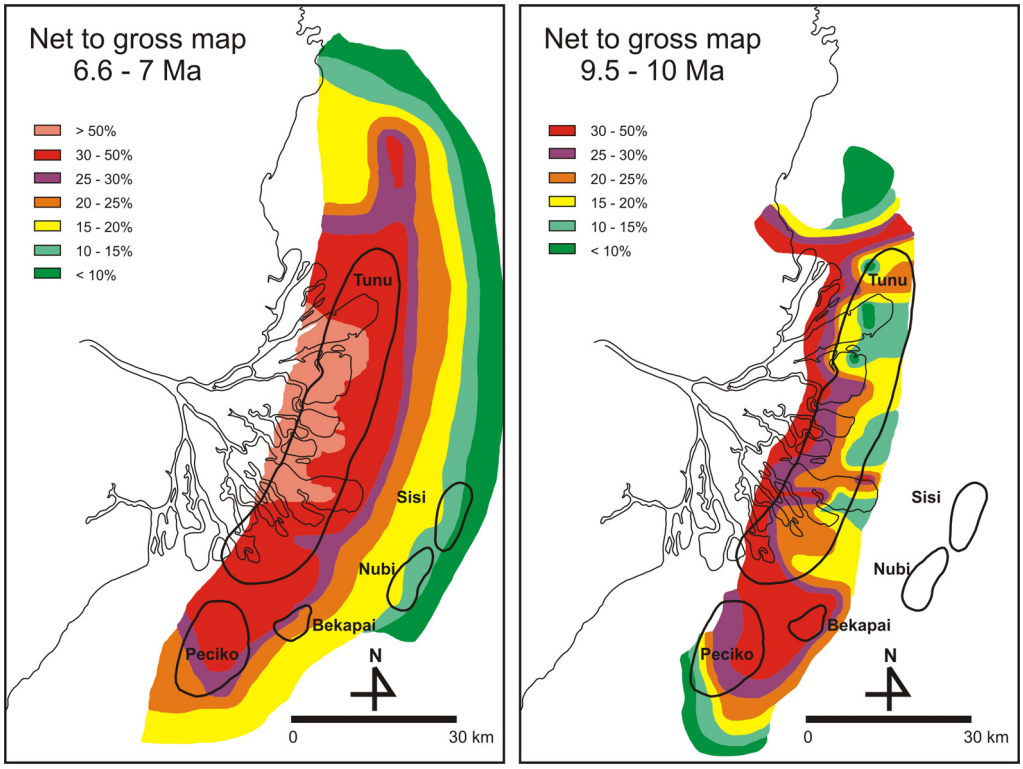

Figure 2.9 Distribution of sands and mudrocks on the Median Axis in the form of net to gross maps for sediments of age 7–6.6 Ma (left) and 10–9.5 Ma (right) (simplified from Total E&P Indonesie, 2000a).

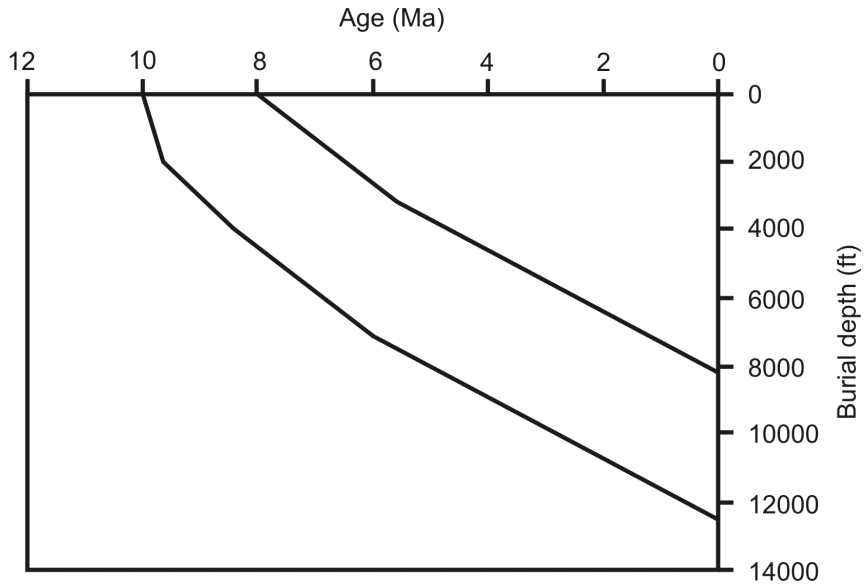

Figure 2.10 Burial history of Neogene section, shelfal area, Lower Kutai Basin (data source: Lambert et al., 2003).

deep water petroleum system. To date, hydrocarbons have only been produced from the Neogene fluvio-deltaic system in the Lower Kutai Basin.

2.2.1 Palaeogene petroleum system

To date, there has been no hydrocarbon production from this petroleum system in the Kutai Basin. The equivalent petroleum system has been proven to generate oil in the Barito Basin, located to the south of the Kutai Basin. Guritno and Chambers (1999) claimed that they had demonstrated the existence of an Eocene petroleum system in the Lower Kutai Basin, even though they failed to find economic hydrocarbon reserves. Their area of investigation was in the northern part of the basin, near the basin margin, where the Neogene sediments are relatively thin. They found that the essential elements of the petroleum system were present as described below.

The source rocks for the Eocene petroleum system are coals and carbonaceous mudrocks, and they have the potential to generate both oil and gas. 1-D basin modelling has shown that the maximum of hydrocarbon generation was in the period 24–17 Ma (Guritno and Chambers, 1999). The generated hydrocarbons then migrated laterally and vertically through faults to the traps. The potential traps are structural closures as well as stratigraphic traps. The potential reservoir rocks are upper Eocene sands of deltaic facies; the carbonate rocks were considered to be too tight and the turbiditic sands were considered to be mineralogically immature so their porosity is relatively low. The regional seal for this petroleum system is formed by Oligocene mudrocks. Guritno and Chambers (1999) noted that the main reasons why they could not find economic hydrocarbon reserves were poor reservoir quality, caused by mineral dissolution due to relatively deep burial, and trap breach due to inversion.

2.2.2 Neogene fluvio-deltaic petroleum system

The hydrocarbons that have been produced in the Kutai Basin have come from the Neogene petroleum system of Middle Miocene–Pliocene age. Recently, the Lower Miocene strata of this petroleum system have also been proposed as a potential petroleum system, although there has been no production as yet (Bachtiar, 2004).

The first researchers who tried to explain the Neogene petroleum system were Oudin and Picard (1982). They analysed the relationship between hydrocarbon generation and overpressured zones in Handil and Bekapai fields. In their model, hydrocarbon migrated vertically from source rocks located beneath the present accumulations, as well as laterally from source rocks located in the synclinal areas.

A complete synthesis of the Neogeone petroleum system was made by Paterson et al. (1997) and Duval et al. (1998), and revisited by Lambert et al. (2003). The schematic model of this petroleum system, describing the essential components of source rock, reservoir, seal, migration, and trapping mechanism, is shown in Figure 2.11.

The main source rocks in this petroleum system are organic-rich mudrocks, coal beds, and even sandy facies deposited in fluvial, deltaic top, tidal plain, and delta front settings. They are mostly classified as Type III source rocks. Although the organic-rich mudrocks are gas prone, Lambert et al. (2003) reported that the oil-generative potential of the Type III organic matter is unusually high. The contribution of hydrocarbon generation from marine mudrocks, located in the deeper part of the Neogene sequence, is thought to be negligible because their organic content is low. Interestingly, isotopic analysis performed by Lambert et al. (2003) showed that the threshold for both gas and oil maturation corresponds to a vitrinite reflectance of 0.6%. Also, their computation shows that the onset of hydrocarbon generation was at 3 Ma, and has continued to the present day.

The reservoirs are the sands in a complex multilayered sequence of intercalated sands and mudrocks. The sands are both fluvial sands and mouth bar sands. An example from Peciko Field, illustrating the complexity of the reservoir,

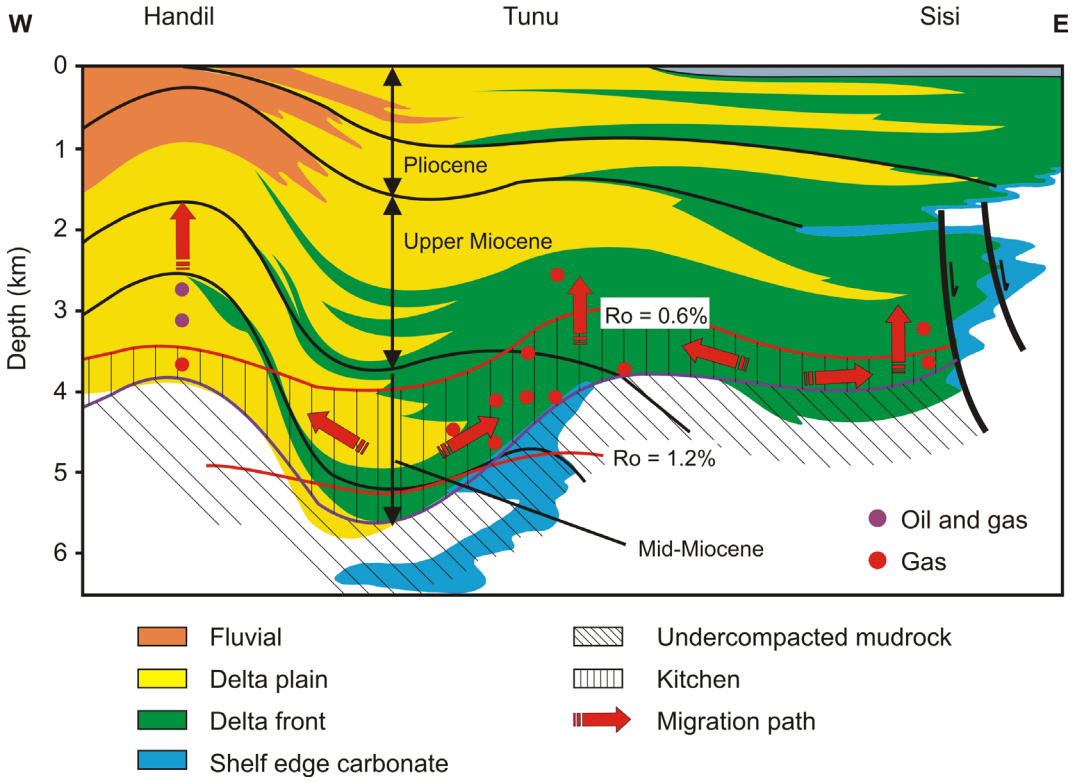

Figure 2.11 Schematic of the Neogene petroleum system (simplified from Duval et al., 1998).

is shown in Figure 2.12. The permeability of the reservoir is very much affected by its clay content and sedimentary structures (e.g., bioturbation). The highest reported permeability is of the order of hundreds of millidarcies, and permeabilities range downwards to the order of 10^{-2} mD (Lambert et al., 2003; Samson et al., 2005).

The seal comprises intraformational marine mudrocks developed during marine flooding surface events. Duval et al. (1998) also noted that these flooding events are coeval throughout the basin, so the seals are widely distributed throughout the basin. As can be seen in Figure 2.11, the migration is proposed to be predominantly lateral migration from the main source rock areas located in the synclinal areas towards the reservoir beds, and then vertically into the traps. Basin modelling work done by Burrus et al. (1992) shows that the migration is short distance migration, around 10-15 km.

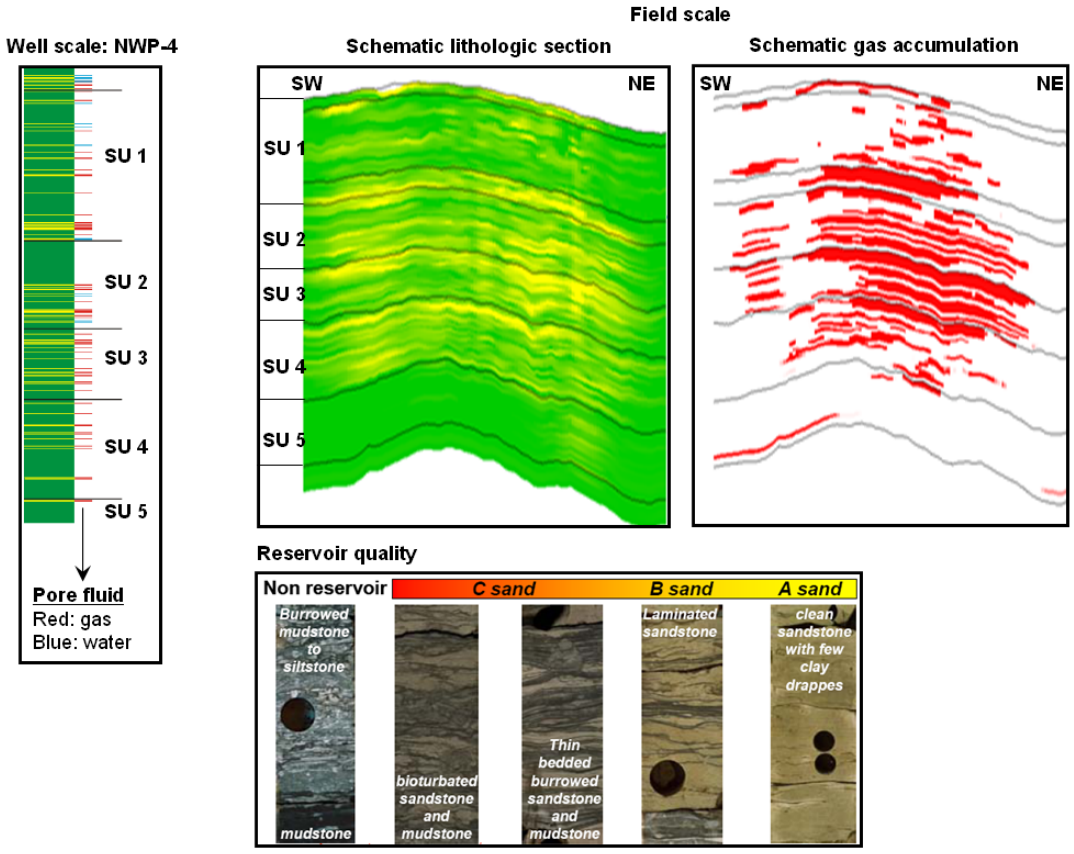

Figure 2.12 Schematic showing complexity of reservoir geometry (stacked sandstone bodies), pore fluid distribution, and reservoir quality (permeability) in the Neogene petroleum system (compiled from Lambert et al., 2003, Samson et al., 2005, and Total E&P Indonesie, 2010a).

The traps have structural and stratigraphic elements with hydrodynamic trapping where there is active lateral reservoir drainage. Structural traps may be simple anticlines or faulted anticlines (e.g., anticlinal rollover in the hanging wall of a fault). Simple anticlines are generally found in the shelfal area (Internal, Median, and External axes), while the faulted anticlines tend to be found in the onshore area. The stratigraphic traps are sand bodies, such as mouth bar sands, confined in mudrock sequences, direct sand pinchouts, or sand channels draped across anticlinal trends (Doust and Noble, 2008).

Grosjean et al. (1994, 2009) and Lambert et al. (2003) pointed out the importance of hydrodynamic elements associated with the structural trapping in

two fields on the Median Axis, i.e., Tunu and Peciko. In both fields, the gas accumulations displaced down-dip from the anticlinal crest, on the northern flank in the Peciko Field (Figure 2.12), and on the western flank in the Tunu Field (Figure 2.13). These researchers (Grosjean et al., 1994; 2009; Lambert et al., 2003) have explained the hydrodynamic trapping as the result of expulsion of water vertically from the overpressured mudrocks into the reservoirs (Figure 1.5). Further discussion on hydrodynamics in the Peciko Field is given in Chapter 5, together with an alternative explanation for the hydrodynamics in the area.

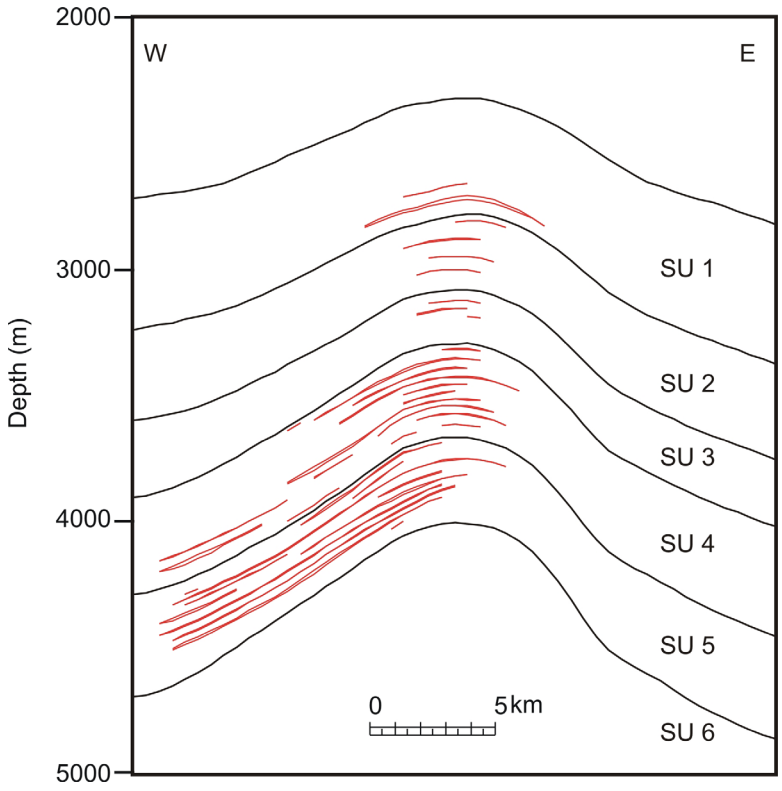

Figure 2.13 Displaced gas accumulations (red) on the western flank of the structure in the Tunu Field, indicating hydrodynamic trapping (simplified from Lambert et al., 2003).

The distribution of oil versus that of gas in the Lower Kutai Basin is an outstanding puzzle (Figure 1.1). Some fields contain both oil and gas (e.g., Bekapai and Handil), while other fields only contain gas (e.g., Tunu and Peciko). Guritno et al. (2003) suggested that the type of hydrocarbon relates to the degree

of faulting. The accumulations of oil relate to a high intensity of faulting, while gas is found in fields where there is a lower intensity of faulting. In their model, as the heavier fluid, oil needs more permeable pathway to migrate to the reservoir. Faults provide such permeable pathways, which is why oil is found in fields with a higher degree of faulting. Where faults are absent, then the oil located in the source rocks remains where it is until it cracks to gas. This explains why in the unfaulted fields, we hardly find any oil. However, their model does not explain why, in some fields, oil is located in shallower reservoirs than some gas accumulations (e.g., Handil and Bekapai). Total E&P Indonesie in-house analysis has offered an explanation for this behaviour: oil in the shallower reservoirs originated by condensation of gas that had migrated into them. It is not the subject of this research to investigate the relative distribution of oil and gas, but the explanations that have been advanced are not conclusive.

2.2.3 Deep water turbidite petroleum system

Guritno et al. (2003) described the discovery of deep water petroleum system in the Lower Kutai Basin (water depths 4000–6000 ft). Saller et al. (2006) stated that the amounts of hydrocarbons discovered are 6 tcf gas and 200 million bbl of oil and condensate.

Interestingly, the source rocks in this petroleum system are sandstone containing coaly fragments, pieces of wood, resinite, and other coaly debris (Saller et al., 2006). The deep water mudrocks are thought not to be source rocks because of their low organic content. The source rocks are of Type III, i.e., they are gas-prone and condensate-prone.

The reservoirs in this petroleum system are Upper Miocene–Pliocene turbiditic sandstones encased in marine mudrocks. The thickness of individual reservoirs can reach 300 ft. Sandstone porosities are 12–35%, and permeabilities are hundreds of millidarcies to darcies. The seals are intra-formational hemipelagic mudrocks. They also provide independent pressure regimes for each reservoir unit. Migration is vertical along faults, from the mature Middle Miocene

source rock. Lateral migration from source rocks located in the synclinal area, as in the shelfal area, is considered to be unlikely because the source rocks in the synclinal area have a very low TOC content.

The dominant trap type in this petroleum system is structural, with some minor stratigraphic trapping. The structural traps are thrust-faulted anticlines, in which the faults provide compartmentalisation of the reservoir units.

CHAPTER 3
THEORETICAL BACKGROUND

This chapter gives the theoretical background for analysis overpressure and compaction in the research area. Firstly, the basic terms that are commonly used in analysing overpressure are given. Then overpressure generating mechanisms are described and the transient nature of overpressure is discussed. Worldwide examples of overpressured basins are briefly reviewed, including the overpressure generating mechanisms. Overpressure estimation methods are then described and the last section reviews the related phenomena of overpressure in form of lateral reservoir drainage and hydrodynamic trapping.

3.1 Basic terminology

Figure 3.1 shows a combined generic depth profile of pore pressure and stress in an overpressured sedimentary basin. It is used in this section to illustrate some basic terms used in overpressure analysis.

Normal hydrostatic pressure

The normal hydrostatic pressure (blue line in Figure 3.1) at any depth is the pore pressure due to an open column of water that reaches up to the surface datum, e.g., sea level. Strictly speaking, atmospheric pressure at the datum should be added to the pressure due to this notional column of water in hydrostatic equilibrium to give the absolute pressure. Neglecting the contribution of atmospheric pressure, the normal hydrostatic water pressure at any point in the subsurface is solely due to the weight of its overlying water column and it is calculated by using the equation:

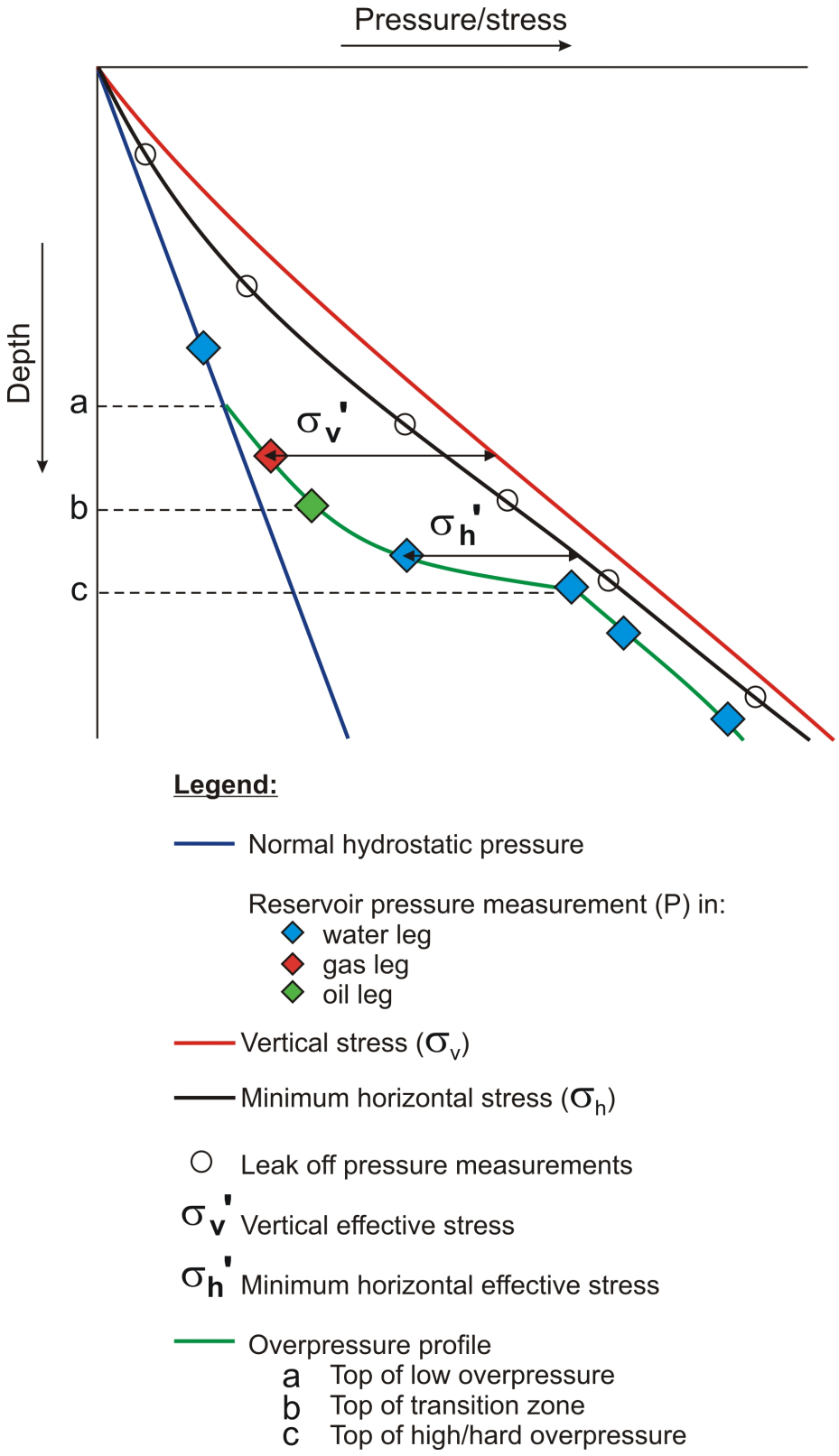

Figure 3.1 Typical pressure/stress – depth profile commonly encountered in a sedimentary basin.

$$P = \rho_w g z$$
or in terms of gradient : (3.1)
$$\frac{dP}{dz} = \rho_w g$$

where P = fluid pressure or pore pressure, ρ_w = density of water, g = gravitational acceleration, and z = depth below a certain datum,. For fresh water with the gradient of 1 g/cc, the hydrostatic gradient is 0.433 psi/ft.

The pore pressures are measured by down-hole pressure instruments such as the repeat formation tester (RFT), the modular dynamic tester (MDT), and the formation interval tester (FIT), or they can be measured during production tests such as the drill stem test (DST). The RFT and MDT are newer technology than the FIT, and they provide high quality pressure data provided that the seal against the borehole wall is effective and the formation is not too tight. In Figure 3.1, the pressure measurements are symbolized by diamonds: blue for measurements in the water leg, red for measurements in the gas leg, and green for measurements in the oil leg.

Vertical stress

The red line in Figure 3.1 is the depth profile of the vertical stress which is defined as the stress acting in the vertical direction. In many basins, where the surface topography is not severe, the vertical stress is essentially due to the weight of the overlying sediments, or overburden, and may be assumed to be a principal stress. It follows that the other two principal stresses must lie in the horizontal plane. The vertical stress is also known as overburden stress or lithostatic stress, and it is calculated by using the equation:

$$\sigma_v = \rho_b g z$$
or in terms of gradient : (3.2)
$$\frac{d\sigma_v}{dz} = \rho_b g$$

where σ_v = vertical stress, ρ_b = bulk density of sediment, and z = depth below a certain datum. A density value of 2.3 g/cm^3 , which is a typical average sediment density from the surface down to around 2 km depth, gives a vertical stress gradient of 1 psi/ft.

Minimum horizontal stress

The black line in Figure 3.1 is the depth profile of the minimum horizontal stress. The minimum horizontal stress is usually obtained from a leak-off test (LOT). White et al. (2002) analysed several pressure values resulting from an LOT test and how best to estimate the minimum horizontal stress. The schematic of the result of the LOT test is shown in Figure 3.2. In performing an LOT, the wellbore pressure is increased gradually by pumping the drilling fluid down the well. The leak-off pressure (LOP) is assigned when there is a departure from the linear relationship between pressure and the volume of the pumped mud. This inflexion is an indicator that the limit of rock elasticity has reached. Hydraulic fractures start to develop at this stage, and the volume of the pumped mud in the borehole will increase compared to the previous stage, as the mud can escape into the fractures. At a certain point, the formation breakdown will be reached (FBP in Figure 3.2), and the fractures will propagate and the pressure in the wellbore will be relatively constant since the mud can escape to the propagated fractures. The pump will be turned off after the fractures have propagated, allowing the wellbore pressure to decrease.

The initial decline of the pressure after the pump has turned off is identified as the instantaneous shut-in pressure (ISIP). The pressure inside the wellbore continues to decrease and the fractures will close again. The fracture closure pressure (FCP) is determined by the 'double tangent' method, i.e. the cross-point between the ISIP line and the stabilised pressure line (point E in Figure 3.2). The LOT can be extended as an XLOT (extended leak-off test). The purpose of the XLOT is to remove all the effects of the rock tensile strength so that the minimum horizontal stress can be determined accurately.

White et al. (2002) stated that ISIP and FCP are the better estimates of the minimum horizontal stress than the LOP, because the LOP is affected by stress perturbation and the hoop stress surrounding the wellbore when inducing or opening a fracture (Inglis, 1913).

Another test that can give an estimate of fracture pressure is the formation integrity test (FIT). The procedures are similar to the LOT, except that the fluid pressure is increased up to a pre-determined value instead of being increased up to leak-off (Figure 3.2). The pre-determined value corresponds to the mudweight pressure planned for continued drilling of the well. Thus the FIT value is a minimum estimate of the leak-off pressure, and of the minimum horizontal stress: the LOP will not be less than the FIT value.

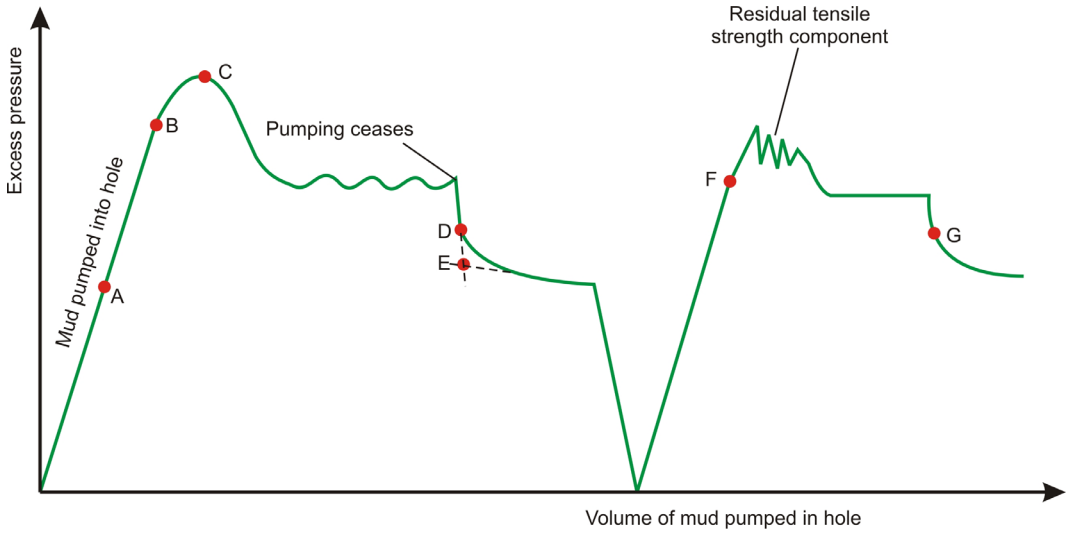

A: Formation integrity test (FIT)
B: Leak-off pressure (LOP)
C: Formation breakdown pressure (FBP)
D: Instantaneous shut-in pressure (ISIP)
E: Fracture closure pressure (FCP)
F: Fracture re-opening pressure (Pr)
G: Second shut-in pressure (SSIP)

Figure 3.2 A schematic of an XLOT test (modified from White et al., 2002).

Effective stress

The difference between vertical stress and pore pressure is defined as the vertical effective stress (Terzaghi and Peck, 1967):

$$\sigma_V' = \sigma_v - P \tag{3.3}$$

Similarly, the principal stresses in the horizontal plane are defined as the differences between the maximum and minimum horizontal stresses and the pore pressure. For the minimum horizontal stress, σ_h, the minimum horizontal effective stress is

$$\sigma_h' = \sigma_h - P \tag{3.4}$$

Unlike pore pressure and vertical stress, vertical effective stress cannot be measured, but is simply obtained by subtracting the pore pressure from the vertical stress. Physically, the effective stress is the stress that is borne by grain-to-grain contacts. The remainder of the vertical stress, which equals the pore pressure as shown by Equation 3.3, is borne by the pore fluid.

Overpressure

By definition, overpressure at any point is the pore pressure excess over the normal hydrostatic pressure. In Figure 3.1, overpressure is present below point ‘a’, which is the depth of the top of overpressure. The green line is the pore pressure profile obtained by interpolation of measured pressure values. The overpressure at any depth is the difference between the pore pressure (green line) and the normal hydrostatic pressure (blue line).

When the overpressure is much smaller than the vertical effective stress, the overpressure is said to be ‘low’, and when it approaches the vertical effective stress, it is said to be ‘high’ or, especially by drilling engineers, ‘hard’. In Figure 3.1, the interval a–b is an interval of low overpressure, the interval b–c is a transition zone, and the interval below point ‘c’ is a zone of high overpressure.

The reservoir is said to be underpressured if its pore pressure is lower than the normal hydrostatic pressure. Underpressure can be caused by reservoir depletion during hydrocarbon production, or by natural phenomena such as in a relatively isolated sand bodies from the recharge area compared to the discharge area (Figure 3.3), in the absence of any overpressure generating mechanisms, for example in the Denver Basin (Belitz and Bredehoeft, 1988).

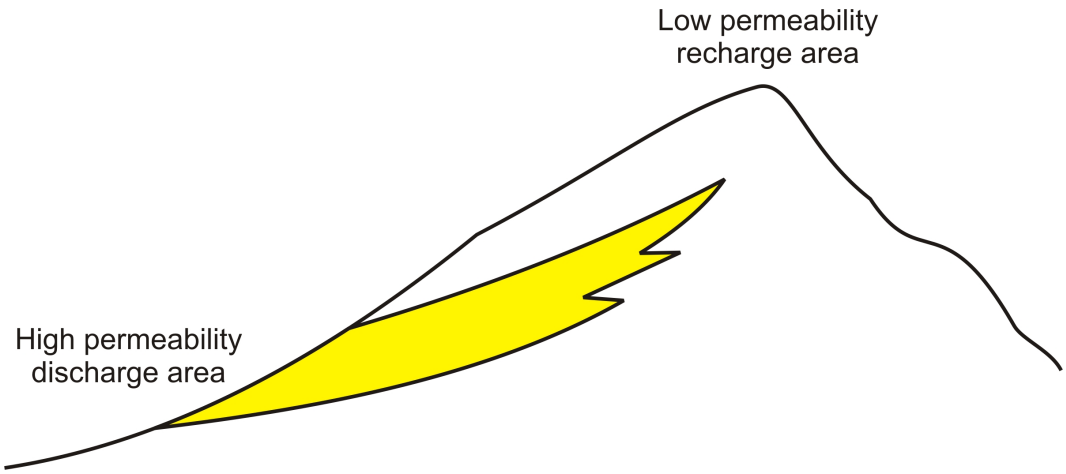

Figure 3.3 Underpressuring due to reservoir isolation from recharge area (modified from Swarbrick and Osborne, 1998).

3.2 Overpressure generating mechanisms

Reviews of overpressure generating mechanisms have been given by Swarbrick et al. (2002), Bowers (2001), Katahara (2006), and Tingay et al. (2009). The mechanisms that are capable of generating high magnitudes of overpressure may be classified as loading mechanisms, in which one or more of the principal stresses acting on the sediment are increased, and unloading mechanisms that involve a decrease in effective stress. Only small magnitudes of overpressure can be generated by hydrocarbon buoyancy, hydraulic head and osmosis. Overpressure is a transient phenomenon because pore fluid flows in the direction of negative overpressure gradient. The redistribution of fluid from overpressured

zones may cause an increase of overpressure in other regions that previously had lower overpressure or normal hydrostatic pressure. Descriptions of each mechanism are given in the following sub-sections.

3.2.1 Loading mechanisms

Disequilibrium compaction

Sediment burial causes an increase in vertical stress, or gravitational loading, which can potentially generate overpressure by disequilibrium compaction. In the disequilibrium compaction process, overpressuring is a result of a competition between the rate of fluid escape and the rate of vertical compaction due to the increase in gravitational loading caused by ongoing sedimentation. For one-dimensional flow, the fluid velocity, *v*, relative to a rigid sediment framework is described by Darcy's equation:

$$v = -\frac{k\rho_w g}{\mu}\frac{d(OP)}{dz} \tag{3.5}$$

where k = permeability of sediment, ρ_w = density of water, g = gravitational acceleration, μ = viscosity of water, and $d(OP)/dz$ is the overpressure gradient.

Tectonic compression

An increase in lateral stress due to tectonic compression can give rise to overpressure, as for the disequilibrium compaction mechanism, caused by gravitational loading. Sediments can compact horizontally, as well as vertically. However, if the pore fluid is not allowed to escape, the pore pressure will increase and the sediments will compact less. Van Ruth et al. (2003) gave an example of the overpressuring due to the increase in lateral stress in Cooper-Eromanga Basin, Australia.

3.2.2 Unloading mechanisms

Unloading mechanisms can generate high overpressures via processes that transfer load from grain-to-grain contacts to the pore fluid (Swarbrick et al., 2002). An influx of pore fluid or conversion of solid matrix material into fluids will automatically increase the pore pressure, if the pore fluid cannot escape from the system. If load-bearing grains are partly transformed into fluid, then some of the stress that was previously carried by the grain-to-grain contacts is transferred to the fluid, resulting in increase in pore pressure (Figure 3.4). Both mechanisms will cause decrease in effective stress. By contrast, the loading mechanisms do not cause the effective stress to decrease but simply prevent the sediments from compacting.

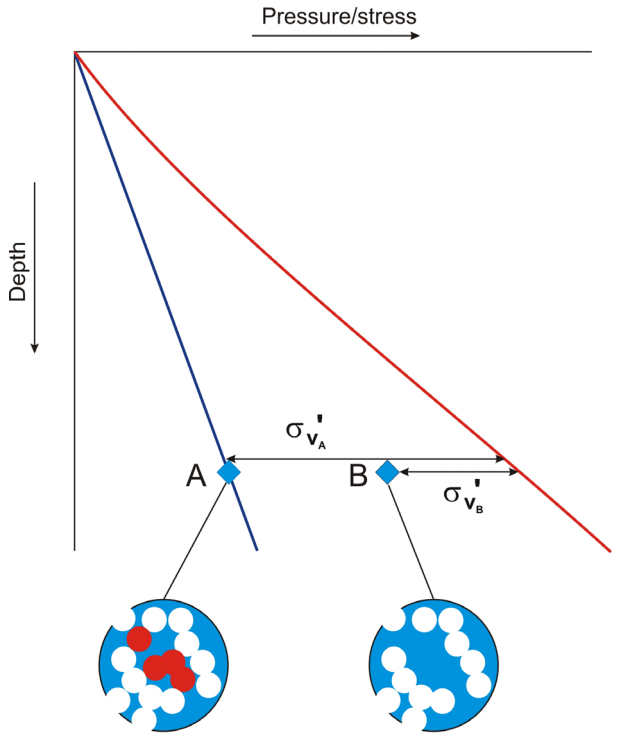

Figure 3.4 Schematic of overpressure generation due to load transfer from load-bearing grains (red) into pore fluid (e.g. due to transformation of load-bearing kerogen into oil and gas) (after Swarbrick and Osborne, 1998).

Among the geological processes causing unloading, either by increasing pore fluid volume of by transferring the load, are clay diagenetic processes such as smectite-illite transformation (e.g., Lahann, 2002), hydrocarbon generation (e.g., Swarbrick et al., 2002), and lateral or vertical transfer (Bowers, 2001; Flemings et al., 2002; Tingay et al., 2009). Other unloading mechanisms are aquathermal pressuring (Barker, 1972), and erosional/exhumation (Katahara and Corrigan, 2002). Each process is described below.

Clay diagenetic processes

Clay diagenetic processes include smectite–illite transformation, further illitization of mixed-layer illite/smectite, and kaolinitization of illite. The clay diagenetic process cause overpressure in two ways: expansion of pore fluid and load transfer.

The clay diagenetic processes are strongly dependent on temperature. Smectite–illite transformation, for which the reaction is (Boles and Franks, 1979):

$$\text{smectite} + K^{+} \rightarrow \text{illite} + \text{silica} + H_2O$$

causes the disappearance of discrete smectite at temperatures around 80°C (Hower et al., 1976; Boles and Franks, 1979). It is very clear from the chemical reaction above that the transformation produces some water. The reaction also causes load transfer from the smectite to the pore water because the smectite is a load-bearing material. Swarbrick et al. (2002) investigated the transformation reaction, and they found the maximum possible volume increase is about 4.1%. Concerning the small volume increase, they concluded that this reaction is a minor contributor to overpressure development. However, they did not account for the overpressure caused by the load transfer. Lahann (2002) and Katahara (2006) pointed out the importance of load transfer as the mechanism that creates high overpressures as a result of smectite–illite transformation.

Illitization of mixed-layer illite/smectite is ongoing at temperatures greater than 80°C (Hower et al., 1976; Boles and Franks, 1979). To date, there is no known minimum temperature limit for the complete illitization of mixed-layer

illite/smectite. The reaction releases free water previously contained in the smectite layers as bound water. The process thus results in ovepressuring in the same manner as for smectite–illite transformation.

Kaolinite transforms to illite at temperatures around 130–140°C (Bjørlykke, 1998). The transformation contributes to overpressure both by release of free water from the reaction and by transferring load from grains to pore fluid as mineral grains are dissolved (Bjørlykke and Hoeg, 1997).

Hydrocarbon generation

Hydrocarbon generation involves two processes: transformation of kerogen containing in the source rock into oil or gas, and cracking of oil into gas (e.g., Swarbrick et al., 2002). The transformation of kerogen into gas may contribute to overpressure through two processes, expansion of pore fluid and transfer of any load that was previously borne by kerogen on to the pore fluid. Oil cracking only contributes to overpressure through expansion of pore fluid.

Swarbrick et al. (2002) stated that the increase of fluid volume could be as high as 75–140 % in the source rock, thus having the potential to create a high magnitude of overpressure. A recent numerical modelling study by Hansom and Lee (2005) showed that oil generation could produce overpressures as high as 6245 psi, while gas generation from oil cracking and kerogen transformation could produce overpressures as high as 11,020 psi. All the calculations above exclude the potential of the load-transfer process in generating the overpressure. Clearly, hydrocarbon generation can generate very high magnitudes of overpressure.

Aquathermal pressuring

The possibility that thermal expansion of pore water could contribute to overpressure was first pointed out by Barker (1972). If a volume of water is heated whilst being perfectly sealed, the pore pressure will increase along the line

of iso-density (Figure 3.5). For example, on heating a sealed body of water with density of 0.99 g/cm^3 from 54.4°C to 93.3°C, the pressure will increase by about 8000 psi.

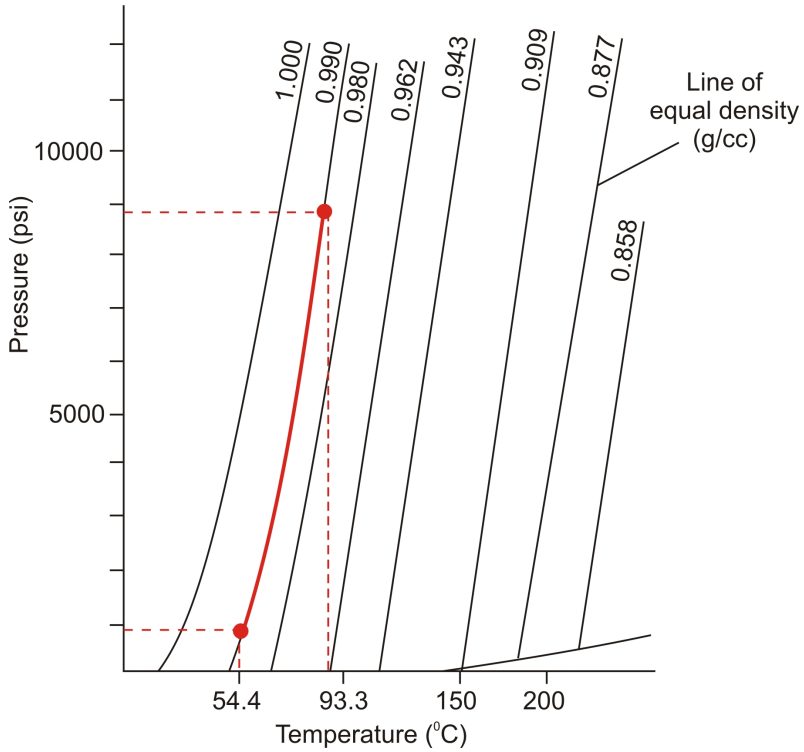

Figure 3.5 Effect of aquathermal pressuring on overpressure development (modified from Osborne and Swarbrick, 1997).

A condition that must be met for aquathermal pressuring to occur is that the pore fluid must be effectively sealed. In real sedimentary basins, there is no perfectly closed system since there is no rock of zero permeability. Once the system starts to leak, the effect of aquathermal pressuring is negligible, as shown by Luo and Vasseur (1992) in a numerical modelling study and by Swarbrick et al. (2002) for a simple numerical example. Aquathermal pressuring may contribute to overpressuring at great depths in sedimentary basins. For depths of interest for hydrocarbon production, down to maximum depths of 5–6 km, aquathermal pressuring cannot contribute significantly to overpressure generation.

Erosional/Exhumation

The effect of erosion on overpressure was investigated by Katahara and Corrigan (2002). If the overburden is removed from a sediment pile, then it will be accompanied by a change in pore pressure due to the poroelastic response (Biot, 1941):

$$\Delta P = B\Delta S_v \tag{3.6}$$

where B is known as Skempton's coefficient. The value of B depends on rock and fluid properties, especially their compressibility. Katahara and Corrigan (2002) pointed out that if the fluid is water, the net effect of the erosional unloading is underpressure because of the low compressibility of water. Conversely, if the fluid is gas, the net effect is overpressure because of its relatively high compressibility value. Katahara and Corrigan (2002) also noted the importance of low permeability seal for the above condition occur. In case of a high permeability seal, the erosion will not build up the gas pressure.

3.2.3 Other minor processes

Hydrocarbon buoyancy

If a reservoir contains hydrocarbons, then there will be some overpressure developed due to the difference in fluid density between the hydrocarbon and pore water (Figure 3.6). The amount of the overpressure generated by buoyancy depends on the difference in density between pore water and hydrocarbon:

$$\Delta P = \left(\rho_w - \rho_{HC}\right)gh \tag{3.7}$$

where ΔP is overpressure, ρ_{HC} is hydrocarbon density, ρ_w is water density, and h is hydrocarbon column height.

Swarbrick et al. (2002) gave an illustrative example of an oil column 1.0 km high with oil of 39°API. The maximum overpressure due to buoyancy at the top of the column is around 290 psi. If the oil were to be replaced by gas, the

overpressure would be around 1090 psi at the top of gas column. A hydrocarbon column 1 km high would be an extreme case, so the effect of hydrocarbon buoyancy is generally only to contribute minor amounts of overpressure.

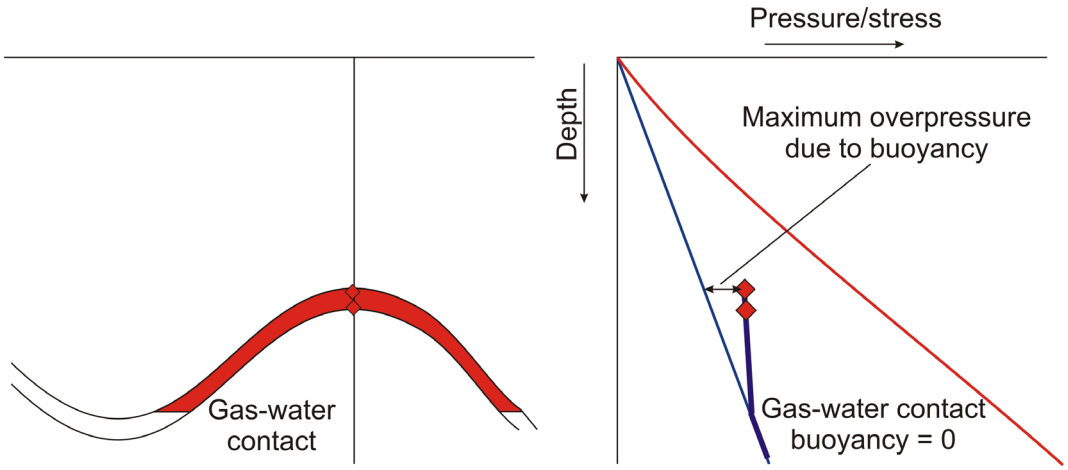

Figure 3.6 Overpressure due to gas buoyancy where the pore water in the water-saturated reservoir is at normal hydrostatic pressure. The maximum overpressure is located in the crest of the structure, while the overpressure due to buoyancy is zero at the gas-water contact.

Hydraulic head

If a reservoir crops out in a high elevation area, then it will have the potential to create overpressure. Assuming that the reservoir is fully water-saturated up to an elevation H above sea level, the hydraulic head is also H, and the corresponding overpressure is $\rho_w gH$ in the static case with no water flow (Figure 3.7). The magnitude of overpressure could be assessed given the elevation of the water table in the reservoir, its permeability, the fluid density and flow velocity (e.g., Bachu and Underschultz, 1995). As an illustrative example, 3.0 km of structural relief for the outcropping reservoir can generate a maximum overpressure of 4350 psi (Swarbrick et al., 2002).

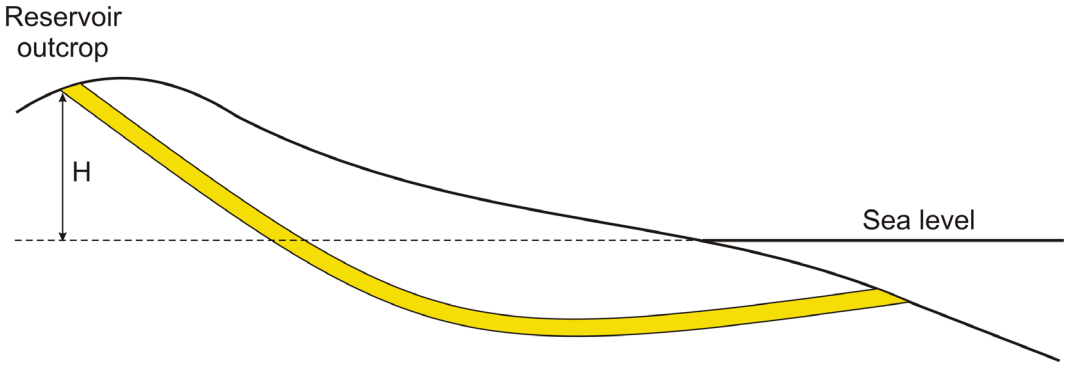

Figure 3.7 Overpressure due to hydraulic head. The maximum head, *H*, due to this mechanism is equal to the elevation of the reservoir at outcrop, and the corresponding overpressure is $\rho_w gH$.

Osmosis

Osmosis is flow of water through a semipermeable membrane due to salinity difference. In the case of sand-mudrock interbeds, the mudrock is the membrane, and the water will flow from higher salinity to lower salinity reservoirs passing the mudrock (Figure 3.8). To be able to create a high magnitude of overpressure, a continuous source of more saline water to the reservoir is required, which is unlikely to be the case. Moreover, Osborne and Swarbrick (1997) pointed out that the porosity of the mudrocks is too high to act as a perfect membrane, so the potential of this process to cause a high magnitude of overpressure is negligible. Their calculation for the typical North Sea mudrocks shows that the maximum overpressure that could be generated through this process is about 435 psi.

3.3 Transient overpressure phenomenon

Overpressure is a transient phenomenon. It will dissipate through time if all overpressure-generating mechanisms become inactive. An example of pressure dissipation is shown in Figure 3.9. In that figure, the shallower section is normally pressured, while the deeper section is overpressured. The overpressure will

dissipate towards the normally pressured section, and it will result in a pressure transition zone at the top of the mudrock dominated sequence in Figure 3.9. The shape of the transition zone depends on the permeability of the sediment and the timing of overpressure generation (Swarbrick, 1997), amongst other factors. For example, a very sharp transition zone suggests a very low permeability in the sediments crossed by the transition zone, while a very broad transition zone can result if overpressure has developed only recently.

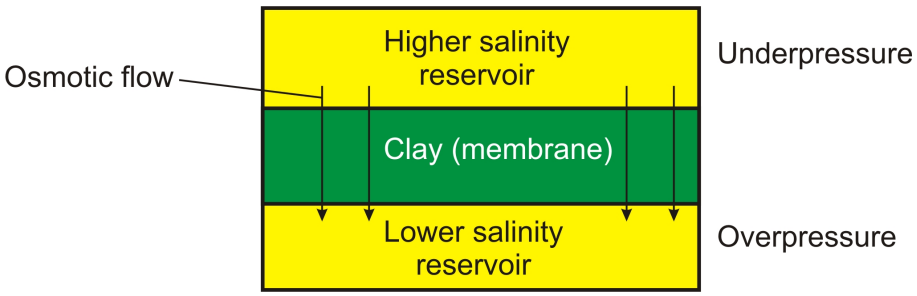

Figure 3.8 Illustration showing overpressure caused by osmotic flow through clay membrane (modified from Swarbrick and Osborne, 1998).

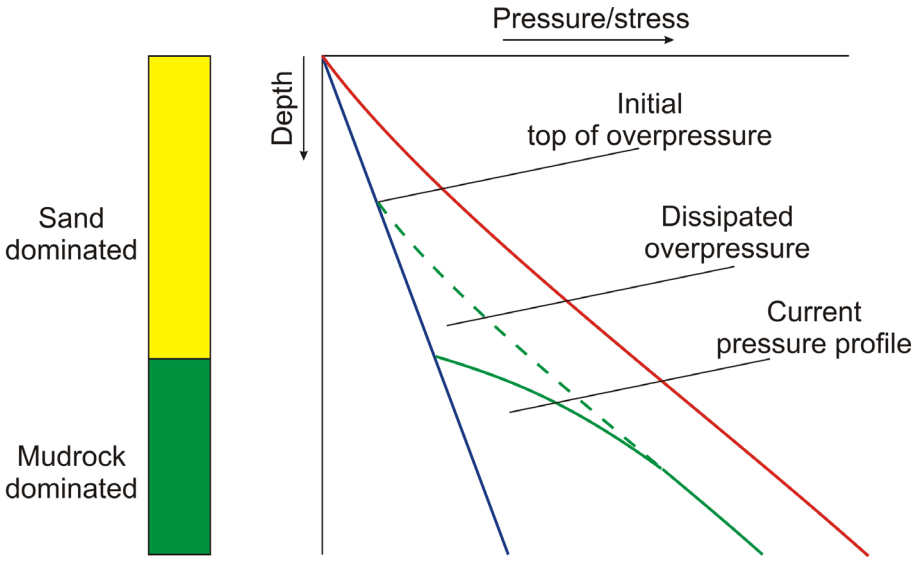

Figure 3.9 Illustration showing overpressure dissipation through a more permeable sequence.

Another mechanism of overpressure generation may occur when a tilted sand body is encased in a mudrock sequence (Figure 3.10). This phenomenon is better known as the centroid effect (Traugott, 1996). The pore pressure–depth profile through the permeable sand body will be hydrostat-parallel. At the base of the sand body, fluid will flow from the adjacent mudrock into the sand body, and the local pressure in the sand body will be less than in the adjacent mudrocks. At the top of the sand body, the pressure differential is reversed, and fluid flows out of the sand into the mudrock. The centroid phenomenon is very well documented in Eugene Island, Gulf of Mexico (Flemings et al., 2002; Bowers, 2001).

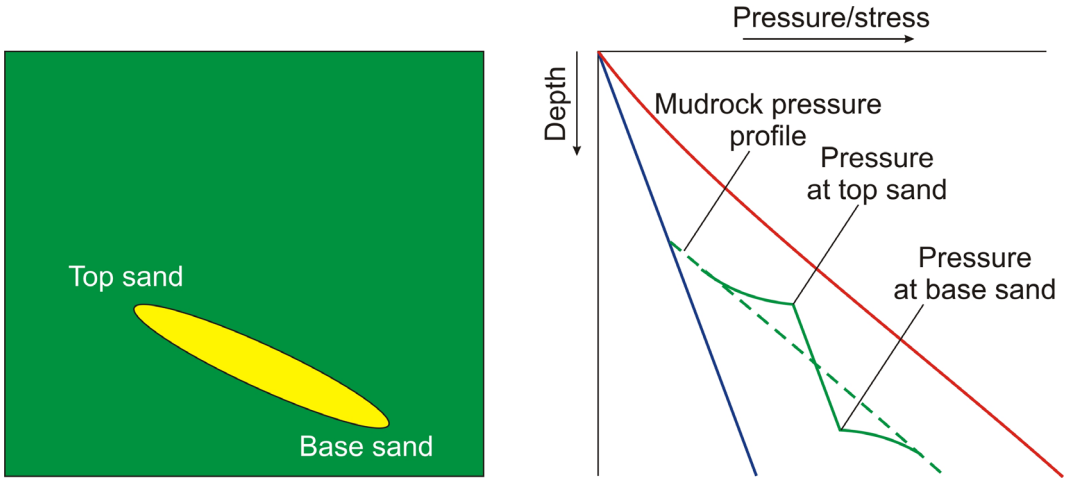

Figure 3.10 Illustration showing 'centroid' effect which causes the pore pressure in the sand to be lower and higher than the regional pore pressure in the mudrock at the base and top of the sand body, respectively.

Tingay et al. (2009) recently investigated overpressuring in the Baram Delta, Brunei. They found that in some areas, overpressure has resulted from vertical transfer of overpressure upwards along faults.

Another important overpressure transfer phenomenon is regional overpressure transfer as observed in the North Sea area (Dennis et al., 2000) (Figure 3.11) and in the Lower Kutai Basin (Grosjean et al., 1994; Lambert et al., 2003; (Figure 1.5). O'Connor and Swarbrick (2008) coined the term 'lateral

reservoir drainage' for this phenomenon. Lateral reservoir drainage causes tilted hydrocarbon-water contacts, as discussed in Sub-section 3.1.5.

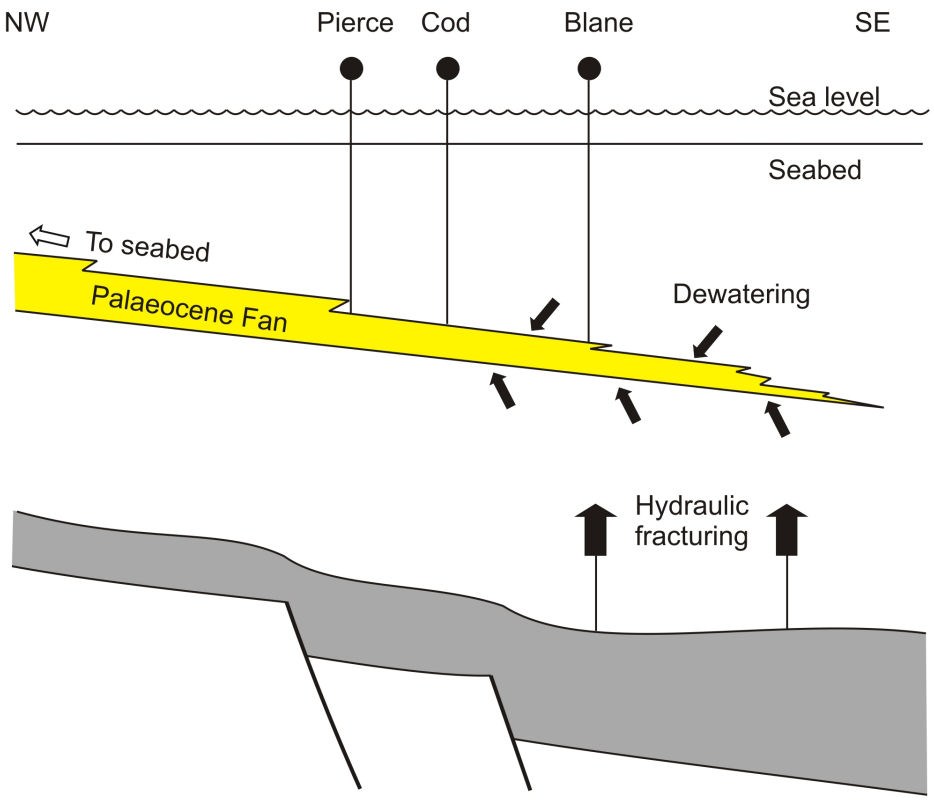

Figure 3.11 Lateral reservoir drainage causing overpressure bleed-off in the Palaeocene fan sandstones of the Central Graben, North Sea (simplified from Dennis et al., 2000).

3.4 Worldwide examples of overpressuring

Worldwide overpressure occurrences are shown in Figure 3.12. Overpressure is present in almost every geological environment and in strata of all ages. In a young geological environment experiencing rapid burial, overpressure is commonly thought to be caused by disequilibrium compaction. Among the many examples are the US Gulf Coast region (Dickinson, 1953; Pennebaker, 1968; Reynolds, 1970), the Lower Kutai Basin (Bois et al., 1994; Bates, 1996; Burrus,

1998), and the prodelta sequence of the Baram Delta (Tingay et al., 2009). As stated in Chapter 1, the hypothesis that overpressure in the Lower Kutai Basin is due to gravitational loading, leading to disequilibrium compaction, will be tested in this research. In a relatively old sedimentary basin, such as the Cooper-Eromanga Basin, South Australia, van Ruth et al. (2003) concluded that lateral stress plays an important role in overpressuring in that basin.

Several researchers have also stressed the importance of the unloading mechanisms of gas generation and clay diagenesis, and also by pressure transfer in relatively young sedimentary sequences. Some examples of basins where these mechanisms have been shown to be active are Haltenbanken and the Northern North Sea (Hermanrud et al., 1998; Teige et al., 1999, 2007), the Eugene Island area of the Gulf of Mexico (Flemings et al., 2002; Bowers, 2001), and the inner shelf of the Baram Delta (Tingay et al., 2009).

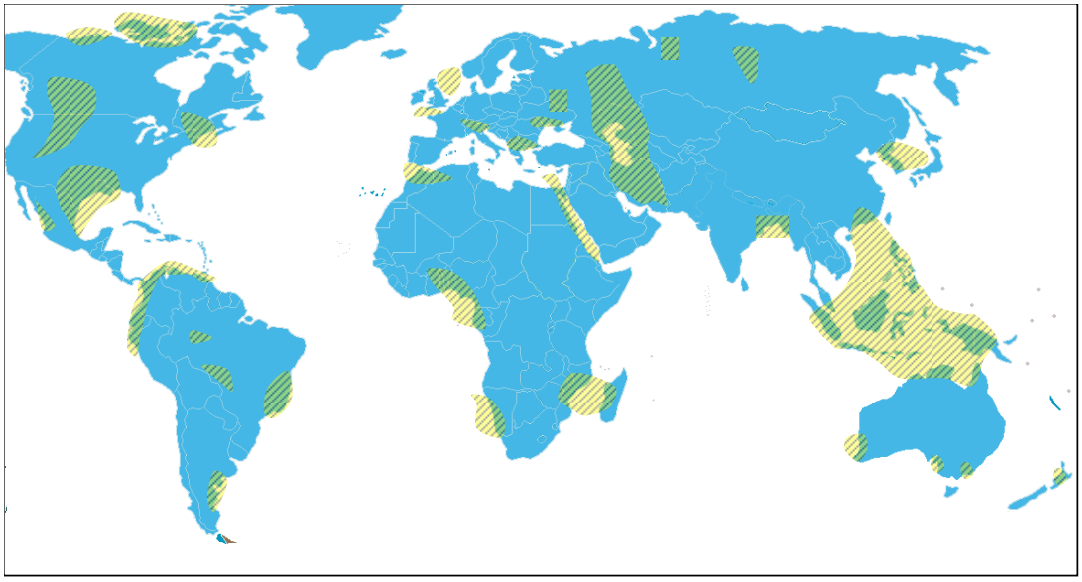

Figure 3.12 Worldwide occurrences of overpressure (shaded areas) (after Mouchet and Mitchell, 1989).

3.5 Overpressure characteristics

3.5.1 Disequilibrium compaction characteristics

Disequilibrium compaction occurs when a mudrock cannot dewater fast enough for the pore fluid to remain in hydrostatic equilibrium as it compacts under increasing vertical and/or lateral stress. Consequently, the mudrock becomes overpressured and its porosity is greater than it would be if the pore pressure were hydrostatic. The circumstances illustrated in Figure 3.13, showing constant porosity and pore pressure parallel to the lithostatic stress below the top of overpressure, are predicated on a series of simplistic assumptions: uniform lithology, no fluid escape, no change in temperature, no diagenesis, and some non-physical behaviour of fluid and mineral compressibility. Nevertheless, these circumstances are commonly approximated in young mudrock successions undergoing rapid burial in sedimentary basins, and are generally considered to be diagnostic of disequilibrium compaction (e.g. Swarbrick et al., 2002).

In wireline logs, the constant porosity resulting from disequilibrium compaction will be evidenced by constant density (density log), constant transit time (sonic log), and constant resistivity (resistivity log). It is important to note that all the wireline log responses above are for mudrock sequences. Therefore, it is necessary to discriminate mudrock from sandstone prior to analysing the wireline log responses. The way this discrimination is done is described in Section 4.2.

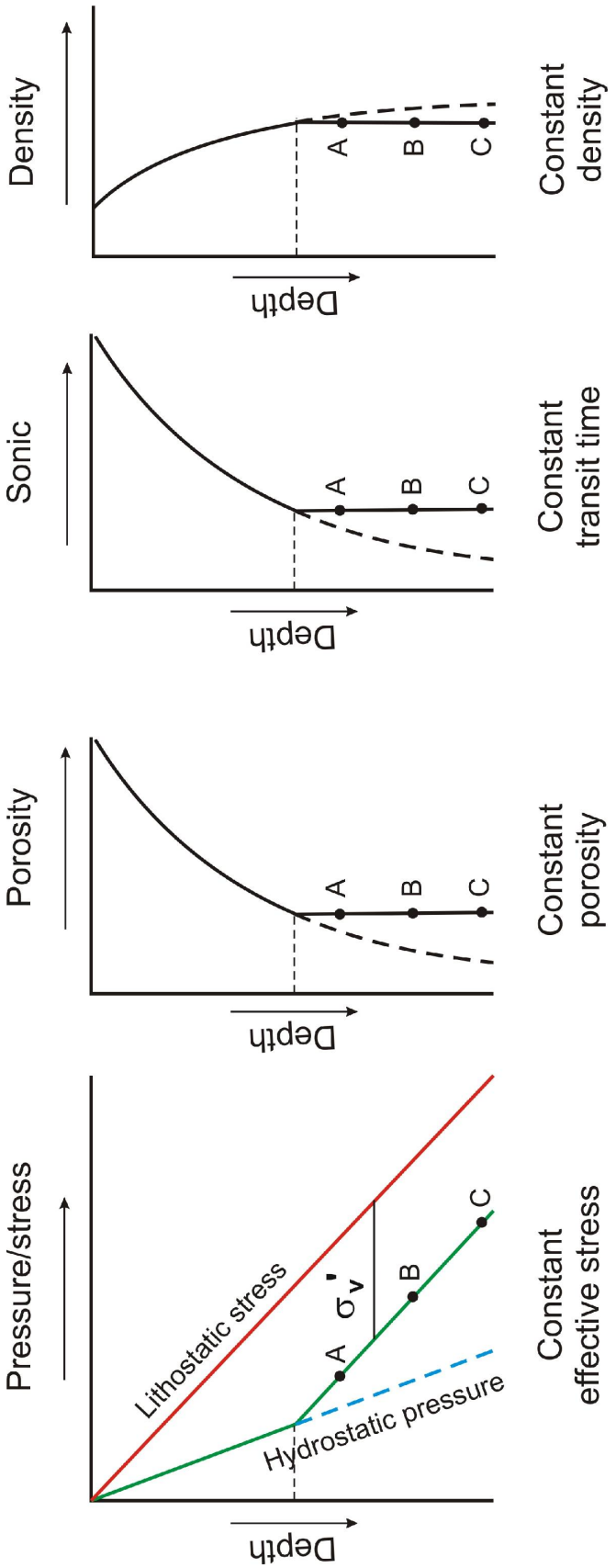

Figure3.13 Cartoon to show the pressure-depth profile and wireline log responses anticipated where overpressure is due to disequilibrium compaction.

3.5.2 Unloading characteristics

At depths where unloading mechanisms of overpressure generation first become active in mudrocks, the density usually continues to increase while the sonic log trend reverses, moving towards higher sonic travel time with increasing depth. The resistivity log trend also reverses, moving towards lower resistivity with increasing depth. The density may reverse a little bit at the bottom of the section, if the pore pressure approaches lithostatic pressure, due to the opening of the microcracks. All these wireline log responses are illustrated schematically in Figure 3.14.

These responses can be explained by the concept of storage pores and connecting pores (Bowers and Katsube, 2002) (Figure 3.15). The storage pores are the biggest contributor to the total bulk porosity of a mudrock, while the connecting pores are only a very minor contributor. Where pore pressure in a mudrock increases due to fluid expansion, the unloading response is essentially elastic opening of the connecting pores, and results in only a very small increase in porosity. Because the density log measures the bulk porosity of the mudrock (e.g., Hermanrud et al., 1998), it is barely affected by the fluid expansion. The increase in porosity that does occur during fluid expansion is predominately due to the opening of flat connecting pores because they are more compliant than the storage pores. The connecting pores have low aspect ratio and therefore they are mechanically flexible. Conversely, the storage pores have high aspect ratio and therefore they are mechanically stiff and barely affected by the unloading. The connecting pores affect the transport properties, sonic velocity and electrical conductivity, and so their opening affects sonic and resistivity logs but has negligible effect on density and neutron logs (Hermanrud et al., 1998). Therefore, we may expect to see log responses as shown in Figure 3.14.

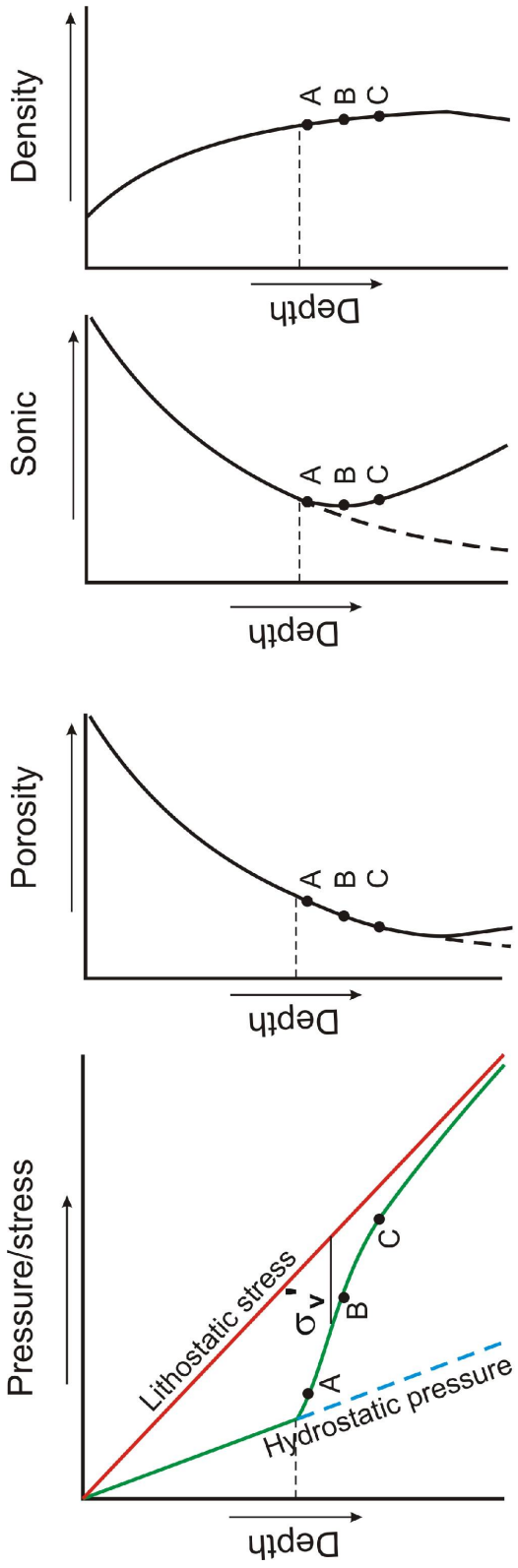

Figure 3.14 Cartoon to show the pressure-depth profile and wireline log responses anticipated where overpressure is due to unloading.

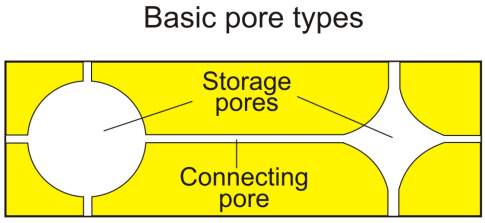

Pore shape	Aspect ratio	Elastic rebound capacity
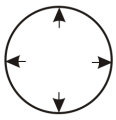	> 0.1	Poor
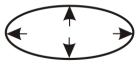	0.001 - 0.1	Good
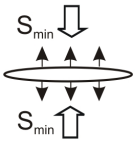	< 0.001	If P < S_{min}: poor If P = S_{min}: good

Figure 3.15 Properties of storage and connecting pores (after Bowers and Katsube, 2002).

3.6 Overpressure estimation methods

In Section 3.5 the wireline log responses to overpressure were described. Departures of the wireline logs from normal compaction trends are indicators of overpressure, either caused by disequilibrium compaction or unloading mechanisms. These departures are key for overpressure estimation from wireline logs.

There are two empirical methods widespread used for estimating overpressure in mudrocks. The first is Eaton's ratio method (Eaton, 1975). The second method is the effective stress method. Both methods stress the importance of the normal compaction trends (NCTs) for the mudrock. Prior to discussing the overpressure estimation method, an overview of mudrock compaction will be given first.

3.6.1 Overview of mudrock compaction

Mudrock compaction may be defined as porosity loss through burial depth. The first and also the most cited empirical relationship between porosity and depth of mudrock sequence was introduced by Athy (1930):

$$\Phi = \Phi_0 e^{-bz} \tag{3.8}$$

where Φ is porosity at any given depth, z, Φ_0 is surface porosity, e is the base for Napierian logarithms, and b is an empirical constant obtained by fitting this exponential-decay function to the porosity–depth data values. Rubey and Hubbert (1959), by expanding Athy's relation, stated that the porosity reduction depends on the vertical effective stress:

$$\Phi = \Phi_0 e^{-\frac{c}{(\rho_b - \rho_w)}\sigma'} \tag{3.9}$$

where c is an empirical constant, ρ_b is bulk density of sediments, ρ_w is water density, and σ_v' is vertical effective stress. The idea behind this equation is to eliminate the effect of high porosity data points, due to overpressure generated by disequilibrium compaction, on Equation 3.8. As explained earlier (Figure 3.13), the disequilibrium compaction overpressure points will cluster in a certain region in porosity-vertical effective stress line, so that it will not affect the functional relationship of Equation 3.9.

Equations 3.8 and 3.9 describe the exponential decay of porosity with increasing burial depth and vertical effective stress, respectively. When porosity is lost purely due to the increase in the principal effective stresses acting on the sediment, the process is termed as mechanical compaction. Mechanical compaction is mainly an irreversible plastic process, with a much smaller elastic component. The exponential decay of porosity with depth, or vertical effective stress, shows that the sediment becomes more resistant to compaction as the porosity decreases and the area of the grain contacts increases.

In contrast to the mudrocks, compaction in sandstones is characterised by a linear porosity reduction with depth (Magara, 1980), which indicates that

sandstone compaction is less affected by the imposed stresses and more affected by chemical and mineralogical agents, such as mineral dissolution and cement precipitation, which are strongly influenced by temperature.

Equations 3.8 and 3.9 are empirical relationships, which may be fitted to mudrock data, that may be describing mechanical compaction, chemical compaction, or a combination of both. Also, there is no reason to suppose that one simple exponential decay function correctly describes the compaction behaviour over a large depth interval, especially when extrapolated beyond the ranges of depth or vertical effective stress for which they were derived.

Recently, several researchers have stressed the importance of chemical compaction in mudrocks. Bjørlykke (1998) argued that, at depth, the dominant process affecting mudrock compaction is chemical compaction caused by dissolution and precipitation of minerals, as in sandstones (Figure 3.16). Chemical compaction is little affected by the imposed stresses, provided that the principal effective stresses are all compressive, and is highly temperature-dependent. The main chemical compaction processes in mudrocks are the transformation of smectite to mixed-layer illite/smectite, illitization of mixed-layer illite/smectite, transformation of kaolinite to illite, and quartz dissolution and reprecipitation.

Mondol et al. (2007) performed laboratory experiments to investigate the mechanical compaction of mudrocks. They used synthetic mixtures of brine-saturated smectite and brine-saturated illite for investigation. Brine-saturated smectite is less compressible than brine-saturated illite and therefore it experiences less mechanical compaction. For the composition of 20% smectite and 80% illite, the experiments showed that below 2 km depth compaction in the laboratory does not reproduce the published porosity–depth profiles in mudrocks (Figure 3.17). They emphasised the importance of chemical compaction as the dominant process in porosity reduction below 2 km depth, as previously proposed by Bjørlykke (1998).

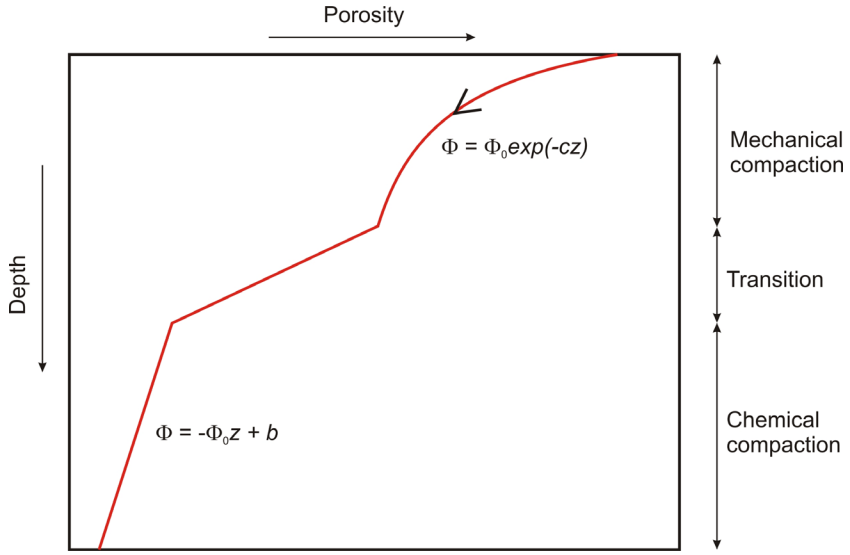

Figure 3.16 Bjorlykke's compaction model dividing compaction into two regimes: mechanical compaction and chemical compaction. The transition between the two regimes is marked by temperatures of around 70–100°C (Bjorlykke, 1998).

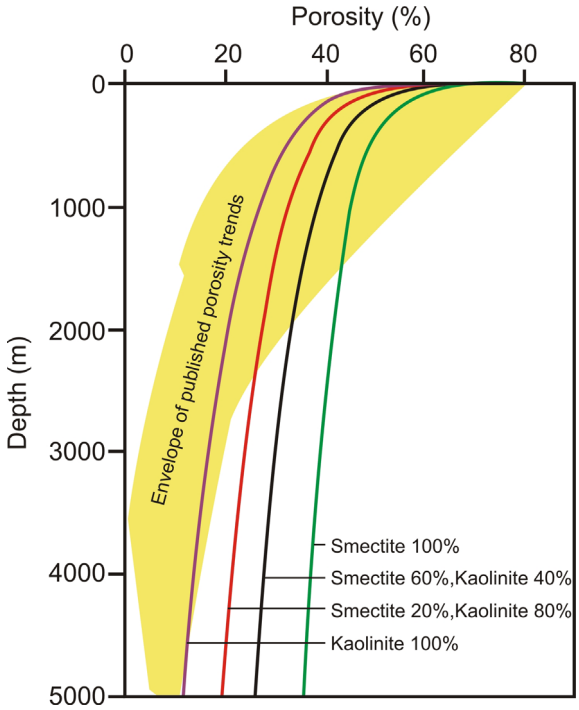

Figure 3.17 Comparison between published porosity trends with laboratory experiments in mechanically compacting synthetic mudrocks of different clay composition (modified from Mondol et al., 2007).

Recently, Thyberg et al. (2010) and Peltonen et al. (2009) have investigated the role of quartz precipitation in chemical compaction of mudrocks. They deduced that the quartz precipitation had mainly resulted from smectite-illite transformation, as described above. The quartz precipitation may also cause the rock framework to be stiffened, so that it becomes overcompacted in a mechanical sense.

3.6.2 Mudrock compaction from wireline data

Direct measurements of mudrock porosity on core samples are very rarely done, so NCTs such as those given by Equations 3.8 and 3.9 are fitted to wireline log data, such as density, sonic travel time (e.g., Issler, 1992), and resistivity (e.g., Magara, 1968). Of these wireline logs, the sonic log has been the most widely used as a proxy for porosity since it is commonly available with relatively high data quality, and it is less affected by bad hole conditions. There are three techniques for determining NCTs from the wireline logs: 1) direct use of the logs as plots of the chosen wireline parameter against depth; 2) plotting wireline parameter versus effective stress; and 3) cross-plotting wireline parameters.

3.6.2.1 Direct use of wireline logs

Sonic log

In early work on pore pressure prediction, several researchers (e.g. Hottman and Johnson, 1965; Jorden and Shirley, 1966; Magara, 1968) empirically fitted sonic velocity–depth profiles with an exponential equation, using linear regression on a semi-log plot, to describe the NCT:

$$\Delta t_n = \Delta t_0 e^{-bz} \tag{3.10}$$

where $\Delta t_n =$ transit time at NCT, $\Delta t_0 =$ transit time at surface, and $b =$ empirical constant obtained by fitting transit time versus depth. This NCT is termed as 2P-

NCT because the Equation 3.10 requires two constants to be determined, i.e. Δt_0 and b. Magara (1976a) also used Equation 3.10 to estimate the amount of erosion in Western Canada Basin.

Equation 3.10 was criticized by Chapman (1983) as being physically incorrect because it allows the transit time to approach zero at large depths (Figure 3.18). Whilst it is reasonable for the porosity to approach zero at depth, as implied by Equation 3.8, the sonic transit time should approach rock-matrix transit time at depth, not zero. In order to take this into account, Chapman (1983) proposed that the form of the sonic velocity–depth NCT should be:

$$\Delta t_n = (\Delta t_0 - \Delta t_m)e^{-bz} + \Delta t_m \qquad (3.11)$$

where Δt_m is the matrix transit time. In Equation 3.11, the transit time does approach the matrix transit time as the porosity approaches zero (Figure 3.18). This NCT is termed as 3P-NCT because Equation 3.11 requires three constants to be determined, i.e. Δt_0, Δt_m, and b.

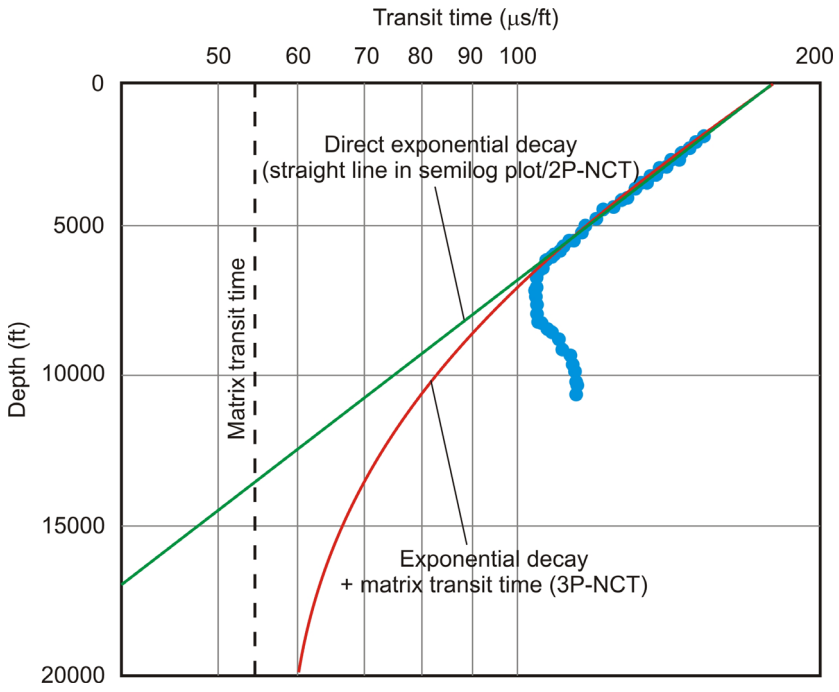

Figure 3.18 Comparison of normal compaction trends (NCTs) between direct exponential decay (2P-NCT) and exponential decay + matrix transit time (3P-NCT).

Whilst Equation 3.10 is clearly wrong, physically, in predicting sonic transit times less than matrix transit times below a certain depth, it is important to bear in mind that Equation 3.11 is still only an empirical relation. The transition in mudrocks from mechanical compaction into chemical compaction with increasing temperature, and therefore with depth, may be too complex to be described accurately with a single exponential-decay term.

Bell (2002) compared four empirical functional relationships between velocity and depth (NCTs) that are commonly used in seismic velocity analysis as well as in pore pressure analysis from seismic data. Each of the equations involves two parameters to be determined empirically. One of the functions he chose was Equation 3.10, which, as already suggested above, should be avoided as a physically impossible NCT at large depths. The others were a power law relationship, a linear relationship, and the square-root relationship, described in that order by the following equations:

$$v_n = v_0 + z^b \tag{3.12}$$

$$v_n = v_0 + bz \tag{3.13}$$

$$v_n = \sqrt{\left(v_0{}^2 + 4bz\right)} \tag{3.14}$$

where v_n is the velocity on the NCT, v_0 is the velocity at the surface velocity, b is a constant, and z is depth. Both v_0 and b are obtained empirically by fitting the velocity data against depth for each function.

Resistivity log

Similar to the sonic log, in early work on pore pressure prediction, several researchers (e.g. Hottman and Johnson, 1965; Magara, 1968) empirically fitted resistivity–depth profiles with an exponential equation, using linear regression on a semi-log plot, to describe the NCT. The equation is:

$$R_n = R_0 e^{bz} \tag{3.15}$$

where R_n = resistivity at NCT, R_0 = resistivity at surface, and b = empirical constant obtained by fitting transit time versus depth. In contrast to the sonic log, the normal resistivity will show exponential increase instead of exponential decay.

Similar to the direct exponential decay for the sonic log, the direct resistivity–depth equations are also physically wrong. In Equation 3.15, the resistivity will keep on increasing to infinity, whereas it should asymptotically approach the matrix resistivity at depth. An alternative equation to describe the NCT from the resistivity log with the same procedure as for the sonic log is:

$$\frac{1}{R_n} = \frac{(R_m - R_0)}{R_0 R_m} e^{-bz} + \frac{1}{R_m} \tag{3.16}$$

where R_n = resistivity on the NCT, R_m = matrix resistivity, and R_0 = resistivity at the surface.

Density log

Prior to constructing the NCT from the density log, the density log values are usually converted to the porosity with the equation:

$$\Phi = \frac{(\rho_m - \rho_b)}{(\rho_m - \rho_f)} \tag{3.17}$$

where ρ_m = matrix density. After the conversion, the NCT can be constructed by using Equation 3.8.

3.6.2.2 Sonic porosity versus effective stress

Work in soil mechanics has suggested that compaction of a mudrock should be analysed by relating vertical effective stress to the void ratio (Burland, 1990):

$$e = e_{100} - Cc \log\left(\frac{\sigma_v}{\sigma_{100}}\right)$$

or, with effective stress as the dependent variable: (3.18)

$$\sigma_v = \sigma_{100} \times 10^{\frac{e_{100} - e}{Cc}}$$

where e is the void ratio, $\Phi/(1-\Phi)$, σ_{100} is 100 kPa, e_{100} is the void ratio at 100 kPa vertical effective stress, and Cc is the compaction coefficient, determined by linear regression from a plot of e versus $\log\sigma_v$.

Clearly, porosity first needs to be obtained from the wireline log parameter. In using the sonic log, the porosity may be calculated by using the empirical relation of Issler (1992):

$$\Phi_s = 1 - \left(\frac{\Delta t_m}{\Delta t}\right)^{1/x} \tag{3.19}$$

where Φ_s is the sonic-derived porosity, Δt is the observed sonic transit time, and x is an empirical constant. Issler (1992) determined x to be 2.19 and Δt_m to be 220 μs/m for mudrocks in the Beaufort-Mackenzie Basin, Canada.

Bowers (1995) proposed an empirical NCT to relate sonic velocity directly to vertical effective stress for mudrocks, which is applicable to overpressured mudrocks as well as hydrostatically pressured mudrocks provided that the overpressure is due to disequilibrium compaction:

$$v = 5000 + a\sigma_v'^{\,b}$$

or, with effective stress as the dependent variable: (3.20)

$$\sigma_v' = \left(\frac{v - 5000}{a}\right)^{1/b}$$

where a and b are empirical constants obtained by linear regression after plotting $\log(v-5000)$ versus $\log\sigma_v'$, v is in ft/s, σ_v' is in psi, and 5000 ft/s is the assumed velocity in the mudrocks at the surface.

3.6.2.3 Cross-plots of wireline parameters

The NCT obtained from cross-plotting wireline parameters is not intended to be used directly for quantitative overpressure estimation, but it is important in analysing the cause of overpressure. The data located on the NCT are said to be normally compacted, including data points for mudrocks that are overpressured

due to disequilibrium compaction, while if they are located outside the NCT they are said to be unloaded.

Bowers (2001) proposed a sonic velocity–density cross-plot to investigate whether mudrocks are overpressured due to unloading mechanisms. In Figure 3.19, the two lines are the upper and lower bounds of the expected NCT relation between velocity and density. The upper bound is obtained from Gardner's velocity–density relation:

$$v = \left(\rho_b / 0.23 \right)^4 \tag{3.21}$$

For the lower bound, Bowers (2001) proposed

$$v = 4790 + 2953(\rho_b - 1.3)^{3.57} \tag{3.22}$$

where v is in ft/s and ρ_b is in g/cc.

Dutta (2002) plotted density versus sonic transit time to investigate compaction behaviour of mudrocks. He discriminated between two stages of mudrock compaction, eodiagenesis and telodiagenesis (Figure 3.19). Katahara (2006) adopted Dutta's compaction stages as smectitic compaction line for eodiagenesis and illitic compaction line for telodiagenesis. Similar to the Bowers' velocity–density relation, the data points on the compaction lines are interpreted as normally compacted, and data points off the compaction lines are interpreted as overpressured due to unloading mechanisms.

3.6.3 Overpressure estimation methods

There are two empirical methods that are commonly used in estimating the overpressure, i.e. Eaton's method (Eaton, 1975) and the effective stress method. A schematic diagram to compare these methods is shown in Figure 3.20. In Eaton's method, the wireline data (sonic and resistivity) are compared with the NCTs at the same depths (Figure 3.20). In contrast, the principle of the effective stress method is that the overpressured mudrock will have the same effective stress value as a mudrock on the normal compaction trend with the same porosity

(Figure 3.20). This is reasonable if the overpressuring is caused by disequilibrium compaction. Below are detailed description of both methods.

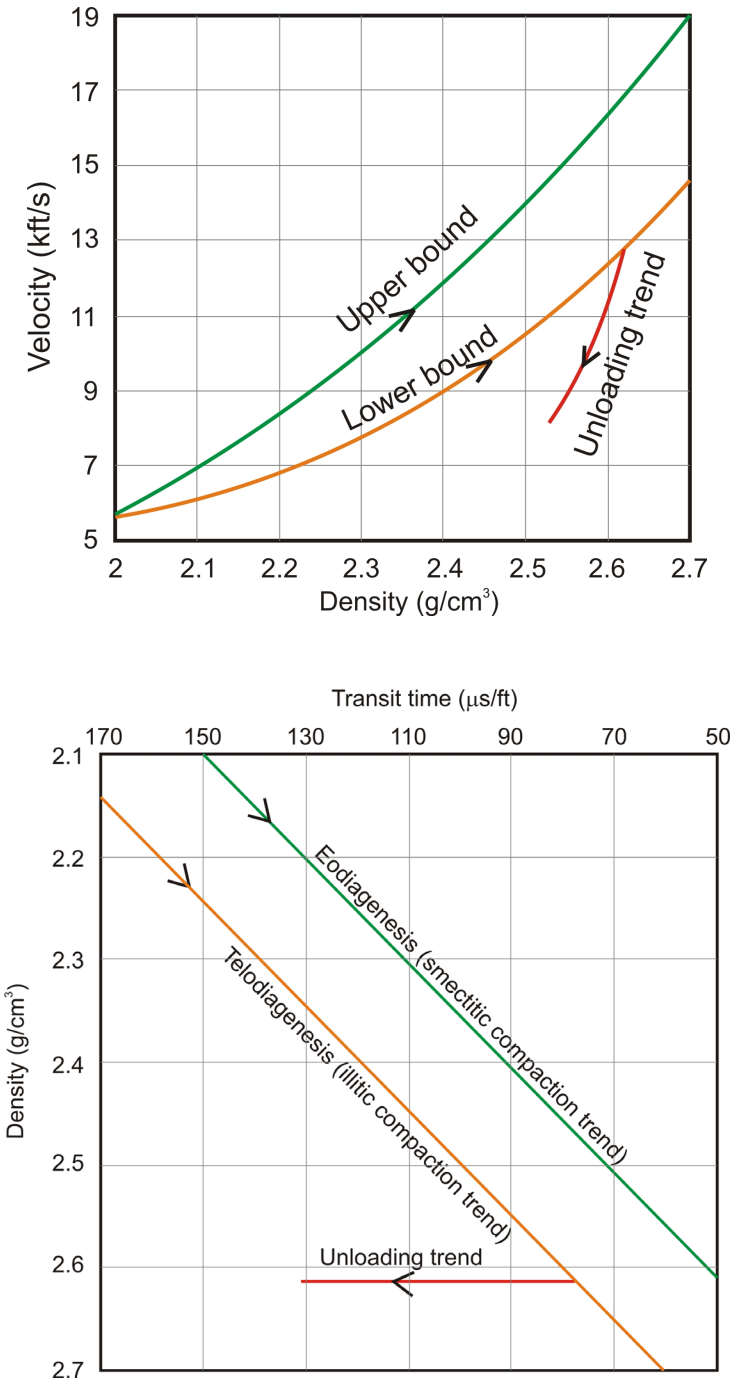

Figure 3.19 Upper panel: sonic velocity–density cross-plot as used by Bowers (2001). Lower panel: Density–sonic transit time cross-plot as used by Dutta (2002).

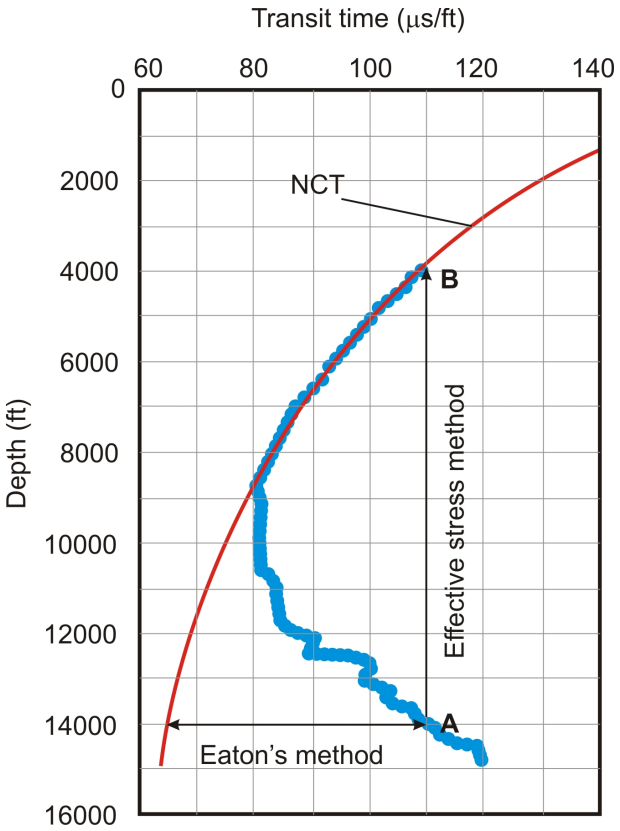

Figure 3.20 Schematic of Eaton's method and the effective stress method. In Eaton's method, pore pressure is estimated by comparing the wireline log reading (sonic in this illustration) with the expected wireline log value for normally compacted mudrocks at the same depth.

Eaton's ratio method

Eaton's method has long been used by companies operating in the Lower Kutai Basin for predicting pore pressure (e.g., Bois et al., 1994). Eaton (1975) performed an empirical statistical analysis for wells exhibiting overpressure in the Gulf of Mexico, and found the following relationships:

$$P = \sigma_v - (\sigma_v - P_n)\left(\frac{\Delta t_n}{\Delta t}\right)^3 \qquad \text{for using the sonic log} \qquad (3.23)$$

$$P = \sigma_v - (\sigma_v - P_n)\left(\frac{R}{R_n}\right)^{1.2} \qquad \text{for using the resistivity log} \qquad (3.24)$$

$$P = \sigma_v - (\sigma_v - P_n)\left(\frac{D_c}{D_{cn}}\right)^{1.2} \quad \text{for the using the corrected 'd' exponent} \qquad (3.25)$$

The subscript *n* denotes the value of the parameter on the normal compaction curve.

An illustration of the information needed to apply Eaton's ratio method (1975) to sonic log data is shown in Figure 3.20. Eaton (1975) did not mention in his paper how the NCT should be determined, but the implication was that it should be determined empirically from mudrocks where the fluid pressure was normal hydrostatic pressure. As can be seen from the above equations, the empirically determined Eaton exponents are 3 for the sonic log and 1.2 for the resistivity log and corrected 'd' exponent.

Some pore pressure analysts commonly adjust the Eaton exponent to fit the estimated pore pressures to reliable downhole pressure measurements in reservoir layers. The process of adjusting this exponent has been described as "cheatin' with Eaton" (P. Heppard, pers. comm.). Because this method is only an empirical method, usage of this method outside the area where the NCT was derived should be treated sceptically. Also, it is important to note that this method does not imply anything about the overpressuring mechanisms, whether loading or unloading. Tingay et al. (2009), citing Mouchet and Mitchell (1989), and Hermanrud et al. (1998) have stated that the exponent of 3 for the sonic log implies that overpressure is generated by disequilibrium compaction. They are not correct, because Eaton (1975) proposed his methodology on empirical grounds for Gulf of Mexico data without giving any consideration to the mechanisms that had generated overpressure there.

Effective stress method

This method is also known as the equivalent depth method (Mouchet and Mitchell, 1989), or the vertical method. The principle of this method is that for a given value of porosity, the overpressured mudrock will possess the same effective stress value as the normally pressured mudrock.

An illustration of the information needed to apply the effective stress method to sonic log data is shown in Figure 3.20. The transit time at Point A equals the transit time in normally pressured mudrock at the depth of 4000 ft (Point B). The effective stress at Point B can be calculated by subtracting the normal hydrostatic pressure from the vertical stress value at that point. Applying the principle of the equivalent depth method, the vertical effective stress at Point A is assumed to be equal to the vertical effective stress at Point B. Hence, the pore pressure at point A can be calculated by subtracting the vertical effective stress value at Point B from the vertical stress value at Point A:

$$P_A = \sigma_{V_A} - \left(\sigma_{V_B} - P_B\right) \tag{3.26}$$

The effective stress method is valid for overpressure caused by disequilibrium compaction provided that the mudrock lithology is the same at the two depths and that the only operative compaction process is mechanical compaction. Where overpressure is caused by an unloading mechanism, the effective stress method will fail to estimate the pore pressure accurately because porosity–effective stress relationships during unloading deviate from the NCT.

Bowers' method

Bowers (1995) proposed a modified effective stress method for estimating pore pressure that would account for overpressure generated by both loading and unloading mechanisms. For the loading mechanism, his method incorporates an empirical NCT relationship between vertical effective stress and velocity as described in Equation 3.20. This equation implies that for a given value of velocity (which is proxy for porosity in the absence of unloading), the overpressured and the normally pressured mudrock will possess the same value of effective stress. This is the principle of the effective stress method. Bowers (1995) further proposed the following relationship between vertical effective stress and velocity in an unloaded mudrock:

$$\sigma'_v = \sigma'_{\max}\left[\frac{1}{\sigma'_{\max}}\left(\frac{v-5000}{A}\right)^{1/B}\right]^U \tag{3.27}$$

where A and B are the same empirical constants as a and b in Equation 3.20, U is another empirical constant, and $\sigma'_{\max}$ is the maximum value of vertical effective stress to which the mudrock has been subjected. For practical application, $\sigma'_{\max}$ may be chosen as the point where sonic or resistivity log starts to reverse. Pore pressure caused by unloading can then be directly calculated by subtracting the vertical effective stress from the vertical stress (Equation 3.3)

3.7 Overpressure implications: lateral reservoir drainage and hydrodynamic trapping

Lateral reservoir drainage (O'Connor and Swarbrick, 2008) can cause hydrodynamic trapping of oil and gas. The first comprehensive analysis of hydrodynamic trapping was given by Hubbert (1953) for hydrodynamic flow caused by hydraulic head, also known as gravity-driven hydrodynamics. Whatever the cause of the lateral overpressure gradient in the reservoir, the principle of gravity-driven hydrodynamics and lateral reservoir drainage is the same: overpressure gradients lead to fluid flow.

Lateral flow of water in reservoir layers affects the migration of hydrocarbons through the reservoir as well as being associated with hydrocarbon trapping. For certain combinations of reservoir dip and overpressure gradient, the gas and oil can migrate in different ways, as shown in Figure 3.21. The focus of this research is more closely related to hydrodynamic trapping, so the effect of lateral reservoir drainage on hydrocarbon migration is not discussed further.

Where hydrocarbons accumulate under lateral reservoir drainage conditions, the hydrocarbon-water contacts are tilted (Figure 3.22). The magnitude of the tilting can be calculated by using (Hubbert, 1953):

$$\tan\theta = \frac{dz}{dx} = \frac{\rho_w}{\rho_w - \rho_{hc}}\frac{dH}{dx} \tag{3.28}$$

where θ is the dip of the hydrocarbon-water contact, ρ_{hc} is the hydrocarbon density, and $\frac{dH}{dx}$ is the overpressure gradient stated in terms of hydraulic head of water, H, given by:

$$H = \frac{OP}{\rho_w g} \tag{3.29}$$

where OP is the overpressure.

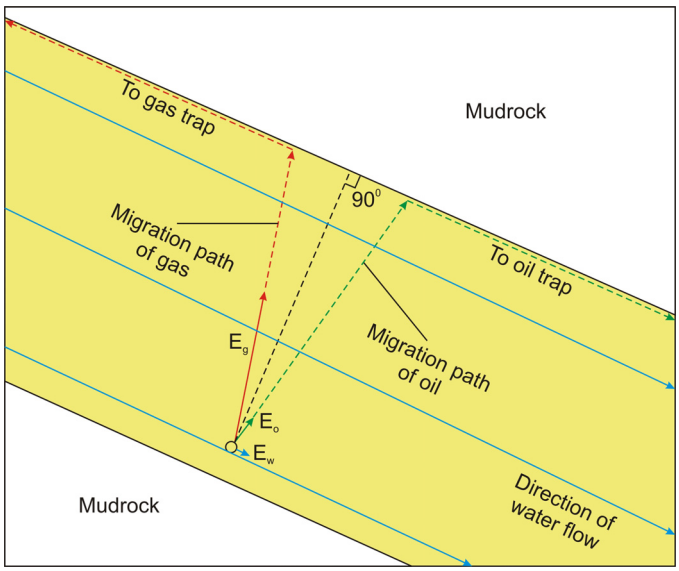

Figure 3.21 Divergent migration of oil and gas due to hydrodynamic condition (simplified from Hubbert, 1953).

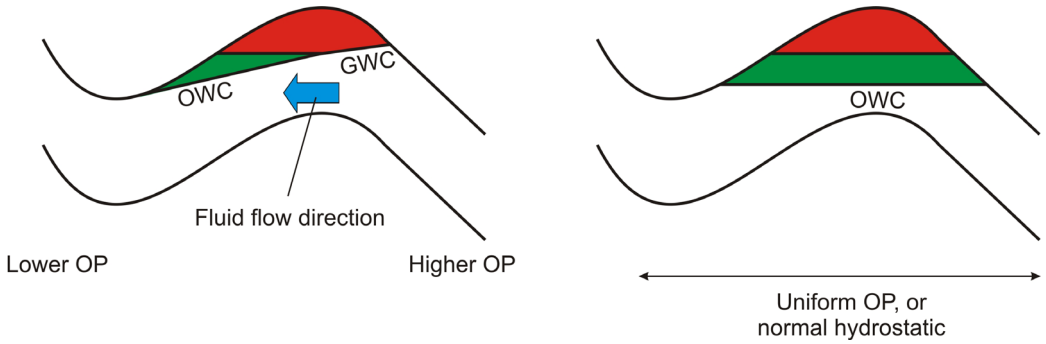

Figure 3.22 Cartoon illustrating the difference between hydrodynamically tilted hydrocarbon water contacts (left panel) and a hydrostatic flat hydrocarbon water contact (right panel).

Overpressure gradients in reservoirs can be detected by mapping overpressure values measured in the water leg (to avoid overpressure due to buoyancy), as performed by Dennis et al. (2000) in North Sea reservoirs. Overpressure gradients can also be detected in pressure–depth plots for multiple wells, as illustrated in Figure 3.23. The plot will be characterized by a single common hydrocarbon pressure gradient accompanied by several water pressure gradients.

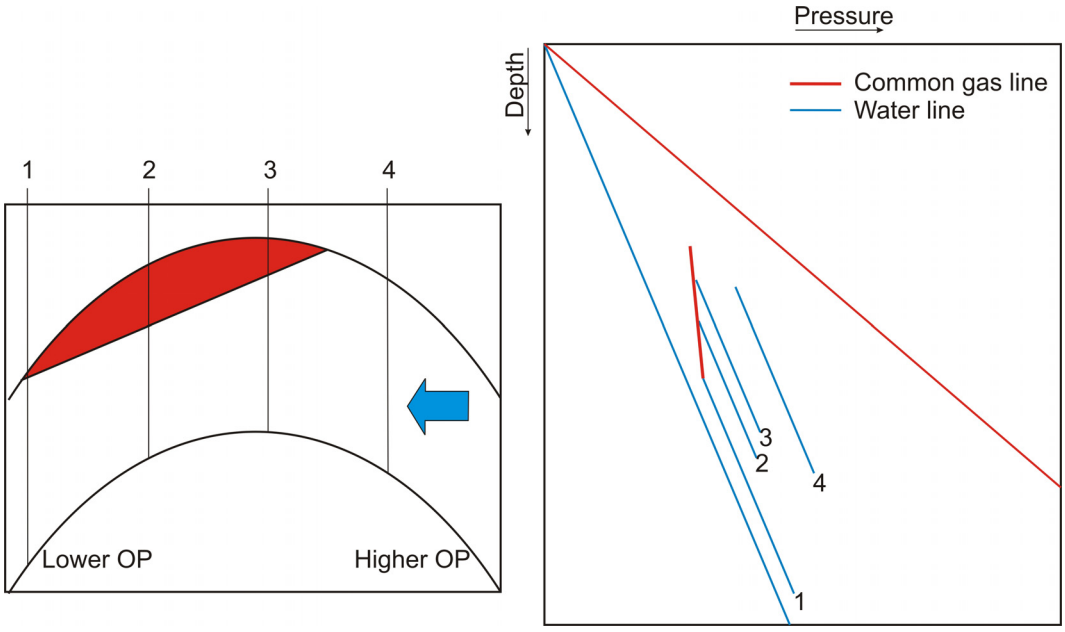

Figure 3.23 Cartoon illustrating one pressure gradient in a single gas accumulation accompanied by different water pressure gradients in different wells, indicating hydrodynamic trapping.

Active lateral reservoir drainage at the present time needs a source of water to maintain the flow. One possible source of active water flow is dewatering of the mudrocks adjacent to the sands (Magara, 1969, 1978; Grosjean et al., 1994; Lambert et al., 2003; O'Connor and Swarbrick, 2008). In this model, the mudrocks dissipate their overpressure through the reservoir, thus maintaining active lateral drainage. This model requires the presence of higher overpressure in the mudrocks. There should still be continuity between sand and mudrock pore

pressures because the mudrock is not completely impermeable. O'Connor and Swarbrick (2008) coined the term 'shoulder effect' to describe the pressure-depth gradients adjacent to the reservoirs in these circumstances (Figure 3.24). Shoulder effects should be observable in the sonic or resistivity logs, as well as on pressure–depth profiles, if pressure discrepancies exist.

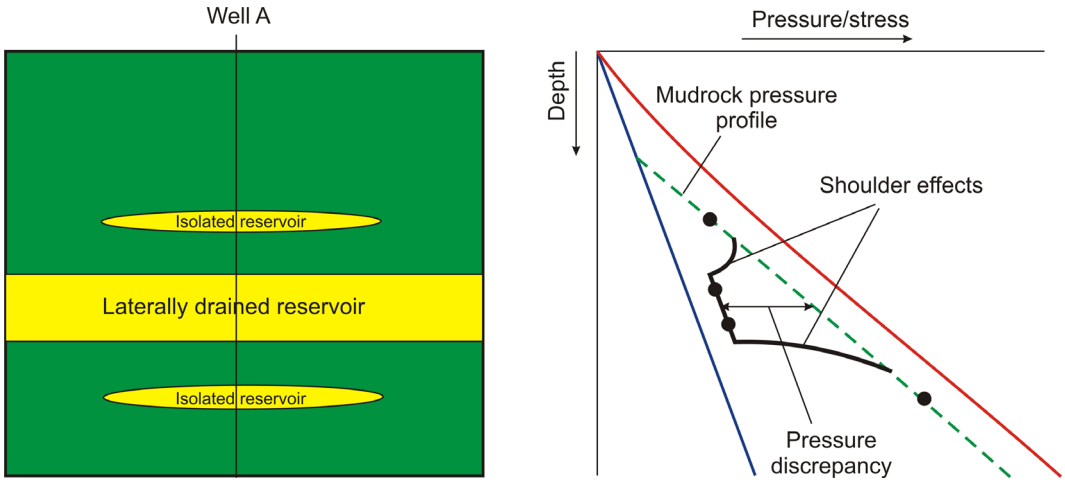

Figure 3.24 Cartoon showing shoulder effects on the pressure–depth profile as a consequence of lateral reservoir drainage. The green dashed line showing sub-lithostatic parallel pressure profile indicates that overpressure is caused by disequilibrium compaction. The higher overpressure in the mudrock compared to the laterally drained reservoir triggers the fluid flow from the mudrocks toward the reservoir, causing the development of the 'shoulder effect'.

Magara (1969, 1978) reported the presence of shoulder effects (Figures 3.25 and 3.26). The first case he discussed, taken from Shiunji gas field, Japan, shows that there is mudrock dewatering through the upper and lower sequences of high permeability rocks (tuff reservoirs). The second case, taken from the Beaufort Basin, Canada, shows the dewatering of intraformational mudrocks into sandstone reservoirs.

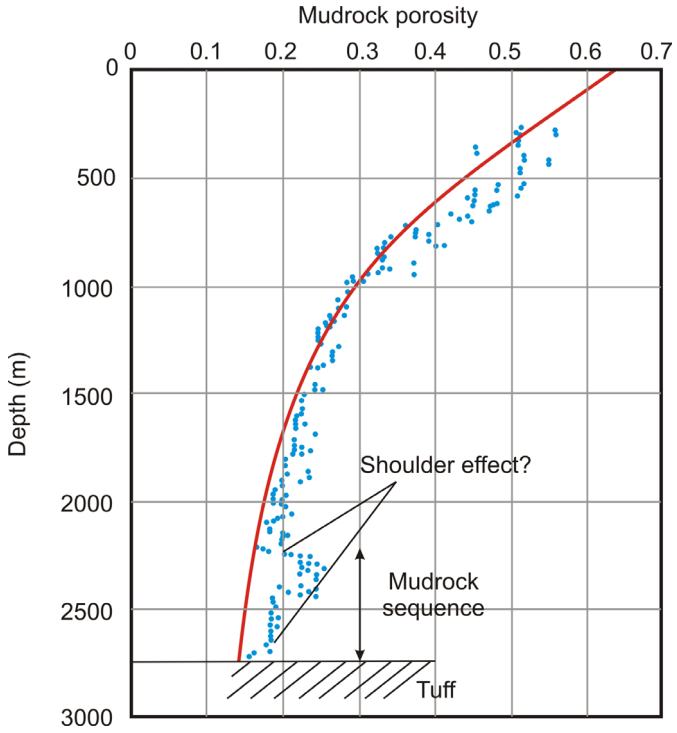

Figure 3.25 Possible shoulder effects at the Shiunji gas field, Japan (simplified from Magara, 1969). The red line indicates the normal compaction trend.

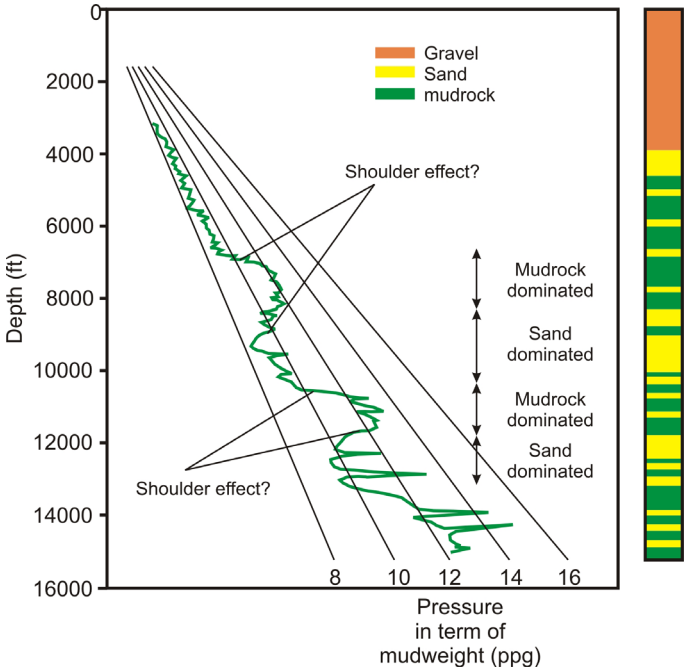

Figure 3.26 Possible shoulder effects in the Taglu Well, Beaufort Basin, Canada (simplified from Magara, 1978).

Schmidt (1973) presented a pore pressure profile estimated from the resistivity log in Pan America A-5 Well, Manchester Field, Lousiana. It seems that there is a shoulder effect in that well (Figure 3.27). However, it is not clear to what extent these 'shoulder effects' are caused by changes in lithology because Schmidt (1973) did not show any lithological information for this well to disciminate between mudrocks and reservoir sands.

Gurevich and Chilingar (1995) reported the presence of pressure discrepancies between reservoirs and mudrocks in the Baku Archipelago, Azerbaijan. They reported pressure discrepancies as high as 40 MPa (Figure 3.28). However, they did not reveal the method used to estimate the pore pressure in the mudrocks, nor did they show a wireline log that could be used to identify the shoulder effect.

O'Connor and Swarbrick (2008) estimated pore pressures in the mudrocks from the sonic log in a well located offshore East India. They presented the shoulder effect as a pore pressure–depth profile, and did not show the sonic log itself (Figure 3.29). They proposed this pore pressure–depth profile as evidence of the presence of lateral reservoir drainage in the area.

Bois et al. (1994) also reported the presence of pressure discrepancies in the Sisi Field, Lower Kutai Basin, as discussed in the introductory chapter (Figure 1.2). Grosjean et al. (1994) and Lambert et al. (2003) proposed that the lateral reservoir drainage in the Tunu and Peciko fields (Figure 1.1) could be sourced by mudrock dewatering (Figure 1.5). As described in Chapter 5, there are strong reasons for scepticism about both these ideas, and one way of testing them is by searching for the shoulder effect.

Dennis et al. (2000) have described lateral reservoir drainage out of the Palaeocene fan sandstones of the Central Graben, North Sea (Figure 3.11). Their model involves fluid flow through pressure compartments in the Jurassic/Triassic strata and hydro-fractured mudrocks located far below the laterally drained reservoir. These sources of water maintain the active lateral reservoir drainage.

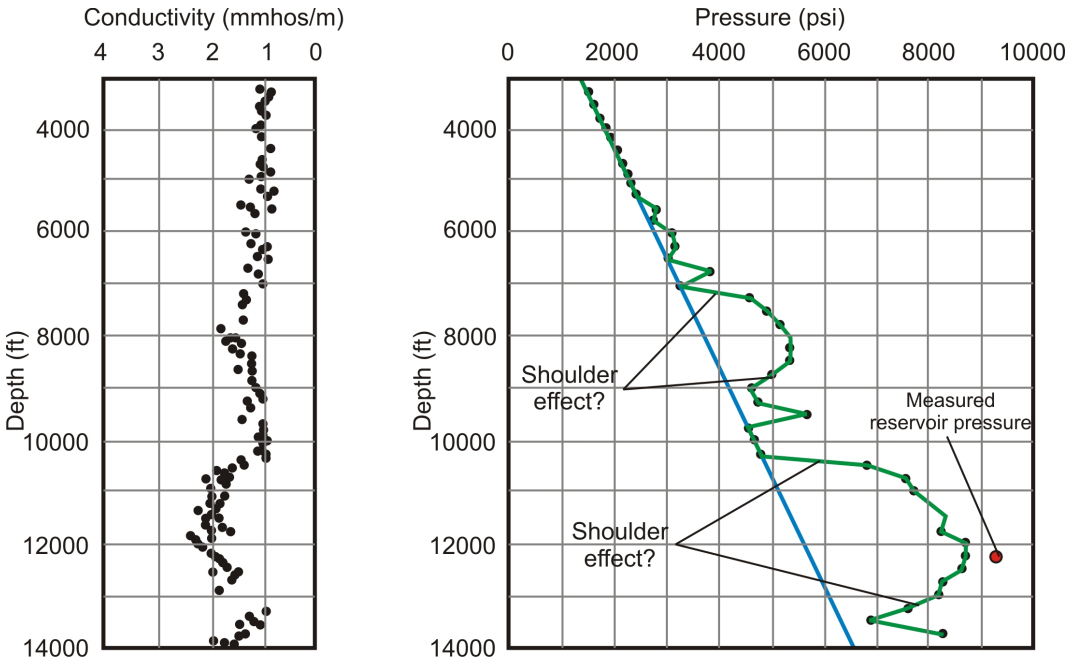

Figure 3.27 Possible shoulder effects in the Pan America A-5 Well, Manchester Field, Louisiana Gulf Coast (simplified from Schmidt, 1973).

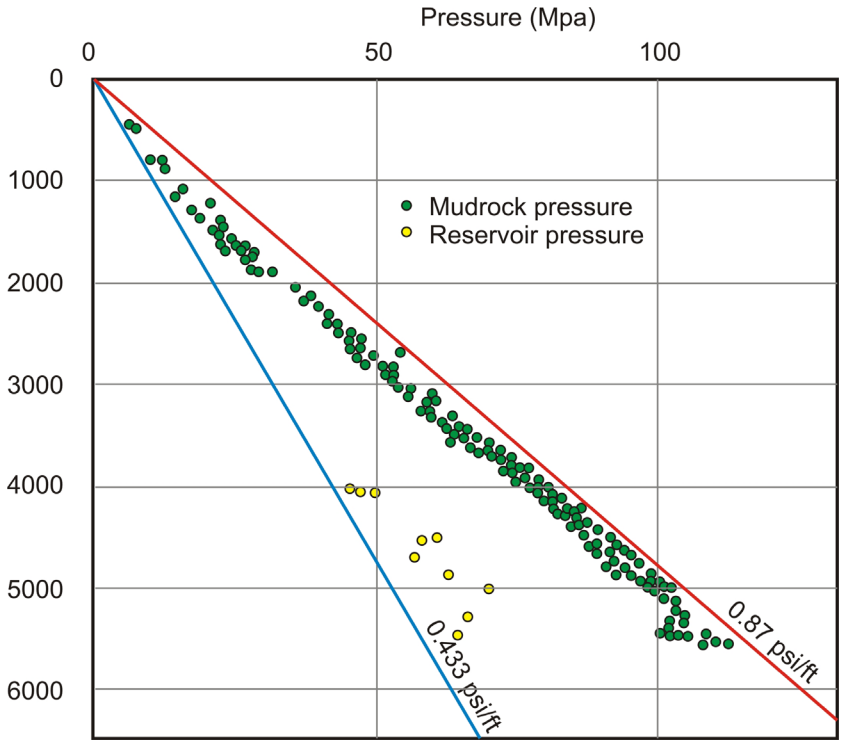

Figure 3.28 Reservoir-mudrock pressure discrepancy in Azerbaijan (simplified from Gurevich and Chilingar, 1995).

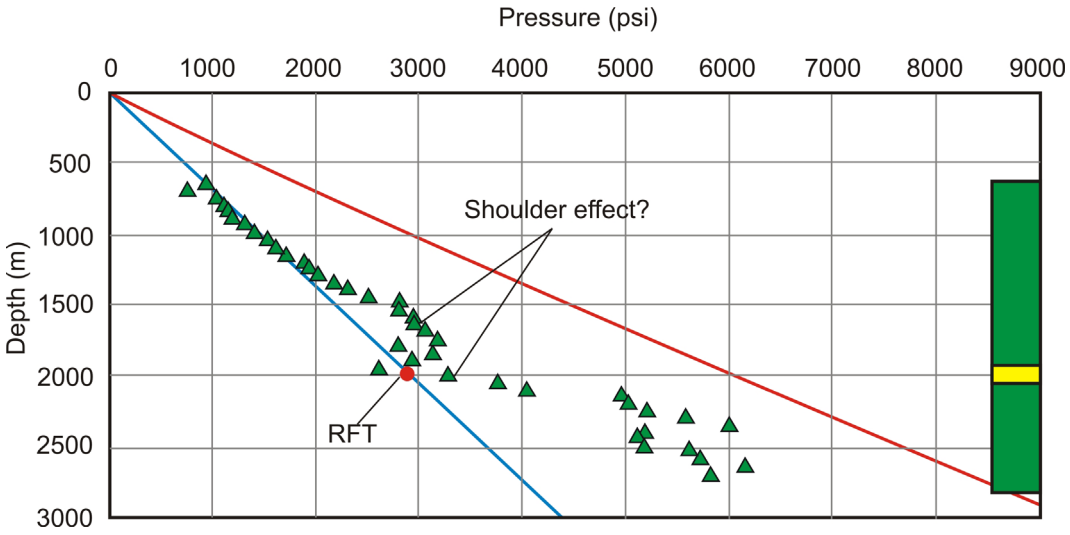

Figure 3.29 Possible shoulder effect from an offshore India well (simplified from O'Connor and Swarbrick, 2008).

CHAPTER 4
RESEARCH METHODOLOGY

The research workflow is shown in Figure 4.1. Broadly, there are three data categories used in this research: pressure data, wireline log suites, and other data such as temperature, vitrinite reflectance, and structural horizons. Each data type is initially processed separately, and the results of each analysis are integrated to analyse overpressure mechanisms and compaction in the Lower Kutai Basin. Details of each process are described in the following sections.

4.1 Pressure data

Typical pressure data available for analysis in this research are shown in Figure 4.2. Most pressure measurements were made with the repeat formation testing (RFT) pressure measurement tool. In some more recent wells, the tool used was the Modular Dynamic Tester, which is the new generation of RFT tool (Ireland et al., 1992). The RFT provides high quality pressure data, compared to data obtained from other measurements, such as a drill stem test (DST) or a formation interval test (FIT). The raw pressure drawdown test in the RFT also can be used to determine reservoir permeability (in Figure 4.2, it is given as the mobility, which is permeability divided by viscosity of the pore fluid). The RFT tool is also capable of doing multiple pressure measurements together with fluid sampling (FA in Figure 4.2) in one run.

The quartz gauge that was used to measure pressure in the RFT tool does so with an associated error of about ± 15 psi (Ireland et al., 1992). The new generation of quartz gauge, i.e., the combinable quartz gauge (CQG), reduces the measurement error to about ± 2.5 psi. An inhouse study by Total E&P Indonesie

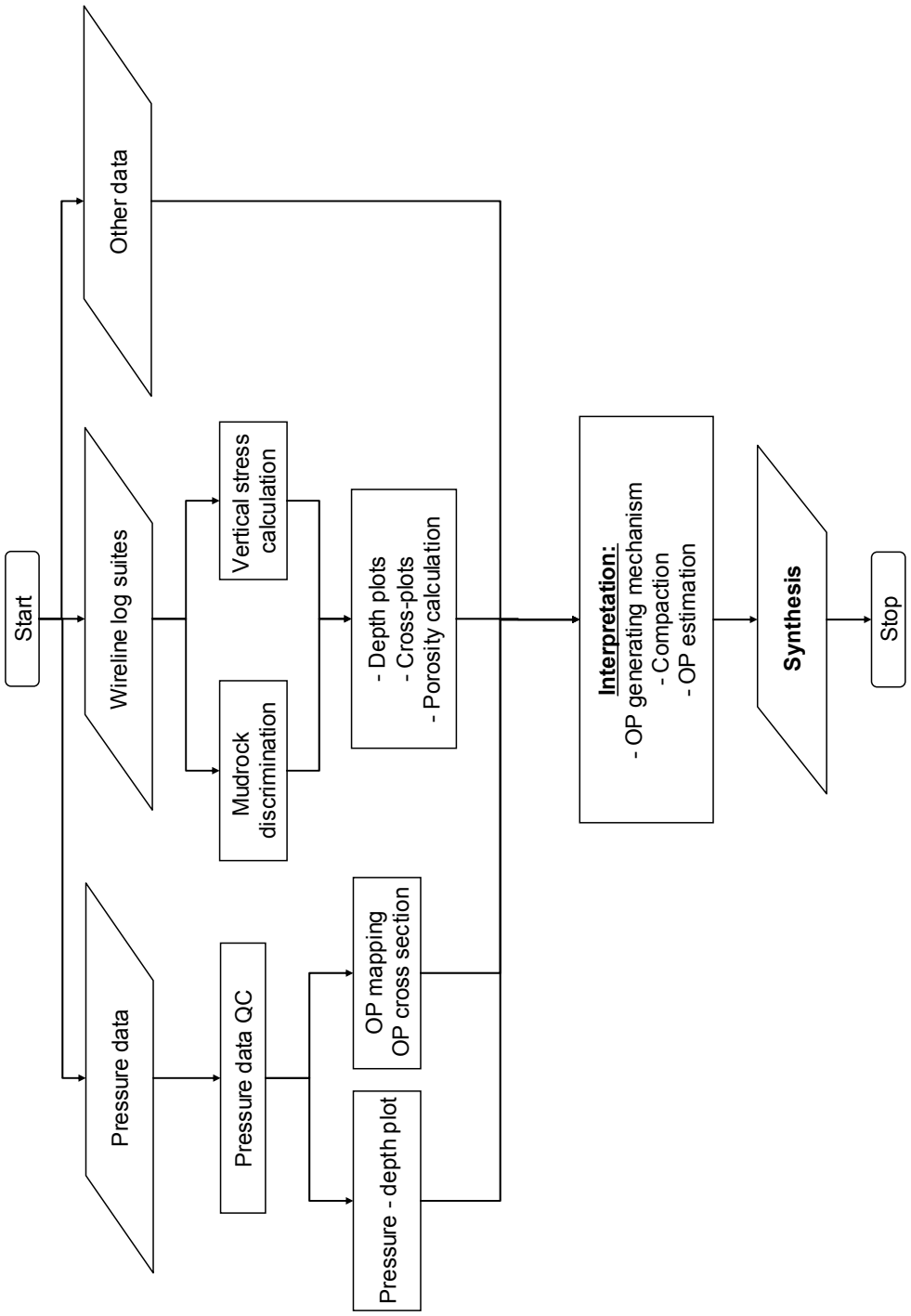

Figure 4.1 Research workflow.

WELL	TVDSS (ft)	TOOL	GAUGE	FP (psi)	EMW (gr/cm^3)	MOB (mD/cp)	FA	FLUID LOG	MARKER	REMARK	DATE
NWP-1	7449.37	RFT	QG	3292	1.01		HC	G	1a-a	GOOD	6/2/1991
NWP-1	7449.37	RFT	QG	3293	1.01	61	N/A	G	1a-a	GOOD	6/2/1991
NWP-1	8003.04	RFT	QG	3610	1.04	14	N/A	G	1d	GOOD	6/2/1991
NWP-1	8608.20	RFT	QG	3906	1.04	4.3	N/A	G	1g	GOOD	6/2/1991
NWP-1	8646.74	RFT	QG	3854	1.02	876	N/A	G	1h	GOOD	6/2/1991
NWP-1	8670.52	RFT	QG	3853	1.02	273	N/A	G	1h	GOOD	6/2/1991
NWP-1	8682.00	RFT	QG	3854	1.02	974	N/A	G	1h	GOOD	6/2/1991
NWP-1	8695.12	RFT	QG	3855	1.02	938	N/A	G	1h	GOOD	6/2/1991
NWP-1	8708.24	RFT	QG	3856	1.02	45	N/A	G	1h	GOOD	6/2/1991
NWP-1	9898.81	RFT	QG	4430	1.03		N/A	G	2g	N.S	6/2/1991
NWP-1	10907.74	RFT	QG	5291	1.12		N/A	G	4a	S.C	6/2/1991
NWP-1	10950.05	RFT	QG	5384	1.13	1.4	N/A	G	4b	GOOD	6/2/1991

Note:

TVDSS	True vertical depth sub sea
TOOL	Downhole pressure instrument
GAUGE	Pressure gauge; QG: quartz gauge
FP	Formation pressure
EMW	Pressure in equivalent mud weight
MOB (mD/cp)	Mobility in Millidarcy per centi poise
FA	Pore fluid analysis from fluid sample
	HC : hydrocarbon
	N/A: not available
FLUID LOG	Pore fluid analysis from wireline logs
	G: gas
	O: oil
	W: water
MARKER	Stratigraphical marker
REMARK	Result of pressure test
	GOOD : reliable pressure data
	N.S. : not stabilised (not enough time to directly determine pressure value)
	S.C. : unreliable pressure data due to mud invasion
	TIGHT : unreliable pressure data due to tight reservoir
DATE	Date of pressure measurement

Figure 4.2 Typical pressure data available for analysis in this research.

shows that the accuracy of the pressure measurements in the Lower Kutai Basin area is in the range of ± 7 to ± 15 psi.

The first step in pressure data processing is a quality check (pressure QC). The workflow for the pressure QC is shown in Figure 4.3. The data are firstly sorted by the result of the pressure test ('REMARK' in Figure 4.2). Only 'GOOD' pressure data are accepted for the next QC; the remainder are discarded. For analysis of overpressure generation mechanisms and hydrodynamics, the pressure data need to be virgin pressure data, unaffected by drawdown due to reservoir depletion. The pressure data that were taken before production was started are designated as Class A pressure data. Data in this class have all come from

exploration and appraisal wells. The pressure data that were taken after production had started, but with no obvious pressure depletion effect, are designated as Class B pressure data. Where Class A data are limited, the Class B data are used with careful consideration. Pressure data that show obvious depletion effects are discarded.

After the pressure QC step, the selected data are then processed by plotting the pressure values versus depth and mapping overpressure for pressure data measured in the water leg. The purpose of the pressure–depth plot is to:

- determine overpressure trend for analysing the overpressure generation mechanism (in combination with wireline log analysis).
- determine overpressure due to buoyancy. Pressure measurements in the hydrocarbon leg are used to calculate the buoyancy effect due to overpressuring, as discussed in Section 3.2.

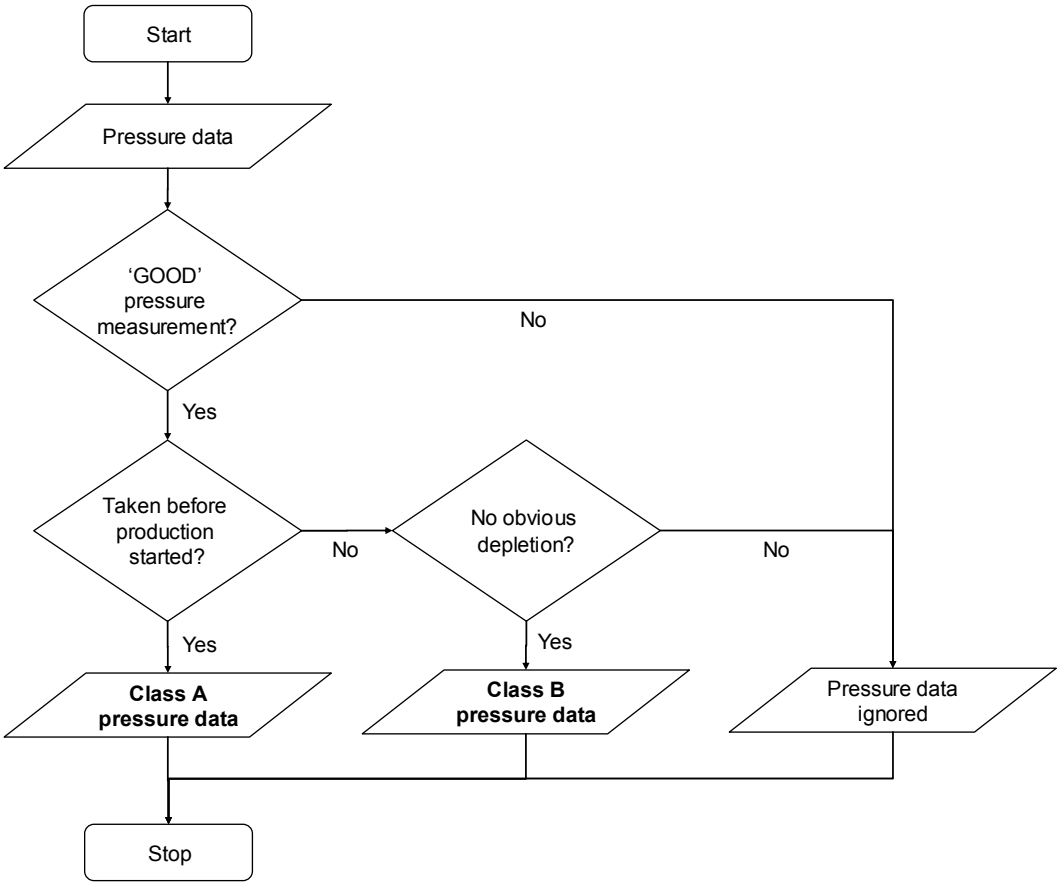

Figure 4.3 Flowchart for pressure QC.

- look for indications of hydrodynamic trapping. Lateral reservoir drainage leading to hydrodynamic trapping can be recognized from the presence of one common hydrocarbon line accompanied by several water lines (Figure 3.23).

Overpressure mapping is performed in order to know direction of fluid flow and the magnitude of overpressure gradient. Both parameters are required to analyse the location of potential hydrodynamic traps, as discussed in Section 3.7.

4.2 Wireline log suites

The wireline log suites to be analysed in this research are gamma ray, density, neutron, sonic, and resistivity logs. For overpressure analysis, two preliminary steps are necessary: 1) vertical stress calculation, and 2) mudrock discrimination.

The vertical stress is calculated by using the density log with the equation

$$\sigma_v = \sum_{i=1}^{n} \rho_b g dz \qquad (4.1)$$

Commonly, the density log in the shallower section is either unavailable or has low data quality due to borehole caving. In that case, an average value of bulk density in the shallow section is estimated from nearby wells. The density log in the shallowest section, typically down to 500 m below seafloor, is unavailable. For this depth interval, the average value of 1.9 g/cm^3 is used. This value can be found in the Ocean Drilling Program Database (ODP) at http://www.odp.tamu.edu. Binh et al. (2007) also used this value to calculate vertical stress in the shallower section in offshore Vietnam.

The density log measures bulk density value every 0.5ft. Therefore, the calculation of the vertical stress is also performed at every depth step, at intervals of 0.5 ft. An example of the vertical stress calculation in the spreadsheet is shown in Figure 4.4.

TVDSS (m)	RHOB (g/cm^3)	Δz	$\Delta\sigma_{vz}$ (PA)	σ_v (PA)	σ_v (psi)	σ_v/z (psi/ft)
479.872				8935216.64	1295.61	0.823
480.024	2.06	0.15	2949.408	8938166.05	1296.03	0.823
480.177	2.06	0.15	3088.764	8941254.81	1296.48	0.823
480.329	2.06	0.15	3068.576	8944323.39	1296.93	0.823
480.482	2.06	0.15	3088.764	8947412.15	1297.37	0.823
480.634	2.06	0.15	3068.576	8950480.73	1297.82	0.823
480.786	2.06	0.15	3068.576	8953549.30	1298.26	0.823
480.939	2.06	0.15	3088.764	8956638.07	1298.71	0.823
481.091	2.06	0.15	3068.576	8959706.64	1299.16	0.823
481.244	2.06	0.15	3088.764	8962795.41	1299.61	0.823
481.396	2.06	0.15	3068.576	8965863.98	1300.05	0.823
481.548	2.06	0.15	3068.576	8968932.56	1300.50	0.823
481.701	2.06	0.15	3088.764	8972021.32	1300.94	0.823
481.853	2.06	0.15	3068.576	8975089.90	1301.39	0.823
482.006	2.06	0.15	3088.764	8978178.66	1301.84	0.823
482.158	2.06	0.15	3068.576	8981247.24	1302.28	0.823
482.31	2.06	0.15	3068.576	8984315.82	1302.73	0.823
482.463	2.06	0.15	3088.764	8987404.58	1303.17	0.824
482.615	2.06	0.15	3068.576	8990473.16	1303.62	0.824
.....	.....	.....	.....	.....	.....	.....
.....	.....	.....	.....	.....	.....	.....
3685.758	2.59	0.15	3820.824	82344071.54	11939.89	0.988

Remaks:

Column 1: Depth
Column 2: Density value
Column 3: Depth interval
Column 4: Vertical stress at each interval depth interval in Pascal
Column 5: Total vertical stress, obtained by cumulative sum of each interval in psi
Column 6: Total vertical stress in psi.
Column 7: Vertical stress gradient in psi/ft.

Figure 4.4 Example of spreadsheet calculation of vertical stress in a well. In this well, the density data start to available at the depth of 480.024 m. Above this depth, the value of 1.9 g/cm^3 for the density is used to calculate the total vertical stress from surface down to 480.024 m.

Estimates of overpressure and compaction trend in the mudrock sections need to be done in a consistent mudrock lithology. Katahara (2008) discussed techniques of discriminating mudrock from sandstone based on their petrophysical properties (Figure 4.5). In sandstone, the grain-to-grain contacts between sand grains produce a continuous load-bearing network. By contrast, in

mudrock, the sand grains float in the load-bearing clay so that sand grains do not provide a continuous load-bearing network. The threshold between a continuous and discontinuous load-bearing network of sand grains should, therefore, be a suitable sand–mudrock discriminant.

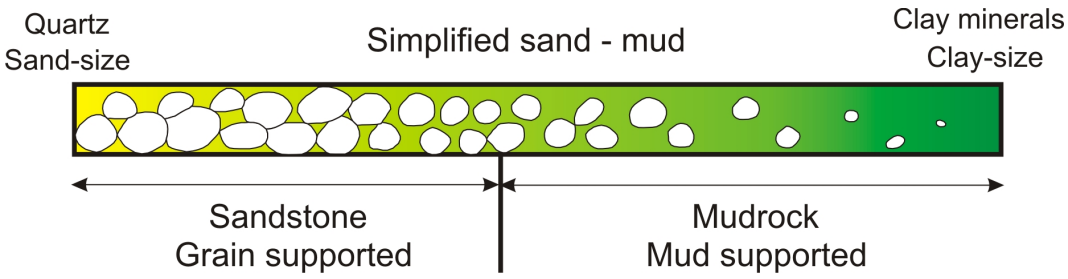

Figure 4.5 Cartoon illustrating the underlying reason why there are differences between the physical characteristics of sandstone and mudrock (modified from Katahara, 2008).

The gamma ray log is commonly used to measure the clay content (Figure 4.6), with a typical threshold at around 65 API units. Katahara (2008) pointed out that the usage of gamma ray is liable to errors since not all mudrocks are highly radioactive, and not all sandstones lack radioactivity. As a basis for sand–mudrock discrimination, he proposed a simple conceptual model of a mudrock as having three constituents: quartz, water, and clay minerals (Figure 4.7). On the cross-plot, mudrocks plot within the triangle defined by the points for the three pure constituents. The clay content is higher below the quartz–water line. An example of applying this technique is shown in Figure 4.8. Katahara (2008) stated that this technique produces a clearer and more reliable discrimination of mudrocks compared to the gamma ray technique (Figure 4.6).

For the purposes of analysis, the wireline log data points for the mudrocks are plotted directly against depth as well as on cross-plots. The cross-plots used here for analysis of overpressure generation mechanisms are of density versus transit time and density versus resistivity, as discussed in Section 3.2.

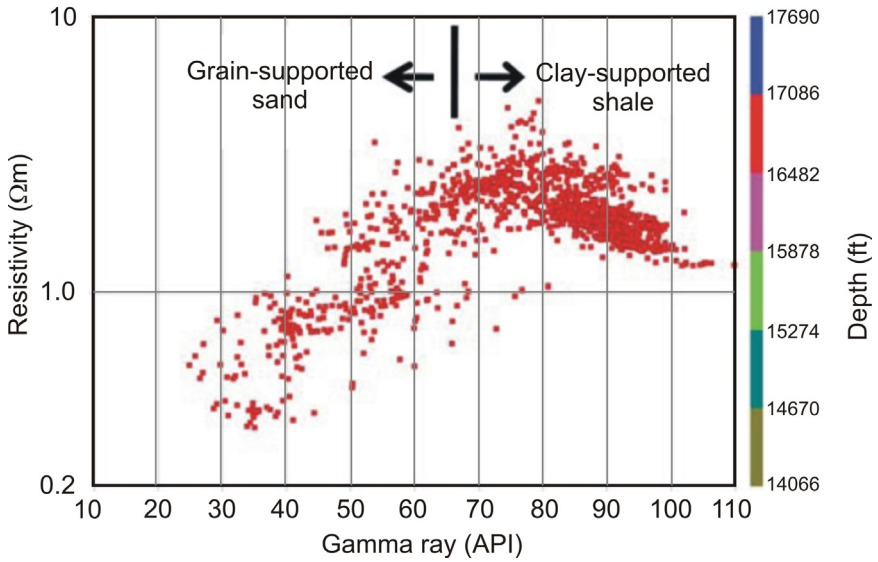

Figure 4.6 Mudrock discrimination based on the gamma ray log (after Katahara, 2008).

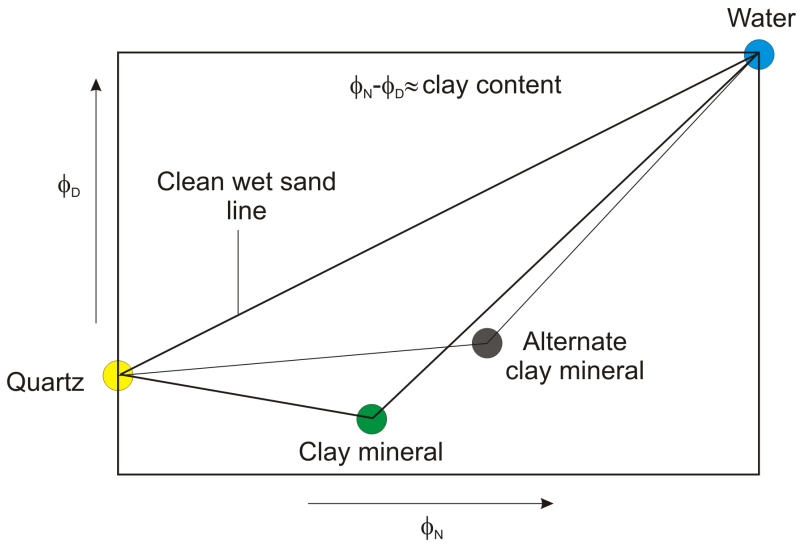

Figure 4.7 Cartoon illustrating where simple three-component mudrocks can lie on a cross-plot of density porosity versus neutron density (modified from Katahara, 2008).

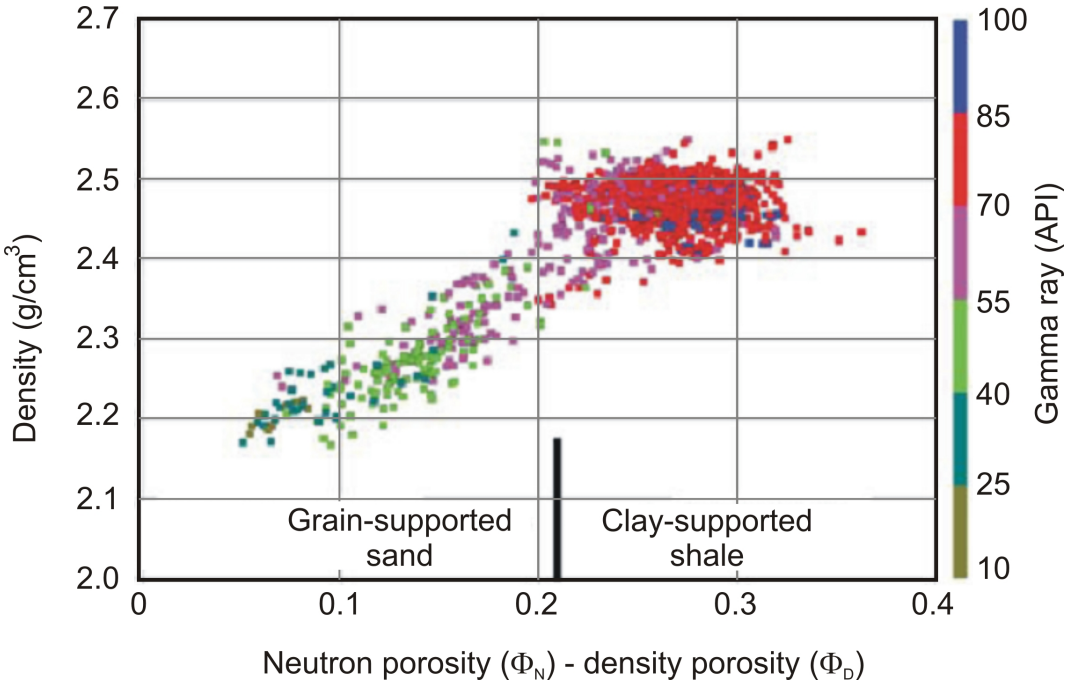

Figure 4.8 Mudrock discrimination based on the difference between neutron porosity and density porosity (after Katahara, 2008).

4.3 Other data

Other data available for analysis in this research are:

- **Temperature data**

  Borehole temperature measurements are available for this research. The data are required to identify the unloading mechanism(s) responsible for overpressure generation and to determine the compaction state of the mudrock (telodiagenesis and eodiagenesis, as discussed in Sub-section 3.6.2).

- **Hydrocarbon maturation data**

  The hydrocarbon maturation data available for this research are vitrinite reflectance. The data have been used to identify the unloading mechanism(s) responsible for overpressure generation.

- **Structural and stratigraphic horizons**

  These data have been used to analyse the possibility of overpressure transference from the deeper strata, and the relationship between overpressuring and stratigraphic condition, i.e. sand deficiency. Overpressure maps and structural horizons can also be correlated to analyse whether hydrodynamic traps are present. The stratigraphic data are in the form of stratigraphic horizons and net to gross (NTG) maps. An example of these data was shown in Figure 2.9.

- **Pore fluid distribution**

  Pore fluid distribution is the type of fluid in where the pressure data is measured, i.e. gas leg, water leg, and oil leg. The data are available either from fluid sampling during pressure tests or from wireline log analysis (dealt with in Section 4.2). The data have been used to determine the hydrocarbon gradient, calculate overpressure due to buoyancy (overpressure data measured in the gas legs), and for hydrodynamic mapping. Hydrodynamic mapping requires pressure data in the water leg only.

- **Water isotopes**

  The results of a water isotopic study (Total E&P Indonesie, 2003b) have been incorporated in the analysis of overpressuring and compaction.

4.4 Interpretation

The interpretation stage requires integrated analysis of all data types to make deductions about the overpressure generating mechanism, the state of compaction of the mudrocks, and overpressure value estimation.

The overpressure generating mechanisms are analysed from the wireline logs in the mudrocks and the cross-plots of those data points together with pressure trend from pressure–depth plots and other data. The first thing to do is to determine whether the overpressure is caused by loading, unloading, or a

combination of both mechanisms. If the cause of overpressure is an unloading mechanism, then other data are used to determine the plausible mechanisms of unloading.

Compaction is analysed by direct inspection of wireline logs in the mudrocks and cross-plots of wireline log parameters, as discussed in Section 3.2. One of the end results of the compaction analysis is an empirical relationship for porosity versus depth in the mudrocks in the research area. This compaction relationship is compared with worldwide published compaction relationships to try to answer a fundamental question about mudrock compaction, i.e., what is the driving mechanism of the mudrock compaction? Is it mechanical compaction (e.g., Magara, 1980; Katahara, 2006), or chemical compaction (e.g., Bjorlykke., 1998)?

The end result of this research is a synthesis of overpressure and compaction in the Lower Kutai Basin, in accordance with the objectives as stated in Section 1.2.

CHAPTER 5
OVERPRESSURE AND COMPACTION IN THE PECIKO FIELD

The content of this chapter has been accepted for publication in Petroleum Geoscience (Ramdhan and Goulty, 2010a). The data from the Peciko Field were analysed first because of the comprehensive nature and high quality of the wireline log suites available. A broader analysis of overpressure and compaction in fields within the shelfal area of the Lower Kutai Basin is given in Chapter 6. The purpose of this analysis at Peciko was to test all the theoretical background (Chapter 3) and the research methodology (Chapter 4), and to choose the most suitable approach for analysis of the whole Lower Kutai Basin.

The Peciko Field was developed using the concept of hydrodynamic trapping (Grosjean et al., 1994; Lambert et al., 2003), and a campaign of reservoir pressure measurements for hydrodynamic analysis purposes has resulted in an excellent pressure database. On average, there are around 70 RFT points in each well. These pressure data are very useful for overpressure analysis because they can be used to determine overpressure distribution, overpressure generating mechanism, and to calibrate methods of pore pressure estimation. The drilling method applied in this field, i.e., using an oil-based mud, has resulted in high quality wireline log suites, especially the density logs, because there is less caving of the borehole, that is commonly the cause of unreliable density log data. Both the abundant pressure data and high quality wireline log suites makes the Peciko Field an ideal place to study overpressure and compaction. Together with the very well documented pore fluid distribution, it also makes this field an ideal area to study lateral reservoir drainage.

This chapter starts with a section on background information available on the Peciko Field, before the analysis of overpressure, compaction, and lateral

reservoir drainage is presented. The analysis of overpressure and compaction comprise analysis of wireline log suites, pressure, temperature, and vitrinite reflectance data. The analysis of lateral reservoir drainage comprises hydrodynamic mapping and the magnitude of the expected tilting of hydrocarbon–water contacts.

5.1 The Peciko Field

The Peciko Field is a gas field located on the Median Axis, in the shelfal area, where the water depth is around 40 m (Figure 1.1). As of 2009, the field contains 3.3 tcf gas (Total Indonesie, 2010b). Structurally, this field is an unfaulted anticline (Figure 5.1). Stratigraphically, the productive interval in the Middle–Upper Miocene succession on the Median Axis, including the Peciko Field, is the Tunu Main Zone (Figure 5.2). The Tunu Main Zone is sub-divided into six intermediate stratigraphic units (SUs), of which only the uppermost five are present in the Peciko Field. They have an average thickness of 300–400 m, based on the presence of third-order maximum flooding surfaces. The reservoirs in this field are dominantly distributary mouth bars (Samson et al., 2005). The dimensions of individual mouth bars are 1–3 m thick and 1500–4000 m wide, and stacked mouth bars attain thicknesses of 10–30 m (Figure 5.3). The burial history of the Tunu Main Zone in this field (Figure 2.10) shows that the sedimentation rate during the last 8 Ma has been fairly constant at around 300 m/Ma.

The temperature data derived from 10 wells shows that the geothermal gradient is around 9.4°C/1000 ft, with the surface temperature of around 30°C (Figure 5.4). Based on this geothermal gradient, and the relatively high surface temperature, this part of the Lower Kutai Basin can be classified as a ‘warm’ basin. There is only one well with vitrinite reflectance data in this field, i.e., PEC-1. The data show that onset of gas generation in this well (vitrinite reflectance > 0.6%) (see Sub-section 2.2.2) is located at a depth around 12,000 ft (Figure 5.5).

Figure 5.6 is a schematic cross-section of the field illustrating the stacked nature of the gas reservoirs and the hydrodynamically tilted gas–water contacts in

the deeper overpressured accumulations. The lateral overpressure gradient has displaced the accumulation from the crest to the northern flank of the structure (Figures 5.6 and 5.7). The existence of hydrodynamically trapped accumulations was identified by Grosjean et al. (1994) and Lambert et al. (2003). The lateral overpressure gradients are sufficiently large to create hydrodynamic traps for gas. For example, in SU3 the lateral overpressure gradient reaches 150 psi/km. Given a gas density of 0.2 g/cm^3, the gas–water contact has a tilt of up to 7°. Detailed discussion of the overpressure gradient is given in Sub-section 5.4.4.

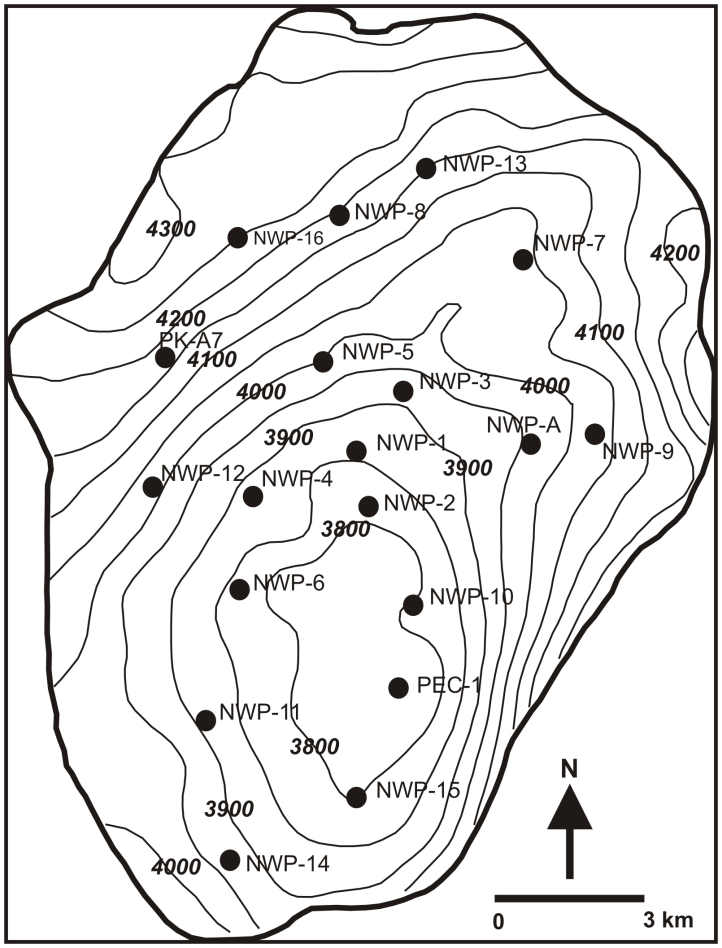

Figure 5.1 Structural map of one stratigraphic horizon within the Tunu Main Zone at the Peciko Field. The depth contour interval is 200 ft. The thick line demarcates the lateral extent of hydrocarbon accumulations in all reservoirs.

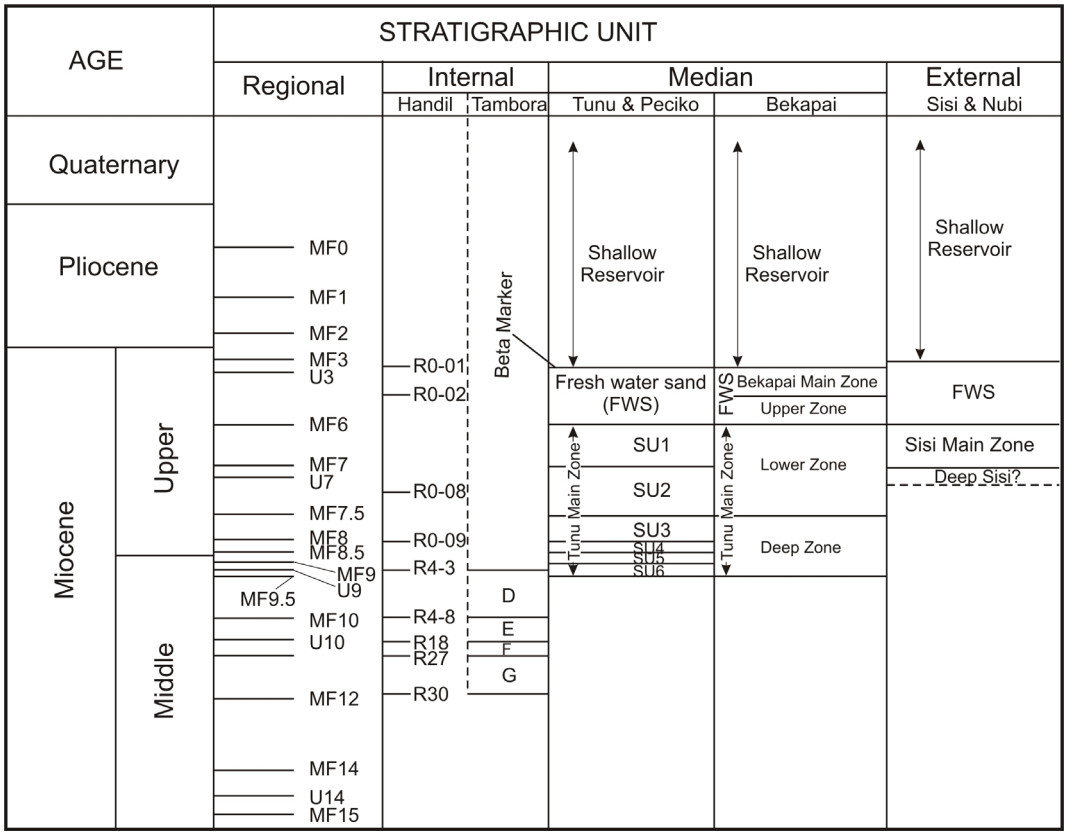

Figure 5.2 Stratigraphic column of the shelfal area Lower Kutai Basin, including the Peciko Field (simplified from Total E&P Indonesie, 2000b).

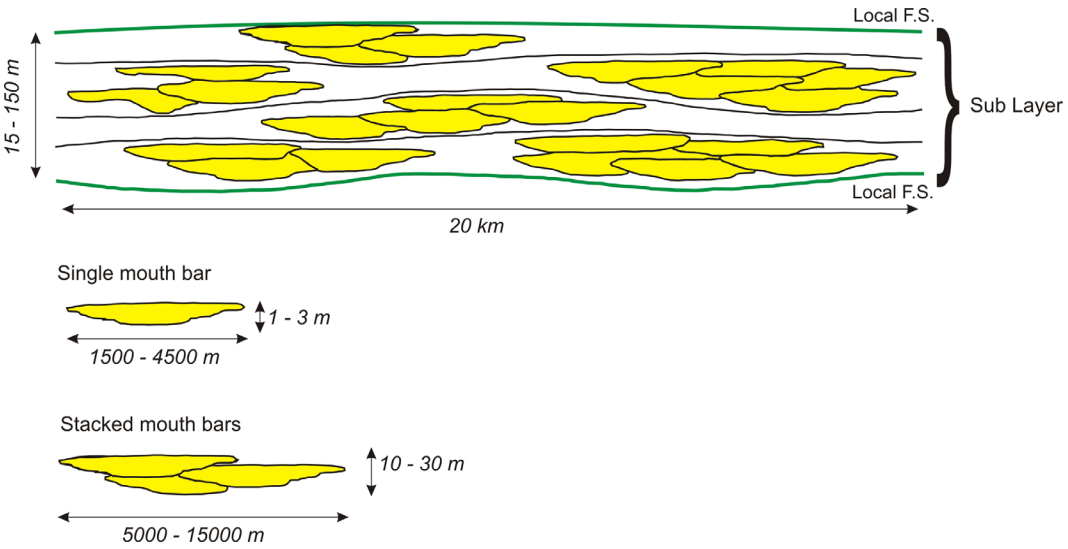

Figure 5.3 Schematic section showing stacked mouth bars in a stratigraphic interval between two local flooding surfaces (after Samson et al., 2005).

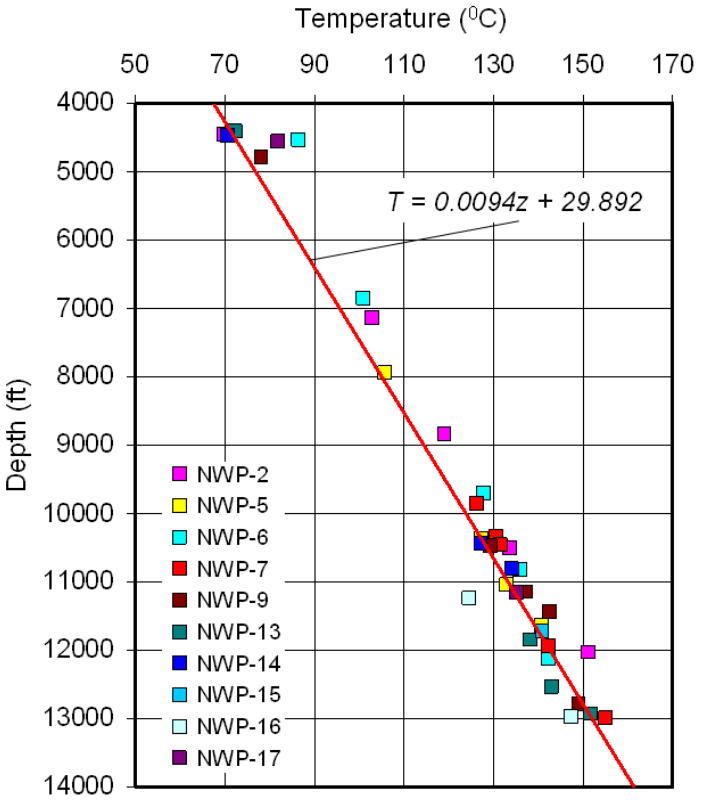

Figure 5.4 Thermal gradient in the Peciko Field.

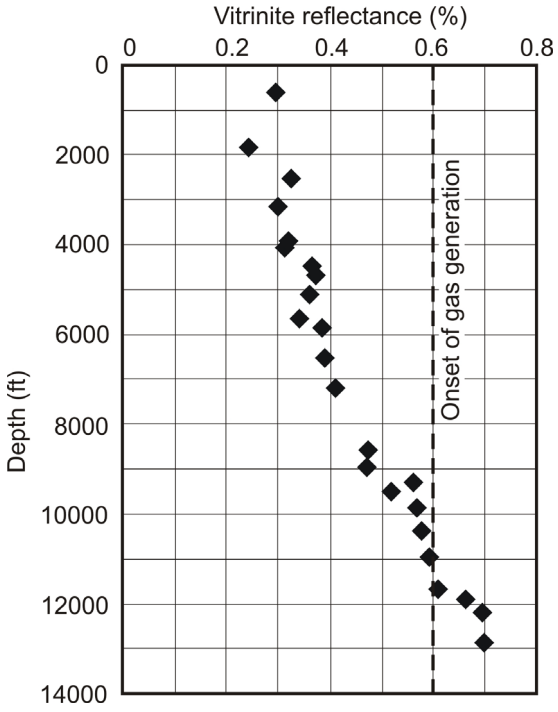

Figure 5.5 Vitrinite reflectance data from well PEC-1.

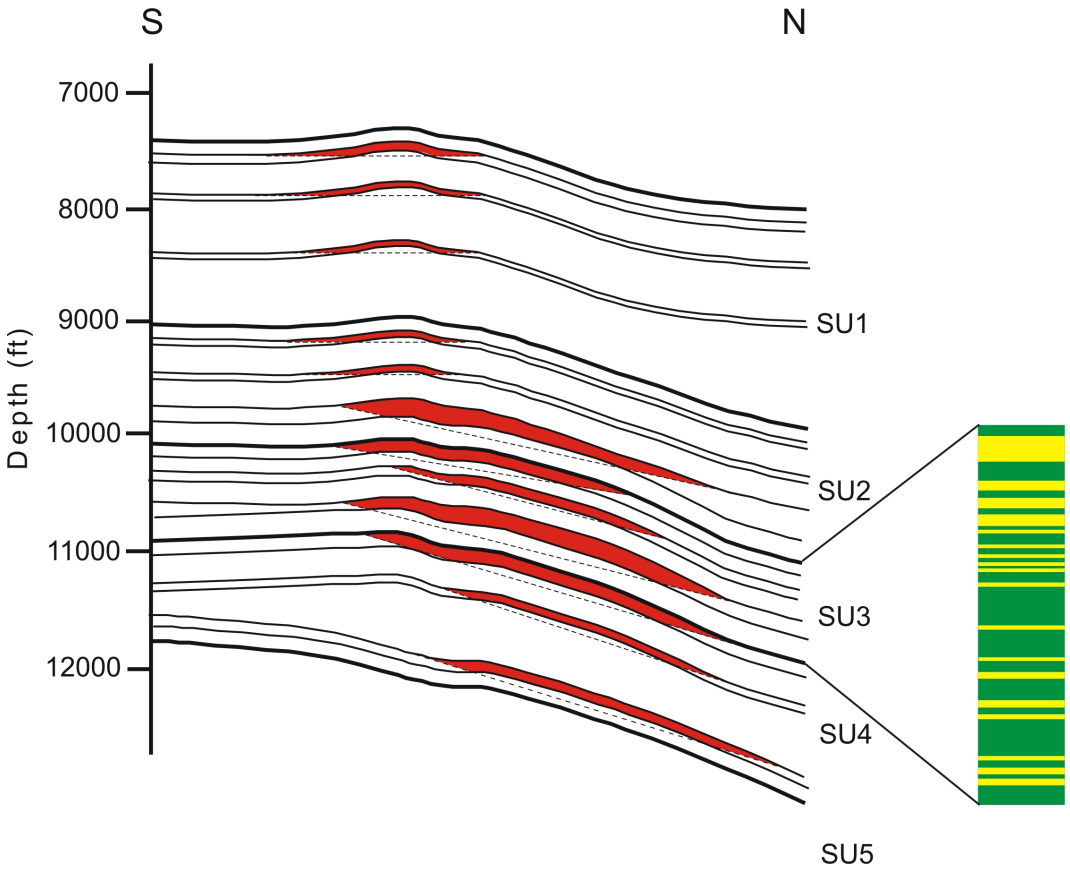

Figure 5.6 Schematic section through the Peciko Field showing gas accumulations (red) with tilted GWCs in the Tunu Main Zone. SU1 – SU5 are stratigraphic units of the Tunu Main Zone. A simplified lithological column for SU3 is shown on the right: yellow denotes sand-rich interval and green mudrock intervals.

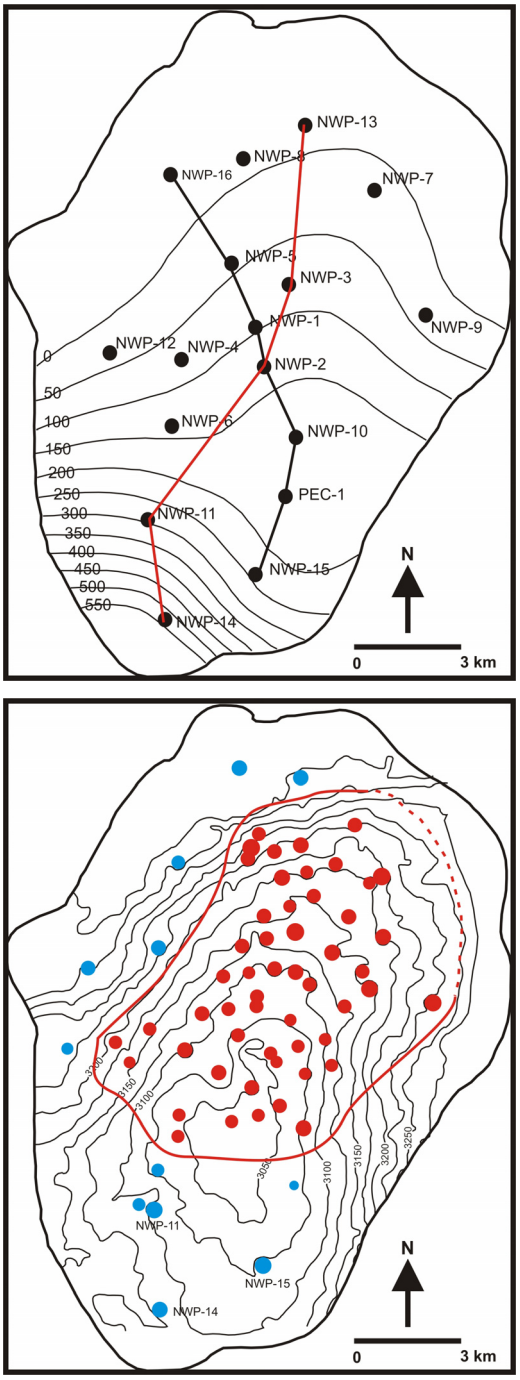

Figure 5.7 Upper: lateral overpressure distribution in the uppermost reservoir of SU3 in the Peciko Field before production started. Overpressure contours are at intervals of 50 psi. Lower: pore fluid distribution in the same stratigraphic unit showing that the gas accumulation is located on the north flank of the structure. Red line: limit of the gas accumulation in this stratigraphic unit. Diameter of the well symbols is proportional to reservoir thickness.

5.2 Pressure data

The pressure data available for analysis come from 17 wells. The number of Class A pressure data is 1200 points. Pressure-depth plots for all Class A data points are shown in Figure 5.8. Each data point has been grouped based on its fluid status (water, gas, or possible gas). It is assigned as possible gas if the result of wireline log analysis only shows minor indication of gas, for example, where there is no clear separation in neutron-density cross-plot.

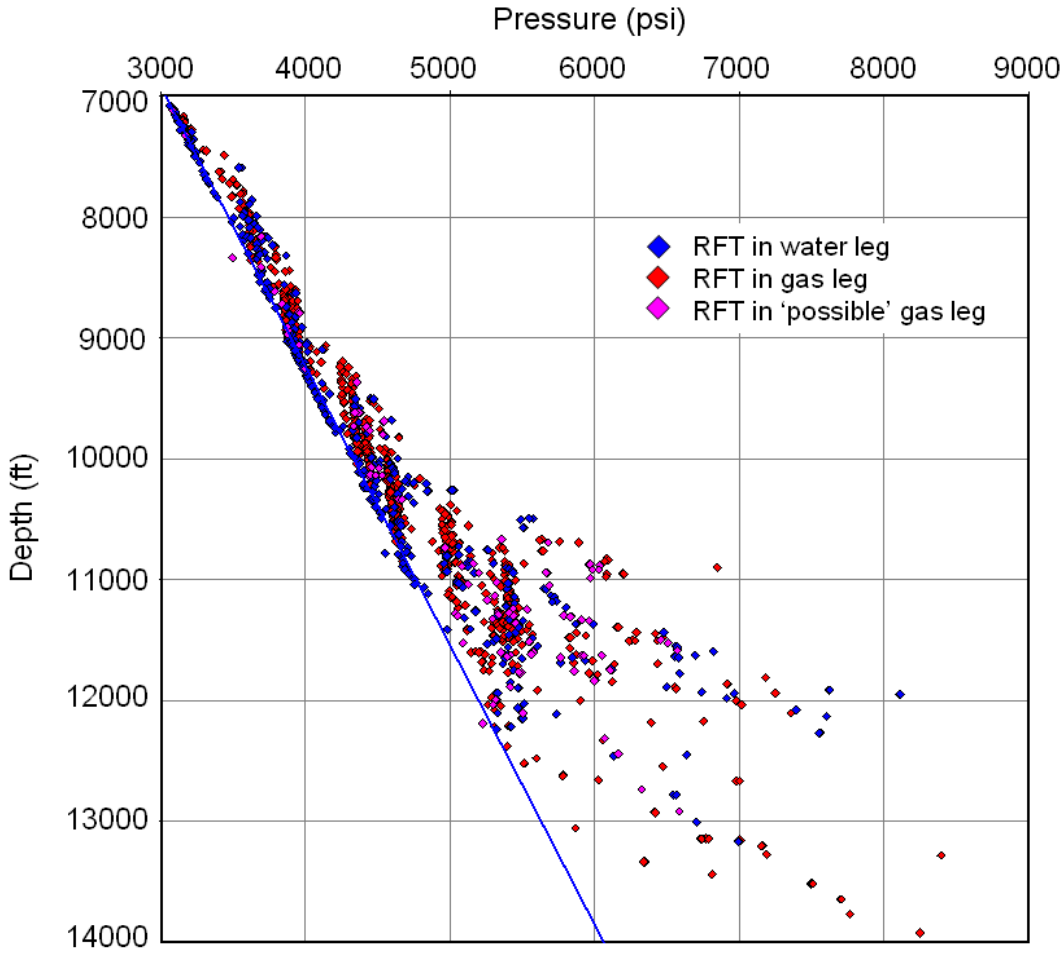

Figure 5.8 Pressure–depth plot for all Class A pressure data.

From Figure 5.8, several separate major gas pools, which correspond to different stratigraphic units, can be recognised. An example of a pressure-depth plot in an intermediate stratigraphic layer is shown in Figure 5.9. The complete pressure-depth plot for each intermediate stratigraphic layer is given in Appendix 1a. In Figure 5.10, it can be seen clearly that in stratigraphic layer SU3a (the uppermost layer of SU3), there is one gas line accompanied by several water lines. This is very indicative of the presence of lateral reservoir drainage and hydrodynamically trapped hydrocarbons.

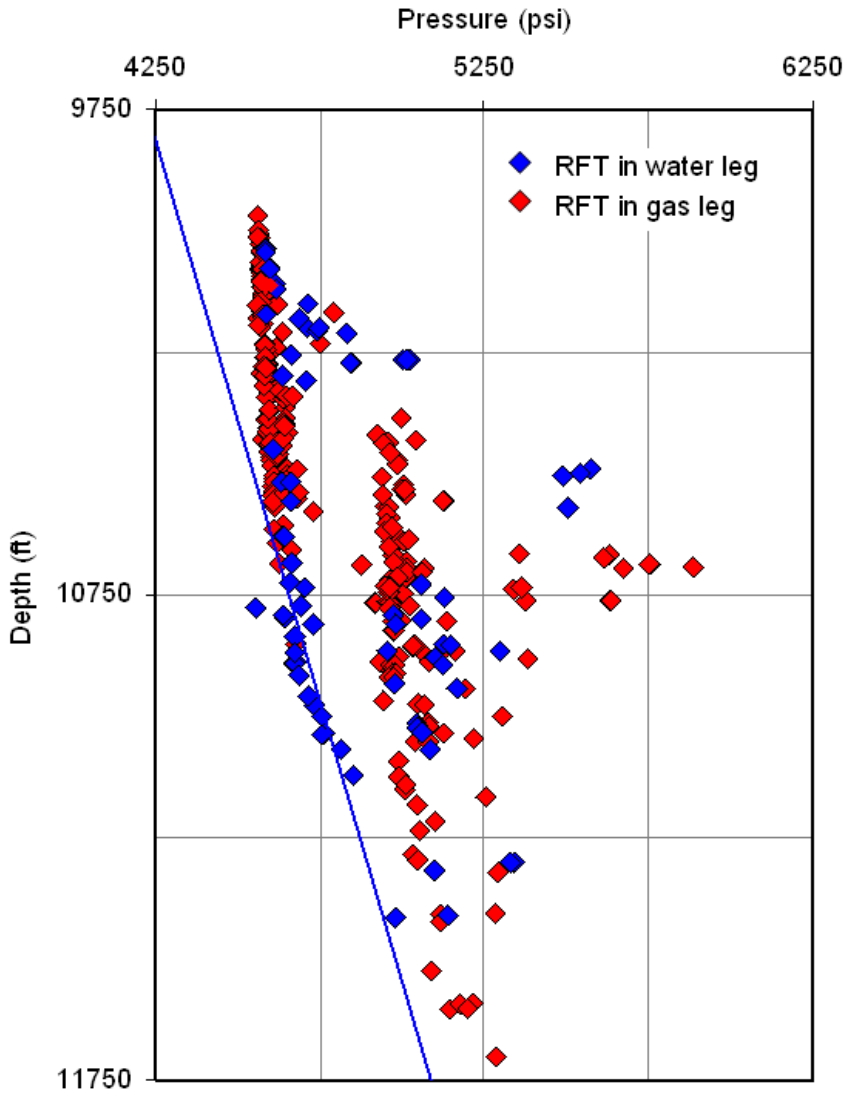

Figure 5.9 Pressure–depth plot in stratigraphic layer SU3 in the Peciko Field.

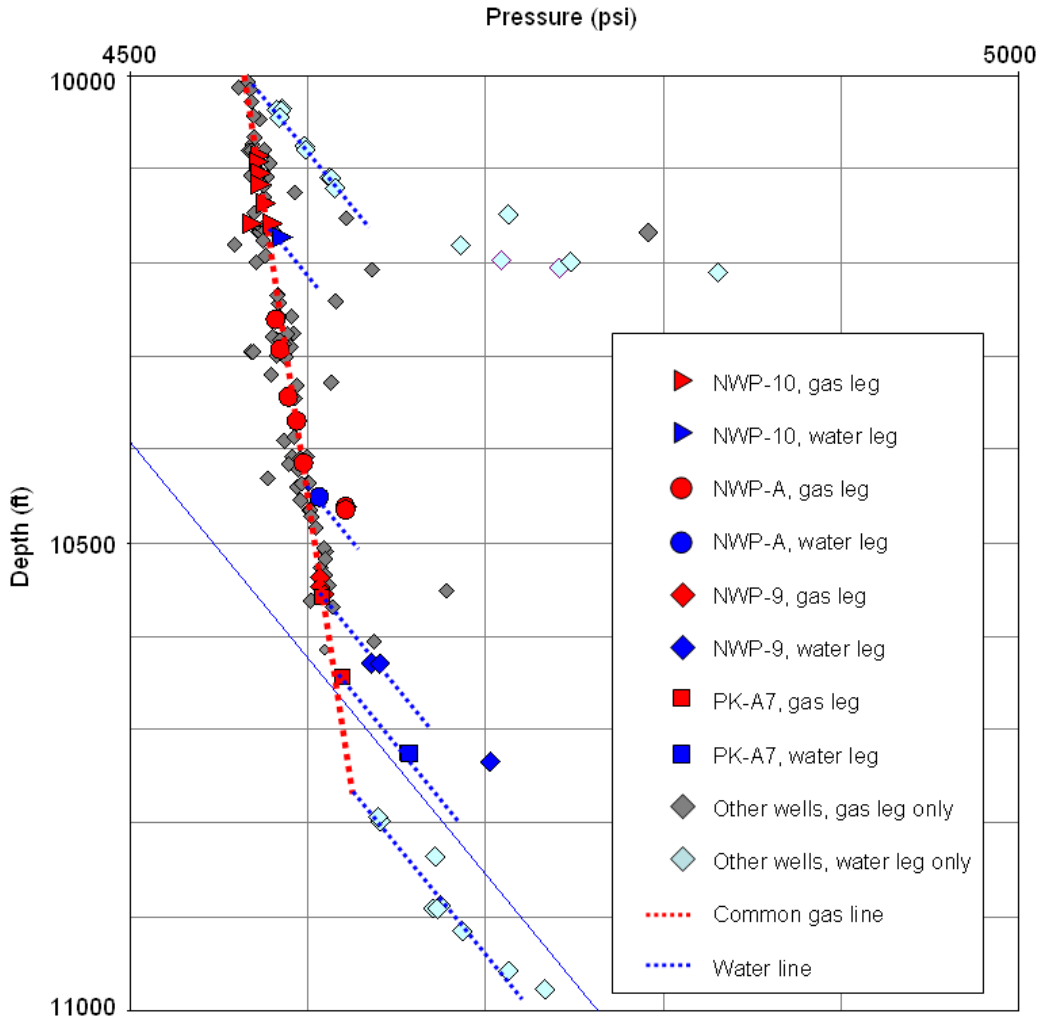

Figure 5.10 Pressure–depth plot for stratigraphic layer SU3a showing hydrodynamically tilted gas-water contacts: one gas line accompanied by several water lines.

A typical pressure-depth plot for an individual well is shown in Figure 5.11. The complete pressure-depth plot for all 16 wells is given in Appendix 1b. All depths are given as TVDSS because the water depth at these wells does not exceed 60 ft. The overpressured zone in this field can be divided into two: a low overpressure zone and a transition zone into high overpressure. The low overpressure zone is characterised by a pressure trend that is close to the vertical stress gradient, while the transition zone has a pressure gradient that is far higher than the lithostatic stress gradient. None of the wells in the Peciko Field

encounters the zone of very high overpressure; they all terminated within the transition zone. A south-north cross-section (Figure 5.12) shows that both top of low overpressure and top of the transition zone deepen to the north, where the strata are more sand-rich (Figure 2.8).

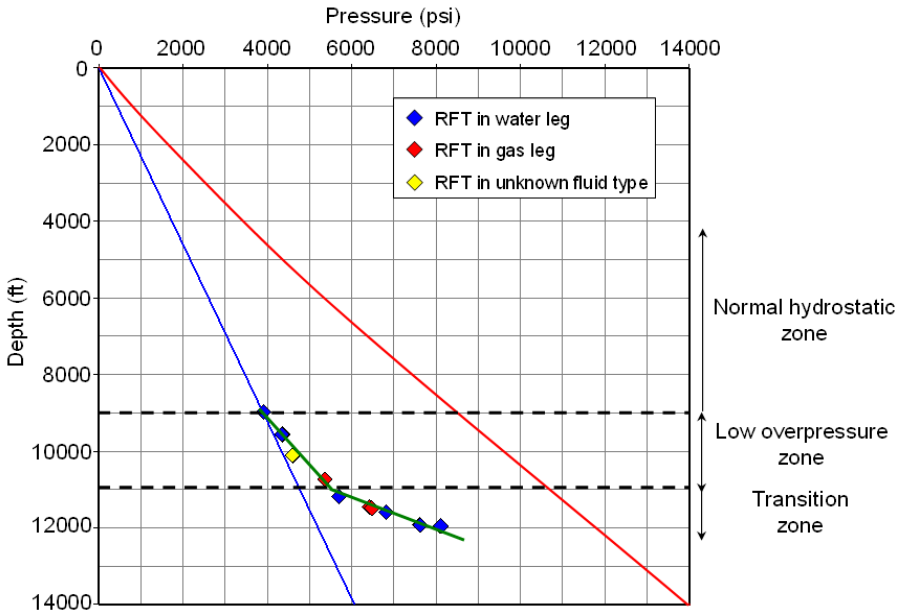

Figure 5.11 Typical overpressure profile in the Peciko Field.

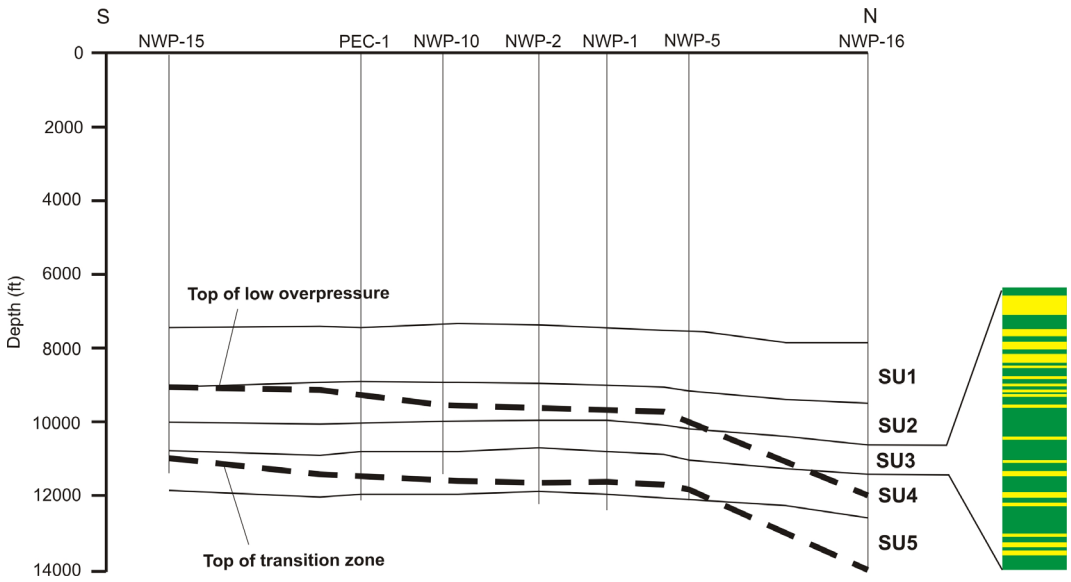

Figure 5.12 Overpressure cross-section in the Peciko Field showing that both top of overpressure and the top of the transition zone deepen to the north.

5.3 Wireline log suites

The wireline log suites available for analysis come from 16 wells (NWP-1 – NWP-16). Discrimination of mud-rich intervals from more silty and sandy intervals was done by cross-plotting density against the difference between neutron porosity and porosity estimated from the density log (Katahara, 2006). To infer porosity from the density log, a matrix density of 2.72 g/cm^3 was used, based on clay mineralogical analysis performed by Total E&P Indonesie. A fluid density of 1.05 g/cm^3 was used, based on formation water analysis performed by Total E&P Indonesie. The data do not show a clear difference in gradient as in Katahara (2006) (Figure 5.13), and therefore an arbitrary threshold value of 0.18 was chosen (i.e., $\Phi_N - \Phi_D > 0.18$) to ensure that the pressure analysis was consistently performed in the mud-rich intervals. Tests showed that the compaction trend for the mudrock data had low sensitivity to the choice of threshold value.

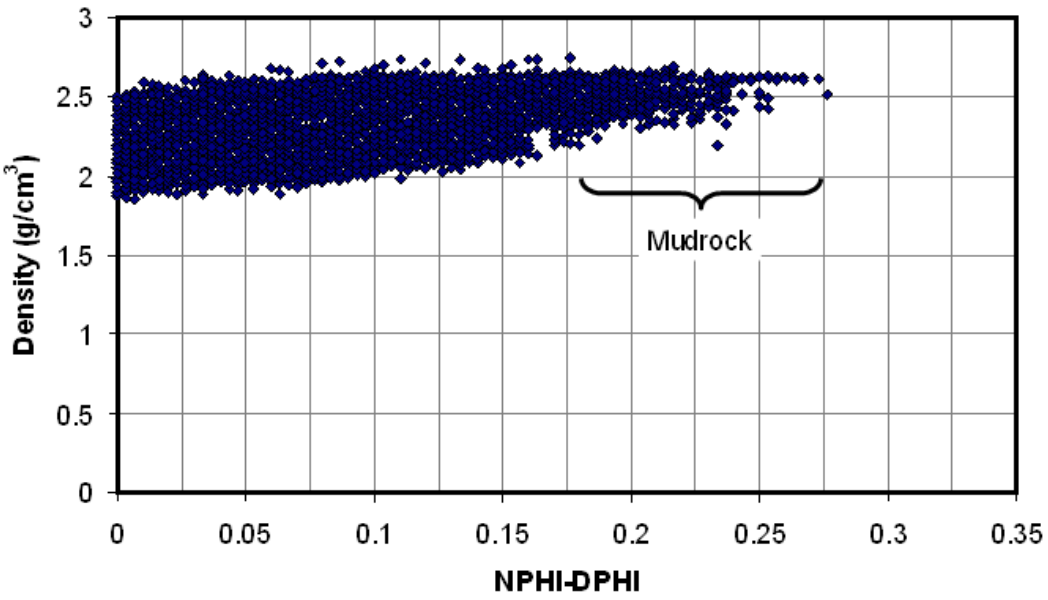

Figure 5.13 Sand-mudrock discrimination in the Peciko Field.

The raw density log was also used to calculate vertical stress in this field. Examples from wells NWP-9 and NWP-16 are shown in Figure 5.14. The complete results of the calculations in 16 wells shown on pressure-depth plots in

Appendix 1b. The vertical stress in each well does not differ significantly, and the trend can be approximated with a power law equation. For NWP-9, the equation is:

$$\sigma_v = 0.3856 z^{1.0984} \quad (5.1)$$

where σ_v is in psi and z is in ft.

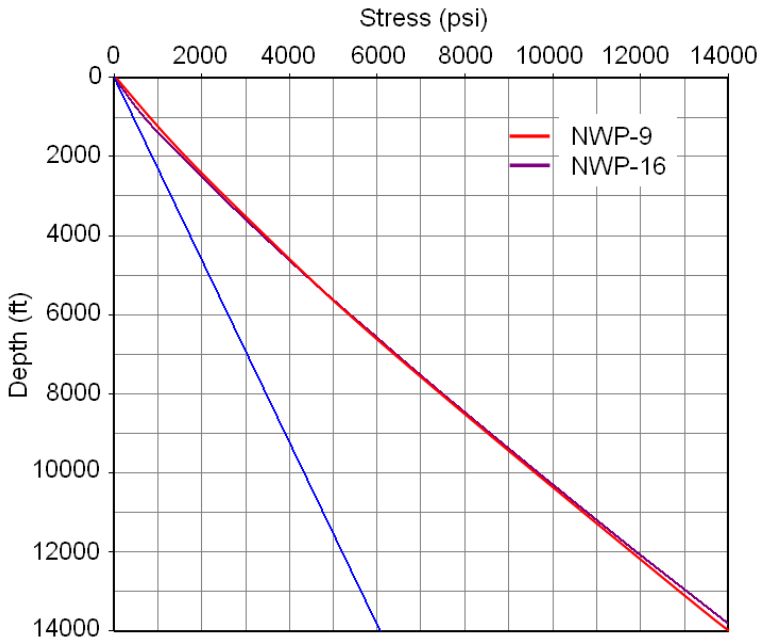

Figure 5.14 Examples of vertical stress in wells NWP-9 and NWP-16.

The complete wireline log response for the mudrocks in all 16 wells is given in Appendix 1b. For analysis of overpressure, the data from three wells, PEC-1, NWP-9, and NWP-16 (locations in Figure 5.1), are presented to illustrate the findings. PEC-1 was chosen as typical example of a well on the crest of the structure and because source rock maturation data are available from it (Figure 5.5), although it does contain a relatively small number of RFT points and no density log was run in this early well. NWP-9 was chosen because it encounters the highest overpressure value in the Peciko Field. NWP-16 is located downflank in the northern part of the field where top of overpressure is deeper. It is the deepest well in the field and was chosen to make a comparison of the wireline log responses with those from well NWP-9.

5.4 Data analysis

5.4.1 Overpressure generating mechanisms

Observation

The pressure-depth plot for well PEC-1 (Figure 5.15) is typical of wells in this field, except that top of overpressure is located at slightly greater depth further north (Figure 5.12). The overpressure initially increases slowly with depth below the top of low overpressure at ~9500 ft and then more rapidly through the transition zone. The top of the transition zone is at ~11,300 ft. The top of transition zone is picked where vertical effective stress starts to decrease as depth increases.

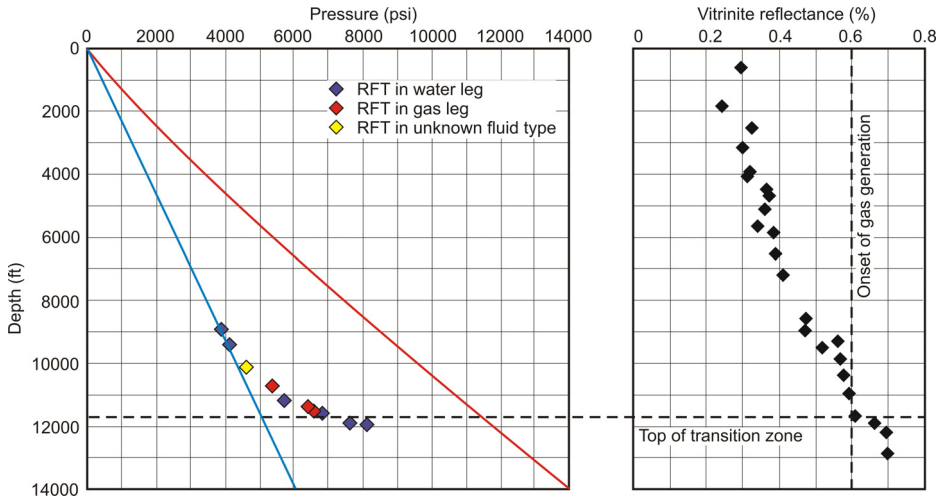

Figure 5.15 Pressure data from well PEC-1 showing that top of the transition zone coincides with the onset of gas generation.

As mentioned previously, well PEC-1 is the only well in the Peciko Field from which vitrinite reflectance data are available (Figure 5.5 and 5.15). There is a correlation between the top of the transition zone into hard overpressure and the vitrinite reflectance value of 0.6% (threshold for onset of gas generation) (see

Sub-section 2.2.2). The pressure-depth plot, wireline log suites for the mudrock section, and simplified lithological column of the Tunu Main Zone for NWP-9 are shown in Figure 5.16. The pressure-depth plot for well NWP-9 indicates that the top of low overpressure is at a depth of ~11,000 ft, although there is a good RFT measurement showing ~300 psi of overpressure in an isolated sand body at ~10,000 ft depth. The top of the transition into hard overpressure is around 12,000 ft depth, where reversals can be seen in the trends of both the sonic and resistivity logs through the mudrocks. The density log, by contrast, shows no obvious reversal, but it shows consistently high value of density, around 2.6 g/cm^3, in the depth interval 11,000–13,000 ft. The sonic and resistivity reversals without an accompanying density reversal are clear evidence for overpressure generation by an unloading mechanism, as discussed in Sub-section 3.5.2. Moreover, the high density values (~2.6 g/cm^3) also show that the porosity of the mudrock is very low, ~7%. It is unlikely that the mudrock is experiencing disequilibrium compaction with this low porosity value.

Cross-plots of density against sonic and resistivity log values for mudrocks in well NWP-9 are shown in Figure 5.17, with data points colour-coded at intervals of 1000 ft. The illitic compaction trend was determined empirically from data in the 16 appraisal wells at the Peciko Field, and differs slightly from Dutta's (2002) trend (Figure 3.19). The purpose of plotting this trend is to aid identification of unloading, which may be indicated by departures from this trend. The average geothermal gradient of around 9.4°C/1000 ft plus surface temperature of 30°C gives an estimated temperature of nearly 80°C at 5000 ft depth. This temperature is sufficient for discrete smectite to have disappeared, transformed into mixed layer illite/smectite (Hower et al., 1976; Boles and Franks, 1979). Based on this fact, all data below 5000 ft are used to derive the illitic compaction trend. The data above 5000 ft show considerable scatter so the smectitic compaction trend could not be constructed with confidence. The illitic compaction trend relating density to transit time is:

$$\rho = -0.0049\Delta t + 2.973 \qquad (5.2)$$

where ρ is density in g/cm^3 and Δt is transit time in μs/ft.

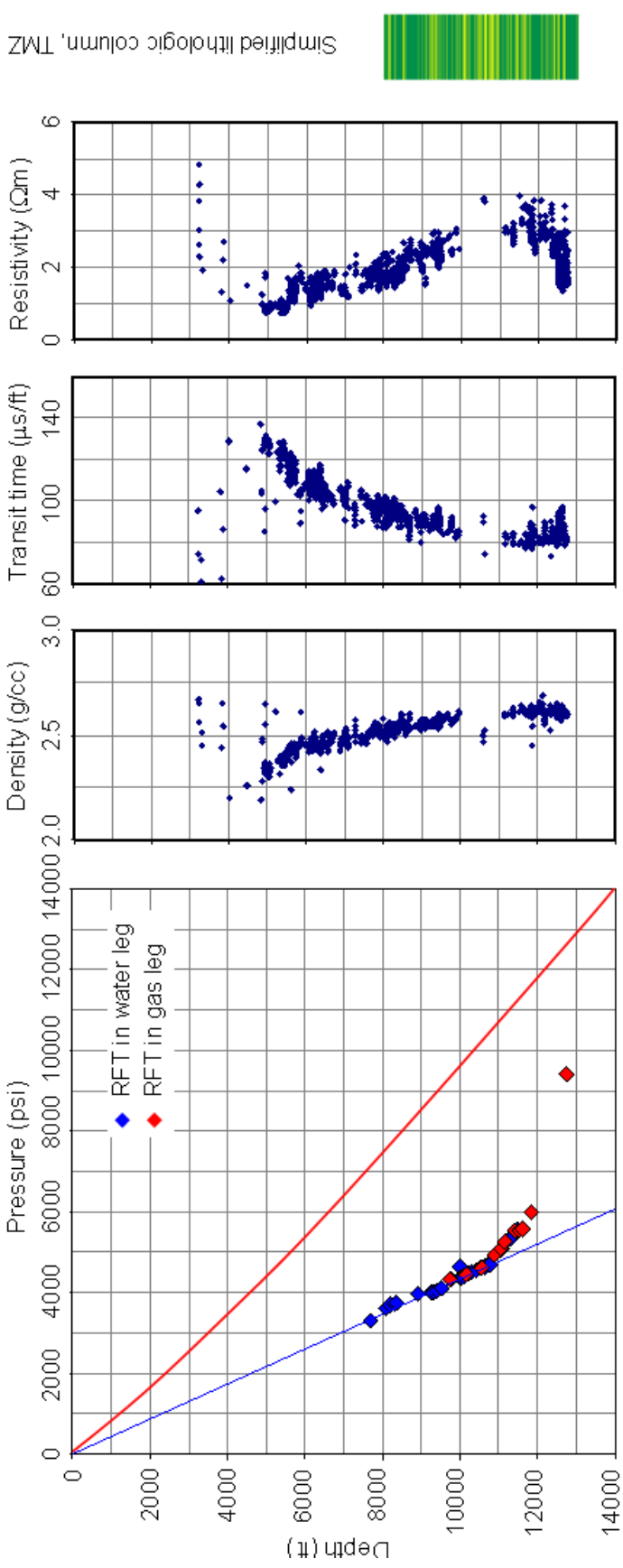

Figure 5.16 Pressure–depth plot, wireline log suites in the mudrock section, and simplified lithological column for the Tunu Main Zone in well NWP-9, Peciko Field.

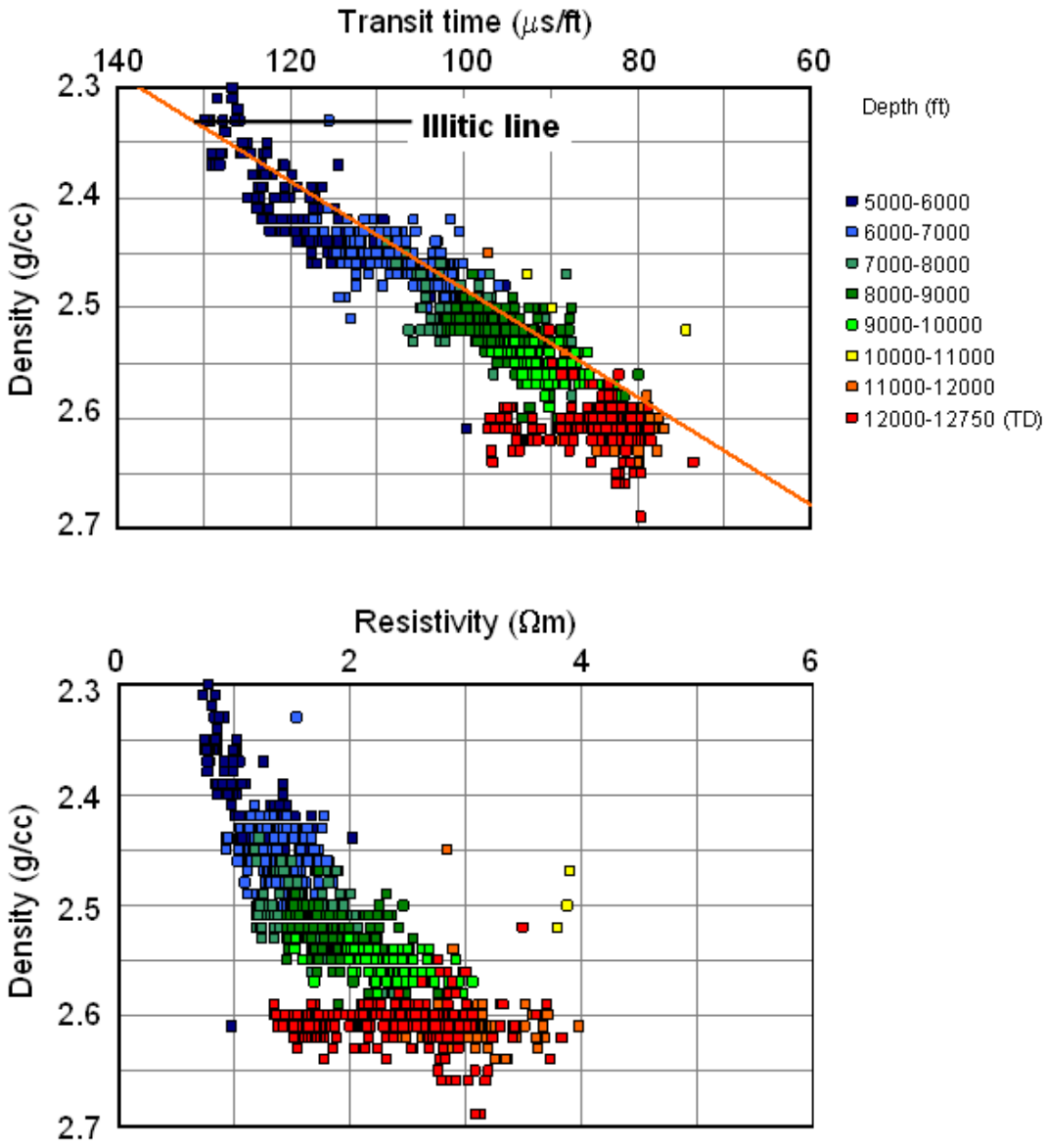

Figure 5.17 Cross-plots of density against sonic transit time and resistivity in mudrocks in well NWP-9, Peciko Field.

Both density-sonic and density-resistivity cross-plots in NWP-9 show clear unloading responses at a depth of ~12,000 ft. The data points coloured red in the deepest interval show changes in trend, with increased sonic transit time and decreased resistivity but no decrease in density. These observations provide clear evidence that the generating mechanism for the transition zone is an unloading process. Data points in the depth range 5000–12,000 ft on the density-sonic cross-

plot fall on, or close to, the illitic compaction trend. The unloading response can also be clearly observed in several other wells, such as NWP-2, NWP-3, NWP-4, and NWP-10 (Appendix 1b).

The pressure-depth plot, wireline log suites for the mudrock section, and simplified lithological column of the Tunu Main Zone for NWP-16 are shown in Figure 5.18. The pressure-depth plot for well NWP-16 appears to converge slightly towards the lithostatic gradient with increasing depth, but it is not clear whether the well has entered the expected transition zone into hard overpressure. The wireline logs appear to display asymptotic trends towards the bottom of the well, without any clear indication of reversals, although it is possible that the trends of both sonic and resistivity logs are on the point of reversing at the bottom of the well. Both density-sonic and density-resistivity cross-plots also show no clear response of unloading (Figure 5.19).

Interpretation

The observations provide clear evidence that the generating mechanism for the transition into high overpressure zone is an unloading process. There are two candidates causing overpressuring in this field, clay diagenesis and gas generation. Among the clay diagenesis processes (see Sub-section 3.2.2), transformation of discrete smectite to mixed-layer illite/smectite can be ruled out as the cause of overpressuring in this field since the depth of transformation (5000 ft) is located far above the top of low overpressure (9500–12,000 ft). Presumably, lateral reservoir drainage was responsible for draining pressure that may be produced by the transformation. The NTG maps for the Median Axis region of the lower Kutai Basin show a progressive upward increase in NTG at the Peciko Field from SU5 up to SU3 (Figure 2.9), which is consistent with effective lateral drainage above the overpressured zone.

Pressure–depth plots show that the top of low overpressure is at depths of 9500–12,000 ft, corresponding to estimated temperatures of 120–140°C, and there is a transition zone into high overpressure at depths of 11,500–14,000 ft,

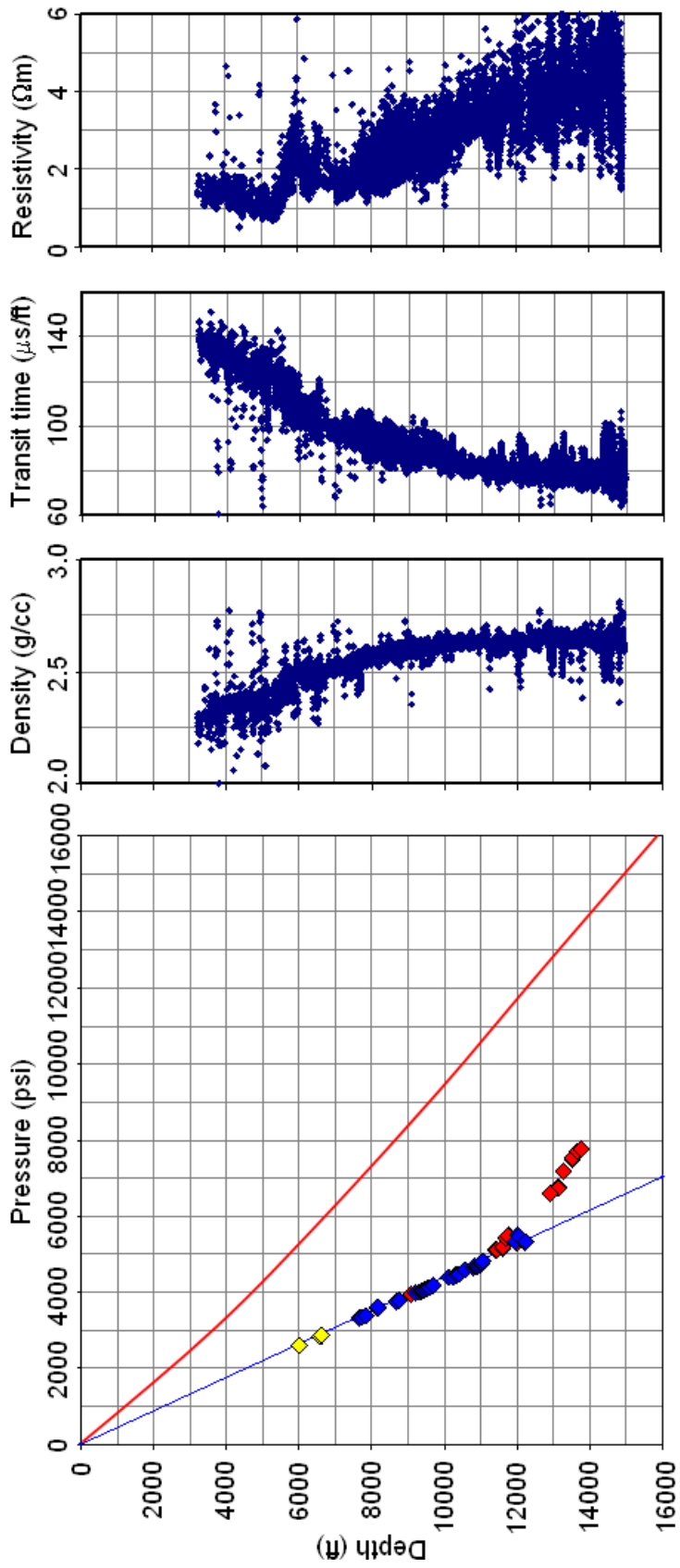

Figure 5.18 Pressure–depth plot, wireline log suites in the mudrock section, and simplified lithological column for the Tunu Main Zone in well NWP-16, Peciko Field.

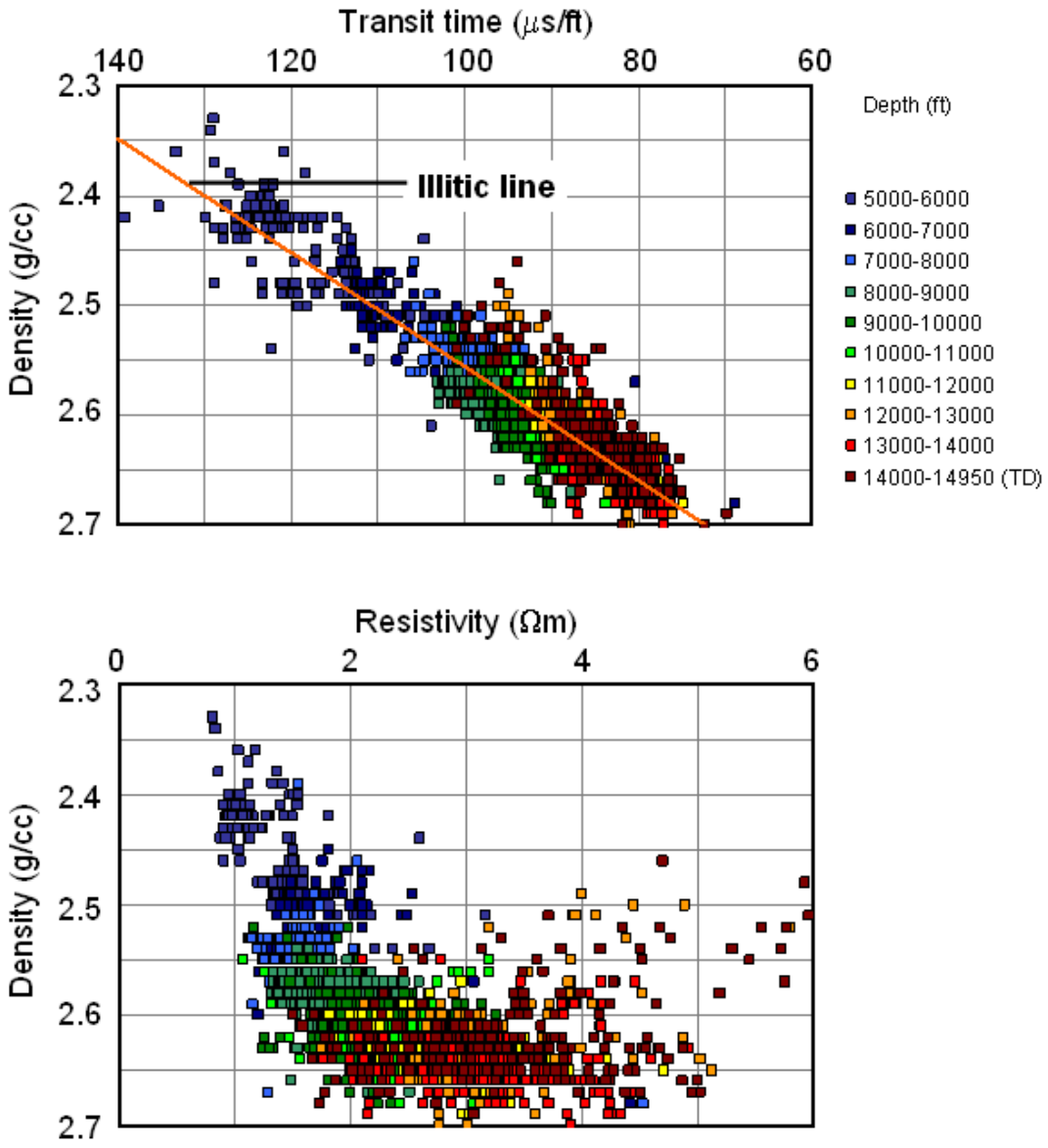

Figure 5.19 Cross-plots of density against sonic transit time and resistivity in mudrocks in well NWP-16, Peciko Field.

corresponding to estimated temperatures of 140–160°C. Illitization of mixed-layer illite/smectite is ongoing at temperatures greater than 80°C (Hower et al., 1976; Boles and Franks, 1979) and thus it may contribute to the observed overpressure. Kaolinte transforms to illite at temperatures ~130–140°C in basin settings (Bjorlykke, 1998) and it can also contribute to the observed overpressure. This temperature roughly corresponds to that estimated at the depth of the transition

zone. Furthermore, the dissolution of kaolinite and precipitation of illite may reduce porosity and permeability at this depth, and thereby help to maintain high overpressure in the deeper strata.

Gas generation, generated both directly from kerogen and from oil cracking to gas, seems likely to be another process to be responsible for unloading overpressuring in the Peciko Field. Data from PEC-1 shows that there is a correlation between high overpressure and vitrinite reflectance values above 0.6%, which is the onset of gas generation (Lambert et al., 2003). Other data from neighbouring fields show a good correlation of high overpressure with vitrinite reflectance, as discussed in the next chapter.

To the south and east of the Peciko Field, the sands within the Tunu Main Zone peter out as the depositional environment changes from the shelf break setting to deep marine. Since the organic carbon content of the deep marine sediment is low and its potential for hydrocarbon generation is negligible (Sub-section 2.2.3), there is unlikely to be significant lateral transfer of overpressure generated by gas generation from the synclinal area to the southwest. However, there may be lateral transfer of overpressure generated by clay diagenesis.

There are two possible ways of explaining how the low overpressure was generated: by disequilibrium compaction, or by vertical transfer from the zone of high overpressure below. This issue is considered in the next sub-section, since its resolution depends upon the compaction state of the mudrock.

5.4.2 Compaction

Plots of all wells with density logs, NWP-1 to NWP-16, are shown in Figure 5.20. The density log, as discussed in Sub-section 3.5.2, is a more reliable indicator of the bulk porosity of the sediments than the sonic and resistivity logs. The density values continue gradually to increase downwards through the zone of low overpressure (Figure 5.20), showing that compaction continues down to the TD of all the wells, independent of overpressuring. Based on this observation, loading and disequilibrium compaction cannot possibly be responsible for all the

overpressure in the zone of low overpressure. The origin of the low overpressure, above the transition zone into hard overpressure, has probably resulted from passive transmission of pore fluid from the highly overpressured zone below (vertical transfer).

Plotting the data from 16 wells in Figure 5.20, in which the depth to top of overpressure varies, may obscure trends, so plot of density against depth for the individual wells are given in Appendix 1b.

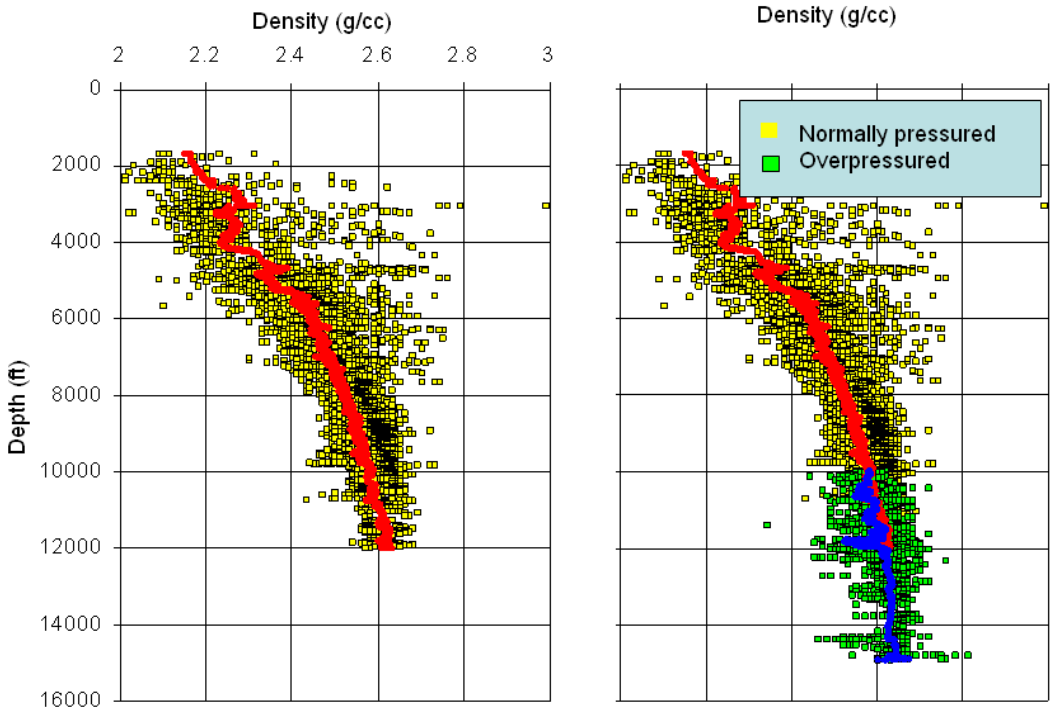

Figure 5.20 Composite density plot for mudrocks, defined by $\Phi_N - \Phi_D > 0.18$, in all the NWP wells, Peciko Field: left figure for hydrostatically pressured interval only; and right figure for all the density log data. The red and blue lines are running averages of the data, using a window length of 100 ft, for the hydrostatically pressured and overpressured section, respectively.

The continuous compaction below the top of overpressure and down to TD is consistent with ongoing chemical compaction. The effective stress appears to have no influence on compaction and the mudrocks are likely to be stiffened by

chemical compaction so that they are overconsolidated in a mechanical sense (Bjorlykke and Hoeg, 1997; Bjorlykke, 1998, 1999).

An empirical exponential relationship between density-derived porosity and depth in the Peciko Field is shown in Figure 5.21. As mentioned previously, there are two exponential relations. The first relation is for the first 5000 ft, and this is the smectitic compaction line (eodiagenesis). Unfortunately, the data in the first 6000 ft show considerable scatter so the compaction line cannot be constructed with confidence. The second relation is for 6000 ft depth to TD, and this is the illitic compaction line (telodiagenesis) (Figure 5.21). A comparison between the latter compaction relation in the Peciko Field and worldwide published compaction relationships is included in Chapter 7.

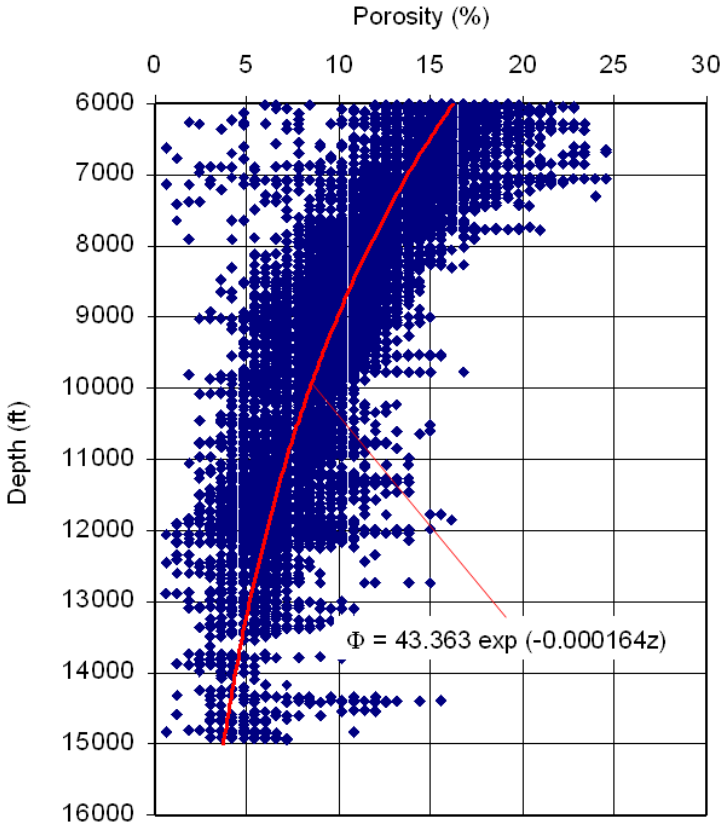

Figure 5.21 Empirical fitting exponential-decay curve for porosity as a function of depth for the depth interval of 6000 – 15,000 ft derived from 16 density logs in the Peciko Field.

5.4.3 Overpressure estimation

Wells NWP-9 and NWP-16 were chosen for overpressure estimation analysis. As mentioned earlier, the highest overpressure encountered in this field is in NWP-9. NWP-16 was chosen because the deepest top of overpressure is in this well. The sonic log is used to estimate overpressure in both wells.

Prior to estimating the overpressure in the mudrocks, the first step is to construct the normal compaction trends (NCTs) for the sonic transit time versus depth. The NCTs were derived by fitting the data to hydrostatically pressured interval from 6000–11,000 ft depth in all 16 wells. The choice of this depth interval was based on the fact that over a large depth interval above the top of overpressure, the mudrocks are located on the illitic compaction trend. The various NCTs are shown in Figure 5.22. The 3P-NCT gives the highest overpressure estimates, and so was used to estimate the overpressure in wells NWP-9 and NWP-16.

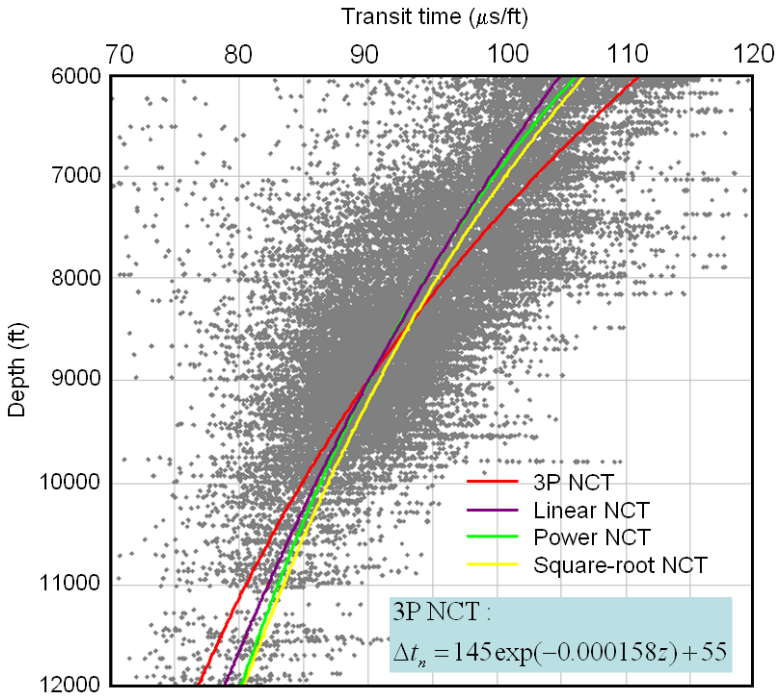

Figure 5.22 Various empirical NCTs for sonic transit time versus depth fitted empirically to mudrock data from the Peciko Field.

Overpressures estimated in wells NWP-9 and NWP-16 are shown in Figures 5.23 and 5.24. In the zone of low overpressure in NWP-9 (Figure 5.23), fair estimates of pore pressure are obtained with the standard exponent of 3 in Eaton's equation, but the measured reservoir pore pressure in the transition zone, near TD, is seriously underestimated. The exponent needs to be increased to ~7 to match the pressure measurement. Several researchers (e.g., Tingay et al., 2009) have stated that if the Eaton's exponent of 3 matches the observed pore pressure, then it is implied that the cause of overpressure is disequilibrium compaction. However, the estimated pore pressure also depends on the choice of the normal compaction trend. For example, if we choose the square root normal compaction trend (Figure 5.22), then the estimated pore pressure will be lower than the observed pore pressure. Therefore, it is best to avoid making any interpretation of overpressure generating mechanism based on the overpressure estimation method.

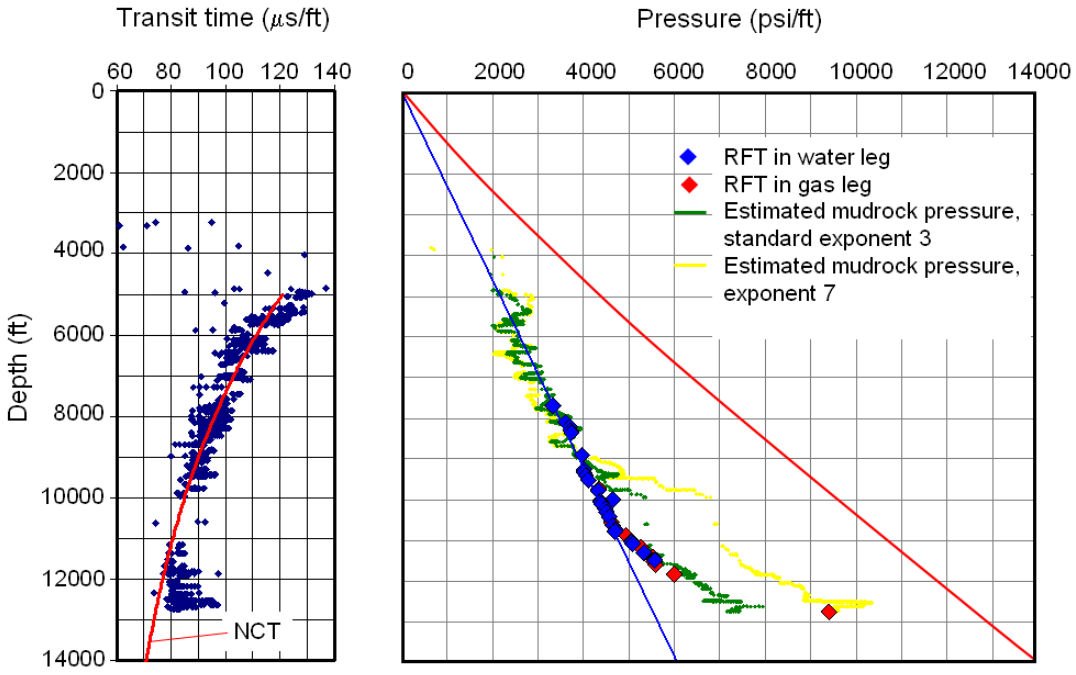

Figure 5.23 Estimated pore pressure profiles in the mudrocks in well NWP-9 using 3P-NCT + Eaton's Method with exponents 3 and 7.

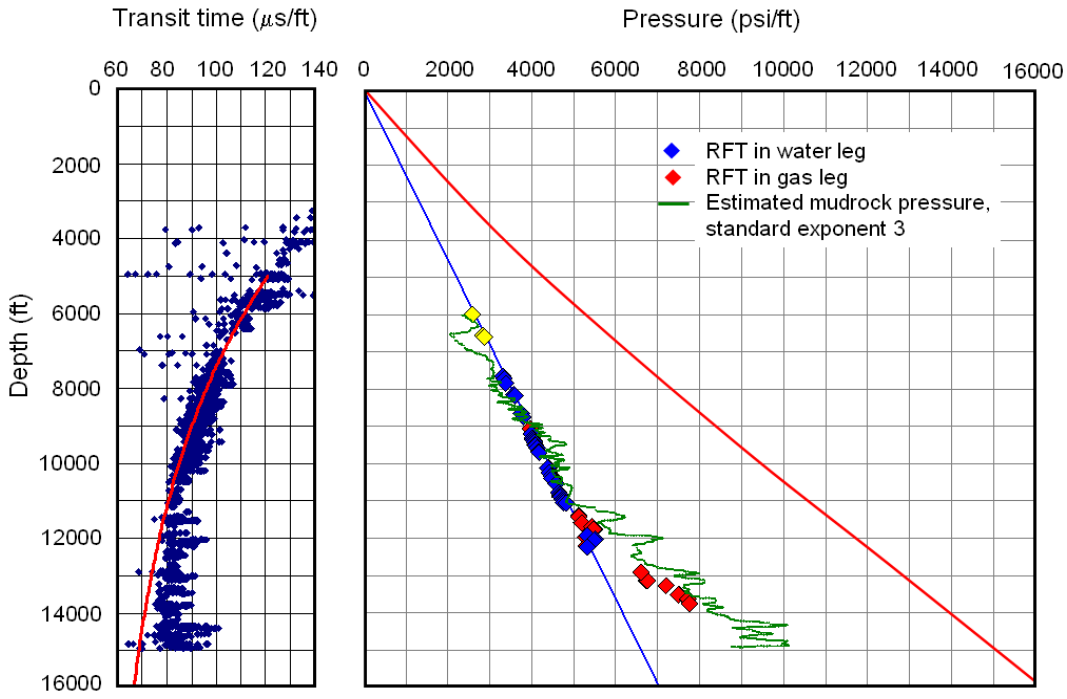

Figure 5.24 Estimated pore pressure profile in the mudrocks in well NWP-16 using 3P-NCT + Eaton's Method with exponent 3.

The same technique applied to well NWP-16, using the standard exponent of 3, predicts overpressure in the 11,000–12,000 ft depth interval, where the pore pressure is hydrostatic (Figure 5.24). Bois et al. (1994) used this overestimation as evidence for pore pressure discrepancies, but their interpretation is in serious doubt, as discussed below.

Bois et al. (1994) used a simple exponential decay function for the sonic log normal compaction trend (2P-NCT/Equation 3.10) and Eaton's equation (Equation 3.23) with the standard exponent 3 for estimating pore pressure in some Sisi wells. Their estimated pore pressure (Figure 1.2) resulted in a pressure discrepancy in the shallower section and pressure equilibrium (i.e., sand pressure = mudrock pressure) at TD in the Sisi wells. The same technique, if applied to the Peciko wells, will result in similar equilibrium between sand and mudrock pressures (Figure 5.25). However, as mentioned in Sub-section 3.6.2, the simple exponential decay of sonic travel time with depth (2P-NCT/Equation 3.10) cannot

be correct, since such exponential decay will cause the matrix transit time to approach zero at large depths, which is physically unreasonable. Therefore, the evidence for inferring that there are sand–mudrock pressure discrepancies in the Peciko Field is very unconvincing.

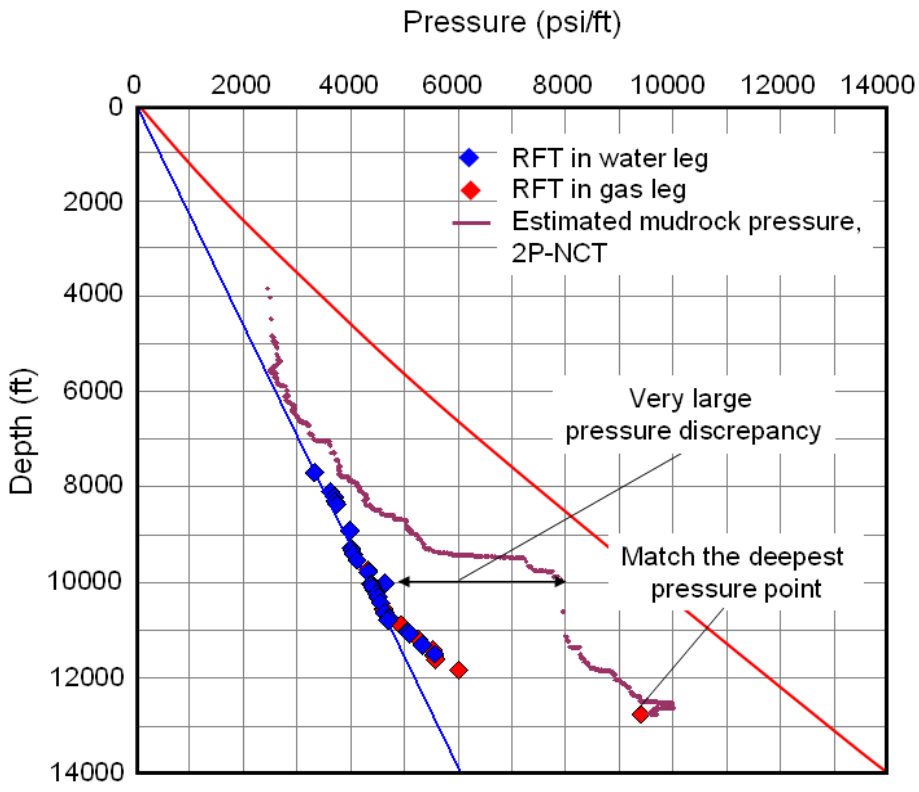

Figure 5.25 Estimated pore pressure profile in the mudrocks in well NWP-9 using 2P-NCT + Eaton's Method with exponent 3.

A more appropriate empirical method to estimate overpressure due to unloading is Bowers' (2001) method. It is discussed in the next chapter since it requires very high pore pressure data to derive the unloading curve (Equation 3.27), and none of the pore pressure measurements in the Peciko Field are sufficiently high to apply it.

5.4.4 Lateral reservoir drainage

An example of the presence of the existence of lateral reservoir drainage in the Peciko Field, leading to hydrodynamically tilted gas-water contacts was described in Section 5.1. The overpressure maps for several stratigraphic layers where mapping was possible are shown in Appendix 1c.

The previous hydrodynamic model (Figure 1.5) explained the maintenance of active lateral reservoir drainage by expulsion of water from overpressured and undercompacted mudrocks, as demonstrated by the presence of sand–mudrock pressure discrepancies. It has been demonstrated above that the interpretation of sand–mudrock pressure discrepancies is very weak because it resulted from the wrong empirical method (2P-NCT + Eaton's method). Moreover, this research has revealed that the cause of overpressure in the Peciko Field is an unloading mechanism, and the mudrock is in an overcompacted state. In the following paragraphs, it is demonstrated that pressure discrepancies do not exist in the Peciko Field.

If pressure discrepancies exist, then the shoulder effect (Figure 3.24) should be observable in the sonic log. The sonic logs from 16 wells have been examined, and no clear evidence of shoulder effects was found (Figure 5.26). The absence of the shoulder effect is in accordance with Deming's work (Deming, 1994), which strongly suggests that thinly interbedded sand–mudrock sequences cannot possibly maintain such huge pressure discrepancies on geological time scales.

It is proposed that active lateral reservoir drainage at the present time is maintained by water expulsion resulted from gas generation and clay diagenesis (Figure 5.27). Consequently, the lateral reservoir drainage may be present anywhere in the basin, as long as both processes are active and there is overpressure variation. The potential for active lateral drainage leading to hydrodynamic trapping in other fields is discussed in Chapter 6.

As a final point here, the relatively limited temperature data in Figure 5.27 show that the top of the transition zone coincides with an isotherm. This

observation supports the interpretation that gas generation and clay diagenesis, which are temperature-driven, are the main causes of overpressuring. On the other hand, it seems that the top of overpressure does not coincide with the facies distribution since it crosses a relatively sand-rich interval as shown in Figure 5.28.

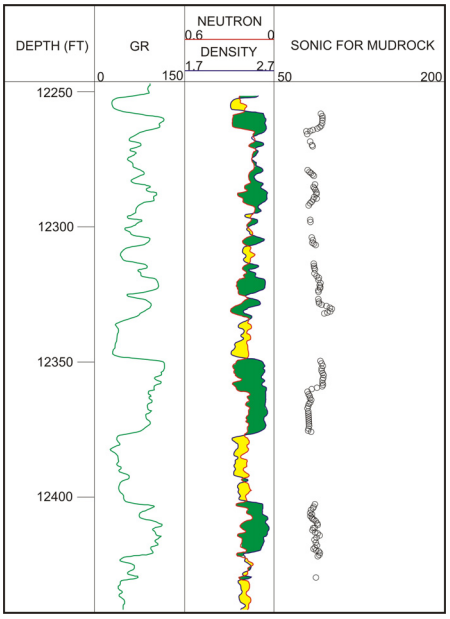

Figure 5.26 Typical sonic log through a sand-mudrock sequence in the Peciko Field, showing the absence of shoulder effect (taken from NWP-16).

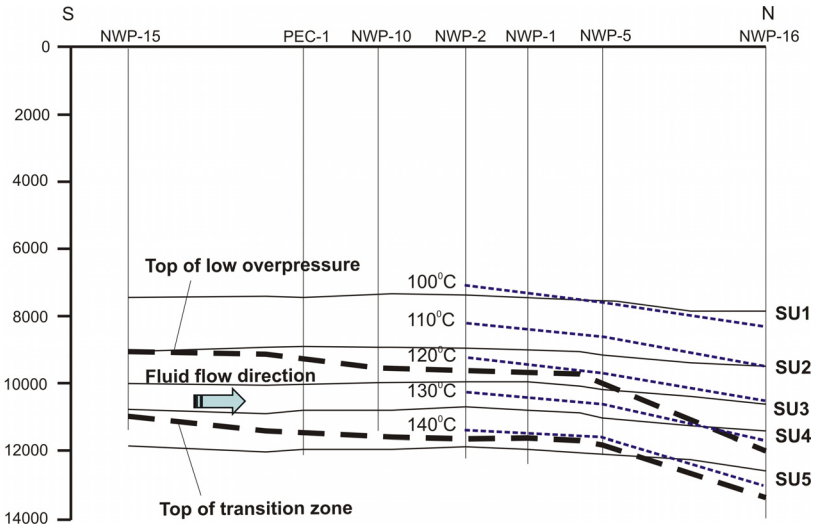

Figure 5.27 A south-north cross-section showing that the top of the transition zone into hard overpressure follows the 140°C isotherm.

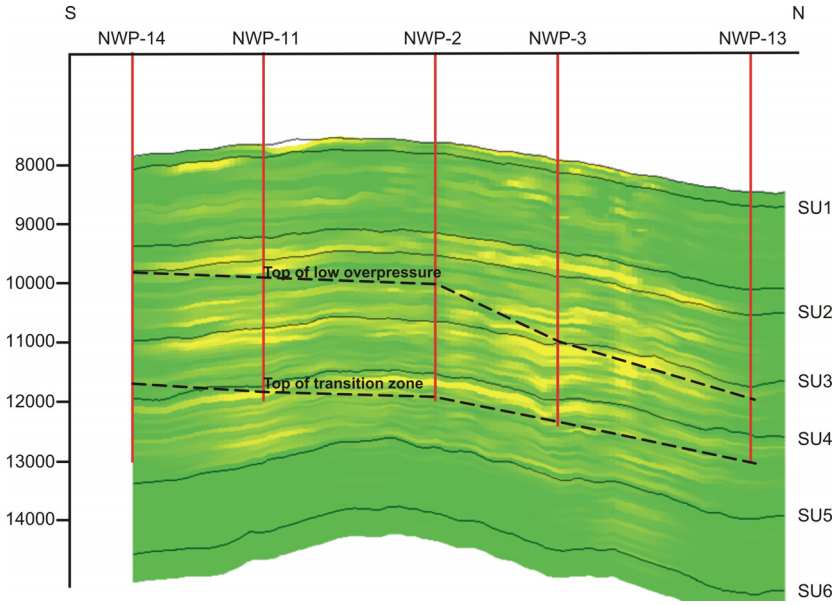

Figure 5.28 Top of overpressure in relation to sand-mudrock facies distribution.

5.5 Summary

The following points summarise the main results from the Peciko Field:

- Overpressure in the Peciko Field is caused by an unloading mechanism, or mechanisms.
- The overpressuring in the Peciko Field does not provide convincing evidence for the existence of sand–shale pressure discrepancies.
- The unloading may be caused by clay diagenesis, i.e., illitization of mixed layer illite/smectite and kaolinitization of illite, and by gas generation.
- The smectite-illite transformation taking place in the shallower section does not contribute to the overpressuring due to effective lateral reservoir drainage in the shallow section.
- Compaction proceeds down to the TD of well independent of overpressuring, which implies that the mudrocks are overcompacted in a mechanical sense.
- The equation relating porosity to depth for the interval of 6000 – 15,000 ft is:

$$\Phi = 43.363\exp(-0.000164z) \qquad (5.3)$$

- Active lateral reservoir drainage is maintained by water flow resulting from clay diagenesis and gas generation.

CHAPTER 6
OVERPRESSURE AND COMPACTION IN THE LOWER KUTAI BASIN

The content of this chapter has been submitted for publication to AAPG Bulletin (Ramdhan and Goulty, 2010b). The objective of this chapter is to analyse whether the explanations for overpressuring and compaction at the Peciko Field are also applicable for the whole Lower Kutai Basin.

The chapter starts with an analysis of overpressuring and compaction in Section 6.1, moving from the easternmost part of the basin, the deep water area, to the shelfal area (External, Median, and Internal axes), and then to the onshore area (see Figure 1.1 for the locations). Interpretation of these data is given in Section 6.2, including consideration of the implications for hydrodynamics. The issue about what overpressure estimation method is suitable when overpressure has been generated by unloading is addressed in Section 6.3. The outcome of this chapter is a comprehensive understanding of overpressuring and compaction in the Lower Kutai Basin.

6.1 Data analysis

6.1.1 Deep water area

The deep water area is still classified as an exploration area, so neither pressure data nor wireline log suites have been released yet. The analysis of overpressuring in the area will be inferred from the results of the analysis on the shelfal area, combined with the geological conditions in the deep water area.

Stratigraphically, the deep water area is dominated by marine mudrock sediments of Pliocene age, which encase turbidite sand reservoirs sourced from

shelfal sediments (Guritno et al., 2003). Confinement of the reservoirs in the mudrock sequences (Figure 2.7) prevents lateral reservoir drainage from occurring in this area. This information will be used for some speculation concerning the overpressure behaviour in the deep water area in Sub-section 6.2.1.

6.1.2 External Axis

The field located on the External Axis is the Sisi–Nubi Field. Originally Sisi and Nubi were regarded as two separate fields, but it was later realised that some of the hydrocarbon accumulations extended across the whole structure. This field is a faulted anticlinal trap (Figure 6.1). The structural map in the Figure 6.1 is for the top of Beta marker, which is the top of the Fresh Water Sand Stratigraphic Unit (Figure 5.2). The maximum water depth in these fields is around 50 m. Stratigraphically, the productive interval is located in the upper part of the Upper Miocene, and comprises both the Sisi Main Zone and the Fresh Water Sand (Figure 5.2). In terms of field development, both fields are still at the appraisal stage.

6.1.2.1 Pressure data

As of 2008, there are 19 wells in the Sisi–Nubi Field. Because the field is still at the appraisal stage, all 'GOOD' pressure measurements in this well can be categorised as Class A pressure data.

There are ~1200 Class A pressure data available for analysis in these fields. A pressure–depth plot for all the Class A data is shown in Figure 6.2. The pressure–depth plot for each stratigraphic interval is shown in Appendix 2a. In this main text, the pressure–depth plots for two stratigraphic intervals are discussed: the Shallow Reservoir Zone, which overlies the Fresh Water Sand and extends upwards into the Quaternary, and the Sisi Main Zone (Figures 6.3 and 6.4). The pressure data from the Shallow Reservoir Zone are interesting since they show a consistent shift from normal hydrostatic pressure.

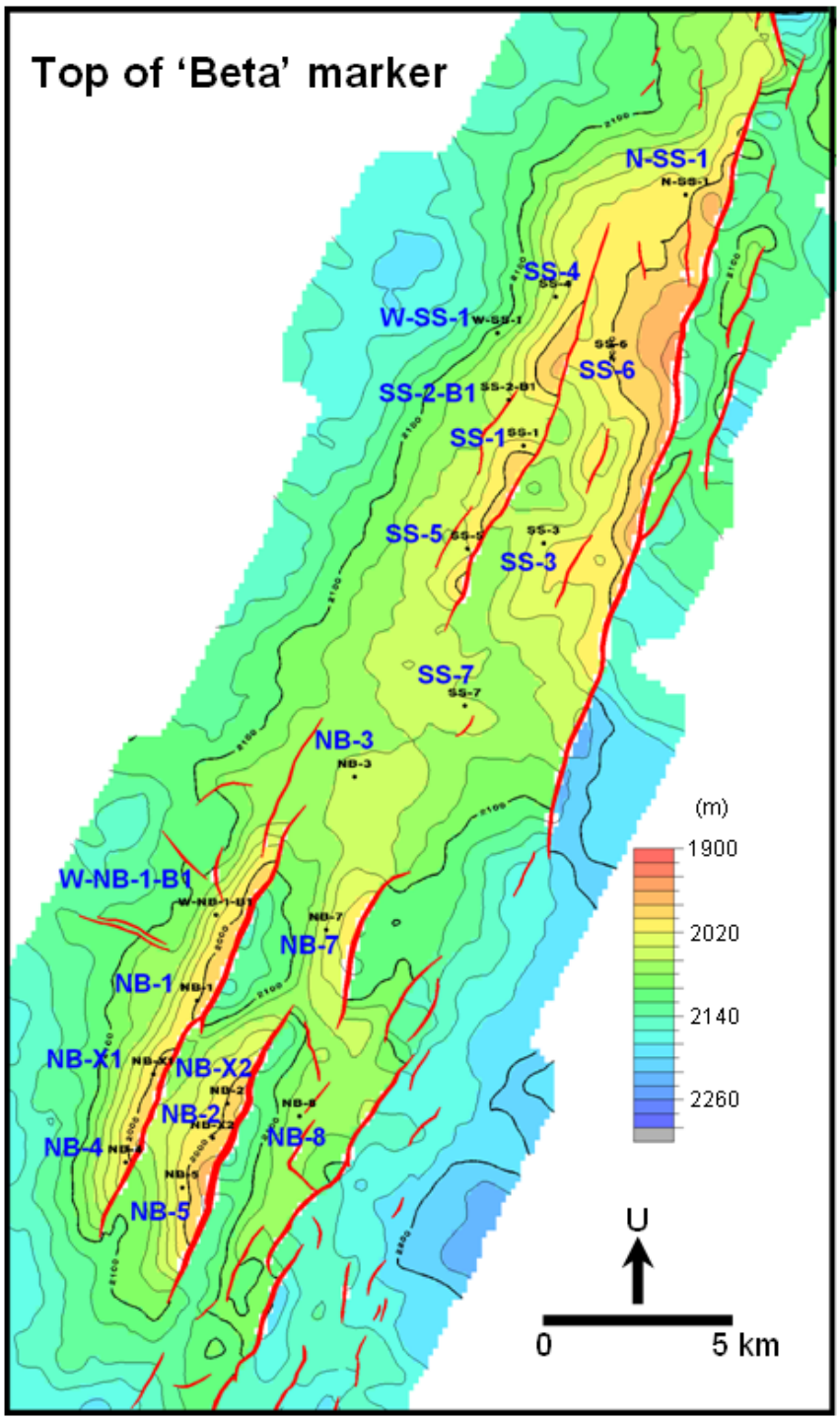

Figure 6.1 Structural map of the Sisi–Nubi Field at the top of the Beta marker (Total E&P Indonesie, 1995).

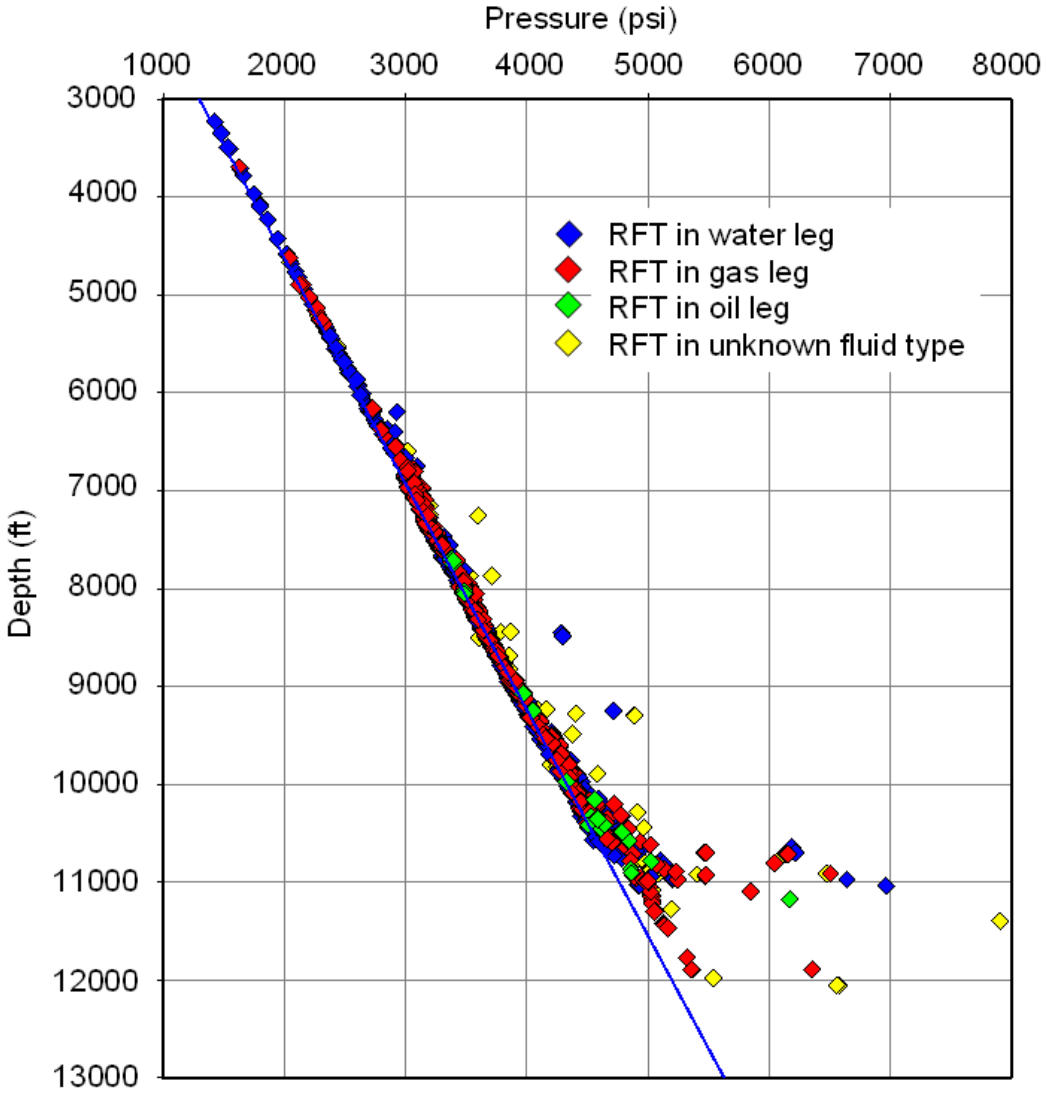

Figure 6.2 Pressure–depth plot for all Class A pressure data, Sisi–Nubi Field.

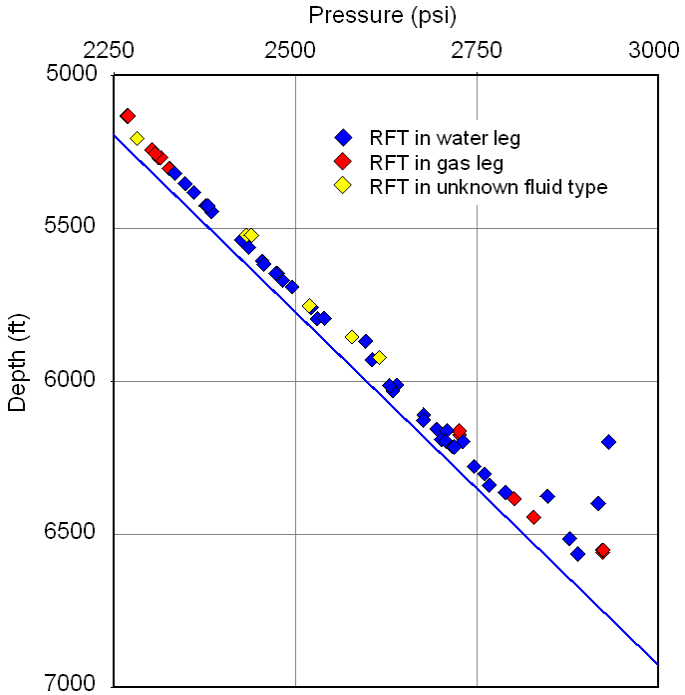

Figure 6.3 Pressure–depth plot for the Shallow Reservoir Zone, Sisi–Nubi Field, showing a constant shift in the water pressure from the normal hydrostatic line.

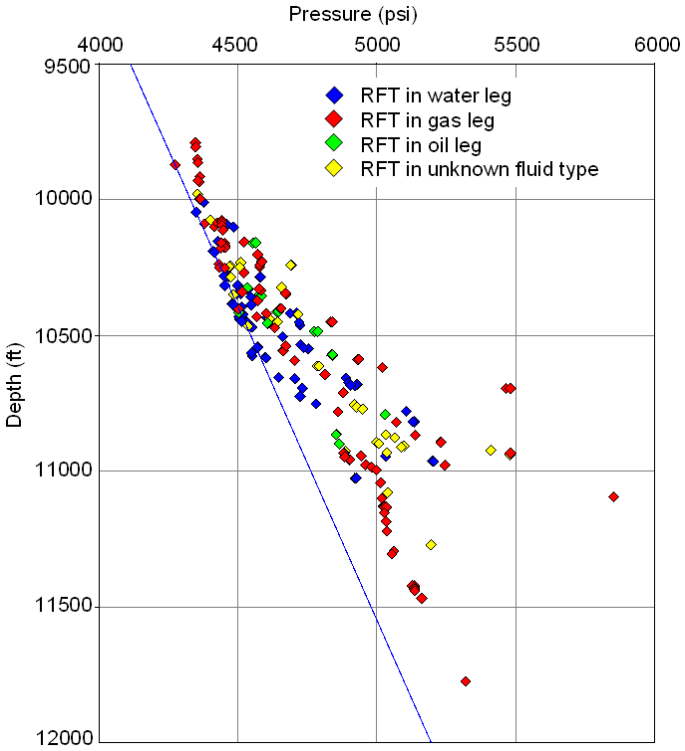

Figure 6.4 Pressure–depth plot for the Sisi Main Zone, Sisi–Nubi Field.

The pressure in the water leg in the Shallow Reservoir Zone shows a consistent excess of just over 40 psi, on average, above the normal hydrostatic pressure (Figure 6.3). This very slightly overpressured condition may be caused by hydraulic head. The highest elevation in the onshore area where the Upper Miocene strata crops out is about 200 m, and it will give a maximum overpressure of:

$P = \rho g h = 1000 \times 9.8 \times 200 = 1{,}960{,}000$ Pa ≈ 284 psi.

Given that the distance from the Sisi–Nubi Field to the onshore area is about 50 km, 40 psi overpressure means that there is an overpressure drop of ~244 psi/50 km, or about 172 m of head in 50 km. This lies within the range of hydraulic head drop for regional groundwater flow (e.g. Domenico and Schwartz, 1990).

Several gas accumulations can be identified from the pressure–depth plot for the Sisi Main Zone (Figure 6.4), although they are not as clear as in the Peciko Field (Figures 5.8 and 5.9). The lack of clarity may be caused by the lower density of pressure measurements, or it may reflect true conditions, with most of the reservoirs being compartmentalized, either by faults or by poor reservoir connectivity.

As in the Peciko Field, all wells in the External Axis were terminated in the transition zone. The pressure–depth plot for a single well, which is typical for wells in the Sisi–Nubi Field, is shown in Figure 6.5. There are four wells in the Sisi–Nubi Field that encountered the overpressured zone: SS-3-ST1, SS-4, NB-5, and W-NB-1 (Appendix 2b). Unlike the Peciko Field, the zone of low overpressure is absent from this axis; instead, the pressure trend abruptly changes from normal hydrostatic pressure into the transition zone into high overpressure. This characteristic will be analysed using wireline log and vitrinite reflectance data, in the following sub-section.

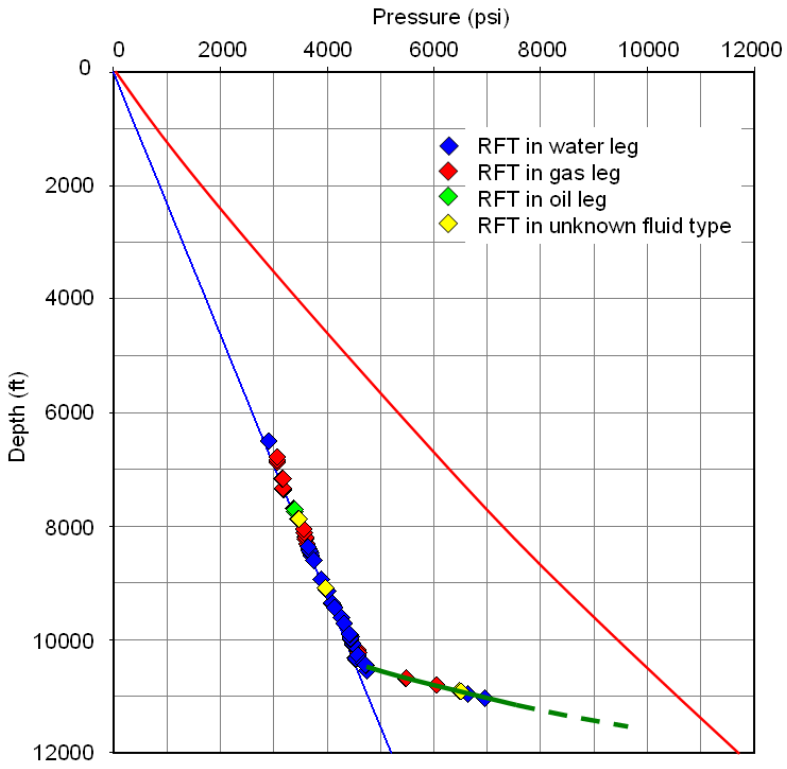

Figure 6.5 Overpressure profile in well NB-5, Nubi Field.

6.1.2.2 Wireline log suites

Wireline logs from wells exhibiting overpressure on this axis, SS-3-ST1, SS-4, NB-5, and W-NB-1, are available for analysis, together with vitrinite reflectance data from well SS-1. Complete wireline log responses for the mudrocks are shown in Appendix 2b. In this main text, two wells are discussed: SS-1 and SS-4.

In SS-1, there is a clear reversal in sonic and resistivity at a depth around 11,250 ft, whereas the density log remains approximately constant at values slightly greater than 2.6 g/cm^3 down to TD (Figure 6.6). These log responses comprise evidence of unloading, confirmed by the density-sonic and density-resistivity cross-plots (Figure 6.7). Interestingly, the same phenomenon as in well PEC-1 (Figure 5.15) is observed, i.e., the sonic and resistivity log reversals occur around the same depth as the onset of gas generation (Figure 6.8). It is unfortunate that there are no pressure data in the reversal section due to the absence of reservoirs.

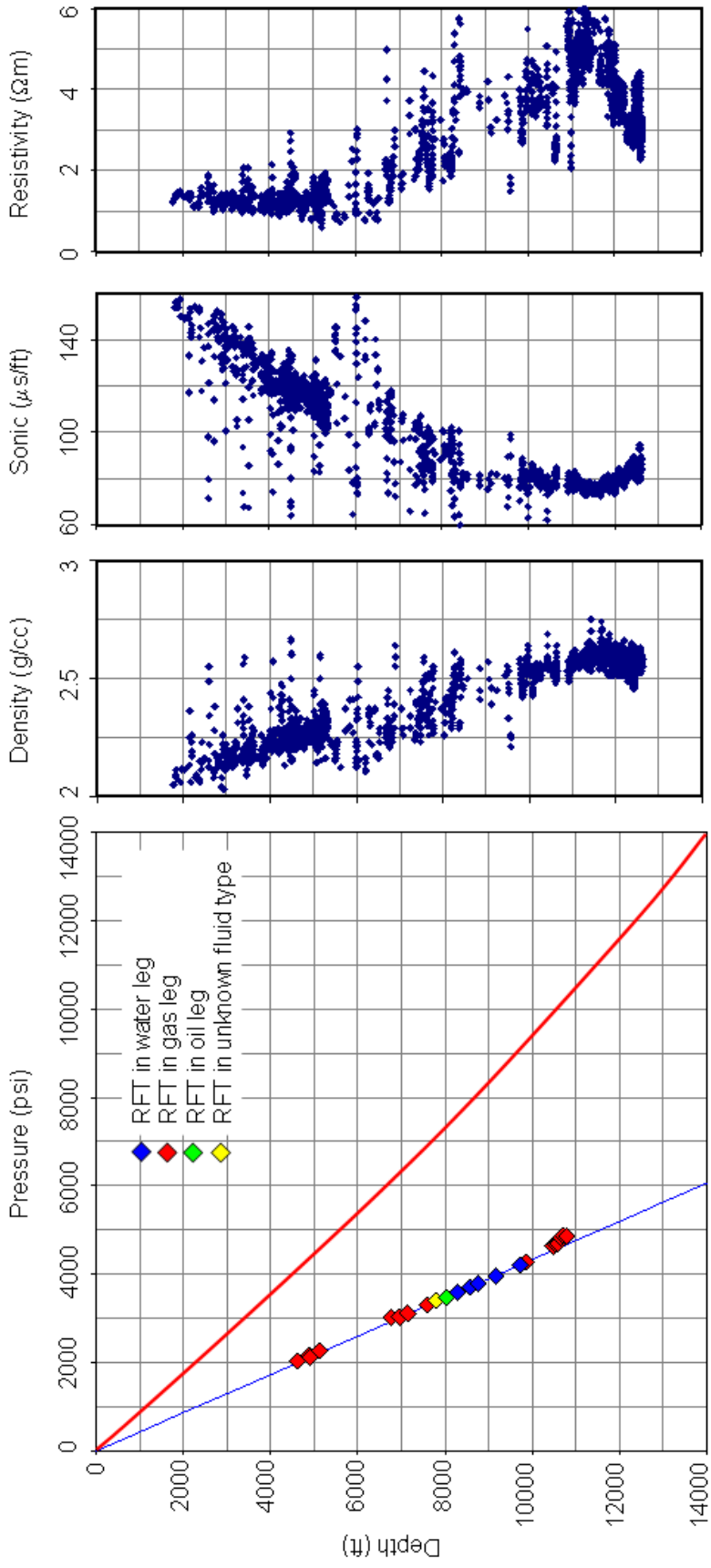

Figure 6.6 Pressure–depth plot and wireline log values in the mudrocks for well SS-1, Sisi Field.

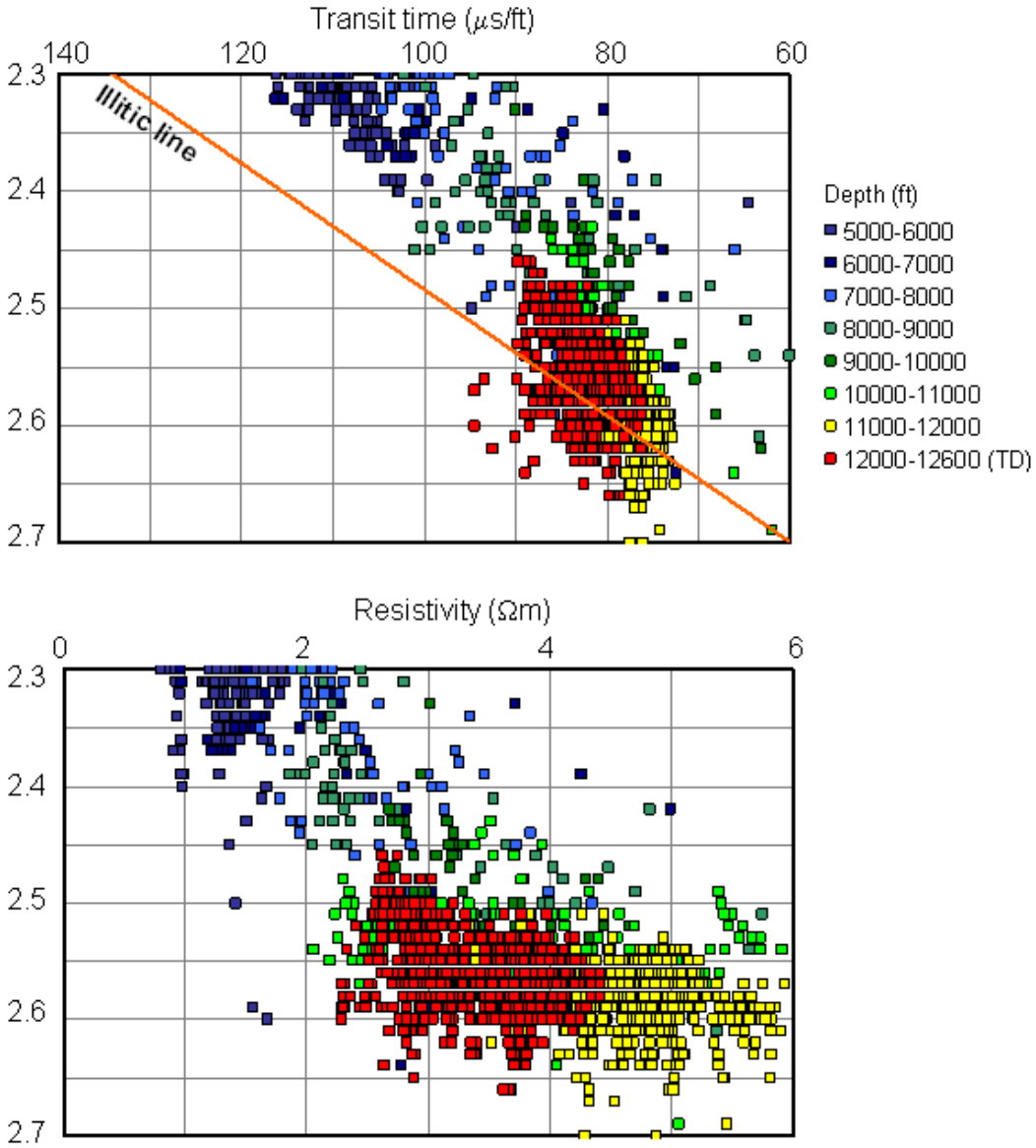

Figure 6.7 Cross-plots of density against sonic transit time and resistivity in mudrocks in well SS-1, Sisi–Nubi Field.

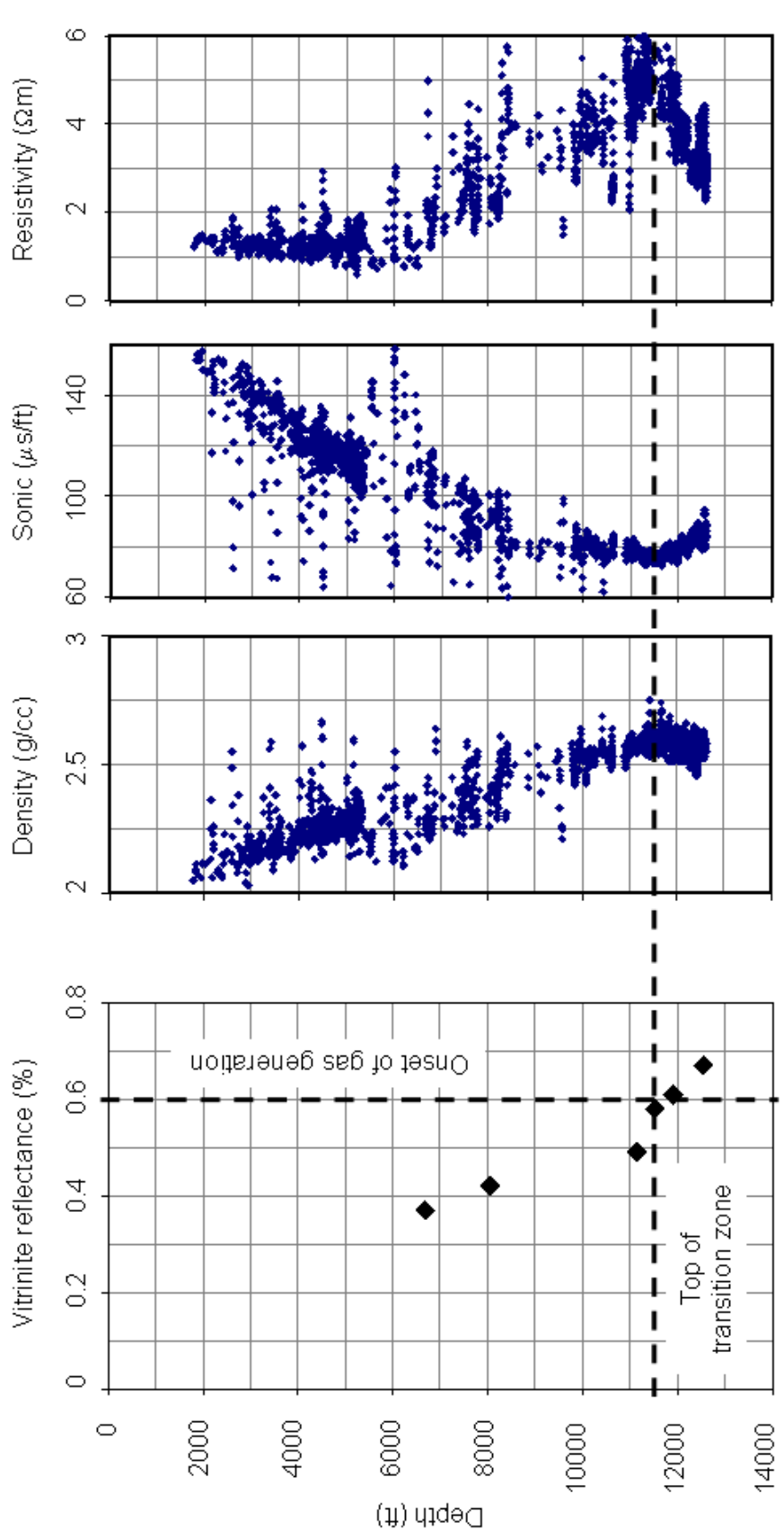

Figure 6.8 Vitrinite reflectance data from well SS-1,Sisi Field showing that the top of the overpressure transition zone coincides with the onset of gas generation.

The SS-4 well shows similar behaviour to SS-1, except that the depth of sonic and resistivity reversals is around 11,000 ft (Figure 6.9). There is a pressure point in the reversal section showing that there is an overpressured reservoir. Also, these log responses are evidence of unloading, as confirmed by density-sonic and density resistivity cross-plots (Figure 6.10).

6.1.3 Median Axis

The Median Axis is the most prolific axis in terms of both reserves and hydrocarbon production in the Lower Kutai Basin. This axis contains the giant Bekapai Oil and Gas Field (De Matharel et al., 1980), the giant Peciko Gas Field (Lambert et al., 2003), and the super giant Tunu Gas Field (Lambert et al., 2003).

The structure of the Bekapai Field is a faulted anticline (Figure 6.11). Based on the presence of the major faults, the field is divided into three compartments: west, central, and east compartments. Production to date has been from the west compartment. The central and east compartments are still in the appraisal and exploration stages, respectively, and the number of wells is very limited. The stratigraphic interval that is the biggest contributor to hydrocarbon production from this field is the Bekapai Main Zone, in the upper part of the Fresh Water Sand (Figure 5.2). The oil comes only from this zone. Other contributing intervals are the Shallow Reservoir Zone and the Tunu Main Zone.

The Peciko and Tunu fields, as discussed earlier in Chapter 5, are unfaulted anticlinal structures with gas trapped hydrodynamically in the deeper reservoirs (Figures 2.12 and 2.13). The productive interval in both fields is the Tunu Main Zone (Figure 5.2).

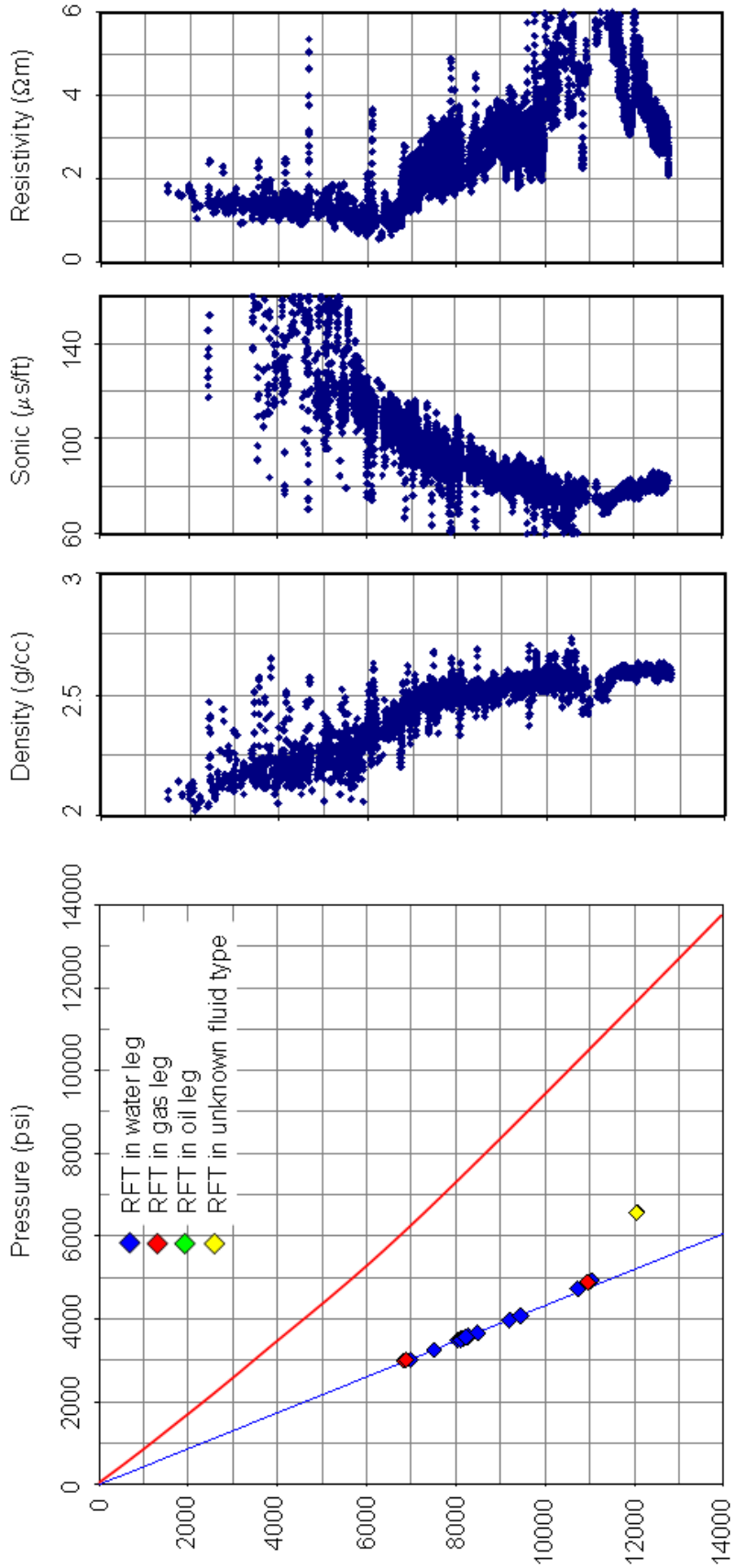

Figure 6.9 Pressure–depth plot and wireline log values in the mudrocks for well SS-4, Sisi Field.

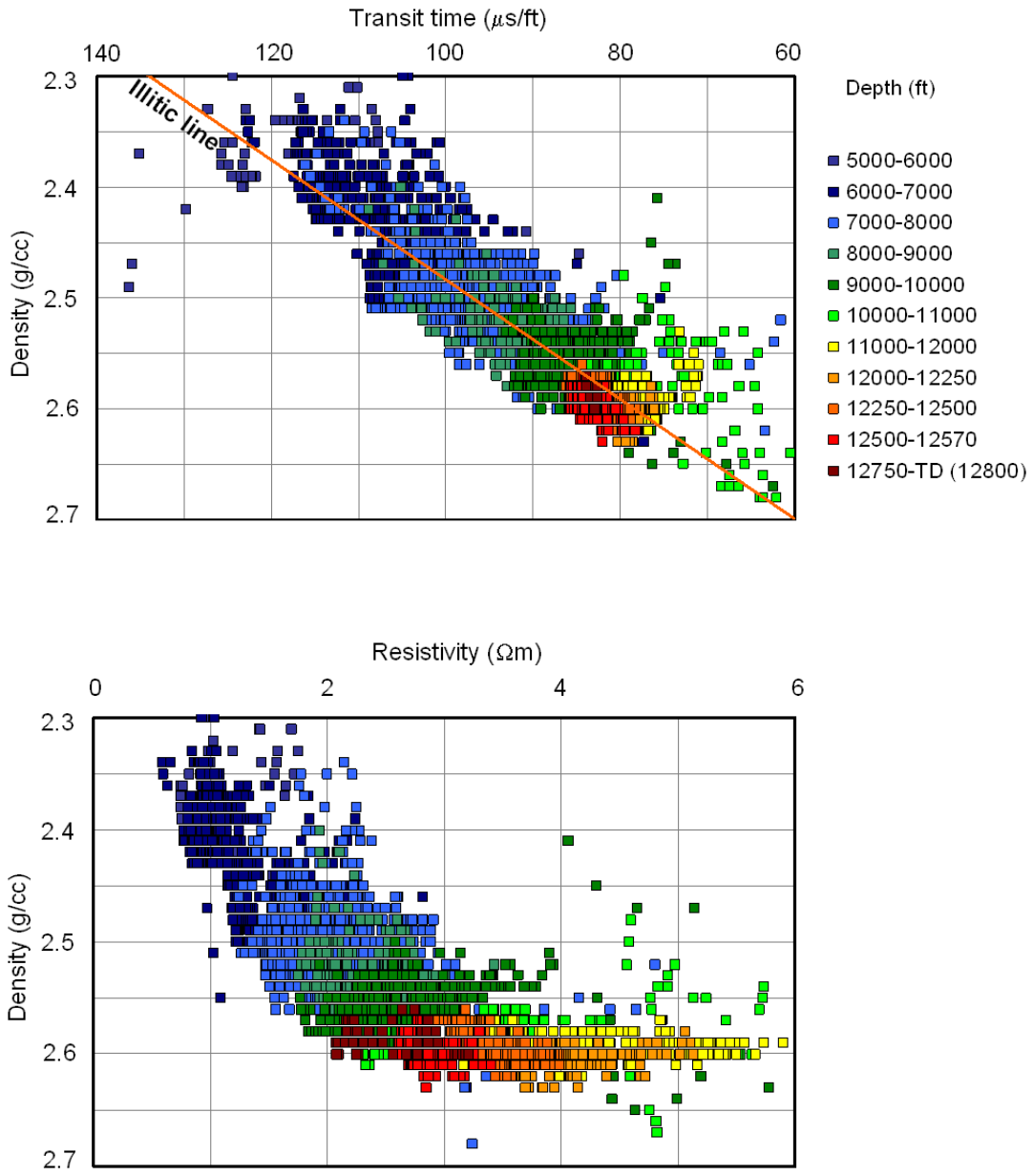

Figure 6.10 Cross-plots of density against sonic transit time and resistivity in mudrocks in well SS-4, Sisi–Nubi Field.

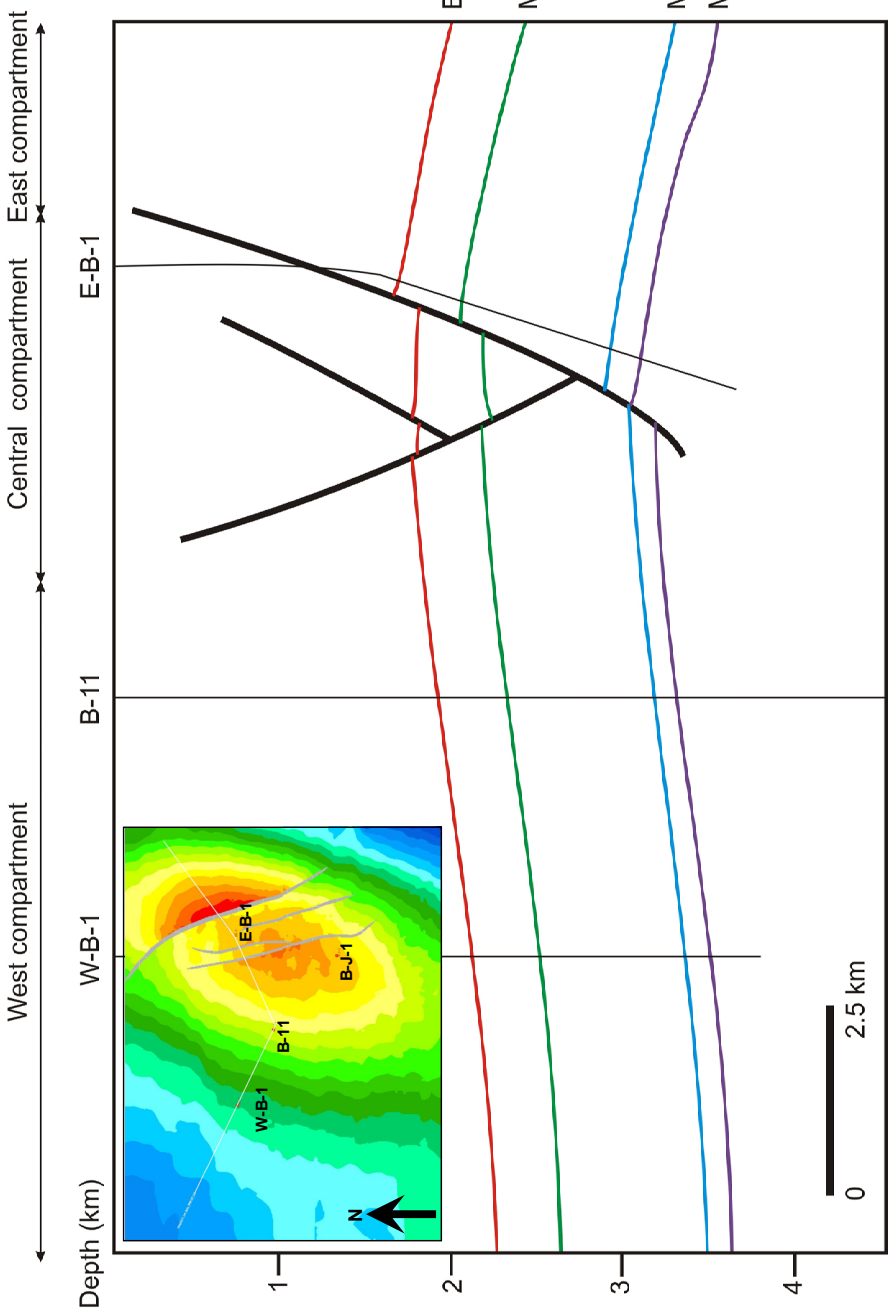

Figure 6.11 Vertical section through the Bekapai Field showing main faults and some stratigraphic horizons. Unfortunately, only the two deeper horizons are marked on Figure 5.2 (Total E&P Indonesie, 2010c).

6.1.3.1 Pressure data

Bekapai

There are ~90 Class A and ~100 Class B pressure data available for analysis in this field. The Class B data are included because the number of Class A data is limited. The pressure–depth plot for all the Class A and B data is shown in Figure 6.12. There are not enough data to analyse pressure–depth plots for each stratigraphic interval in this field. Due to this limitation, sets of data points belonging to the same hydrocarbon accumulations cannot be identified from the pressure–depth plot.

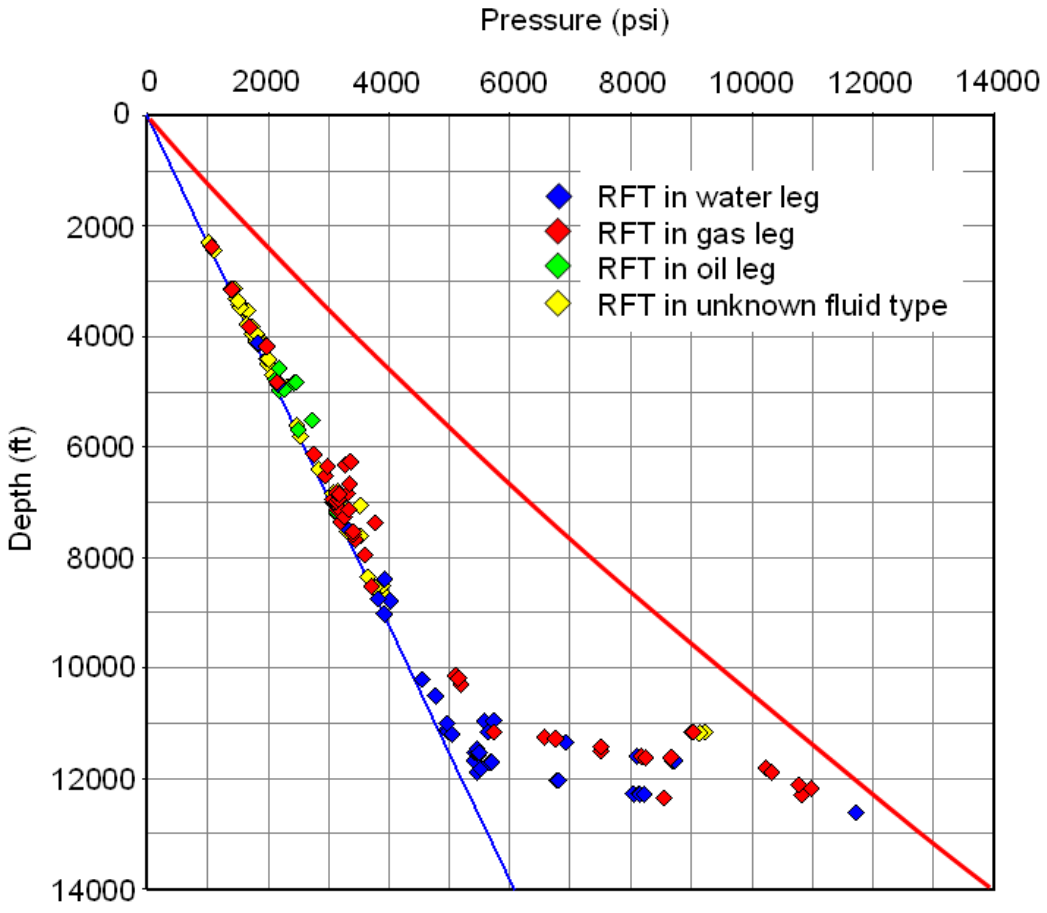

Figure 6.12 Pressure–depth plot for all Class A and B pressure data, Bekapai Field.

Three wells have encountered the overpressured zone in this field: B-J-1, B-11, and W-B-1 (Figure 6.13). These wells are located in the crestal, flank, and synclinal areas of the western compartment of the structure, respectively. The top of overpressure is shallower in the synclinal area.

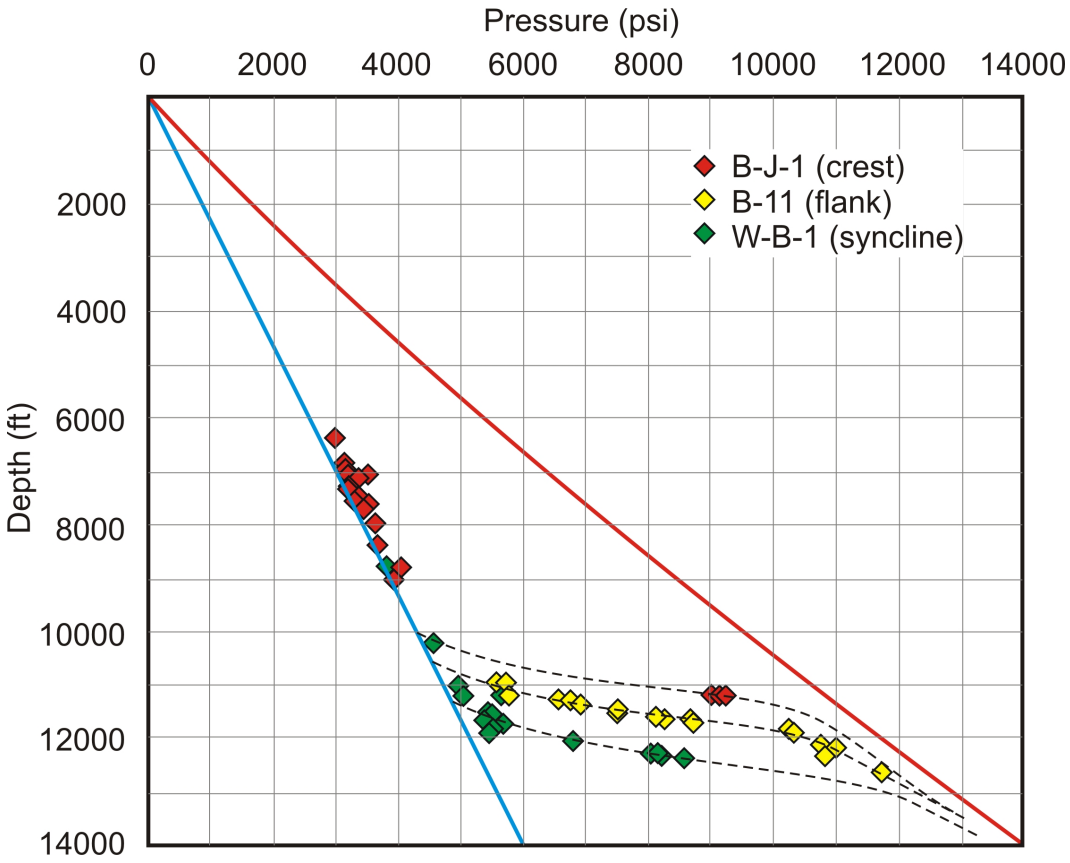

Figure 6.13 Pressure–depth plot for wells B-J-1, B-11, and W-B-1, Bekapai Field, showing that the top of overpressure is shallower at the crest.

Well B-11 encountered very high overpressure. Also, there is no low overpressure zone in this field; instead the pressure trend abruptly changes from normal hydrostatic pressure into the transition zone into high overpressure.

Tunu

There are ~1000 Class A and ~3500 Class B pressure data available for analysis in this field. The Class B data are included because the number of Class A data is limited, considering the size of the field, which is almost 3.5 times the area of Peciko (Figure 1.1). The pressure–depth plot for all the Class A and B data is shown in Figure 6.14.

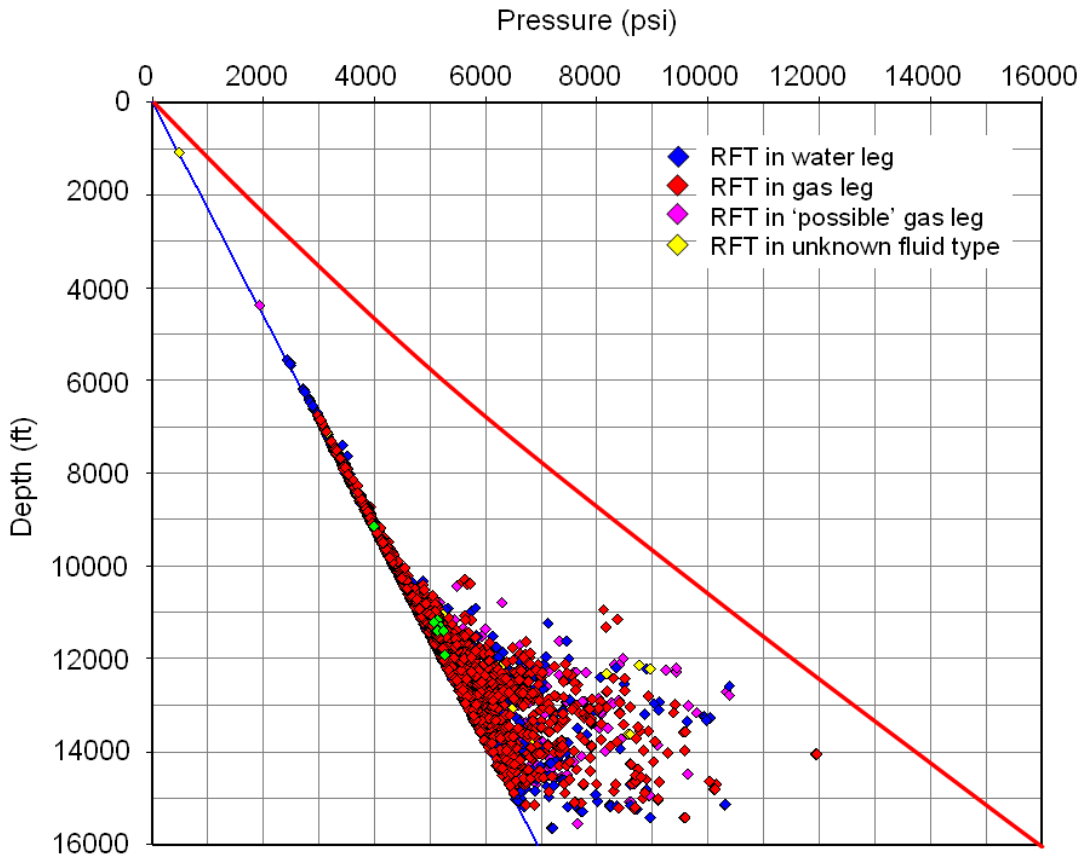

Figure 6.14 Pressure–depth plot for all Class A and B pressure data, Tunu Field.

The pressure–depth plots for each stratigraphic interval within the Tunu Main Zone are shown in Appendix 3a. Typical pressure–depth plots for two stratigraphic intervals within the Tunu Main Zone are shown in Figures 6.15 and 6.16. For SU1, the uppermost section of the Tunu Main Zone (Figure 5.2), the pressure in the water leg is consistently higher than the normal hydrostatic

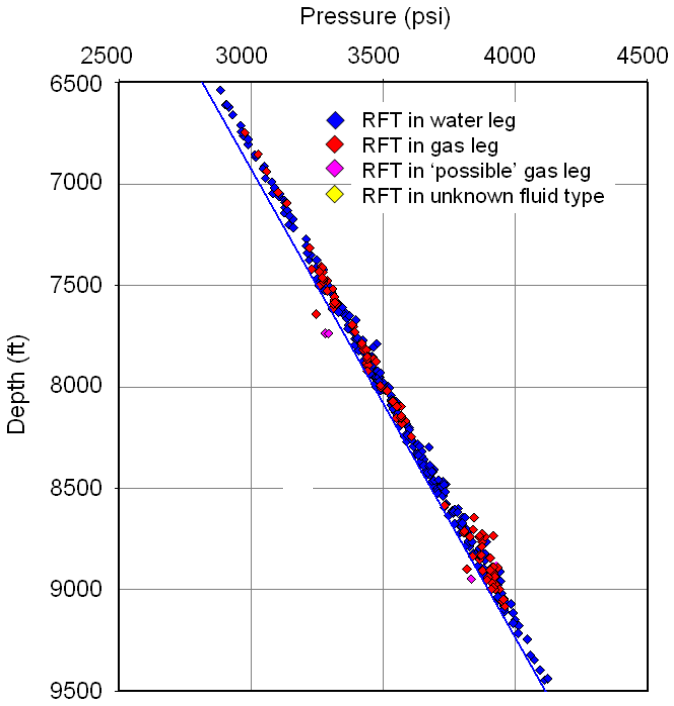

Figure 6.15 Pressure–depth plot in SU1, Tunu Main Zone, Tunu Field.

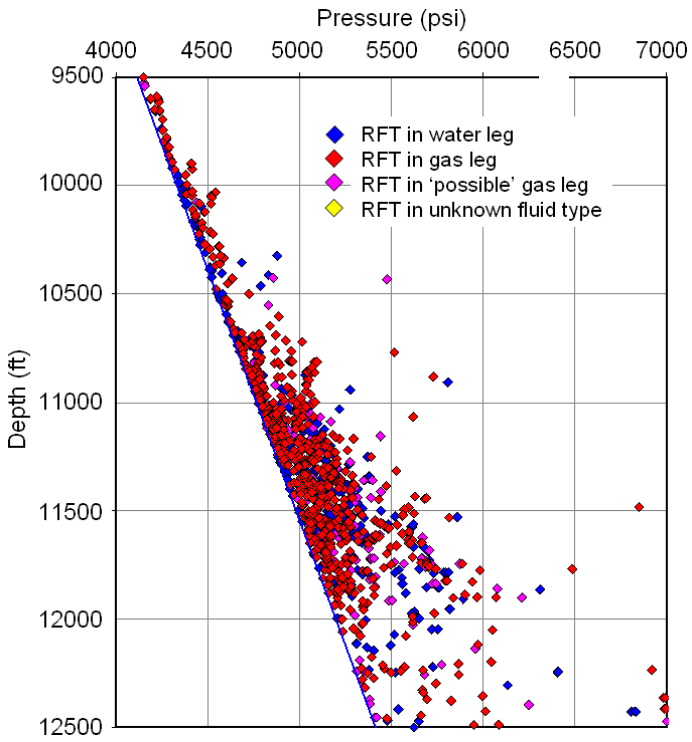

Figure 6.16 Pressure–depth plot in SU-4, Tunu Main Zone, Tunu Field.

pressure, by ~40 psi on average (Figure 6.15), just as observed on the External Axis. The same explanation may apply, i.e., the slight overpressure in the Tunu Field may also be due to hydraulic head. The slight overpressure can be observed down into the underling interval of SU3 (Appendix 3a).

Several gas accumulations can be identified from the pressure–depth plot for SU4 (Figure 6.16), although they are not as clear as in the Peciko Field (Figures 5.8 and 5.9). The lack of clarity may be caused by the lower density of pressure measurements compared to the Peciko Field.

A typical pressure–depth plot for a single well is shown in Figure 6.17. As on the External Axis, most wells in this field were terminated in the transition zone. There is no low overpressure zone in this field, and the pressures abruptly change from normal hydrostatic pressure into the transition into high overpressure, as in the Bekapai Field. The top of overpressure in this field also varies, and is shallower on the western flank of the structure (Figures 6.18 and 6.19). The overpressure value also varies in the same stratigraphic unit, leading to the presence of hydrodynamic trapping in this field, as discussed by Lambert et al. (2003) (see Sub-section 2.2.2).

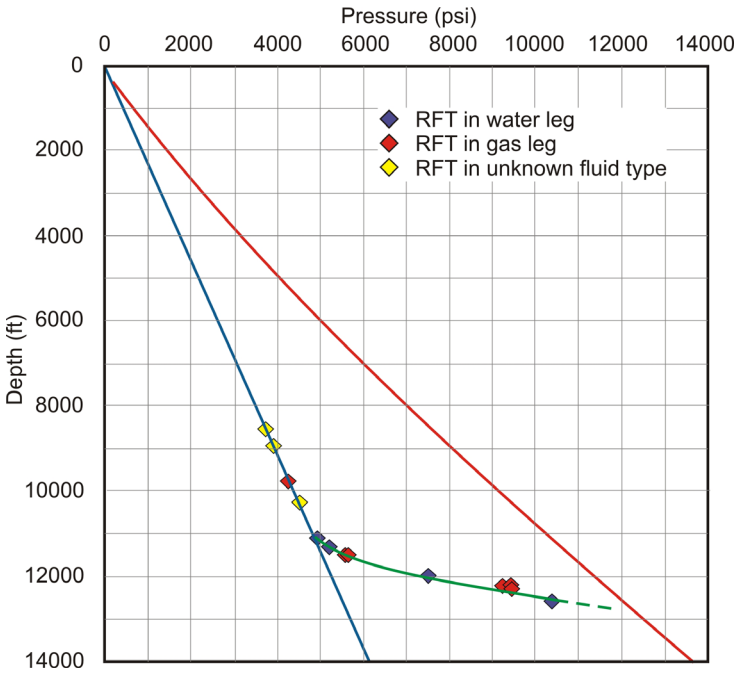

Figure 6.17 Overpressure profile in well TN-G6, Tunu Field.

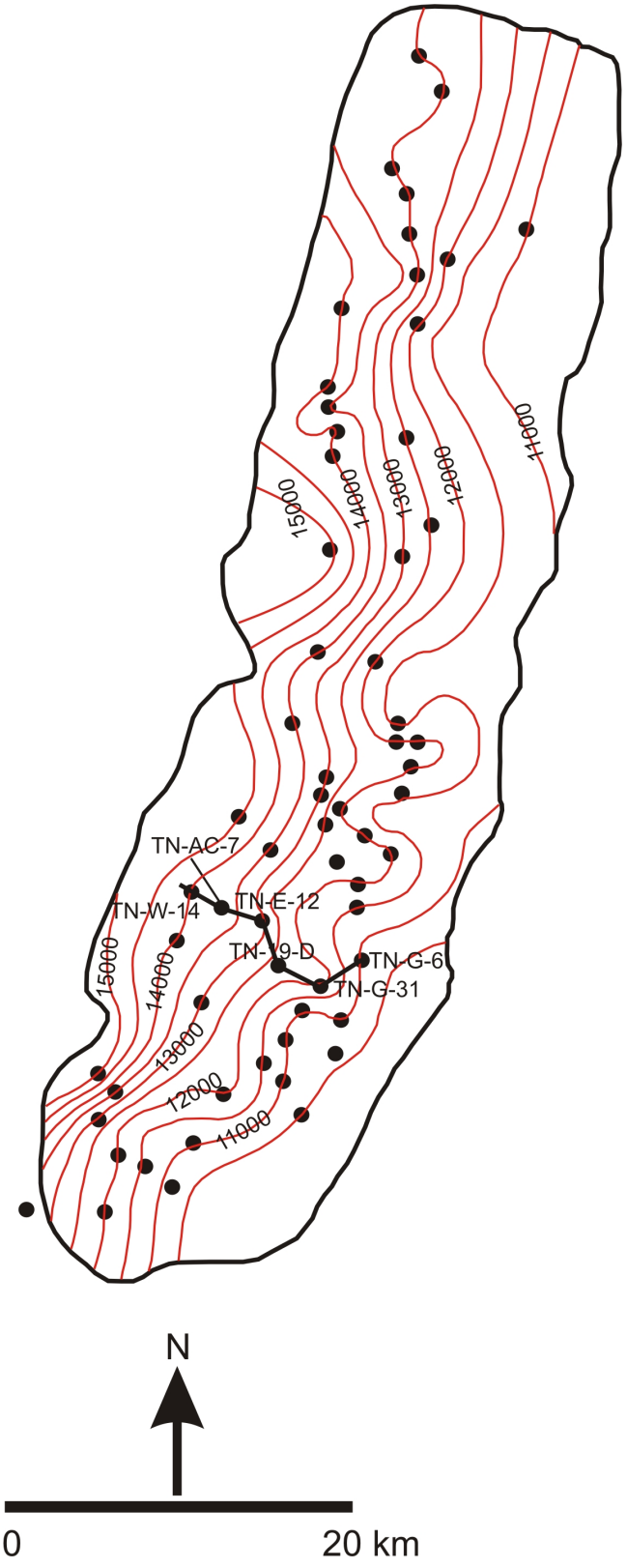

Figure 6.18 Map of depth to top of overpressure in the Tunu Field.

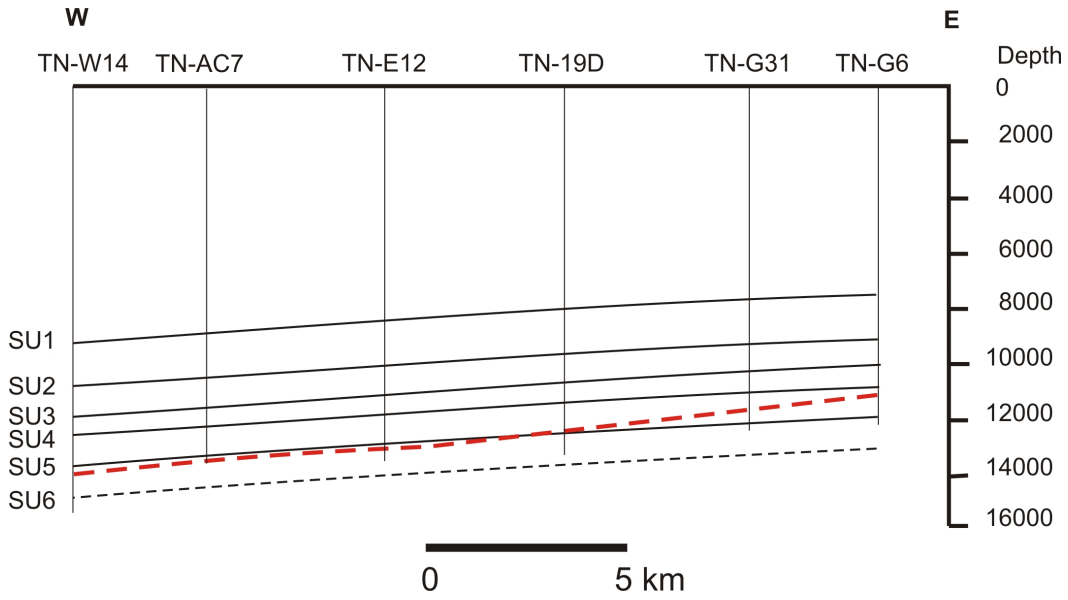

Figure 6.19 West-east cross-section showing variation in depth of top of overpressure relative to stratigraphic horizons in the Tunu Field.

6.1.3.2 Wireline log suites

Bekapai

Wireline logs for three wells that encountered overpressure in the Bekapai Field, i.e., B-J-1, B-11, and W-B-1 are available for analysis. Complete wireline log responses for the mudrocks in those wells are shown in Appendix 3b. In this main text, B-11 is discussed since the well penetrated into the zone of very high overpressure.

The B-11 well encountered the pressure transition zone at a depth of 11,000 ft (Figure 6.20). Unfortunately, the compaction trend in the mudrock beds down to 11,000 ft is not clearly defined because of poor hole conditions caused by the use of a water-based mud in a sandy environment, so there is considerable scatter in the log responses above that depth. Nevertheless, the wireline log responses (Figure 6.20) show clear reversals, at around 11,000 ft on the sonic and resistivity logs, and around 12,000 ft on the density log. These log responses comprise evidence of unloading, confirmed by density-sonic and density-

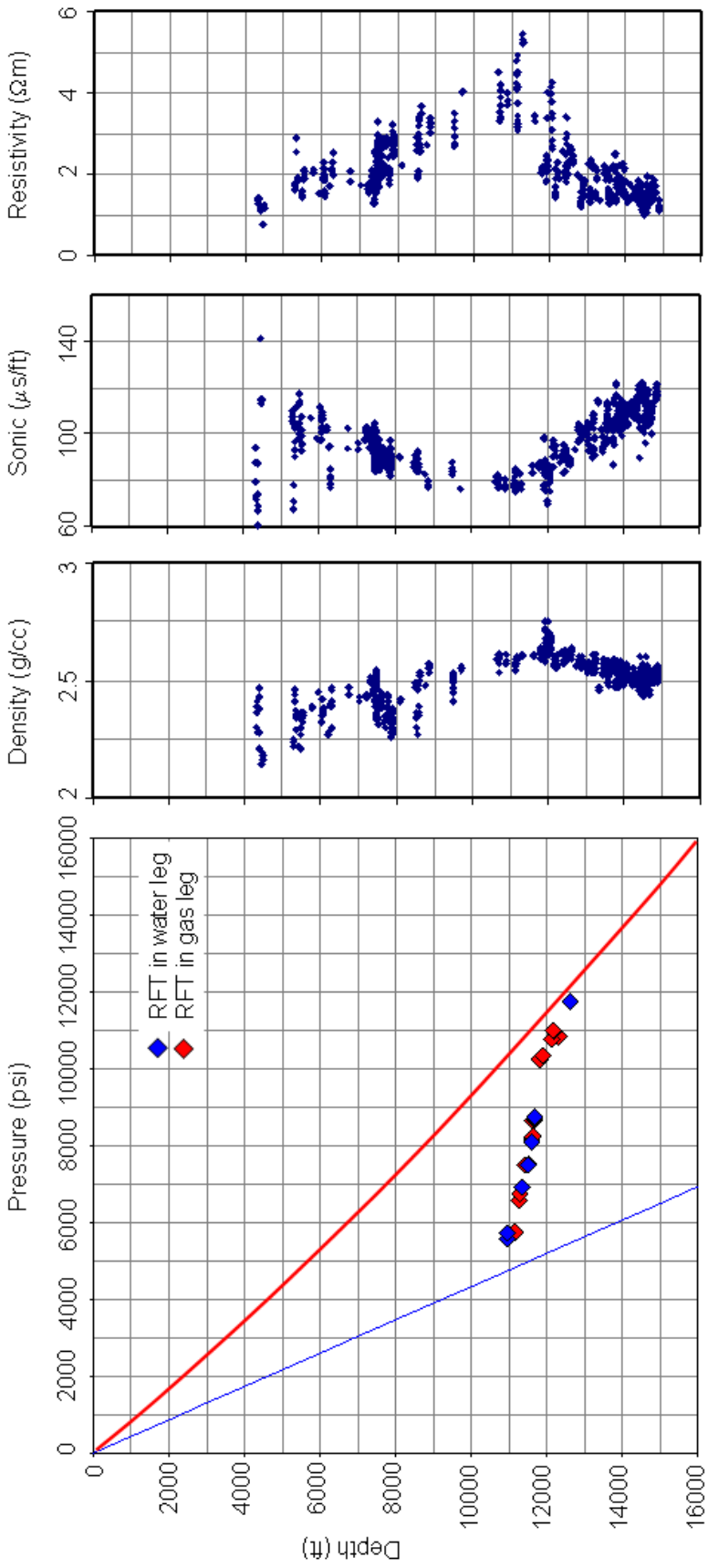

Figure 6.20 Pressure–depth plot and wireline log values in the mudrocks in well B-11, Bekapai Field.

resistivity cross-plots (Figure 6.21). The unloading trend on the density-sonic cross-plot is unusually strong. The cause of the density reversal in well B-11 is interpreted as a result of microcracks opening due to the very high overpressure.

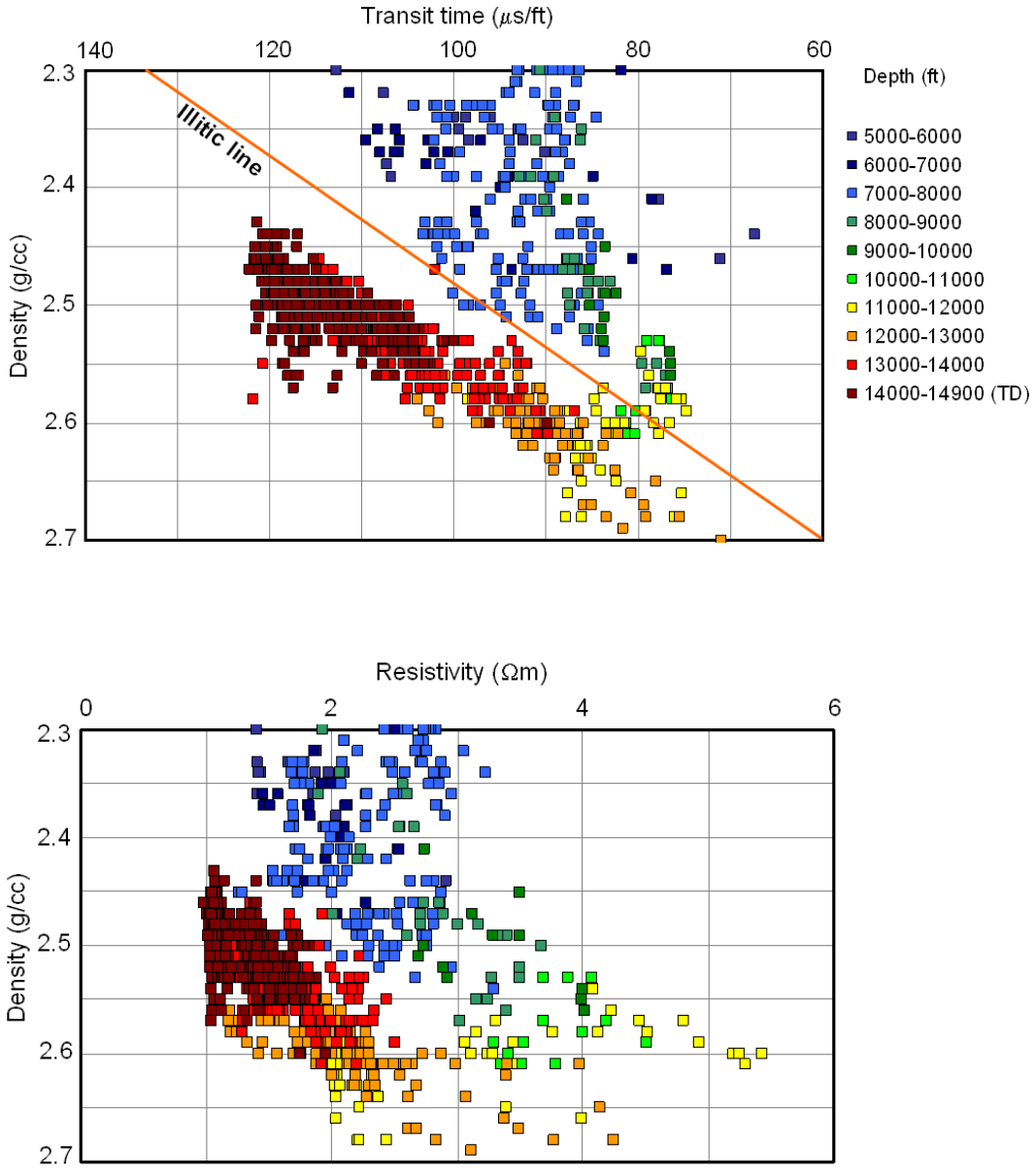

Figure 6.21 Cross-plots of density against sonic transit time and resistivity in mudrocks in well B-11, Bekapai Field.

Tunu

It is very unfortunate that in the super giant Tunu Field there are no complete wireline log suites. During the earlier stages of field development, drilling was done with water-based mud, which caused caving because of the high sand content, resulting in missing sections in the wireline logs. During the later stages of development, oil-based mud was used, but not all wireline logging tools were run.

The wireline log responses through the mudrocks for well TN-G6 are shown in Figure 6.22 and for several other overpressured wells at Tunu in Appendix 3c. No sonic log is available from well TN-G6.

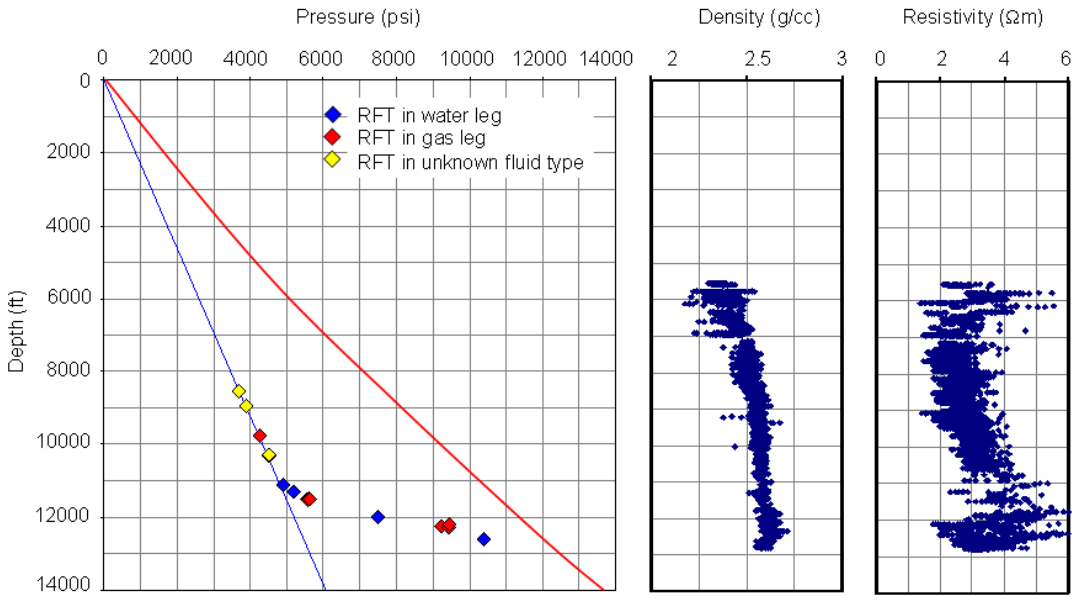

Figure 6.22 Pressure–depth plot and wireline log values in the mudrocks in well TN-G6, Tunu Field.

The resistivity log contains a reversal at a depth just above 12,000 ft, approximately corresponding to the top of the pressure transition zone. The density log response continues to increase down to 12,500 ft, where there is just a hint of reversal that cannot be identified with confidence, registering density values above 2.6 g/cm^3 in the overpressured section. Other overpressured wells

(Appendix 3c) also show that in the overpressured section, the density values are above 2.6 g/cm^3. It is inferred, therefore, that the cause of overpressure in this well is also an unloading mechanism.

6.1.4 Internal Axis

The Handil, Tambora, and Nilam fields are located on the Internal Axis (Figure 1.1). The structure at Handil is a faulted anticline (Figure 6.23), whereas Tambora and Nilam are unfaulted anticlines (Figure 6.24). The Handil field is divided into north and south compartments by the Main Fault.

The productive zones in the Tambora and Nilam are the same, i.e., D – G zones in the upper part of the Middle Miocene interval. For the Handil Field, there are productive zones in the Upper Miocene interval as well as in the upper part of the Middle Miocene interval (Figure 5.2).

6.1.4.1 Pressure data

Handil

There are ~70 Class A and ~170 Class B pressure data available for analysis in this field. The Class B data are included because the number of Class A data is limited. The pressure–depth plot for all the Class A and B data is shown in Figure 6.25.

Most wells in the Handil Field were terminated in the zone of normal hydrostatic pressure. However, one well encountered high overpressure, i.e., H-9-B1 (Figure 6.26). The top of overpressure in this well is located at a depth around 9500 ft where there is a very abrupt transition into very high overpressure, close to lithostatic stress, and the zone of high overpressure continues to TD.

There is an interesting variation in the depth to the top of overpressure in the field (Figure 6.27). KRB-1 and KRB-2 are located in the northern compartment, and KRB-3, KRB-4 and W-H-1 are located in the southern

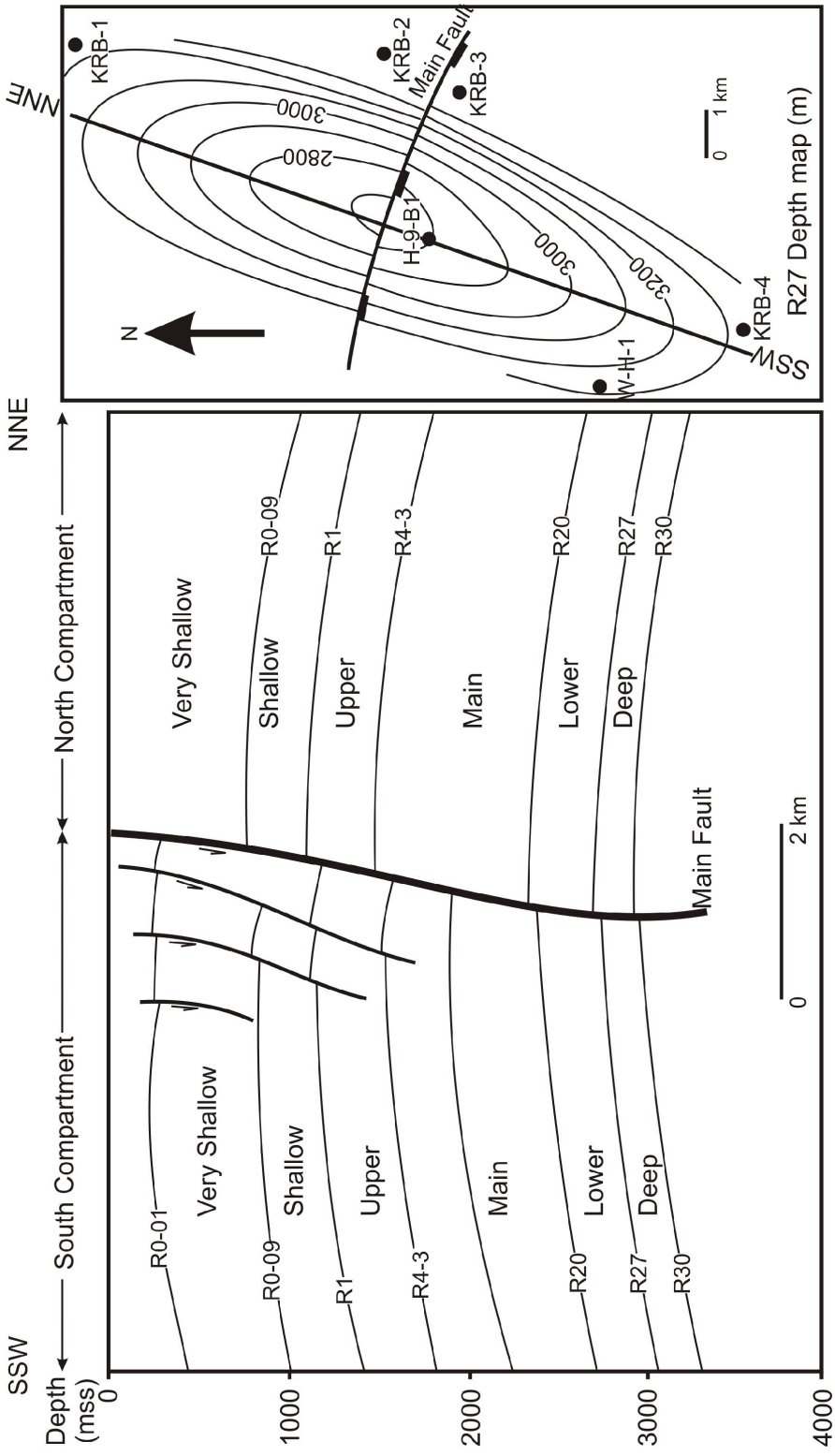

Figure 6.23 Structure of the Handil Field (after Bellorini et al., 1989) for horizon R27 in the Middle Miocene (Figure 5.2).

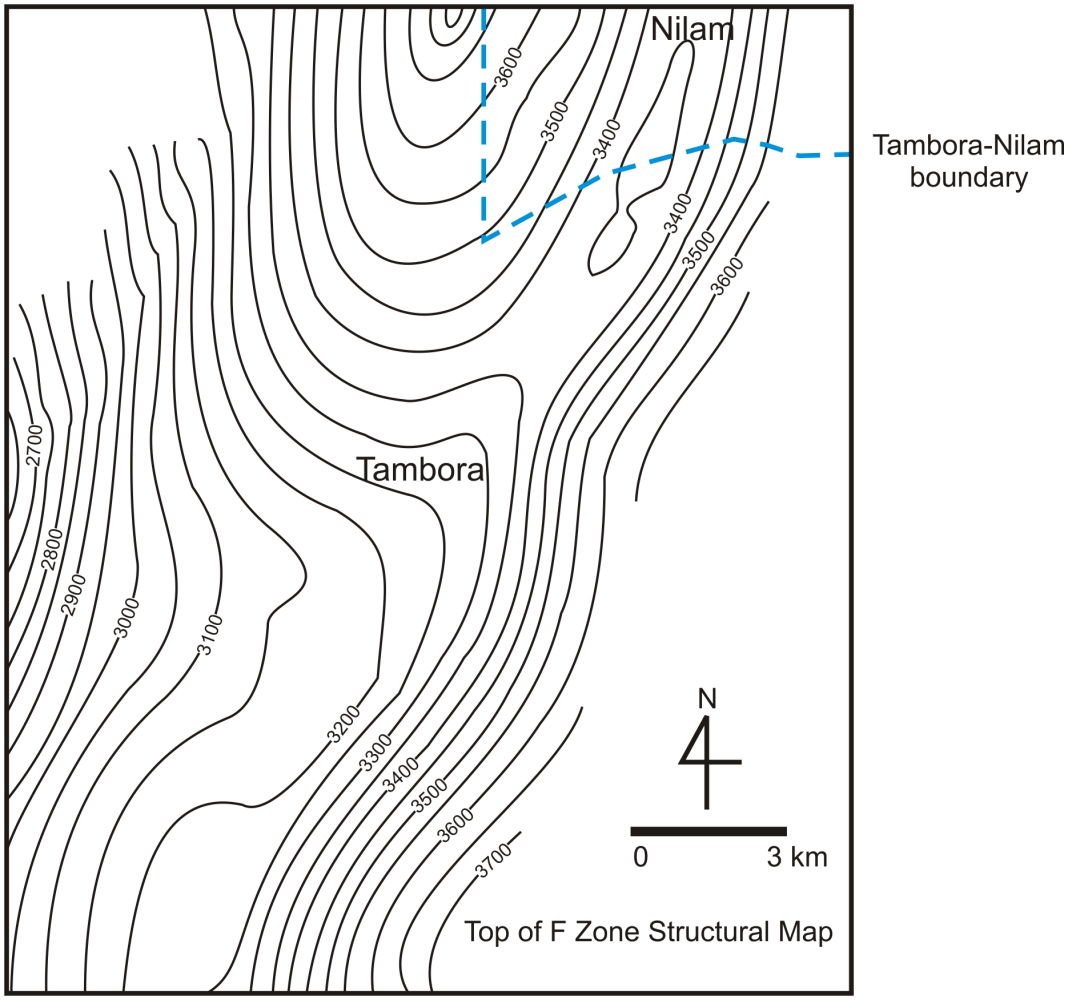

Figure 6.24 Structural map of the Nilam and Tambora fields at the top of F Zone (see Figure 5.2 for stratigraphic column) (Total E&P Indonesie, 2003c).

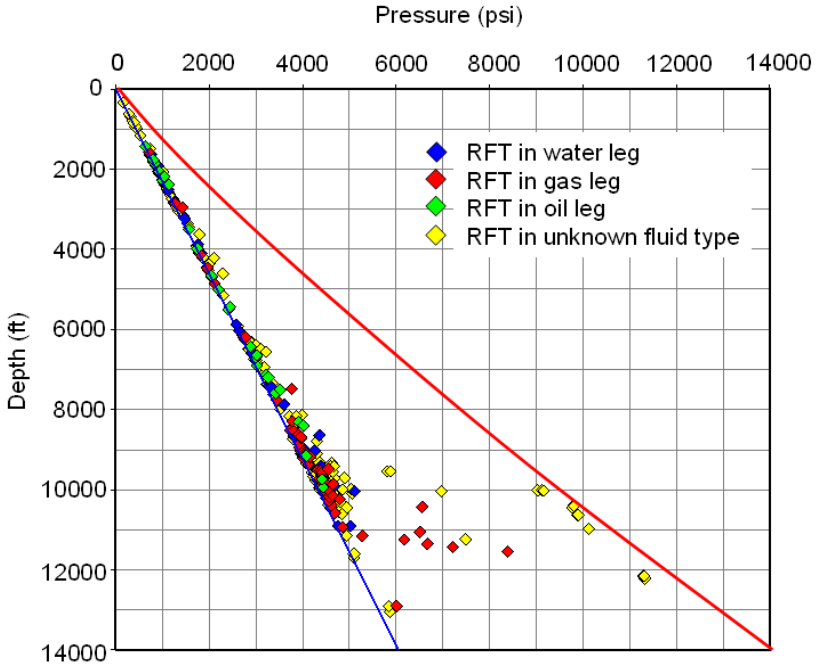

Figure 6.25 Pressure–depth plot for all Class A and B pressure data, Handil Field.

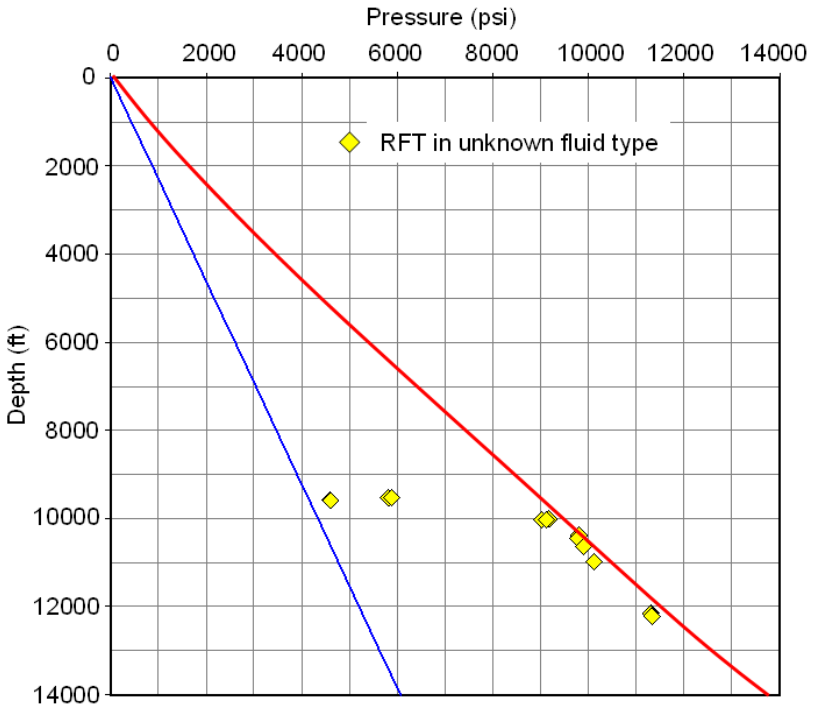

Figure 6.26 Pressure–depth plot for well H-9-B-1, Handil Field.

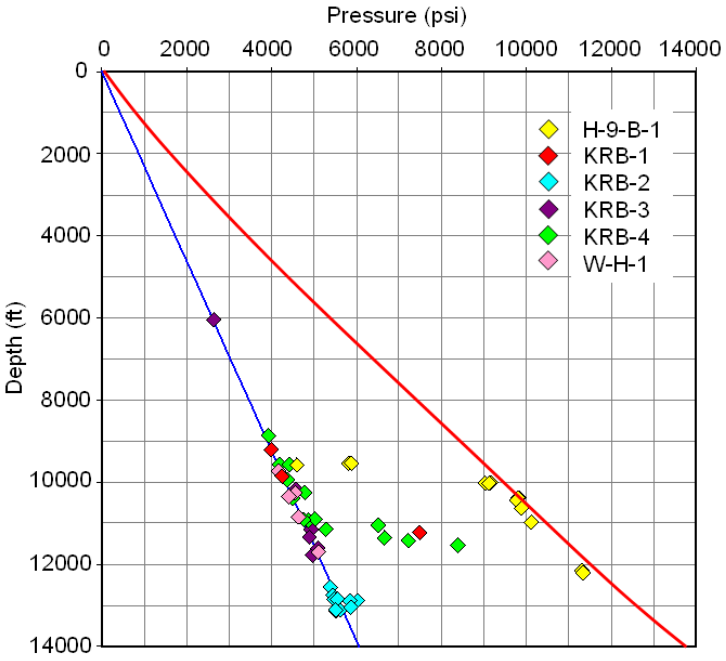

Figure 6.27 Pressure–depth plot showing top of overpressure for wells located in the Handil Field (see Figure 6.23 for well locations).

compartment. The top of overpressure is located somewhere in the range 10,000–11,200 ft in KRB-1, deeper than 13,000 ft in KRB-2, deeper than 11,700 in KRB-3, at 11,000 ft in KRB-4, and deeper than 11,700 ft in W-H-1 (Figure 6.27). Using H-9-B1 as the reference well located at the crest of the structure, it seems that the top of overpressure is deeper on the flanks to the north-east, east, and south-west.

Tambora

There are ~45 Class A and ~80 Class B pressure data available for analysis in this field. The Class B data are included because the number of Class A data is limited. The pressure–depth plot for all the Class A and B data is shown in Figure 6.28.

Most wells in the Tambora Field were also terminated in the zone of normal hydrostatic pressure. There is one recent well, drilled in 2009, that encountered high overpressure, i.e. TM-84. The pressure–depth plot for this well is shown in Figure 6.29. The top of overpressure in this well is located at ~13,150

ft depth, and below this depth the pressure changes abruptly to very high overpressure, close to lithostatic stress.

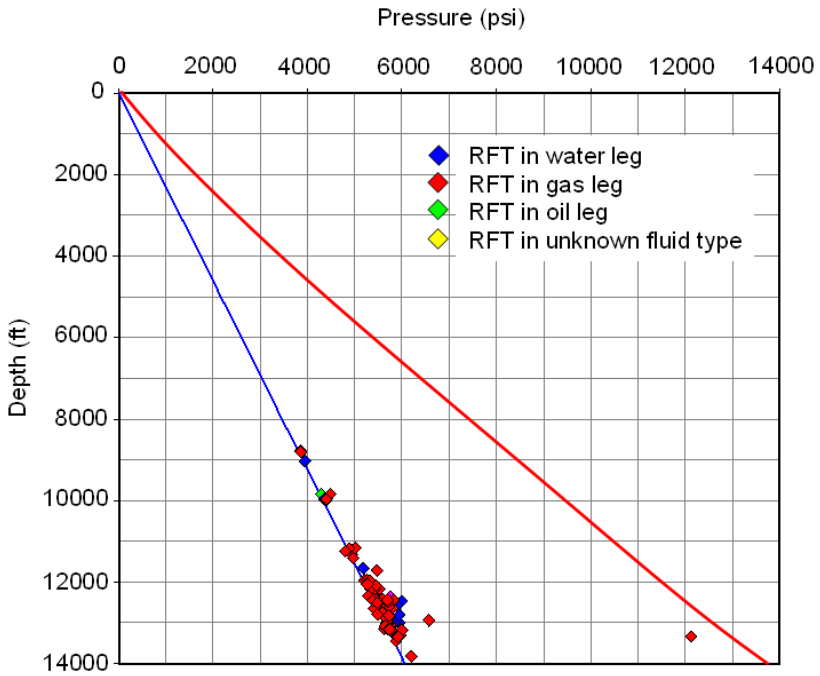

Figure 6.28 Pressure–depth plot for all Class A and B pressure data, Tambora Field.

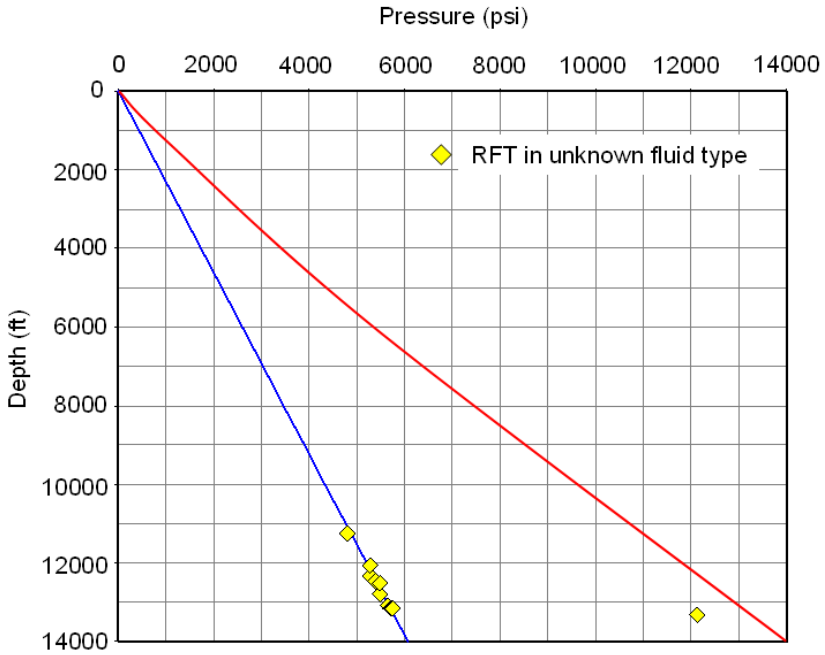

Figure 6.29 Pressure–depth plot for well TM-84, Tambora Field.

Nilam

There are ~160 Class A and ~330 Class B pressure data available for analysis in this field. The Class B data are also included because the number of Class A data is limited. The pressure–depth plot for all the Class A and B data is shown in Figure 6.30.

Most wells in the Nilam Field were also terminated in the zone of normal hydrostatic pressure. There is one well, NLM-109X, that encounters high overpressure (Figure 6.31) The top of overpressure in this well is located somewhere in the range 13,000–13,750 ft, and again from the top of overpressure the pressure increases abruptly to very high overpressure, close to the lithostatic stress, and remains high down to TD.

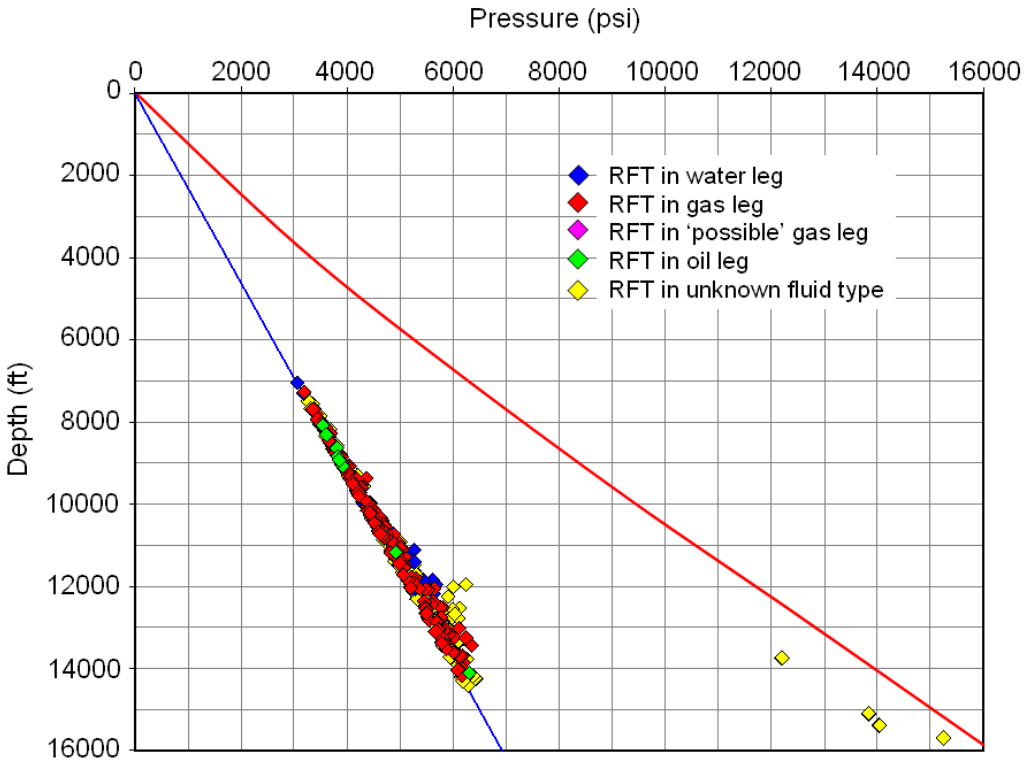

Figure 6.30 Pressure–depth plot for all Class A and B pressure data, Nilam Field.

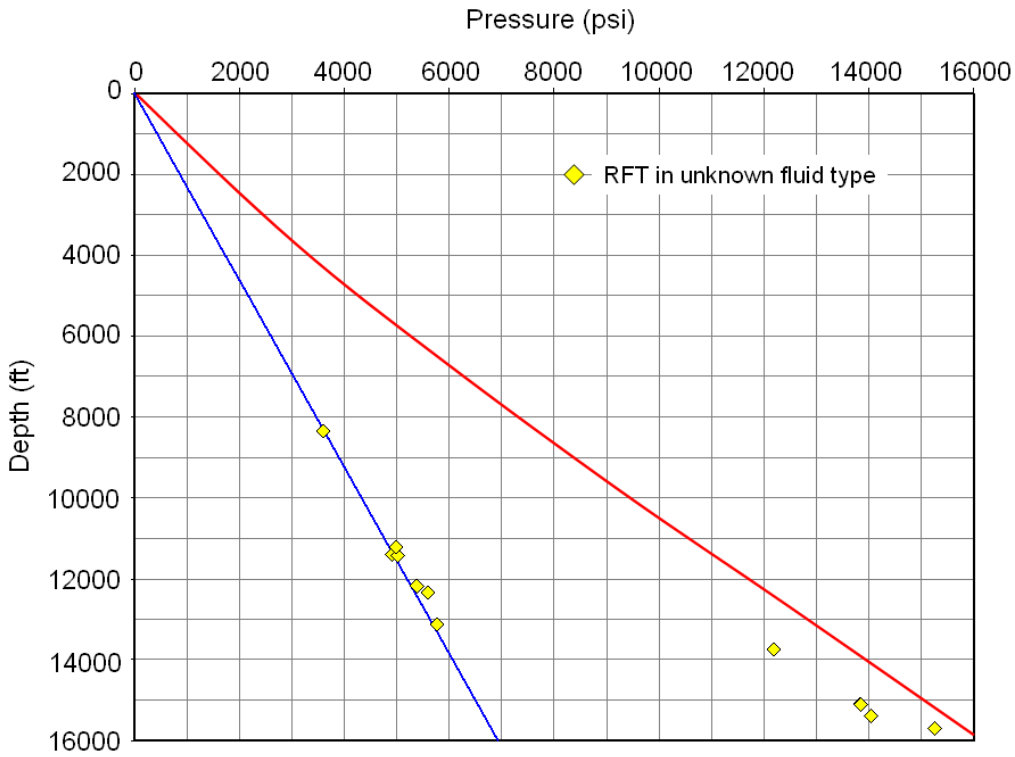

Figure 6.31 Pressure–depth plot for well NLM-109X, Nilam Field.

6.1.4.2 Wireline log suites

Handil

Of the three wells encountering overpressure in the Handil Field, H-9-B1, KRB-1, and KRB-4, only wireline log suites from H-9-B1 can be used to analyse overpressuring in this field. The other two wells have poor wireline log suites because drilling was done with water-based mud in a sand-rich environment, leading to bad hole conditions.

In the H-9-B1 well, the density log was only run in the overpressured section, but sonic and resistivity logs were run over a long interval (Figure 6.32). There is a clear reversal on the sonic log around 9,500 ft and less clear reversals on the resistivity log, somewhere between 8900 ft and 9500 ft, and on the density log around 10,000 ft. These log responses are evidence of unloading, confirmed by the density-sonic cross-plot (Figure 6.33). The characteristics of the pressure-

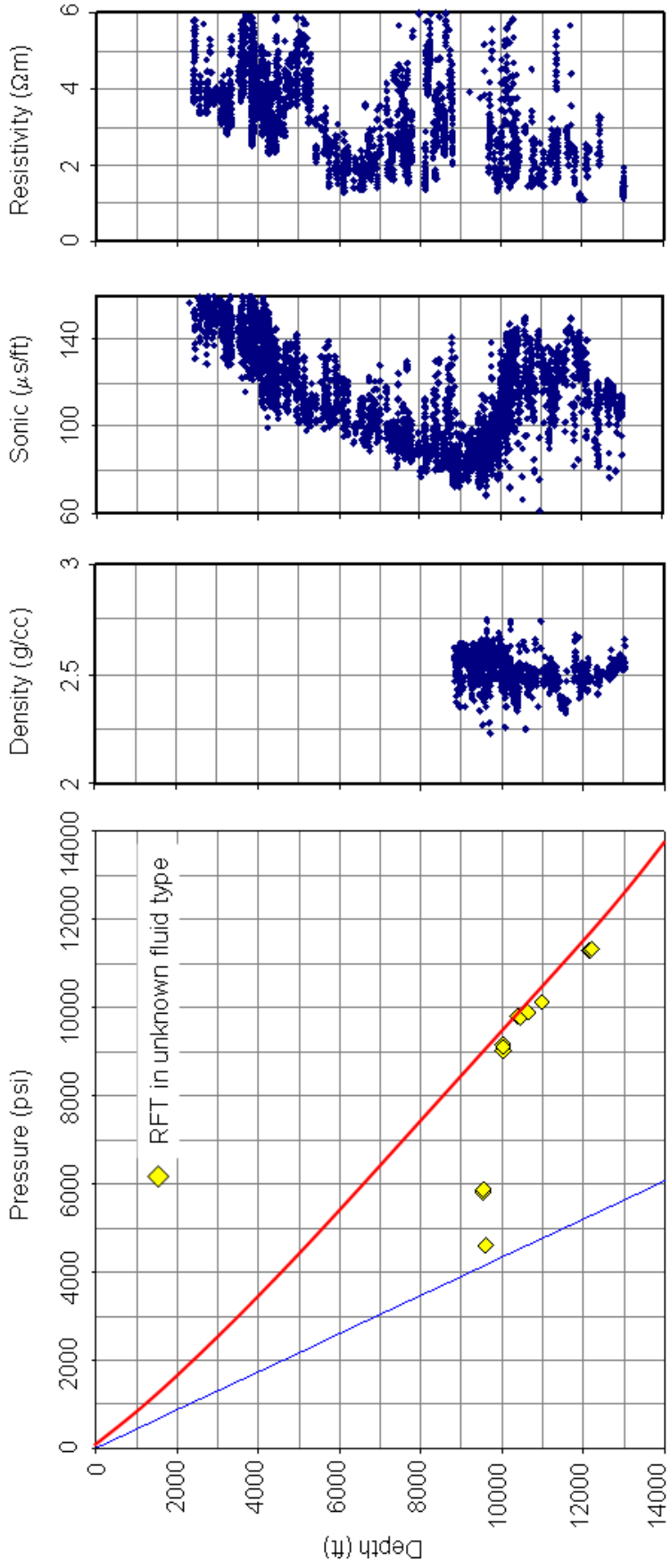

Figure 6.32 Pressure–depth plot and wireline log values in the mudrocks in well H-9-B1, Handil Field.

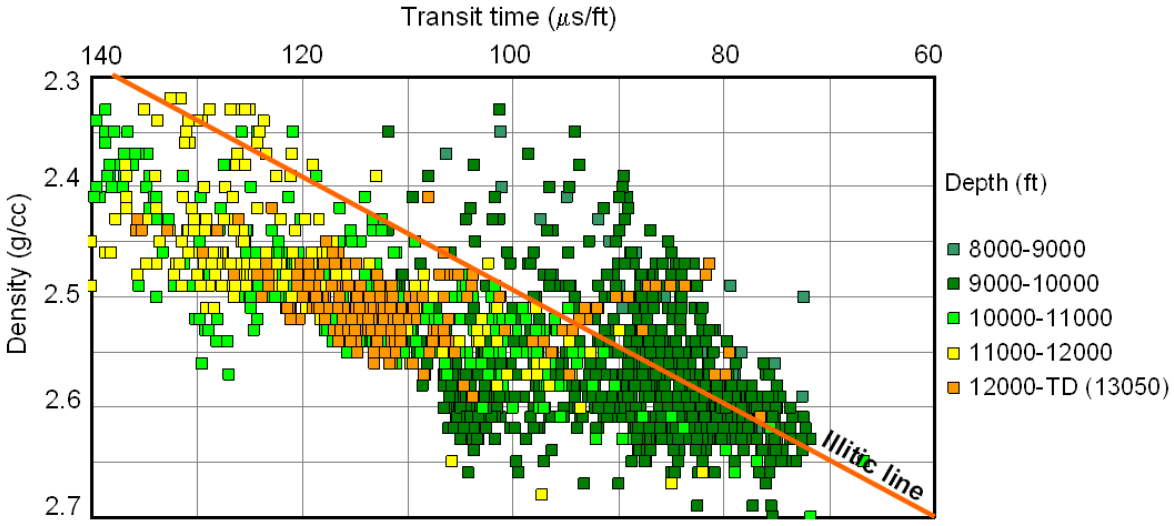

Figure 6.33 Cross-plot of density against sonic transit time in mudrocks in well H-9-B1, Handil Field.

depth profile and the wireline log responses are very similar to the B-11 well in the Bekapai Field: the top of transition zone corresponds to the reversals on the sonic and resistivity logs, and the density reversal is found where the pore pressure approaches the lithostatic stress. Based on these correlations, we again interpret the cause of overpressuring to be unloading processes, and the density reversal as being caused by the opening of microcracks.

Tambora

For the overpressured well TM-84 in the Tambora Field, there is only a relatively good quality density log in the overpressured section. Caving of the borehole wall causes a scattering of the log response towards low density values, but there are many data points around 2.6 g/cm^3 at depths below 11,000 ft (Figure 6.34). Based on this log response, with a high density value that appears to change little through a sharp transition to hard overpressure, interpret the cause of overpressure in this well is again interpreted to be an unloading mechanism.

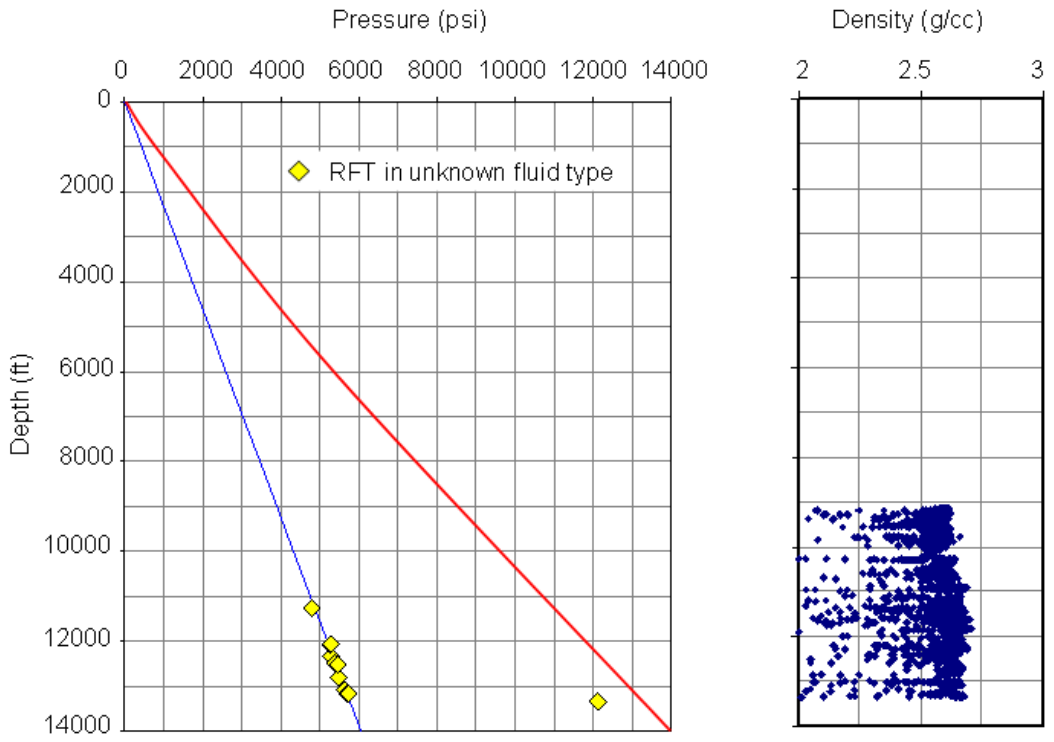

Figure 6.34 Pressure–depth plot and density log values in the mudrocks in well TM-84, Tambora Field.

Nilam

It is very unfortunate that the wireline log quality for well 109X in the Nilam Field, where very high overpressure is encountered (Figure 6.31), is unreliable for the purposes of overpressure and compaction analysis.

6.1.5 Onshore area

There are two main fields to be analysed in the onshore area, i.e., Mutiara and Semberah fields (Figure 1.1). The structure of each field is a thrust-faulted plunging anticline (Figures 6. 35 and 6.36).

The reservoir zones are located within the Middle Miocene interval. In Figure 6.35b, it can also be seen that the all Upper Miocene sediments have been eroded from the Mutiara Field.

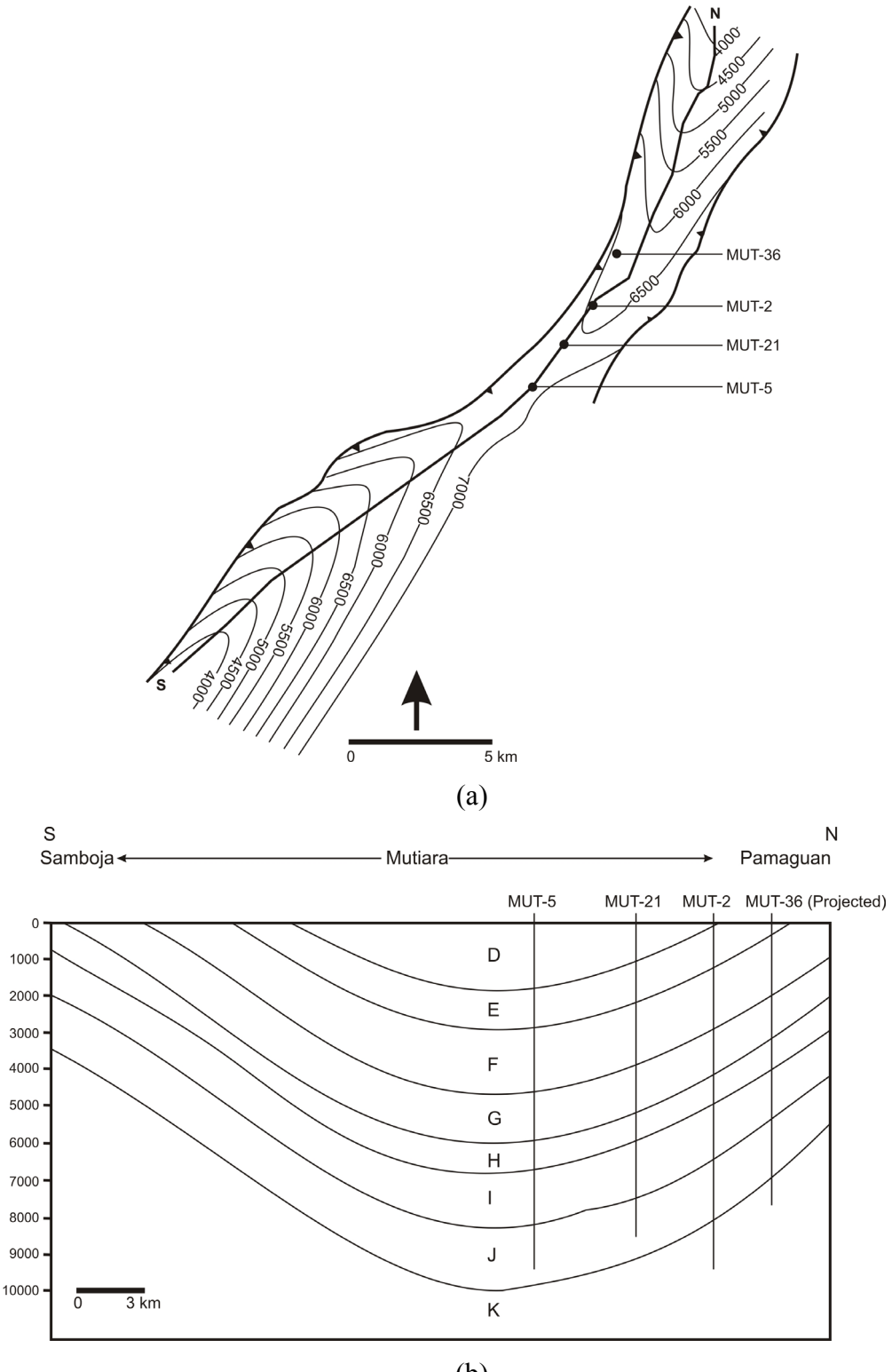

Figure 6.35 Structure of the Mutiara Field: (a) map for one stratigraphic horizon; and (b) south-north cross-section (modified from Safarudin and Manulang, 1989).

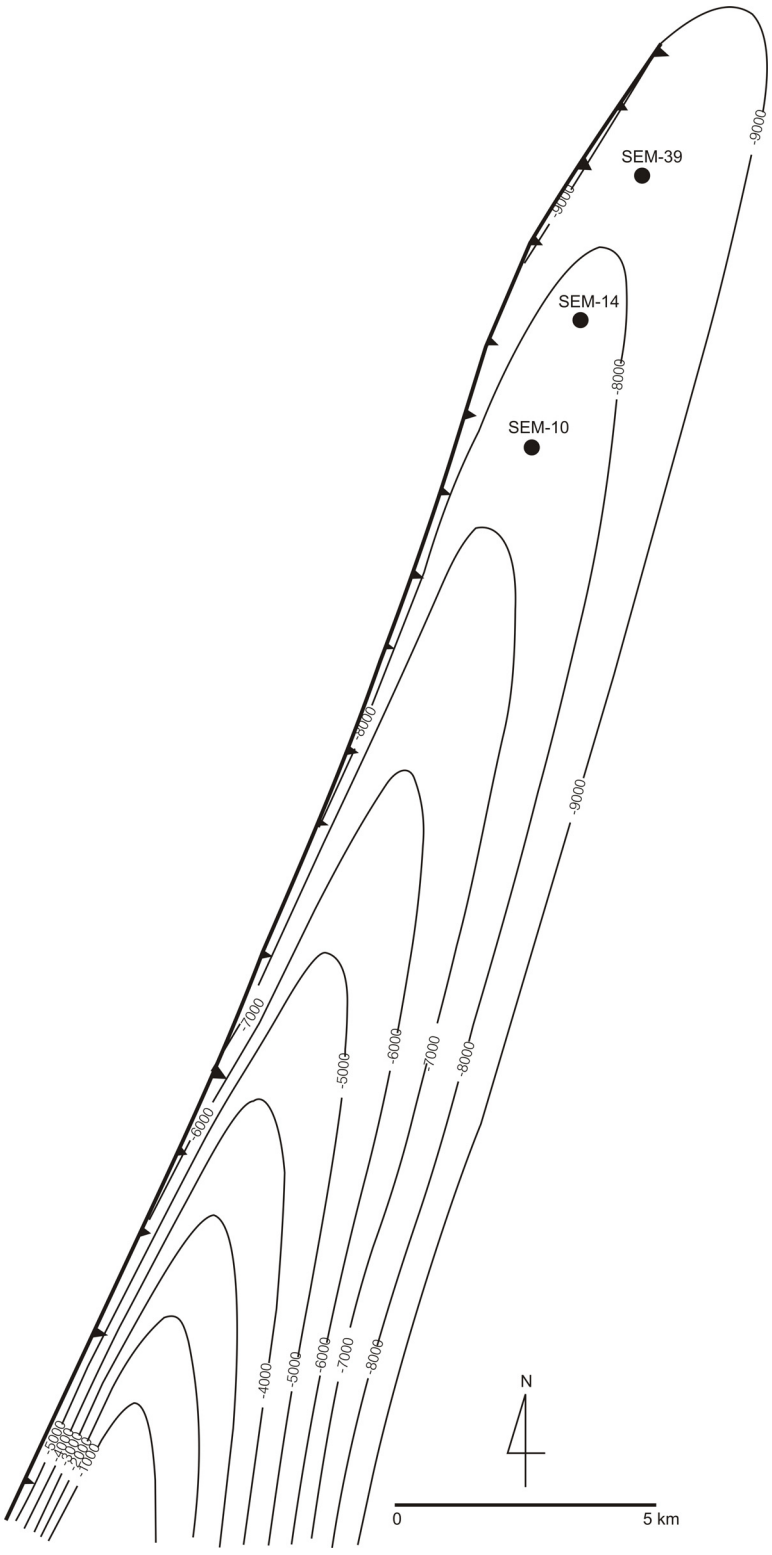

Figure 6.36 Structural map for one stratigraphic horizon in the Semberah Field (modified from Ramdhan, 2002).

6.1.5.1 Pressure data

Mutiara

There are ~430 Class A pressure data available for analysis in this field. No pressure data were taken from production wells, so there are no Class B data. A pressure–depth plot for all the data is shown in Figure 6.37.

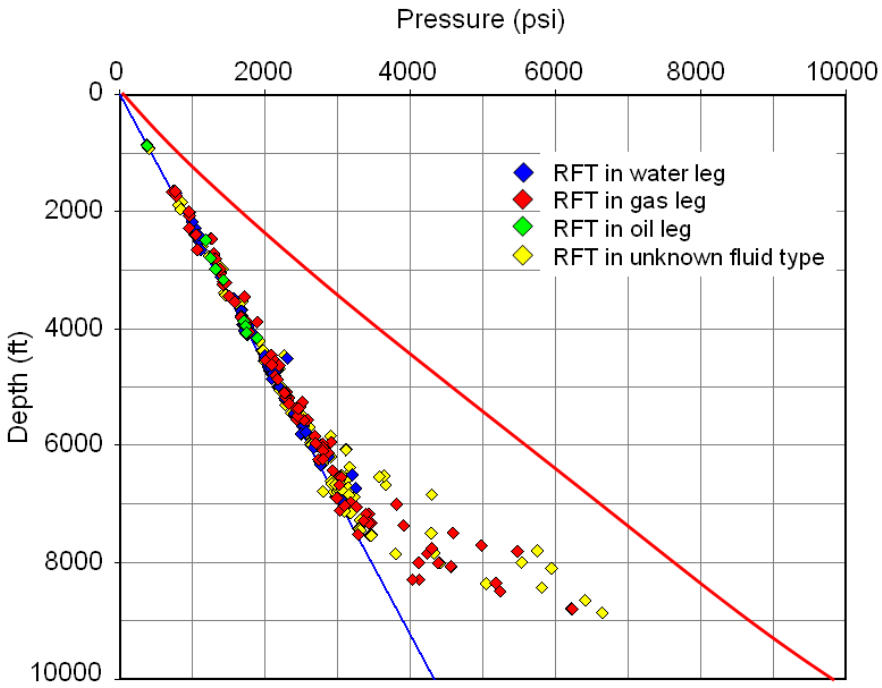

Figure 6.37 Pressure–depth plot for all Class A pressure data, Mutiara Field.

Five wells encountered overpressure in this field: MUT-1, MUT-2, MUT-5, MUT-21, and MUT-36. The pressure–depth plot for MUT-21, which is a typical overpressured well in this field, are shown in Figure 6.38. Pressure–depth plots for the other four overpressured wells are given in Appendix 4a. The pressure data from well MUT-21 indicate that the top of overpressure is at ~7000 ft depth, and below this depth down to TD the pore pressure trend is sub-parallel to the lithostatic stress.

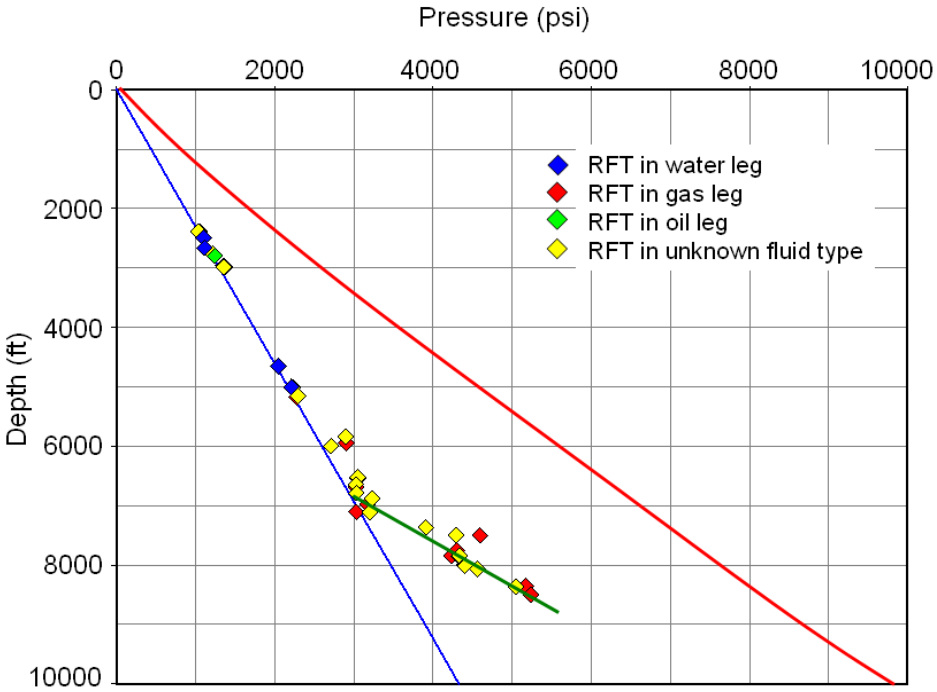

Figure 6.38 Pressure–depth plot for well MUT-21, Mutiara Field.

Semberah

There are ~160 Class A pressure data available for analysis in this field, taken from exploration and appraisal wells. No pressure data were taken from production wells, so there are no Class B data. A pressure–depth plot for all the data is shown in Figure 6.39.

Five wells encountered overpressure in this field: SEM-10, SEM-12, SEM-14, SEM-24, and SEM-39. The pressure–depth plot for SEM-39, which is a typical overpressured well that encounters the zone of very high overpressure is shown in Figure 6.40. Pressure–depth plots for the other four overpressured wells are given in Appendix 4b. The pressure data from well SEM-39 indicate that the top of overpressure is located somewhere in the range 7000–9000 ft. From 9000 ft depth down to around 11,000 ft, the pore pressure trend converges gently with the lithostatic stress profile. The top of the transition zone into very high overpressure is located somewhere in the range 11,000–13,000 ft. This behaviour will also be analysed by incorporating wireline log data in the next sub-section.

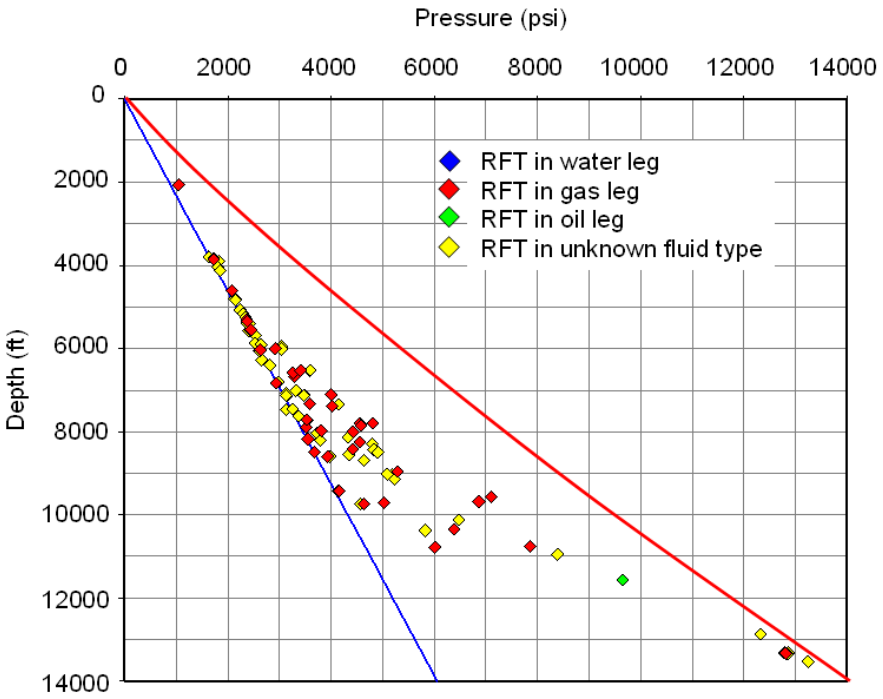

Figure 6.39 Pressure–depth plot for all Class A pressure data, Semberah Field.

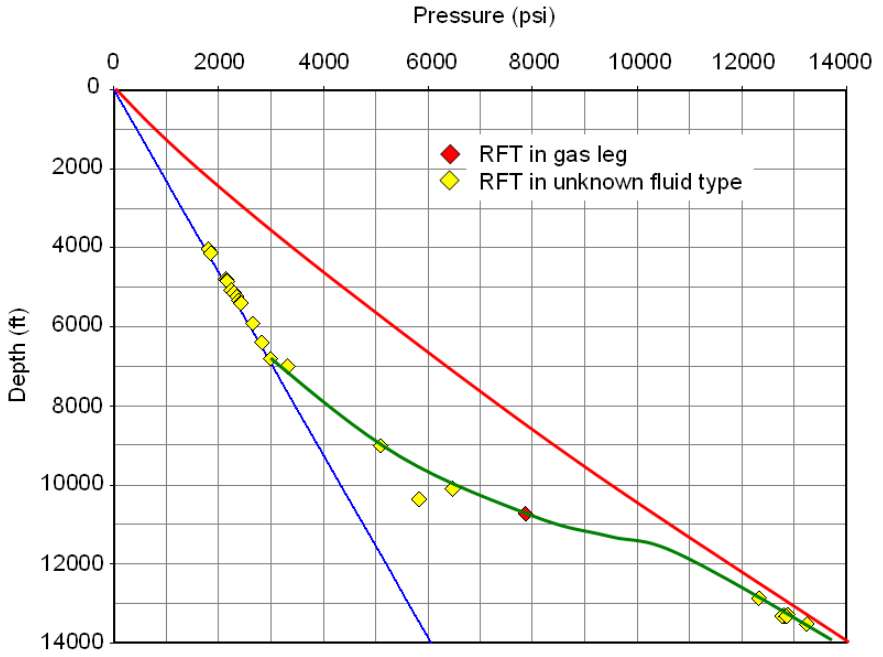

Figure 6.40 Pressure–depth plot for well SEM-39, Semberah Field.

6.1.5.2 Wireline log suites

Mutiara

The wireline log responses through the mudrocks in well MUT-21, which is a typical well, are shown in Figure 6.41, and those for the other overpressured wells in the Mutiara Field can be seen in Appendix 4a. Generally, the wireline log suites have poor quality due to drilling with water-based mud in a sand-rich environment, leading to bad hole conditions.

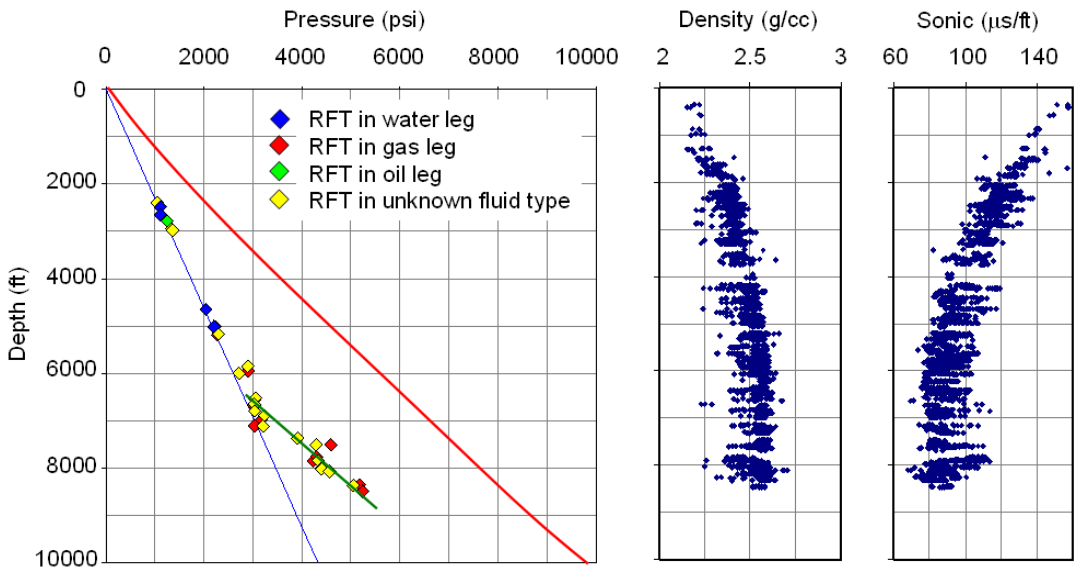

Figure 6.41 Pressure–depth plot and wireline log values in the mudrocks in well MUT-21, Mutiara Field.

As can be seen in Figure 6.41, the overpressured section in the well MUT-21 does not correlate with any clear reversal in density and/or sonic log. Below the top of overpressure, the pore pressure trend is approximately lithostat-parallel, and this is probably the reason why there is no sonic reversal. If the overpressure is due to unloading, then for there to be a reversal on the sonic log, the overpressure value needs to be sufficiently high to cause a reduction in vertical

effective stress with increasing depth. One important point concerning the density log is that the density values registered in the overpressured section are greater than 2.6 g cm^{-3}, which suggests that, as in other wells, the mudrocks are overcompacted and weighs against disequilibrium compaction as the cause of overpressuring in this field.

Based on these log responses circumstances, there are two possible causes of overpressuring in this well: 1) unloading, with subsequent dissipation of overpressure on exhumation, and 2) vertical transfer from more highly overpressured strata at depth. To decide which of these possibilities is more likely, analysis of the Semberah field below is helpful.

Semberah

The wireline log responses through the mudrocks in the overpressured wells in the Semberah Field are shown in Appendix 4b. The wireline responses in well SEM-39, which encounters the zone of high overpressure, are shown in Figure 6.42. Generally, the wireline log suites have poor quality due to drilling with a water-based mud in a sand-rich environment, leading to bad hole conditions.

As can be seen in Figure 6.42, the sonic and resistivity reversals start around 9000 ft, whereas the density reversal starts around 10,000 ft. The density-sonic cross-plot has considerable scatter, yet nevertheless displays a clear unloading trend (Figure 6.43), similar to those in the Bekapai and Handil wells (Figures 6.21 and 6.33). Based on these responses, it may be inferred that the same unloading mechanisms as in other fields described above are responsible for overpressure generation.

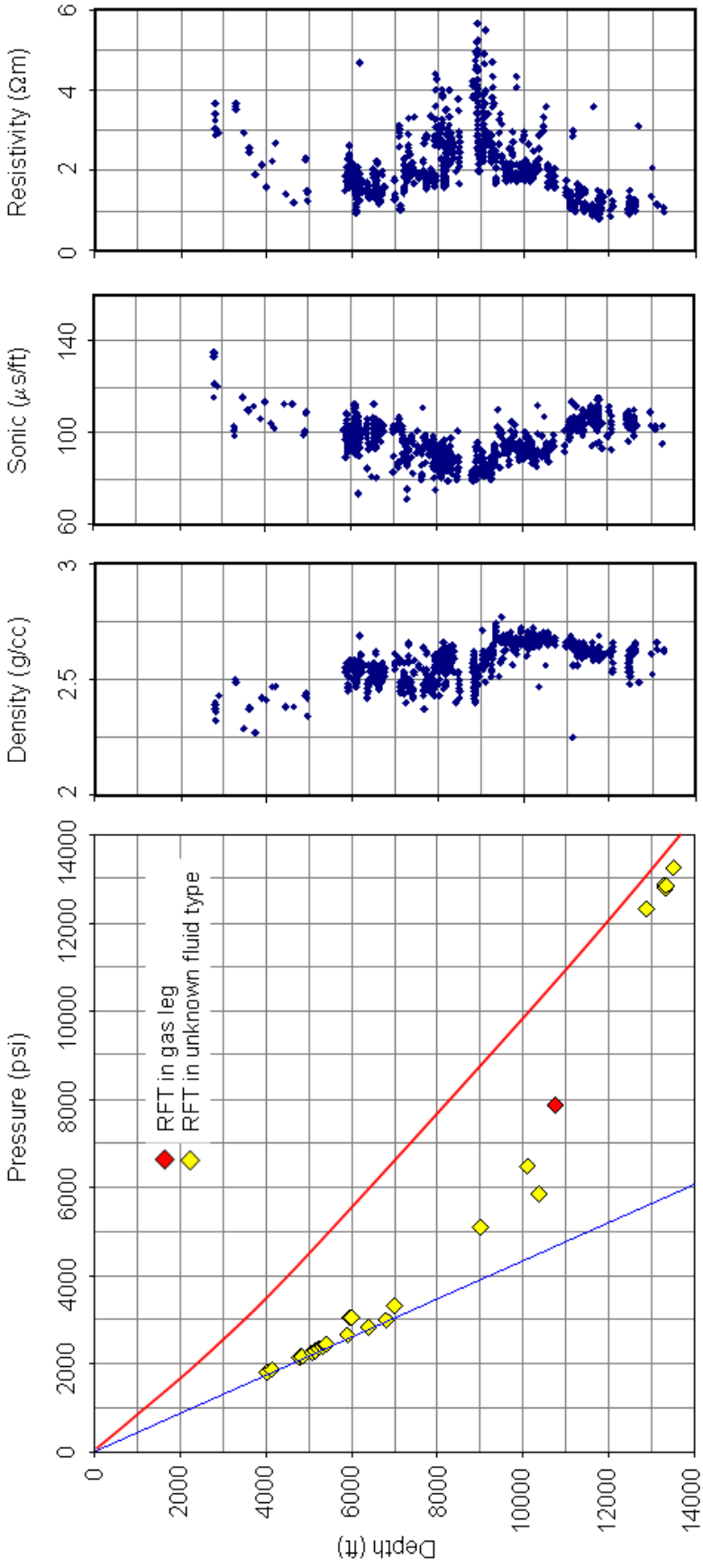

Figure 6.42 Pressure–depth plot and wireline log values in the mudrocks in well SEM-39, Semberah Field.

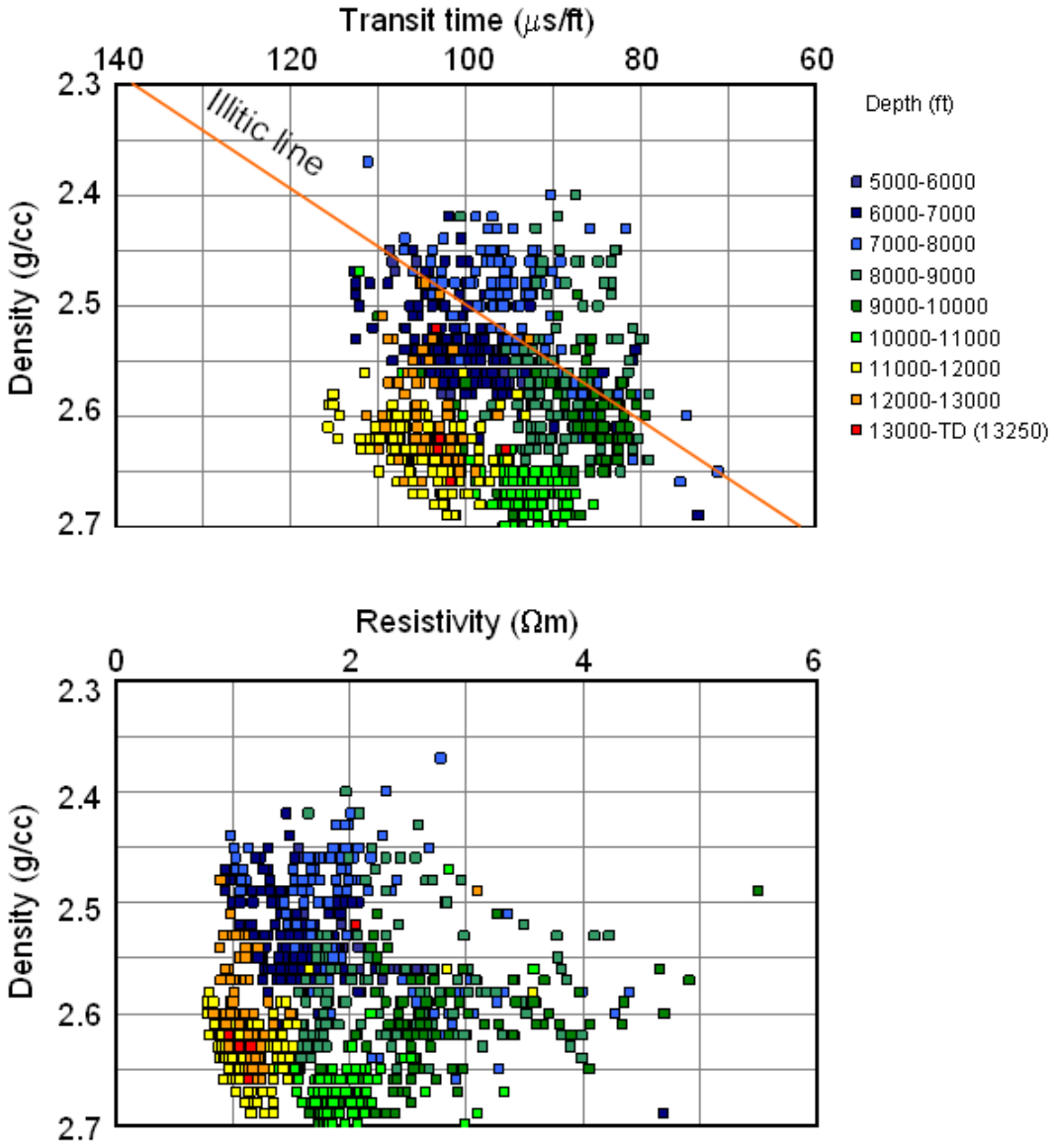

Figure 6.43 Cross-plots of density against sonic transit time and resistivity in mudrocks in well SEM-39, Semberah Field.

6.2 Interpretation

6.2.1 Overpressure distribution and its characteristics

Overpressure is present throughout the shelfal and onshore areas in the Lower Kutai Basin, as shown in Figure 6.44.

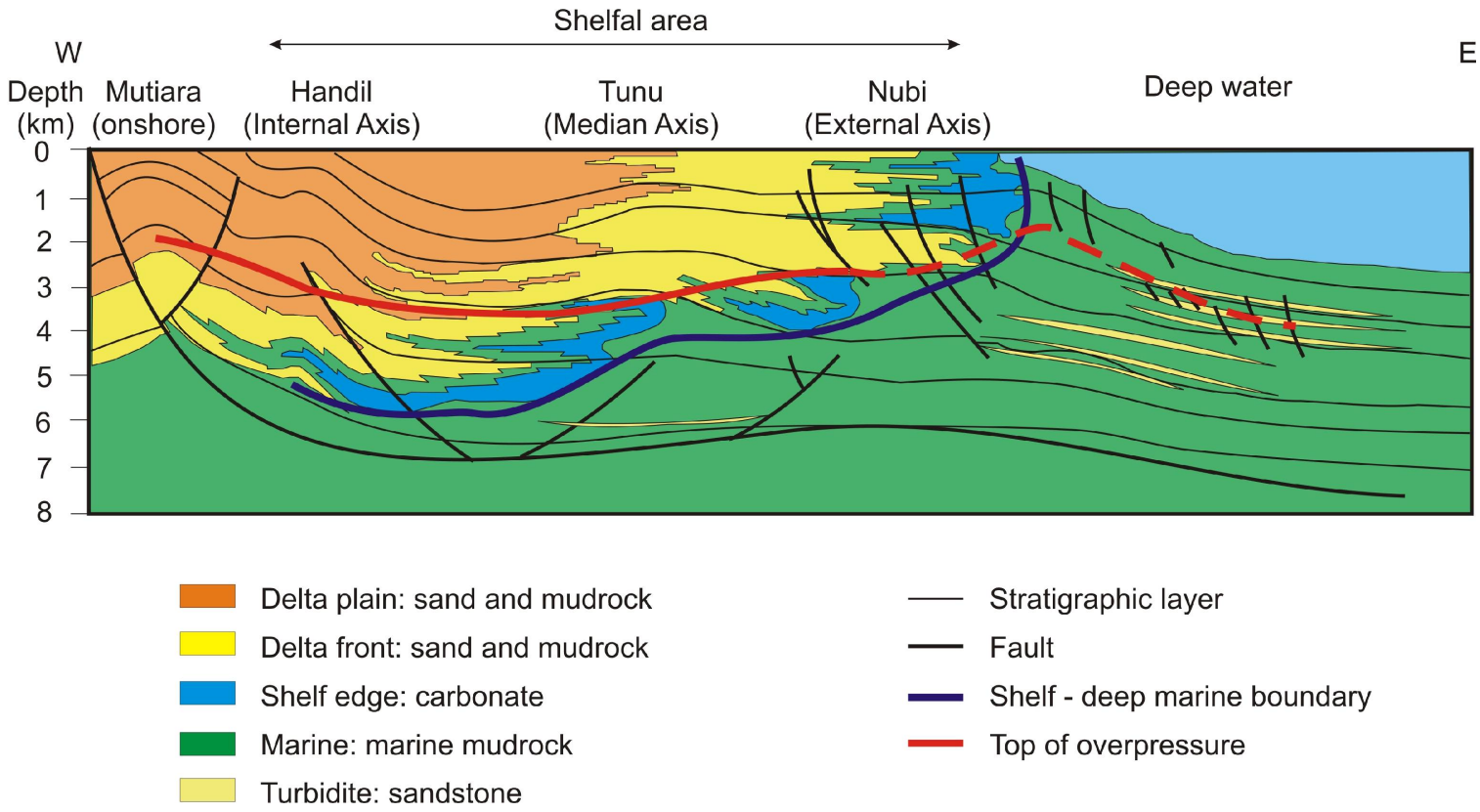

Figure 6.44 Schematic west-east geological cross-section of the Lower Kutai Basin (after Total E&P Indonesie, 2003a) and top of overpressure. Top of overpressure comes from several wells in the Mutiara, Handil, Tunu, Sisi–Nubi, and the deep water area located close to the line of section.

According to Bates (1996), at several locations in the onshore area the top of overpressure is very shallow, and even very near to the ground surface, but this circumstance is not evident in Figure 6.44.

In almost every field in the shelfal and onshore areas, the depth of the top of overpressure varies and cross-cuts stratigraphic boundaries. It has been demonstrated in Sub-section 5.4.4 that this variation leads to hydrodynamic trapping in the Peciko Field. Another example of variation in the depth to the top of overpressure is in the Tunu Field (Figures 6.18 and 6.19), where Lambert et al. (2003) identified it as being associated with hydrodynamic trapping (Figure 2.13).

Pressure profiles are generally similar for fields located in the same area of the basin. Typical forms of pressure profile in each area are shown in Figure 6.45.

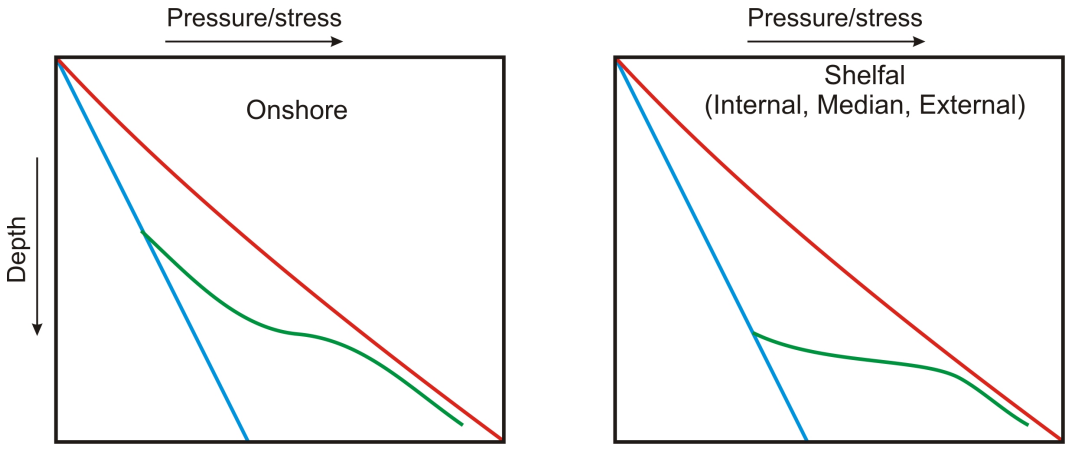

Figure 6.45 Characteristic overpressure profiles in each area of the Lower Kutai Basin.

In the shelfal area, except at the Peciko Field, the pressure profile changes abruptly from normal hydrostatic pressure into a transition zone to high overpressure. For example, in well B-11, Bekapai Field, the increment of pressure is about 0.27 g/cm^3 mudweight equivalent for every 100 m before the pressure profile converges asymptotically with the lithostatic gradient (Figure 6.20). In the Peciko Field, there is a zone of low overpressure above the transition zone into high overpressure. In the onshore area, there is a relatively long low-medium overpressure zone, somewhat similar to that observed in the Peciko Field, before

the transition zone into high overpressure is reached. These pressure profiles can be used as guidance in pre-drill prediction in each area in the Lower Kutai Basin.

6.2.2 Overpressure generating mechanisms and compaction

The observations above result in clear evidence that, not only in the Peciko Field, but also in shelfal and onshore areas, the transition into high overpressure is caused by an unloading process. When presenting the well data above, it was repeatedly emphasised that density logs show continuous increase in density values to around 2.6 g/cm^3 down to depths below the top of overpressure, as observed both on pressure–depth plots and by reversals on sonic and resistivity logs. These values of density, in combination with the high geothermal gradient of 0.0094°C/ft and the average surface temperature of 30°C in the onshore and shelfal areas (Figure 6.46), indicate that substantial chemical compaction of the mudrock has taken place.

An interesting question is whether disequilibrium compaction has made any contribution at all to the overpressure, or whether only unloading processes have contributed. The question is addressed first by considering the compaction state of the mudrocks, then with reference to the results of isotopic analysis of formation water, done as an in-house study by Total E&P Indonesie (2003b), and finally by addressing the candidate unloading mechanisms for overpressure generation.

The thermal gradient in the Lower Kutai Basin (Figure 6.46) gives an estimated temperature of 90°C at 6600 ft depth. Discrete smectite tends to have disappeared from basin mudrocks by the depth where this temperature is reached (Hower et al., 1976; Boles and Franks, 1979). Clauer et al. (1999) investigated clay mineralogy in the Tunu Field, on the Median Axis (Figure 1.1). At sampling depths below 7700 ft, they found that the clay fraction consists of mixed-layer illite/smectite, kaolinite/dickite, detrital illite, and chlorite. In the depth range 9000–14,000 ft where top of overpressure is reached in most wells, ongoing illitization of mixed-layer illite/smectite and the conversion of kaolinite to illite

are likely to occur (Bjorlykke, 1998). Both these clay diagenetic reactions release quartz which is subsequently precipitated as microcrystalline cement, as observed by Thyberg et al. (2010). Some dissolution and reprecipitation of detrital quartz is also likely to be occurring (Bjorkum, 1995).

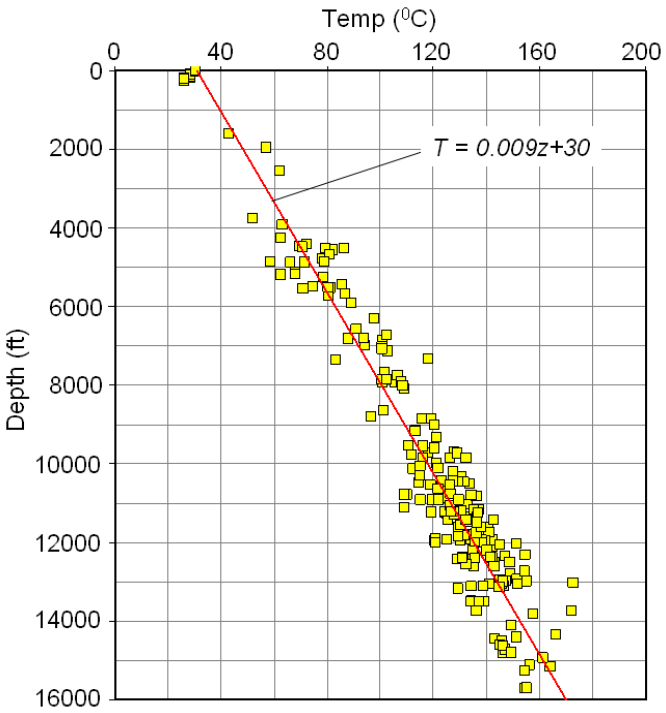

Figure 6.46 Geothermal gradient of the Lower Kutai Basin.

The high density value around 2.6 g/cm^3 in mudrocks at the depths where the top of overpressure is encountered suggest that chemical compaction has taken place. These densities are comparable to the highest densities recorded at similar depths in overcompacted Jurassic mudrocks on the Halten Terrace, deep water Norway (Hermanrud et al., 1998).

In Chapter 5, it was shown that in the Peciko Field, density values continue to increase smoothly below top of overpressure, even though the vertical effective stress has reached its maximum value at the top of overpressure in each well (Figure 5.20). Thus, compaction appears to continue with increasing depth, independent of vertical effective stress. Figure 5.20 constitutes strong evidence for

ongoing chemical compaction below the top of overpressure, and for discounting disequilibrium compaction as a mechanism that contributes to the generation of overpressure in this field. Given the high average density, in excess of 2.6 g/cm^3, reached at the depths where the overpressure transition zone is reached in all wells, the preferred interpretation is that the mudrocks in the overpressured intervals are overcompacted as a result of diagenesis.

An isotopic study of formation water performed in-house by Total E&P Indonesie (2003b) shows the importance of the contribution of water originating from mudrock compaction to the present day formation water in the reservoirs. The original aim of the study was to explain the decrease of water salinity with depth on the Median and External axes (Figure 6.47).

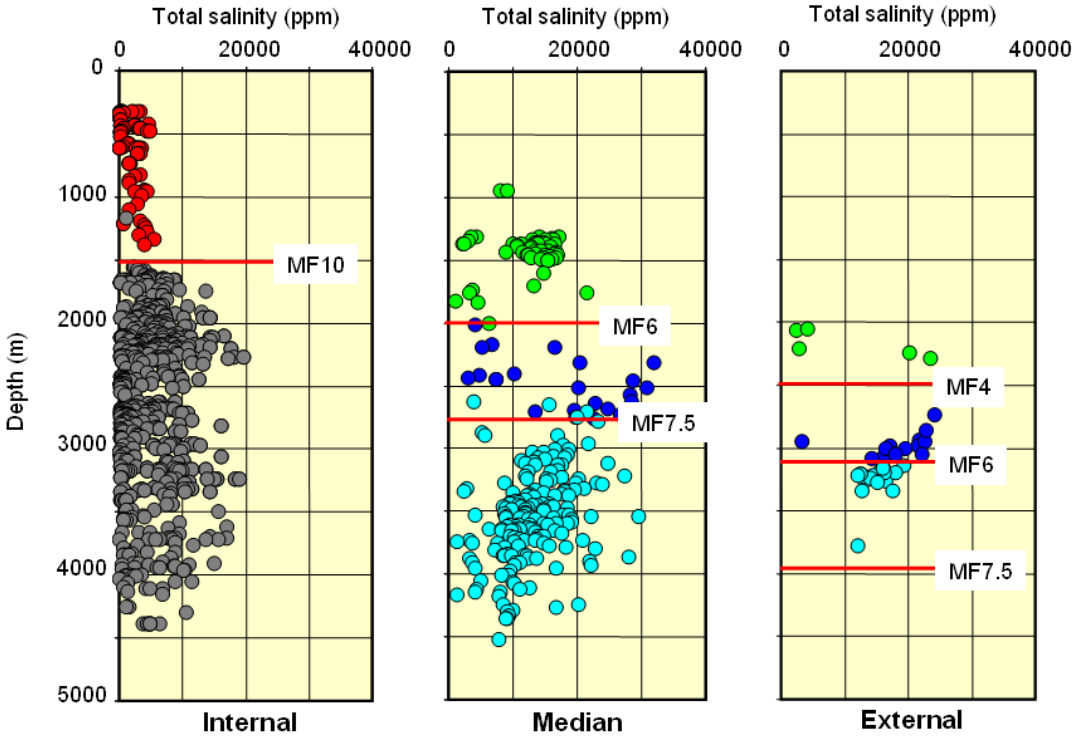

Figure 6.47 Salinity variations across the Internal, Median, and External axes (Total E&P Indonesie, 2003b).

The deuterium (D) and oxygen-18 (^{18}O) isotopes data from the Median and External axes show that there are shifts in the data for both isotopes from the expected lines for 'normal' formation water (Figure 6.48). The 'normal' lines result from mixing river and sea water isotopic compositions, assuming that there is no contribution from other sources. Both isotopes are enriched compared to the 'normal' isotopic lines.

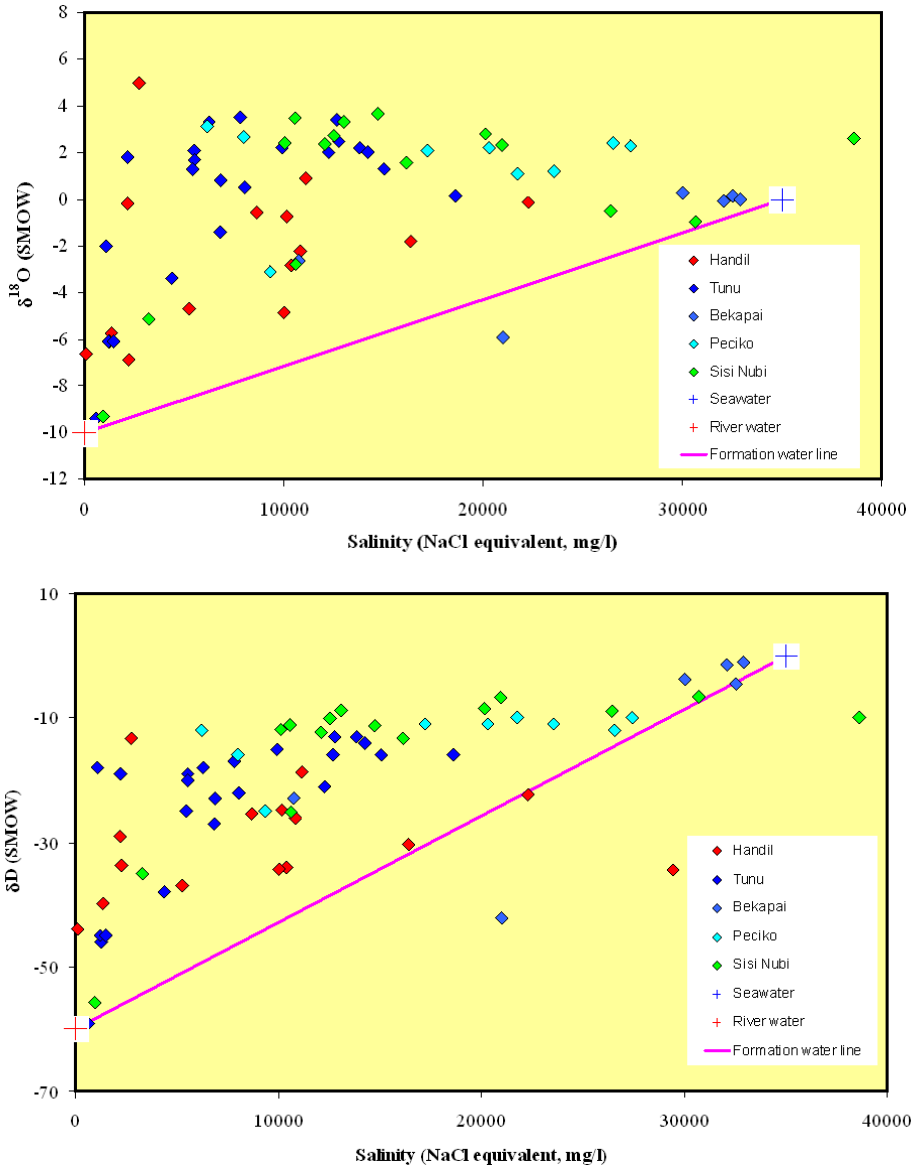

Figure 6.48 Enrichment of deuterium (D) and oxygen-18 (^{18}O) isotopes compared to the 'normal' lines for formation water (Total E&P Indonesie, 2003b).

There are two candidate mechanisms to explain the isotopic enrichment: thermal re-equilibration (enrichment due to increase of temperature), or mixing of the formation water with sources (the third source) other than river water and sea water. Results of the study revealed that thermal re-equilibration is not the cause because it requires the temperature of the reservoir to increase with the isotope enrichment, and this is not the case in the study area. It is likely that the formation water has a component from a third source (Figure 6.49). Furthermore, the third source was interpreted as compaction water expelled from the mudrock. The compaction water has low salinity, because of ion filtration through clay, causing chloride depletion. This explains why the third source has low salinity.

The study revealed that the compaction water has contributed significantly, in the range of 12–54% with an average around 30%, to the total volume of formation water in the reservoirs at the present time, and this is the cause of decrease in salinity with increasing depth on the Median and External axes. The expulsion of a significant amount of water from the mudrocks implies substantial compaction. This circumstance supports the interpretation given in this thesis that there is no contribution from disequilibrium compaction to the overpressuring, at least in the shelfal area.

As in the Peciko Field, there are two unloading mechanisms that occur internally within mudrock which could be responsible for overpressure generation, clay diagenesis and gas generation. It is also plausible that there is some vertical transfer from below, associated with sub-vertical cracks opening to cause the reversals in density log (e.g. Figure 6.20).

Vitrinite reflectance data from the Sisi-Nubi, Tunu, Peciko, Handil, and Nilam fields are shown in Figures 6.8, 6.50, and 6.51. In all fields except the Tunu Field, the top of the transition zone into hard overpressure, where sonic and resistivity logs display reversals, coincides with the vitrinite reflectance threshold value of 0.6% for gas generation. In the Tunu Field, only vitrinite reflectance values below the threshold were measured in the hydrostatically pressured intervals down to 14,000 ft, and the composite plot shows vitrinite reflectance values that approach 0.6% at that depth, but do not exceed it. Taken together, the

vitrinite reflectance data suggest a strong correlation between the top of transition zone into hard overpressure and gas generation.

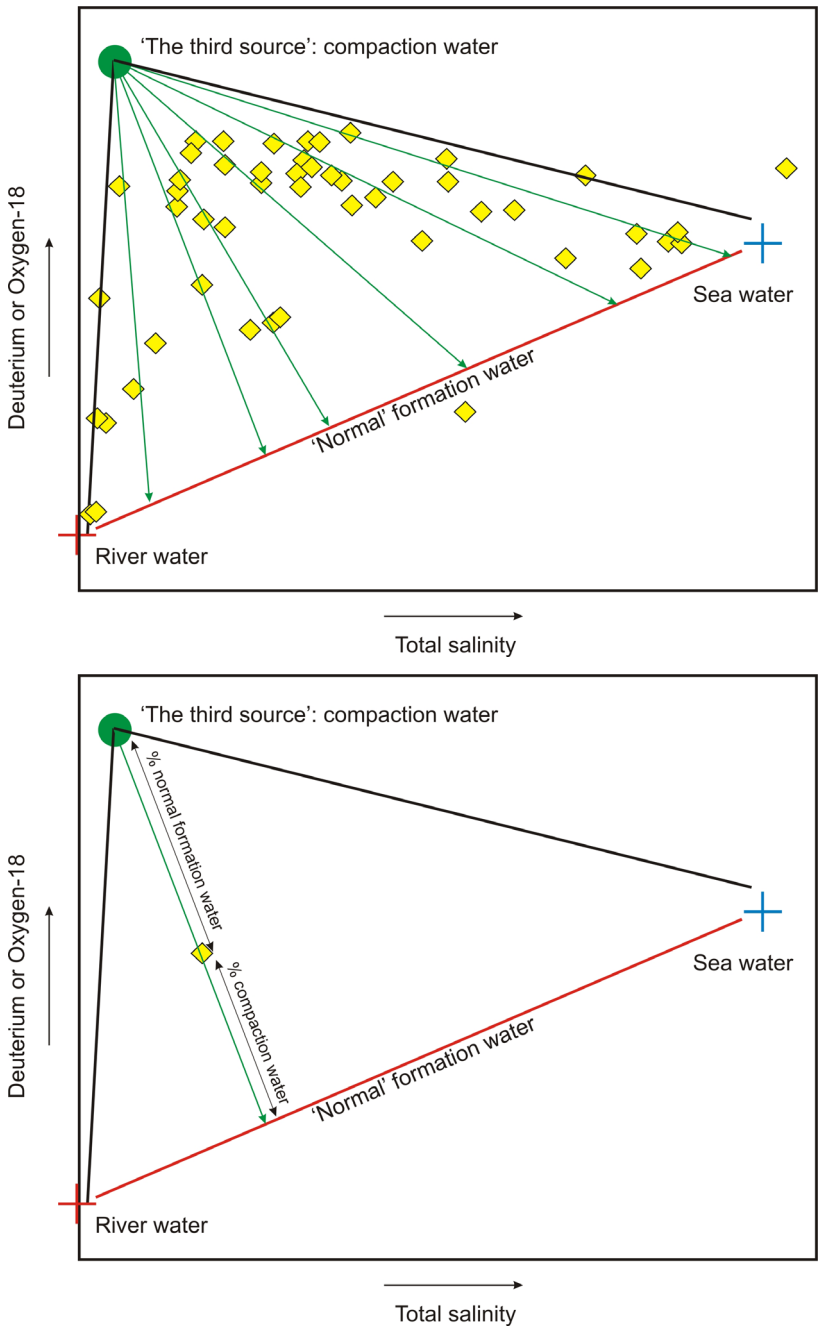

Figure 6.49 Mixing formation water with the third source (compaction water) as the cause of isotope enrichment. Bottom panel: example of calculation of compaction water contribution to the observed formation water composition (after Total E&P Indonesie, 2003b).

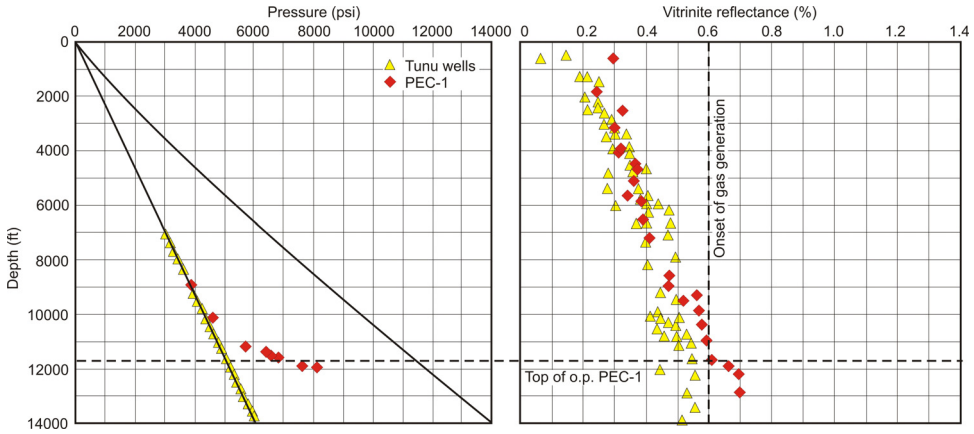

Figure 6.50 Composite pressure–depth plot and vitrinite reflectance data for wells in the Tunu Field and well PEC-1, Peciko Field. All the vitrinite reflectance data from the Tunu Field come from depth intervals in the respective wells where the pore pressure is known to be hydrostatic.

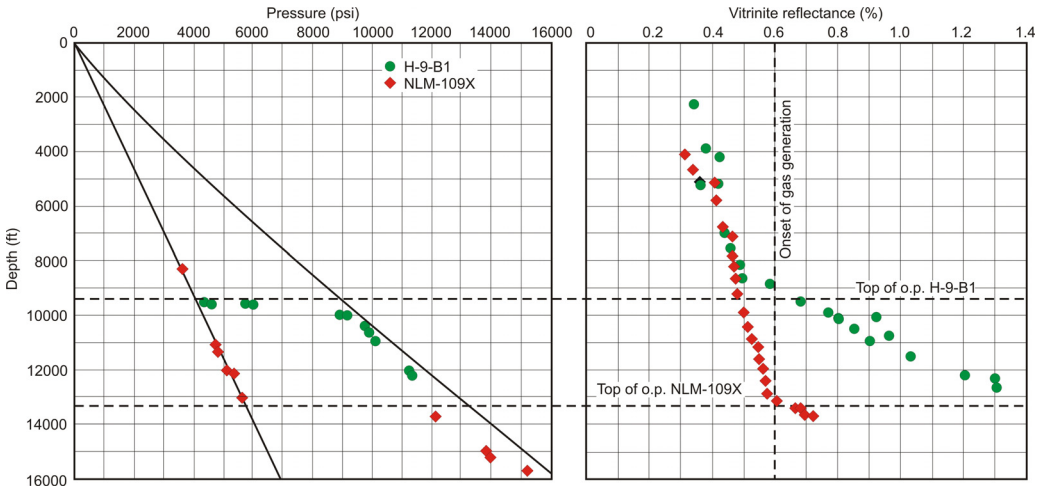

Figure 6.51 Pressure–depth plot and vitrinite reflectance data for wells H-9-B1, Handil Field and NLM-109X, Nilam Field.

There are no appropriate data to quantify the amounts of fluid expansion caused by gas generation and clay diagenesis, but both processes are plausibly responsible for overpressure generation, with the gas generation process being dominant. Reversals on density logs may be due to cracks opening to permit vertical transmission of fluid, so vertical pressure transfer may be a third mechanism contributing to the observed overpressure, but gas generation and

diagenesis are also likely to be the primary processes responsible for generating the fluid that is expelled from greater depths.

6.2.3 Hydrodynamic implications

Lateral reservoir drainage has been proven to cause hydrodynamic trapping in the Peciko and Tunu fields (Sub-section 5.4.4). In both fields, there are sufficient pressure data to perform overpressure mapping to determine fluid flow directions, as given in Figure 5.7 and Appendix 1c for the Peciko Field.

In other fields where the number of pressure data is not sufficient, the top of overpressure variation could be used to detect the presence of lateral reservoir drainage leading to hydrodynamic trapping. In almost all fields the top of overpressure varies, and commonly increases with depth in one lateral direction across the field. An example of this variation in the Bekapai Field is shown in Figure 6.52. The top of overpressure is deeper on the western flank of the structure, implying that the fluid flow direction is towards the west. It is possible that in the overpressured depth interval in this field, hydrodynamically trapped flank accumulations may be found, as in the Peciko and Tunu fields.

In the Handil Field, the top of overpressure is deeper in all flank directions, north-east, east, and south-west (Figure 6.27). Thus fluid flow may be outwards in all directions. Possibly there is vertical fluid transfer up the main fault in the vicinity of well H-9-B1. Unfortunately, the spatial coverage of the pressure data is insufficient to draw firm conclusions.

At shallower depths, it seems that fluid flow direction is governed by hydraulic head from the onshore area. The evidence for this is the slight overpressure at shallow depths in the Fresh Water Zone in the Sisi–Nubi and Tunu fields. It is interesting to consider the pore fluid distribution in relation to the possible effect of hydraulic head in this shallower zone. In the Tunu Field, the shallow reservoir is dominated by water, while it is a hydrocarbon-bearing zone in the Sisi–Nubi Field. As a speculation, meteoric water driven by the hydraulic head may have flushed the hydrocarbons from the Fresh Water Zone in the Tunu Field,

so that all hydrocarbons have been displaced and subsequently trapped in the Sisi–Nubi Field, where the structure is bounded by faults.

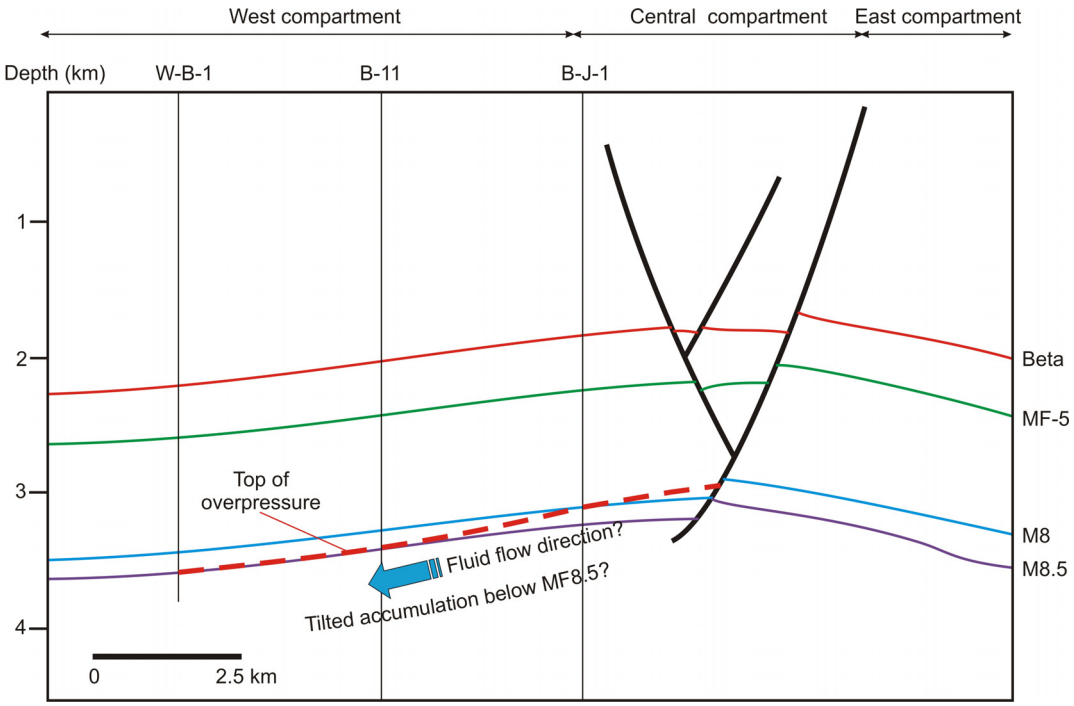

Figure 6.52 Possible hydrodynamically tilted hydrocarbon accumulation in the very deep zone, Bekapai Field.

6.3 Overpressure estimation

As discussed in Sub-section 3.6.3, Bowers (1995) pointed out the importance of understanding the overpressure generating mechanism prior to estimating pore pressure from log responses in mudrocks. Experience in the Peciko Field shows that application of the standard Eaton method with exponent 3 (Eaton, 1975) tends to underestimate overpressures that are caused by fluid expansion mechanisms. In the Lower Kutai Basin, where it has been inferred that overpressure is caused by unloading mechanisms, including gas generation and clay diagenesis, empirical constants in Equation 3.27 (Bowers, 1995) need to be determined.

A plot of vertical effective stress against velocity data for multiple wells in the basin (Figure 6.53) shows a clear and consistent virgin curve. Data points

from unloaded mudrocks lie above the normal compaction curve. Fitting the hydrostatically pressured data points yielded the following form for the virgin curve:

$$\sigma'_v = \left(\frac{v - 5000}{11.661} \right)^{1/0.7529} \tag{6.1}$$

The unloaded data points were used to find the exponent U in Equation 3.20, yielding the unloading relationship:

$$\frac{\sigma'_v}{\sigma'_{max}} = \left[\frac{1}{\sigma'_{max}} \left(\frac{v - 5000}{11.661} \right)^{1/0.7529} \right]^8 \tag{6.2}$$

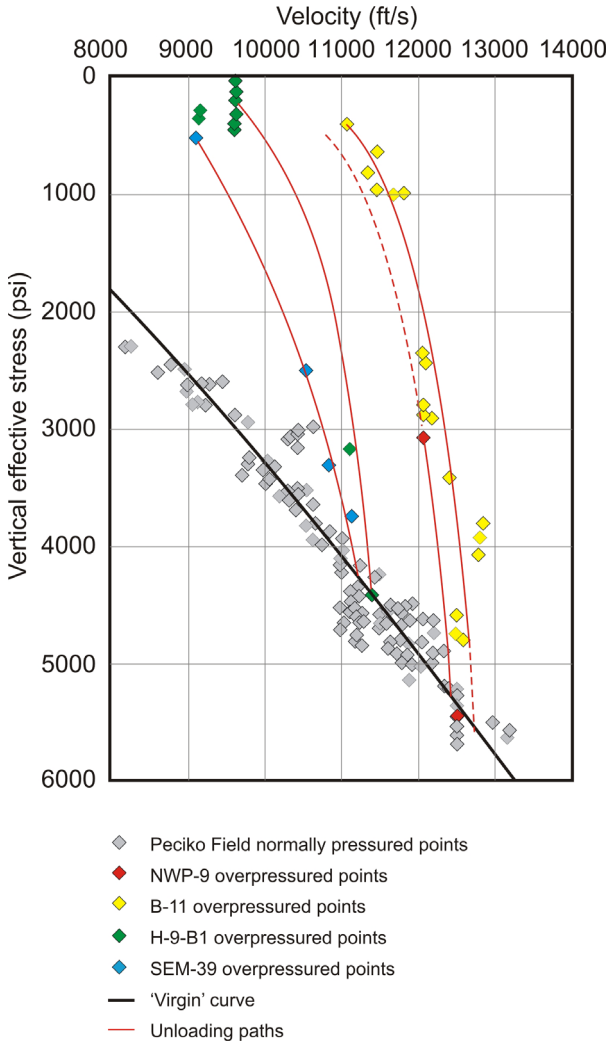

Figure 6.53 Plot of velocity versus vertical effective stress showing the normal compaction trend (the'virgin' curve) and unloading paths.

The result of applying Equation 6.2 to well B-11, Bekapai Field is shown in Figure 6.54. The maximum effective stress experienced by the mudrocks, which is required in the calculation, was obtained from the depth where the sonic and resistivity logs start to reverse, and is assumed to be constant throughout the overpressured section. This method appears to give fairly good estimates of overpressure in the mudrocks, assuming that they are in continuity with the measured pore pressures in the sands.

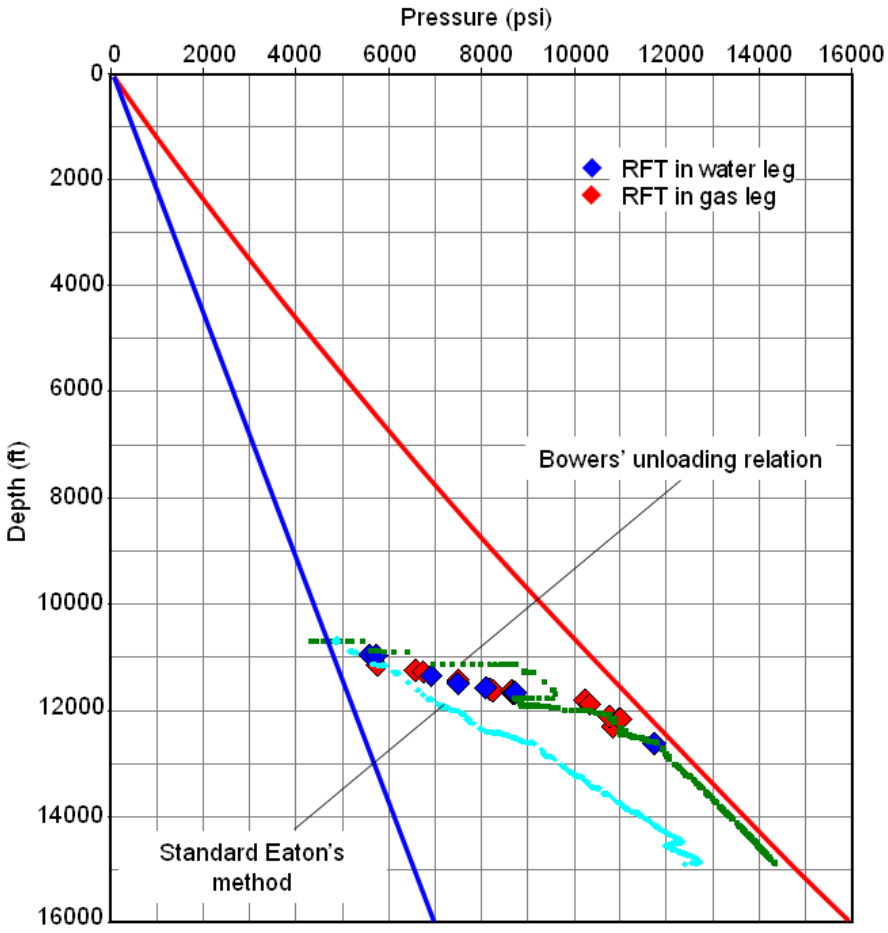

Figure 6.54 Application of Bowers' unloading relation and standard Eaton's method in predicting overpressure in mudrocks in well B-11, Bekapai Field.

6.4 Summary

The following points summarise the main findings of this chapter:

1. Overpressure is present in all areas in the Lower Kutai Basin.
2. On the field scale, the top of overpressure varies, and commonly increases with depth in one lateral direction across the field.
3. Overpressure in the shelfal and onshore areas is caused by an unloading mechanism or mechanisms. The plausible causes of unloading are clay diagenesis and gas generation.
4. The overpressured zones can be detected from reversals on the sonic and resistivity logs around the top of the transition zone into high overpressure.
5. Compaction in the shelfal area is independent of vertical effective stress, and by the depths where the top of overpressure is encountered, the mudrocks are overcompacted in a mechanical sense.
6. It seems that lateral reservoir drainage occurs in all fields except on the deep water area.
7. Overpressure can be estimated by applying Bowers' relation for an unloading mechanism.

CHAPTER 7
DISCUSSION

In this chapter, the research problems outlined in Chapter 1 and the research objectives are discussed. In section 7.1, the reasons why previous workers in the Lower Kutai Basin attributed the overpressure to disequilibrium compaction are reviewed, and a summary of the evidence for the radically different interpretation contained in this thesis is given. Section 7.2 is concerned with overpressure detection and estimation. The role of overpressure in the petroleum system, including hydrodynamic trapping, is discussed in Section 7.3. The last item for discussion is to put the overpressuring and compaction in the Lower Kutai Basin into a wider context by comparing the mudrock compaction trend at Peciko with examples of other basins. This comparison is made in Section 7.4, and a new hypothesis concerning the porosity–temperature compaction trend for mudrocks in the chemical compaction regime is proposed.

7.1 Overpressuring and compaction in the Lower Kutai Basin

It is instructive to review the reasons why previous workers have considered the primary mechanism of overpressure generation in the Lower Kutai Basin to be disequilibrium compaction. By the early 1990s, disequilibrium compaction was well established as a primary mechanism of overpressure generation in Tertiary successions, following early work on Gulf Coast wells (Dickinson, 1953; Dickey et al., 1968). Thus during early exploration of the Lower Kutai Basin, explorationists would have been expecting disequilibrium compaction to have generated overpressure in rapidly buried Miocene successions. Wherever reversals were observed on sonic logs, they were attributed to enhanced porosities due to disequilibrium compaction (e.g. Bois et al., 1994; Bates, 1996; Burrus, 1998).

Sonic logs were preferred for pore pressure prediction in mudrocks principally because the sonic log is less influenced by bad hole conditions than density and neutron logs (Bois et al., 1994). Where good density logs were recorded, reversals on them were also ascribed to disequilibrium compaction, even though the reduction in density nowhere near matched the equivalent depth for reduction in sonic velocity. For example, near the base of the B-11 well at Bekapai (Figure 6.20), at a depth of 14,800 ft, the sonic transit time is 110 μs/ft, the same value as at 5000 ft depth. The density log shows a reversal at 12,000 ft from a maximum value greater than 2.6 g/cm^3. At 14,800 ft, the density has reduced to 2.5 g/cm^3, and was attributed by Burrus (1998) to disequilibrium compaction even though the density at 5000 ft is only 2.1 g/cm^3. Clearly, disequilibrium compaction does not provide a satisfactory explanation for those observations, as discussed more generally by Kooi (1997): at the very least, substantial chemical compaction is indicated.

The sharp nature of the pressure transition zones in several fields was not anticipated, and also influenced interpretation of the pore pressure regime. Several kicks and some internal blowouts occurred in the early phase of exploration drilling in the shelfal area of the Lower Kutai Basin. According to Bois et al. (1994), following a severe kick in the SISI-2b well, Sisi Field, pore pressure estimates using the d' exponent and indices from gas shows were reconsidered. They wrote, “At this time, it was realised how misleading were the pressure measurements obtained in reservoirs. It was thereafter decided to forbid their use for that purpose.” They conducted a regional study of mudrock pore pressures based on sonic logs, and confirmed what they thought were large discrepancies between reservoir and mudrock pore pressures. However, although Bois et al. (1994) recognised that the choice of the normal compaction trend is of the utmost importance, they extrapolated the normal compaction trend from shallow depths, where they were confident that mudrock pore pressures were hydrostatic, either by “visual estimation” or by calculated regression, in which they used a simple exponential decay function for sonic transit time (2P-NCT):

$$\Delta t_n = \Delta t_0 e^{-cz} \qquad (7.1)$$

where *c* is a constant. The trend in Equation (7.1) grossly underestimates the sonic transit time for hydrostatically pressured mudrocks when extrapolated to large depths, because Δt_n becomes less than Δt_{ma}. Consequently, measured sonic velocities at depth are always less than those predicted for hydrostatically pressured mudrocks by such incorrect normal compaction curves.

Bates (1996) only studied the onshore part of the Lower Kutai Basin, including the Badak and Nilam Fields on the northern part of the Internal Axis but not the Tambora and Handil fields located on the present-day Mahakam Delta (Figure 1.1). He considered the primary mechanism for generation of overpressure to be disequilibrium compaction because of the basinwide distribution and scale of overpressuring. With the benefit of hindsight, this vague reasoning seems unconvincing. He further claimed that overpressuring is independent of hydrocarbon generation, temperature, geological age, uplift and tectonic effects. Yet he partially contradicted himself by explaining that where the top of overpressure is shallow, it is because of uplift. Furthermore, the vitrinite reflectance data from Nilam (Figure 6.51) are taken from his paper. Bates (1996) also reported that in the Lower Miocene in the western part of the basin, the anticlinal cores expose highly sheared, very low density claystones which exhibit evidence of rapid dewatering. We have no data to confirm whether that is so, but there is no doubt that the distribution of overpressure onshore is more complex than in the shelfal area, where our study is focused, because of uplift.

A final point worth making in defence of earlier workers is that most early exploration wells terminated in the transition zone into hard overpressure. It now seems reasonable to suppose that the hard overpressure zone is ubiquitous throughout the basin, and overpressures in it are much higher than those which could be explained by disequilibrium compaction.

In summary, the reasons why the disequilibrium compaction interpretation appears to be wrong, at least for the shelfal area of the basin, are mainly based on density behaviour in the mudrocks. The density logs do not display reversals at the same depths as sonic and resistivity logs: where density reversals have been observed, they are distinctly deeper. The composite density plot from 16 appraisal

wells in the Peciko Field (Figure 5.20) shows that density continues to increase below the top of overpressure, which is where the vertical effective stress reaches its maximum value in each well. Where density logs display reversals, the densities are still very high in comparison to densities at the same vertical effective stresses in hydrostatically pressured mudrocks at shallower depths. For example, the density is 2.6 g/cm^3 at 12,600 ft (3840 m) in well B-11, at Bekapai, where the vertical effective stress is less than 500 psi (3 MPa) and 2.5 g/cm^3 at 10,500 ft (3200 m) depth in well H-9-B1, at Handil, where the vertical effective stress is even less.

Moreover, the isotopic water study described in Sub-section 6.2.2 shows a significant contribution of compaction water to the observed present-day composition of the formation water. This circumstance indicates that the mudrock has been compacted significantly, which is contrary to the disequilibrium compaction hypothesis.

Sonic logs have also been examined, without success, for evidence of any shoulder effects (O'Connor et al., 2008) above the transition zone into hard overpressure. If there really were pore pressure discrepancies between mudrocks and reservoirs at those depths, we would expect a shoulder effect to be present.

7.2 Overpressure detection and estimation

Based on the pressure–depth profiles and overpressure distribution analysed in Chapter 6, several points can be made as guidance for the detection and estimation of overpressure in the Lower Kutai Basin:

Pre-drill prediction

In a mature area, the information on tops of overpressure from offset wells are of paramount information compared to other data. The top of overpressure in the planned well can be estimated by interpolation of the depths to the top of overpressure in the offset wells. In the absence the sufficient data from the offset

wells, the top of overpressure can still be estimated by applying this rule of thumb: the top of overpressure is usually deeper on the flank of structures in the shelfal and onshore areas. Information on source rock maturation would also be very helpful in detecting the top of overpressure in the shelfal area, where the shallower reservoir sands are laterally drained, because the top of overpressure tends to coincide with the onset of gas generation there.

After the top of overpressure in the planned well has been estimated, the following characteristics of pressure-depth profiles can be used as guidance:

- Shelfal area: from the top of overpressure down to TD, a very sharp change in the slope of the pressure-depth profile is expected at the top of the transition zone into high overpressure.
- Onshore area: from the top of overpressure down to TD, a zone of low to medium overpressure with a pressure-depth profile sub-parallel to the lithostatic stress may be anticipated, until the top of the very sharp transition zone into high overpressure is reached.

Prediction while drilling

For the onshore and shelfal areas, overpressure prediction while drilling is essentially the search for sonic and/or resistivity reversals. The sonic log is usually run in logging while drilling (LWD). In the absence of reservoir, a reversal can be used as an indicator that drilling has encountered a transition zone into high overpressure. Overpressure inside the reversal could then be estimated by using Bowers' relation, given by Equation (6.2). For drilling in the shelfal area, Total E&P Indonesie relies on the gas-while-drilling indicator as the best method of overpressure detection. If the background gas, i.e., the gas contained in the mudrock, stays above 2%, then the drilling mudweight is raised. This method of detection is consistent with the result of this research that gas generation is one of the causes of overpressure generation in this area. Furthermore, in the Peciko Field the top of the transition zone into high overpressure follows the 140°C isotherm. Therefore, measurement of temperature while drilling would be useful

to analyse the top of the transition zone, but there are enormous practical difficulties because of the cooling effect of circulating drilling mud. Applying the results of this research in combination with Total E&P Indonesie's established method will result in safe and efficient drilling of wells in this area.

7.3 Role of overpressure in the petroleum system

A major result of this research is that that overpressuring in the onshore and shelfal areas is caused by gas generation. Thus source rocks must be distributed widely on the shelfal and onshore areas. That may explain why the Lower Kutai Basin, and especially the shelfal area, is very prolific for gas.

The density reversals in the zone of high overpressure are attributed to the opening of microcracks. The cracks will promote hydrocarbon migration vertically from the overpressured section.

The most important role of overpressuring in the Lower Kutai Basin is to cause hydrodynamic trapping of hydrocarbons due to lateral variations in overpressure. This trapping mechanism has been proven to be operative in the Peciko and Tunu fields. It is also possible that hydrocarbons are trapped hydrodynamically in other fields below the top of overpressure.

Variation in the depth to the top of overpressure might be used as an early indication of the presence of hydrodynamic trapping. In this discussion, the Bekapai Field will be used as an example. The wells B-J-1, located at the crest of the structure, B-11, located on the flank, and W-B-1, located in the synclinal area, show that the top of overpressure varies in this field (Figure 6.52). It is located around horizon MF 8 in B-J-1 and around horizon MF8.5 in B-11 and W-B-1, so the top of overpressure crosses stratigraphy. Given the absence of faulting, these observations suggest that hydrodynamic flow is occurring through the overpressured reservoirs in this field. The direction of the flow is towards the western flank of the area. Tilted hydrocarbon accumulations may be present on the western flank of the Bekapai Field, as in the Tunu Field and on the northern flank of the Peciko Field (Figure 6.52).

7.4 Global comparison

7.4.1 Overpressuring

In the introductory chapter, it was stated that the shelfal area of the Lower Kutai Basin provides a unique example of overpressuring compared to other Neogene sedimentary basins in the world: it is a young basin, experiencing continuous sedimentation with relatively high temperatures. Swarbrick et al. (2002) compiled reported sedimentation rates in several basins world-wide where overpressuring could possibly be produced by disequilibrium compaction (Figure 7.1). This chart includes the Lower Kutai Basin. However, disequilibrium compaction requires a combination of a high sedimentation rate and low permeability of the sedimentary system. The massive lateral drainage of reservoir sands in the upper section of the Lower Kutai Basin, due to good connectivity to outcrop, assisted by higher NTG in the onshore and shelfal areas, allows the mudrocks to dewater, so they are at normal hydrostatic pressure to depths around 3 km below the sea bed. Thus the circumstances in the Lower Kutai Basin are rather unique: it is a young Neogene basin where the sedimentation rate is moderately high, yet the overpressuring is caused by an unloading mechanism.

The conclusion that overpressure is generated by unloading is plausible because of the relatively warm conditions in the Kutai Basin and the source rock distribution. The geothermal gradient of 9.4°C/1000 ft and the surface temperature of 30°C cause smectite–illite transformation to occur at relatively shallow depths, and it is estimated that discrete smectite has disappeared at about 6000 ft below sea bed. The deltaic depositional environment at low latitudes has resulted in the widespread deposition of gas-prone source rocks with high TOC.

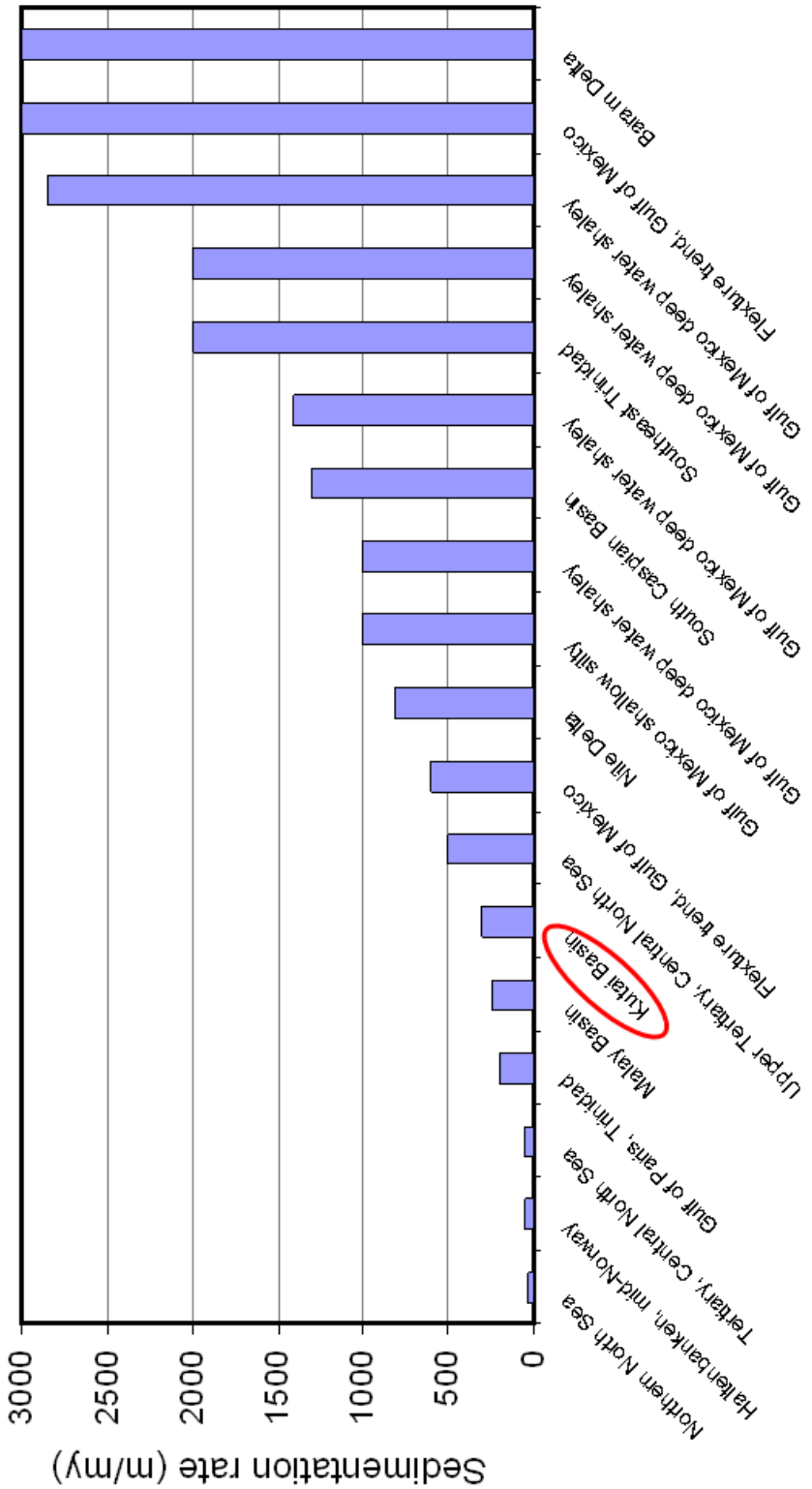

Figure 7.1 Average rates of sedimentation in various basins around the world (data source: Swarbrick et al., 2002).

7.4.2 Compaction

Six historically important published compaction curves have been chosen for comparison with the porosity–depth profile derived empirically for mudrocks in the Peciko Field. They are the compaction curves of Athy (1953), Dickinson (1953), Magara (1968), Sclater and Christie (1980), Baldwin and Butler (1985) (referred to as Baldwin-Butler 1 and 2 here), and Hansen (1996) (Figure 7.2).

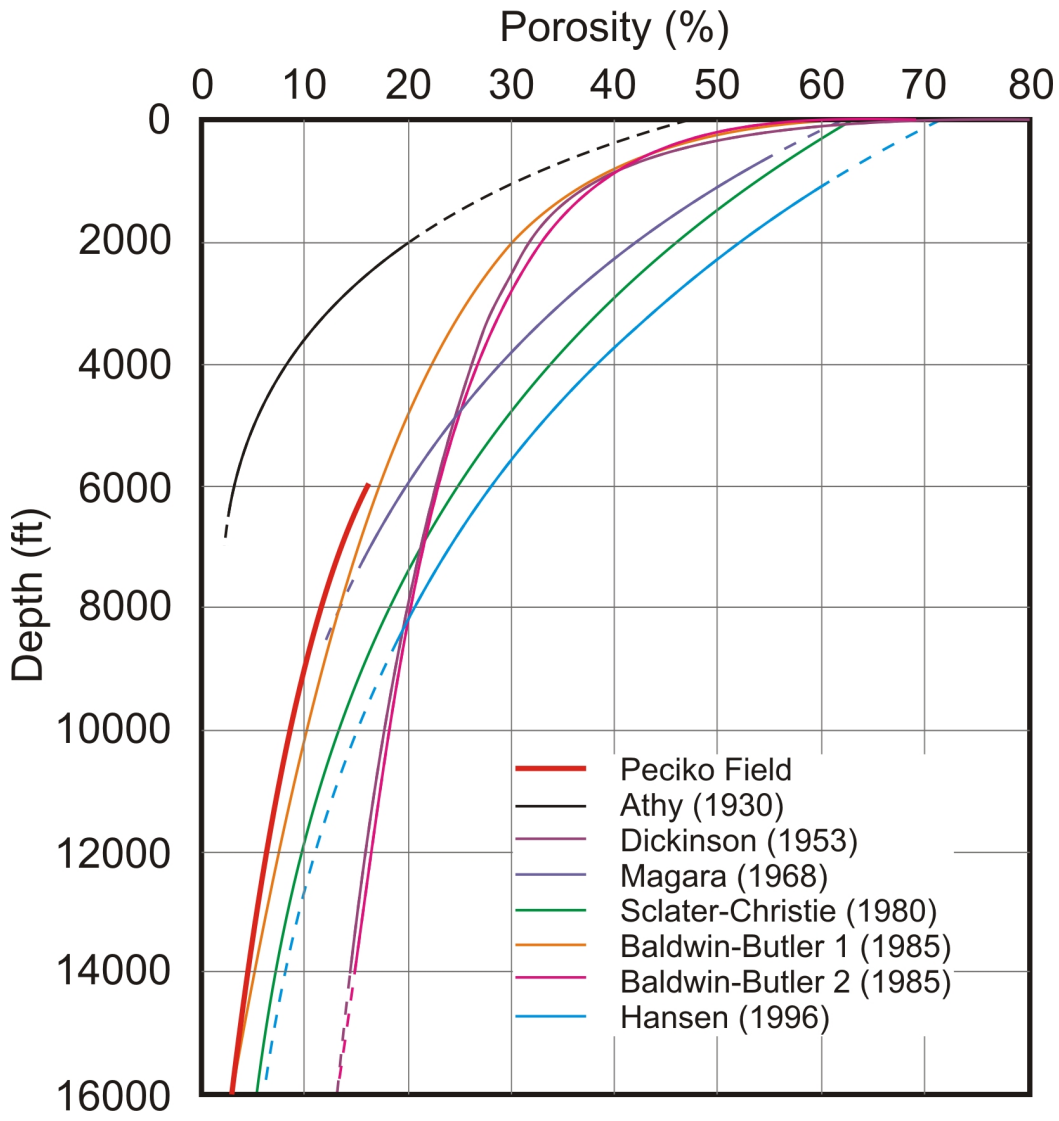

Figure 7.2 Comparison of the porosity–depth compaction trend at Peciko with other published compaction trends.

Athy (1930) first proposed that porosity decays exponentially with depth. He constructed a porosity-depth curve for sedimentary rocks of Permian–Pennsylvanian age in the Oklahoma oilfields. The depth range where the equation was constructed was at 2000–6400 ft. He also recognised that in the area where the data were taken, a thickness of 1400 ft of the uppermost sediments had been eroded. He obtained porosity values from laboratory porosity measurements on 200 samples of cuttings and sidewall cores. Athy's (1930) compaction curve has stimulated much subsequent research into mudrock compaction. Notably, Rubey and Hubbert (1959) proposed that exponential decay of porosity with effective stress would be more appropriate to describe mechanical compaction in order to allow for the mudrocks being overpressured by disequilibrium compaction.

Dickinson (1953) constructed a porosity-depth curve in the form of an exponential decay for the Tertiary Gulf Coast area down to the depth of 15,000 ft. He stated that he obtained porosity values from some density measurements (density-derived porosity) and 'estimates used by geophysicists'. His data include the undercompacted section starting at depths of around 10,000 ft, as indicated by low density values at depth.

Magara (1968) constructed a porosity-depth curve in the form of an exponential decay for well Shiunji SK-21, Nagaoka Plain, Japan. The mudrock layers used to construct the equation are located in a volcanic sequence, and the depth range where the equation was constructed was 250–2200 ft within normally compacted mudrocks. He derived porosity values from the resistivity log.

Sclater and Christie (1980) constructed a porosity-depth curve in the form of an exponential decay for North Sea mudrock data down to the depth of 8 km. Their equation is:

$$\Phi = 63\exp(-0.00051z) \qquad (7.2)$$

where Φ is in % and z is in m. They derived porosity from sonic data using Magara's (1976b) transformation of sonic to porosity. In addition, they stated explicitly that the constant 63 is the surface porosity (%).

Baldwin and Butler (1985) compiled previously published compaction curves, and then proposed that the compaction relationship between porosity and

depth is better described by expressing depth as a power law function of solidity,

$$S = 1 - \Phi \tag{7.3}$$

They constructed different power law equations for normally compacted and undercompacted mudrocks. The equation for undercompacted mudrocks was taken from Dickinson's curve (1953). Their equations are:

$$z = 6.02S^{6.35} \tag{7.4}$$

for normally compacted mudrocks (Baldwin–Butler 1), and

$$z = 15S^{8} \tag{7.5}$$

for undercompacted mudrocks (Baldwin–Butler 2), where z is in km and S is expressed as a fraction.

Hansen (1996) constructed exponential and linear functions to describe the decay of porosity with depth in sedimentary rocks of Cretaceous–Tertiary age on the Norwegian Shelf. His equations are:

$$\Phi = 71\exp(-0.00051z) \tag{7.6}$$

for exponential decay, and

$$\Phi = 62 - 0.00018z \tag{7.7}$$

for linear decay

where porosity is in % and z is in m. The data used for construction of these relationships came from the depth range 1000–8500 ft, which explains why the surface porosity values at $z = 0$ are so different. Part of the area has experienced Late Cenozoic uplift and erosion, so Hansen (1996) was careful to choose only normally compacted mudrocks in his analysis, avoiding those that are overcompacted. He derived the porosity values from sonic logs, calibrated with density-derived porosities measured from cuttings and sidewall cores using 2.72 g/cm^3 as the matrix density value. He also stated that it is questionable whether his equations should be applied to mudrocks at depths below 8500 ft.

In terms of depth of investigation, there are two compaction trends that can be compared with the Peciko Field: those of Sclater and Christie (1980) and the Baldwin-Butler 1 curve (Baldwin and Butler, 1985), which was chosen in preference to the Baldwin-Butler 2 curve because it was stated that the former was derived from normally compacted mudrocks. It can be seen in Figure 7.2 that the

Peciko curve is close to Baldwin-Butler 1, but it is significantly different from the Sclater-Christie curve.

In order to test the hypothesis put forward in this thesis that the mudrocks in the Peciko Field are overcompacted below 6000 ft depth, due to the complete transformation of discrete smectite to mixed-layer illite/smectite at temperatures of 90°C, these three curves have all been converted here into trends of porosity versus temperature. To convert depth into temperature, the following geothermal gradients were used:

$$T = 0.0089z + 23.33 \quad (7.8)$$

in the Gulf Coast area from Burst (1969) for the Baldwin-Butler 1 curve,

and

$$T = 0.0091z + 10 \quad (7.9)$$

in the North Sea area from Harper (1971) for the Sclater-Christie curve, and

$$T = 0.0094z + 30 \quad (7.10)$$

for the Peciko Field. Temperatures are in degrees Celsius and depths in feet for all three geothermal gradients.

All three compaction curves align on to a single trend at temperatures above 90°C (Figure 7.3). Thus it is tentatively suggested that the chemical compaction trend for mudrocks in sedimentary basins at temperatures higher than 90°C is independent of variables other than temperature, i.e., independent of age, depth of burial, and effective stress. Clearly, this hypothesis should be tested further.

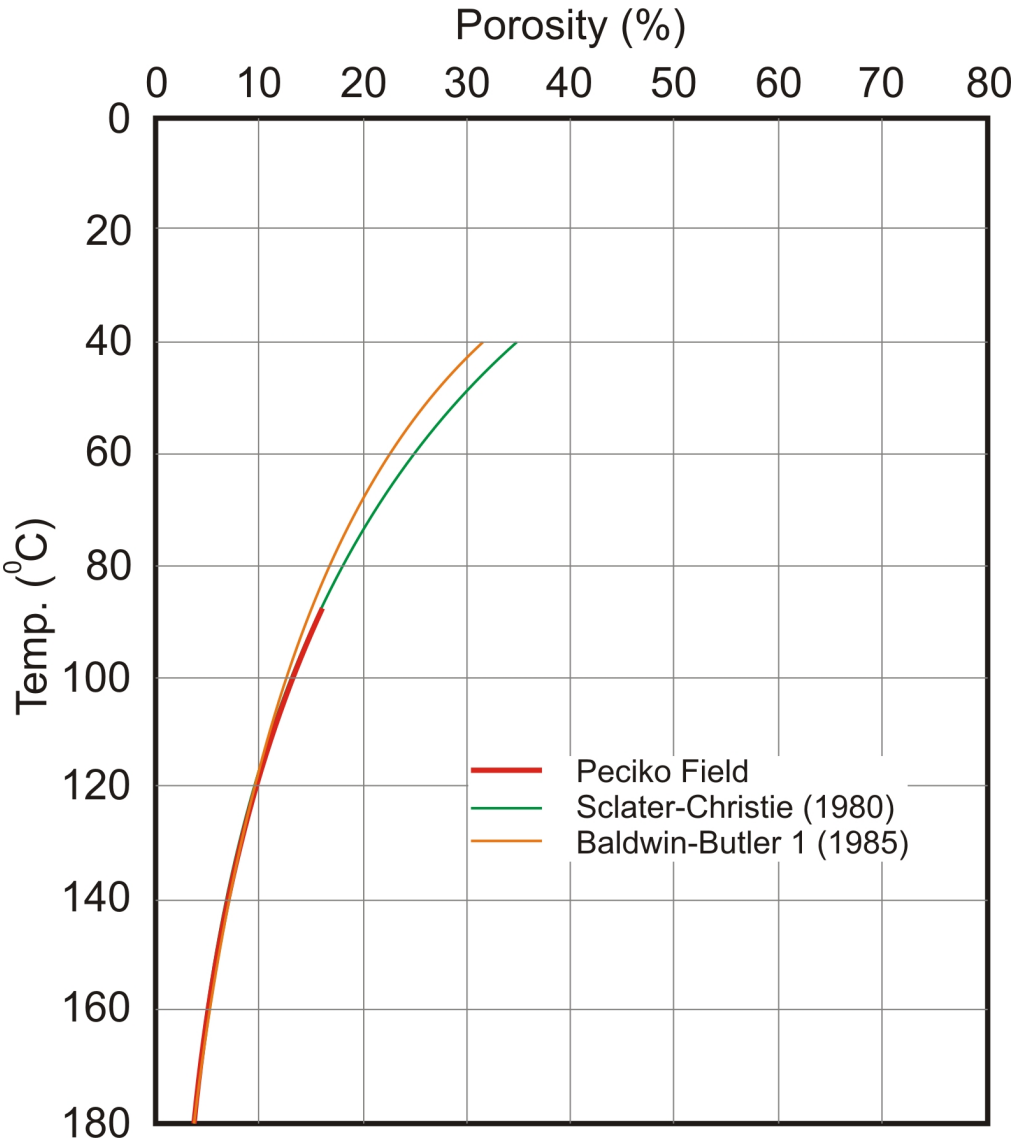

Figure 7.3 Porosity–temperature compaction trends for mudrocks in the Peciko Field compared to the Sclater–Christie curve and Baldwin-Butler 1.

CHAPTER 8
CONCLUSIONS AND SUGGESTIONS FOR FUTURE RESEARCH

8.1 Main findings

In this section, the main findings are given in sub-sections with headings that correspond to the objectives of this research listed in Section 1.2.

8.1.1 The cause of overpressure

The cause of overpressure in the shelfal and onshore areas of the Lower Kutai Basin is interpreted to be one or more unloading mechanisms. In most fields in the shelfal area, the pore pressure profile steps up directly from hydrostatic pressure into the transition zone into high overpressure, whereas overpressure increases more gradually with depth in the onshore area, passing through a substantial depth interval with intermediate overpressure. The top of the transition zone into high overpressure, which is the top of overpressure in most fields investigated here, can be recognized from sonic and resistivity log reversals. Where density log reversals are observed, they tend to be at distinctly greater depths than the sonic and resistivity log reversals, as shown clearly on cross-plots. Further, the cause of the density log reversal is interpreted as the opening of microcracks at very high overpressure. These log responses imply that overpressure is generated by unloading mechanisms.

This interpretation contradicts earlier interpretations that overpressure in the Lower Kutai Basin is primarily due to disequilibrium compaction, and also contradicts the notion that there are pore pressure discrepancies between sands and mudrocks around the top of overpressure.

Vitrinite reflectance data from five fields suggest that the onset of gas generation coincides with the top of overpressure. Thus gas generation is implicated as a principal mechanism of overpressure generation, and it is reasonable to assume that ongoing clay diagenesis also contributes. In the shelfal area, all the smectite originally deposited in the overpressured sediments probably converted to mixed layer smectite–illite while the sediment was still hydrostatically pressured. Nevertheless, other chemical compaction processes are likely to be active in the overpressured succession, including illitization of mixed layer smectite–illite, illitization of kaolinite, and quartz dissolution and reprecipitation. Density log reversals coincide with hard overpressure, close to the lithostatic stress, which may have caused opening of cracks to promote vertical migration of pore fluids. Thus vertical transfer is another candidate unloading mechanism that contributes to overpressure, although it is recognised that the primary causes of overpressure at greater depths than the TDs of the wells are again likely to be gas generation and diagenesis.

8.1.2 The state of mudrock compaction

Density logs from 16 appraisal wells in the Peciko Field show that compaction continues below the top of overpressure, independent of vertical effective stress. This observation is clear evidence of ongoing chemical compaction, and shows that at least the overpressured mudrocks are mechanically overcompacted. These wells yield an exponential decrease in porosity with depth:

$$\Phi = 43.363 \exp(-0.000164 z) \qquad (8.1)$$

where Φ is in percent and z is in ft, for mudrocks in the depth interval 6000–15,000 ft. This porosity–depth trend appears to be shifted to lower porosity values, at each depth, than other published porosity–depth trends for hydrostatically pressured mudrocks because of the higher temperatures in the Lower Kutai Basin. Converting the Peciko compaction trend for mudrocks and those of Sclater and Christie (1980) and Baldwin and Butler (1985) into porosity–temperature trends, shows an excellent fit at temperatures above 90°C.

8.1.3 Overpressure detection and estimation

Overpressure detection and estimation is discussed comprehensively in Section 7.2. Basically, the recommended methods for overpressure detection amount to the search for sonic and resistivity reversals. Meanwhile, overpressure can be estimated by using Bowers' relation for overpressure generated by unloading mechanisms. The empirical constants are given in Equation 6.2.

8.1.4 Relationship between overpressure and the petroleum system

The most obvious relationship between overpressure and the petroleum system in the shelfal area of the Lower Kutai Basin is the lateral reservoir drainage which causes hydrodynamic trapping. Lateral reservoir drainage was already known to cause hydrodynamically tilted gas-water contacts in the Peciko and Tunu fields (Grosjean et al., 1994; Lambert et al., 2003). In other fields where the overpressure measurements in the water leg are not sufficient to produce overpressure maps, variation in the stratigraphic level of the top of overpressure could be used as an early indicator to the presence of tilted hydrocarbon-water contacts.

One important conclusion from this research is that gas generation is a principal cause of overpressure in the Lower Kutai Basin. It implies that the gas source rocks are widely distributed in the basin, although quantification has not been possible in this thesis.

8.1.5 Comparison of overpressure and compaction with other basins

This research reveals that overpressure in the Lower Kutai Basin is caused by unloading mechanisms. To date there is no other Neogene Basin worldwide where the role of disequilibrium compaction has been discounted. Therefore, the Lower Kutai Basin is probably unique in terms of overpressure generating mechanism in young sedimentary basins.

Regarding the state of compaction, comparison of porosity–temperature profiles in mudrocks in the Lower Kutai Basin and other basins worldwide suggests an intriguing possibility that mudrock compaction depends only on temperature at temperatures greater than 90°C, as discussed in Sub-section 7.4.2. Clearly, this hypothesis needs to be tested further, as discussed in Sub-section 8.2 below.

8.2 Future research

This research indicates that the studies listed here need to be performed in order to comprehensively understand overpressure and hydrodynamics in the Lower Kutai Basin.

Clay diagenetic study

This research reveals that below 6000 ft the discrete smectite has disappeared and the mudrock compaction is located on the illitic compaction trend. XRD analysis can be used to find the proportions of different minerals present in the mudrocks. It is also hypothesized in this study that the mudrocks are overcompacted as a consequence of quartz cementation resulting from smectite–illite transformation. SEM analysis could be used to test this hypothesis.

Mudrock compaction trends at temperatures above 90°C

It was shown in Figure 7.3 that the porosity–temperature compaction trend for mudrocks in the Peciko Field closely matched the Sclater-Christie and Baldwin-Butler 1 compaction trends for mudrocks, when the latter two trends were converted from porosity–depth to porosity–temperature trends. Without further work, it is not possible to say whether the similarity in these three compaction curves is by chance, or whether they are following a generic porosity–temperature compaction trend for mudrocks above 90°C. It would be desirable to determine empirically such porosity–temperature compaction trends for mudrocks in other

basins worldwide, and to investigate to what extent they vary with mudrock composition, geological age, and effective stress.

Lateral reservoir drainage modelling

Lateral reservoir drainage has thought to be responsible for hydrodynamic trapping in the Peciko Field. It also causes the top of overpressure to be deeper in the shelfal area. It is interesting to know how much water has laterally drained and how lateral drainage has impacted hydrocarbon migration. These questions could be answered by performing basin modelling of lateral reservoir drainage in the research area.

Overpressuring in the syn-rift sequence (Palaeogene) on the onshore area and its relationship with structural development in the Kutai Basin

None of the data available to study overpressure have come from the Palaeogene synrift sequence in the Lower Kutai Basin. As mentioned in Sub-section 2.1.2, overpressuring in the synrift sequence has been cited by almost all researchers in support of their hypotheses concerning the structural development of the basin. Analysis of the data from this sequence will provide not only the information on overpressure relevant to the structural evolution of the basin, but also a comprehensive understanding of overpressuring in the Lower Kutai Basin since the basin started to develop.

Overpressuring in the deep water area

As mentioned earlier, the deep water area is still classified as an exploration area so the data has not been released yet. The data from deep water area will provide important new information about overpressure and compaction since the area has not been laterally drained. One of the findings of this research is that overpressure in the shelfal area is relatively deep because the conversion of smectite to mixed layer illite/smectite does not build overpressure there because of lateral reservoir drainage. Data from deep water wells could be used to test this hypothesis. Moreover, compaction analysis from the Peciko Field shows that the mudrocks

are overcompacted at the depths where the overpressure is encountered. If the top of overpressure in the deep water area is really shallower than in the shelfal area, it will be interesting to see whether the mudrocks are clearly overcompacted at shallower depths. This test could be done by comparing the density data from the overpressured section of the deep water area with the normally pressured section from the shelfal area.

APPENDICES

APPENDIX 1. PECIKO FIELD

Appendix 1a

Pressure–depth plots for intermediate stratigraphic units, as shown in Figure 5.2

Appendix 1a Pressure-depth plot for intermediate stratigraphic units, Peciko Field

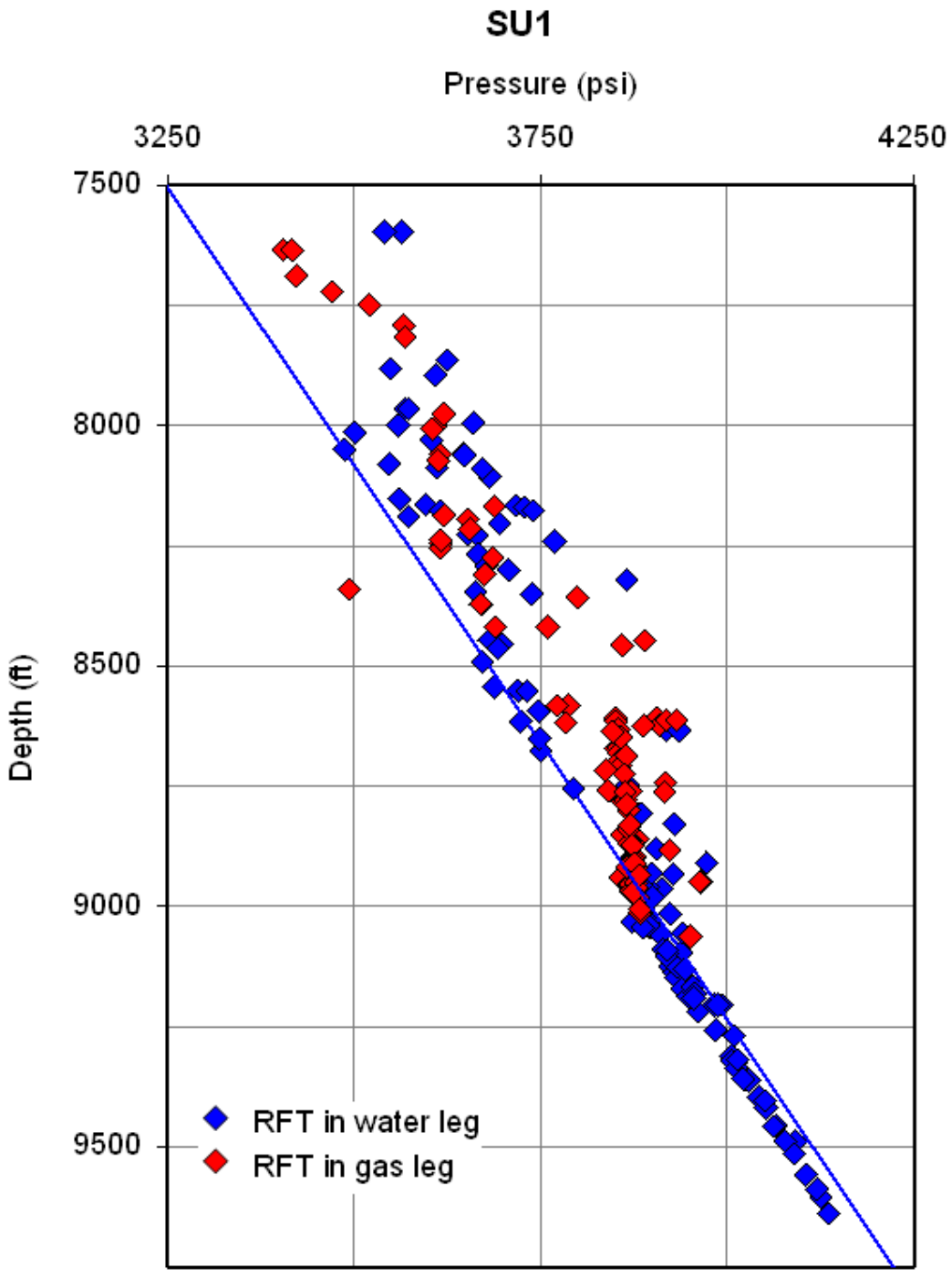

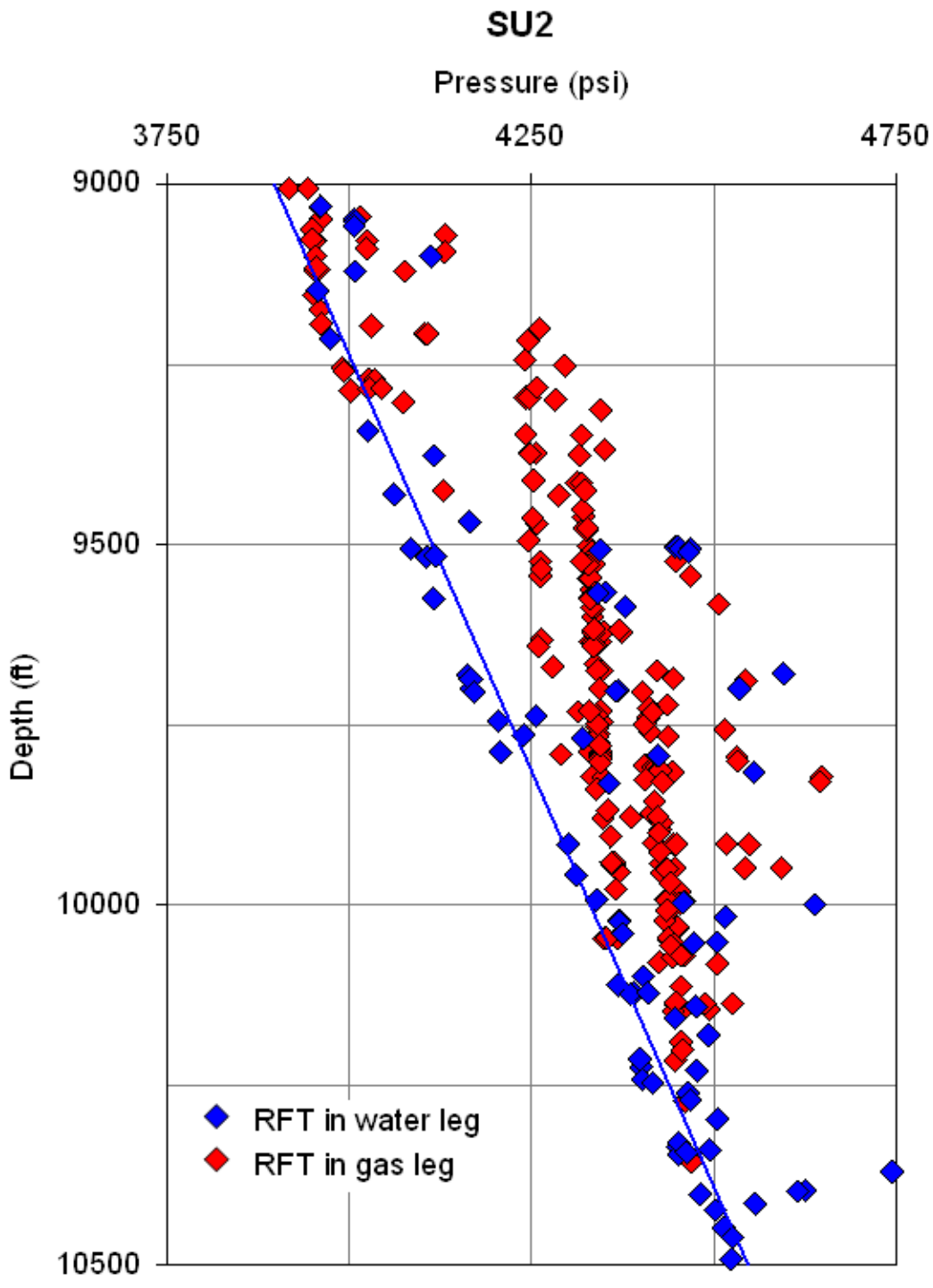
SU2
Pressure (psi)
3750
4250
4750
9000
9500
10000
10500
Depth (ft)
RFT in water leg
RFT in gas leg

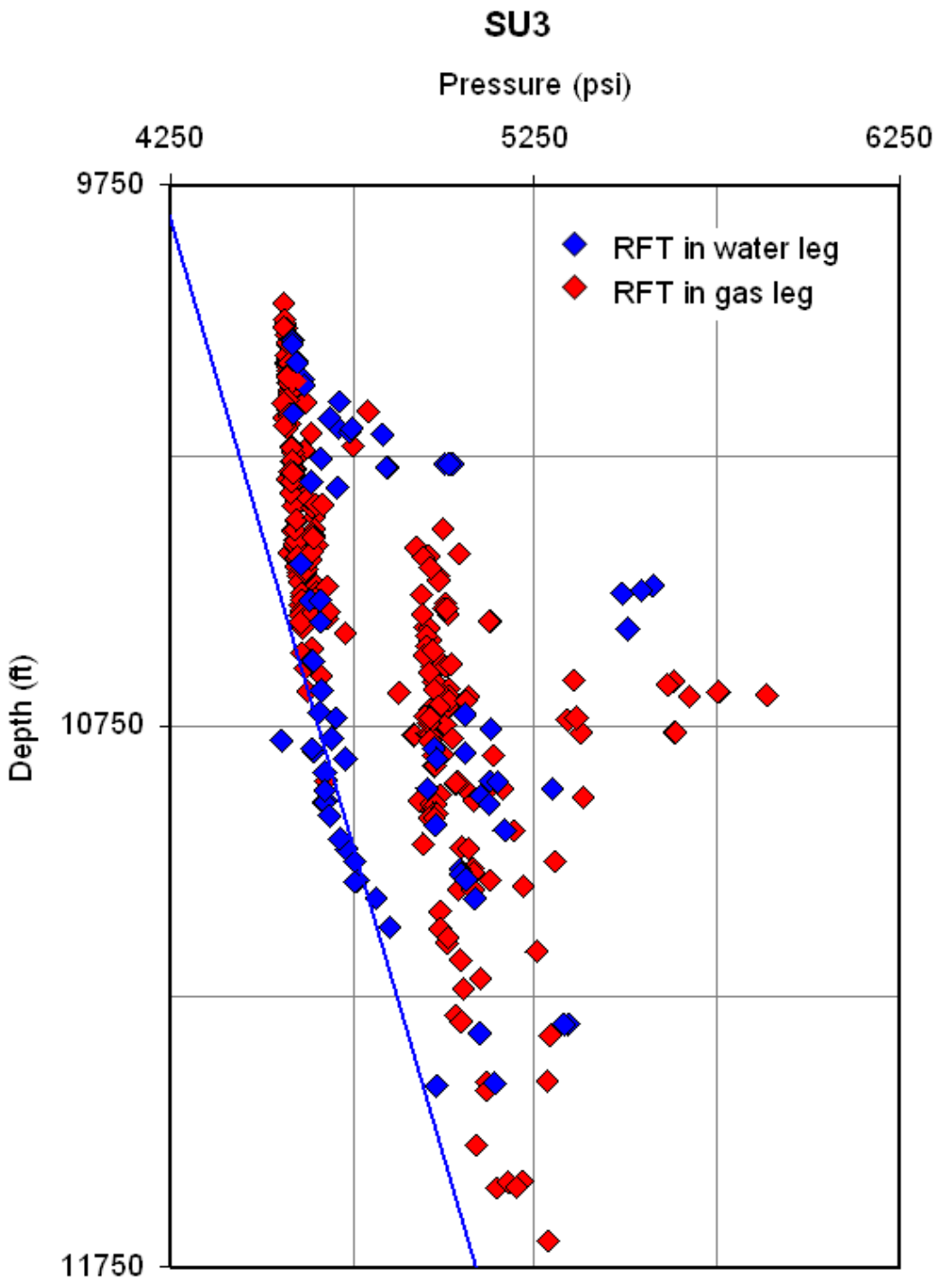
SU3
Pressure (psi)
4250
5250
6250
9750
10750
11750
Depth (ft)
RFT in water leg
RFT in gas leg

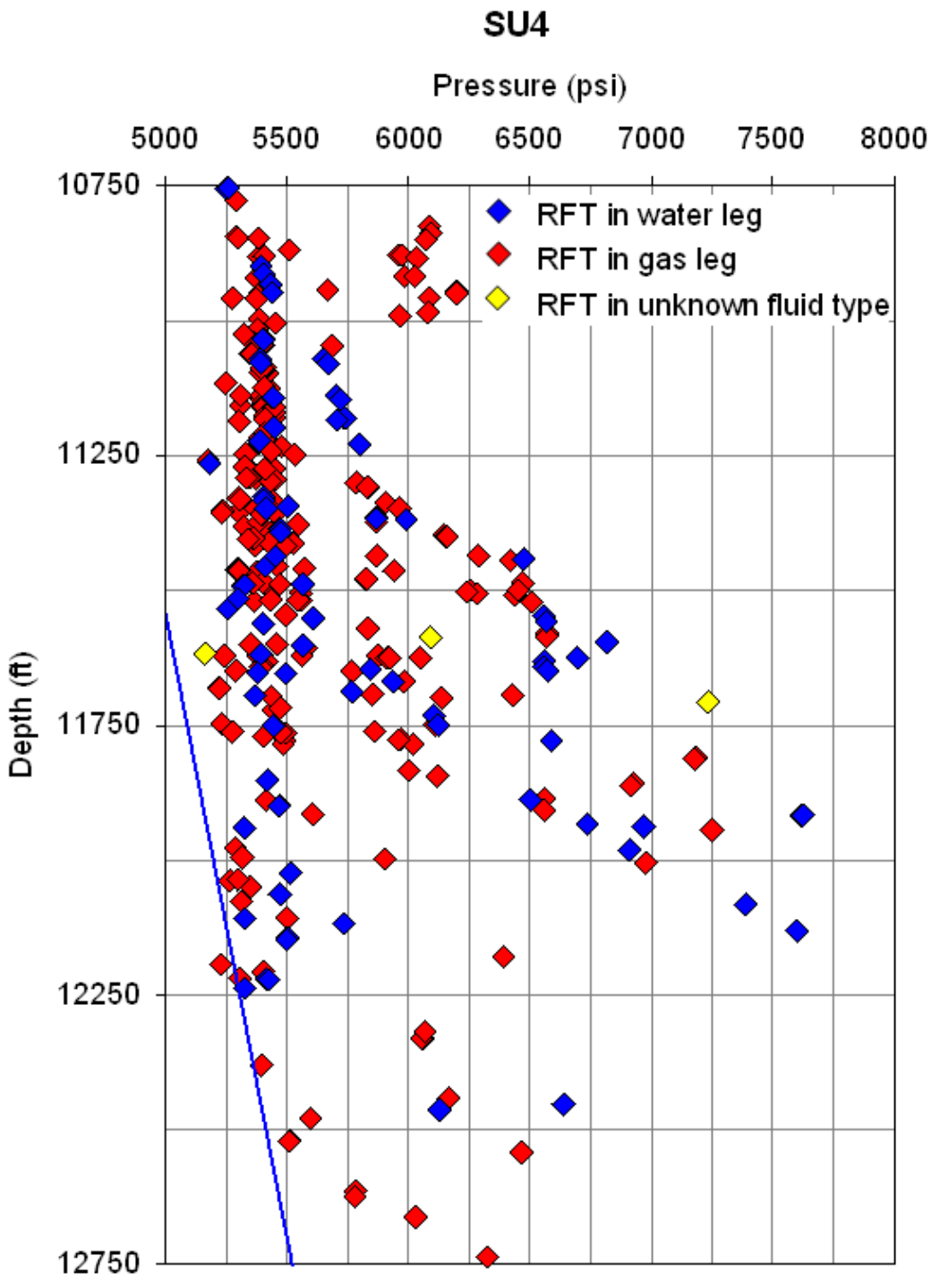
SU4
Pressure (psi)
5000
5500
6000
6500
7000
7500
8000
10750
11250
11750
12250
12750
Depth (ft)
RFT in water leg
RFT in gas leg
RFT in unknown fluid type

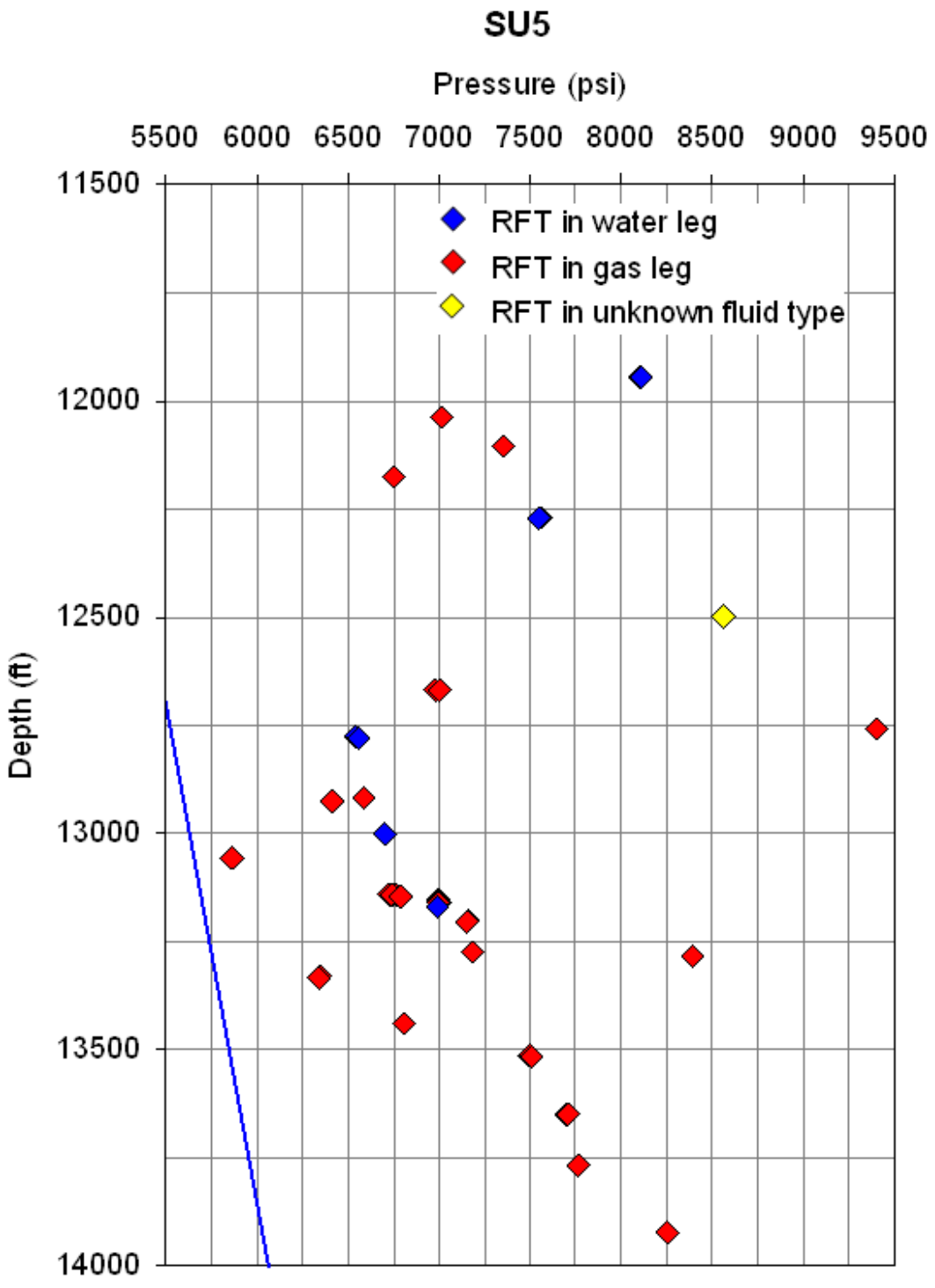
SU5
Pressure (psi)
5500
6000
6500
7000
7500
8000
8500
9000
9500
11500
12000
12500
13000
13500
14000
Depth (ft)
RFT in water leg
RFT in gas leg
RFT in unknown fluid type

APPENDIX 1. PECIKO FIELD

Appendix 1b

Pressure–depth plots, wireline log responses, and cross-plots for mudrocks in 16 wells

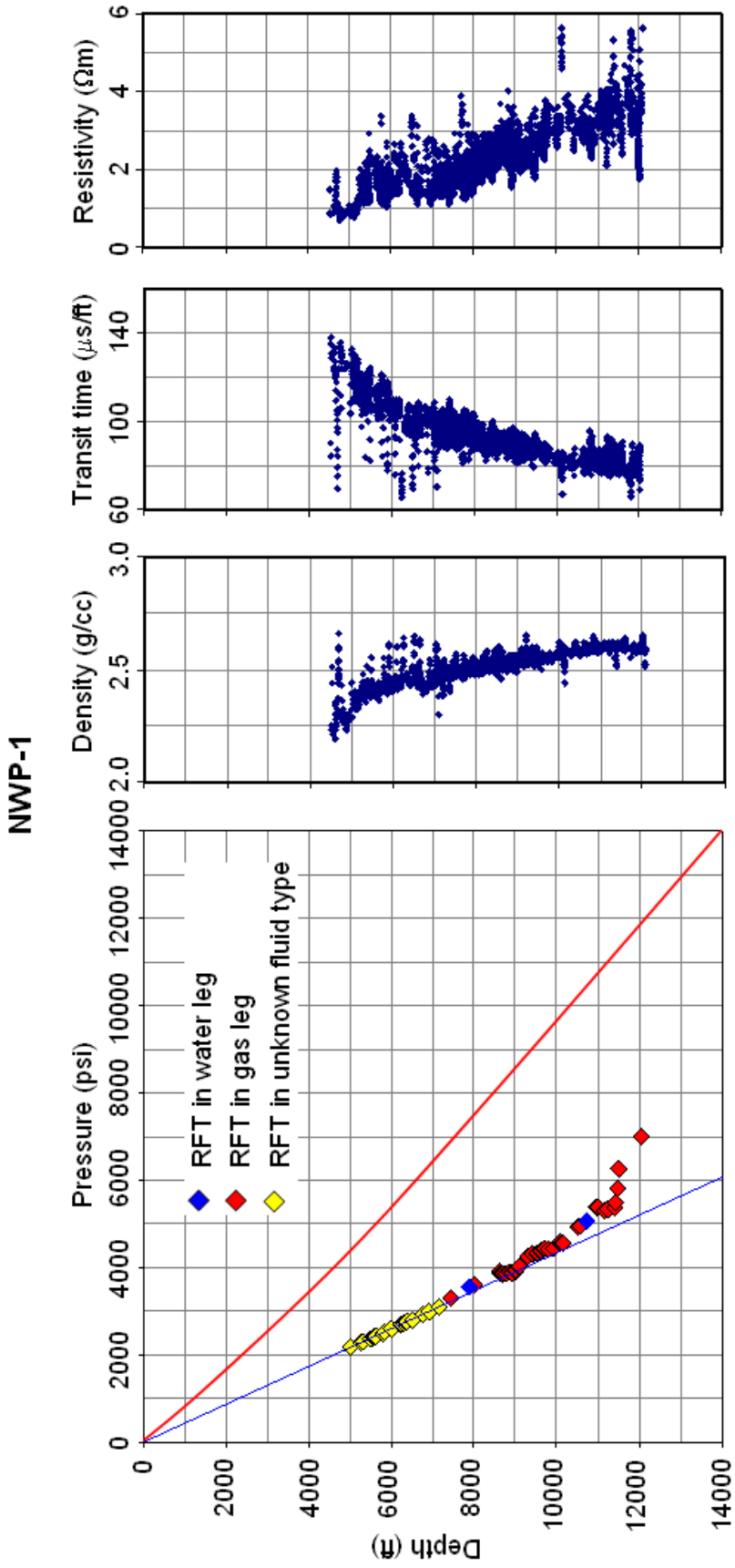
NWP-1
Resistivity (Ωm)
0
2
4
6
Transit time (μs/ft)
60
100
140
Density (g/cc)
2.0
2.5
3.0
Pressure (psi)
0
2000
4000
6000
8000
10000
12000
14000
RFT in water leg
RFT in gas leg
RFT in unknown fluid type
Depth (ft)
0
2000
4000
6000
8000
10000
12000
14000

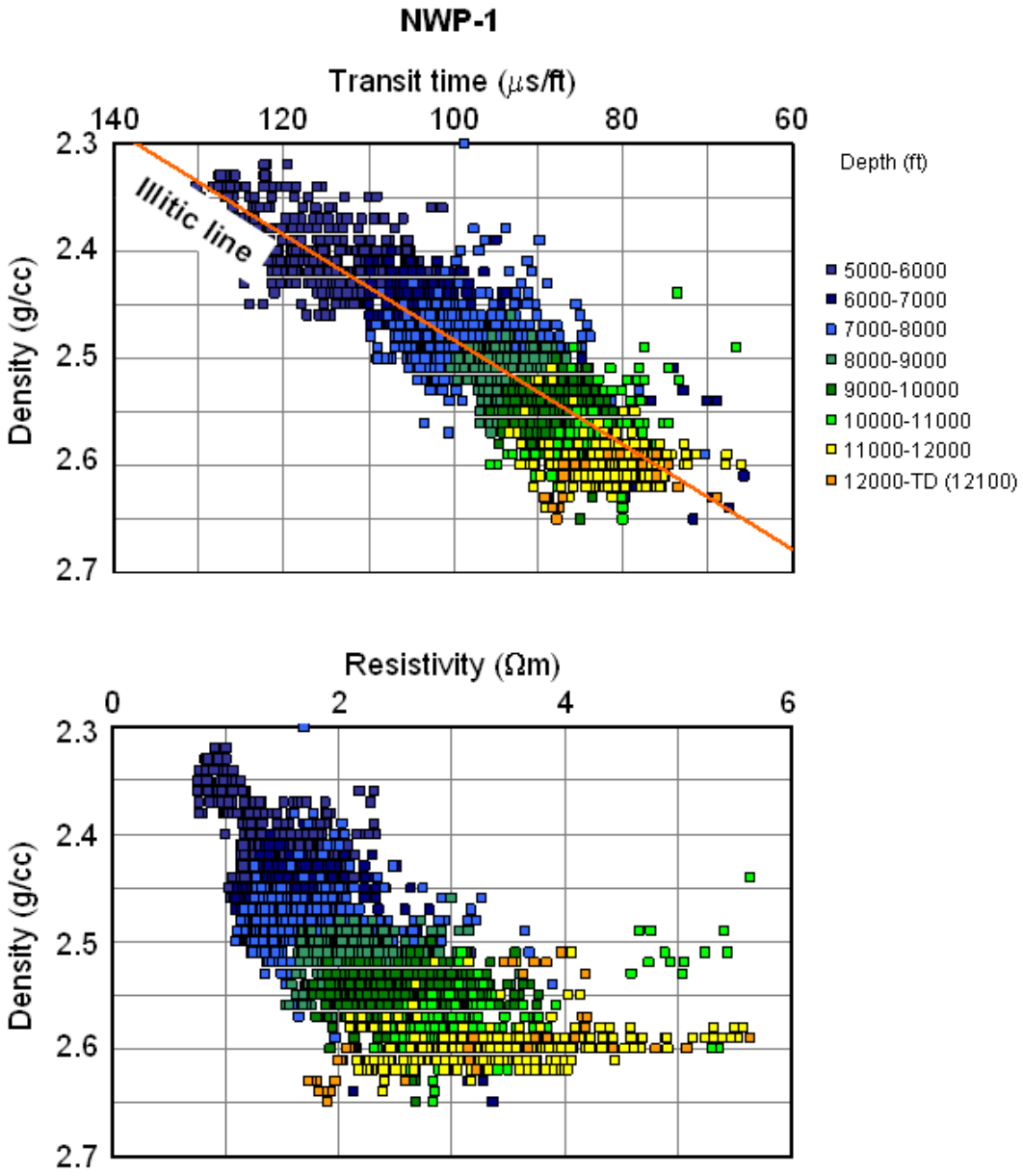
NWP-1
Transit time (μs/ft)
140
120
100
80
60
2.3
2.4
2.5
2.6
2.7
Density (g/cc)
Illitic line
Depth (ft)
5000-6000
6000-7000
7000-8000
8000-9000
9000-10000
10000-11000
11000-12000
12000-TD (12100)
Resistivity (Ωm)
0
2
4
6
2.3
2.4
2.5
2.6
2.7
Density (g/cc)

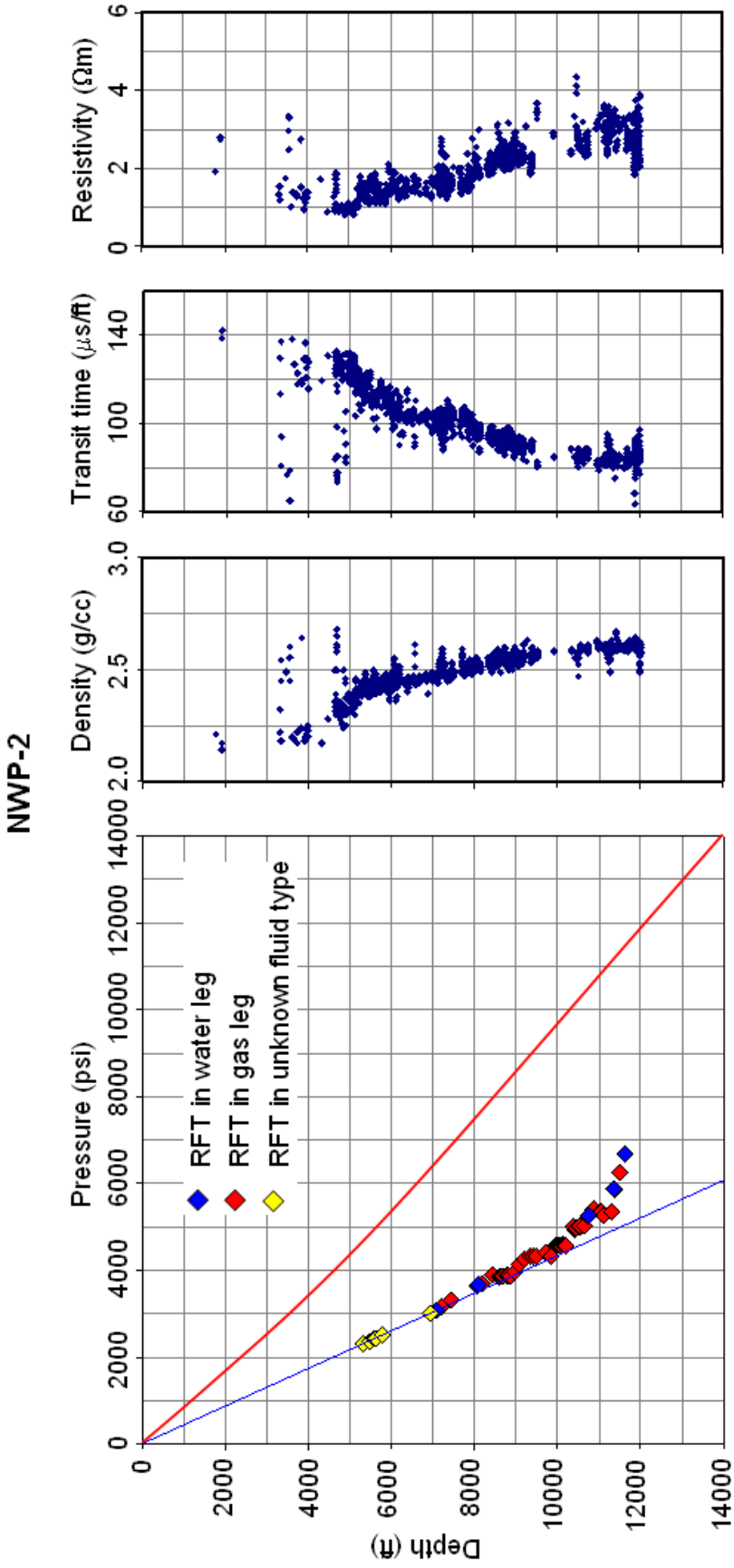
NWP-2
Resistivity (Ωm)
0
2
4
6
Transit time (μs/ft)
60
100
140
Density (g/cc)
2.0
2.5
3.0
Pressure (psi)
0
2000
4000
6000
8000
10000
12000
14000
RFT in water leg
RFT in gas leg
RFT in unknown fluid type
Depth (ft)
0
2000
4000
6000
8000
10000
12000
14000

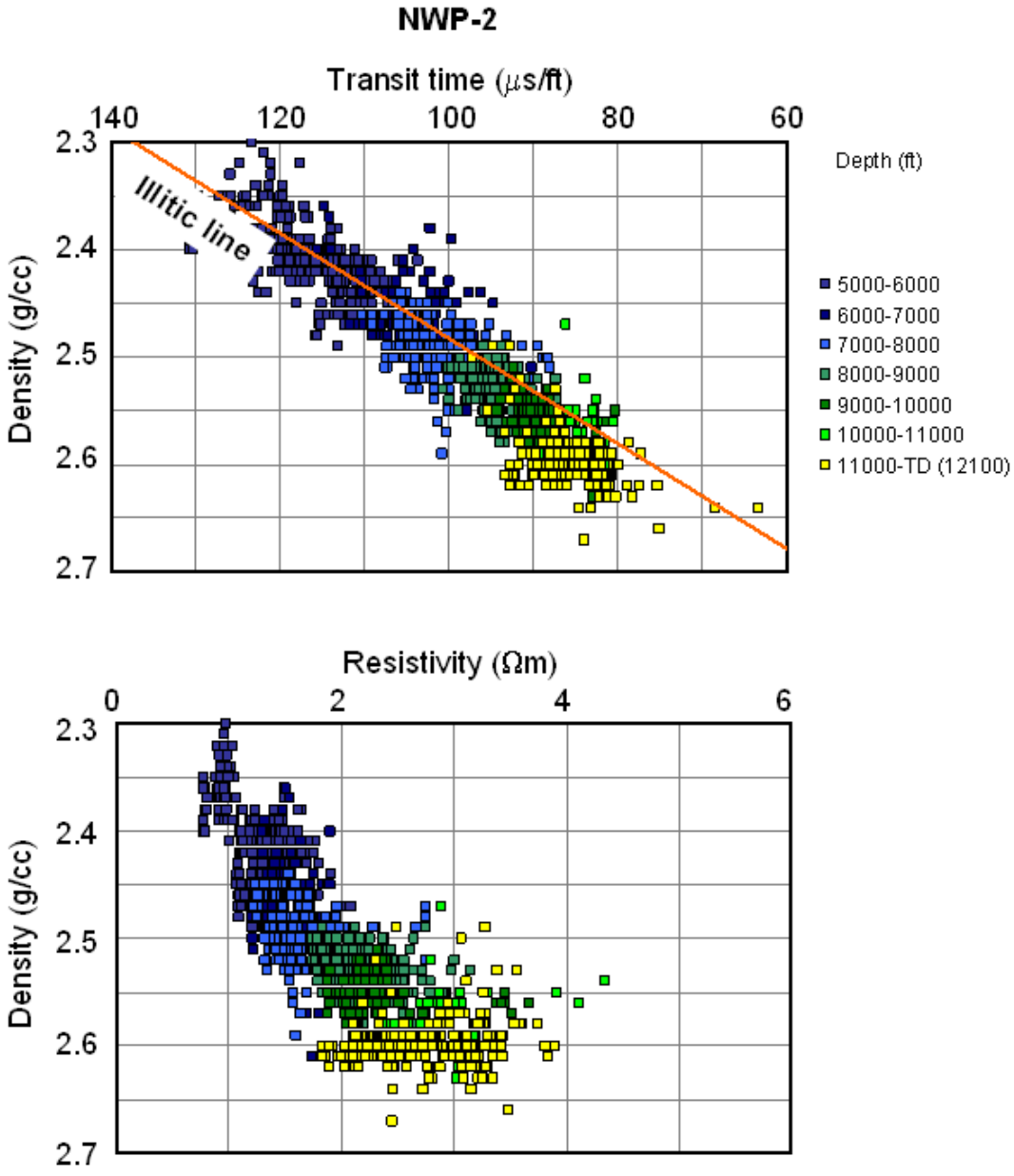
NWP-2
Transit time (μs/ft)
140
120
100
80
60
Density (g/cc)
2.3
2.4
2.5
2.6
2.7
Illitic line
Depth (ft)
5000-6000
6000-7000
7000-8000
8000-9000
9000-10000
10000-11000
11000-TD (12100)
Resistivity (Ωm)
0
2
4
6
Density (g/cc)
2.3
2.4
2.5
2.6
2.7

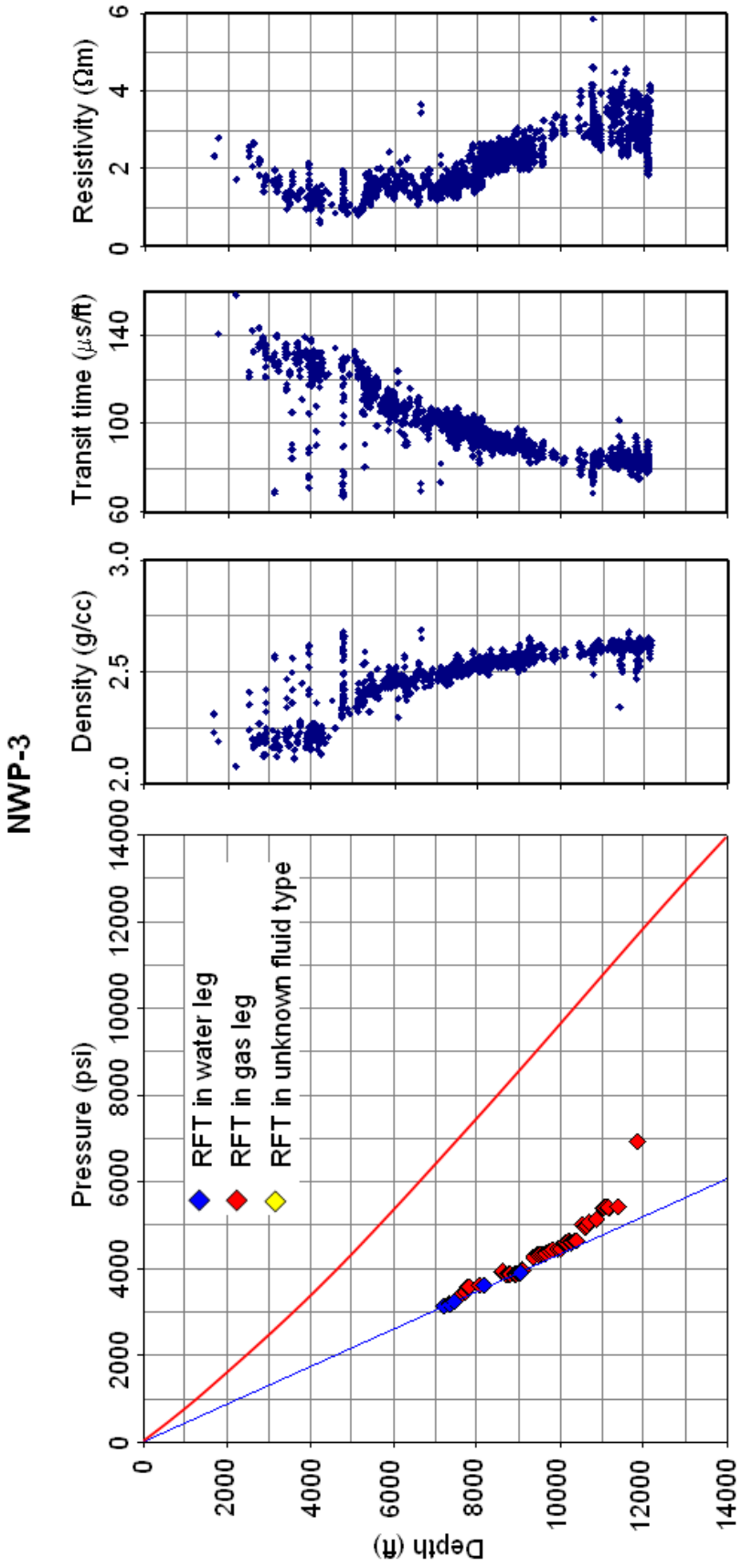
NWP-3
Resistivity (Ωm)
0
2
4
6
Transit time (μs/ft)
60
100
140
Density (g/cc)
2.0
2.5
3.0
Pressure (psi)
0
2000
4000
6000
8000
10000
12000
14000
RFT in water leg
RFT in gas leg
RFT in unknown fluid type
Depth (ft)
0
2000
4000
6000
8000
10000
12000
14000

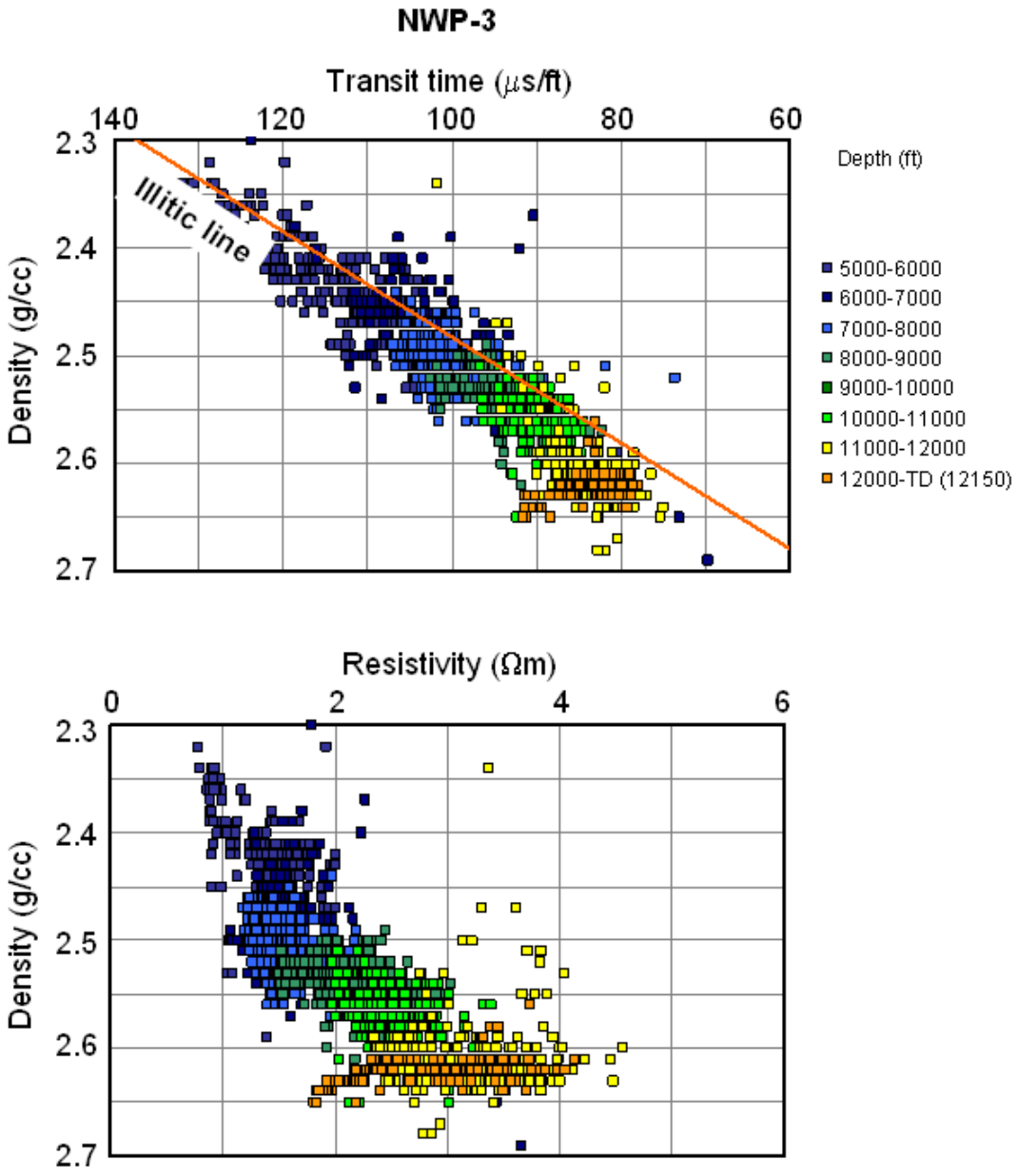
NWP-3
Transit time (μs/ft)
140
120
100
80
60
Density (g/cc)
2.3
2.4
2.5
2.6
2.7
Illitic line
Depth (ft)
5000-6000
6000-7000
7000-8000
8000-9000
9000-10000
10000-11000
11000-12000
12000-TD (12150)
Resistivity (Ωm)
0
2
4
6
Density (g/cc)
2.3
2.4
2.5
2.6
2.7

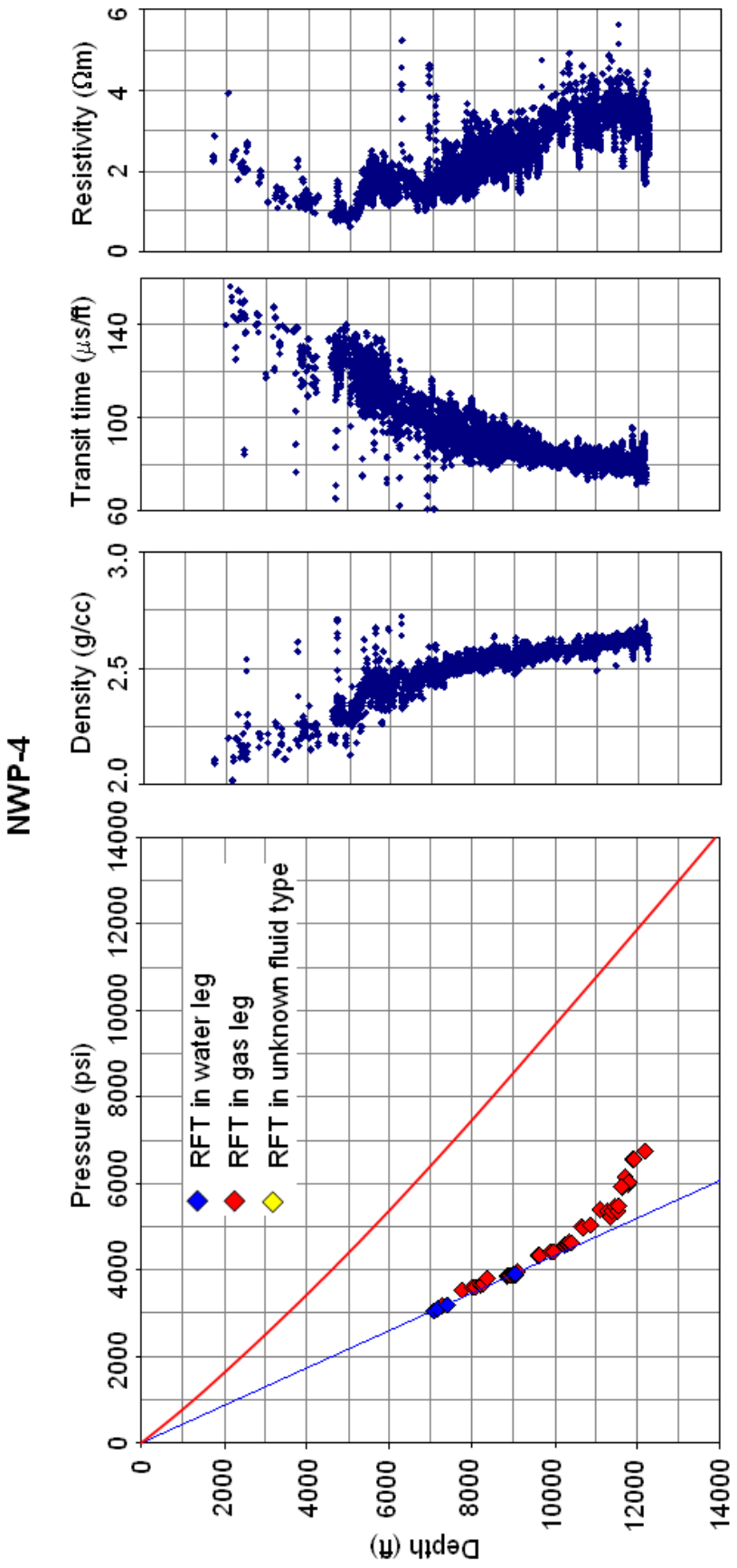
NWP-4
Resistivity (Ωm)
0
2
4
6
Transit time (μs/ft)
60
100
140
Density (g/cc)
2.0
2.5
3.0
Pressure (psi)
0
2000
4000
6000
8000
10000
12000
14000
RFT in water leg
RFT in gas leg
RFT in unknown fluid type
Depth (ft)
0
2000
4000
6000
8000
10000
12000
14000

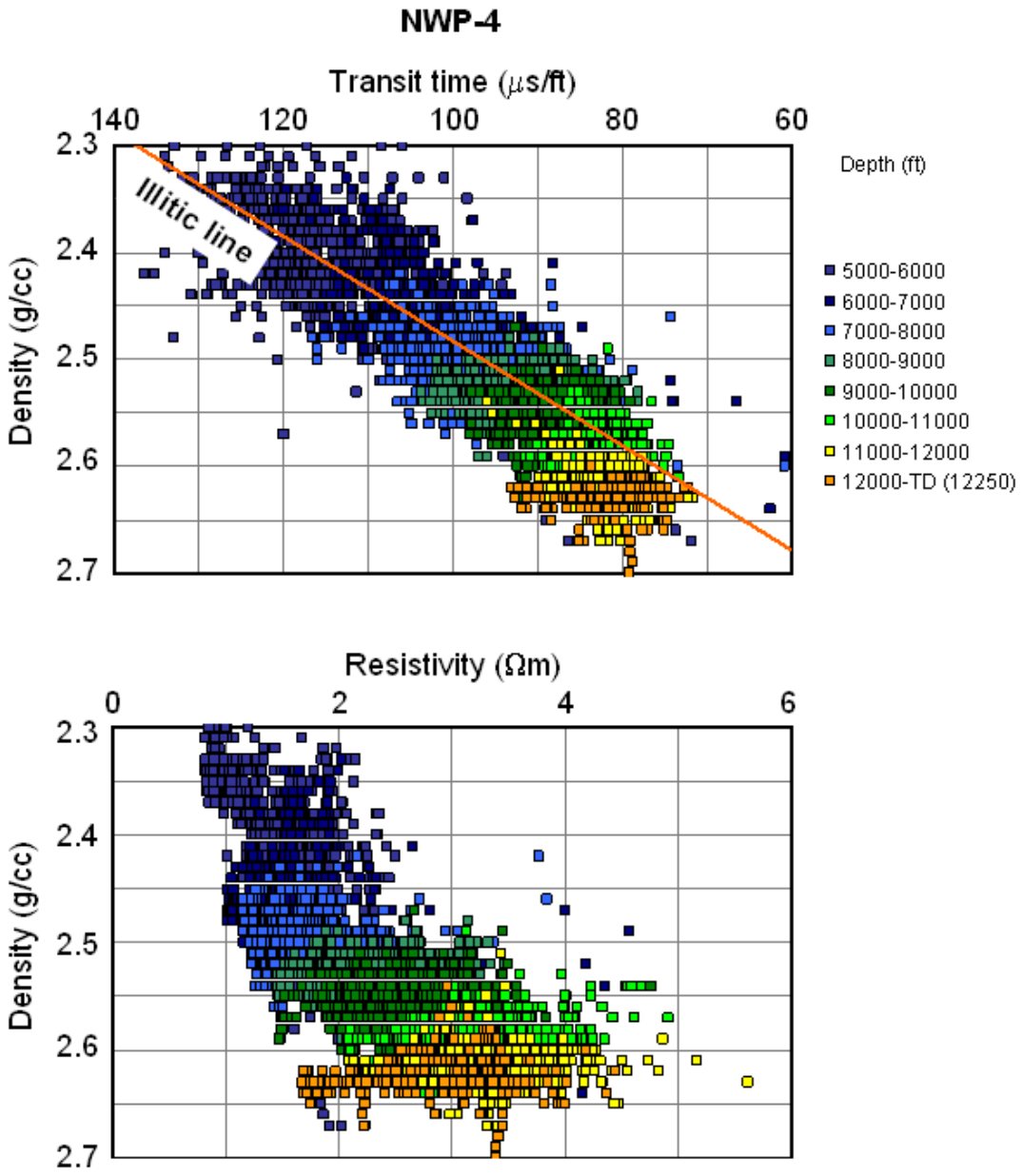
NWP-4
Transit time (μs/ft)
140
120
100
80
60
Density (g/cc)
2.3
2.4
2.5
2.6
2.7
Illitic line
Depth (ft)
5000-6000
6000-7000
7000-8000
8000-9000
9000-10000
10000-11000
11000-12000
12000-TD (12250)
Resistivity (Ωm)
0
2
4
6

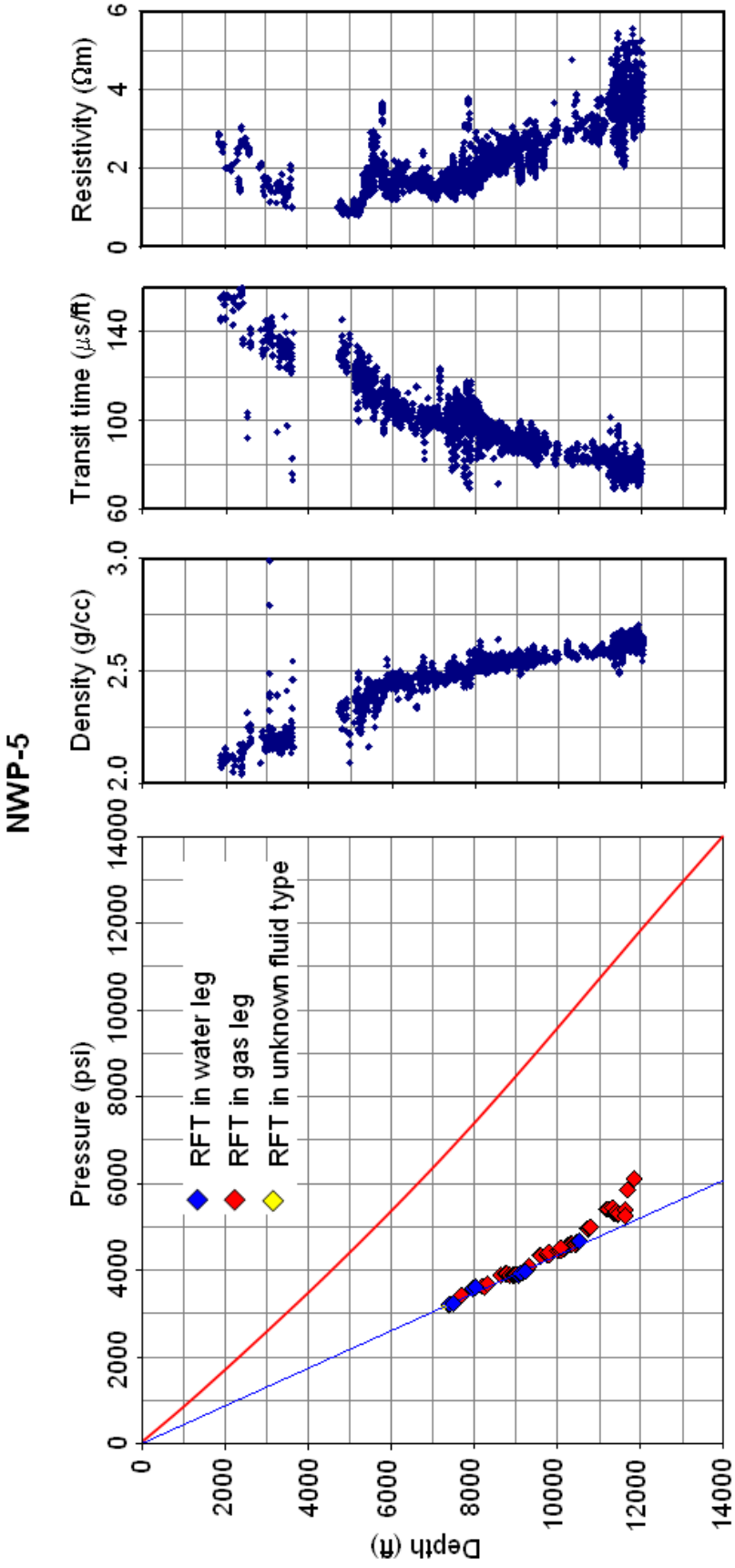
NWP-5
Resistivity (Ωm)
0
2
4
6
Transit time (μs/ft)
60
100
140
Density (g/cc)
2.0
2.5
3.0
Pressure (psi)
0
2000
4000
6000
8000
10000
12000
14000
RFT in water leg
RFT in gas leg
RFT in unknown fluid type
Depth (ft)
0
2000
4000
6000
8000
10000
12000
14000

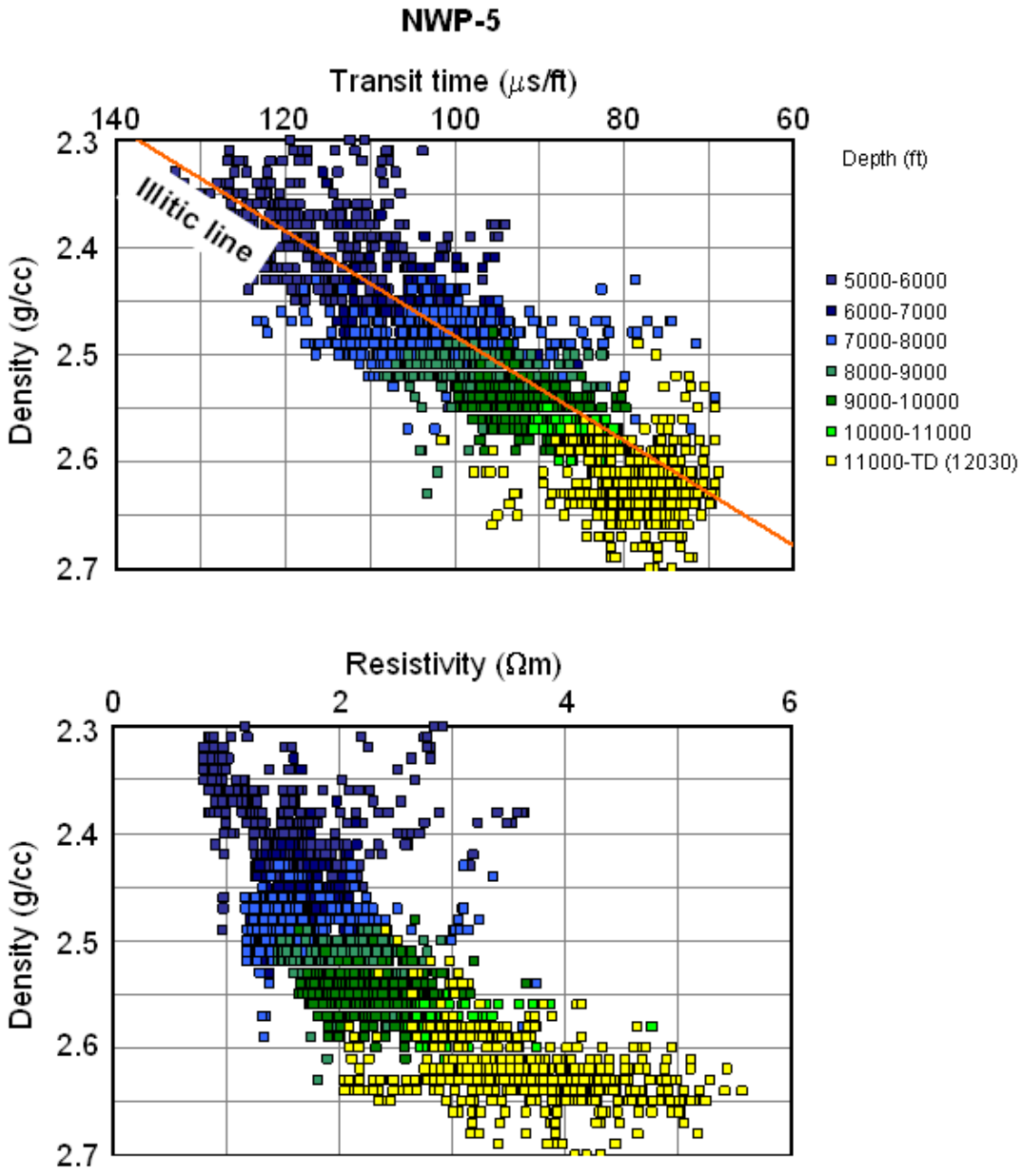
NWP-5
Transit time (μs/ft)
140
120
100
80
60
Density (g/cc)
2.3
2.4
2.5
2.6
2.7
Illitic line
Depth (ft)
5000-6000
6000-7000
7000-8000
8000-9000
9000-10000
10000-11000
11000-TD (12030)
Resistivity (Ωm)
0
2
4
6
Density (g/cc)
2.3
2.4
2.5
2.6
2.7

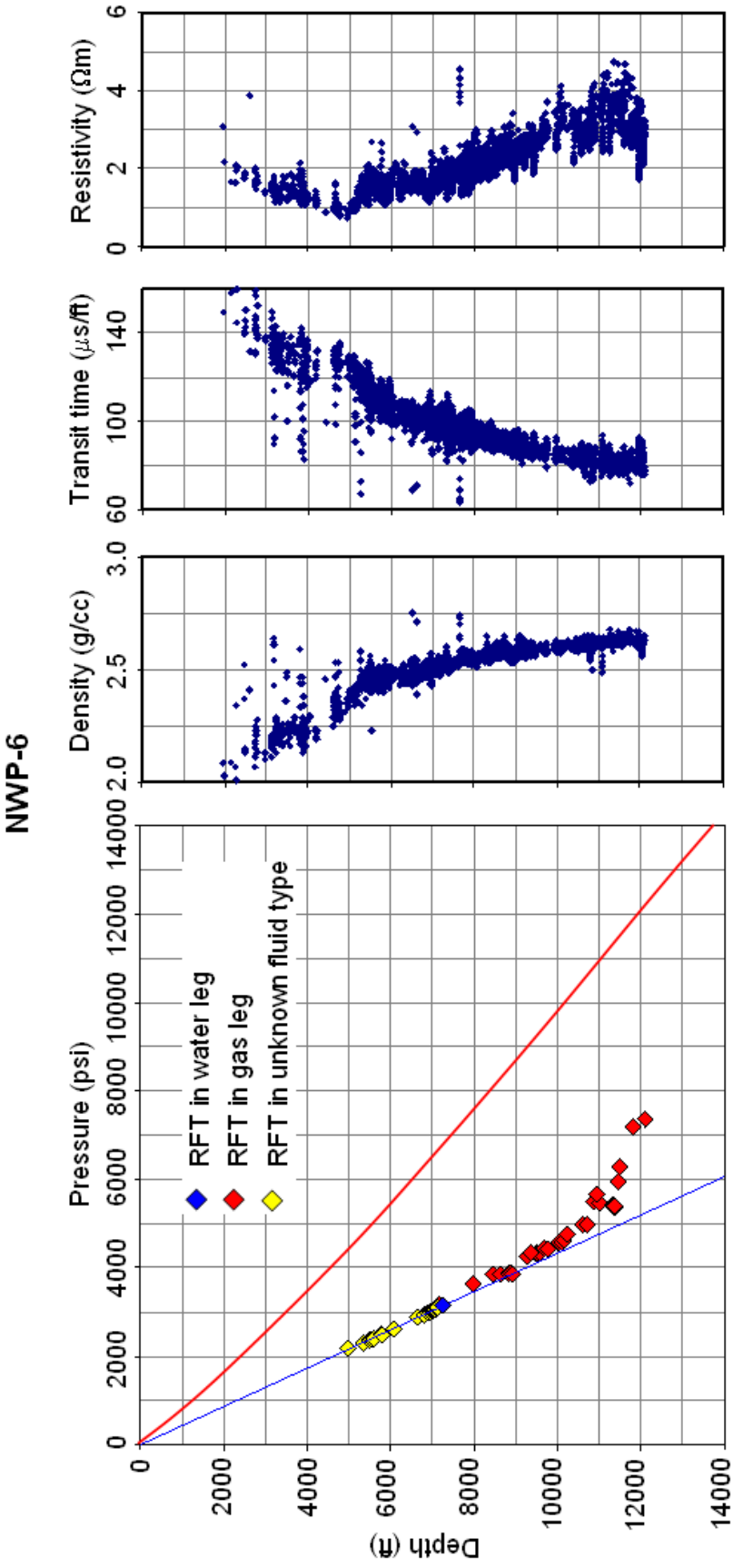
NWP-6
Resistivity (Ωm)
0
2
4
6
Transit time (μs/ft)
60
100
140
Density (g/cc)
2.0
2.5
3.0
Pressure (psi)
0
2000
4000
6000
8000
10000
12000
14000
RFT in water leg
RFT in gas leg
RFT in unknown fluid type
Depth (ft)
0
2000
4000
6000
8000
10000
12000
14000

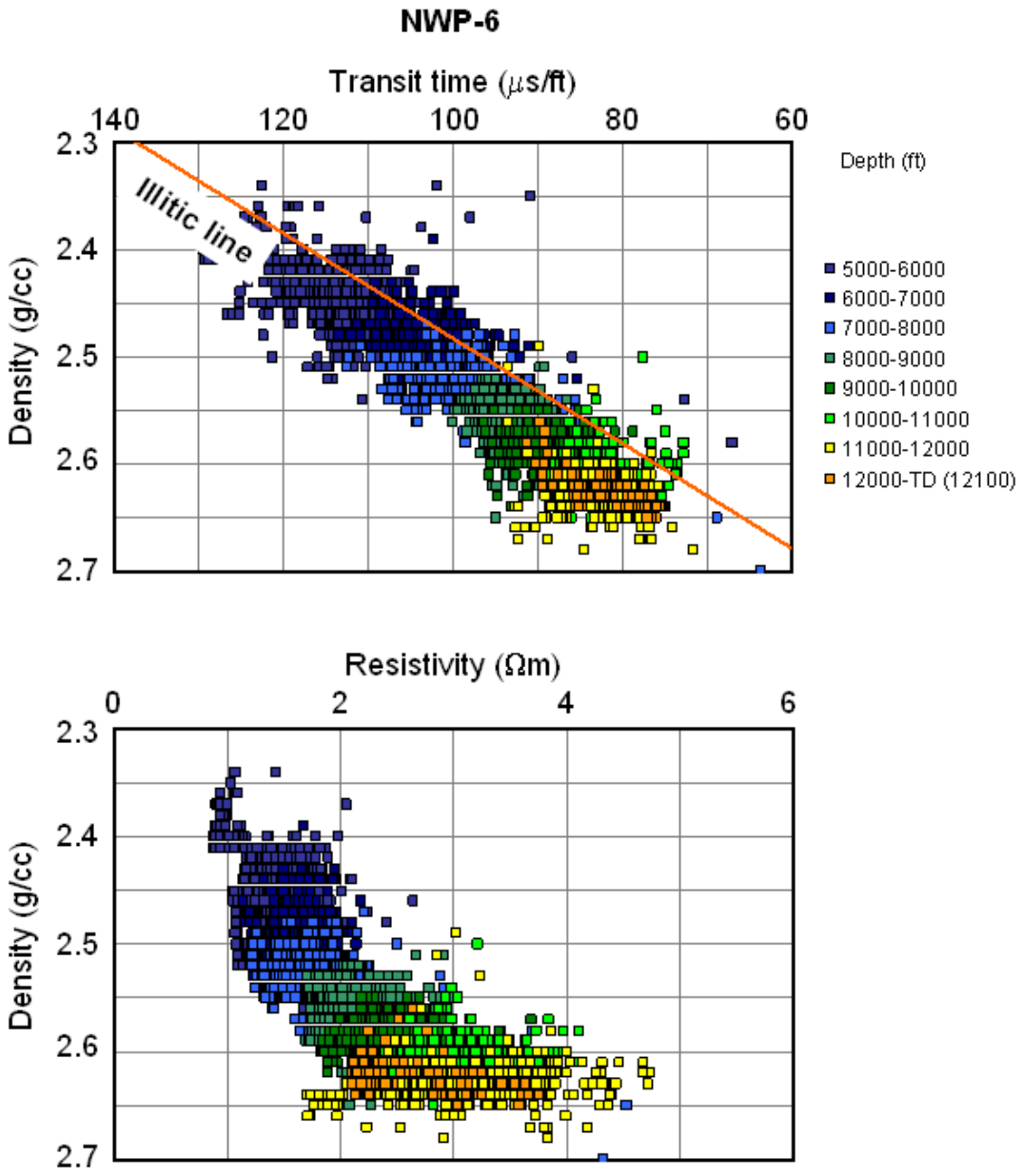
NWP-6
Transit time (μs/ft)
140
120
100
80
60
Density (g/cc)
2.3
2.4
2.5
2.6
2.7
Illitic line
Depth (ft)
5000-6000
6000-7000
7000-8000
8000-9000
9000-10000
10000-11000
11000-12000
12000-TD (12100)
Resistivity (Ωm)
0
2
4
6
Density (g/cc)
2.3
2.4
2.5
2.6
2.7

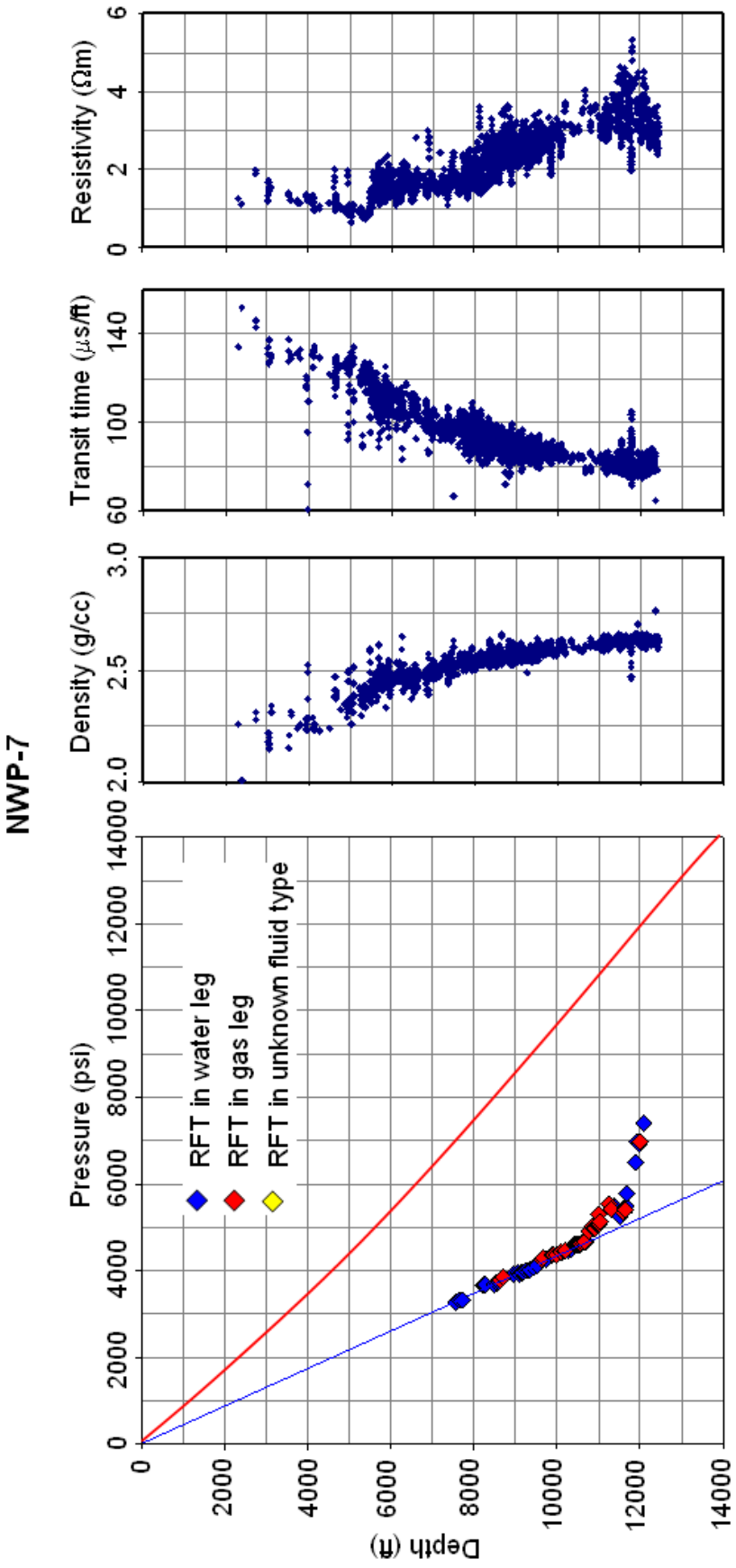
NWP-7
Resistivity (Ωm)
0
2
4
6
Transit time (μs/ft)
60
100
140
Density (g/cc)
2.0
2.5
3.0
Pressure (psi)
0
2000
4000
6000
8000
10000
12000
14000
RFT in water leg
RFT in gas leg
RFT in unknown fluid type
Depth (ft)
0
2000
4000
6000
8000
10000
12000
14000

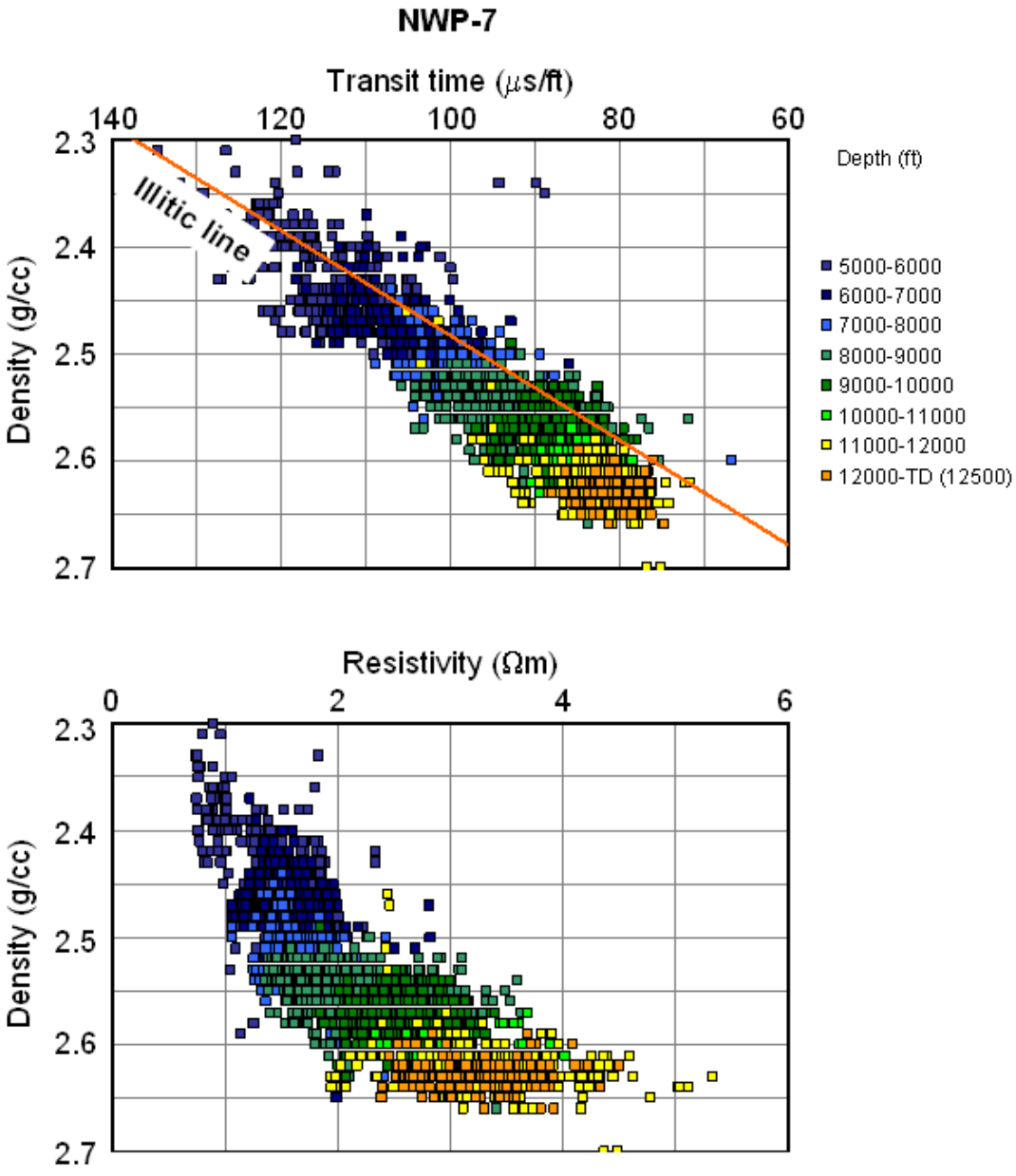
NWP-7
Transit time (μs/ft)
140
120
100
80
60
Density (g/cc)
2.3
2.4
2.5
2.6
2.7
Illitic line
Depth (ft)
5000-6000
6000-7000
7000-8000
8000-9000
9000-10000
10000-11000
11000-12000
12000-TD (12500)
Resistivity (Ωm)
0
2
4
6
Density (g/cc)
2.3
2.4
2.5
2.6
2.7

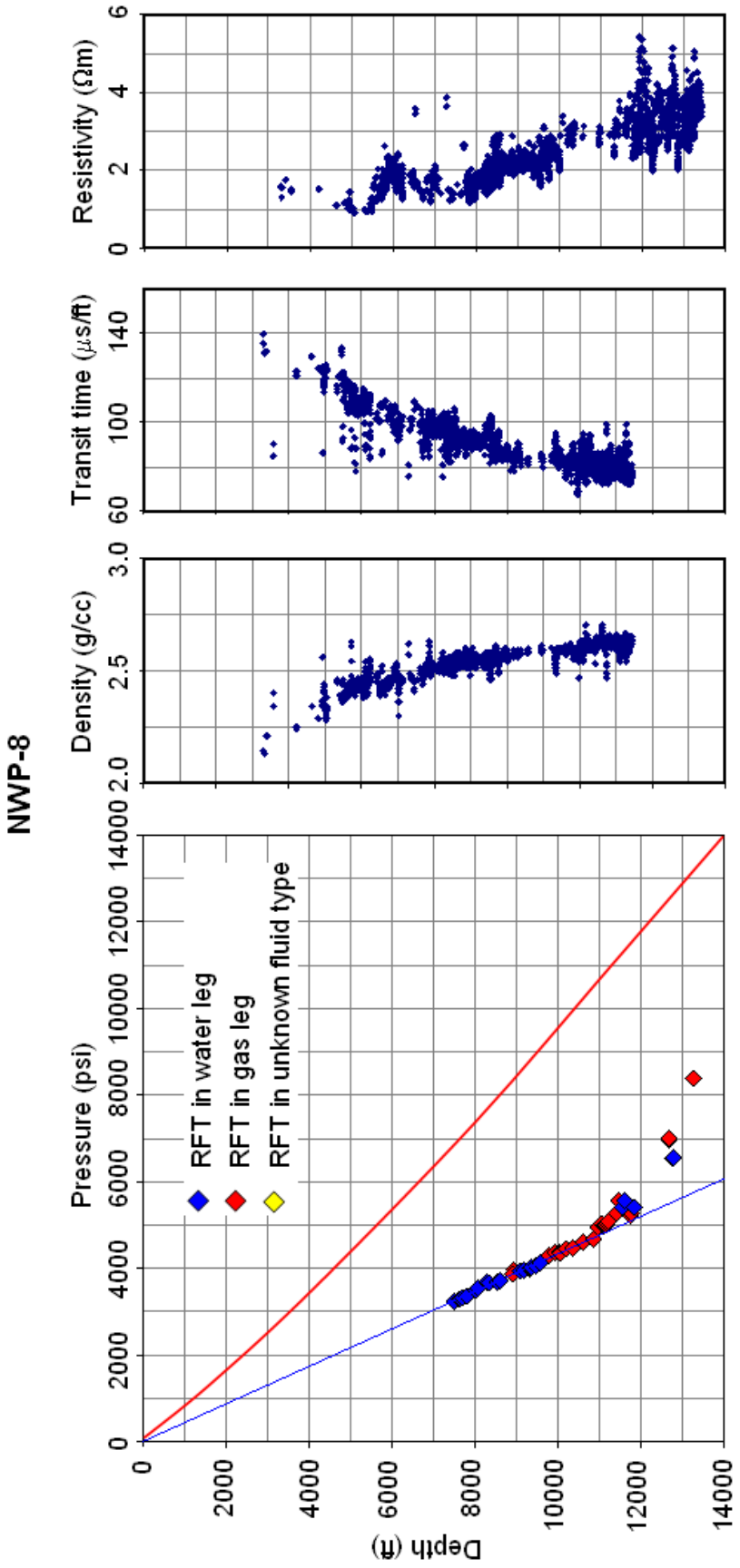
NWP-8
Resistivity (Ωm)
0
2
4
6
Transit time (μs/ft)
60
100
140
Density (g/cc)
2.0
2.5
3.0
Pressure (psi)
0
2000
4000
6000
8000
10000
12000
14000
RFT in water leg
RFT in gas leg
RFT in unknown fluid type
Depth (ft)
0
2000
4000
6000
8000
10000
12000
14000

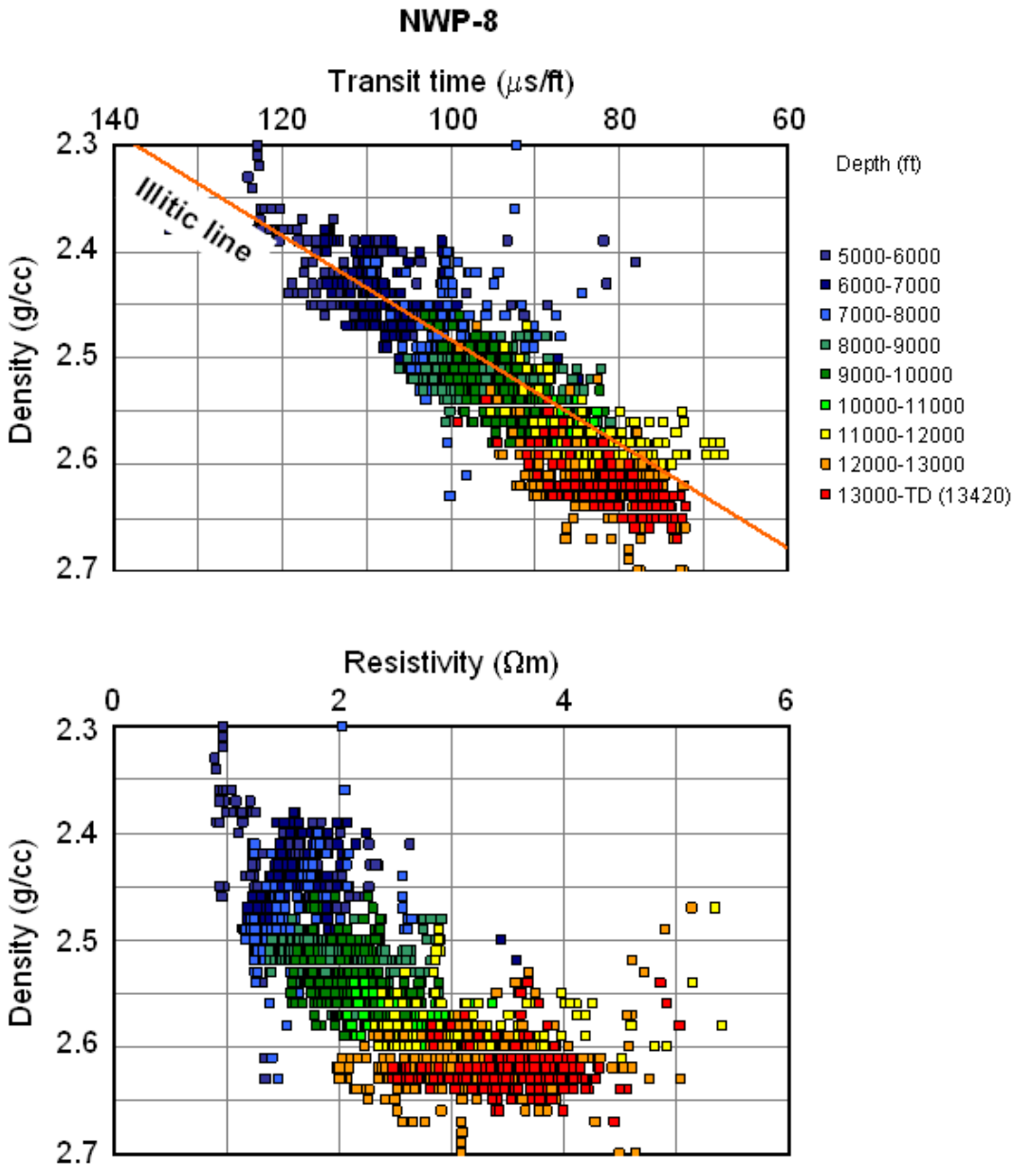
NWP-8
Transit time (μs/ft)
140
120
100
80
60
Density (g/cc)
2.3
2.4
2.5
2.6
2.7
Illitic line
Depth (ft)
5000-6000
6000-7000
7000-8000
8000-9000
9000-10000
10000-11000
11000-12000
12000-13000
13000-TD (13420)
Resistivity (Ωm)
0
2
4
6
Density (g/cc)
2.3
2.4
2.5
2.6
2.7

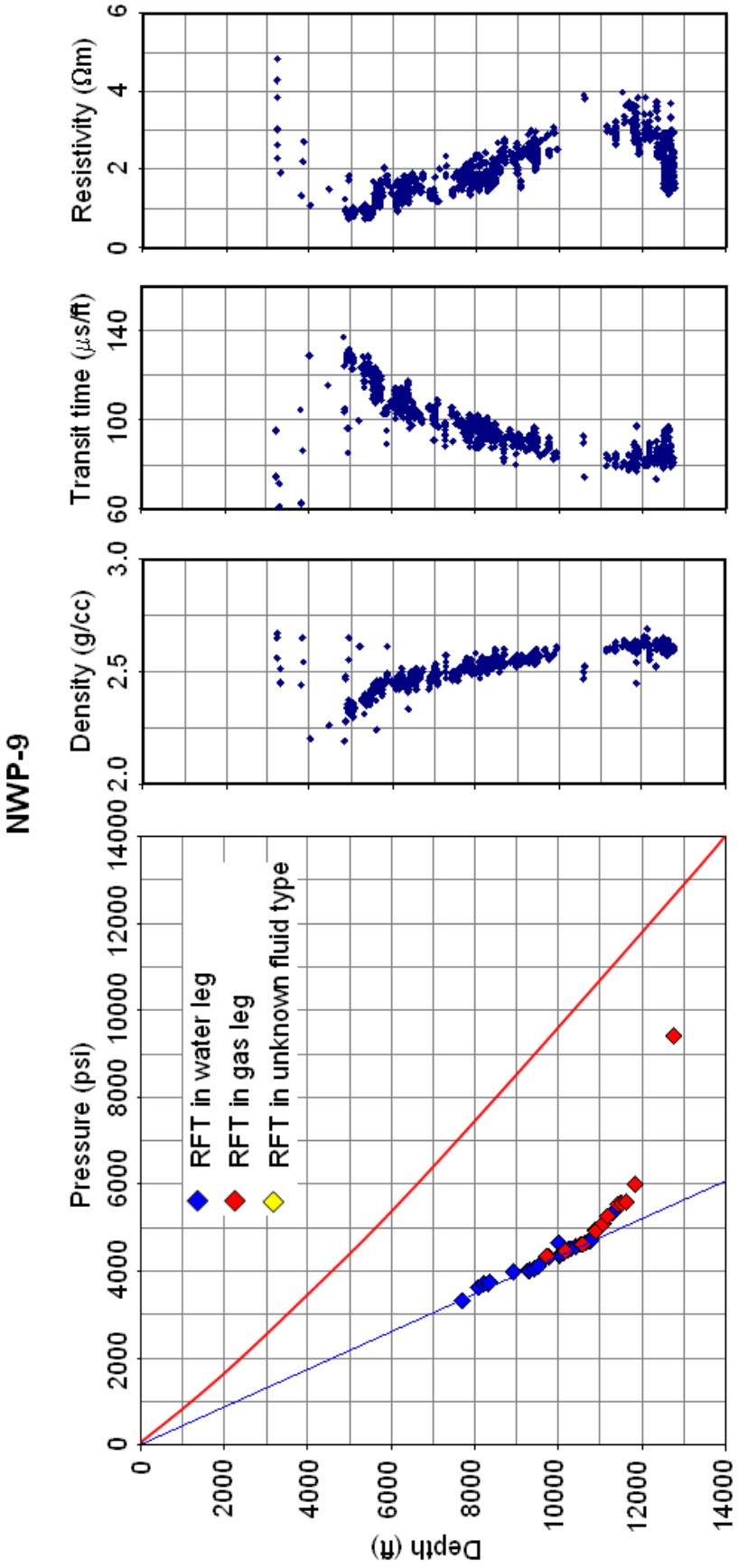
NWP-9
Resistivity (Ωm)
0
2
4
6
Transit time (μs/ft)
60
100
140
Density (g/cc)
2.0
2.5
3.0
Pressure (psi)
0
2000
4000
6000
8000
10000
12000
14000
RFT in water leg
RFT in gas leg
RFT in unknown fluid type
Depth (ft)
0
2000
4000
6000
8000
10000
12000
14000

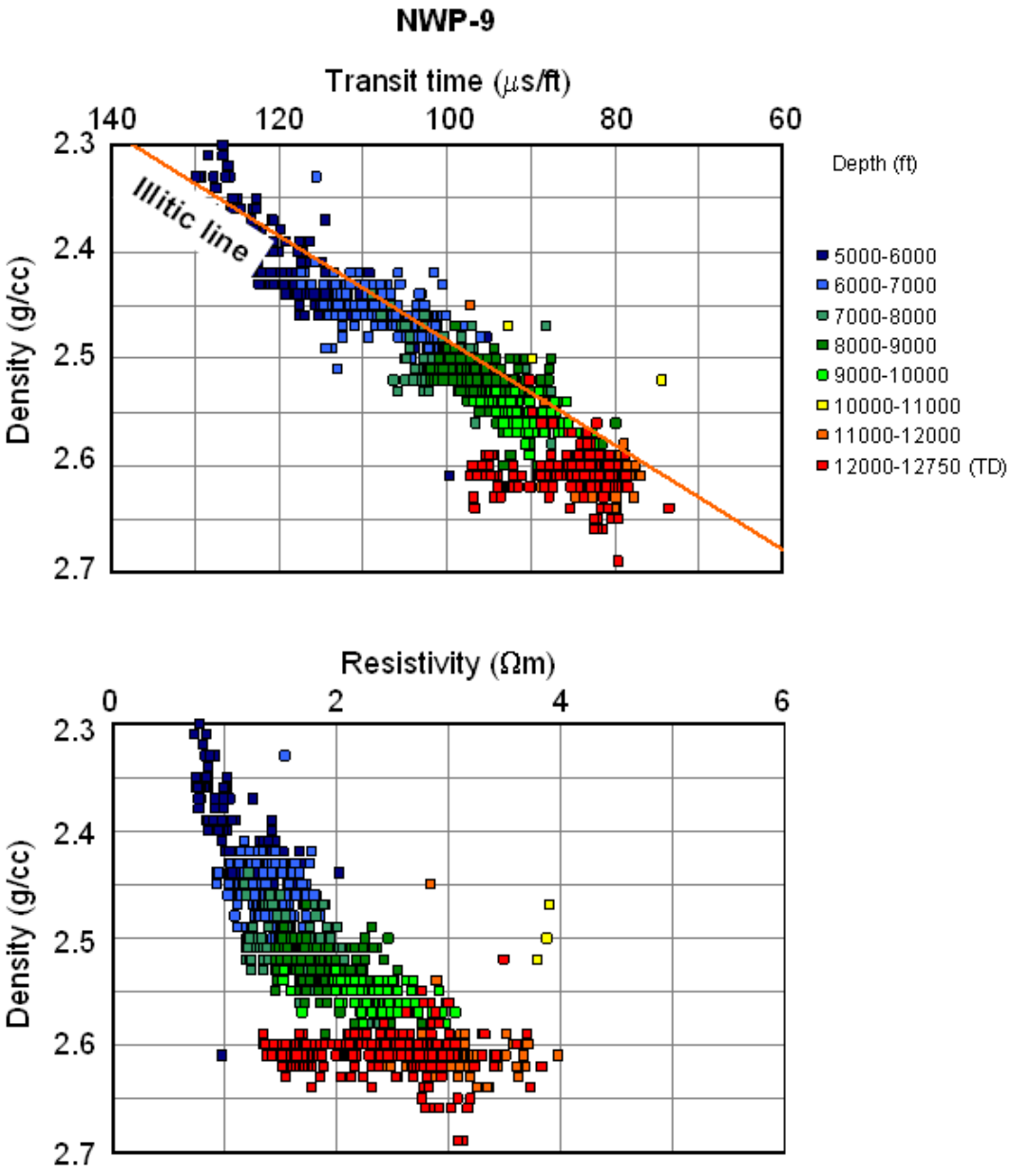
NWP-9
Transit time (μs/ft)
140
120
100
80
60
Density (g/cc)
2.3
2.4
2.5
2.6
2.7
Illitic line
Depth (ft)
5000-6000
6000-7000
7000-8000
8000-9000
9000-10000
10000-11000
11000-12000
12000-12750 (TD)
Resistivity (Ωm)
0
2
4
6

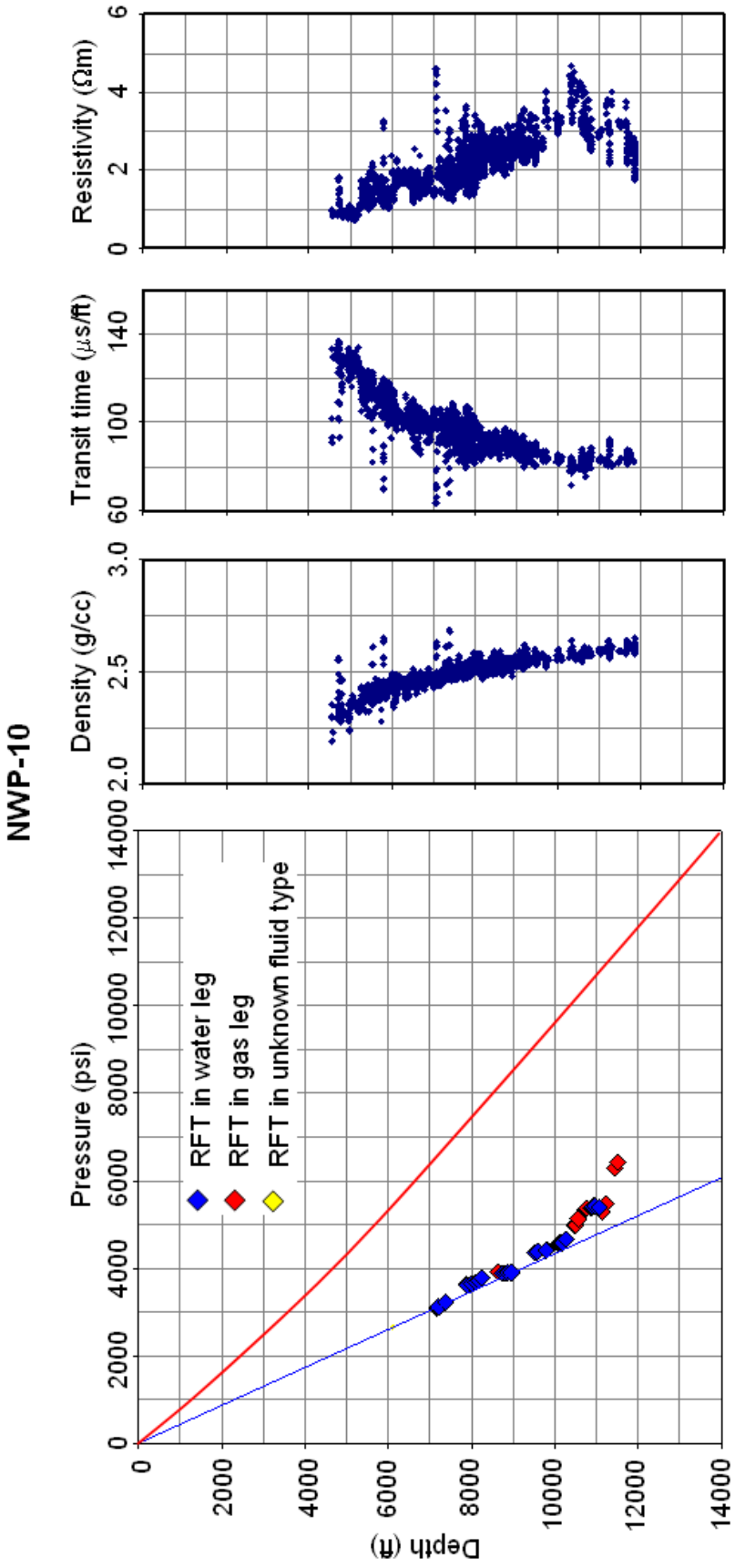
NWP-10
Resistivity (Ωm)
0
2
4
6
Transit time (μs/ft)
60
100
140
Density (g/cc)
2.0
2.5
3.0
Pressure (psi)
0
2000
4000
6000
8000
10000
12000
14000
RFT in water leg
RFT in gas leg
RFT in unknown fluid type
Depth (ft)
0
2000
4000
6000
8000
10000
12000
14000

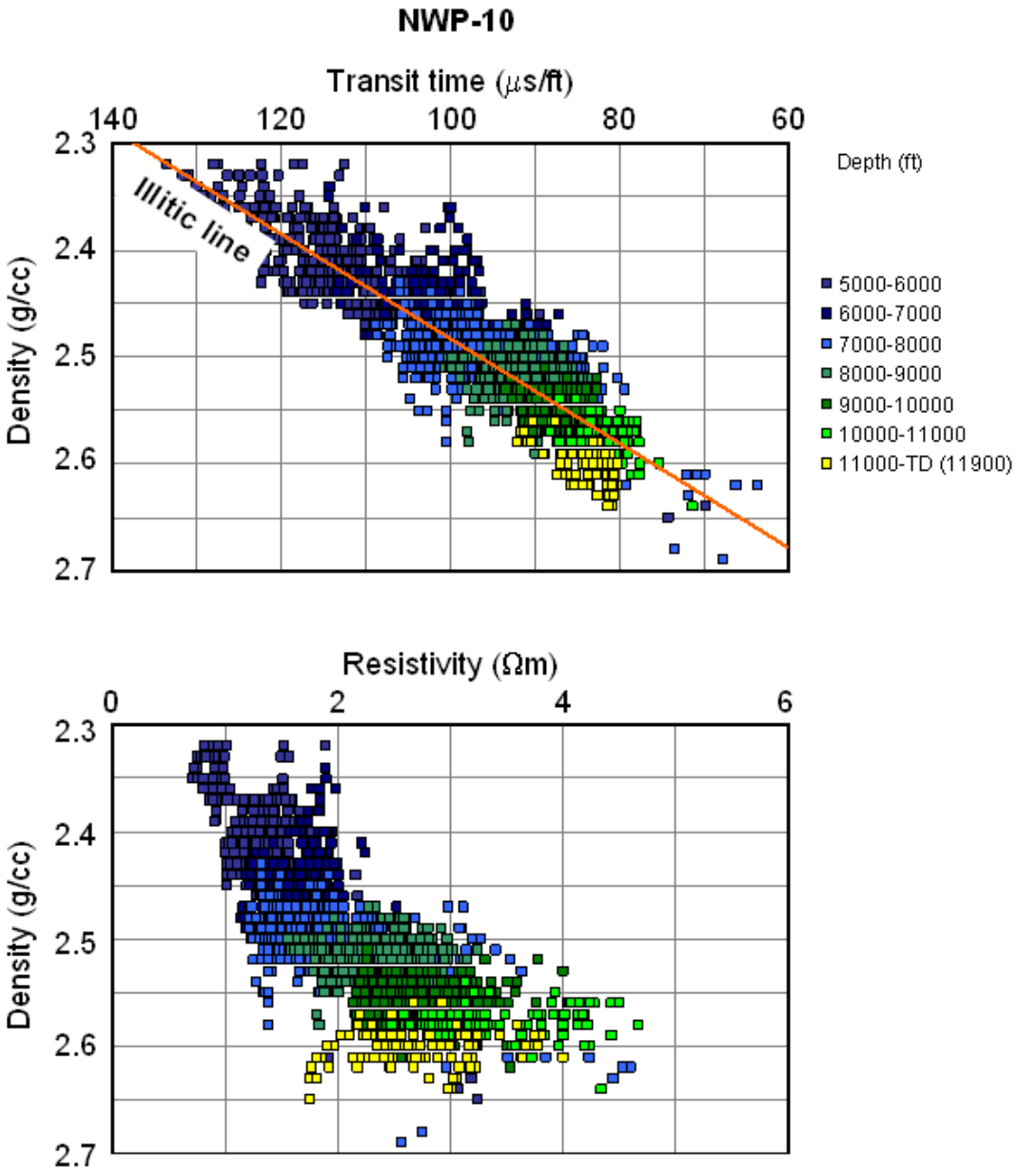
NWP-10
Transit time (μs/ft)
140
120
100
80
60
Density (g/cc)
2.3
2.4
2.5
2.6
2.7
Illitic line
Depth (ft)
5000-6000
6000-7000
7000-8000
8000-9000
9000-10000
10000-11000
11000-TD (11900)
Resistivity (Ωm)
0
2
4
6
Density (g/cc)
2.3
2.4
2.5
2.6
2.7

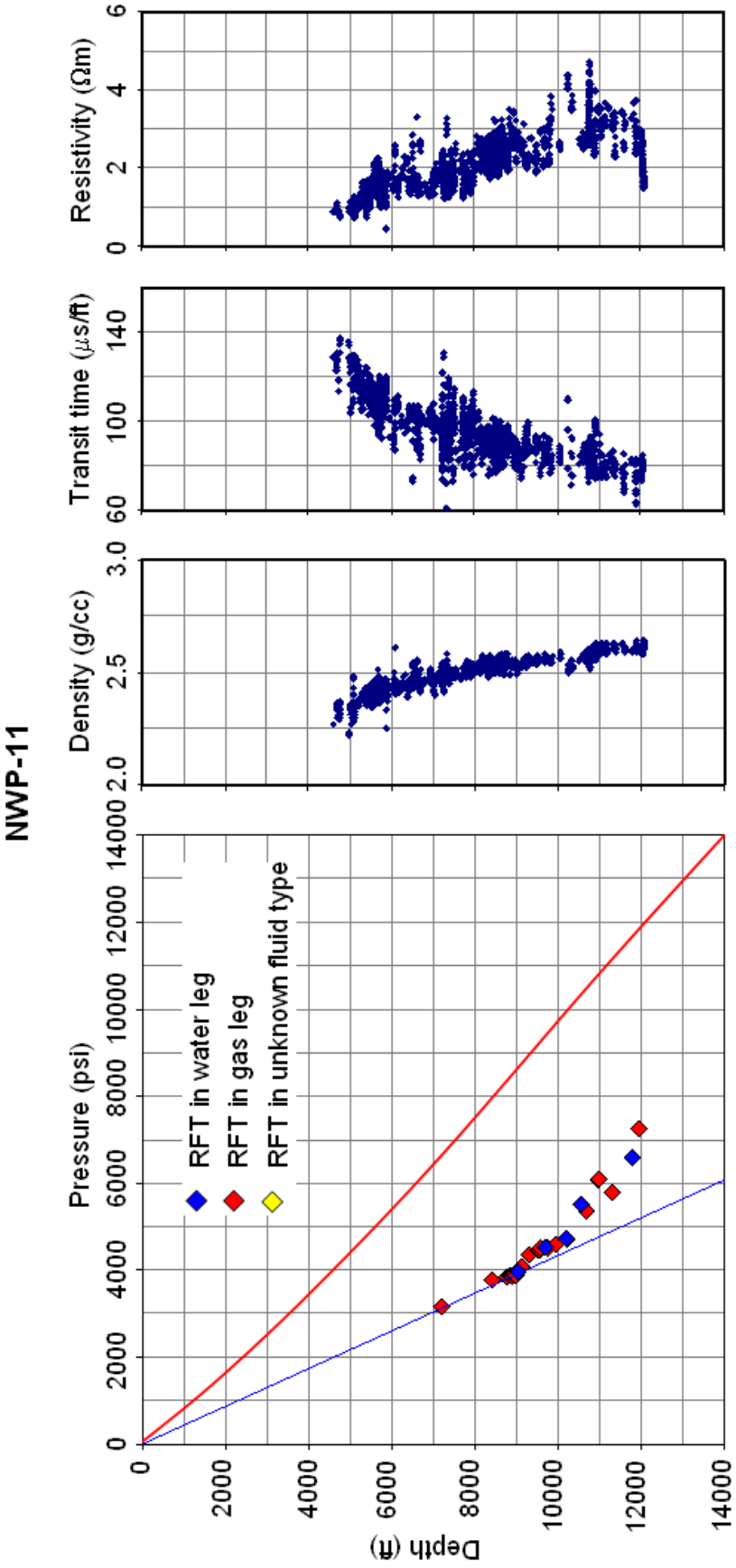
NWP-11
Resistivity (Ωm)
0
2
4
6
Transit time (μs/ft)
60
100
140
Density (g/cc)
2.0
2.5
3.0
Pressure (psi)
0
2000
4000
6000
8000
10000
12000
14000
RFT in water leg
RFT in gas leg
RFT in unknown fluid type
Depth (ft)
0
2000
4000
6000
8000
10000
12000
14000

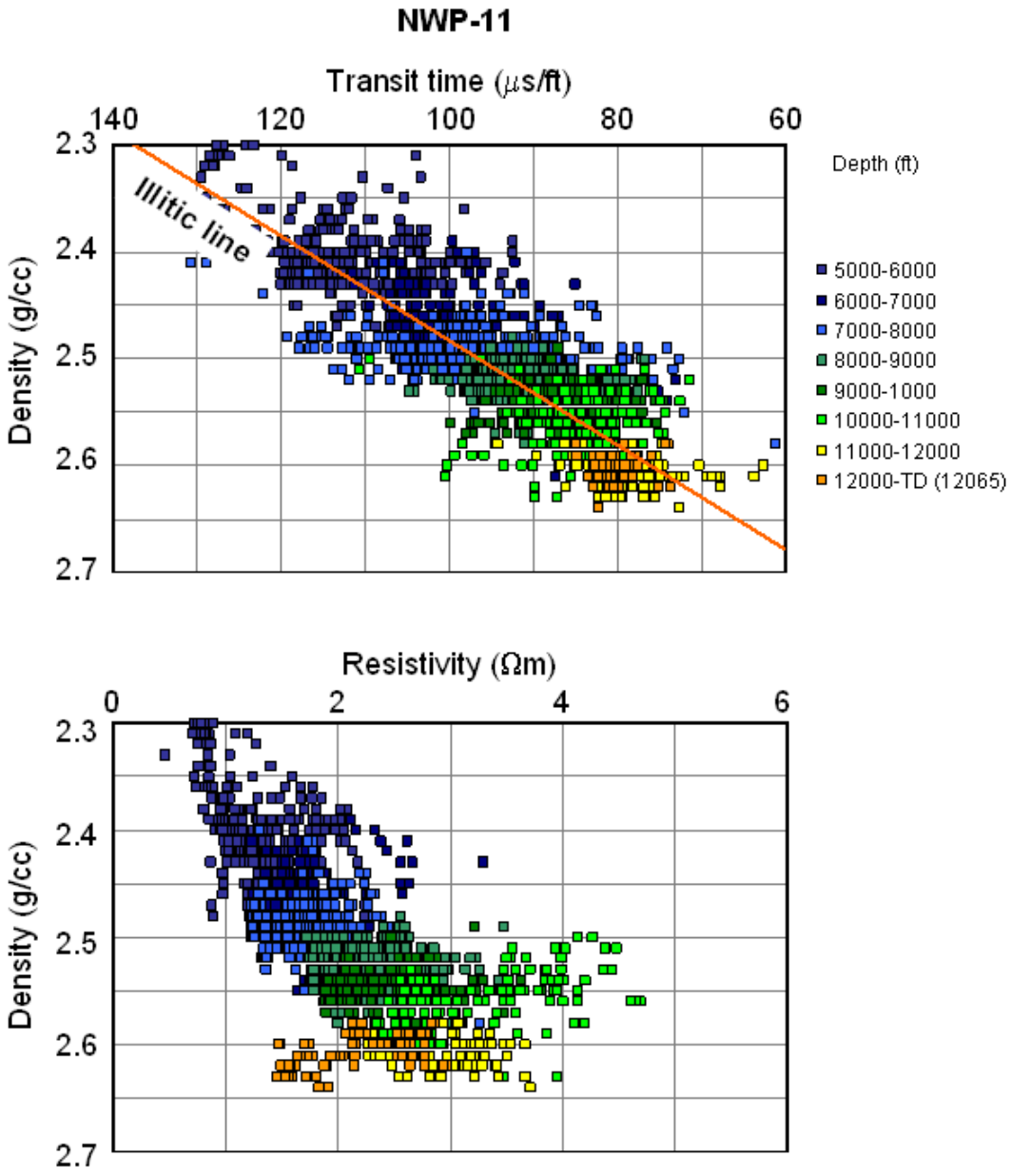
NWP-11
Transit time (μs/ft)
140
120
100
80
60
Density (g/cc)
2.3
2.4
2.5
2.6
2.7
Illitic line
Depth (ft)
5000-6000
6000-7000
7000-8000
8000-9000
9000-1000
10000-11000
11000-12000
12000-TD (12065)
Resistivity (Ωm)
0
2
4
6

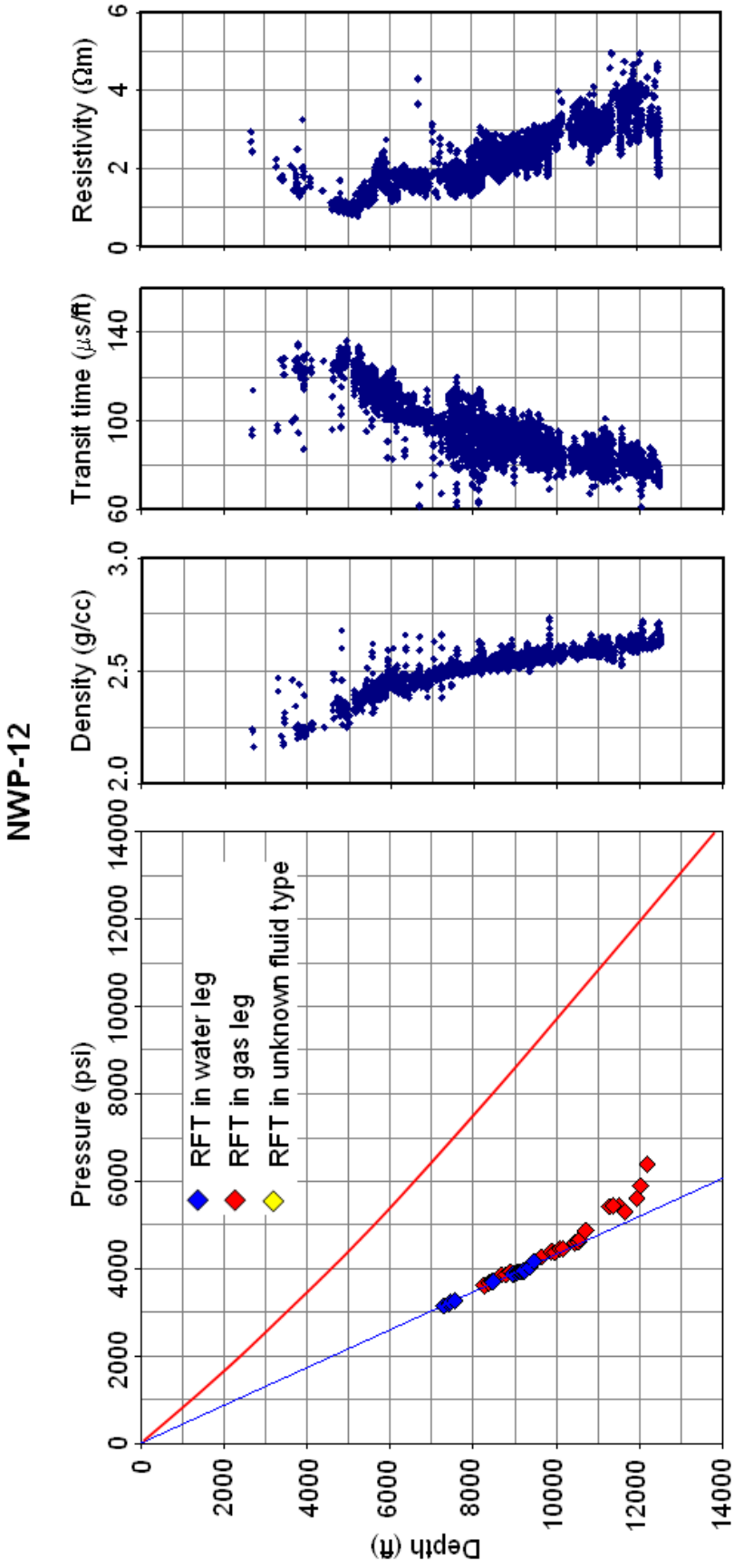
NWP-12
Resistivity (Ωm)
0
2
4
6
Transit time (μs/ft)
60
100
140
Density (g/cc)
2.0
2.5
3.0
Pressure (psi)
0
2000
4000
6000
8000
10000
12000
14000
RFT in water leg
RFT in gas leg
RFT in unknown fluid type
Depth (ft)
0
2000
4000
6000
8000
10000
12000
14000

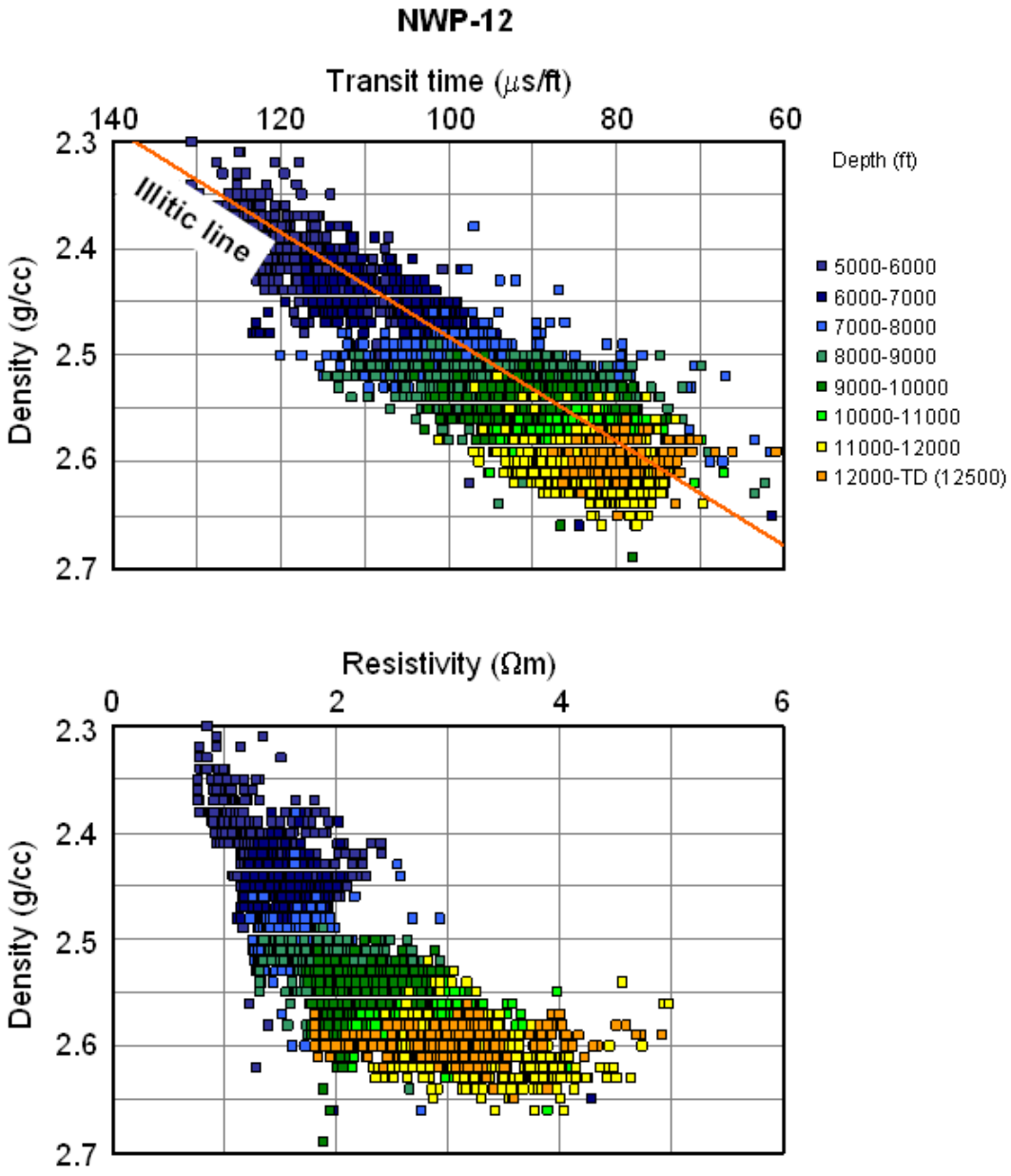
NWP-12
Transit time (μs/ft)
140
120
100
80
60
Density (g/cc)
2.3
2.4
2.5
2.6
2.7
Illitic line
Depth (ft)
5000-6000
6000-7000
7000-8000
8000-9000
9000-10000
10000-11000
11000-12000
12000-TD (12500)
Resistivity (Ωm)
0
2
4
6
Density (g/cc)
2.3
2.4
2.5
2.6
2.7

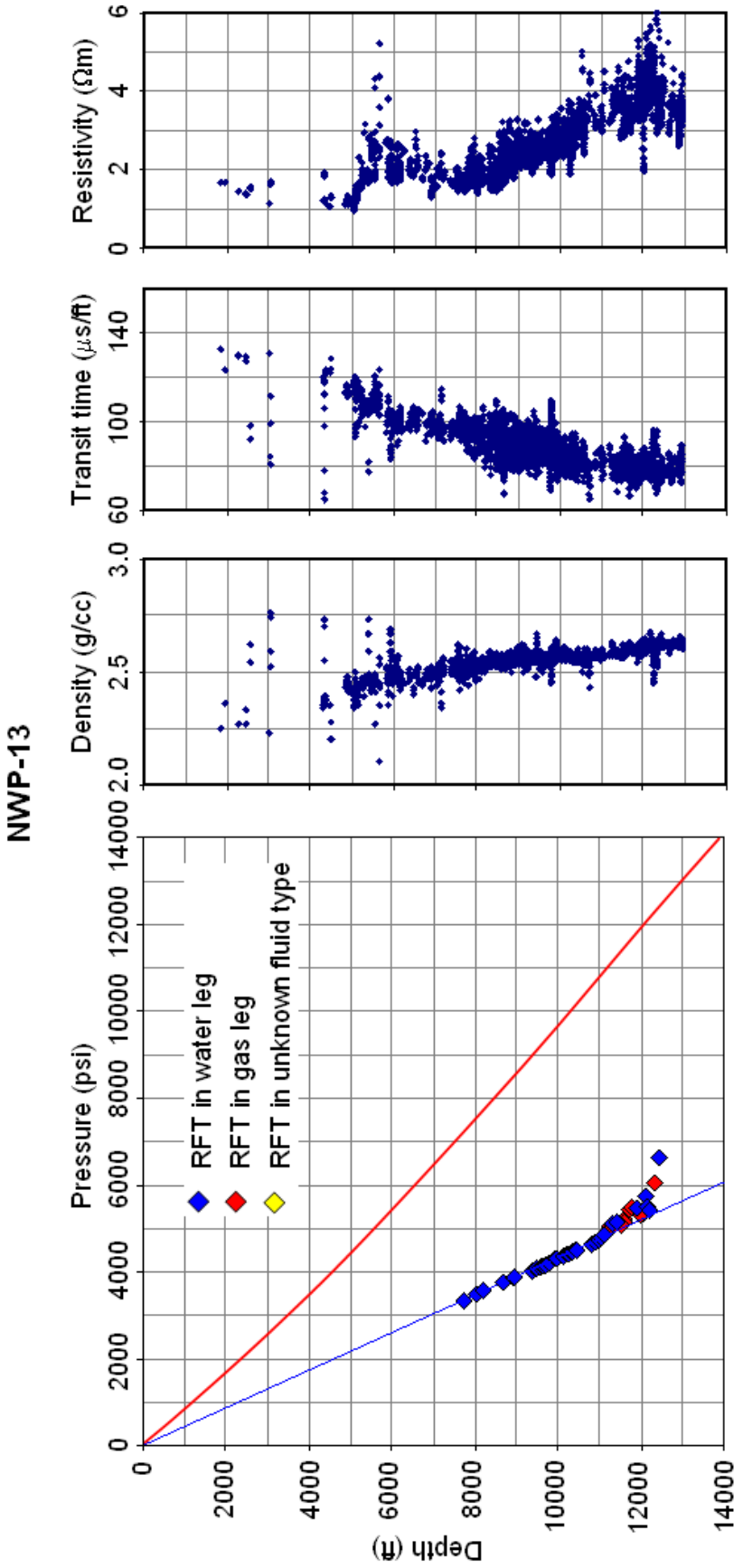
NWP-13
Resistivity (Ωm)
0
2
4
6
Transit time (μs/ft)
60
100
140
Density (g/cc)
2.0
2.5
3.0
Pressure (psi)
0
2000
4000
6000
8000
10000
12000
14000
RFT in water leg
RFT in gas leg
RFT in unknown fluid type
Depth (ft)
0
2000
4000
6000
8000
10000
12000
14000

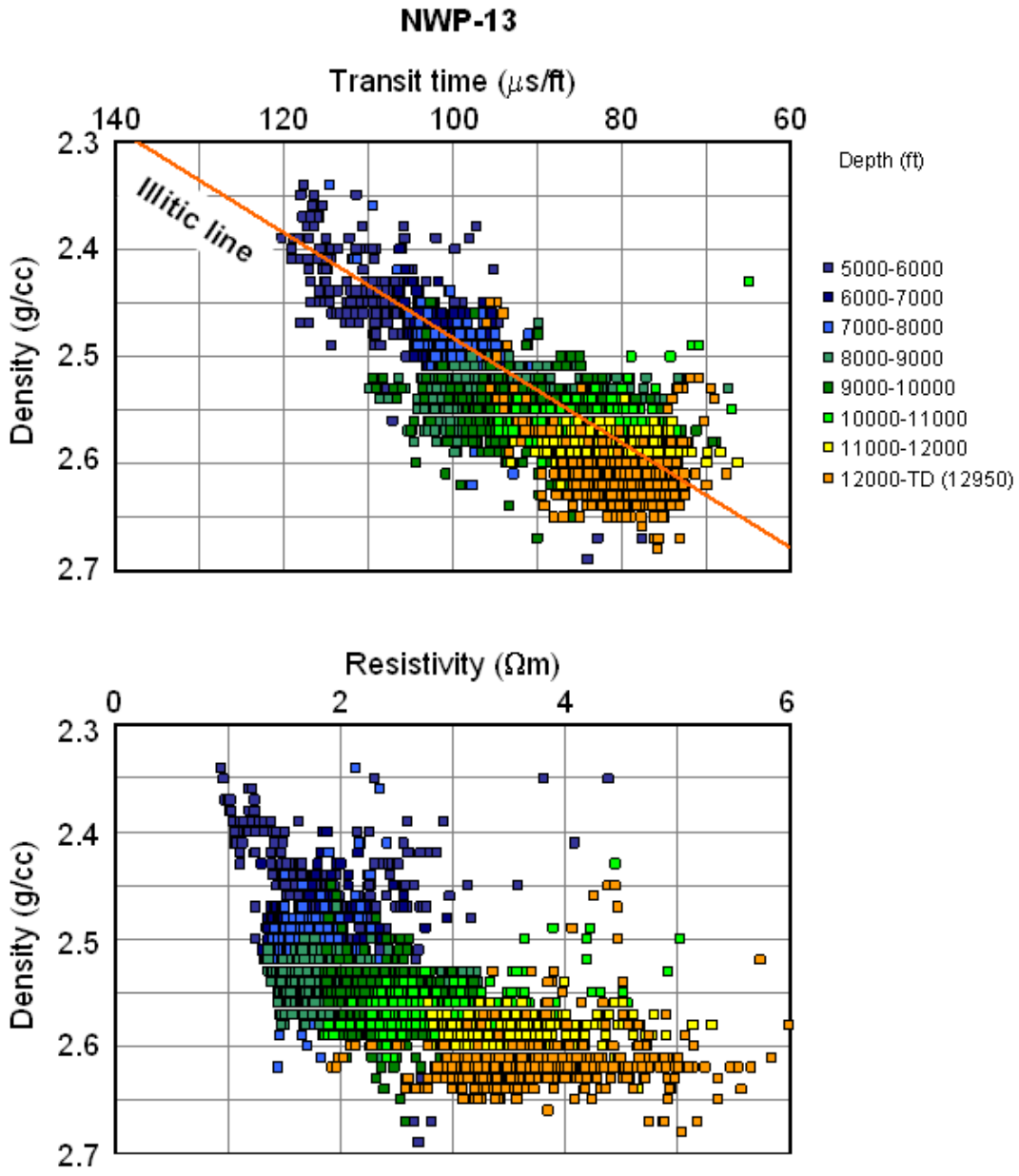
NWP-13
Transit time (μs/ft)
140
120
100
80
60
Density (g/cc)
2.3
2.4
2.5
2.6
2.7
Illitic line
Depth (ft)
5000-6000
6000-7000
7000-8000
8000-9000
9000-10000
10000-11000
11000-12000
12000-TD (12950)
Resistivity (Ωm)
0
2
4
6
Density (g/cc)
2.3
2.4
2.5
2.6
2.7

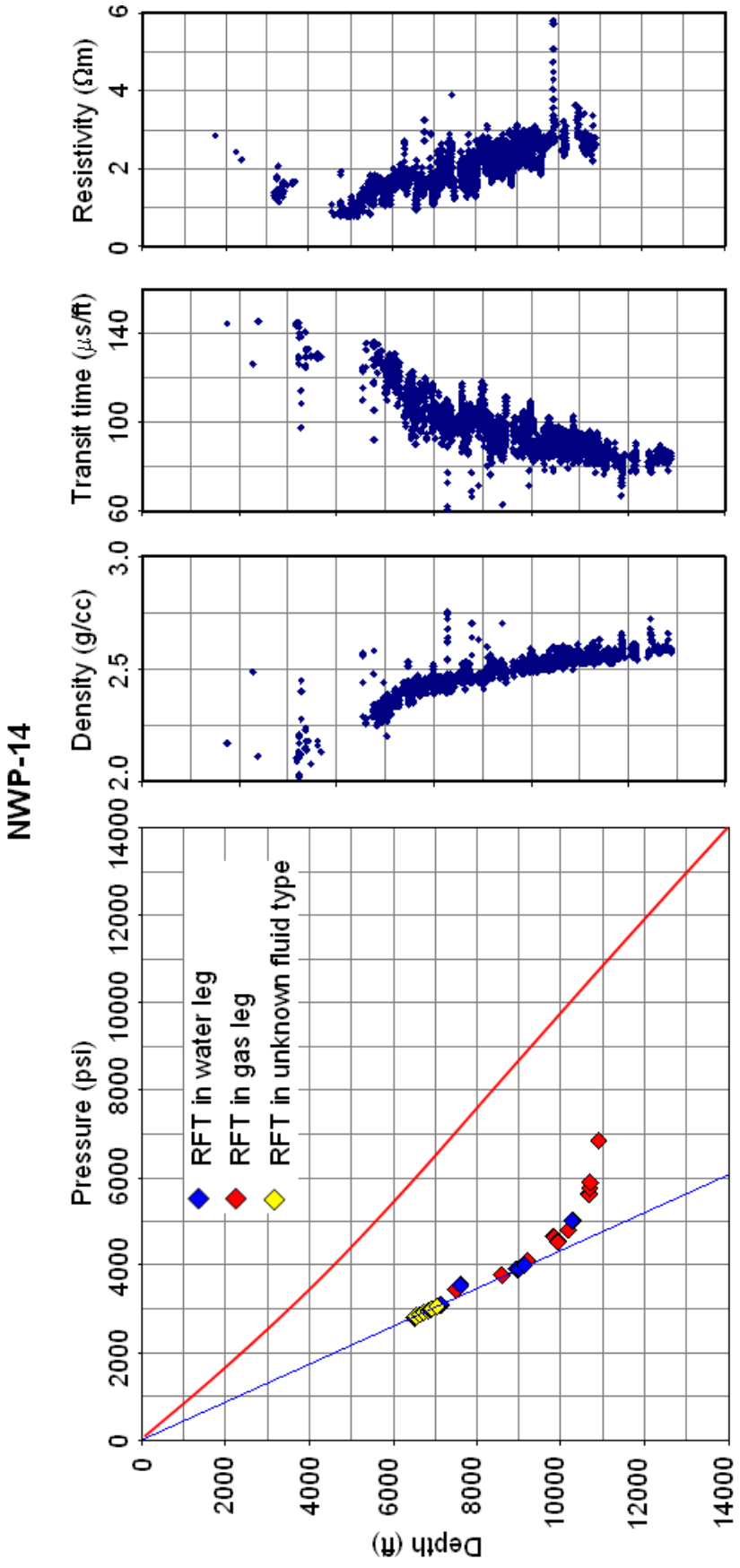
NWP-14
Resistivity (Ωm)
0
2
4
6
Transit time (μs/ft)
60
100
140
Density (g/cc)
2.0
2.5
3.0
Pressure (psi)
0
2000
4000
6000
8000
10000
12000
14000
RFT in water leg
RFT in gas leg
RFT in unknown fluid type
Depth (ft)
0
2000
4000
6000
8000
10000
12000
14000

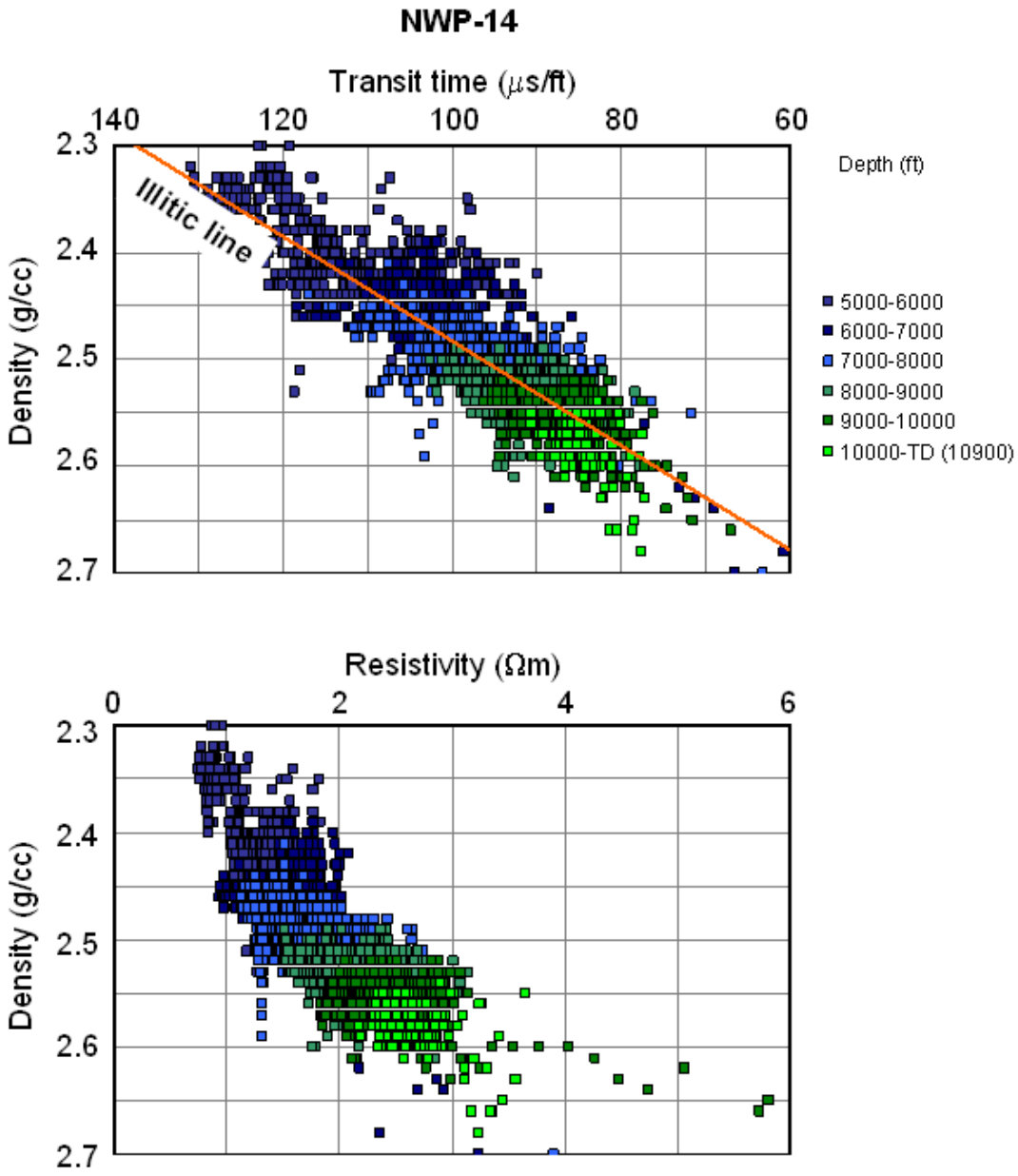
NWP-14
Transit time (μs/ft)
140
120
100
80
60
Density (g/cc)
2.3
2.4
2.5
2.6
2.7
Illitic line
Depth (ft)
5000-6000
6000-7000
7000-8000
8000-9000
9000-10000
10000-TD (10900)
Resistivity (Ωm)
0
2
4
6
Density (g/cc)
2.3
2.4
2.5
2.6
2.7

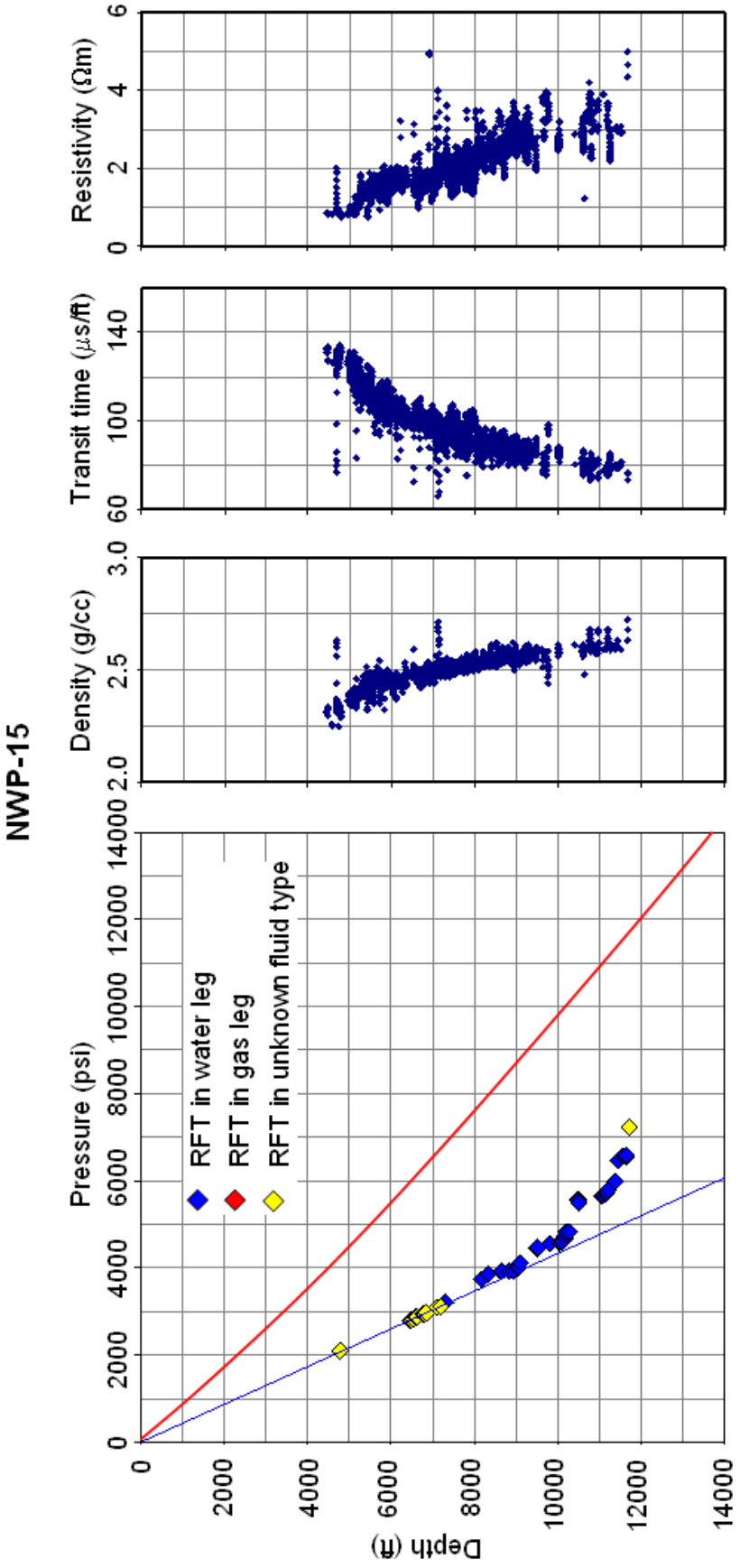
NWP-15
Resistivity (Ωm)
0
2
4
6
Transit time (μs/ft)
60
100
140
Density (g/cc)
2.0
2.5
3.0
Pressure (psi)
0
2000
4000
6000
8000
10000
12000
14000
RFT in water leg
RFT in gas leg
RFT in unknown fluid type
Depth (ft)
0
2000
4000
6000
8000
10000
12000
14000

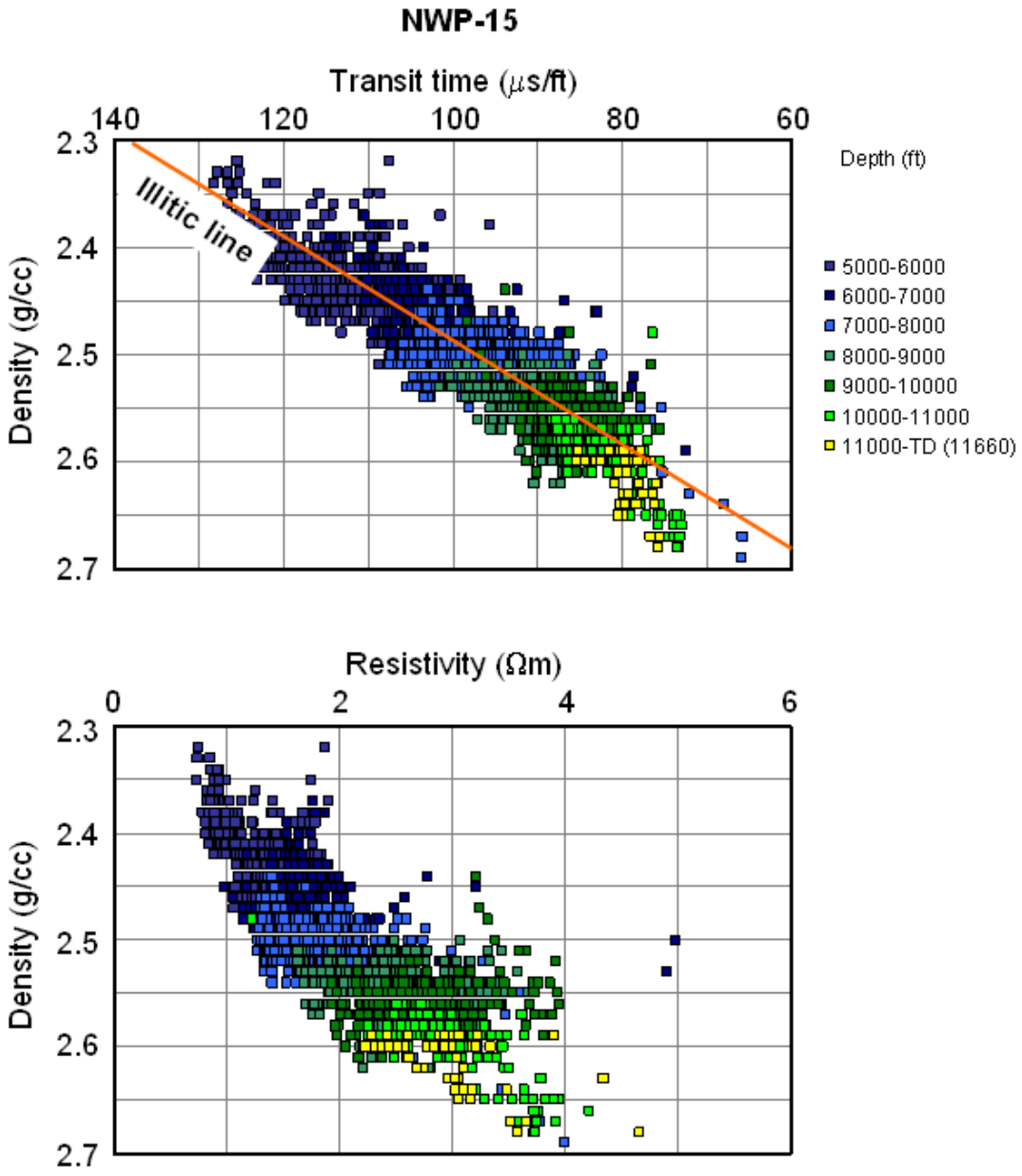
NWP-15
Transit time (μs/ft)
140
120
100
80
60
Density (g/cc)
2.3
2.4
2.5
2.6
2.7
Illitic line
Depth (ft)
5000-6000
6000-7000
7000-8000
8000-9000
9000-10000
10000-11000
11000-TD (11660)
Resistivity (Ωm)
0
2
4
6
Density (g/cc)
2.3
2.4
2.5
2.6
2.7

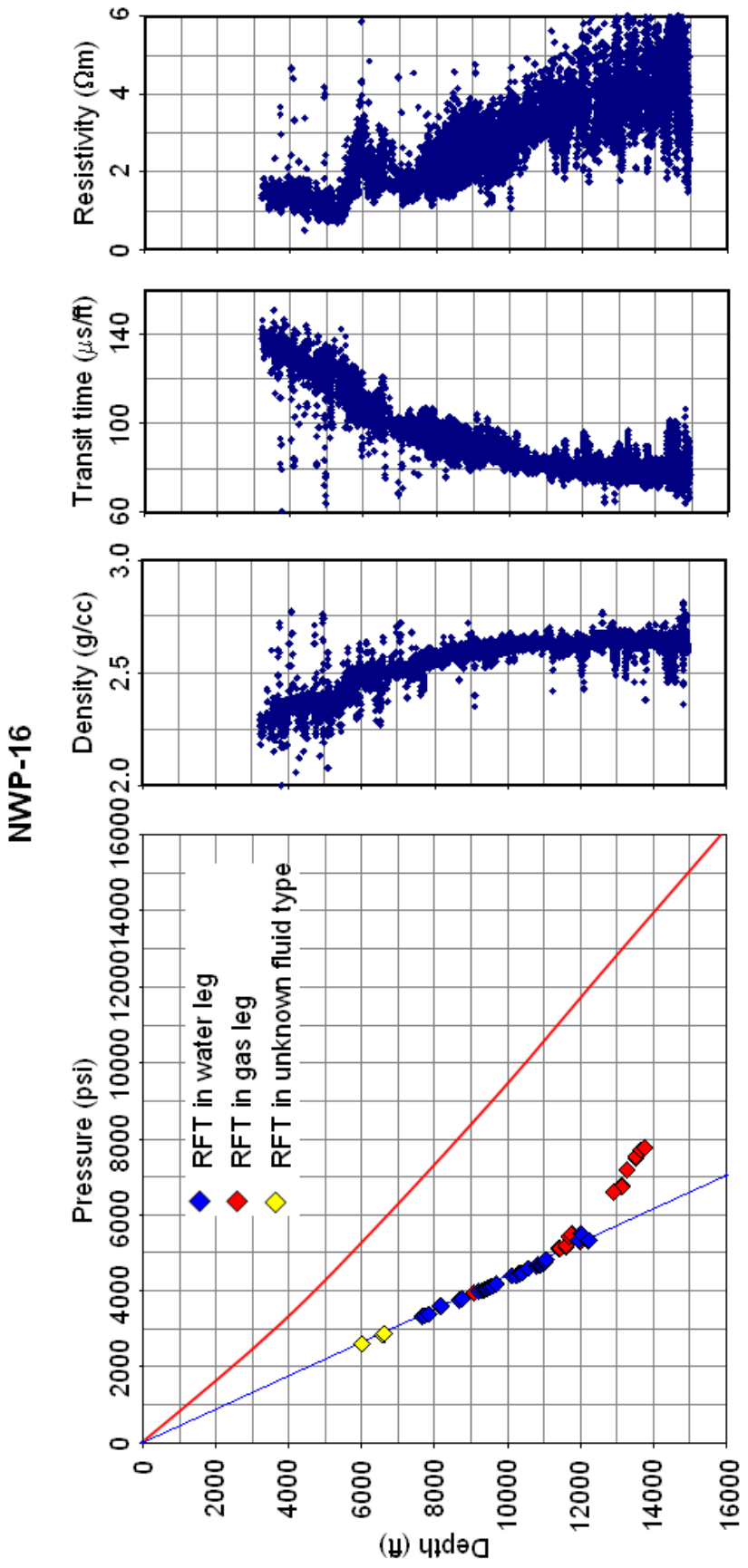
NWP-16
Resistivity (Ωm)
0
2
4
6
Transit time (µs/ft)
60
100
140
Density (g/cc)
2.0
2.5
3.0
Pressure (psi)
0
2000
4000
6000
8000
10000
12000
14000
16000
RFT in water leg
RFT in gas leg
RFT in unknown fluid type
Depth (ft)
0
2000
4000
6000
8000
10000
12000
14000
16000

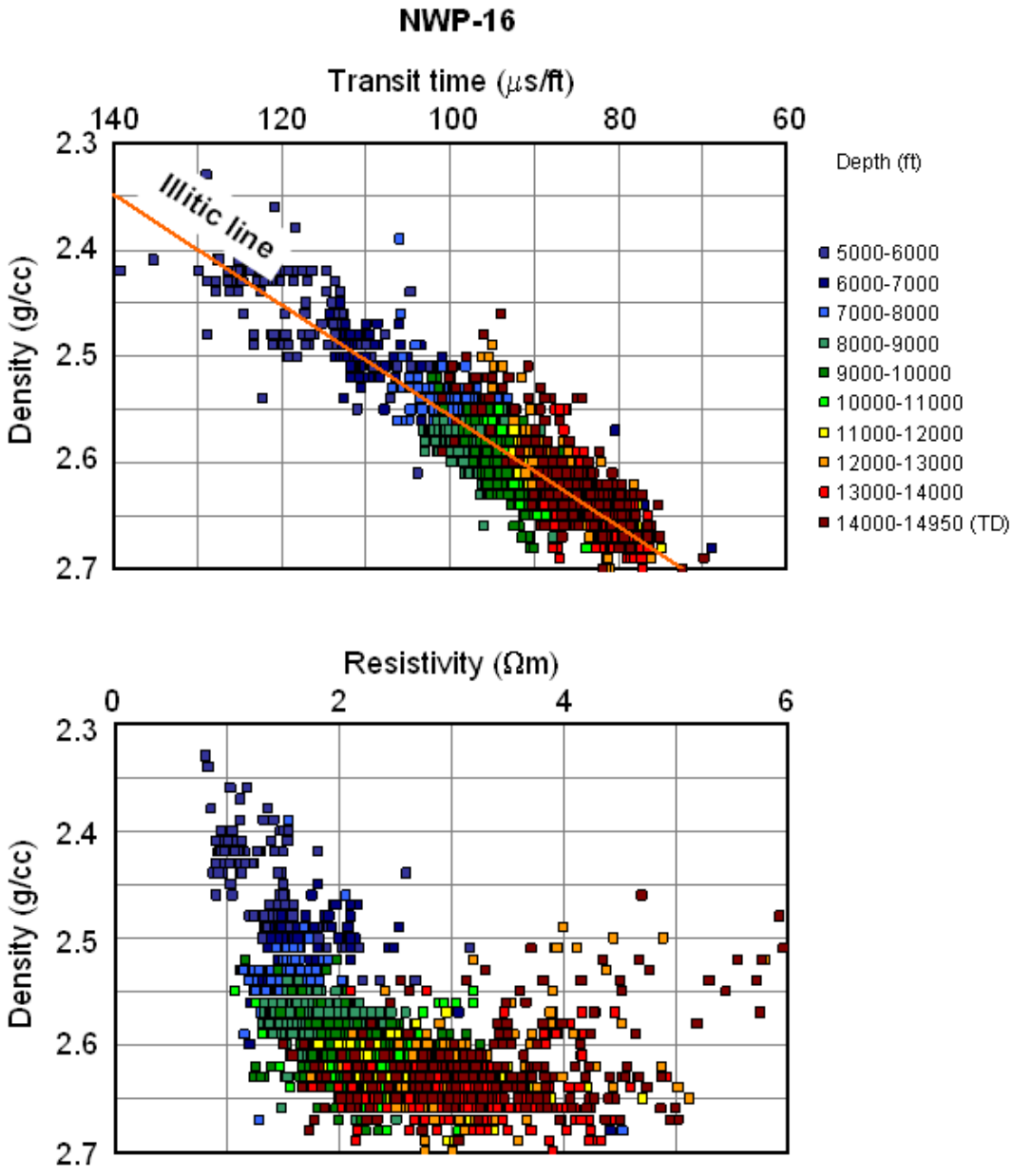
NWP-16
Transit time (μs/ft)
140
120
100
80
60
Density (g/cc)
2.3
2.4
2.5
2.6
2.7
Illitic line
Depth (ft)
5000-6000
6000-7000
7000-8000
8000-9000
9000-10000
10000-11000
11000-12000
12000-13000
13000-14000
14000-14950 (TD)
Resistivity (Ωm)
0
2
4
6
Density (g/cc)
2.3
2.4
2.5
2.6
2.7

APPENDIX 1. PECIKO FIELD

Appendix 1c

Overpressure map in selected stratigraphic units, as shown in Figure 5.2

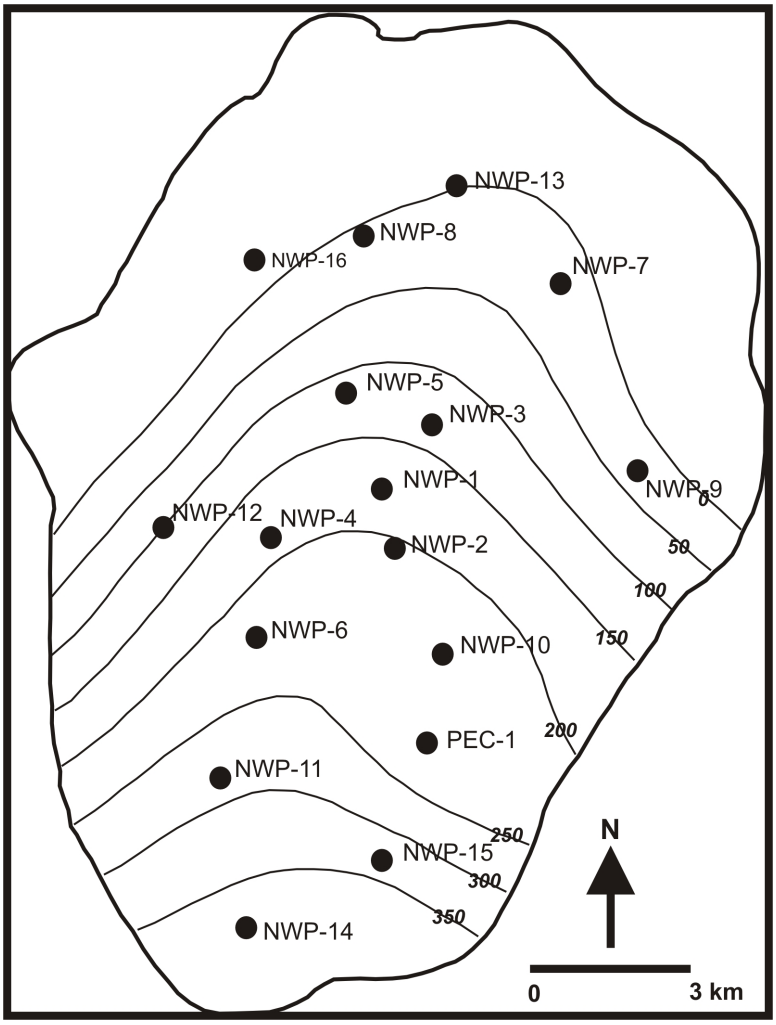

Overpressure map in SU2e (overpressure value is in psi)

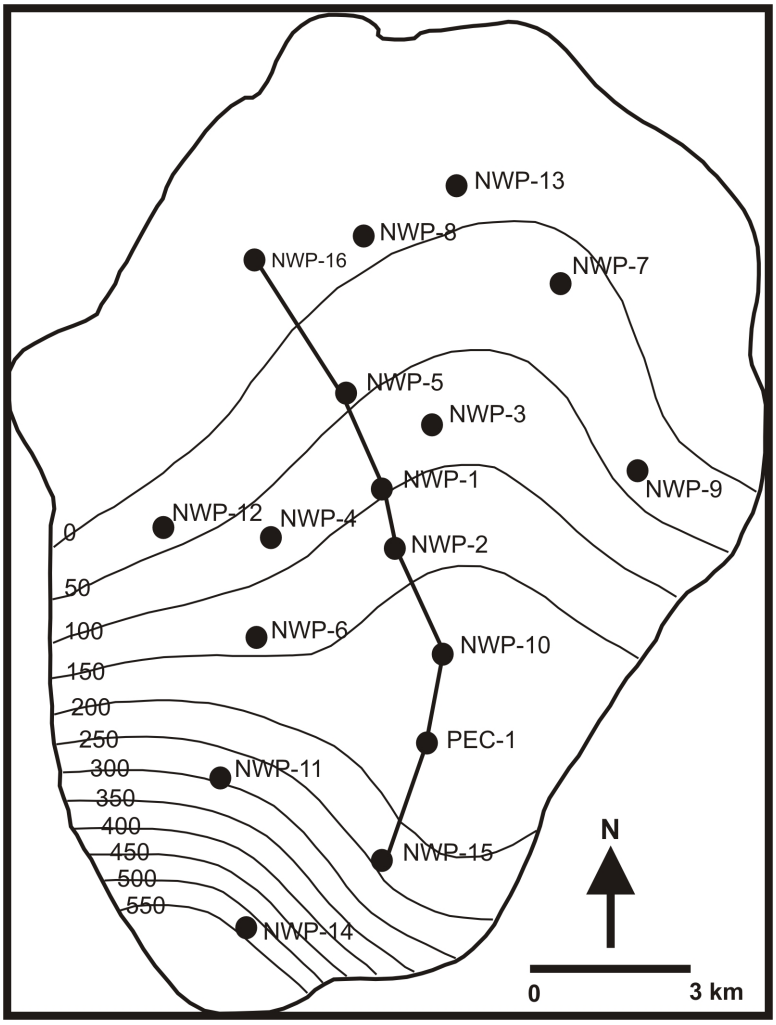

Overpressure map in SU3a (overpressure value is in psi)

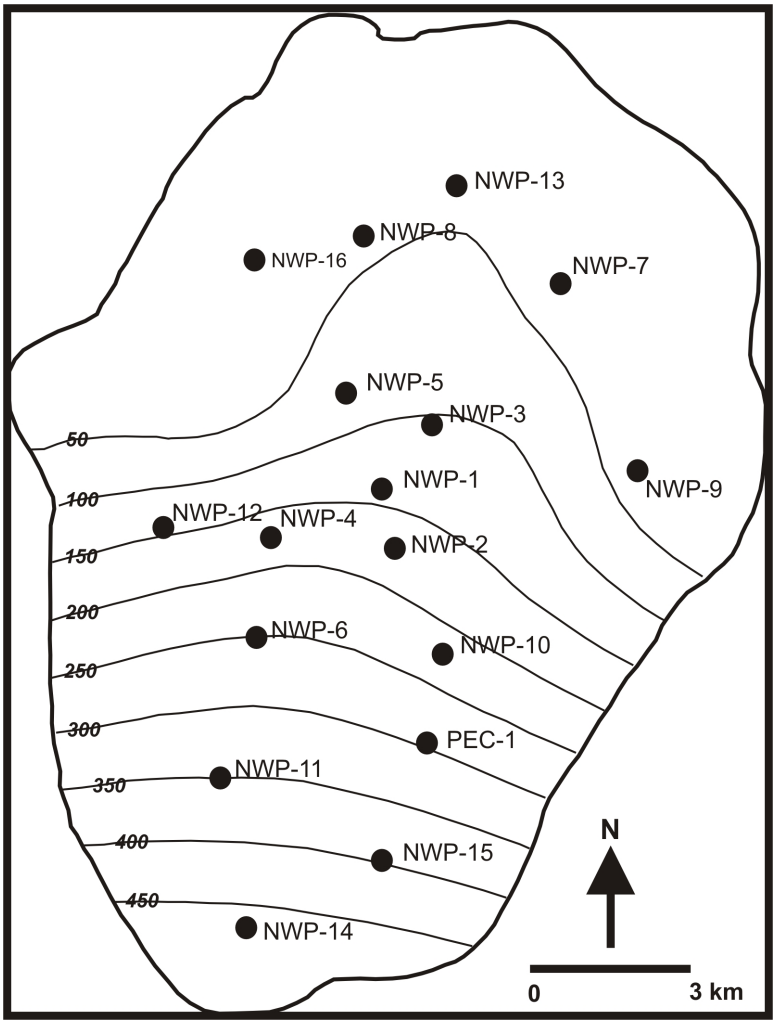

Overpressure map in SU3c (overpressure value is in psi)

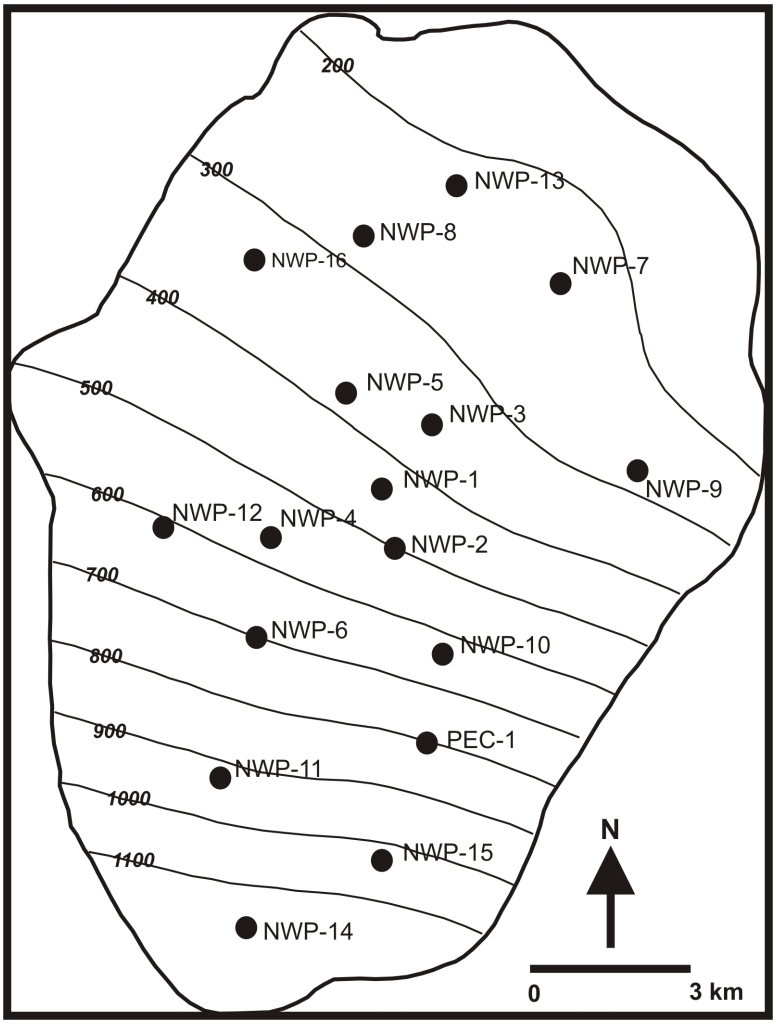

Overpressure map in SU3e (overpressure value is in psi)

APPENDIX 2. EXTERNAL AXIS

Appendix 2a

Pressure–depth plots for each stratigraphic unit,
as shown in Figure 5.2

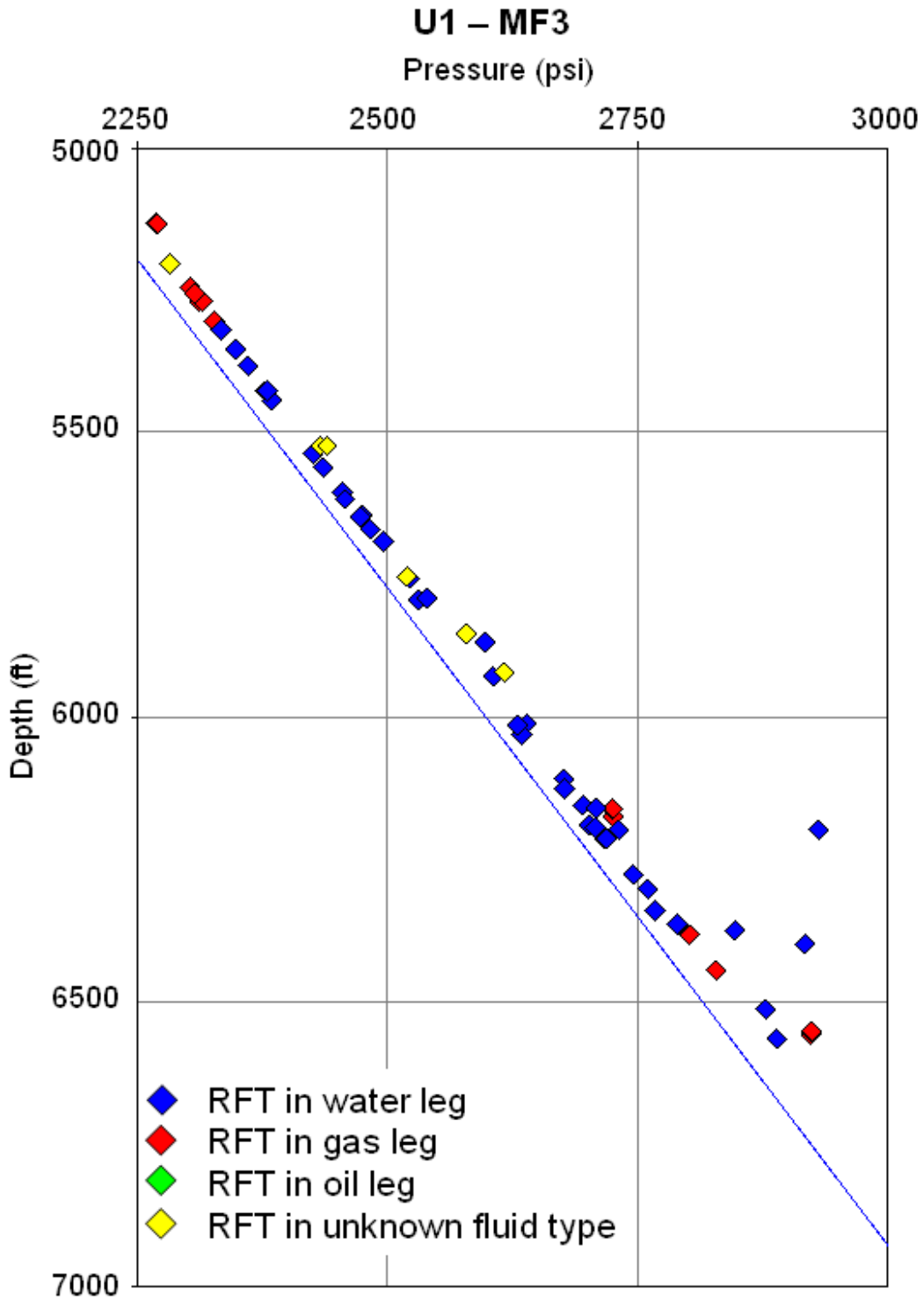
U1 – MF3
Pressure (psi)
2250
2500
2750
3000
5000
5500
6000
6500
7000
Depth (ft)
RFT in water leg
RFT in gas leg
RFT in oil leg
RFT in unknown fluid type

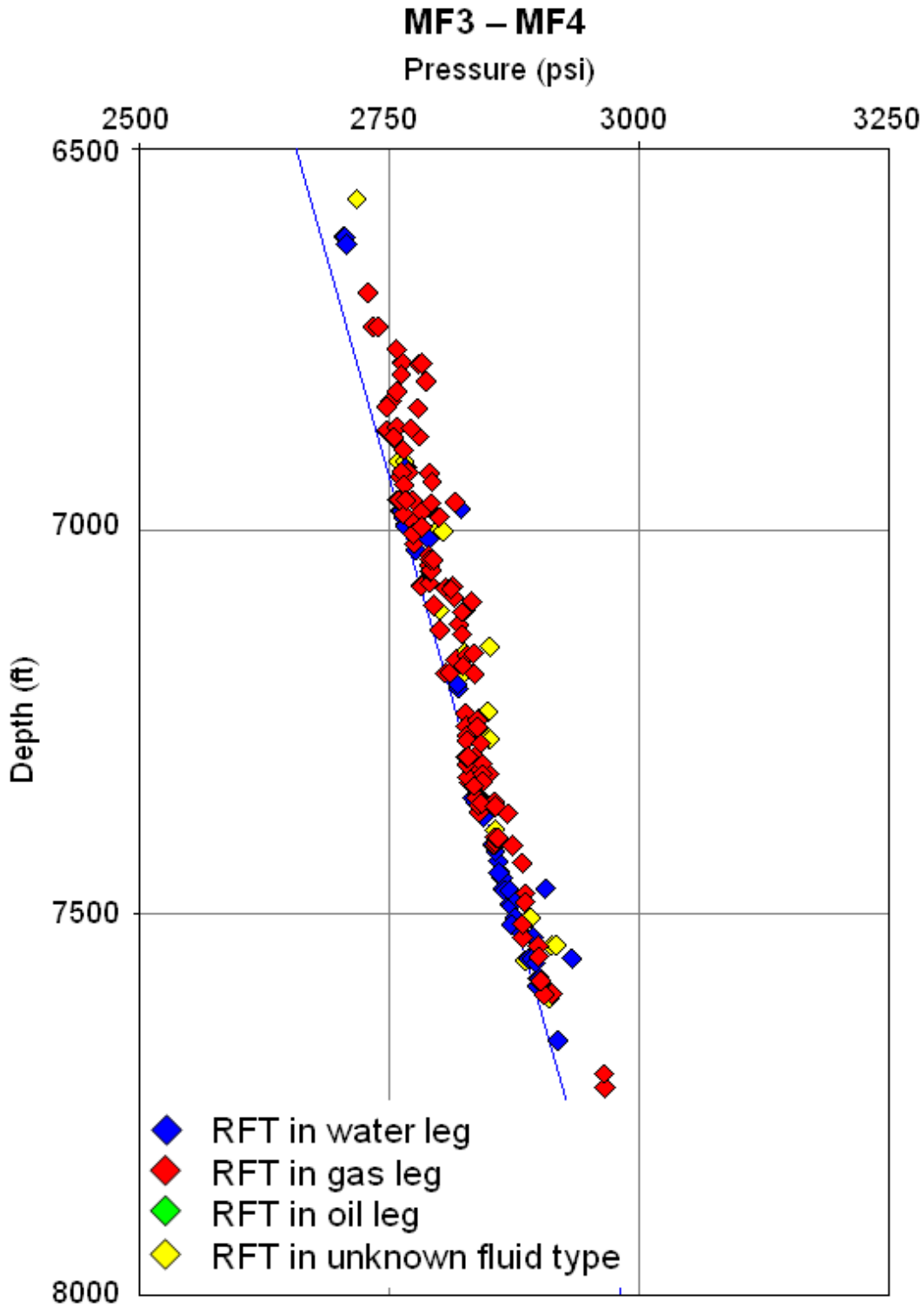
MF3 – MF4
Pressure (psi)
2500
2750
3000
3250
6500
7000
7500
8000
Depth (ft)
RFT in water leg
RFT in gas leg
RFT in oil leg
RFT in unknown fluid type

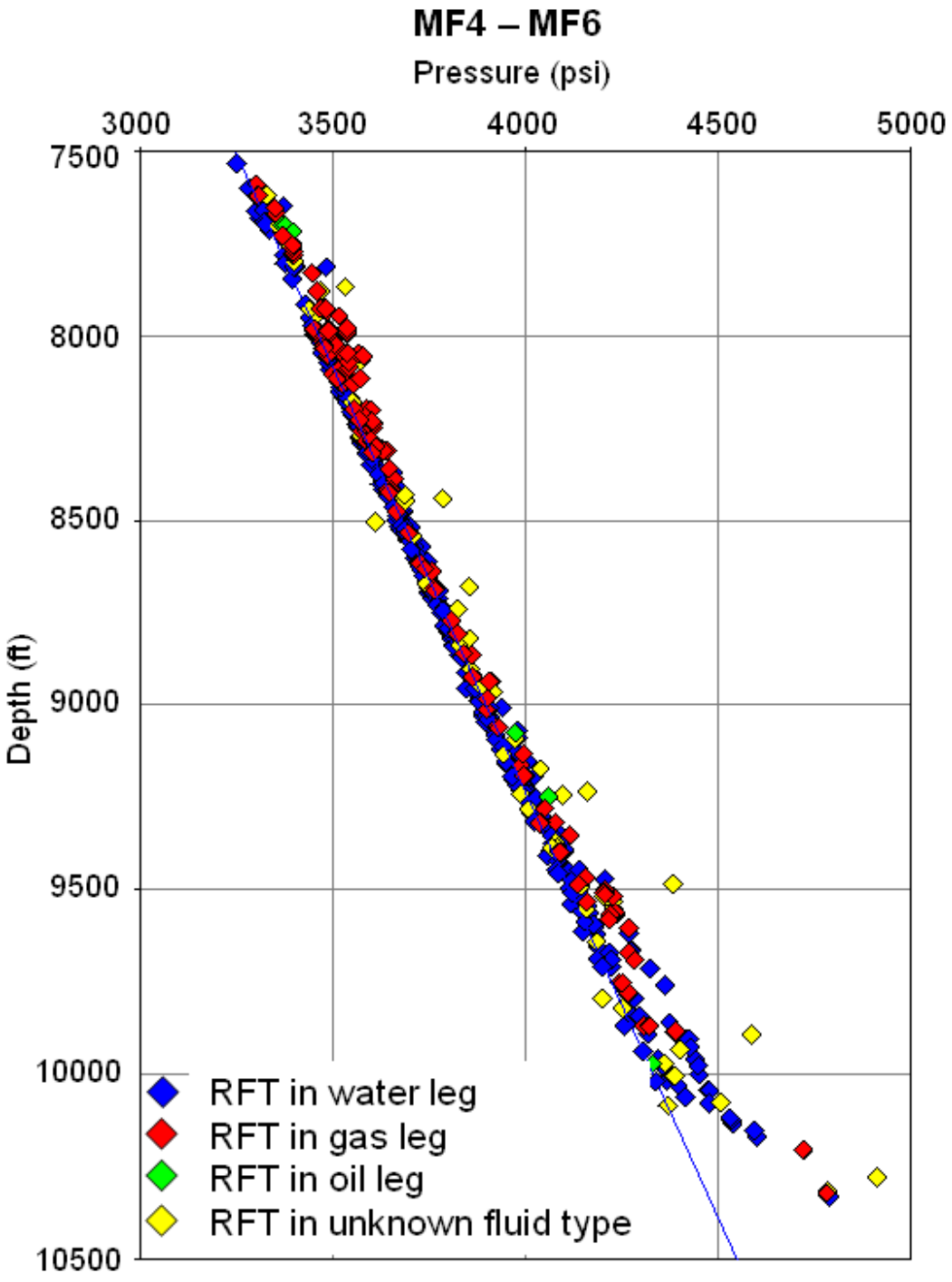
MF4 – MF6
Pressure (psi)
3000
3500
4000
4500
5000
Depth (ft)
7500
8000
8500
9000
9500
10000
10500
RFT in water leg
RFT in gas leg
RFT in oil leg
RFT in unknown fluid type

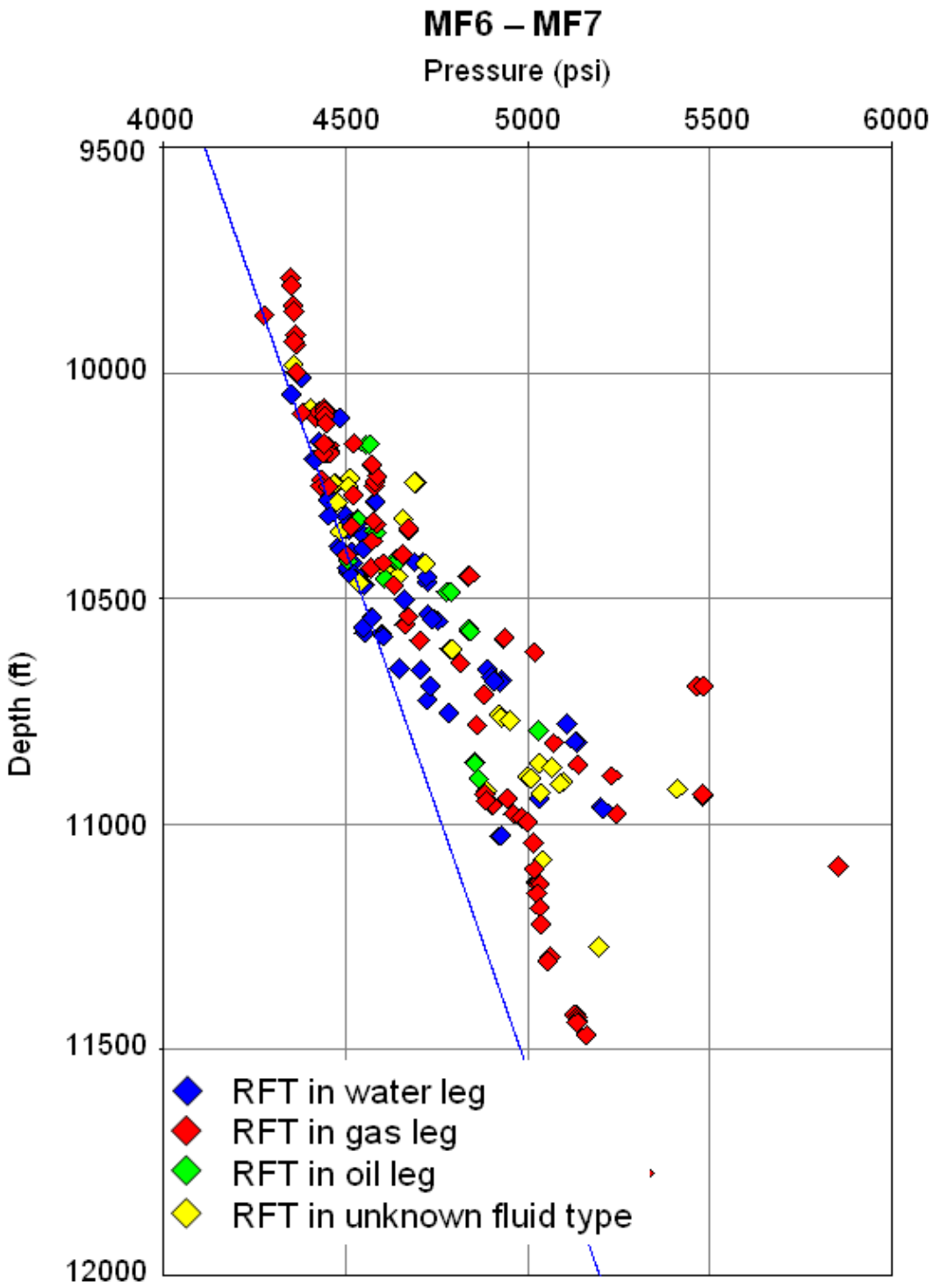
MF6 – MF7
Pressure (psi)
4000
4500
5000
5500
6000
9500
10000
10500
11000
11500
12000
Depth (ft)
RFT in water leg
RFT in gas leg
RFT in oil leg
RFT in unknown fluid type

APPENDIX 2. EXTERNAL AXIS

Appendix 2b

Pressure–depth plots, wireline log responses, and cross-plots for mudrocks in overpressured wells

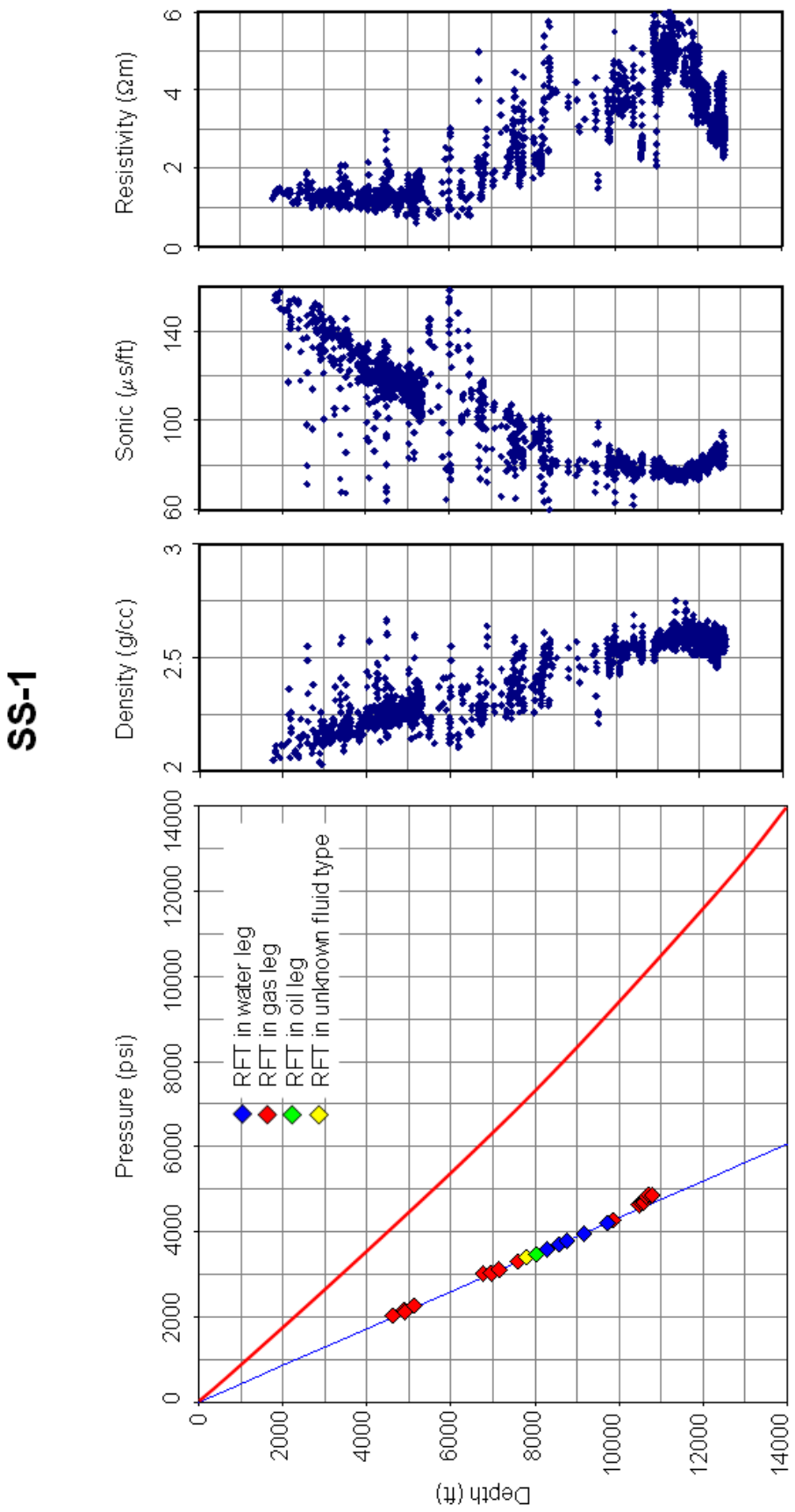
SS-1
Resistivity (Ωm)
0
2
4
6
Sonic (μs/ft)
60
100
140
Density (g/cc)
2
2.5
3
Pressure (psi)
0
2000
4000
6000
8000
10000
12000
14000
RFT in water leg
RFT in gas leg
RFT in oil leg
RFT in unknown fluid type
Depth (ft)
0
2000
4000
6000
8000
10000
12000
14000

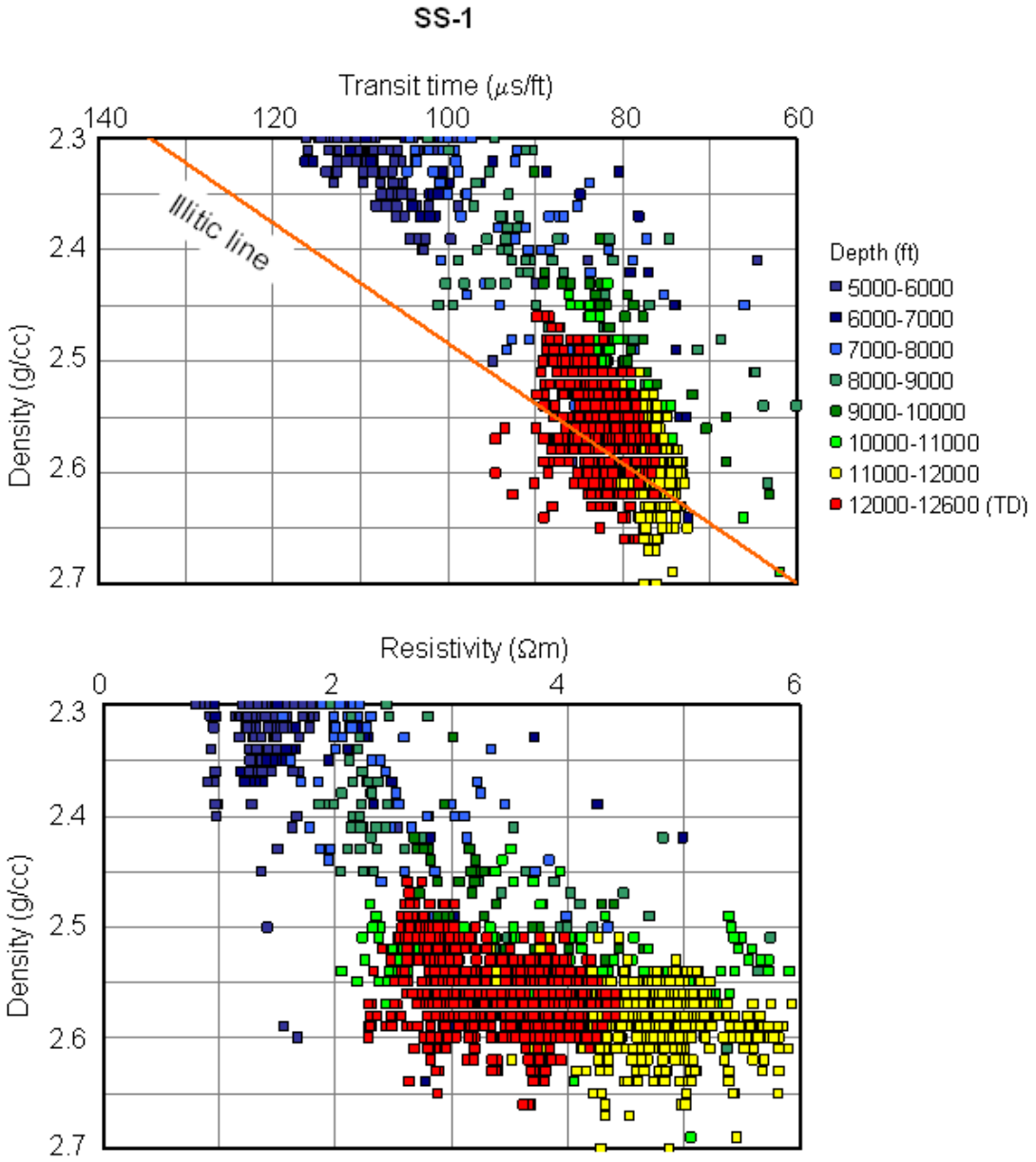
SS-1
Transit time (μs/ft)
140
120
100
80
60
2.3
2.4
2.5
2.6
2.7
Density (g/cc)
Illitic line
Depth (ft)
5000-6000
6000-7000
7000-8000
8000-9000
9000-10000
10000-11000
11000-12000
12000-12600 (TD)
Resistivity (Ωm)
0
2
4
6

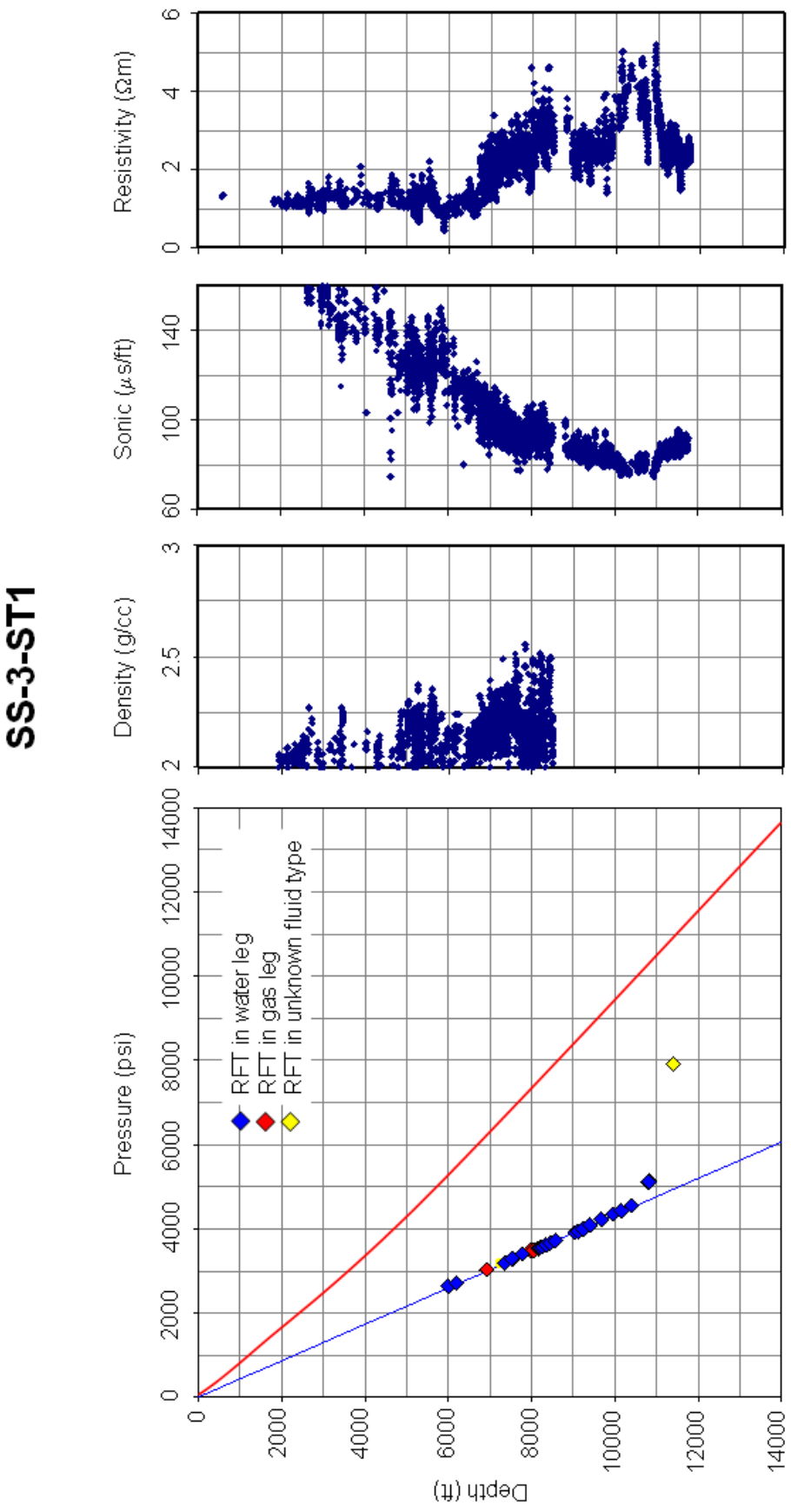
SS-3-ST1
Resistivity (Ωm)
0
2
4
6
Sonic (μs/ft)
60
100
140
Density (g/cc)
2
2.5
3
Pressure (psi)
0
2000
4000
6000
8000
10000
12000
14000
RFT in water leg
RFT in gas leg
RFT in unknown fluid type
Depth (ft)
0
2000
4000
6000
8000
10000
12000
14000

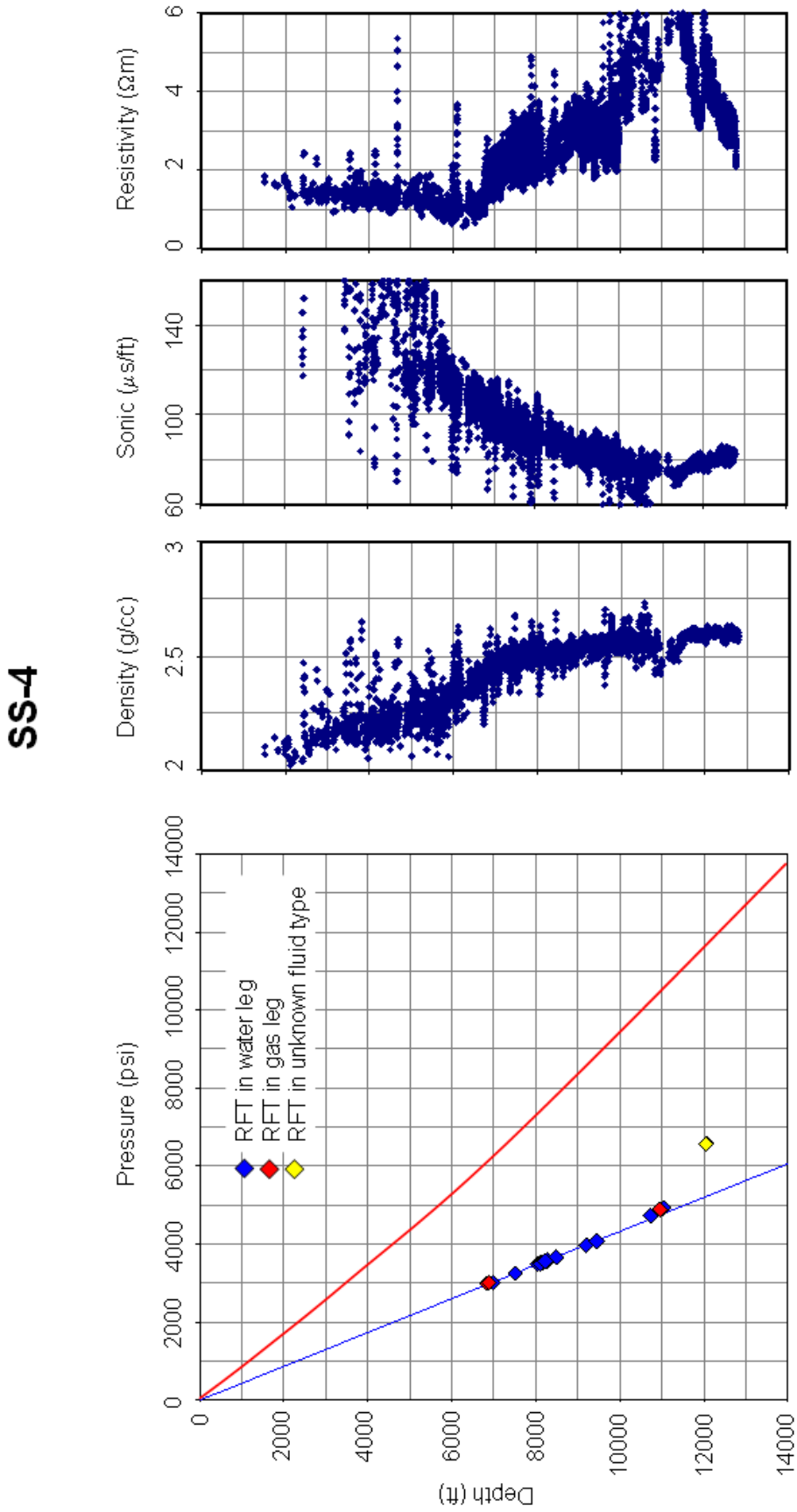
SS-4
Resistivity (Ωm)
0
2
4
6
Sonic (μs/ft)
60
100
140
Density (g/cc)
2
2.5
3
Pressure (psi)
0
2000
4000
6000
8000
10000
12000
14000
RFT in water leg
RFT in gas leg
RFT in unknown fluid type
Depth (ft)
0
2000
4000
6000
8000
10000
12000
14000

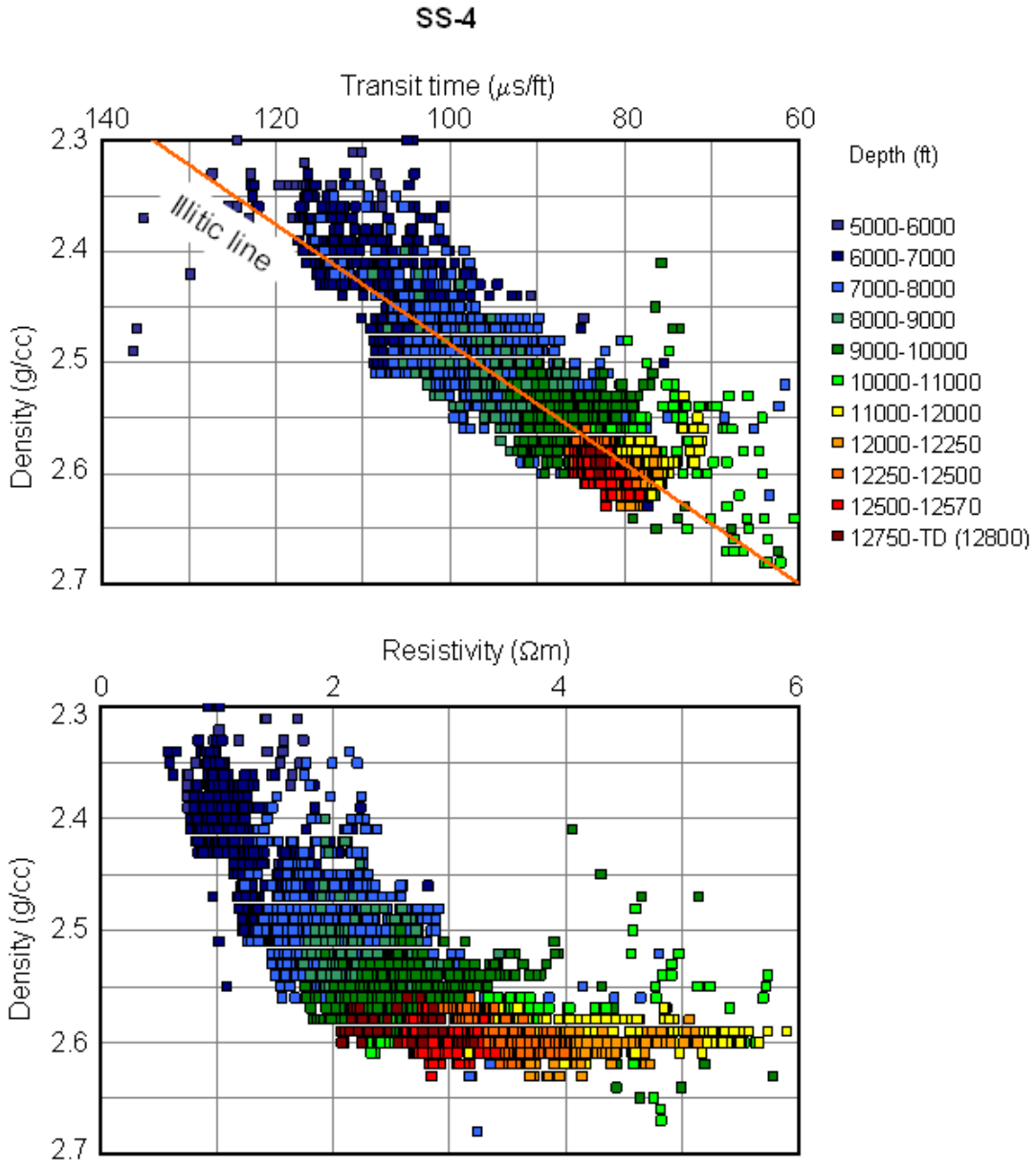
SS-4
Transit time (μs/ft)
140
120
100
80
60
Density (g/cc)
2.3
2.4
2.5
2.6
2.7
Illitic line
Depth (ft)
5000-6000
6000-7000
7000-8000
8000-9000
9000-10000
10000-11000
11000-12000
12000-12250
12250-12500
12500-12570
12750-TD (12800)
Resistivity (Ωm)
0
2
4
6
Density (g/cc)
2.3
2.4
2.5
2.6
2.7

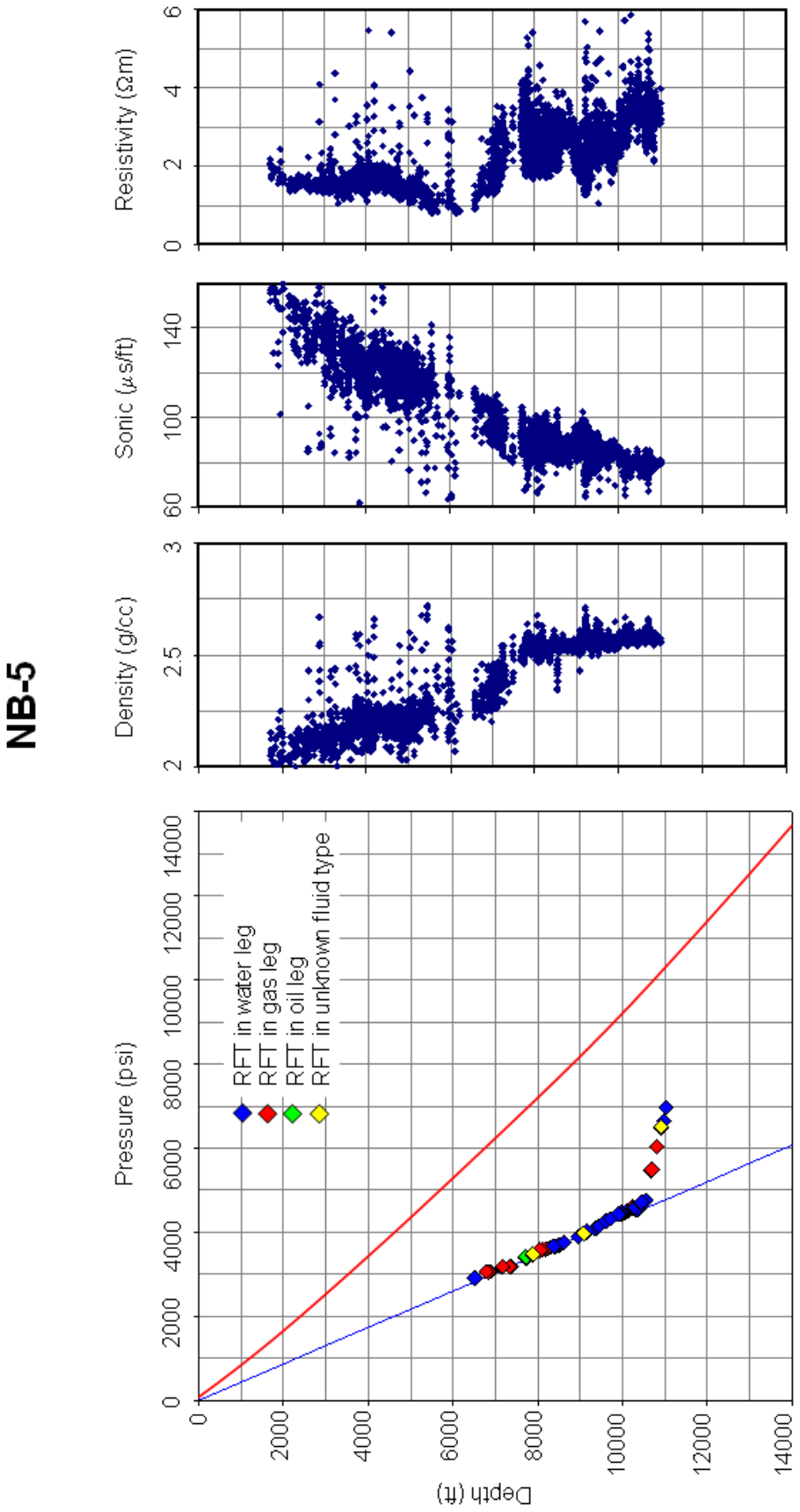
NB-5
Resistivity (Ωm)
0
2
4
6
Sonic (μs/ft)
60
100
140
Density (g/cc)
2
2.5
3
Pressure (psi)
0
2000
4000
6000
8000
10000
12000
14000
RFT in water leg
RFT in gas leg
RFT in oil leg
RFT in unknown fluid type
Depth (ft)
0
2000
4000
6000
8000
10000
12000
14000

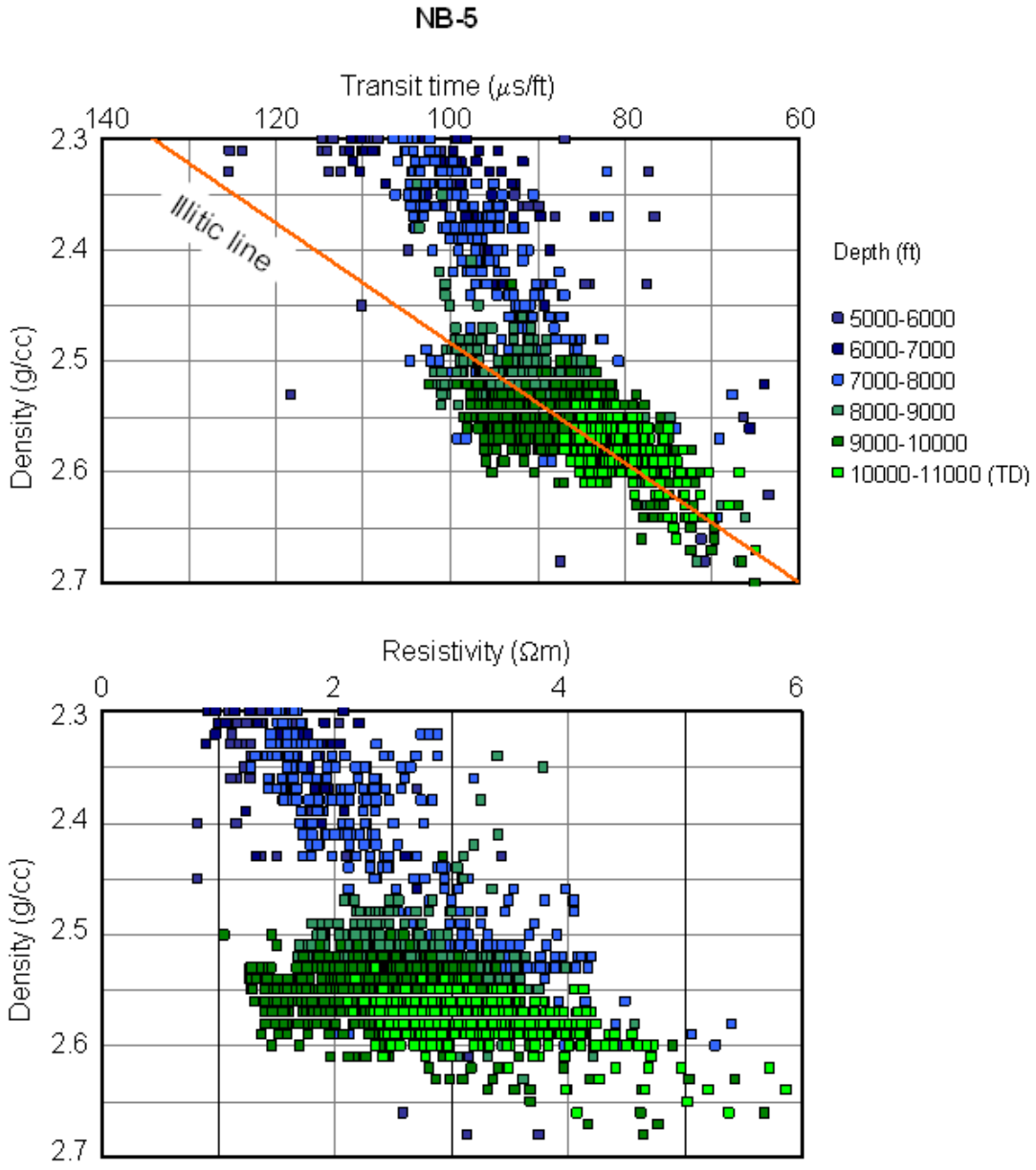
NB-5
Transit time (μs/ft)
140
120
100
80
60
2.3
2.4
2.5
2.6
2.7
Density (g/cc)
Illitic line
Depth (ft)
5000-6000
6000-7000
7000-8000
8000-9000
9000-10000
10000-11000 (TD)
Resistivity (Ωm)
0
2
4
6
2.3
2.4
2.5
2.6
2.7
Density (g/cc)

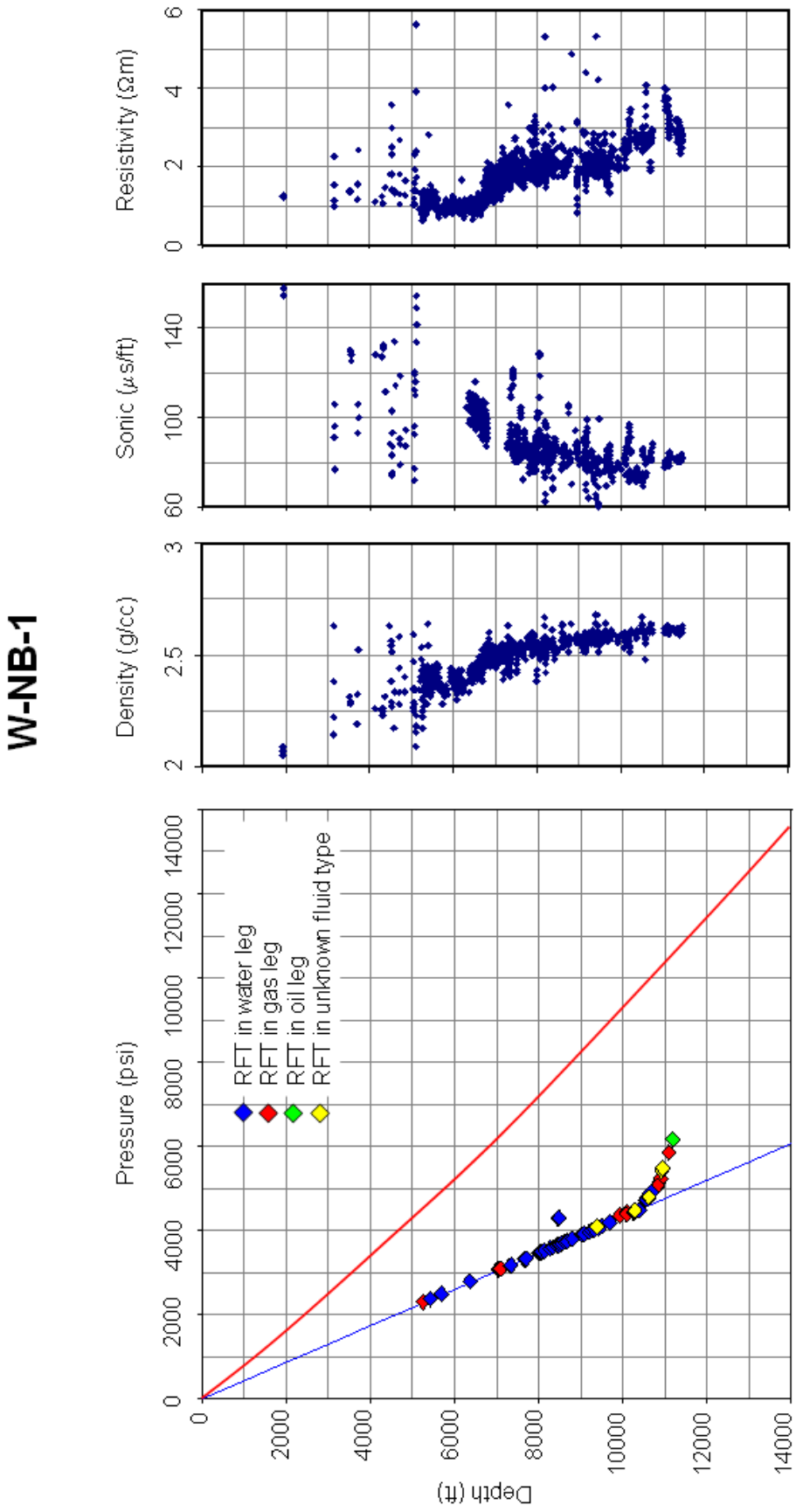
W-NB-1
Resistivity (Ωm)
0
2
4
6
Sonic (μs/ft)
60
100
140
Density (g/cc)
2
2.5
3
Pressure (psi)
0
2000
4000
6000
8000
10000
12000
14000
RFT in water leg
RFT in gas leg
RFT in oil leg
RFT in unknown fluid type
Depth (ft)
0
2000
4000
6000
8000
10000
12000
14000

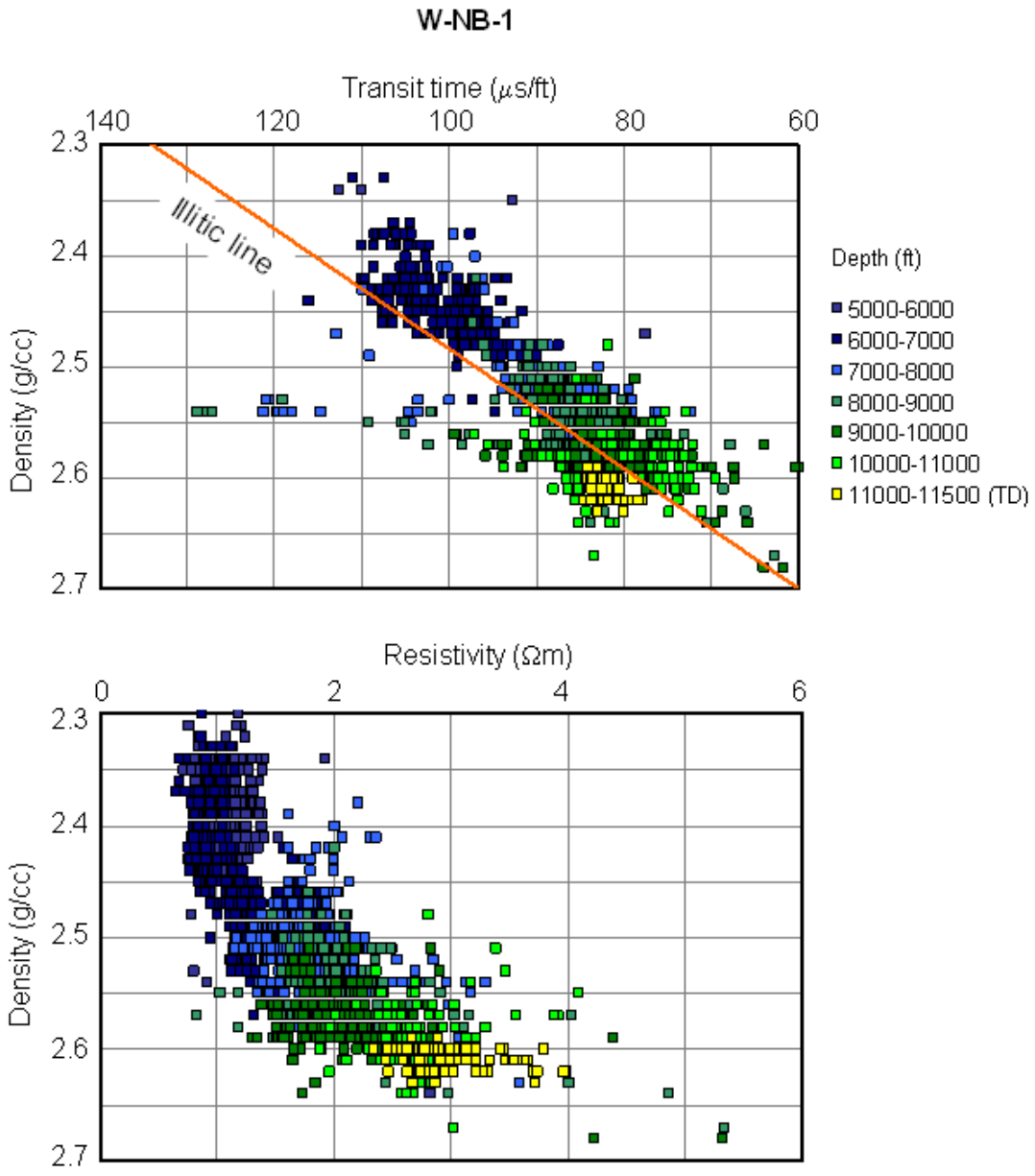
W-NB-1
Transit time (μs/ft)
140
120
100
80
60
2.3
2.4
2.5
2.6
2.7
Density (g/cc)
Illitic line
Depth (ft)
5000-6000
6000-7000
7000-8000
8000-9000
9000-10000
10000-11000
11000-11500 (TD)
Resistivity (Ωm)
0
2
4
6
2.3
2.4
2.5
2.6
2.7
Density (g/cc)

APPENDIX 3. MEDIAN AXIS

Appendix 3a

Pressure–depth plots for intermediate stratigraphic units, Tunu Field, as shown in Figure 5.2

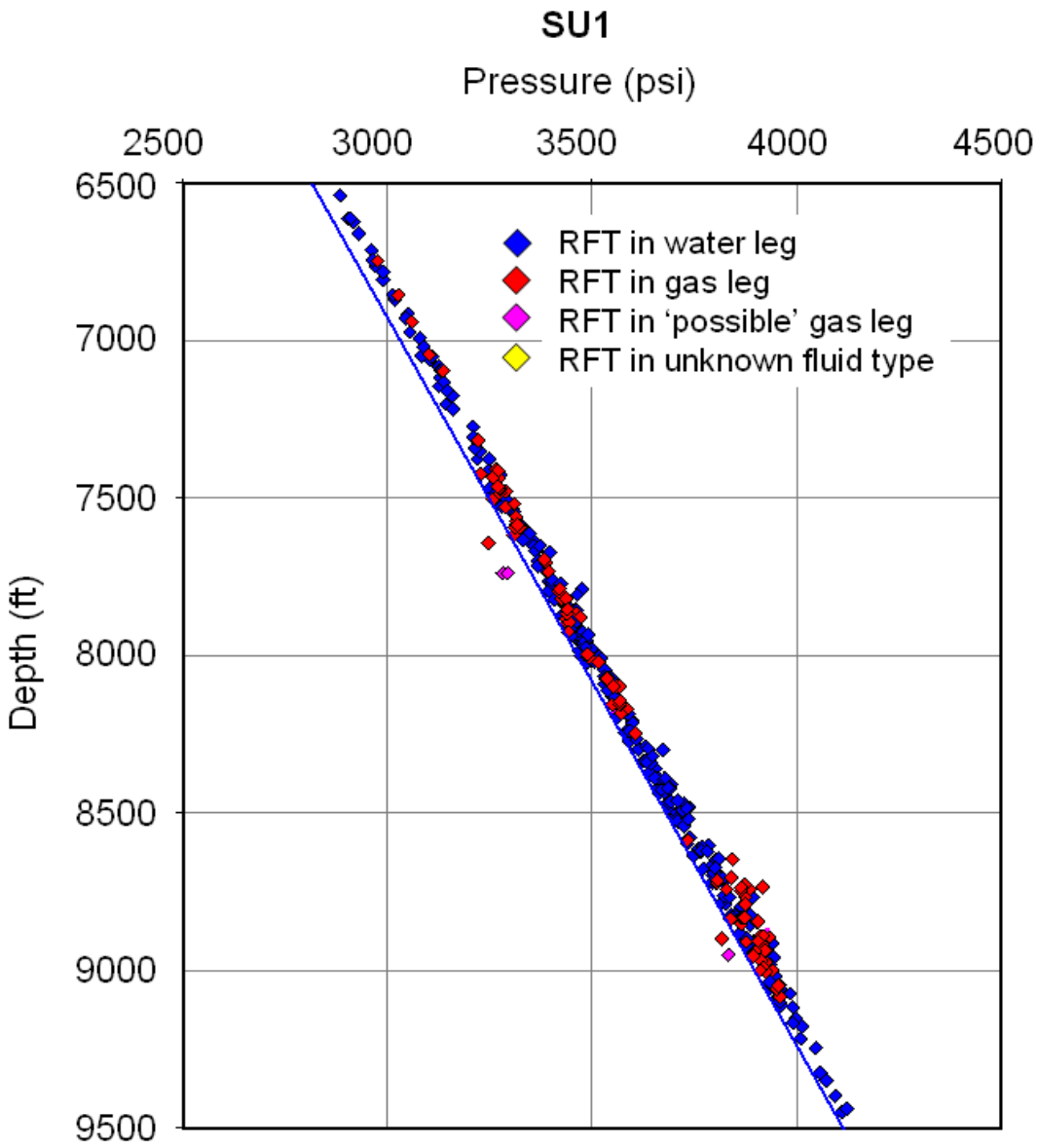
SU1
Pressure (psi)
2500
3000
3500
4000
4500
6500
7000
7500
8000
8500
9000
9500
Depth (ft)
RFT in water leg
RFT in gas leg
RFT in 'possible' gas leg
RFT in unknown fluid type

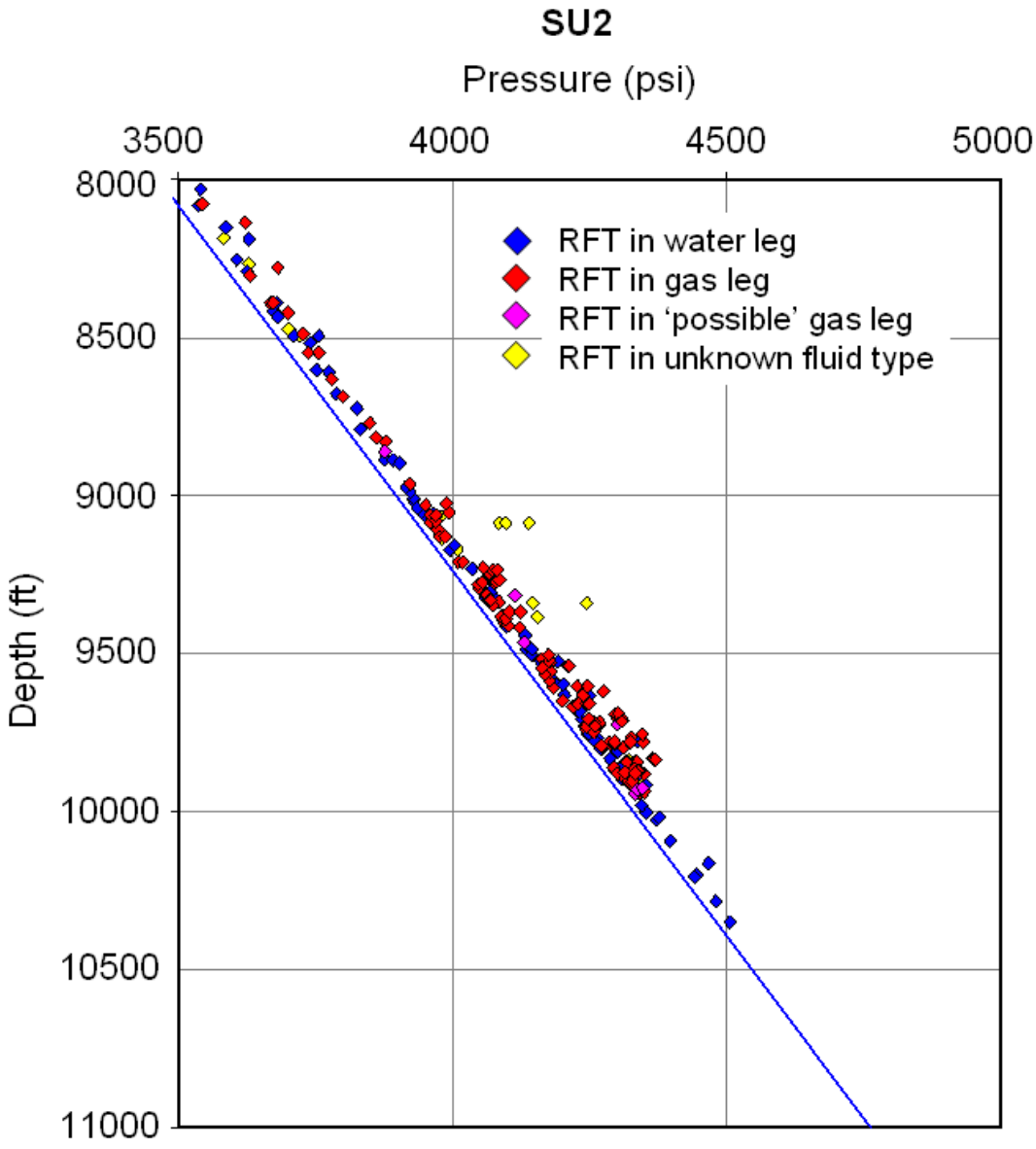
SU2
Pressure (psi)
3500
4000
4500
5000
8000
8500
9000
9500
10000
10500
11000
Depth (ft)
RFT in water leg
RFT in gas leg
RFT in 'possible' gas leg
RFT in unknown fluid type

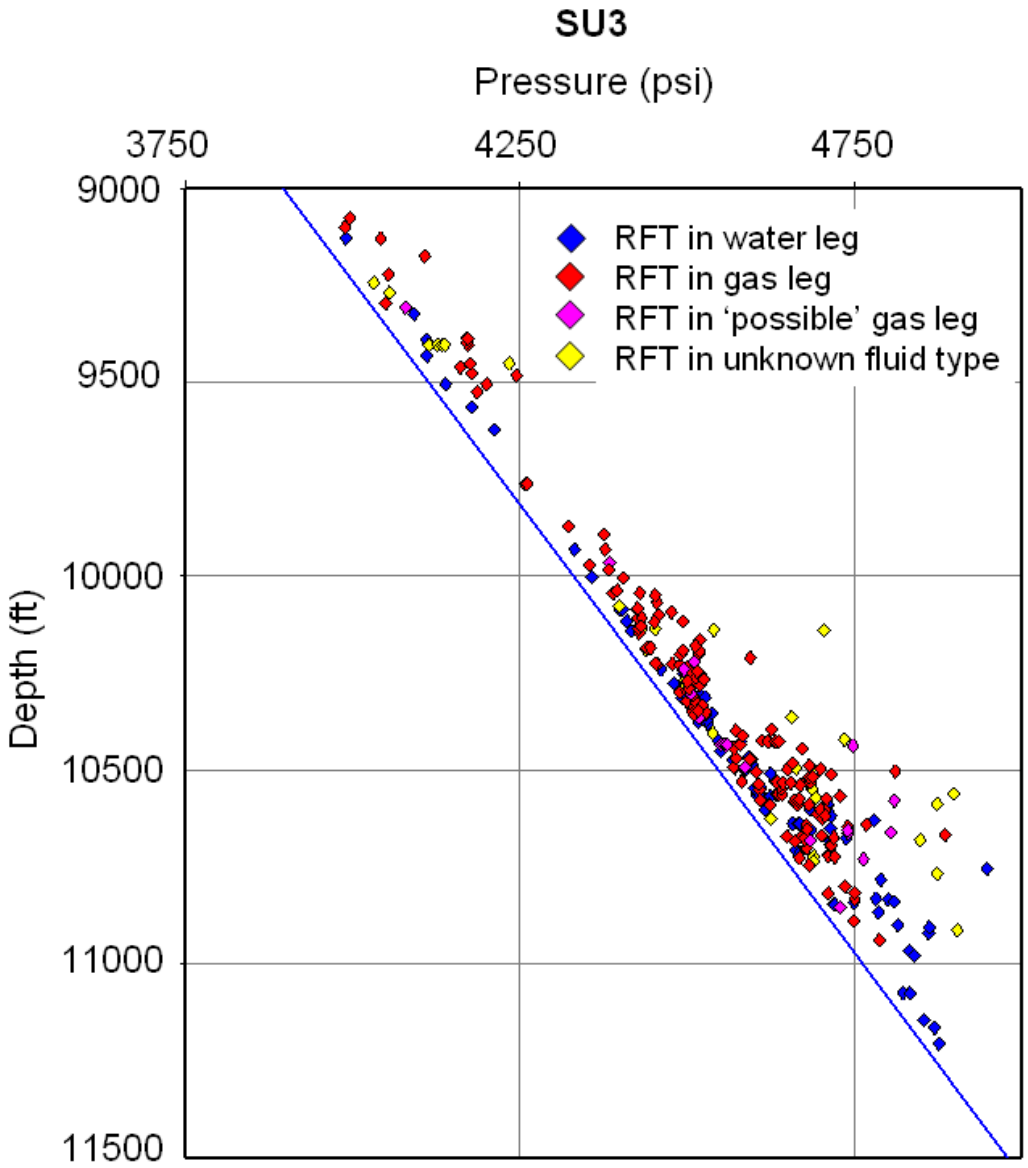
SU3
Pressure (psi)
3750
4250
4750
9000
9500
10000
10500
11000
11500
Depth (ft)
RFT in water leg
RFT in gas leg
RFT in 'possible' gas leg
RFT in unknown fluid type

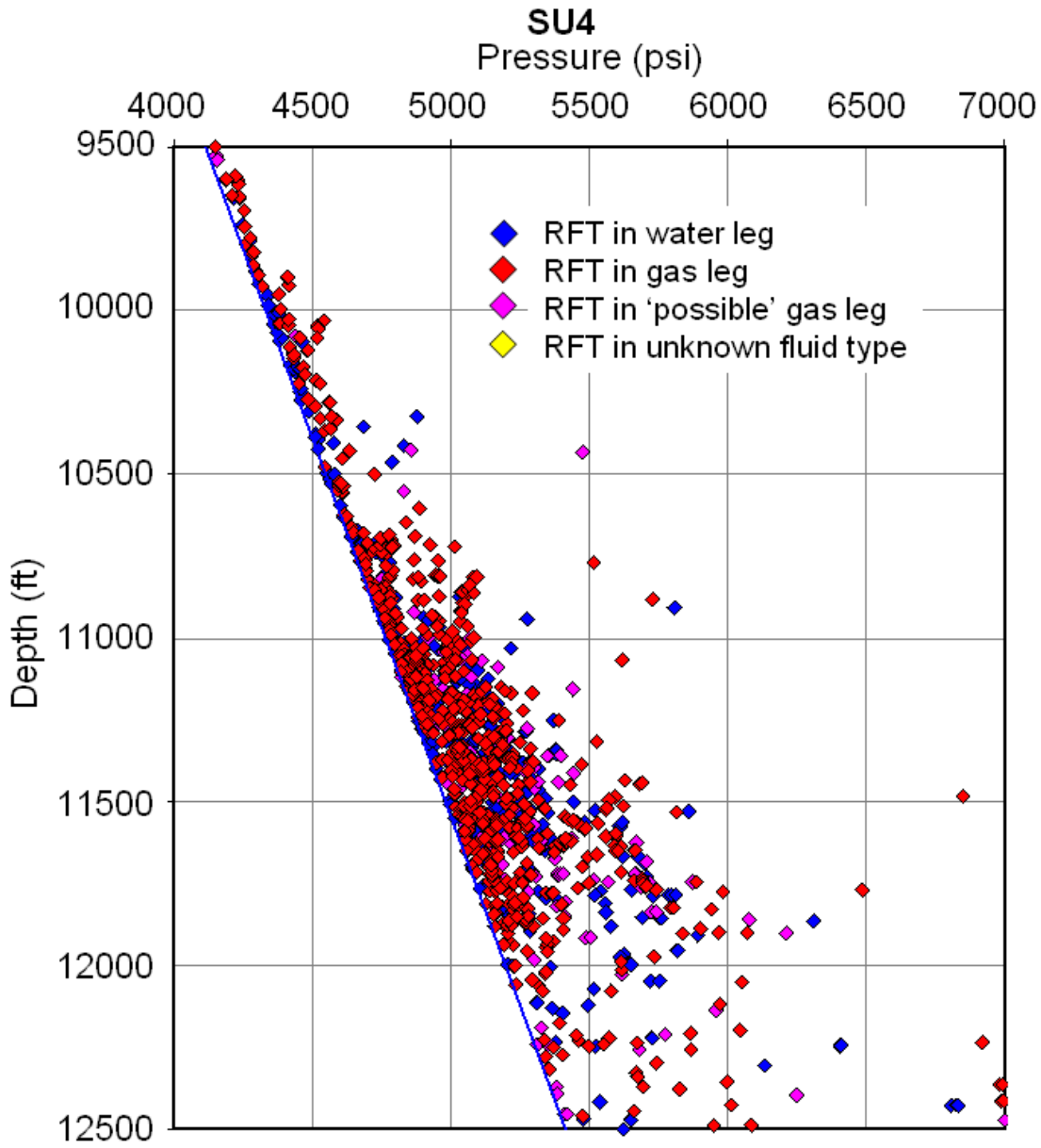
SU4
Pressure (psi)
4000
4500
5000
5500
6000
6500
7000
9500
10000
10500
11000
11500
12000
12500
Depth (ft)
RFT in water leg
RFT in gas leg
RFT in 'possible' gas leg
RFT in unknown fluid type

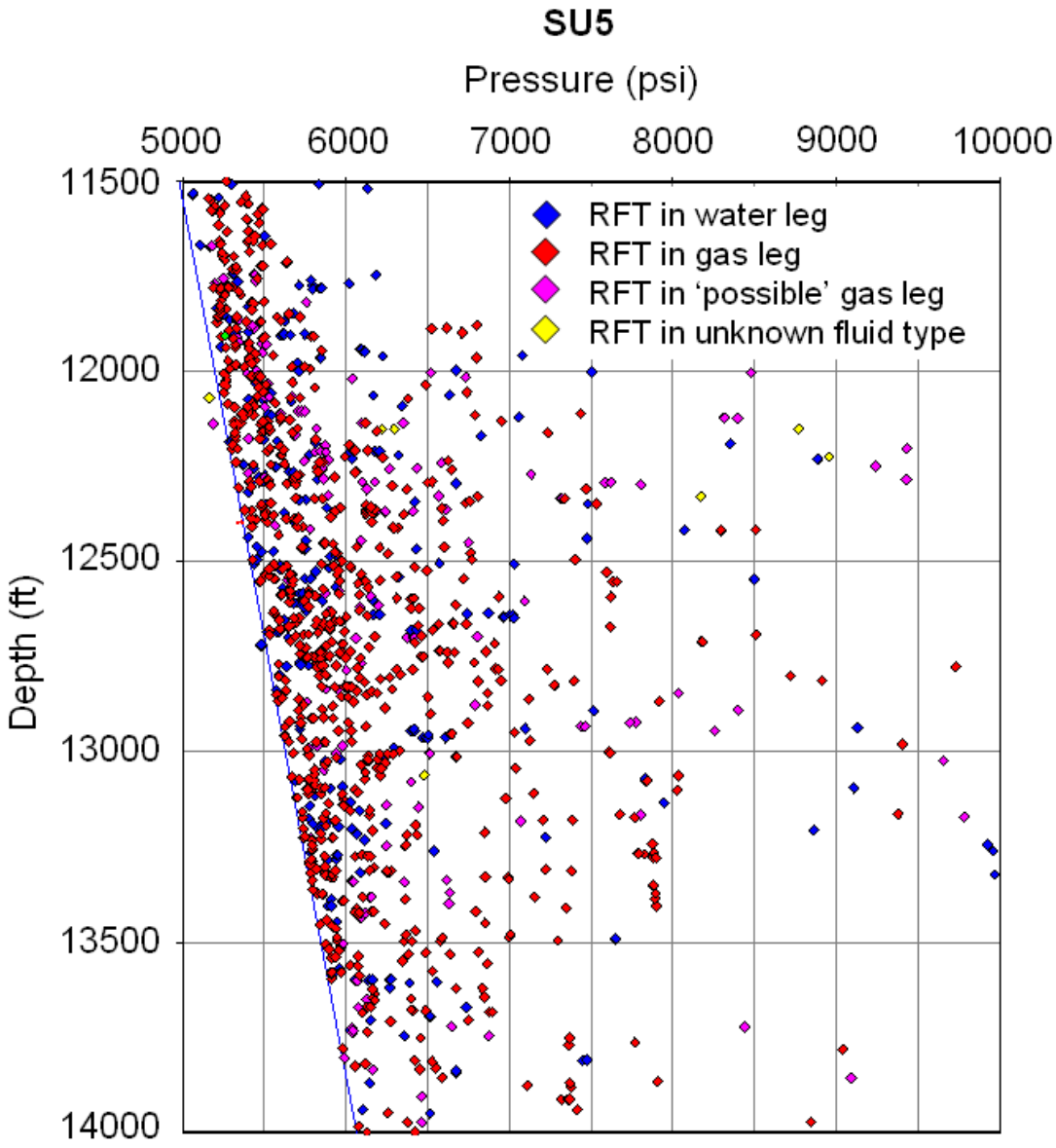
SU5
Pressure (psi)
5000
6000
7000
8000
9000
10000
11500
12000
12500
13000
13500
14000
Depth (ft)
RFT in water leg
RFT in gas leg
RFT in 'possible' gas leg
RFT in unknown fluid type

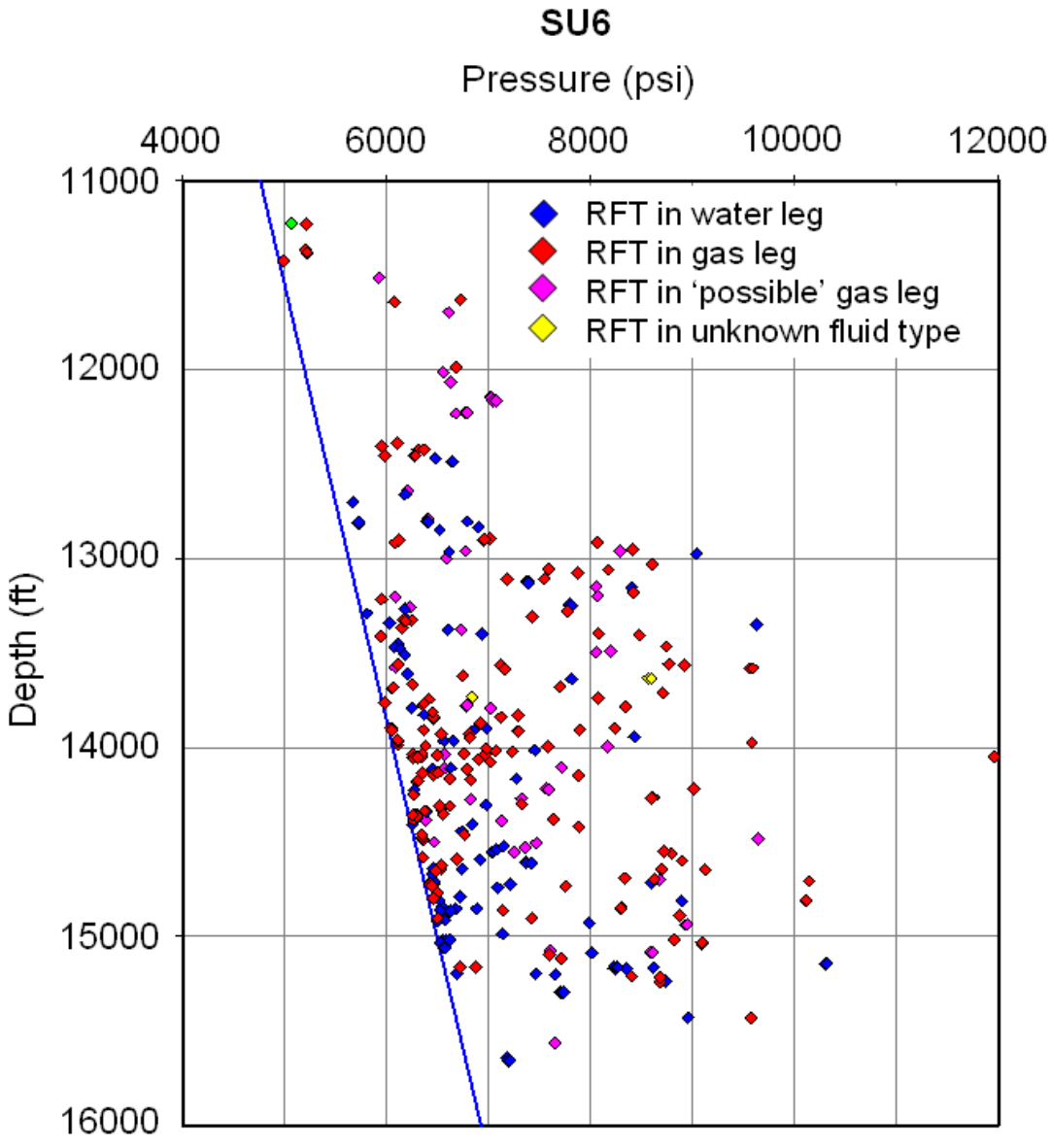
SU6
Pressure (psi)
4000
6000
8000
10000
12000
11000
12000
13000
14000
15000
16000
Depth (ft)
RFT in water leg
RFT in gas leg
RFT in 'possible' gas leg
RFT in unknown fluid type

APPENDIX 3. MEDIAN AXIS

Appendix 3b

Pressure–depth plots, wireline log responses, and cross-plots for mudrocks in overpressured wells, Bekapai Field

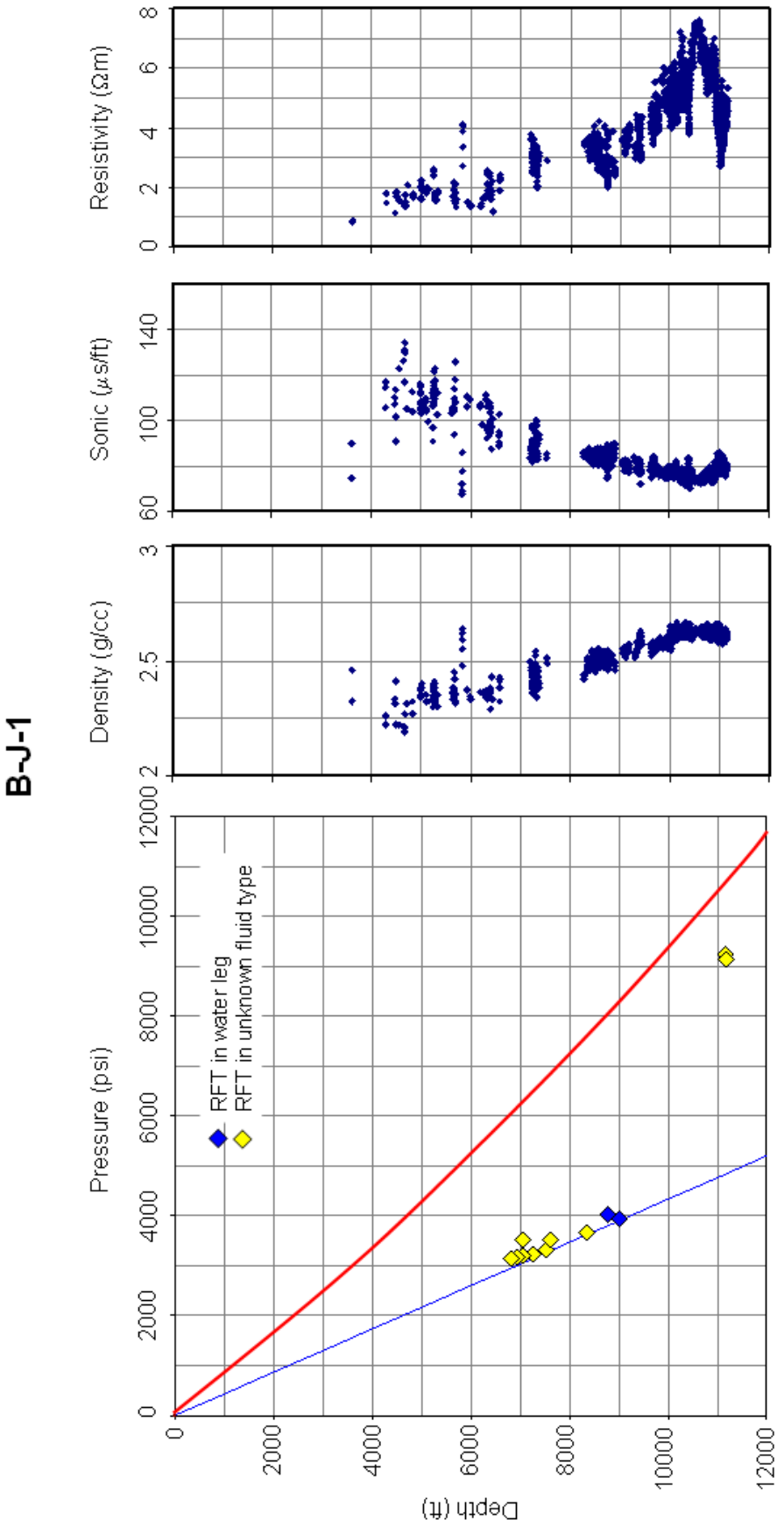
B-J-1
Resistivity (Ωm)
0
2
4
6
8
Sonic (μs/ft)
60
100
140
Density (g/cc)
2
2.5
3
Pressure (psi)
0
2000
4000
6000
8000
10000
12000
RFT in water leg
RFT in unknown fluid type
Depth (ft)
0
2000
4000
6000
8000
10000
12000

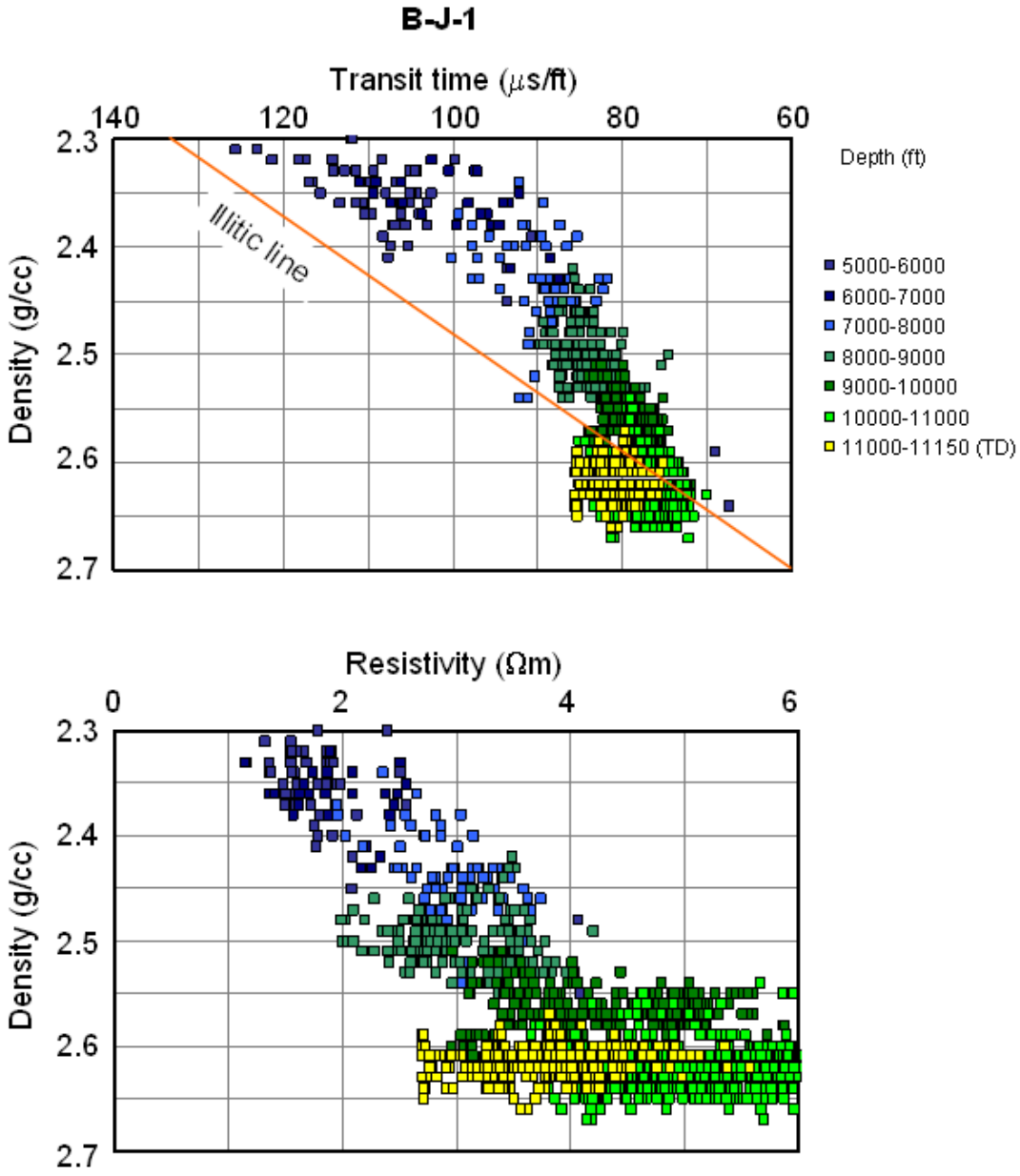
B-J-1
Transit time (μs/ft)
140
120
100
80
60
Density (g/cc)
2.3
2.4
2.5
2.6
2.7
Illitic line
Depth (ft)
5000-6000
6000-7000
7000-8000
8000-9000
9000-10000
10000-11000
11000-11150 (TD)
Resistivity (Ωm)
0
2
4
6
Density (g/cc)
2.3
2.4
2.5
2.6
2.7

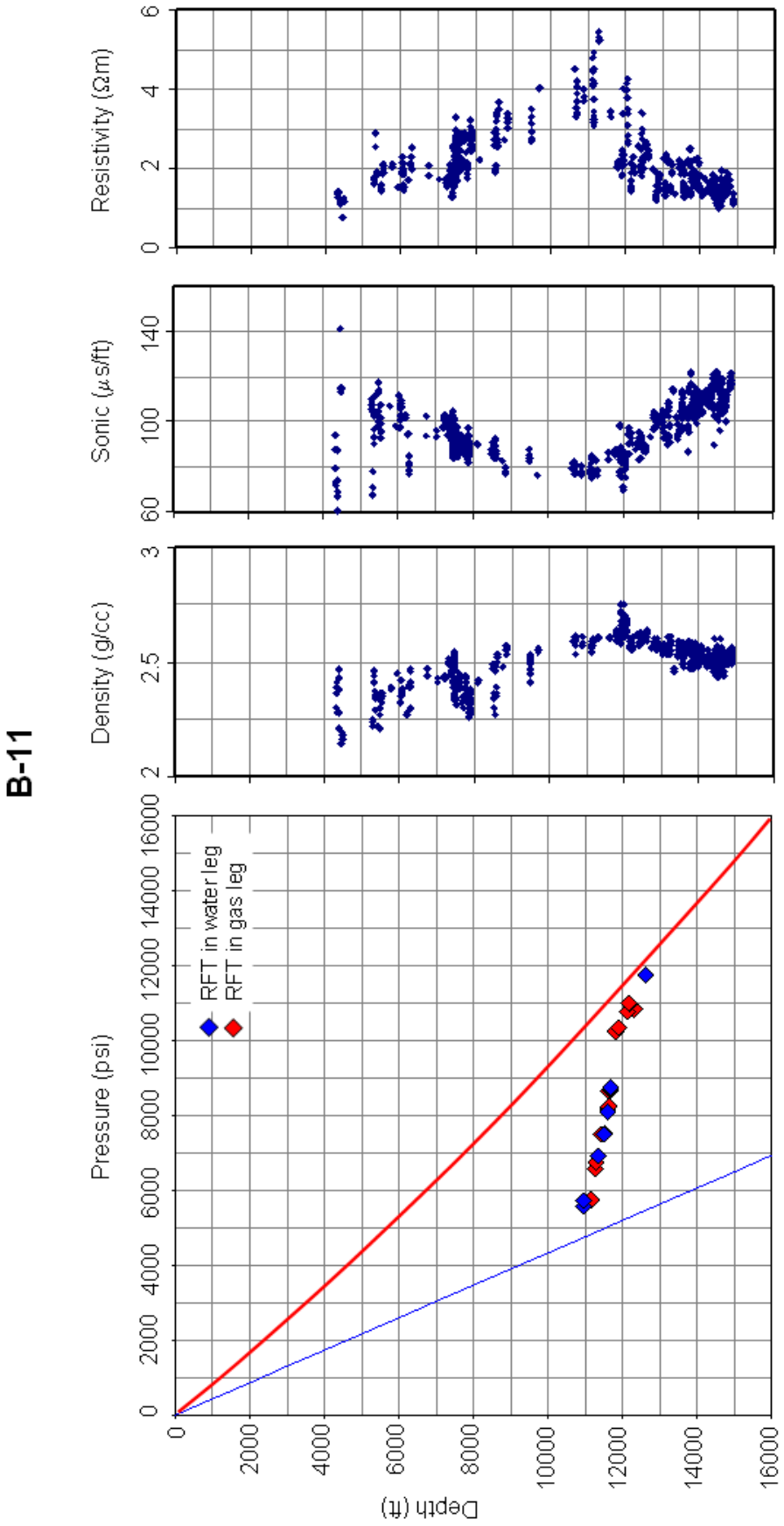
B-11
Resistivity (Ωm)
0
2
4
6
Sonic (μs/ft)
60
100
140
Density (g/cc)
2
2.5
3
Pressure (psi)
0
2000
4000
6000
8000
10000
12000
14000
16000
RFT in water leg
RFT in gas leg
Depth (ft)
0
2000
4000
6000
8000
10000
12000
14000
16000

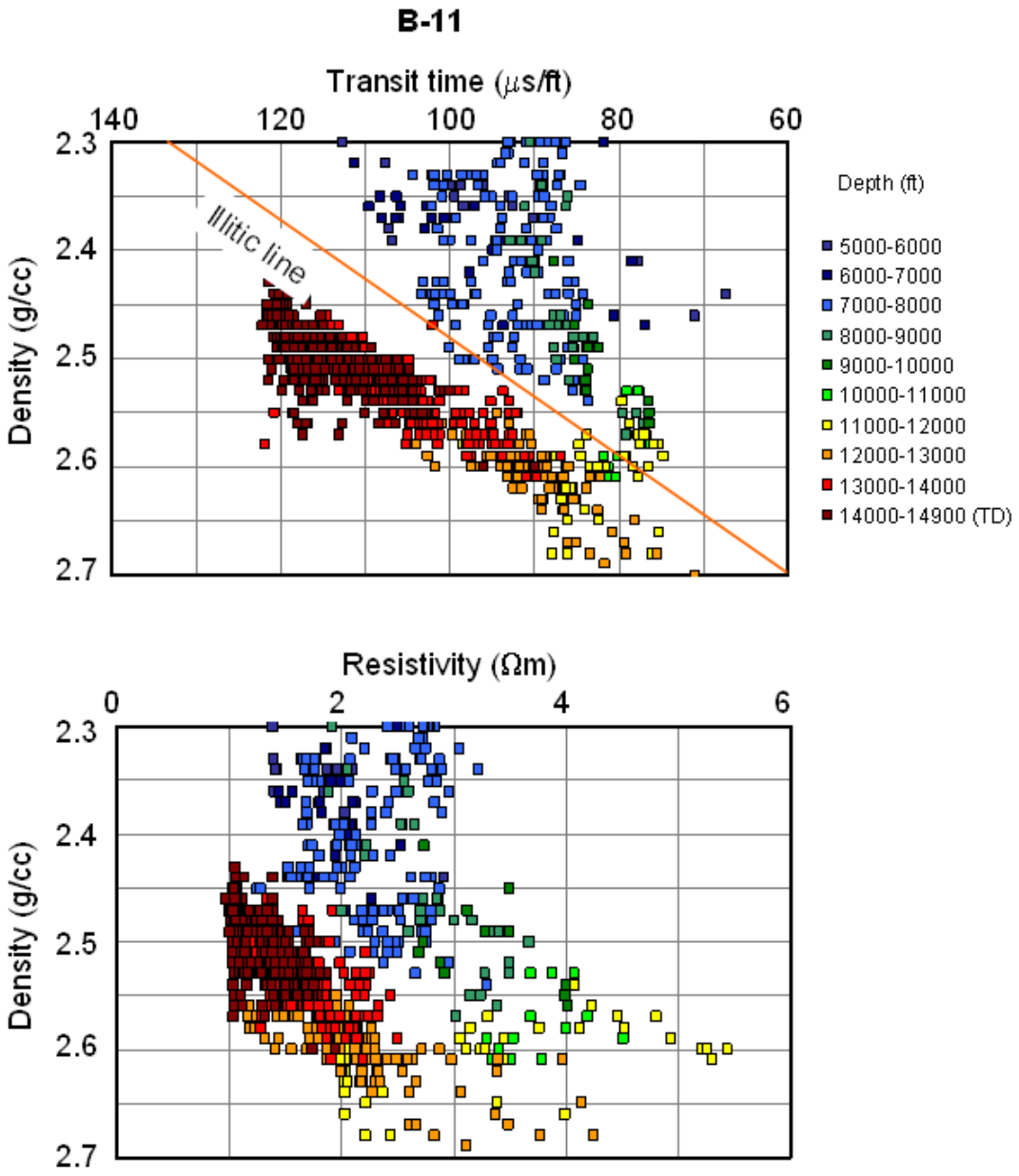
B-11
Transit time (μs/ft)
140
120
100
80
60
Density (g/cc)
2.3
2.4
2.5
2.6
2.7
Illitic line
Depth (ft)
5000-6000
6000-7000
7000-8000
8000-9000
9000-10000
10000-11000
11000-12000
12000-13000
13000-14000
14000-14900 (TD)
Resistivity (Ωm)
0
2
4
6
Density (g/cc)
2.3
2.4
2.5
2.6
2.7

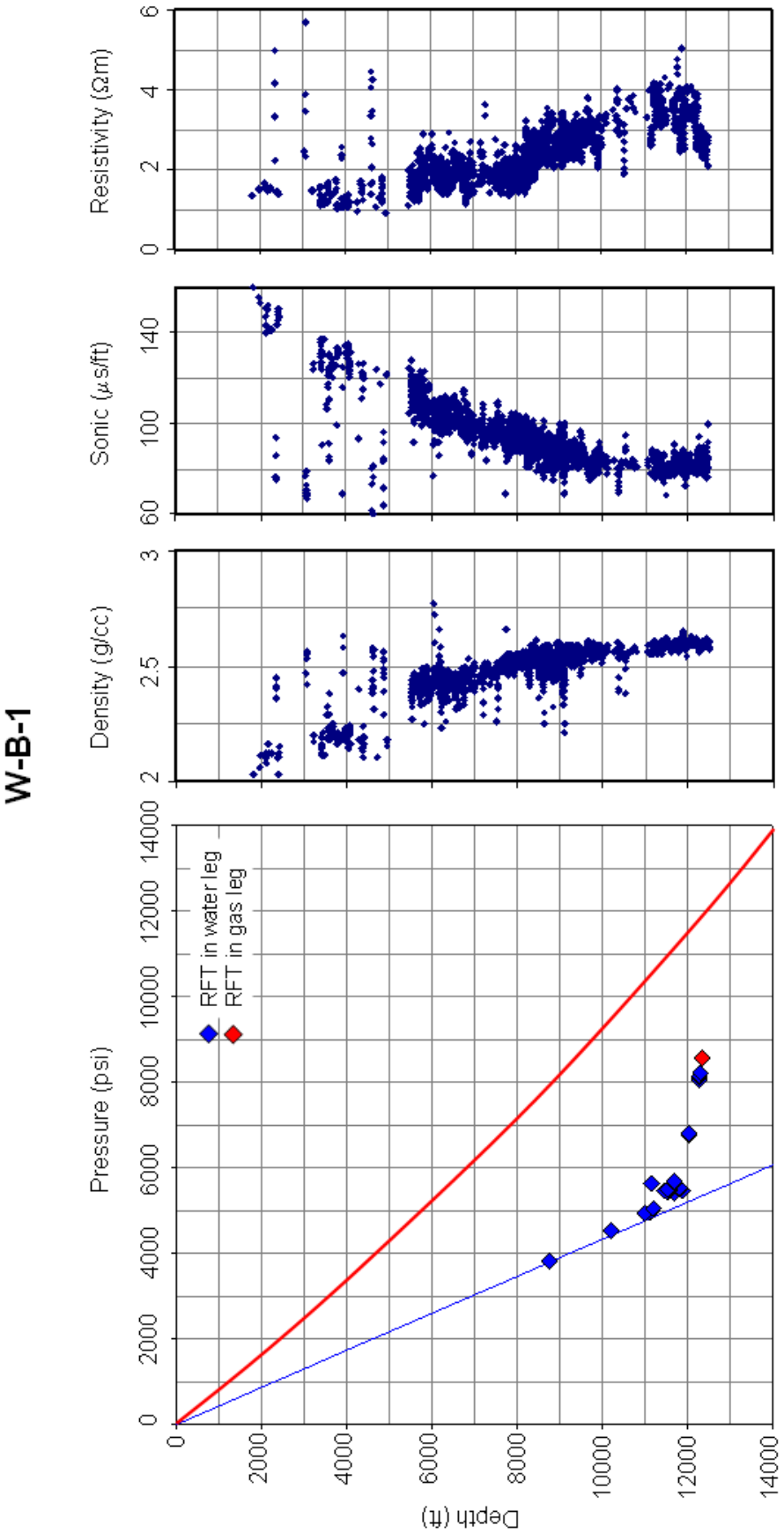
W-B-1
Resistivity (Ωm)
0
2
4
6
Sonic (μs/ft)
60
100
140
Density (g/cc)
2
2.5
3
Pressure (psi)
0
2000
4000
6000
8000
10000
12000
14000
RFT in water leg
RFT in gas leg
Depth (ft)
0
2000
4000
6000
8000
10000
12000
14000

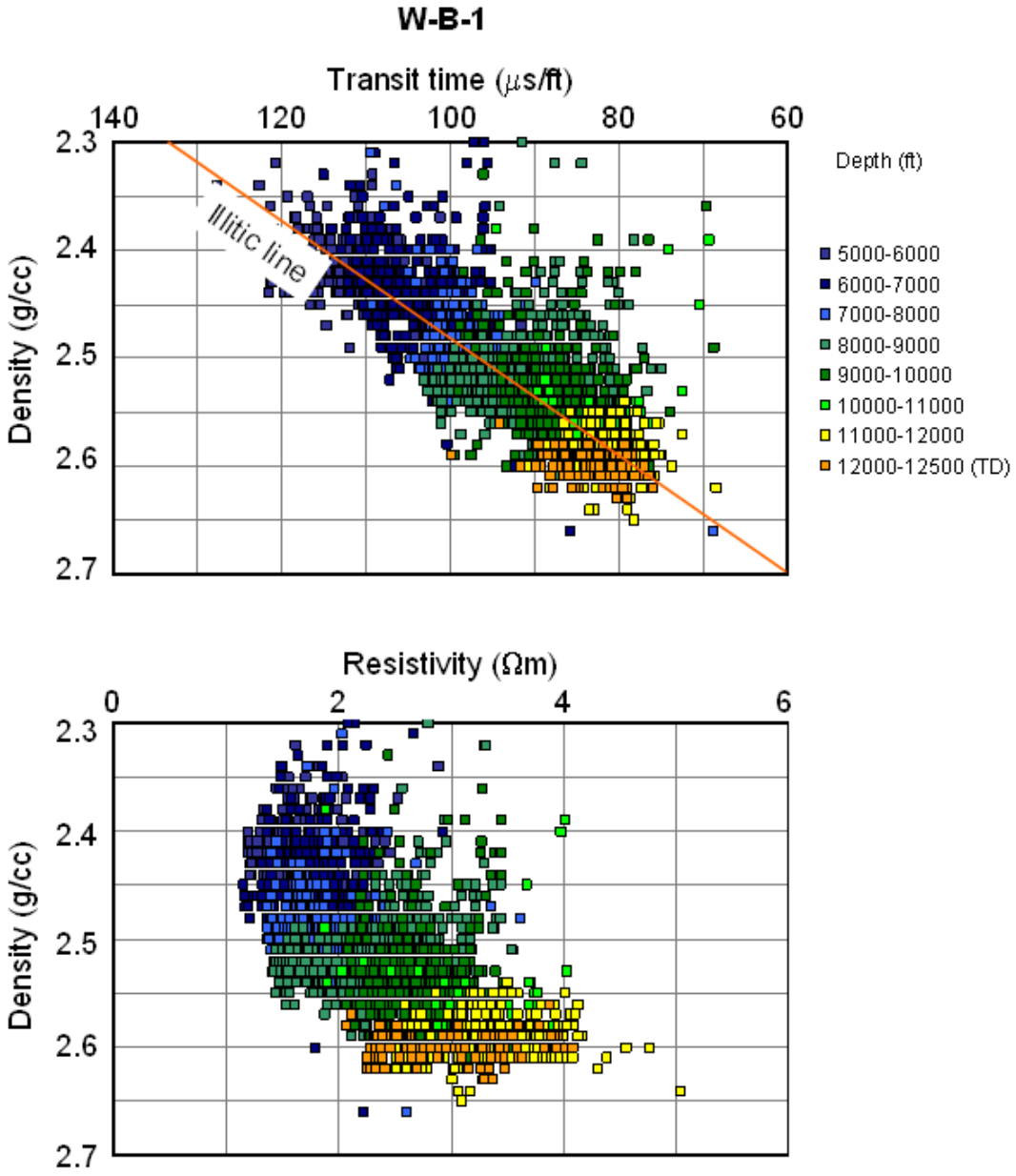
W-B-1
Transit time (μs/ft)
140
120
100
80
60
Density (g/cc)
2.3
2.4
2.5
2.6
2.7
Illitic line
Depth (ft)
5000-6000
6000-7000
7000-8000
8000-9000
9000-10000
10000-11000
11000-12000
12000-12500 (TD)
Resistivity (Ωm)
0
2
4
6
Density (g/cc)
2.3
2.4
2.5
2.6
2.7

APPENDIX 3. MEDIAN AXIS

Appendix 3c

Pressure–depth plots, wireline log responses, and cross-plots for mudrocks in overpressured wells, Tunu Field

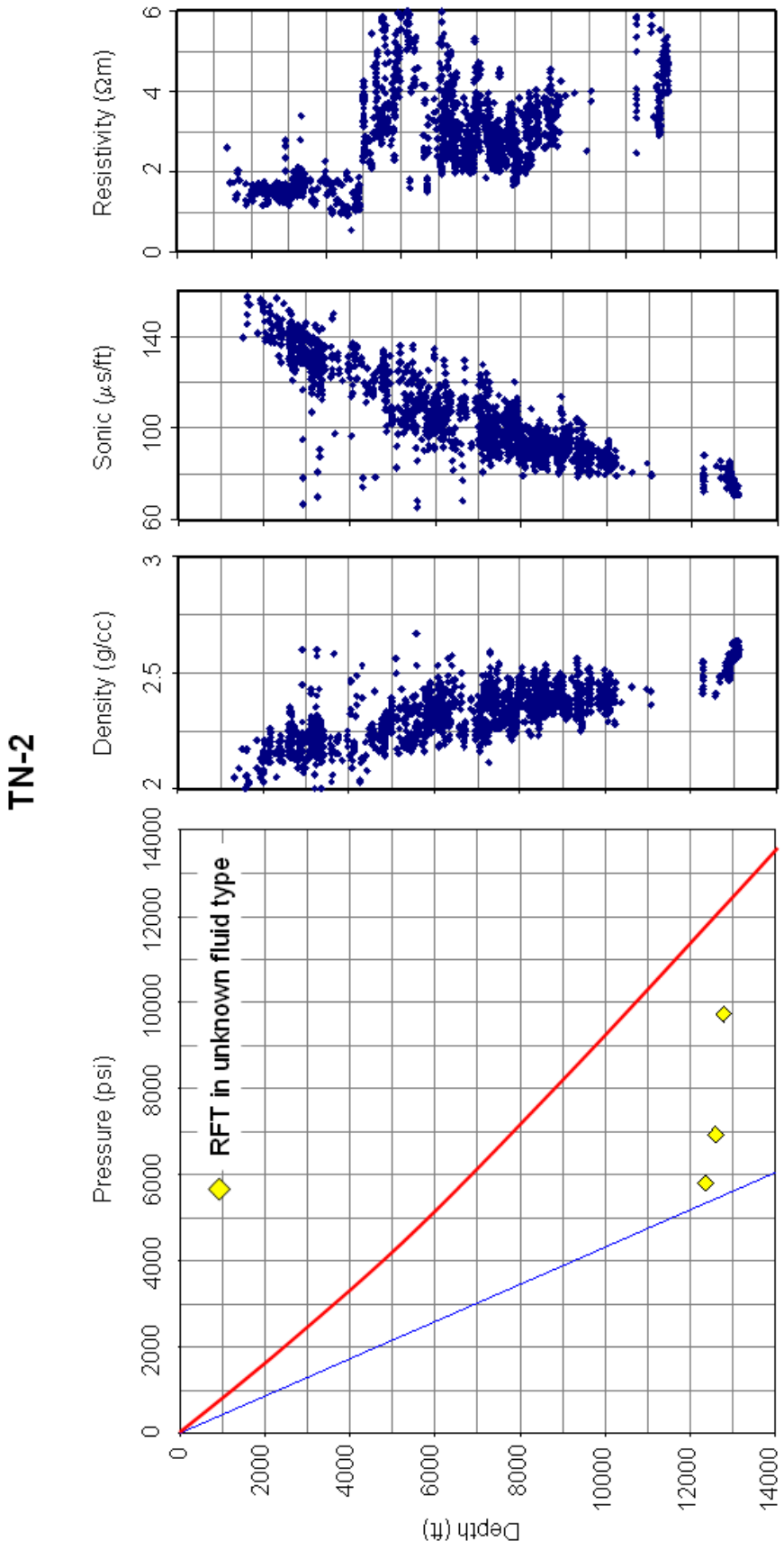
TN-2
Resistivity (Ωm)
0
2
4
6
Sonic (μs/ft)
60
100
140
Density (g/cc)
2
2.5
3
Pressure (psi)
0
2000
4000
6000
8000
10000
12000
14000
RFT in unknown fluid type
Depth (ft)
0
2000
4000
6000
8000
10000
12000
14000

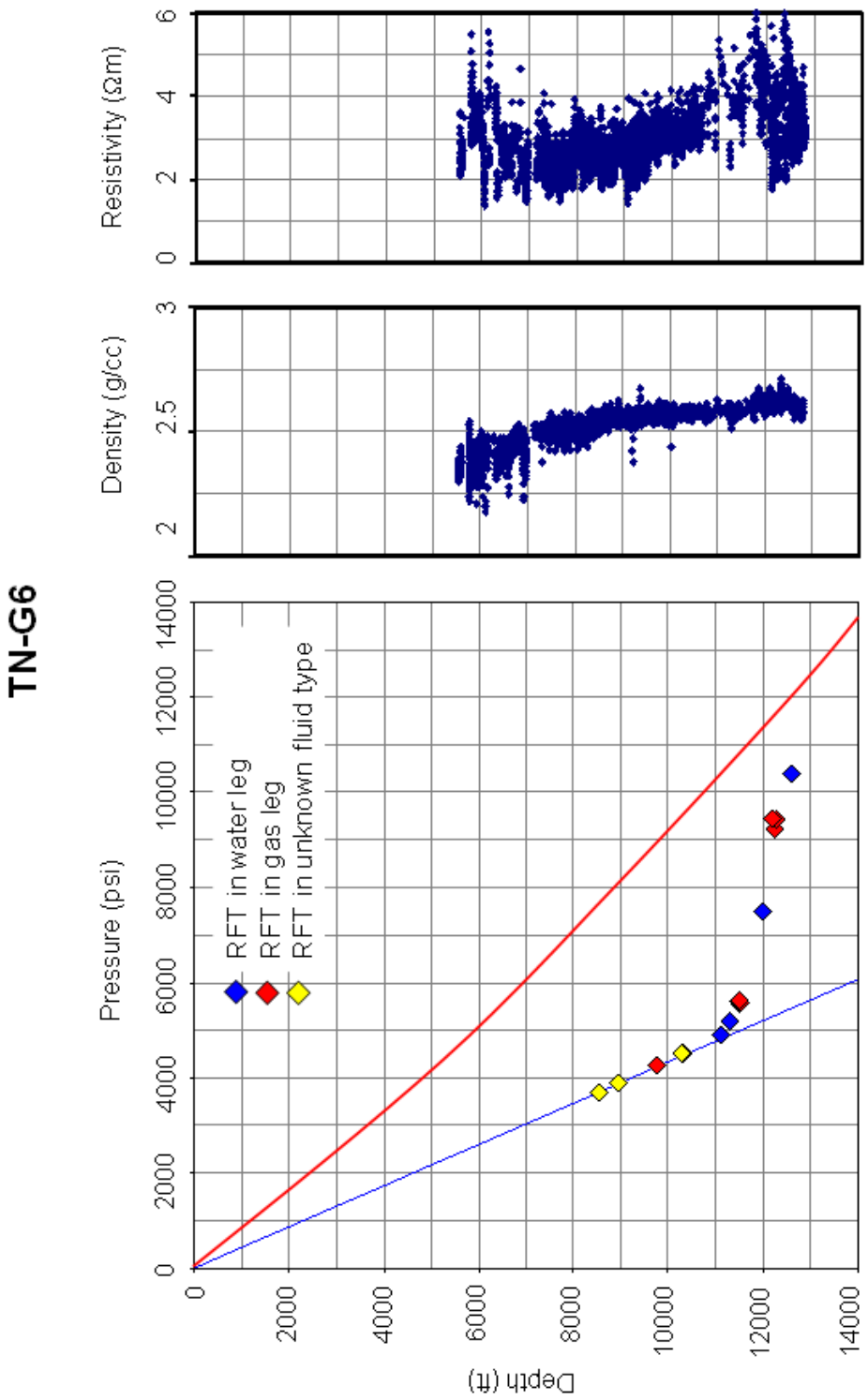
TN-G6
Resistivity (Ωm)
0
2
4
6
Density (g/cc)
2
2.5
3
Pressure (psi)
0
2000
4000
6000
8000
10000
12000
14000
RFT in water leg
RFT in gas leg
RFT in unknown fluid type
Depth (ft)
0
2000
4000
6000
8000
10000
12000
14000

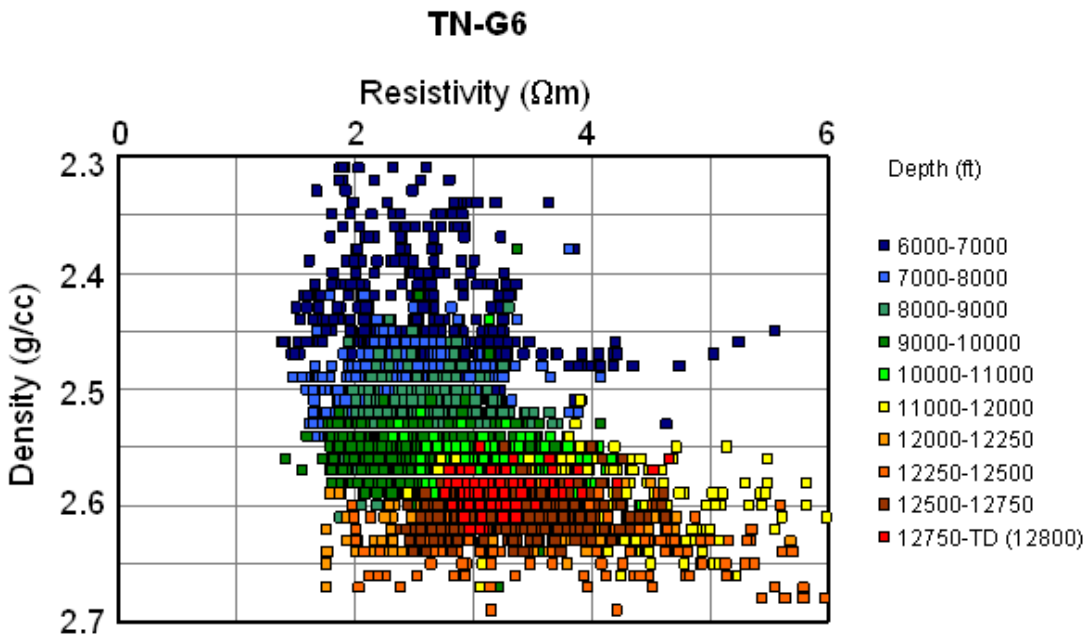
TN-G6
Resistivity (Ωm)
0
2
4
6
Density (g/cc)
2.3
2.4
2.5
2.6
2.7
Depth (ft)
6000-7000
7000-8000
8000-9000
9000-10000
10000-11000
11000-12000
12000-12250
12250-12500
12500-12750
12750-TD (12800)

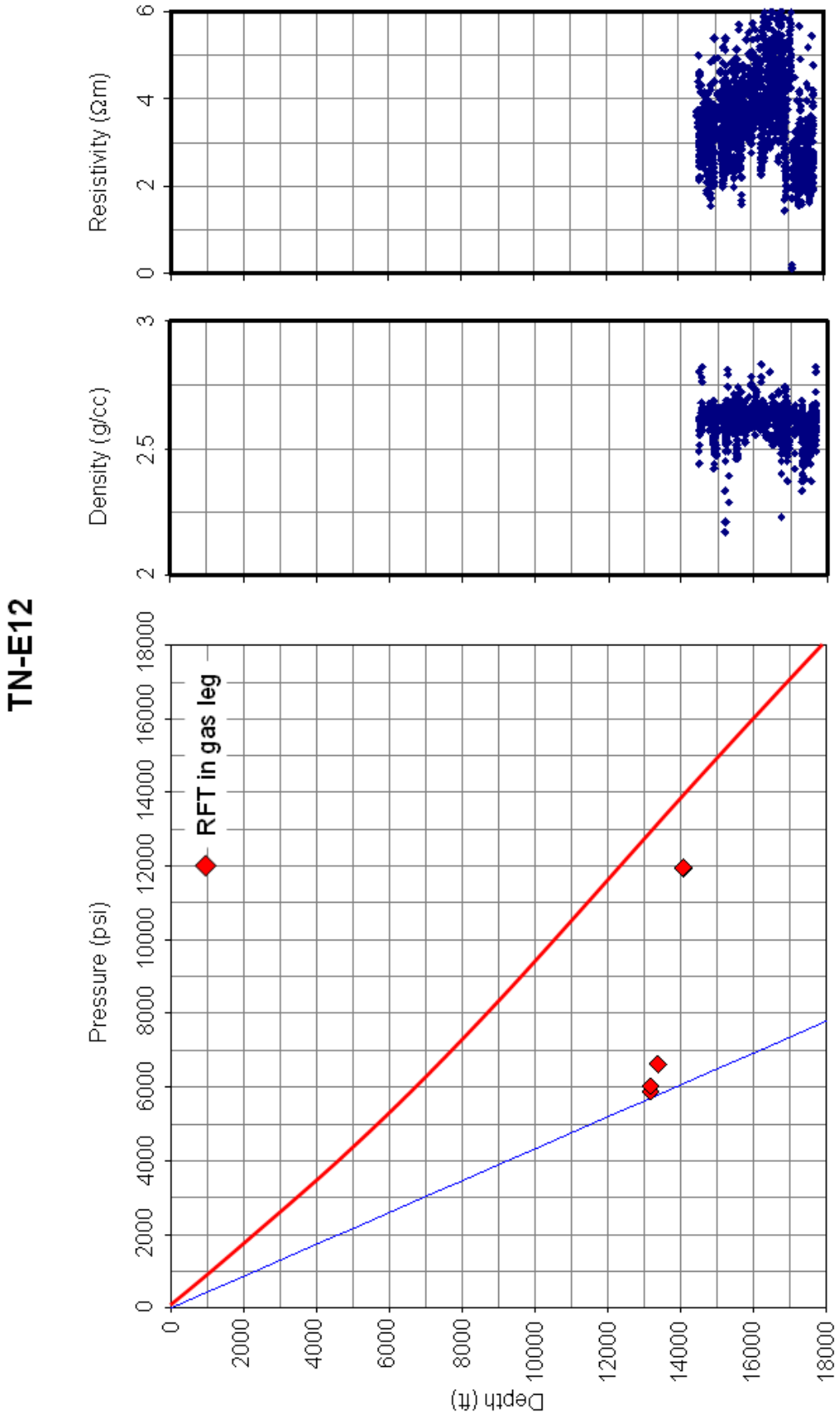
TN-E12
Resistivity (Ωm)
0
2
4
6
Density (g/cc)
2
2.5
3
Pressure (psi)
0
2000
4000
6000
8000
10000
12000
14000
16000
18000
RFT in gas leg
Depth (ft)
0
2000
4000
6000
8000
10000
12000
14000
16000
18000

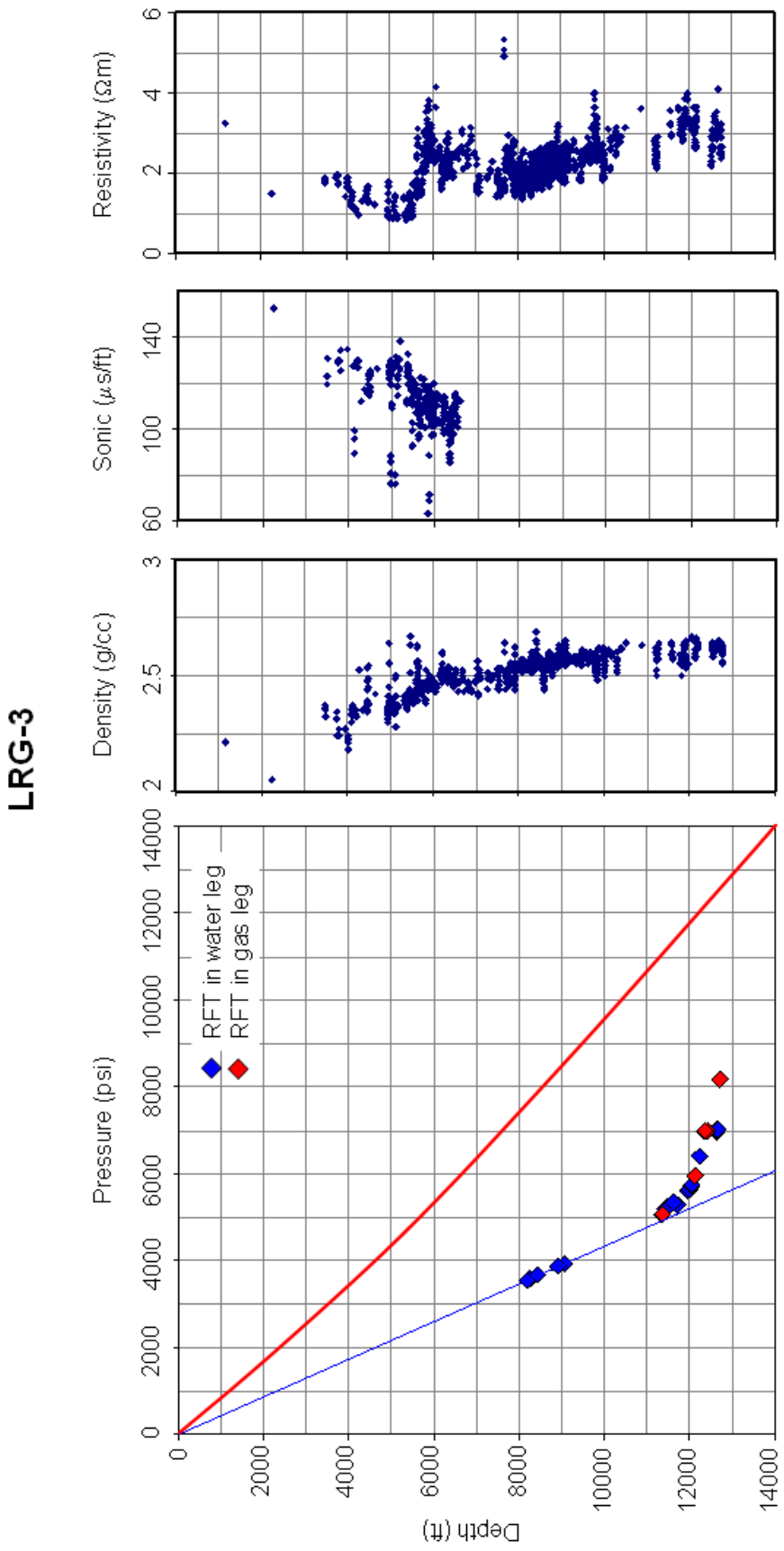
LRG-3
Resistivity (Ωm)
0
2
4
6
Sonic (μs/ft)
60
100
140
Density (g/cc)
2
2.5
3
Pressure (psi)
0
2000
4000
6000
8000
10000
12000
14000
RFT in water leg
RFT in gas leg
Depth (ft)
0
2000
4000
6000
8000
10000
12000
14000

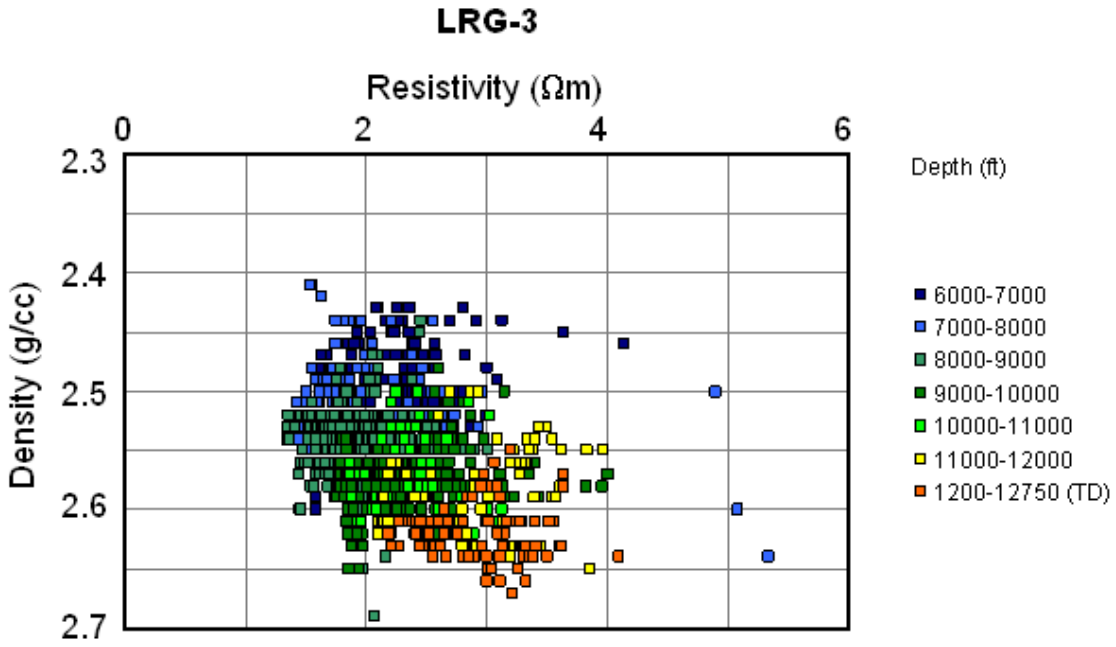
LRG-3
Resistivity (Ωm)
0
2
4
6
Density (g/cc)
2.3
2.4
2.5
2.6
2.7
Depth (ft)
6000-7000
7000-8000
8000-9000
9000-10000
10000-11000
11000-12000
1200-12750 (TD)

APPENDIX 4. ONSHORE AREA

Appendix 4a

Pressure–depth plots, wireline log responses, and cross-plots for mudrocks in overpressured wells, Mutiara Field

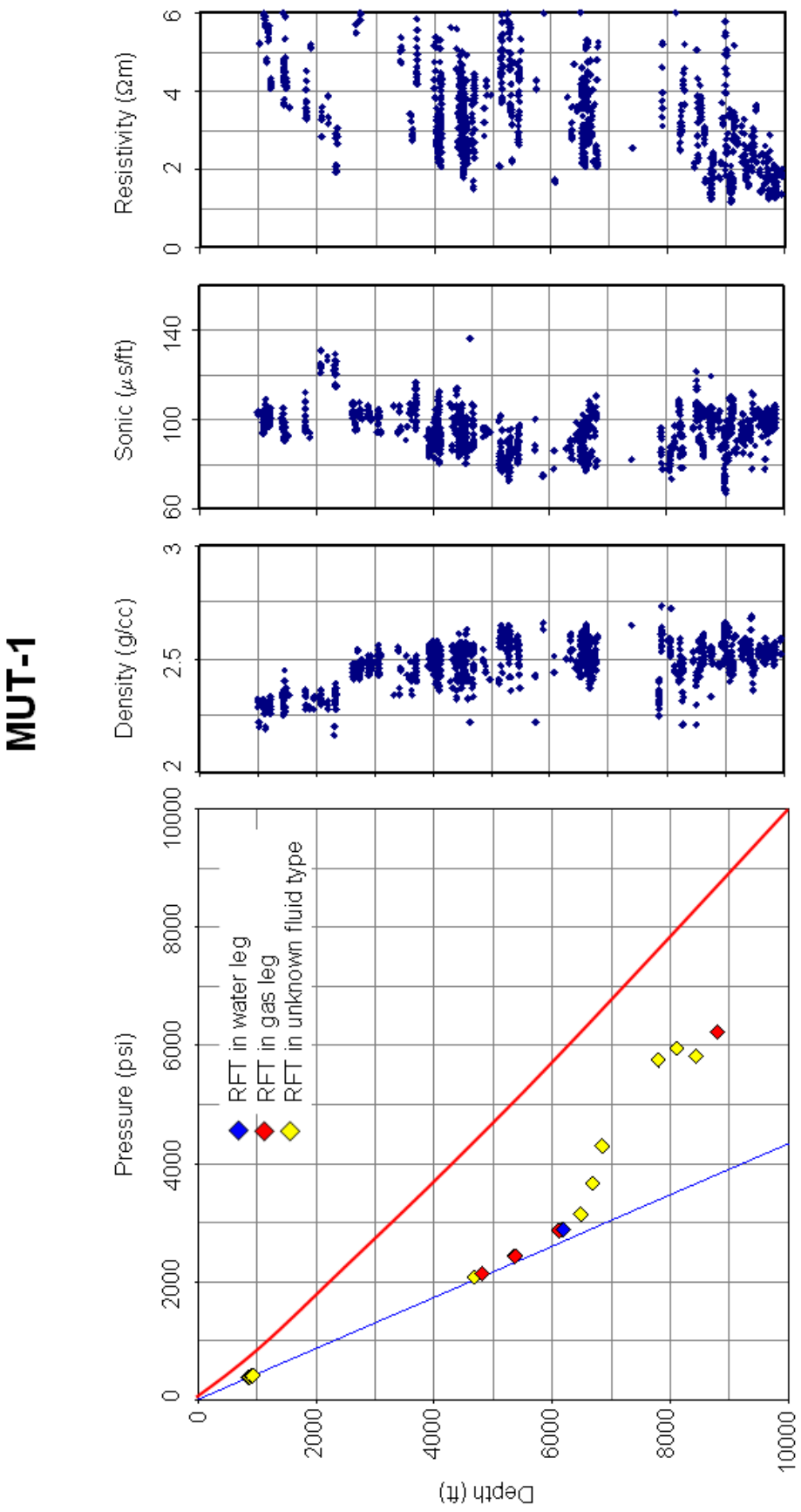
MUT-1
Resistivity (Ωm)
0
2
4
6
Sonic (μs/ft)
60
100
140
Density (g/cc)
2
2.5
3
Pressure (psi)
0
2000
4000
6000
8000
10000
RFT in water leg
RFT in gas leg
RFT in unknown fluid type
Depth (ft)
0
2000
4000
6000
8000
10000

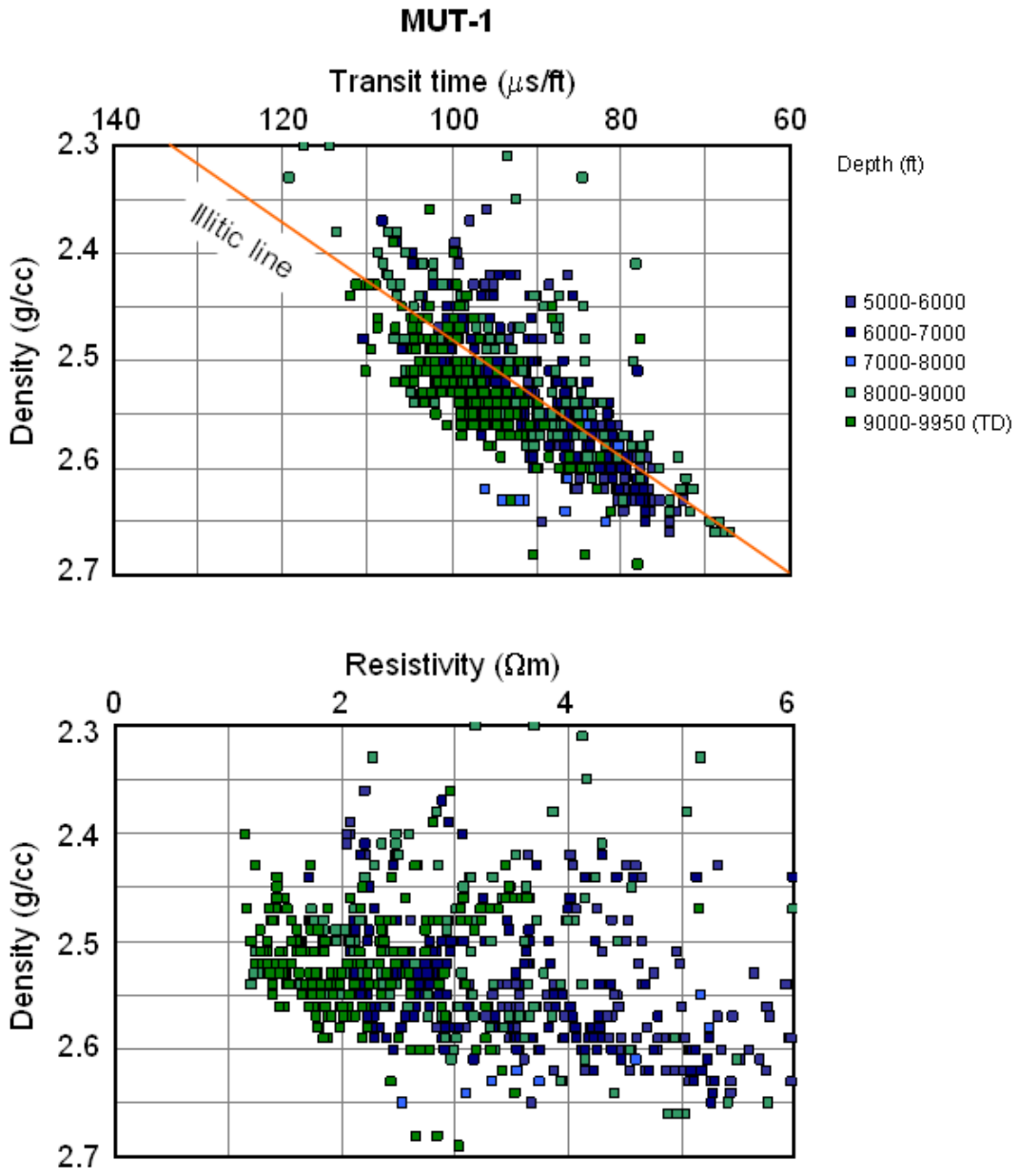
MUT-1
Transit time (μs/ft)
140
120
100
80
60
Density (g/cc)
2.3
2.4
2.5
2.6
2.7
Illitic line
Depth (ft)
5000-6000
6000-7000
7000-8000
8000-9000
9000-9950 (TD)
Resistivity (Ωm)
0
2
4
6
Density (g/cc)
2.3
2.4
2.5
2.6
2.7

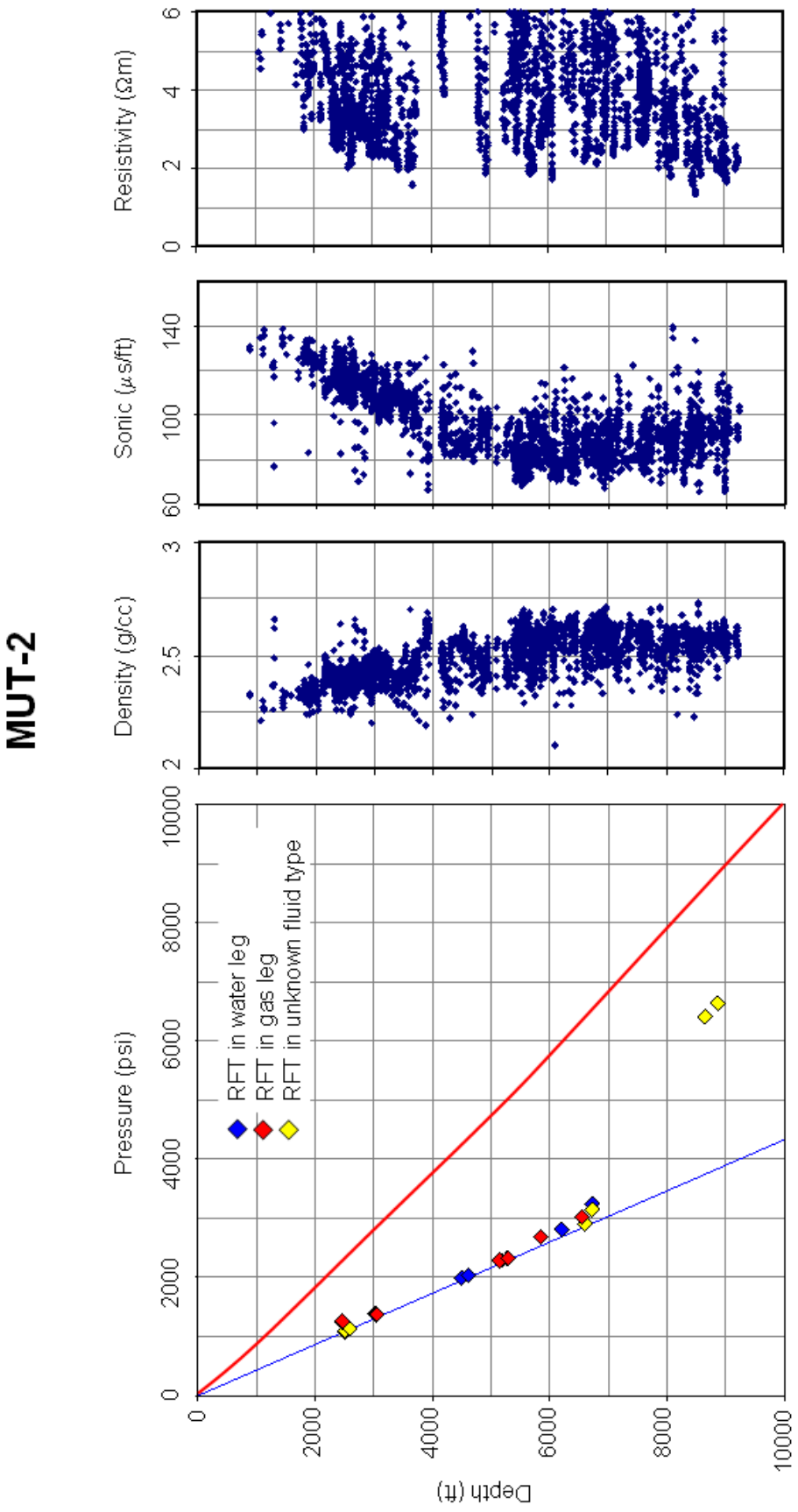
MUT-2
Resistivity (Ωm)
0
2
4
6
Sonic (μs/ft)
60
100
140
Density (g/cc)
2
2.5
3
Pressure (psi)
0
2000
4000
6000
8000
10000
RFT in water leg
RFT in gas leg
RFT in unknown fluid type
Depth (ft)
0
2000
4000
6000
8000
10000

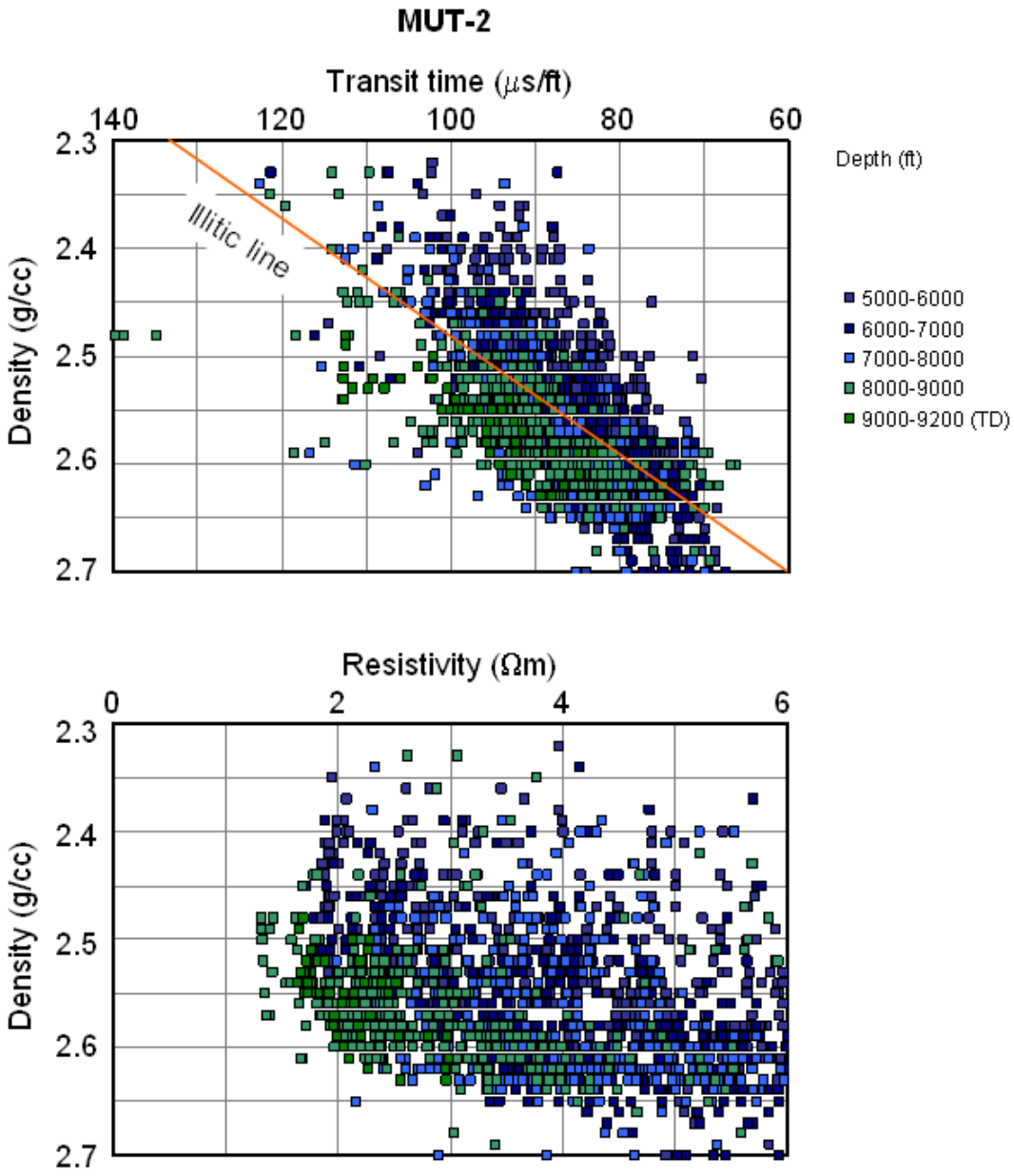
MUT-2
Transit time (μs/ft)
140
120
100
80
60
Density (g/cc)
2.3
2.4
2.5
2.6
2.7
Illitic line
Depth (ft)
5000-6000
6000-7000
7000-8000
8000-9000
9000-9200 (TD)
Resistivity (Ωm)
0
2
4
6
Density (g/cc)
2.3
2.4
2.5
2.6
2.7

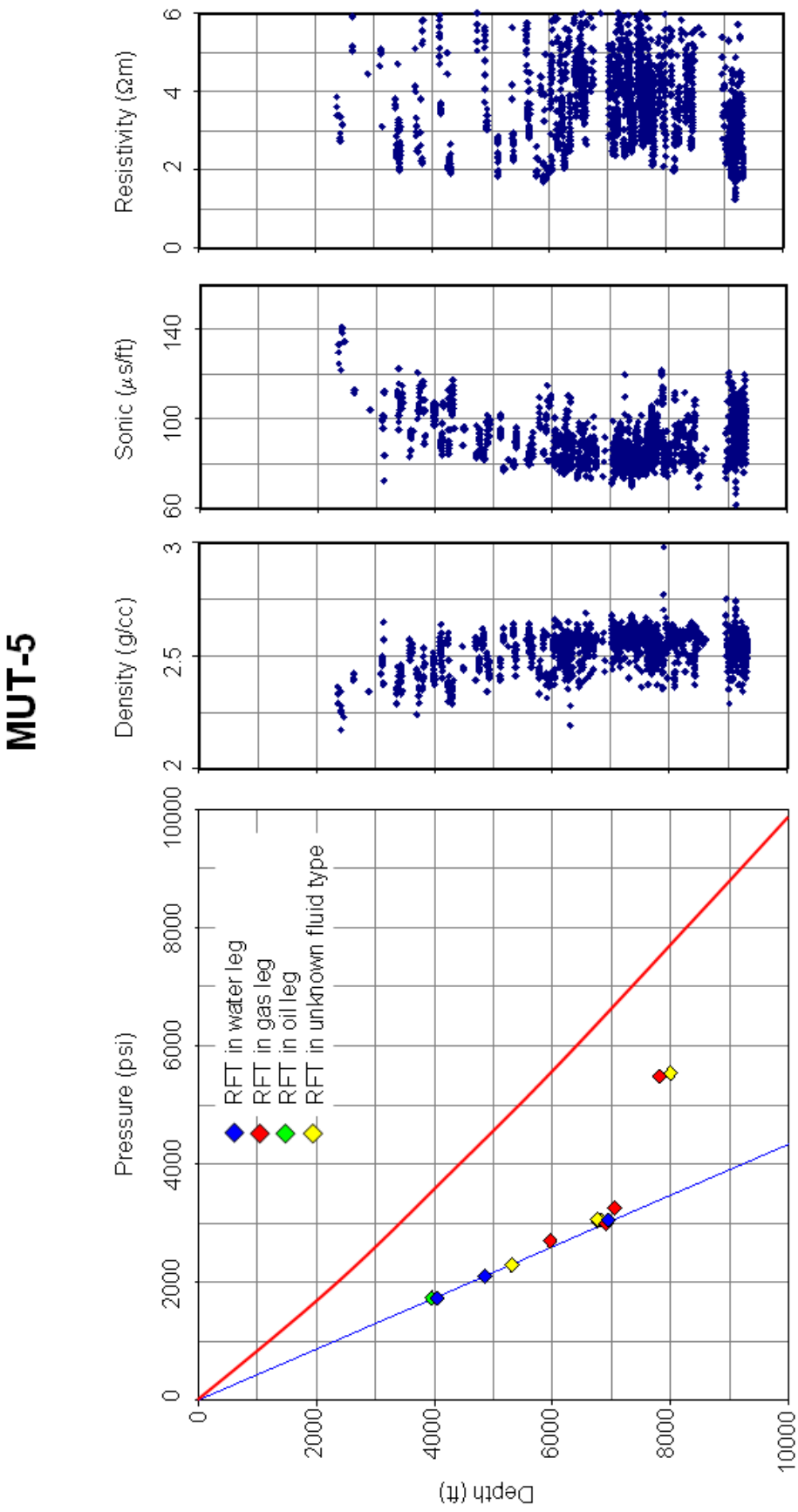
MUT-5
Resistivity (Ωm)
0
2
4
6
Sonic (μs/ft)
60
100
140
Density (g/cc)
2
2.5
3
Pressure (psi)
0
2000
4000
6000
8000
10000
RFT in water leg
RFT in gas leg
RFT in oil leg
RFT in unknown fluid type
Depth (ft)
0
2000
4000
6000
8000
10000

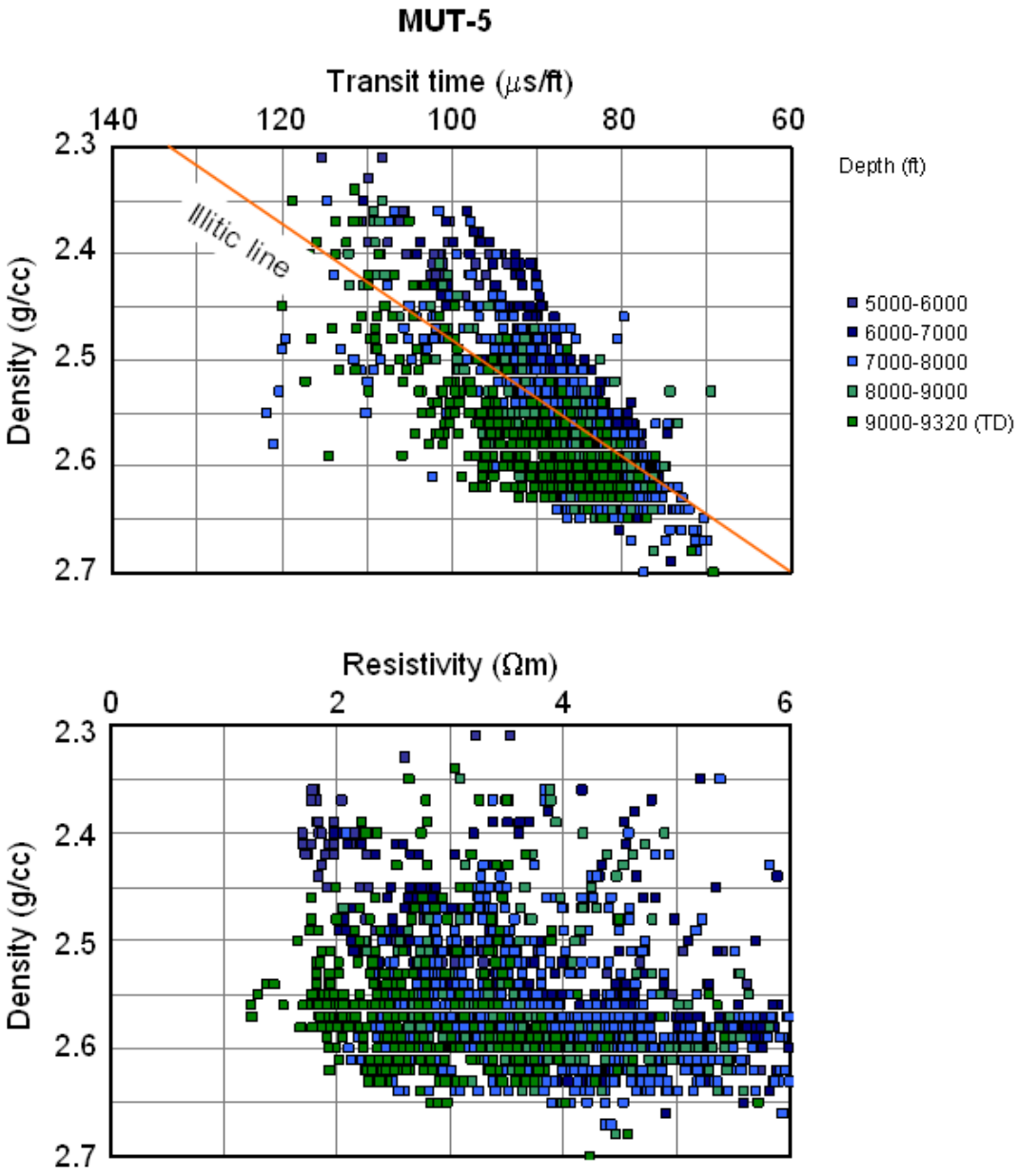
MUT-5
Transit time (μs/ft)
140
120
100
80
60
Density (g/cc)
2.3
2.4
2.5
2.6
2.7
Illitic line
Depth (ft)
5000-6000
6000-7000
7000-8000
8000-9000
9000-9320 (TD)
Resistivity (Ωm)
0
2
4
6
Density (g/cc)
2.3
2.4
2.5
2.6
2.7

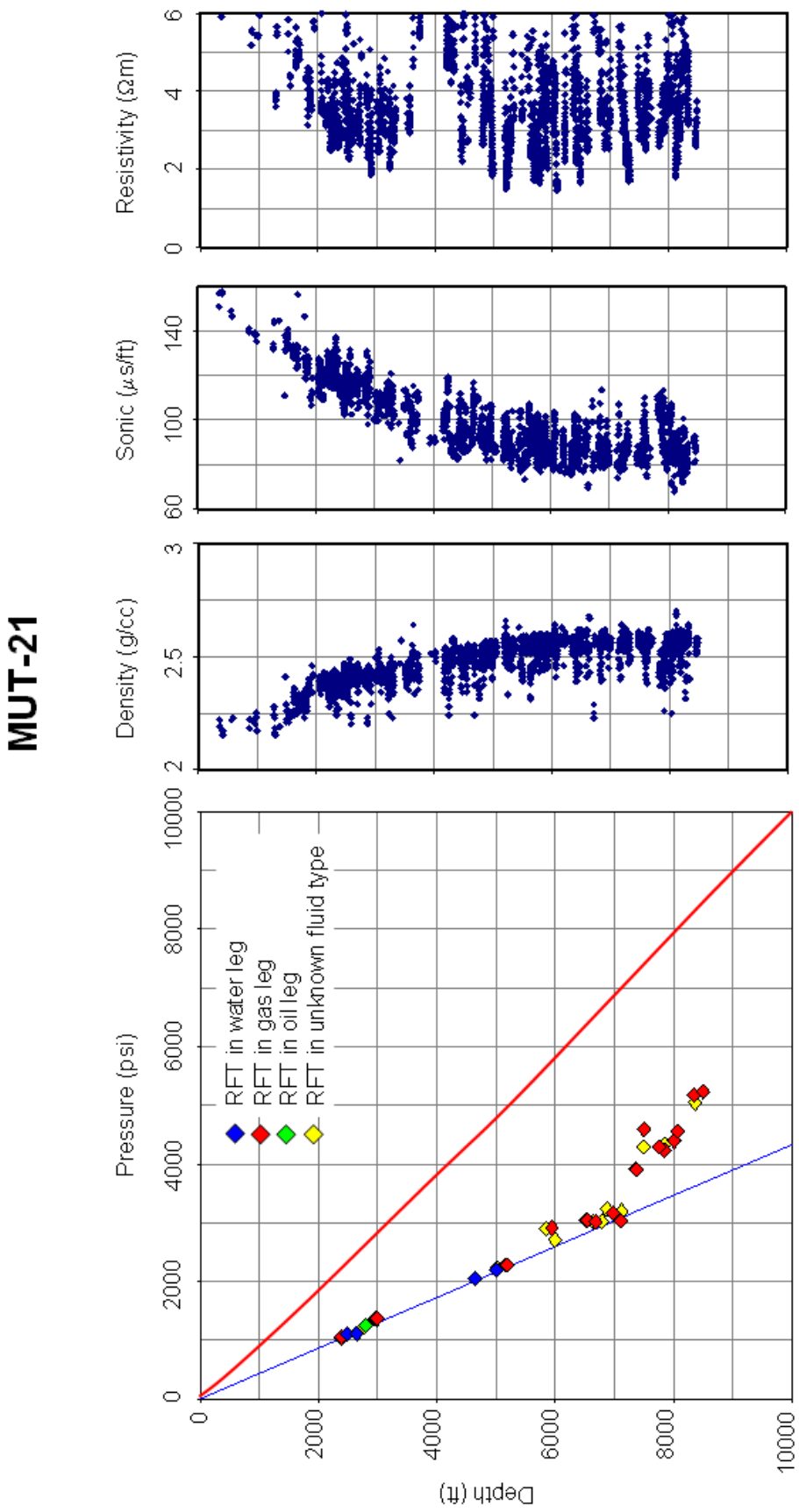
MUT-21
Resistivity (Ωm)
0
2
4
6
Sonic (μs/ft)
60
100
140
Density (g/cc)
2
2.5
3
Pressure (psi)
0
2000
4000
6000
8000
10000
RFT in water leg
RFT in gas leg
RFT in oil leg
RFT in unknown fluid type
Depth (ft)
0
2000
4000
6000
8000
10000

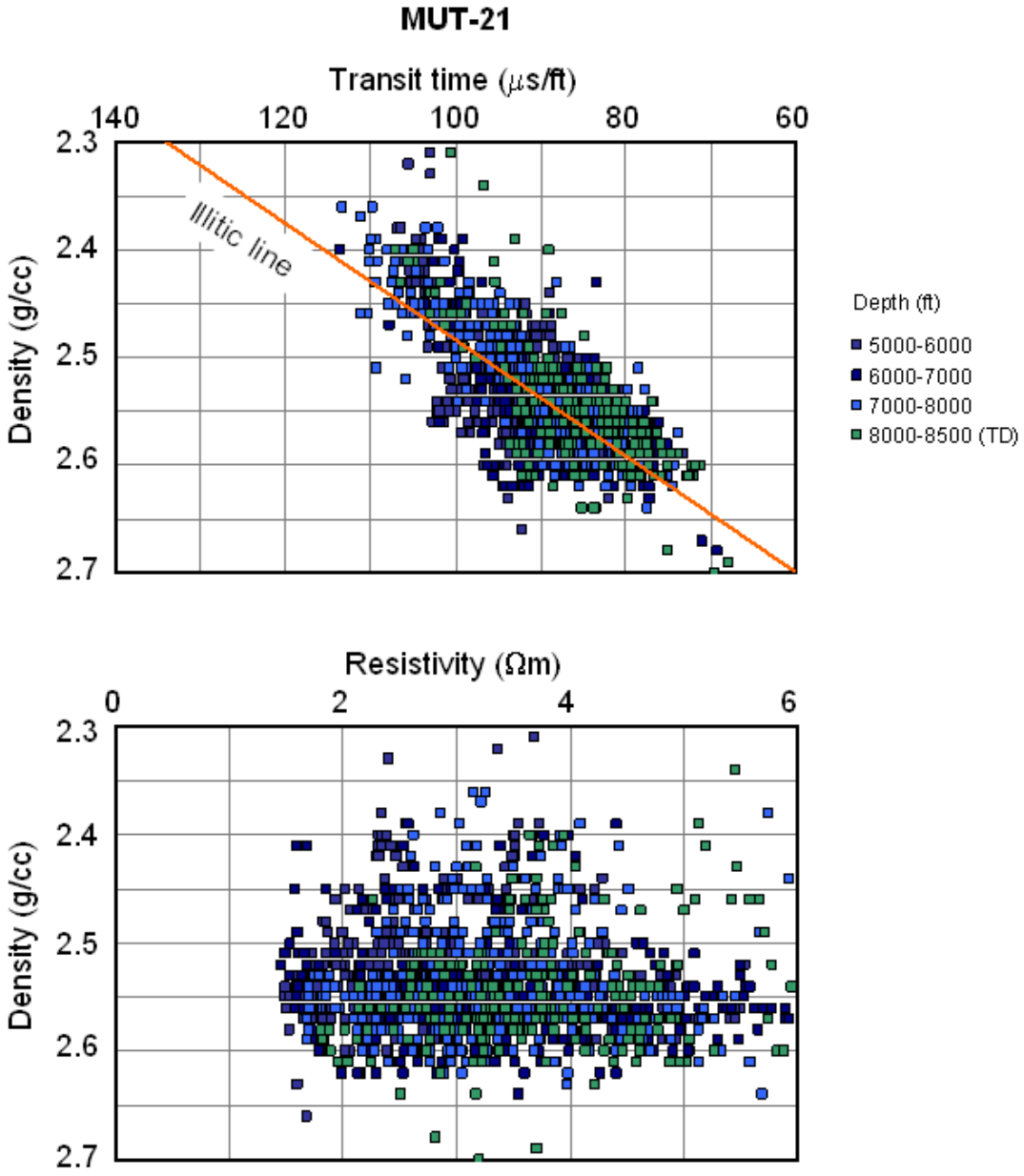
MUT-21
Transit time (μs/ft)
140
120
100
80
60
Density (g/cc)
2.3
2.4
2.5
2.6
2.7
Illitic line
Depth (ft)
5000-6000
6000-7000
7000-8000
8000-8500 (TD)
Resistivity (Ωm)
0
2
4
6
Density (g/cc)
2.3
2.4
2.5
2.6
2.7

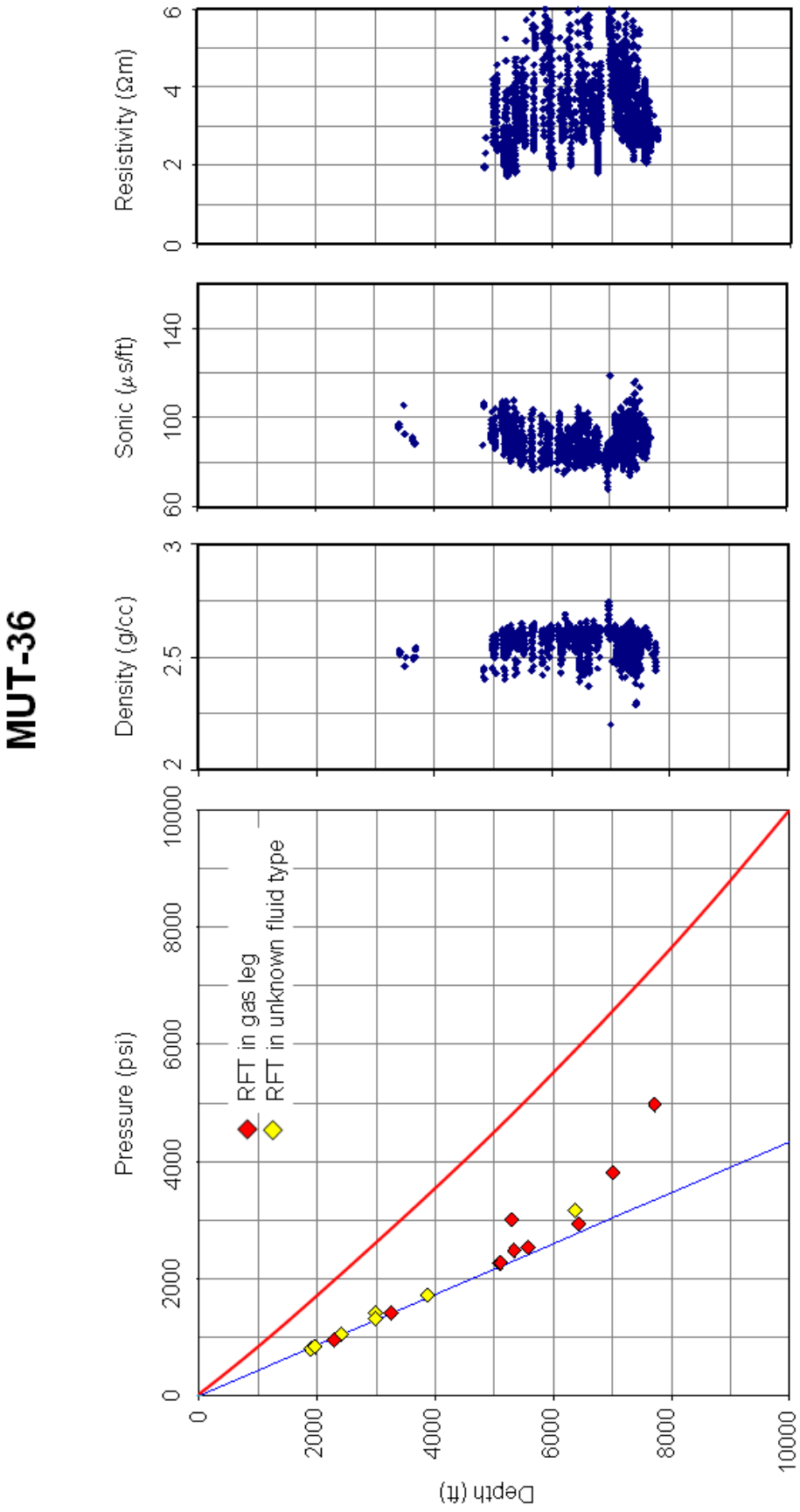
MUT-36
Resistivity (Ωm)
0
2
4
6
Sonic (μs/ft)
60
100
140
Density (g/cc)
2
2.5
3
Pressure (psi)
0
2000
4000
6000
8000
10000
RFT in gas leg
RFT in unknown fluid type
Depth (ft)
0
2000
4000
6000
8000
10000

APPENDIX 4. ONSHORE AREA

Appendix 4b

Pressure–depth plots, wireline log responses, and cross-plots for mudrocks in overpressured wells, Semberah Field

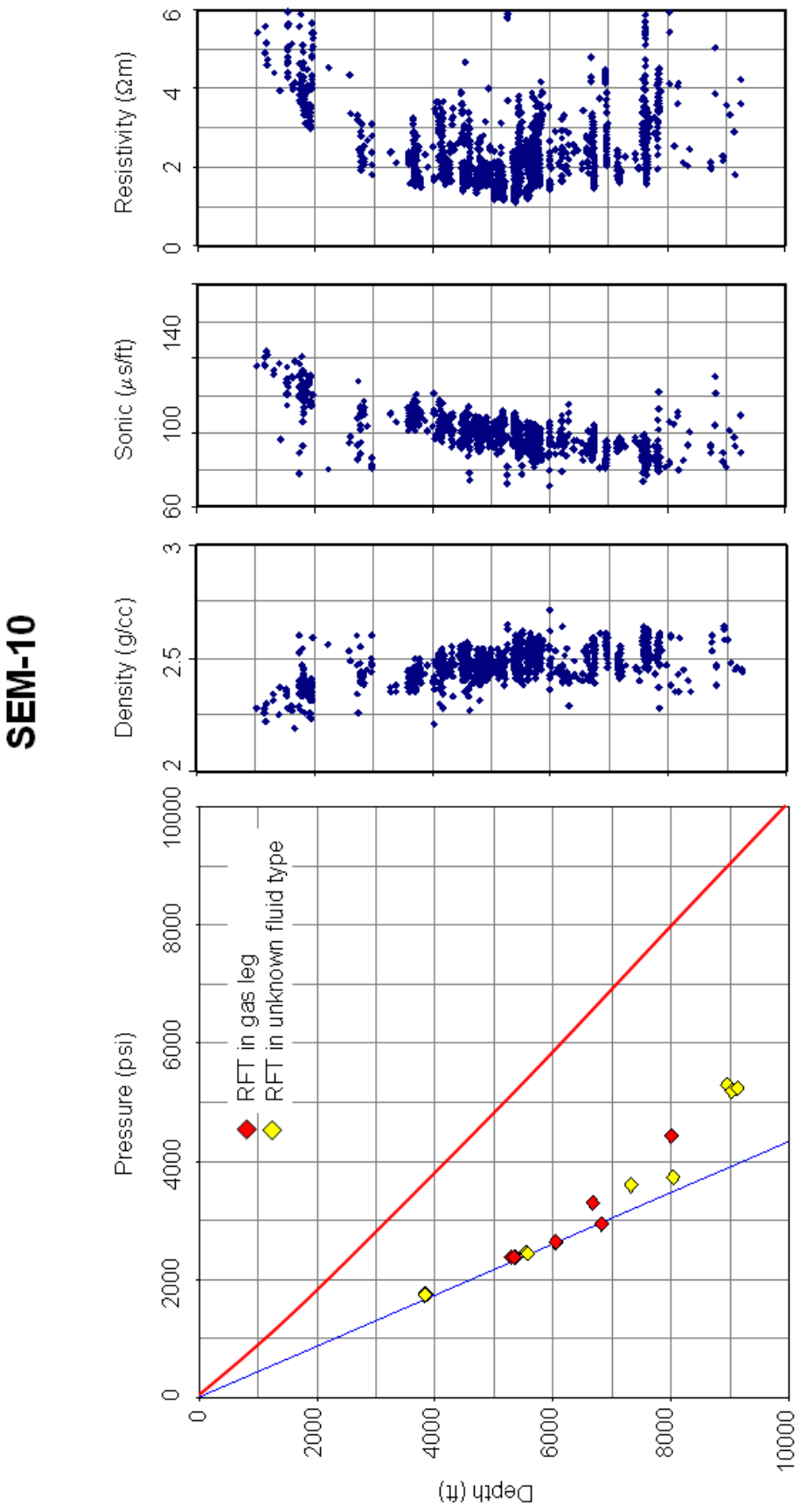
SEM-10
Resistivity (Ωm)
0
2
4
6
Sonic (μs/ft)
60
100
140
Density (g/cc)
2
2.5
3
Pressure (psi)
0
2000
4000
6000
8000
10000
RFT in gas leg
RFT in unknown fluid type
Depth (ft)
0
2000
4000
6000
8000
10000

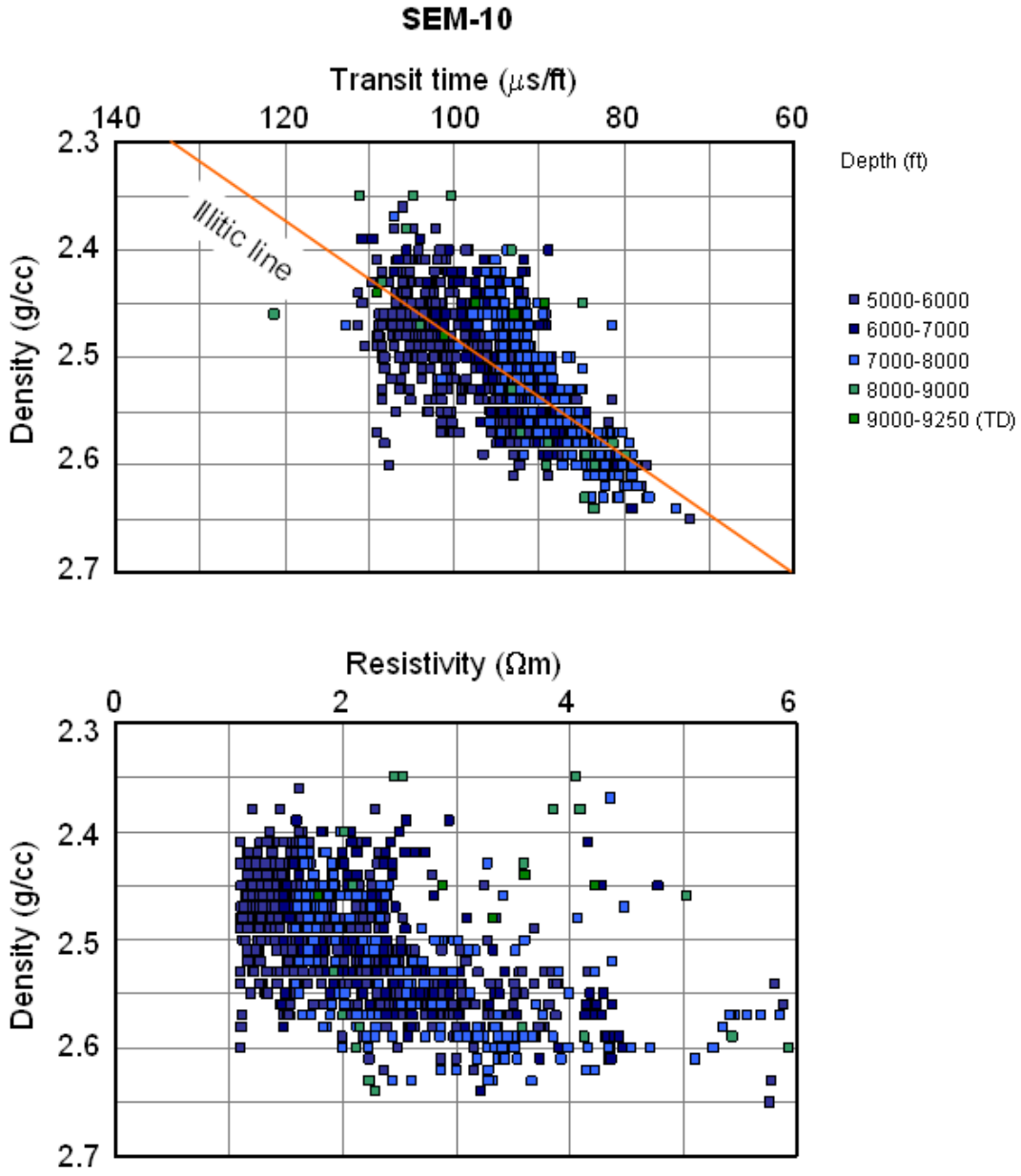
SEM-10
Transit time (μs/ft)
140
120
100
80
60
Density (g/cc)
2.3
2.4
2.5
2.6
2.7
Illitic line
Depth (ft)
5000-6000
6000-7000
7000-8000
8000-9000
9000-9250 (TD)
Resistivity (Ωm)
0
2
4
6
Density (g/cc)
2.3
2.4
2.5
2.6
2.7

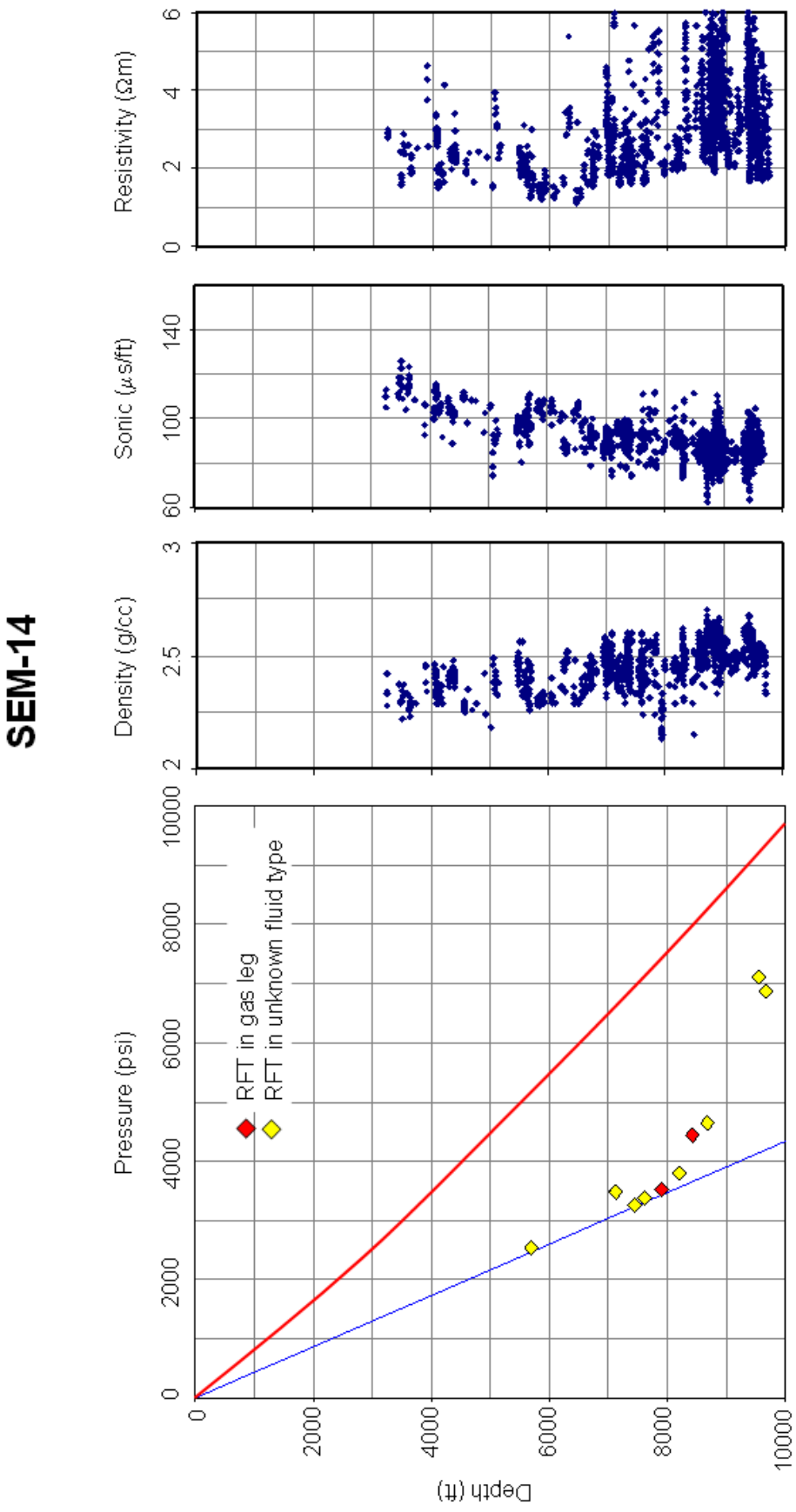
SEM-14
Resistivity (Ωm)
0
2
4
6
Sonic (μs/ft)
60
100
140
Density (g/cc)
2
2.5
3
Pressure (psi)
0
2000
4000
6000
8000
10000
RFT in gas leg
RFT in unknown fluid type
Depth (ft)
0
2000
4000
6000
8000
10000

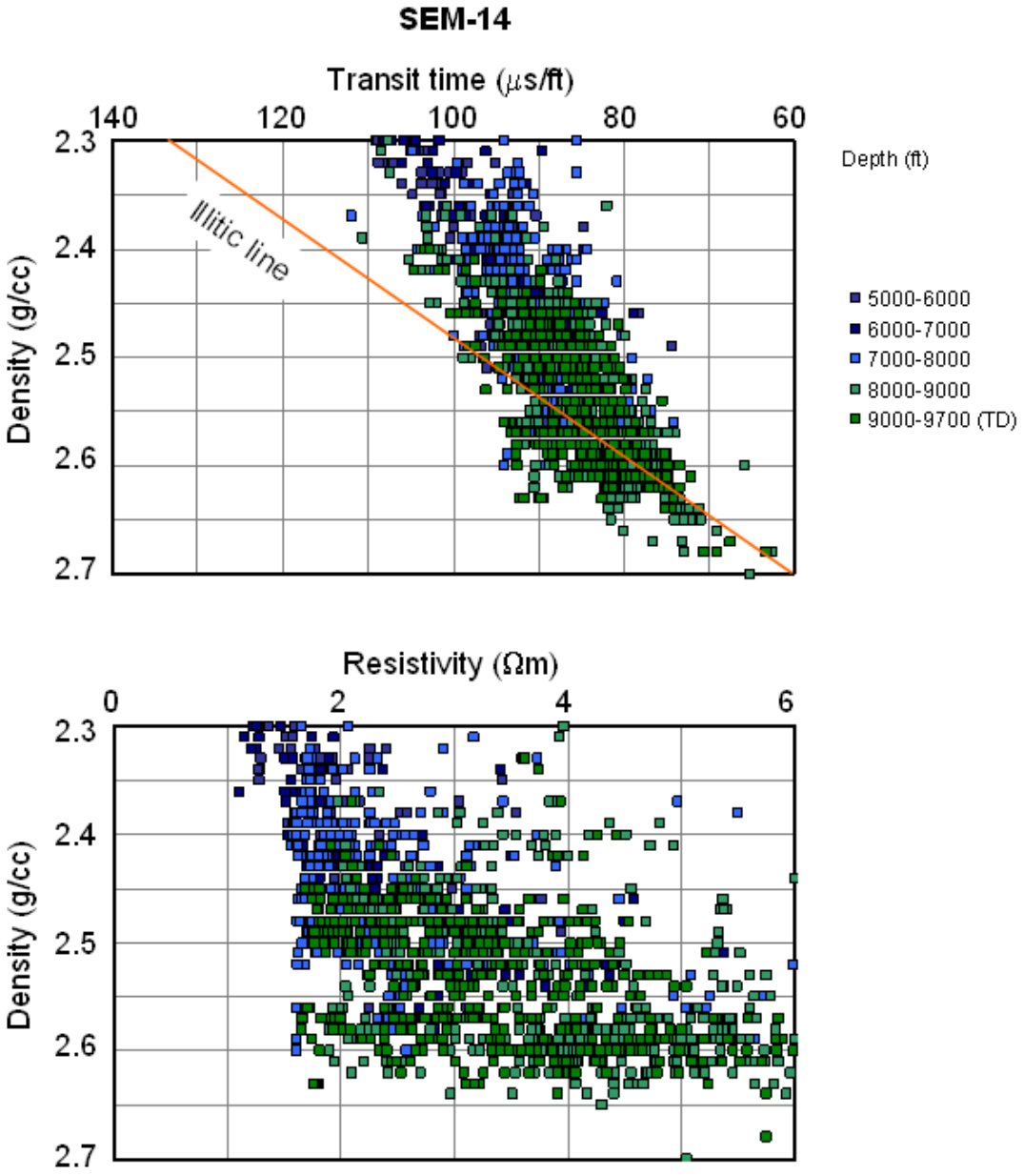
SEM-14
Transit time (μs/ft)
140
120
100
80
60
Density (g/cc)
2.3
2.4
2.5
2.6
2.7
Illitic line
Depth (ft)
5000-6000
6000-7000
7000-8000
8000-9000
9000-9700 (TD)
Resistivity (Ωm)
0
2
4
6
Density (g/cc)
2.3
2.4
2.5
2.6
2.7

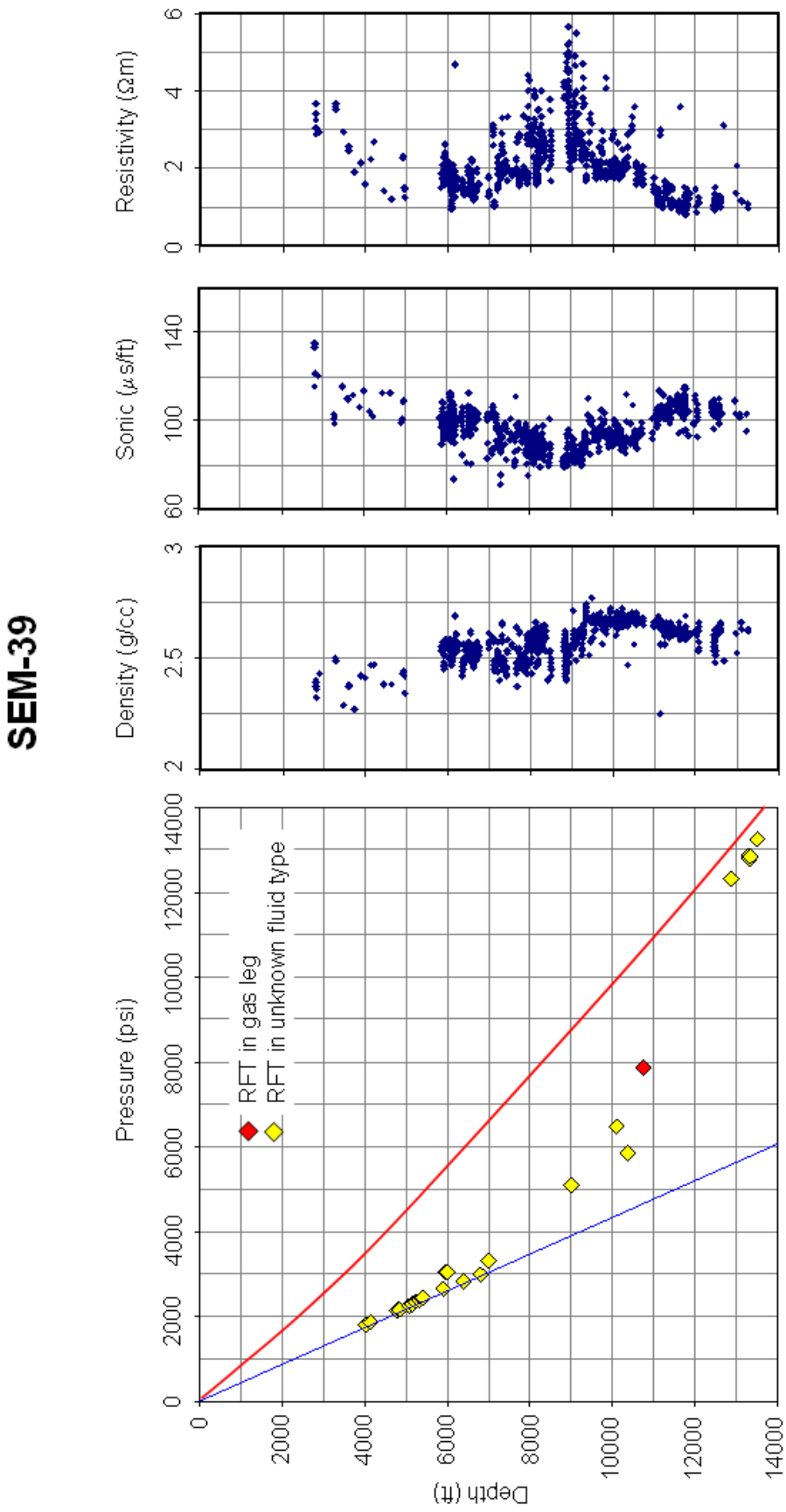
SEM-39
Resistivity (Ωm)
0
2
4
6
Sonic (μs/ft)
60
100
140
Density (g/cc)
2
2.5
3
Pressure (psi)
0
2000
4000
6000
8000
10000
12000
14000
RFT in gas leg
RFT in unknown fluid type
Depth (ft)
0
2000
4000
6000
8000
10000
12000
14000

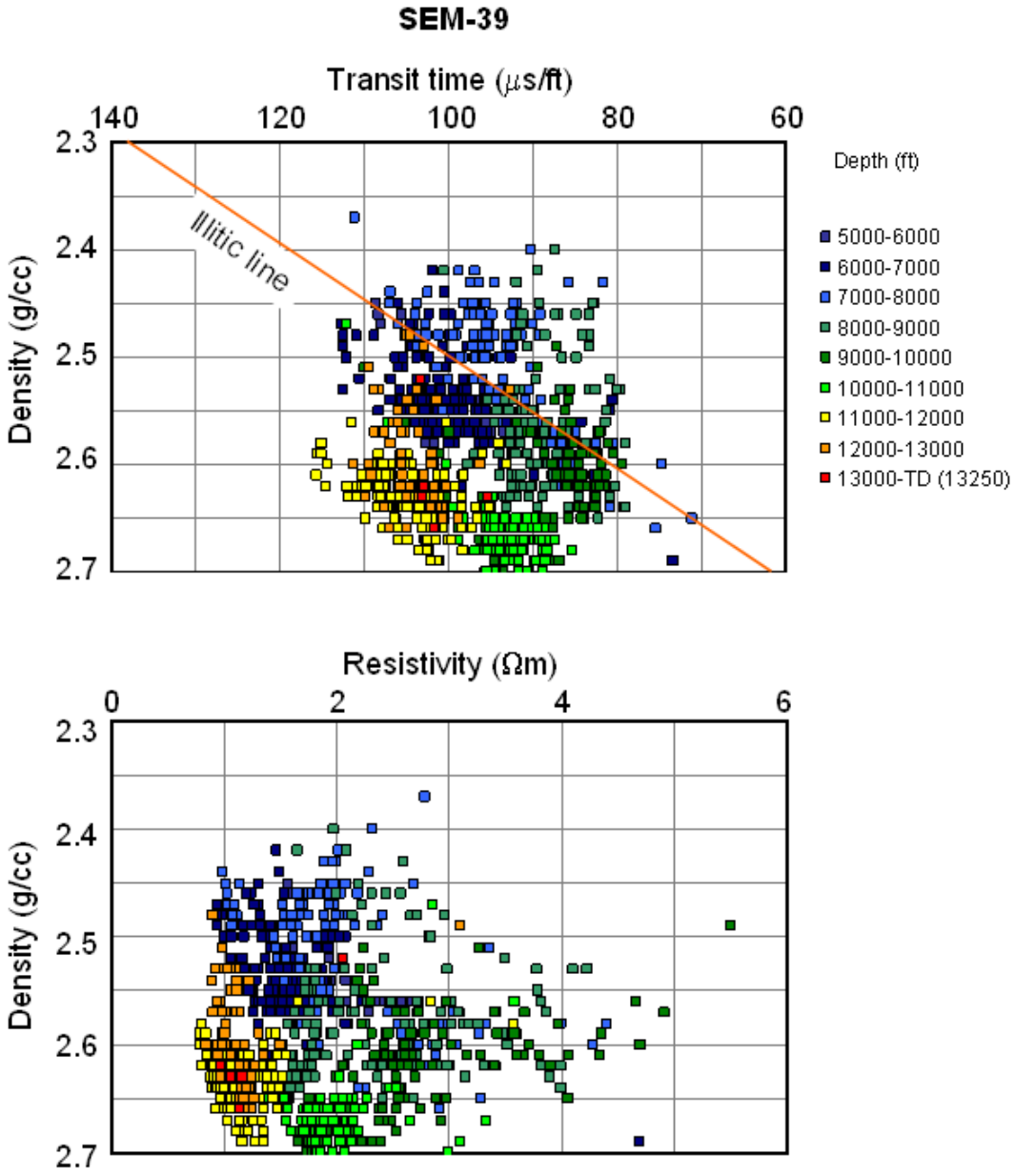
SEM-39
Transit time (μs/ft)
140
120
100
80
60
Density (g/cc)
2.3
2.4
2.5
2.6
2.7
Illitic line
Depth (ft)
5000-6000
6000-7000
7000-8000
8000-9000
9000-10000
10000-11000
11000-12000
12000-13000
13000-TD (13250)
Resistivity (Ωm)
0
2
4
6
Density (g/cc)
2.3
2.4
2.5
2.6
2.7

REFERENCES

Allen, G.P. & Chambers, J.L.C. 1998. *Sedimentation in the Modern and Miocene Mahakam Delta*. Field Trip Guide Book, Indonesian Petroleum Association, Jakarta.

Athy, L.F. 1930. Density, porosity, and compaction of sedimentary rocks. *AAPG Bulletin*, **14**, 1-24.

Bachtiar, A. 2004. *The Sequence Stratigraphy Framework of the Lower Miocene Source Rock in the Lower Kutai Basin*. PhD Dissertation, Institute of Technology Bandung, Unpublished.

Bachu, S. & Underschultz, J.R. 1995. Large-scale underpressuring in Mississippian-Cretaceous succession, Southwestern Alberta Basin. *AAPG Bulletin*, **79**, 989-1004.

Baldwin, B. & Butler, C.O. 1985. Compaction curves. *AAPG Bulletin*, **69**, 622-626.

Barker, C. 1972. Aquathermal pressuring – role of temperature in development of abnormal-pressure zones. *AAPG Bulletin*, **80**, 2068-2071.

Bates, J.A. 1996. Overpressuring in the Kutai Basin: distribution, origins, and implications for the petroleum system. *In: Indonesian Petroleum Association, Proceedings 25th Annual Convention*, 93-115.

Belitz, K. & Bredehoeft, J.D. 1988. Hydrodynamics of the Denver Basin: explanation of sub-normal fluid pressures. *AAPG Bulletin*, **72**, 1334-1359.

Bell, D.W. 2002. Velocity estimation for pore-pressure prediction. *In:* Huffman, A.R. & Bowers, G.L. (eds.), *Pressure Regimes in Sedimentary Basins and their Prediction*. AAPG, Tulsa, Memoir **76**, 177-215.

Bellorini, J.P., Debertrand, T. & Umar, M.I. 1989. Handil Field development example of geological reservoir study. *In: Indonesian Petroleum Association, Proceedings 18th Annual Convention*, 91-106.

Binh, N.T., Tokunaga, T., Son, H.P. & Binh, M.V. 2007. Present-day stress and pore pressure fields in the Cuu Long and Nam Con Son Basins, offshore Vietnam. *Marine and Petroleum Geology,* **24**, 607-615.

Biot, M.A. 1941. General theory of three-dimensional consolidation. *Journal of Applied Physics*, **12**, 155-164.

Bjørkum, P.A. 1995. How important is pressure in causing dissolution of quartz in sandstones? *Journal of Sedimentary Research*, **66**, 147-154.

Bjørlykke, K. 1998. Clay mineral diagenesis in sedimentary basins: a key to the prediction of rock properties: examples from the North Sea Basin. *Clay Minerals*, **33**, 15–34.

Bjørlykke, K. 1999. Principal aspects of compaction and fluid flow in mudstones. *In:* Aplin, A.C., Fleet, A.J. & Macquaker, J.H.S. (eds.) *Muds and Mudstones: Physical and Fluid-Flow Properties*. Geological Society, London, Special Publications, **158**, 73-78.

Bjørlykke, K. & Høeg, K. 1997. Effects of burial diagenesis on stresses, compaction and fluid flow in sedimentary basins. *Marine and Petroleum Geology*, **14**, 267-276.

Bois, M., Grosjean, Y. & de Pazzis, L. 1994. Shale compaction and abnormal pressure evaluation application to the offshore Mahakam. *In: Indonesian Petroleum Association, Proceedings 23rd Annual Convention*, 245-259.

Boles, J.R. & Franks, S.G. 1979. Clay diagenesis in Wilcox sandstones of southwest Texas: implications of smectite diagenesis on sandstone cementation. *Journal of Sedimentary Petrology*, **49**, 55-70.

Bowers, G.L. 1995. Pore pressure estimation from velocity data: accounting for overpressure mechanisms besides undercompaction. *SPE Drilling and Completion*, paper IADC/SPE 27488.

Bowers, G.L. 2001. Determining an appropriate pore-pressure estimation strategy. *Offshore Technology Conference*, paper OTC 13042.

Bowers, G.L. & Katsube, T.J. 2002. The role of shale pore structure on the sensitivity of wire-line logs to overpressure. *In:* Huffman, A.R. & Bowers,

G.L. (eds.), *Pressure Regimes in Sedimentary Basins and their Prediction*. AAPG, Tulsa, Memoir **76**, 43-60.

Burland, J.B. 1990. On the compressibility and shear strength of natural clays. *Geotechnique*, **40**, 329-278.

Burrus, J. 1998. Overpressure models for clastic rocks, their relation to hydrocarbon expulsion: a critical reevaluation. *In:* Law, B.E., Ulmishek, G.F. & Slavin, V.I. (eds.) *Abnormal Pressures in Hydrocarbon Environments*. AAPG, Tulsa, Memoir **70**, 35-63.

Burrus, J., Brosse, E., Choppin de Janvry, G., Grosjean, Y. & Oudin, J.L. 1992. Basin modelling in the Mahakam Delta based on integrated 2D model Temispack. *In: Indonesian Petroleum Association, Proceedings 21st Annual Convention*, 23-43.

Burst, J.F. 1969. Diagenesis of Gulf Coast clayey sediments and its possible relation to petroleum migration. *AAPG Bulletin*, **53**, 73-93.

Chambers, J.L.C. & Daley, T.E. 1995. A tectonic model for the onshore Kutai Basin, East Kalimantan, based on an integrated geological and geophysical interpretation. *In: Indonesian Petroleum Association, Proceedings 24th Annual Convention*, 111-130.

Chambers, J.L.C. & Daley, T.E. 1997. A tectonic model for the onshore Kutai Basin, east Kalimantan. *In:* Fraser, A., Matthews, S. & Murphy, R.W. (eds.) *Petroleum Geology of Southeast Asia*. Geological Society of London, Special Publication **126**, 375-393.

Chambers, J.L.C., Carter, I., Cloke, I.R., Craig, J., Moss, S.J. & Paterson, D.W. 2004. Thin-skinned and thick-skinned inversion-related thrusting – A structural model for the Kutai Basin, Kalimantan, Indonesia. *In:* McClay, K.R. (ed.) *Thrust Tectonics and Hydrocarbon Systems*. AAPG, Tulsa, Memoir **82**, 614-634.

Chapman, R.E. 1983. *Petroleum Geology*. Elsevier, Amsterdam, 415p.

Clauer, N., Rinckenbach, T., Weber, F., Sommer, F., Chaudhuri, S. & O'Neil, J.R. 1999. Diagenetic evolution of clay minerals in oil-bearing Neogene

sandstones and associated shales, Mahakam Delta Basin, Indonesia. *AAPG Bulletin*, **83**, 62-87.

Cloke I.R., Moss, S.J. & Craig, J.C. 1997. The influence of basement reactivation on the extensional and inversion history of the Kutai Basin, eastern Kalimantan. Journal of the Geological Society, London, **17**, 137-141.

De Matharel, M., Lehmann, P. & Oki, T. 1980. Geology of the Bekapai Field. *In:* Halbouty, M.T. (ed.) *Giant Oil and Gas Fields of the Decade 1968-1978.* AAPG, Tulsa, Memoir **30**, 459-469.

Deming, D. 1994. Factors necessary to define a pressure seal. AAPG Bulletin, 78, 1005-1009.

Dennis, H., Baillie, J., Holt, T. & Wessel-Berg, D. 2000. Hydrodynamic activity and tilted oil-water contacts in the North Sea. *In*: Ofstad, K., Kittilsen, J.E. & Alexander-Marrack, P. (eds.) *Improving the Exploration Process by Learning from the Past. NPF*, Amsterdam, Special Publication **9**, 171-185.

Dickey, P.A., Shriram, C.R. & Paine, W.R. 1968. Abnormal pressures in deep wells of Southwestern Louisiana. *Science*, **160**, 609-615.

Dickinson, G. 1953. Geological aspects of abnormal reservoir pressures in Gulf Coast, Louisiana. *AAPG Bulletin*, **37**, 410-432.

Domenico, P.A. & Schwartz, F.W. 1990. *Physical and Chemical Hydrogeology*. John Wiley and Sons, Inc., New York, 824p.

Doust, H. & Noble, R. 2008. Petroleum systems of Indonesia. *Marine and Petroleum Geology*, **25**, 103-129.

Dutta, N.C. 2002. Deepwater geohazard prediction using prestack inversion of large offset P-wave data and rock model. *The Leading Edge*, **21**, 193-198.

Duval, B.C., Cassaigneau, C., Choppin de Janvry, G., Loiret, B., Leo, M., Alibi & Grosjean, Y. 1998. Impact of the petroleum system approach to exploration and appraisal efficiency in the Mahakam Delta. *In: Indonesian Petroleum Association, Proceedings 26th Annual Convention*, 277-290.

Eaton, B.A. 1975. The equation for geopressure prediction from well logs. *SPE*, Paper No. 5544, 11p.

Ferguson, A. & McClay, K. 1997. Structural modelling within the Sanga-Sanga PSC, Kutai Basin, Kalimantan: its application to paleochannel orientation studies and timing of hydrocarbon entrapment. *In:* Howes, J.V.C. & Noble, R.A. (eds.), *Indonesian Petroleum Association, Proceedings of the Petroleum Systems of SE Asia and Australasia Conference*, 709-726.

Flemings, P.B., Stump, B.B., Finkebeiner, T. & Zoback, M. 2002. Flow focusing in overpressured sandstones: theory, observation, and applications. *American Journal of Science*, **502**, 827-855.

Goulty, N.R. 1998. Relationship between porosity and effective stress in shales. *First Break*, **16**, 413-419.

Grosjean, Y., Choppin de Janvry, G. & Duval, B.C. 1994. Discovery of a giant in a mature deltaic province: Peciko, Indonesia. Presented at the 14th World Petroleum Congress, May–June 1994, Stavanger, Norway.

Grosjean, Y., Zaugg, P. & Gaulier, J-M. 2009. Burial hydrodynamics and subtle hydrocarbon trap evaluation: from the Mahakam Delta to the South Caspian Sea. Presented at International Petroleum Technology Congress, Paper 13962.

Gurevich, A.E. & Chilingar, G.V. 1995. Abnormal pressures in Azerbaijan: a brief critical review and recommendations. *Journal of Petroleum Science and Engineering*, **13**, 125–135.

Guritno, E. & Chambers, J.L.C. 1999. North Runtu PSC: the first proven Eocene petroleum play in the Kutai Basin. *In: Indonesian Petroleum Association, Proceedings 27th Annual Convention,* CD-ROM, 20p.

Guritno, E., Salvadori, L., Syaiful, M., Busono, I., Mortimer, A., Hakim, F.B., Dunham, J., Decker, J. & Algar, S. 2003. Deep water Kutei Basin: a new petroleum system. In: *In: Indonesian Petroleum Association, Proceedings 29th Annual Convention*, CD-ROM, 20 p.

Hall, R. 2002. Cenozoic geological and plate tectonic evolution of SE Asia and the SW Pacific: computer-based reconstructions, model and animations. *Journal of Asian Earth Sciences*, **20**, 353-432.

Hall, R. 2009. Hydrocarbon basins in SE Asia: understanding why they are there. *Petroleum Geoscience*, **15**, 131-146.

Hall, R., Cloke, I.R., Nur'aini, S., Puspita, S.D., Calvert, S.J. & Elders, C.F. 2009. The North Makassar Straits: what lies beneath? *Petroleum Geoscience*, **15**, 147-158.

Hansen, S. 1996. A compaction trend for Cretaceous and Tertiary shales on the Norwegian shelf based on sonic transit time. *Petroleum Geoscience* **2**, 159-166.

Hansom, J. & Lee, M-K. 2005. Effects of hydrocarbon generation, basal heat flow and sediment compaction on overpressure development: a numerical study. *Petroleum Geoscience*, **11**, 353-360.

Harper, M.L. 1971. Approximate geothermal gradients in the North Sea Basin. *Nature*, **230**, 235-236.

Hermanrud, C., Wensaas, L., Teige, G.M.G., Vik, E., Nordgård Bolås, H.M. & Hansen, S. 1998. Shale porosities from well logs on Haltenbanken (Offshore Mid-Norway) show no influence of overpressuring. *In:* Law, B.E., Ulmishek, G.F. & Slavin, V.I. (eds.) *Abnormal Pressures in Hydrocarbon Environments*. AAPG, Tulsa, Memoir **70**, 65-87.

Hottman, C.E. & Johnson, R.K., 1965. Estimation of formation pressures from log-derived shale properties. *Journal of Petroleum Technology*, 717-722.

Hower, J., Eslinger, E.V., Hower, M.E. & Perry, E.A. 1976. Mechanism of burial and metamorphism of argillaceous sediment: 1. Mineralogical and chemical evidence. *Geological Society of America Bulletin*, **87**, 725-737.

Hubbert, M.K. 1953. Entrapment of petroleum under hydrodynamic conditions. *AAPG Bulletin*, **45**, 1954-2026.

Inglis, C.E. 1913. Stresses in a plate due to the presence of cracks and sharp corners. *Transactions of the Institution of Naval Architects,* **55**, 219–230.

Ireland, T., Joseph, J., Colley, N., Reigner, P., Richardson, S. 1992. The MDT tool: a wireline testing breakthrough. *Oil Field Review*, 58-65.

Issler, D.R. 1992. A new approach to shale compaction and stratigraphic restoration, Beaufort-Mackenzie Basin and Mackenzie Corridor, Northern Canada. *AAPG Bulletin*, **76**, 1170-1189.

Jorden, J.R. & Shirley, O.J. 1966. Application of drilling performance data to overpressure detection. *Journal of Petroleum Technology*, 1387-1394.

Katahara, K. 2006. Overpressure and shale properties: stress unloading or smectite-illite transformation? *76th SEG Annual Meeting*, Expanded Abstracts, 1520-1524.

Katahara, K. 2008. What is shale to a petrophysicist? *The Leading Edge*, **27**, 738-741.

Katahara, K.W. & Corrigan, J.D. 2002. Effect of gas on poroelastic response to burial or erosion. In: Huffman, A.R. & Bowers, G.L. (eds.) *Pressure Regimes in Sedimentary Basins and Their Prediction*, AAPG, Tulsa, Memoir **76**, 73-78.

Lahann, R. 2002. Impact of smectite diagenesis on compaction modeling and compaction equilibrium. *In:* Huffman, A.R. & Bowers, G.L. (eds.) *Pressure Regimes in Sedimentary Basins and Their Prediction*, AAPG, Tulsa, Memoir **76**, 61-72.

Lambert, B., Duval, B.C., Grosjean, Y., Umar, I.M. & Zaugg, P. 2003. The Peciko case history: impact of an evolving geological model on the dramatic increase of gas reserves in the Mahakam Delta. *In:* Halbouty, M.T. (ed.) *Giant Oil and Gas Fields of the Decade 1990–1999*. AAPG, Tulsa, Memoir **78**, 297-320.

Luo, X. & Vasseur, G. 1992. Contributions of compaction and aquathermal pressuring to geopressure and the influence of environmental conditions. *AAPG Bulletin*, **76**, 1550-1559.

Magara, K. 1968. Compaction and migration of fluids in Miocene mudstone, Nagaoka Plain, Japan. *AAPG Bulletin*, **52**, 2466-2501.

Magara, K. 1969. Upward and downward migrations of fluids in the subsurface. *Bulletin of Canadian Petroleum Geology*, **17**, 20-46.

Magara, K. 1976a. Thickness of removed sedimentary rocks, paleopore pressure, and paleotemperature, southwestern part of Western Canada Basin. *AAPG Bulletin*, **60**, 554-565.

Magara, K. 1976b. Water expulsion from clastic sediments during compaction: directions and volumes. *AAPG Bulletin*, **60**, 543-553.

Magara, K. 1978. The significance of the expulsion of water in oil-phase primary migration. *Bulletin of Canadian Petroleum Geology*, **26**, 123-131.

Magara, K. 1980. Comparison of porosity-depth relationships of shale and sandstone. *Journal of Petroleum Geology*, **3**, 175-185.

McClay, K., Dooley, T., Ferguson, A. & Poblet, J. 2000. Tectonic evolution of the Sanga-Sanga Block, Mahakam Delta, Kalimantan, Indonesia. *AAPG Bulletin*, **84**, 765-786.

Mondol, N.H., Bjørlykke, K., Jahren, J. & Hoeg, K. 2007. Experimental mechanical compaction of clay mineral aggregates – changes in physical properties in mudstones during burial. *Marine and Petroleum Geology*, **24**, 289-311.

Moss, S.J., Chambers, I., Cloke, I., Carter, A., Satria, D., Ali, J.R. & Baker, S. 1997. New observations on the sedimentary and tectonic evolution of the Tertiary Kutai Basin, east Kalimantan. *In:* Fraser, A., Matthews, S. & Murphy, R.W. (eds.) *Petroleum Geology of Southeast Asia*. Geological Society of London, Special Publication **126**, 395-417.

Moss, S.J. & Chambers, J.L.C. 1999. Depositional modelling and facies architecture of rift and inversion episodes in the Kutai Basin, Kalimantan, Indonesia. *In: Indonesian Petroleum Association, Proceedings 27th Annual Convention*, 467-486.

Mouchet, J-P. & Mitchell, A. 1989. *Abnormal Pressures While Drilling*. Elf Aquitaine, Boussens, Manual Techniques **2**, 255p.

O'Connor, S., Swarbrick, R. & Jones, D. 2008. Where has all the pressure gone? Evidence from pressure reversals and hydrodynamic flow. *First Break*, **26**(9), 55-61.

O'Connor, S.A. & Swarbrick, R.E. 2008. Pressure regression, fluid drainage and a hydrodynamically controlled fluid contact in the North Sea, Lower Cretaceous, Britannia Sandstone Formation. *Petroleum Geoscience*, **14**, 115-126.

Osborne, M.J. & Swarbrick, R.E. 1997. Mechanisms for generating overpressure in sedimentary basins: a reevaluation. *AAPG Bulletin*, **81**, 1023-1041.

Ott, H.L. 1978. The Kutai Basin: a unique structural history. *In: Indonesian Petroleum Association, Proceedings 11th Annual Convention*, 307-316.

Oudin, J.L. & Picard, P.F. 1982. Genesis of hydrocarbons in Mahakam Delta and the relationship between their distribution and the overpressured zone. *In: Indonesian Petroleum Association, Proceedings 11th Annual Convention*, 181-202.

Paterson, D.W., Bachtiar, A., Bates, J.A., Moon, J.A. & Surdam, R.C. 1997. Petroleum system of the Kutei Basin, Kalimantan, Indonesia. *In:* Howes, J.V.C. & Noble, R.A. (eds), *Indonesian Petroleum Association, Proceedings of the Petroleum Systems of SE Asia and Australasia Conference*, 709-726.

Peltonen, C., Marcussen, O., Bjørlykke, K. & Jahren, J. 2009. Clay mineral diagenesis and quartz cementation in mudstones: the effects of smectite to illite reaction on rock properties. *Marine and Petroleum Geology*, **26**, 887-898.

Pennebaker, E.S. 1968. Seismic data indicate depth and magnitude of abnormal pressure. *World Oil*, **166**, 73-82.

Pertamina BPPKA. 1997. *Petroleum Geology of Indonesia Basins: Principles, Methods, and Application*, **v. XI***: Kutai Basin*, 134p.

Ramdhan, A.M. 2002. *The Relationship between Hydrodynamics of Groundwater and Hydrocarbon Accumulation in Zone I072A, Semberah Field*. Institute of Technology Bandung, MSc thesis, unpublished.

Ramdhan, A.M. & Goulty, N.R. 2010a. Overpressure generating mechanisms in the Peciko Field, Lower Kutai Basin, Indonesia. *Petroleum Geoscience*, in press.

Ramdhan, A.M. & Goulty, N.R. 2010b. Overpressure and shale compaction in the Lower Kutai Basin, Indonesia – a radical reappraisal. *AAPG Bulletin,* submitted.

Reynolds, E.B. 1970. Predicting overpressure zones with seismic data. *World Oil*, **171**, 78-82.

Rubey, W.W. & Hubbert, M.K. 1959. Role of fluid pressure in mechanics of overthrusting faulting, II. Overthrust belt in geosynclinals area of Western Wyoming in light of fluid-pressure hypothesis. *Geological Society of America Bulletin*, **70**, 167-206.

Safarudin & Manulang, M.H. 1989. Trapping mechanism in Mutiara Field, Kutei Basin, East Kalimantan. *In: Indonesian Petroleum Association, Proceedings 18th Annual Convention*, 31-54.

Samson, P., Dewi-Rochette, T. & Lescoeur, M. 2005. Peciko geological modeling: optimizing fluid distribution and model resolution of a giant gas field in a shale-dominated deltaic environment. *Asia Pacific Oil & Gas Conference*, SPE paper 93253.

Saller, A., Lin, R. & Dunham, J. 2006. Leaves in turbidite sands: the main source of oil and gas in the deep-water Kutei Basin, Indonesia. *AAPG Bulletin*, **90**, 1585-1608.

Schmidt, G.W. 1973. Interstitial water composition and geochemistry of deep Gulf Coast shales and sandstones. *AAPG Bulletin*, **57**, 321-337.

Sclater, J.G. & Christie, P.A.F. 1980. Continental stretching: an explanation of the post-mid-Cretaceous subsidence of the Central North Sea Basin. *Journal of Geophysical Research*, **85**, 3711-3739.

Swarbrick, R.E. 1997. Characteristics of overpressured basins and influence of overpressure on the petroleum system. *In:* Howes, J.V.C. & Noble, R.A. (eds.), *Indonesian Petroleum Association, Proceedings of the Petroleum Systems of SE Asia and Australasia Conference*, 859-865.

Swarbrick, R.E. & Osborne, M.J. 1998. Mechanisms that generate abnormal pressures: an overview. *In:* Law, B.E., Ulmishek, G.F. & Slavin, V.I. (eds.) *Abnormal Pressures in Hydrocarbon Environments*. AAPG, Tulsa, Memoir **70**, 13-34.

Swarbrick, R.E., Osborne, M.J. & Yardley, G.S. 2002. Comparison of overpressure magnitude resulting from the main generating mechanisms. *In:* Huffman, A.R. & Bowers, G.L. (eds.) *Pressure Regimes in Sedimentary Basins and their Prediction*. AAPG, Tulsa, Memoir **76**, 1-12.

Teige, G.M.G., Hermanrud, C., Wensaas, L. & Nordgård Bolås, H.M. 1999. The lack of relationship between overpressure and porosity in North Sea and Haltenbanken shales. *Marine and Petroleum Geology*, **16**, 321-335.

Teige, G.M.G., Hermanrud, C., Wensaas, L. & Nordgård Bolås, H.M. 2007. Geological constraints of pore pressure detection in shales from seismic data. *Basin Research*, **19**, 33-50.

Terzaghi, K. & Peck, R.B. 1967. *Soil Mechanics in Engineering Practice 2nd Edition*. John Wiley & Sons, New York, 729 p.

Thyberg, B., Jahren, J., Winje, T., Bjørlykke, K., Faleide, J.I. & Marcussen, O. 2010. Quartz cementation in Late Cretaceous mudstones, northern North Sea: changes in rock properties due to dissolution of smectite and precipitation of micro-quartz crystals. *Marine and Petroleum Geology*, in press.

Tingay, M.R.P., Hillis, R.R., Swarbrick, R.E., Morley, C.K. & Damit, A.R. 2009. Origin of overpressure and pore-pressure prediction in the Baram province, Brunei. *AAPG Bulletin*, **83**, 51-74.

Total E&P Indonesie 1995. *Sisi-Nubi Field*. Unpublished Report.

Total E&P Indonesie 2000a. *Net to Gross map of the Median Axis*. Unpublished Report.

Total E&P Indonesie 2000b. *Stratigraphic column of the Lower Kutai Basin*. Unpublished Report.

Total E&P Indonesie 2003a. *The Lower Kutai Synthesis*. Unpublished Report.

Total E&P Indonesie 2003b. *Mahakam Formation Water Salinity Study*. Unpublished Report.

Total E&P Indonesie 2003c. *Tambora Field*. Unpublished Report.

Total E&P Indonesie 2010a. *Pore Fluid Distribution, Peciko Field*. Unpublished Report.

Total E&P Indonesie 2010b. *Peciko Field – Main Zone*. Unpublished Report.

Total E&P Indonesie 2010c. *Bekapai Field*. Unpublished Report.

Traugott, M.O. 1996. The pore pressure centroid concept. *Reducing Drilling Risk – Compaction and Overpressure Current Research*, Abstract, IFP, Paris.

Van de Weerd, A.A. & Armin, R.A. 1992. Origin and evolution of Tertiary hydrocarbon bearing basins in Kalimantan (Borneo), Indonesia. *AAPG Bulletin*, **76**, 1778-1803.

Van Ruth, P., Hillis, R., Tingate, P. & Swarbrick, R.E. 2003. The origin of overpressure in 'old' sedimentary basins: and example from the Cooper Basin, Australia. *Geofluids*, **3**, 125-131.

White, A.J., Traugott, M.O. & Swarbrick, R.E. 2002. The use of leak-off tests as means of predicting minimum in-situ stress. *Petroleum Geoscience*, **8**, 189-193.